

Department of Applied Geology

The Proterozoic geological history of the Irumide belt, Zambia

Bert De Waele

**This thesis is presented for the Degree of
Doctor of Philosophy
of
Curtin University of Technology**

Submitted July 2004

This thesis contains no material, which has been accepted for the award of any other degree or diploma in any university.

To the best of my knowledge and belief this thesis contains no material previously published by any other person except where due acknowledgment has been made.

10th March 2005

Bert De Waele

ABSTRACT

The Irumide belt is an elongate crustal province characterised by Mesoproterozoic tectonism and magmatism that stretches over a distance of approximately 900 kilometers from central Zambia to the Zambia-Tanzania border and northern Malawi. It is bounded to the northwest by largely undeformed Palaeoproterozoic basement lithologies of the Bangweulu block and is truncated to the northeast by Mesoproterozoic and Neoproterozoic transcurrent shear zones within reactivated parts of the Palaeoproterozoic Ubendian belt. To the southeast and south, Irumide lithologies were reworked within the Neoproterozoic Lufilian and Zambezi belts, and to the east by the East African Orogen.

Lithologies in the Irumide belt comprise a Palaeo- to Mesoproterozoic complex of gneisses and granitoids and a supracrustal succession of quartzites and pelites. A three-fold subdivision was accepted prior to this study; (1) Palaeoproterozoic granites and gneisses forming the Irumide basement, (2) a supracrustal succession of quartzites and metapelites called the Muva Supergroup, (3) various deformed and undeformed granitoids intruding both the Palaeoproterozoic basement and Muva Supergroup and considered to be pre-Irumide (1.4 Ga) and syn-, late- to post-Irumide (1.1-0.95 Ga). The age of Irumide tectonism itself was poorly constrained between 1.4 and 1.0 Ga. The basement units comprise the Mkushi Gneiss in the southwest and the Luwalizi Granite, Mwambwa River and Mulungwizi Gneisses in the northeast. These units have been correlated with the Palaeoproterozoic Bangweulu block and Ubendian belt in the past. These basement units are structurally and in places unconformably overlain by a metasedimentary succession of quartzites and metapelites, which in the southwest has been called the Kanona Group, and in the northeast the Manshya River Group. Both sequences have been correlated with similar quartzite-pelite successions on the Bangweulu block, termed the Mporokoso Group, and, together with a second cycle reworked unit on the Bangweulu block called the Kasama Formation, were collectively grouped into the Muva Supergroup. Both basement and supracrustals have been deformed, metamorphosed and intruded by a host of granitoids which, based on structural fabrics, were subdivided into pre-, syn-, late- and post-tectonic suites with respect to Irumide tectonism. Due to the lack of reliable geochronological constraints, this subdivision had remained untested until now.

All units in the Irumide belt have been strongly affected by compressional tectonics, resulting in northwest-directed thrusting onto the Bangweulu block basement and extensive crustal shortening. Minor southeast-verging structures form part of locally developed backthrusts within an overall northwest-vergent tectonic regime. At least parts of the Irumide basement were affected by Irumide tectonism, but large-scale thrusting was mainly accommodated along a basal decollement at the basement-cover interface. Extensive shortening is exemplified by tight- to isoclinal folding within the supracrustal sequence, ranging from upright to recumbent. Thrusts developed where shortening could not be accommodated by tight folding, which produced tectonic duplication within the metasedimentary pile, making formation-to-formation correlations across the belt tenuous at best. Irumide tectonism has been reported to affect the base of the Mporokoso Group on the Bangweulu block, where folding along the Luongo shear zone occurred contemporaneously with thermal resetting of biotite dated at ~1.0 Ga (K-Ar dates). Metamorphic parageneses record low- to medium-pressure/medium- to high-temperature conditions. Metamorphic grades range from greenschist facies in the northwestern foreland, to upper amphibolite facies in the southeast, with local granulites. Peak Irumide metamorphism, recorded in metamorphic zircon rim overgrowths, has been dated in this study at 1.02 Ga. Metamorphism to the southeast, across the younger Karoo grabens, had previously been constrained at 1.05 Ga, indicating an across strike diachronous development of metamorphism for the Irumide belt.

The lithological units identified and dated as part of this study in the Irumide belt include: (1) limited Neoarchaean rocks emplaced at 2.73 Ga and representing the oldest rocks in the Bangweulu block; (2) ca. 2.05-1.85 Ga volcano-plutonic complexes and gneisses representing the most important components in the Bangweulu block; (3) an extensive quartzite-metapelite succession with minor carbonate forming the Mporokoso, Kanona and Manshya River groups, and deposited at ca. 1.8 Ga; (4) granitoids emplaced between 1.65-1.55 Ga; (5) deposition of the Kasama Formation between 1.43 and 1.05 Ga (second-cycle reworking of the Mporokoso Group); (6) voluminous syn- to post-kinematic Irumide granitoids emplaced between 1.05-0.95 Ga. In addition, a minor suite of 1.36-1.33 Ga anorogenic plutons (nepheline syenite and biotite granite) have been identified in the far northeastern Irumide belt, but were not included in this study.

Whole-rock geochemical data for magmatic rocks in northern Zambia, predominantly from within the Irumide belt, indicate uniform crust-dominated patterns. Overall high REE contents and trace element characteristics indicate the significant participation of older crust in the generation of all magmatic suites. The data are insufficient to conclusively demonstrate that this crustal melting was associated with either intra-plate, volcanic arc or post-collisional/extensional collapse. A limited number of Sm/Nd isotopic data for the entire range of magmatic suites corroborate the highly reworked nature of parent magmas, with all samples characterised by strongly negative $\epsilon_{\text{Nd}}(\text{T})$ values and T_{DM} model ages between 2.2 and 3.2 Ga.

The geochronological data presented in this thesis show that the Irumide belt includes a Palaeoproterozoic basement complex comprising units as old as 2.73 Ga, but mostly made up of granitic gneisses ranging in age between 2.05 and 1.93 Ga, while granitic and volcanic units of the Bangweulu block to the northwest were dated at 1.87-1.86 Ga. Detrital zircon age data from quartzites and zircon crystallisation ages of interlayered tuffs within the Muva Supergroup indicate a depositional age of between 1.88 and 1.85 Ga, with local derivation from locally recognised basement units, although similarly aged rocks of the Tanzania craton to the northeast are also a possible source. The detrital record of the Muva Supergroup shows that the various components of the Bangweulu block, including 2.73, 2.05-1.93 and 1.87-1.86 Ga units, were assembled by the time of deposition of the Muva Supergroup at around 1.8 Ga.

Both the basement units and the Muva Supergroup were intruded by a previously unknown magmatic suite of biotite granites between 1.65-1.55 Ga, the first record of such a magmatic event in central Africa.

The new data presented in this thesis allow a critical assessment of previously proposed regional correlations between Mesoproterozoic terranes in central and southern Africa. Significant temporal differences between the Irumide belt and the Kibaran belt, Choma-Kalomo block and Namaqua-Natal belts had previously not been detected due to the poor quality, low resolution or limited size of isotopic data sets. The new data set produced in this study indicates a distinct and separate tectono-magmatic history for each of these terranes, therefore precluding previously suggested correlations. In particular, the presumed southeastward continuation of the Irumide belt across the Neoproterozoic Zambezi belt into the Choma-Kalomo block is precluded by the data presented in this thesis. This new

geochronological framework allows for significant spatial separation of the Kalahari and Congo cratons prior to the Neoproterozoic closure of the Damara-Lufilian-Zambezi ocean, and is therefore in support of palaeogeographic models of Rodinia which either place the Congo and Kalahari cratons as distinct and separate fragments within the supercontinent, or show one or both of the two cratons not to form part of it. Currently, available data are not able to determine the tectonic setting or the palaeogeographic location of the Irumide belt, and as a result it is unclear whether it developed within Rodinia as a collisional orogen, at its margin as an accretionary orogen, or was not associated with Rodinia at all.

DEDICATION

I dedicate this thesis to three geologists, colleagues and personal friends who have sadly passed away during the course of this PhD research.

Professor Chris McA. Powell, Director of the Tectonics Special Research Centre (TSRC), sadly passed away en route from South Africa to London in July 2001. Chris, together with Michael Wingate, can be “blamed” for motivating me to apply for the International Post Graduate Scholarship (IPRS) at Curtin University, which allowed me to embark on the research presented in this PhD thesis. I vividly remember my last discussions with Chris earlier that month at the IGCP 418 field meeting in Durban, South Africa, when we talked about the fieldwork I had just finished in Zambia. There are no words to express the shock I felt, when upon my return to Perth later that same month, I heard the news of his death.

Dr. Crispin Katongo, a young aspiring Zambian geologist, with whom I became firm friends when he joined the University of Zambia in 1997, passed away in July 2004 at the University Teaching Hospital in Zambia. I last saw Crispin at the 2004 Geoscience Africa conference in Johannesburg earlier this month, which Crispin left prematurely due to ill health. Crispin still attended most of the talks, and had the same unfailing sense of humour characteristic of him. Upon my arrival in Zambia a week later, Crispin had been admitted to the hospital, and died early the following morning. I attended his funeral along with all his Zambian colleagues, feeling bereft of a personal friend and aware of the tremendous sense of loss to the Zambian geological community.

Professor Henri (Ali Basira) Kampunzu succumbed to terminal cancer in late November 2004 at the Midrand Park Hospital in Johannesburg, South Africa. Henri, like Chris, was a man of great charisma and formidable character, whose sudden death left the geoscience community paralysed for a few weeks. Henri could be regarded a beacon for African geology and was instrumental to a lot of African geoscientific initiatives over the past decades. I first met Henri in Botswana in 1998, and we had become firm friends over the years. Henri was always happy to engage in discussions related to my PhD research, and offered ongoing support until his untimely death.

ACKNOWLEDGEMENTS

This PhD research would not have been possible without the financial support of an International Postgraduate Research Scholarship (IPRS) through Curtin University of Technology, and research funding by the Tectonics Special Research Centre (TSRC). The entire undertaking was admirably supervised by Dr. Ian C.W. Fitzsimons, whose constructive criticism provided invaluable support that led to, what I hope, is a good thesis.

This thesis is the result of many years of fieldwork in Zambia, some of it predating the actual start of the IPRS awarded to me. I'd therefore like to thank the staff at the University of Zambia, in particular Dr. Francis Tembo, the late Dr. Crispin Katongo, Mr. Simon Nkemba and Mr. Willy Nundwe, whose support, understanding and company, both prior to and during my PhD research, were very important to me. I'd also like to acknowledge Dr. Simon Johnson for his ongoing support and assistance.

The staff of TSRC, both at Curtin University of Technology and the University of Western Australia, deserves special mention, as without the scientific environment they provide, the necessary stimuli of research would have been significantly different. I'd like to single out the late Professor Chris McA. Powell and Professor Peter Cawood for constructive comments, and Drs. Michael Wingate and Sasha Nemchin for discussions and hands-on assistance in laboratory techniques and data manipulation.

Fellow student Dr. Gary Love helped me master the art of mineral separation, while Dr. Pete Kinny and Professor Bob Pidgeon showed me a thing or two on preparing SHRIMP mounts. Dr. Allen Kennedy must be commended for suffering me as a learning analyst on the SHRIMP instruments. Various of my SHRIMP instrumental setups have been done by Michael Wingate and Sasha Nemchin, to whom I am indebted for the useful data these sessions produced. I derived the art of treating SHRIMP data from Michael Wingate, Sasha Nemchin, Pete Kinny, Keith Sircombe and Alan Collins.

I'd like to thank Drs. David Pritchard and John Watling for assistance in the geochemical analyses of my samples at the Department of Applied Chemistry of Curtin University of Technology. Dr. Ron Watkins, Prof. Svetlana Bogdanova and the late

Professor Henri Kampunzu are gratefully acknowledged for their assistance in the treatment of geochemical data.

Many fruitful discussions with Drs. Luc Tack, Max Fernandez-Alonso and Jean-Paul Liégeois of the Museum for Central Africa in Tervueren (Belgium) have to a varying degree influenced my developing ideas on African geology in general, and the evolution of the Irumide belt specifically. I thank the staff at the museum for their ongoing support towards my research.

I'd like to thank all my fellow postgraduate students at both nodes of TSRC (Curtin University of Technology and the University of Western Australia), for reminding me that I was not alone in my "suffering". I specifically thank Huntly Cutten, Bregje Hulscher, Matt Greentree and Sandi Occhipinti for putting up with me.

Finally, I thank Tineke and my two kids, Hannah and Toto, for sharing exciting times with me *downunder*.

TABLE OF CONTENTS

INDEX OF TABLES	VII
INDEX OF FIGURES	XIII
1 CHAPTER 1: INTRODUCTION	1
1.1 REGIONAL GEOLOGICAL SETTING OF THE STUDY AREA	1
1.2 A SUMMARY OF PREVIOUS WORK ON THE IRUMIDE BELT	4
1.3 AIMS OF THIS STUDY	9
1.4 METHODOLOGY	10
1.4.1 Fieldwork planning	10
1.4.2 Sampling method	11
1.4.3 Sample preparation	11
1.4.3.1 Preliminary crushing	12
1.4.3.2 Mineral separation	12
1.4.3.3 Preparation of whole rock powder	13
1.4.4 SHRIMP dating	13
1.4.5 Major and trace element geochemistry	14
1.4.6 Isotope geochemistry	14
1.5 STRUCTURE OF THIS THESIS	15
2 CHAPTER 2: LITHOSTRATIGRAPHY	17
2.1 INTRODUCTION	17
2.2 PREVIOUS WORK	18
2.3 BASEMENT ROCKS	28
2.3.1 Archaean granitoids	28
2.3.2 Undeformed basement of the Bangweulu block	28
2.3.3 Deformed basement of the Irumide belt	31
2.3.3.1 The Palaeoproterozoic Mkushi Gneiss	37
2.3.3.2 The Mulungwizi and Mwambwa River Gneiss	40
2.3.3.3 The Luwalizi and Lubu Granite Gneiss	42
2.4 THE MUVA SUPERGROUP	44
2.4.1 Mporokoso Group	45
2.4.2 Kasama Formation	48
2.4.3 Mafingi Group	49
2.4.4 Manshya River Group s.s. (northeastern Irumide belt)	49
2.4.5 Kanona Group (Manshya River Group, southwestern Irumide belt)	53
2.4.6 Volcanic rocks in the Muva Supergroup	60
2.4.6.1 The Katibunga Volcanics	60
2.4.6.2 The Luswa River Volcanics	62
2.4.6.3 The Ilondola Volcanics	64
2.4.6.4 The Kachinga Tuffs	67
2.4.6.5 The Mututa Ridge volcanics	70
2.5 IRUMIDE GRANITOIDS	71
2.5.1 Strongly deformed Irumide granitoids	71
2.5.1.1 Mutangoshi Gneissic Granite and Musalango Gneiss	71
2.5.1.2 Lukamfwa Hill Granite Gneiss	74
2.5.1.3 The Mivula Syenite and Ntendele metatonalite	76
2.5.2 Late-Irumide granitoids	76

2.5.2.1	The Bemba batholith (Lufila Granite)	77
2.5.2.2	Chilubanama Granite	78
2.5.2.3	Porphyritic granites	79
2.6	DISCUSSION	82
3	CHAPTER 3: STRUCTURE AND METAMORPHISM	85
3.1	INTRODUCTION	85
3.2	STRUCTURE	85
3.2.1	Introduction	85
3.2.2	Previous work	86
3.2.3	Irumide structures	88
3.2.4	Late- to post-Irumide doming	91
3.2.5	Lufilian and Zambezi structures	92
3.3	METAMORPHISM	92
3.4	SUMMARY	94
4	CHAPTER 4: ZIRCON U-PB SHRIMP GEOCHRONOLOGY	97
4.1	INTRODUCTION	97
4.2	INSTRUMENTATION AND METHODOLOGIES	98
4.3	U-Pb SHRIMP ZIRCON GEOCHRONOLOGY	100
4.3.1	Magmatic zircon	100
4.3.2	Detrital zircon	102
4.3.3	Metamorphic zircon	102
4.4	ROCKS DATED IN THIS STUDY	103
4.5	ARCHAEOAN AND PALAEOPROTEROZOIC BASEMENT	111
4.5.1	Kapiri Mposhi granite gneiss	111
4.5.2	Mkushi Gneiss	113
4.5.2.1	Sample MK3	113
4.5.2.2	Sample MK5	116
4.5.2.3	Sample CC10	117
4.5.2.4	Sample KN1	119
4.5.2.5	Samples SER 6-6 and SER 6-7 (migmatitic gneiss)	121
4.5.3	Luwalizi Granite Gneiss	127
4.5.3.1	Sample ISK1	127
4.5.3.2	Sample ISK2	129
4.5.4	Lubu Granite Gneiss (sample ML2)	130
4.5.5	Bangweulu Granitoids and Luapula Volcanics	132
4.5.5.1	Sample MA1	133
4.5.5.2	Sample MA2	134
4.5.5.3	Sample MA3	135
4.5.5.4	Sample MA5	137
4.5.5.5	Sample MA9	139
4.6	MUVA SUPERGROUP	140
4.6.1	Detrital provenance of the Mporokoso Group (sample MA6)	140
4.6.2	Detrital provenance of the Kasama Formation (sample KAS)	143
4.6.3	Detrital provenance of the Manshya River Group (sample IL14)	145
4.6.4	The basal conglomerate of the Kanona Group (sample MK8)	148
4.6.5	Luswa River Volcanic (sample ZM31)	150
4.6.6	Kachinga Tuff (sample IS20)	151
4.6.7	Katibunga Volcanic (sample KB5)	153

4.7	STRONGLY DEFORMED IRUMIDE GRANITOIDS	154
4.7.1	The Mutangoshi Gneissic Granite	154
4.7.1.1	Sample MTGG1	155
4.7.1.2	Sample MTGG2	158
4.7.2	The Musalango Gneiss (sample LW10)	160
4.7.3	Lukamfwa Hill Granite Gneiss	162
4.7.3.1	Sample SER6-2c	162
4.7.3.2	Sample 6-3	165
4.7.3.3	Sample SR12	167
4.7.3.4	Sample ND2	169
4.8	MILDLY DEFORMED TO UNDEFORMED IRUMIDE GRANITOIDS	170
4.8.1	The Lufila Granite (Bemba batholith, sample SH8)	171
4.8.2	Luswa River leuco-syenite gneiss (sample LW2)	172
4.8.3	The Chilubanama (grey) Granite	174
4.8.3.1	Sample ZM32	174
4.8.3.2	Sample MTG4	176
4.8.3.3	Sample LW1	179
4.8.4	Porphyritic granites	181
4.8.4.1	Sample KK1	181
4.8.4.2	Sample MH4	183
4.8.4.3	Sample MH9c	186
4.8.4.4	Sample CC5	187
4.8.4.5	Sample CC8	189
4.8.4.6	Sample MK7	191
4.8.4.7	Sample FW1	193
4.8.4.8	Sample FW2	194
4.8.4.9	Sample CHT6	197
4.8.4.10	Sample KN2A	199
4.8.4.11	Sample KN5	201
4.8.4.12	Sample KN7	203
4.8.4.13	Sample KN8	205
4.8.4.14	Sample ND1	208
4.8.4.15	Sample ND4	210
4.8.4.16	Sample ND5	212
4.8.4.17	Sample SASA2	214
4.8.4.18	Sample SER 5-3	216
4.8.4.19	Sample SER 6-4	218
4.8.4.20	Sample SQG	220
4.8.4.21	Sample ZM36	222
4.8.4.22	Sample CHL5	224
4.9	DISCUSSION	226
4.9.1	The basement of the Irumide belt and the Bangweulu block	226
4.9.2	The Muva Supergroup	227
4.9.2.1	The Mporokoso Group	227
4.9.2.2	The Kasama Formation	229
4.9.2.3	The Manshya River Group (northeastern Irumide belt)	230
4.9.2.4	The Kanona Group (southwestern Irumide belt)	231
4.9.3	Strongly deformed granitoids in the Irumide belt	233
4.9.4	Weakly or undeformed Irumide granitoids	234
4.9.5	Peak metamorphism in the Irumide belt	234

4.9.6	Xenocrystic zircon	235
4.9.7	Redefining the Bangweulu block	237
4.9.8	Redefining the Muva Supergroup	238
4.9.9	Summary	239
5	CHAPTER 5: MAJOR AND TRACE ELEMENT GEOCHEMISTRY	245
5.1	INTRODUCTION	245
5.2	THE ARCHAEO (GROUP I) KAPIRI MPOSHI GRANITE-GNEISS	250
5.2.1	Major element geochemistry	250
5.2.2	Trace elements geochemistry	252
5.2.3	Geotectonic interpretation	254
5.3	PALAEOPROTEROZOIC GROUP II GRANITIDS OF THE IRUMIDE BELT	255
5.3.1	Major element geochemistry	256
5.3.2	Trace element geochemistry	258
5.3.3	Geotectonic interpretation	261
5.4	PALAEOPROTEROZOIC MANSA PLUTONO-VOLCANIC SUITE	262
5.4.1	Major element geochemistry	263
5.4.2	Trace element geochemistry	265
5.4.3	Geotectonic interpretation	269
5.5	PALAEOPROTEROZOIC (GROUP III) VOLCANICS IN THE IRUMIDE BELT	269
5.5.1	Major element geochemistry	272
5.5.2	Trace elements	276
5.5.3	Geotectonic interpretation	286
5.6	PALAEO-MESOPROTEROZOIC (GROUP IV) GRANITIDS	287
5.6.1	Major element geochemistry	288
5.6.2	Trace element geochemistry	291
5.6.3	Geotectonic interpretation	296
5.7	LATE-MESOPROTEROZOIC IRUMIDE GRANITIDS	296
5.7.1	Major element geochemistry	300
5.7.2	Trace element geochemistry	304
5.7.3	Geotectonic interpretation	309
5.8	DIFFERENTIATION TRENDS	310
5.9	DISCUSSION	315
6	CHAPTER 6: SM-ND ISOTOPE GEOCHEMISTRY	319
6.1	INTRODUCTION	319
6.2	SELECTION OF SAMPLES	321
6.3	PALAEOPROTEROZOIC (GROUP II) GRANITIDS	323
6.4	PALAEOPROTEROZOIC (GROUP III) MANSA GRANITIDS AND VOLCANICS	324
6.5	PALAEOPROTEROZOIC (GROUP III) IRUMIDE VOLCANICS	325
6.5.1	The Luswa River Tuff	325
6.5.2	The Kachinga Tuff	325
6.5.3	The Katibunga Volcanics	326
6.6	PALAEO-MESOPROTEROZOIC (GROUP IV) GRANITIDS	326
6.7	IRUMIDE (GROUP V) GRANITIDS	327
6.8	DISCUSSION	327
7	CHAPTER 7: DISCUSSION	331
7.1	REGIONAL CORRELATIONS OF THE IRUMIDE BELT	331
7.1.1	Introduction	331
7.1.2	Previous geochronological constraints on Irumide tectonism	332

7.1.3	Previously proposed correlations	333
7.1.3.1	The central African Kibaran belt	333
7.1.3.2	Southeastward extension of the Irumide belt	335
7.1.3.3	The Choma-Kalomo block of southern Zambia	337
7.1.3.4	Mesoproterozoic events in the Kalahari craton	340
7.2	REGIONAL TECTONIC INTERPRETATION	342
7.2.1	Background	342
7.2.2	The nature of the foreland and basement to the Irumide belt	344
7.2.3	Supracrustal sequences	345
7.2.4	Granitoids within the Irumide belt	347
7.2.5	Timing of Irumide tectonism	348
7.2.6	Metamorphic grade	350
7.3	THE RODINIA HYPOTHESIS	351
7.3.1	Conclusions	355
8	APPENDIX A: LIST OF SAMPLES COLLECTED DURING THIS STUDY	359
9	APPENDIX B: MINERAL SEPARATION	363
9.1	CRUSHING	363
9.2	WASHING	363
9.3	MINERAL SEPARATION	364
9.3.1	LST separation	364
9.3.2	Magnetic separation	365
9.3.3	MI Heavy Liquid Separation	367
10	APPENDIX C: SHRIMP ANALYTICAL PROCEDURE	369
10.1	SHRIMP II	369
10.1.1	The Source	370
10.1.2	The Mass Analysers	371
10.1.3	The Detector	372
10.2	ZIRCON SELECTION AND MOUNTING	372
10.3	IMAGING	374
10.4	ANALYTICAL TECHNIQUE (SHRIMP)	374
10.5	STANDARDISATION AND CALIBRATION OF SHRIMP II	375
10.6	DATA QUALITY AND PROCESSING	377
10.7	CORRECTION FOR COMMON Pb	378
10.8	COMPOSITION OF COMMON Pb	380
11	APPENDIX D: GEOCHEMICAL PROCEDURES	381
11.1	DETERMINING WATER CONTENT	381
11.2	DETERMINING CARBONATE AND ORGANIC CONTENT (LOI)	381
11.3	HYDROFLUORIC ACID DIGESTION (ICP-MS)	381
11.4	SAMPLE FUSION (ICP-OES)	382
11.5	ANALYSIS OF TRACE AND RARE EARTH ELEMENTS THROUGH ICP-MS	382
11.6	EXTERNAL STANDARDS	385
11.7	BLANKS	388
11.8	CALIBRATION	388
11.9	DATA QUALITY AND PROCESSING	388
11.10	ANALYSIS OF MAJOR ELEMENTS THROUGH ICP-OES.	393
11.11	ANALYSIS OF K AND Na USING ATOMIC ABSORPTION SPECTROMETRY	394
11.12	CALCULATION AND PLOTTING TOOLS	394

11.13	NORMALISATION VALUES	395
12	APPENDIX E: ISOTOPE GEOCHEMISTRY	399
12.1	MASS SPECTROMETRY	399
12.2	SAMPLE DIGESTION AND SPIKING	400
12.3	CHEMICAL SEPARATION	402
12.3.1	Separation of REE from lighter elements	402
12.3.2	Separation of Sm and Nd	403
12.4	SAMPLE LOADING	404
12.5	OPERATING PROCEDURES	406
12.6	INTERNAL INSTRUMENT CORRECTIONS	406
13	APPENDIX F: SHRIMP ANALYTICAL DATA	409
14	APPENDIX G WHOLE ROCK GEOCHEMISTRY ANALYTICAL DATA	433
15	REFERENCES	451

INDEX OF TABLES

Table 2-1:	Different magmatic suites recognised in the Irumide belt, Bangweulu block and adjacent Lufilian belt.....	19
Table 2-2:	Previously published and unpublished Proterozoic age data (> ca. 950 Ma) for Zambia (refer to Figure 2-5 using grid square for locations). Italics date growth of metamorphic zircon	27
Table 4-1:	Typical characteristics of zircons from different sources (Rubatto and Gebauer, 2000).	97
Table 4-2:	Crystallisation ages of xenocrystic zircon in the Irumide belt obtained as part of this study. *denotes % concordance of the zircon age; ** denotes the igneous crystallisation age of the host rock.	236
Table 4-3:	Different magmatic suites recognised in the Bangweulu block and the Irumide belt, based on zircon U-Pb geochronological data presented in this study.....	239
Table 4-4:	Zircon U-Pb SHRIMP crystallisation ages for magmatic rocks obtained in this study (left: sorted alphabetically by sample name; right: sorted by age). @ denotes metamorphic zircon rims.	241
Table 5-1	Modal composition of sample KMP1 calculated from major element geochemistry.	250
Table 5-2:	Modal composition of Group II granitoids in the Irumide belt calculated from major element chemistry.	257
Table 5-3:	Modal composition of the Mansa Volcanics and Mansa Granitoids of the Bangweulu block calculated from major element chemistry.	263
Table 5-4:	Modal composition of Group III volcanics in the Irumide belt.....	273
Table 5-5:	Modal composition of Group IV granitoids in the Irumide belt.	289
Table 5-6:	Modal composition of Group V granitoids in the Irumide belt	301
Table 6-1:	Present day isotopic ratios of a reservoir of chondritic or depleted mantle composition.	320
Table 6-2:	Sm-Nd isotopic data for igneous lithologies in the Irumide belt and the Bangweulu block.	323
Table 8-1	: Samples collected during this study. ¹ thin section made; ² whole-rock major and trace geochemistry conducted; ³ zircon U-Pb SHRIMP date obtained; ⁴ isotope geochemistry conducted.....	359
Table 9-1	Typical settings for the Frantz Magnetic Separator and resultant mineral separates obtained.....	366
Table 11-1	Measured values for standards (weight %, major elements).....	385
Table 11-2	Quoted values for standards (weight %, major elements)	385
Table 11-3	Measured values for standard (ppm, trace elements)	386
Table 11-4	Quoted values for standards (ppm, trace elements).....	387
Table 11-5	Duplicate analyses (major elements)	389
Table 11-6	Duplicate analyses (trace elements)	390
Table 11-7	Minimum Detection Limits for major elements analyses by ICP-OES method.	392
Table 11-8	Minimum Detection Limits for trace analyses by ICP-MS method	392
Table 11-9	Wavelengths used on ICP-OES	394
Table 11-10:	Normalisation values for CI-chondrite after McDonough and Sun (1995).....	395
Table 11-11:	Normalisation values for Primordial Mantle after Sun and McDonough (1989).....	396
Table 11-12:	Normalisation values for N-MORB after Pearce (1996b).....	396

Table 11-13:	Normalisation values for Ocean-Ridge Granitoid after Pearce et al. (1984a).....	397
Table 12-1	Typical filament configuration for a mass spectrometer run of Sm, Nd, Rb and Sr.....	406
Table 13-1	SHRIMP analytical data for sample KMP-1 (biotite granite gneiss, Kapiri Mposhi map sheet). Spot name ending with r denotes an analysis on a rim.	409
Table 13-2	SHRIMP analytical data for sample MK-3 (biotite granite gneiss, Mkushi map sheet). Spot names ending with r denote analyses on a rim, spot names ending with c denote analyses on core.	409
Table 13-3	SHRIMP analytical data for sample MK-5 (pink granite gneiss, Mkushi map sheet). Spot names ending with r denote analyses on a rim, spot names ending with c denote analyses on core.....	410
Table 13-4	SHRIMP analytical data for sample CC-10 (porphyritic granite, Chin'gombe Mission map sheet).	410
Table 13-5	SHRIMP analytical data for sample KN-1 (biotite granite gneiss, Kanona map sheet).....	410
Table 13-6	SHRIMP analytical data for sample ISK-1 (Luwalizi Granite Gneiss, Isoka map sheet).....	411
Table 13-7	SHRIMP analytical data for sample ISK-2 (Luwalizi Granite Gneiss, Isoka map sheet).....	411
Table 13-8	SHRIMP analytical data for sample MA1 (Mansa Granite, Mansa map sheet).	411
Table 13-9	SHRIMP analytical data for sample MA2 (Mansa Granite, Mansa map sheet).	412
Table 13-10	SHRIMP analytical data for sample MA3 (Mansa Volcanic, Mansa map sheet).	412
Table 13-11	SHRIMP analytical data for sample MA5 (Mansa Volcanic, Mansa map sheet).	412
Table 13-12	SHRIMP analytical data for sample MA9 (Musonda Falls Granite, Musonda Falls map sheet).	413
Table 13-13	SHRIMP analytical data for sample MA6 (Quartzite, Kabweluma Formation, Mporokoso Group, Mansa map sheet).	413
Table 13-14	SHRIMP analytical data for sample KAS (Mwela Quartzite, Kasama Formation, Kasama map sheet).	414
Table 13-15	SHRIMP analytical data for sample IL14 (Chembewesu Quartzite, Manshya River Group, Ilondola Mission map sheet).	415
Table 13-16	SHRIMP analytical data for sample MK8 (Basal Conglomerate, Kanona Group Group, Mkushi map sheet).	416
Table 13-17	SHRIMP analytical data for sample ZM 31 (Luswa rhyolite, Luswa River map sheet).....	416
Table 13-18	SHRIMP analytical data for sample IS20 (Kachinga rhyolitic tuff, Isoka map sheet).....	416
Table 13-19	SHRIMP analytical data for sample KB-5 (Basalt, Katibunga Mission map sheet).	417
Table 13-20	SHRIMP analytical data for sample MTGG-1 (Mutangoshi Gneissic Granite, Chinsali map sheet). Spot names ending with r denote analyses on a rim, spot names ending with c denote analyses on core.	417

Table 13-21	SHRIMP analytical data for sample MTGG-2 (Mutangoshi Gneissic Granite, Chinsali map sheet). Spot names ending with c denote analyses on core.	418
Table 13-22	SHRIMP analytical data for sample LW-10 (Musalango Gneiss, Luswa River map sheet).	418
Table 13-23	SHRIMP analytical data for sample ML-2 (Lubu Granite Gneiss, Chinsali map sheet).	419
Table 13-24	SHRIMP analytical data for sample SER 6-2 (Lukamfwa Hill Granite Gneiss, Serenje map sheet). Spot names ending with r denote analyses on a rim, spot names ending with c denote analyses on core.	419
Table 13-25	SHRIMP analytical data for sample SER 6-3 (Lukamfwa Hill Granite Gneiss, Serenje map sheet).	420
Table 13-26	SHRIMP analytical data for sample SR12 (Lukamfwa Hill Granite Gneiss, Serenje map sheet).	420
Table 13-27	SHRIMP analytical data for sample ND-2 (biotite granite gneiss, Ndabala map sheet).	420
Table 13-28	SHRIMP analytical data for sample SH8 (Bemba batholith, Chinsali map sheet).	421
Table 13-29	SHRIMP analytical data for sample LW-2 (Luswa River Syenite, Luswa River map sheet).	421
Table 13-30	SHRIMP analytical data for sample ZM32 (Chilubanama Granite, Luswa River map sheet).	421
Table 13-31	SHRIMP analytical data for sample MTG-4 (Chilubanama Granite, Chinsali map sheet). Spot names ending with r denote analyses on a rim, spot names ending with c denote analyses on core.	422
Table 13-32	SHRIMP analytical data for sample LW-1 (Chilubanama Granite, Luswa River map sheet).	422
Table 13-33	SHRIMP analytical data for sample KK-1 (porphyritic granite, Kakulu (Mulungushi) map sheet).	422
Table 13-34	SHRIMP analytical data for sample MH-4 (porphyritic granite, Mita hills map sheet).	423
Table 13-35	SHRIMP analytical data for sample MH-9c (porphyritic granite, Mita hills map sheet).	423
Table 13-36	SHRIMP analytical data for sample CC-5 (porphyritic granite, Chin'gombe Mission map sheet).	423
Table 13-37	SHRIMP analytical data for sample CC-8 (porphyritic granite, Chin'gombe Mission map sheet).	424
Table 13-38	SHRIMP analytical data for sample MK-7 (biotite granite gneiss, Mkushi map sheet). Spot name ending with r denotes analysis on a rim.	424
Table 13-39	SHRIMP analytical data for sample FW-1 (porphyritic granite, Fiwila Mission map sheet).	424
Table 13-40	SHRIMP analytical data for sample FW-2 (aplite cutting porphyritic granite, Fiwila Mission map sheet).	425
Table 13-41	SHRIMP analytical data for sample CHT-6 (porphyritic granite, Chitambo Mission map sheet).	425
Table 13-42	SHRIMP analytical data for sample KN-2a (porphyritic granite, Kanona map sheet).	426
Table 13-43	SHRIMP analytical data for sample KN-5 (porphyritic granite, Kanona map sheet). Spot name ending with r denotes analysis on a rim, spot name ending with c denotes analysis on a core.	426

Table 13-44	SHRIMP analytical data for sample KN-7 (biotite granite gneiss, Kanona map sheet). Spot name ending with r denotes analysis on a rim, spot name ending with c denotes analysis on a core.	426
Table 13-45	SHRIMP analytical data for sample KN-8 (porphyritic granite, Kanona map sheet). Spot name ending with r denotes analysis on a rim, spot name ending with c denotes analysis on a core.	427
Table 13-46	SHRIMP analytical data for sample ND-1 (porphyritic granite, Ndabala map sheet). Spot names ending with r denote analyses on a rim, spot names ending with c denote analyses on core.	427
Table 13-47	SHRIMP analytical data for sample ND-4 (diorite, Ndabala map sheet).	427
Table 13-48	SHRIMP analytical data for sample ND-5 (syenite, Ndabala map sheet).	428
Table 13-49	SHRIMP analytical data for sample SASA 2 (Sasa Granite, Serenje map sheet)	428
Table 13-50	SHRIMP analytical data for sample SER 5-3 (porphyritic granite, Serenje map sheet).....	428
Table 13-51	SHRIMP analytical data for sample SER 6-4 (porphyritic granite, Serenje map sheet).....	429
Table 13-52	SHRIMP analytical data for sample SQG (porphyritic granite, Serenje map sheet).	429
Table 13-53	SHRIMP analytical data for sample ZM 36 (Mununga Granite, Mupamadzi River map sheet).	430
Table 13-54	SHRIMP analytical data for sample CHL-5 (porphyritic granite, Chilonga Mission map sheet).	430
Table 13-55	SHRIMP analytical data for sample SER 6-6 (migmatite, Serenje map sheet). Spot names ending with r denote analyses on a rim, spot names ending with c denote analyses on core.....	431
Table 13-56	SHRIMP analytical data for sample SER 6-7 (migmatite, Serenje map sheet). Spot names ending with r denote analyses on a rim, spot names ending with c denote analyses on core.....	431
Table 14-1:	Major and trace element geochemistry of sample KMP 1 (sample batch #4 collected in 2001 and analysed at Curtin University of Technology; n.a.=not analysed).....	433
Table 14-2:	Major element geochemistry (weight %) of the Mkushi Gneiss and the Luwalizi Granite Gneiss (sample batch #4 collected in 2001 and analysed at Curtin University of Technology; n.a.=not analysed).	433
Table 14-3:	Major element geochemistry (weight %) of the Mansa Granitoids and Volcanics (sample batch #4 collected in 2001 and analysed at Curtin University of Technology; n.a.=not analysed; # denotes suspect analysis (see text for details)).....	434
Table 14-4:	Major element geochemistry (weight %) of the Katibunga Volcanics (samples KV-2, KV4, KV-5, KV-7 and KV-8 of sample batch #2, collected in 1999 and analysed by Chemex Canada; samples KB2, KB3, KB4, KB5 and KB6 of sample batch #3, collected in 2000 and analysed at Curtin University of Technology; n.a.=not analysed).....	434
Table 14-5:	Major element geochemistry (weight %) of the Katibunga and Luswa River Volcanics (sample batch #3 collected in 2000 and analysed at Curtin University of Technology).	434
Table 14-6:	Major element geochemistry (weight %) of the Isoka Volcanics (sample batch #3 collected in 2000 and analysed at Curtin University of Technology).....	435

Table 14-7:	Major element geochemistry (weight %) of the Lukamfwa Hill Granitoids (samples SI/98/2A, SI/98/2B, SI/98/3 and SI/98/10 of sample batch #1 collected in 1998 and analysed at Chemex Canada; samples SER6-2C, SER6-2 and SER6-3 of sample batch #2, collected in 1999 and analysed by Chemex Canada; n.a.=not analysed).	435
Table 14-8:	Major element geochemistry (weight %) of the Lukamfwa Hill Granite Gneiss, the Lubu Granite Gneiss (sample ML2) and the Musalango Gneiss (sample LW10)(samples ND2, SR5, SR7 and SR12 of sample batch #4 collected in 2001 and analysed at Curtin University of Technology; samples ML2 and LW10 of sample batch #3 collected in 2000 and analysed at Curtin University of Technology; n.a.=not analysed).	435
Table 14-9:	Major element geochemistry (weight %) of Porphyritic Granitoids (samples SI/98/5, SI/98/6, SI/98/11, SI/98/12 and SI/98/12B of sample batch #1 collected in 1998 and analysed by Chemex Canada; samples MQG-1, SQG-2, SER5-3, SER6-4 and SER6-6 of sample batch #2 collected in 1999 and analysed by Chemex Canada; n.a.=not analysed).	436
Table 14-10:	Major element geochemistry (weight %) of Porphyritic Granitoids (sample batch #4 collected in 2001 and analysed at Curtin University of Technology; n.a.=not analysed)	436
Table 14-11:	Major element geochemistry (weight %) of Porphyritic Granitoids (sample batch #4 collected in 2001 and analysed at Curtin University of Technology; n.a.=not analysed).	436
Table 14-12:	Major element geochemistry (weight %) of Porphyritic Granitoids (sample batch #4 collected in 2001 and analysed at Curtin University of Technology); sample KN2A was collected from an aplite associated with the porphyritic granite (n.a.=not analysed).	437
Table 14-13:	Major element geochemistry (weight %) of Porphyritic Granitoids (samples SH8, SH9, LW1, LW2, LWC and LW11 of sample batch #3 collected in 2000 and analysed at Curtin University of Technology; samples MTG-4, MTG-5, MGG-2 and MTGG-3 of sample batch #3 collected in 1999 and analysed by Chemex Canada; n.a.=not analysed).	437
Table 14-14:	Major element geochemistry (weight %) of Porphyritic Granitoids (sample batch #4 collected in 2001 and analysed at Curtin University of Technology; n.a.=not analysed).	437
Table 14-15:	Trace element geochemistry (ppm) of the Mkushi Gneiss and the Luwalizi Granite Gneiss (sample batch #4 collected in 2001 and analysed at Curtin University of Technology; n.a.=not analysed).	438
Table 14-16:	Trace element geochemistry (ppm) of the Mansa Granitoids and Volcanics (sample batch #4 collected in 2001 and analysed at Curtin University of Technology; n.a.=not analysed).	439
Table 14-17:	Trace element geochemistry (ppm) of the Katibunga Volcanics (KV samples of sample batch #2, collected in 1999 and analysed by Chemex Canada; samples KB of sample batch #3, collected in 2000 and analysed at Curtin University of Technology; n.a.=not analysed).	440
Table 14-18:	Trace element geochemistry (ppm) of the Katibunga, Luswa River and Ilondola Volcanics (sample batch #3 collected in 2000 and analysed at Curtin University of Technology; n.a.=not analysed).	441
Table 14-19:	Trace element geochemistry (ppm) of the Isoka Volcanics (sample batch #3 collected in 2000 and analysed at Curtin University of Technology; n.a.=not analysed).	442

Table 14-20:	Trace element geochemistry (ppm) of the Lukamfwa Hill Granitoids (samples SI of sample batch #1 collected in 1998 and analysed at Chemex Canada; samples SER of sample batch #2, collected in 1999 and analysed by Chemex Canada; n.a.=not analysed).	443
Table 14-21:	Trace element geochemistry (ppm) of the Lukamfwa Hill Granitoids (samples ND2, SR5, SR7 and SR12 of sample batch #4 collected in 2001 and analysed at Curtin University of Technology; samples ML2 and LW10 of sample batch #3 collected in 2000 and analysed at Curtin University of Technology; n.a.=not analysed).	444
Table 14-22:	Trace element geochemistry (ppm) of Porphyritic Granitoids (samples SI of sample batch #1 collected in 1998 and analysed by Chemex Canada; samples MQG-1, SQG-2, SER5-3, SER6-4 and SER6-6 of sample batch #2 collected in 1999 and analysed by Chemex Canada; n.a.=not analysed).	445
Table 14-23:	Trace element geochemistry (ppm) of Porphyritic Granitoids (sample batch #4 collected in 2001 and analysed at Curtin University of Technology; n.a.=not analysed).	446
Table 14-24:	Trace element geochemistry (ppm) of Porphyritic Granitoids (sample batch #4 collected in 2001 and analysed at Curtin University of Technology; n.a.=not analysed).	447
Table 14-25:	Trace element geochemistry (ppm) of Porphyritic Granitoids (sample batch #4 collected in 2001 and analysed at Curtin University of Technology; n.a.=not analysed).	448
Table 14-26:	Trace element geochemistry (ppm) of Porphyritic Granitoids (samples SH8, SH9, LW1, LW2, LWC and LW11 of sample batch #3 collected in 2000 and analysed at Curtin University of Technology; samples MTG-4, MTG-5, MGG-2 and MTGG-3 of sample batch #3 collected in 1999 and analysed by Chemex Canada; n.a.=not analysed).	449
Table 14-27:	Trace element geochemistry (ppm) of Porphyritic Granitoids (sample batch #4 collected in 2001 and analysed at Curtin University of Technology; n.a.=not analysed).	450

INDEX OF FIGURES

Figure 1-1:	The tectonic provinces of central and southern Africa. (AKC=Angola-Kasai craton; BB=Bangweulu block; CK=Choma-Kalomo block; DB=Damara belt; EAO=East African Orogen; IB=Irumide belt; KB=Kibaran belt; KvC=Kaapvaal craton; LA=Lufilian belt; LIB=Limpopo belt; LuB=foreland to the Lurio belt; MaB=Magondi belt; NaB=Natal belt; NB=Namaqua belt; NW=northwest Botswana rift; SS=Sinclair sequence; RI=Rehoboth inlier; SaB=Saldania belt; TC=Tanzania craton; UB=Ubendian belt; UsB=Usagaran belt; ZB=Zambezi belt; ZC=Zimbabwe craton. Dashed line indicates the approximate position of the cross section by Daly (1986b)(Figure 1-3)3
Figure 1-2:	Overview map showing the location of the Irumide belt (IB) with respect to the Bangweulu block (BB), Choma-Kalomo block (CKB) and various orogenic belts in the region (MG=Mafingi Group; CI=Chewore Inliers; NG=Nyika Granite; boxes indicate the map sheets mapped by Stillman (1965c, box 1), Daly (1995b; 1995a, box 2) and Fitches (1971, box 3)).....8
Figure 1-3:	Schematic crustal cross-section through the Irumide belt into southern Malawi and northwestern – central Mozambique (after Daly, 1986b). The approximate position of the section is indicated on Figure 1-1.9
Figure 2-1:	Overview of the Muva Supergroup of Zambia. The inset shows the location of Zambia (white) in Africa (black). The boxes indicate the areas shown in Figure 2-2, Figure 2-3 and Figure 2-4.22
Figure 2-2:	Simplified geological map of the Bangweulu block. The box indicates the two quarter degree geological sheets (1:100,000) of Mansa and Musonda Falls (shown in detail in Figure 2-6). The map is adapted from the geological map of Zambia (Thieme and Johnson, 1981) and from Andersen and Unrug (1984).23
Figure 2-3:	Overview map of the southwestern Irumide belt, showing simplified geology and the location of mapped quarter degree sheets. Simplified geology is adapted from the 1:1,000,000 geological map of Zambia (Thieme and Johnson, 1981). The inset and boxes indicate the areas shown in detail in Figure 2-9 and Figure 2-10.24
Figure 2-4:	Overview map of the northeastern Irumide belt, showing simplified geology and the location of mapped quarter degree sheets. Simplified geology is adapted from the 1:1,000,000 geological map of Zambia (Thieme and Johnson, 1981). The inset and boxes indicate areas shown in detail in Figure 2-10, Figure 2-11, Figure 2-12 and Figure 2-13.25
Figure 2-5:	Overview of previously published Proterozoic age data for Zambia (refer to Table 2-2). Boxes indicate approximate extent of Figures 2-2, 2-3, 2-4, 2-9, 2-10, 2-11, 2-12 and 2-13; grey areas delineate extent of the Mporokoso Group, Irumide belt and Choma-Kalomo block.....26
Figure 2-6:	Simplified geological map of the Mansa and Musonda Falls map sheets indicating location of samples (regional location indicated on Figure 2-2). Adapted from 1:100,000 geological maps of Mansa and Musonda Falls after Thieme (1970; 1971)30
Figure 2-7:	(a) the Mansa Granite, showing porphyritic K-feldspar in a matrix of q-ksp-pl-chl-bi; (b) photomicrograph of a thin section (crossed polars (xpl)) of sample MA1 (Mansa Granite) showing a coarse-grained q-pl-bi

	assemblage with minor K-feldspar (field of view (f.o.v.) 4.64 mm). The plagioclase is extensively saussuritised. Biotite is variably altered to chlorite. The quartz shows undulose extinction.	31
Figure 2-8:	(a) Fine grained enclaves of volcanic rock within coarse granite. Age data indicate that intrusion of the granite and volcanic rocks was penecontemporaneous; (b) photomicrograph of a thin section (xpl) of sample MA3 showing equigranular quartz and feldspar, in a microcrystalline groundmass of q + ksp + epidote + iron oxides and chl. Rounded microcrystalline zones surrounded by equigranular quartz may represent relict vesicles (f.o.v. 4.64 mm).	31
Figure 2-9:	Simplified geological map of the area around Mkushi showing sample locations for this study, based on published 1:100,000 scale geological maps (includes Kapiri Mposhi, Kakulu (Mulungushi), Mita Hills, Mkushi, Musofu River, Fiwila and Ndabala map sheets and parts of Serenje, Chin'gombe, Luano and Bwana Mkubwa sheets)(Smith, 1965; Stillman, 1965a; 1965b; Moore, 1967a; Cvetcovic, 1992; Reichwalder and Brandon, 1992; Kerr, 1994; Mapani and Moore, 1995a; Carruthers, 2000; Smith, 2000; Chisela, in press). The boxes indicate the approximate position of Figure 2-30 and Figure 2-31. Outlines of quartzite ridges are traced in the Manshya River Group.....	32
Figure 2-10:	Simplified geological map of the region around Kanona showing sample locations for this study, adapted from published 1:100,000 scale geological maps (includes Kasanka (mapped from satellite imagery), Serenje, Kanona, Chitambo, and Mupamadzi sheets) (Cordiner, 1994; Mapani and Moore, 1995a; Van de Velde and De Waele, 1997; Cordiner, 2000). Outlines of quartzite ridges are traced in the Manshya River Group.	33
Figure 2-11:	Simplified geological map of the region around Mpika showing sample locations for this study, adapted from published 1:100,000 scale geological maps (includes Chilonga Mission and Katibunga Mission sheets and parts of Mtofwe and Mupamadzi River sheets)(Cordiner, 1994; Mosley, 1994; Mosley and Marten, 1994; Van de Velde and De Waele, 1997). The white rectangle shows the area of the detailed map in Figure 2-37. Outlines of quartzite ridges are traced in the Manshya River Group.....	34
Figure 2-12:	Simplified geological map of the region around Chinsali showing sample localities for this study, adapted from published 1:100,000 scale geological maps (includes Shiwa N'gandu, Ilondola Mission, Luswa River and Chinsali map sheets)(Daly, 1994a; Sykes, 1994; Ayres, 1998; Lucacik, 1998a). Specific units referred to in the text are: A=Chilubanama Granite; B=Mutangoshi Gneissic Granite; C=Lubu Granite Gneiss; D=Musalango Gneiss; E=Lufila Granite (Bemba Batholith). Outlines of quartzite ridges are traced in the Manshya River Group.	35
Figure 2-13:	Simplified geological map of the region around Isoka showing sample localities for this study, based on published 1:100,000 scale geological maps (includes Malole, Mulilansolo Mission, and Mututa Hills map sheets, and parts of Isoka and Kalungu sheets)(1994c; Daly, 1994b; Van Tuijl and Verhoog, 1995a; 1995b). The rectangle indicates the area of Figure 2-23. Outlines of quartzite ridges are traced in the Manshya River Group.	36
Figure 2-14:	(a) strongly deformed Mkushi Gneiss (Munshiwemba mine), intruded by various generations of chalcopyrite-bearing pegmatites (b).	37

Figure 2-15:	(a) photomicrograph of thin section (xpl) of sample KMP1 (Mkushi Gneiss, Kampoyo Quarry) showing q-pl-ksp-bi-mu assemblage (f.o.v. 2.32 mm); (b) Strongly foliated biotite granite gneiss in Kampoyo quarry. An aplitic melt pocket truncates the foliation.	38
Figure 2-16:	(a) photomicrograph of thin section (xpl) of sample MK3 (Mkushi Gneiss, Munshiwemba Quarry) showing q-pl-(ksp)-bi assemblage, with sericitised matrix and relict coarse q-pl crystals. Biotite defines a strong foliation (f.o.v. 4.64 mm); (b) photomicrograph of thin section (xpl) of sample MK5 (Mkushi Gneiss, Munshiwemba Quarry) showing the less deformed coarse granite gneiss variety, with q-pl-ksp-bi (f.o.v. 4.64 mm).	39
Figure 2-17:	Geological map of northern Zambia, showing published whole rock Rb-Sr dates and localities sampled in this study for detrital provenance (see Chapter 4). MSB=Mambwe schist belt (adapted after Andersen and Unrug, 1984).	41
Figure 2-18:	photomicrograph of thin section (xpl) of sample ISK1 (Luwalizi Granite Gneiss, Isoka area) showing q-pl-(ksp)-bi-ms assemblage (f.o.v. 4.64 mm). ...	42
Figure 2-19:	photomicrograph of thin section of sample ML2 (Lubu Granite Gneiss) showing coarse grained quartz, plagioclase and microcline, with biotite and minor muscovite. Note the myrmekitic intergrowth commonly found in the Lubu Granite Gneiss (f.o.v. 4.64 mm).	43
Figure 2-20:	Simplified stratigraphic columns for the (meta)sedimentary sequences of the Muva Supergroup. The stratigraphic locations of samples collected for a detrital provenance study (see Chapter 4) are indicated with ellipses. Thicknesses are estimated maxima; actual thickness varies strongly along strike.	45
Figure 2-21:	Geological map of northern Zambia, adapted from Andersen and Unrug (1984), showing the subdivision of the Palaeoproterozoic Mporokoso Group into four formations.	47
Figure 2-22:	(a) typical thick bedded quartzite of the Kabweluma Formation (locality of sample MA6 in the Mansa 1:100,000 map sheet). Note the alternating thick and thin beds, a prominent channel-fill structure and the planar bedding (below the dashed line); (b) coarse pebble conglomerate of the Neoproterozoic Luapula beds unconformably overlying the Bangweulu block and Mporokoso Group (Musonda Falls 1:100,000 map sheet; Mr. Willy Nundwe for scale).	48
Figure 2-23:	Geological map adapted from the published Isoka, Mulilansolo Mission and part of Mututa ridge 1:100,000 map sheets (Daly, 1994b; 1994c; Van Tuijl and Verhoog, 1995b). The outlined box shows the area of Figure 2-24.	50
Figure 2-24:	Geological map of the Chimbwe syncline, showing the location of the Kachinga Tuff and localities of samples. The map is adapted after Daly (1994b).	51
Figure 2-25:	Cross bedding structures in quartzites of the Manshya River Group; (a) Luswa River sheet; (b) Chembewesu Hill, Ilondola Mission 1:100,000 map sheet (near location of sample IL14).	52
Figure 2-26	(a) tight folding in a fine laminated quartzite-pelite unit of the Manshya River Group (Ilondola Mission 1:100,000 map sheet); (b) fold nose in quartzite of the Manshya River Group (Shiwa N'gandu 1:100,000 map sheet, Figure 2-4)	52

Figure 2-27:	photomicrograph of thin sections (xpl) of quartzites from the Manshya River Group ((a) a mild grain flattening fabric in sample IL8 (Ilondola Mission 1:100,000 map sheet)(f.o.v. 4.64 mm); (b) photomicrograph of a thin section of sample IS25 (Chimbwe syncline, Isoka 1:100,000 map sheet)(f.o.v. 4.64 mm).	53
Figure 2-28:	(a) photomicrograph of thin section (xpl) of sample IS15 (Isoka 1:100,000 map sheet), showing garnetiferous biotite schist of the Manshya River Group (f.o.v. 2.32 mm); (b) photomicrograph of thin section (xpl) of kyanite schist in the Manshya River Group (sample IS2, Chimbwe syncline, Isoka 1:100,000 map sheet)(f.o.v. 2.32 mm).....	53
Figure 2-29:	(a) panoramic view of dominant quartzite ridges in the Kanona map sheet, southwestern Irumide belt; (b) Crenulated garnet-sillimanite schist near Kamena school, Serenje map sheet.	54
Figure 2-30:	Geological map of the region around Mwendafie ridge and Munshiwemba Quarry (adapted after Stillman (1965a)). Location is shown on Figure 2-9.	56
Figure 2-31:	Geological map of the area around Chengelo school, showing the evaporites and stromatolitic limestones mapped by Kerr (1994). Location is shown on Figure 2-9.	57
Figure 2-32:	(a) strongly deformed conglomerate at the base of the Kanona Group (Kakulu 1:100000 map sheet); (b) alternating thick and thin-bedded quartzites with minor schists in the Kanona Group.....	57
Figure 2-33:	(a) large-scale upright isoclinal parallel fold in quartzite at Kundalila Falls national monument near Serenje; (b) Kundalila Falls drop spectacularly from the quartzite ridge (Mr. Willy Nundwe and Otis Nyirenda for scale).....	58
Figure 2-34:	(a) strongly folded quartzite-pelite sequence of the Kanona Group (Kanona 1:100000 map sheet); (b) parallel folding in quartzite-pelite sequences of the Kanona Group (Kanona 1:100000 map sheet).	58
Figure 2-35:	photomicrographs of thin sections showing strongly crenulated biotite schist in the Kanona Group (a) sample CHL3 (Chilonga Mission 1:100000 sheet); (b) sample MK11 (Mkushi 1:100000 sheet)(f.o.v. 4.64 mm).	59
Figure 2-36:	(a) photomicrograph of thin section showing relict andalusite porphyroblast in biotite schist of the Kanona Group, altered to a shimmer aggregate of biotite, muscovite and iron oxides. Sample CHT5 (Chitambo Mission 1:100000 map sheet), (b) photomicrograph of thin section showing andalusite-sillimanite schist of the Kanona Group (sample MK13; f.o.v. 2.32 mm) showing preserved andalusite and sillimanite aggregate in a foliated groundmass of q + pl + ksp + bi (Mkushi 1:100000 map sheet).....	59
Figure 2-37:	Geological map of the Ibangwe Hill area near Mpika showing the location of samples (Katibunga Mission 1:100000 map sheet, see Figure 2-11 for location), adapted from Mosley and Marten (1994).	61
Figure 2-38:	(a) Pillow structures in (meta)basaltic lavas at Nakalya Hill south of Mpika (see Figure 2-37 for location); (b) detail of a single pillow, outlined by a corona of chalcedonic silica.....	62
Figure 2-39:	(a) Katibunga rhyolite tuff (sample KB1, Figure 2-37); (b) tight, crenulated folding in the Katibunga rhyolite tuff suggesting at least two deformation events (sample KV1; Nakalya Hill, south of Mpika, Figure 2-37).	62
Figure 2-40:	(a) a small flow fold in a rhyolitic lava flow in the Luswa River 1:100000 map sheet; (b) a coarse phenocrystic flow layer (below) overlain by a finer grained flow layer (Luswa River 1:100000 map sheet).	63

Figure 2-41:	cross-bedding structures in pyroclastic volcanics in the Luswa River 1:100000 map sheet implying subaqueous deposition or reworking.	63
Figure 2-42:	photomicrographs of (a) a thin section of sample LW12 (xpl) showing q-pl-ksp-bi±mu (Luswa River 1:100000 map sheet)(f.o.v. 4.64 mm); (b) a thin section (xpl) of sample LW14 showing phenocrysts or clasts of q-pl (Luswa River 1:100000 map sheet)(f.o.v. 2.32 mm).	64
Figure 2-43:	Geological map of the area around Ilondola Mission (Ilondola 1:100000 map sheet), adapted from Lucacik (1998a), showing the location of samples collected from the Ilondola Volcanics.	65
Figure 2-44:	(a) the Ilondola Volcanic. Note the small crenulation of fine layering; (b) weathered and stained crossbedded quartzite northeast of Ilondola Mission, interpreted to contain significant volcanic input (Ilondola Mission 1:100000 map sheet).	66
Figure 2-45:	(a) thin section of sample IL2 showing q-pl-ksp-mu-bi-Feox. Note the Fe-oxide vein in the upper left corner, and the fine crenulation of primary layering (f.o.v. 2.32 mm); (b) detrital kyanite in sample IL3. Note that the kyanite crystal is aligned parallel to the primary layering (both samples from Ilondola Mission 1:100000 map sheet) (f.o.v. 2.32 mm).	66
Figure 2-46:	(a) contact between pelitic sequences of the Kachinga Pelite (below) and a massive rhyolitic tuff flow of the Kachinga Tuff; (b) close-up view of the rhyolitic tuff, showing fine layering (Isoka 1:100000 map sheet).	68
Figure 2-47:	(a) fine layering in the Kachinga Tuff; (b) truncation of the fine layering in the Kachinga Tuff indicating sedimentary processes during deposition (Isoka 1:100000 map sheet).	68
Figure 2-48:	(a) flow fold in the Kachinga Tuff; (b) relict amygdale, filled in by chert (Isoka 1:100000 map sheet).	69
Figure 2-49:	photomicrographs of (a) a thin section (xpl) of sample IS18 showing primary layering defined by opaque minerals (iron oxides). Autoclastic fabrics can be observed, with broken q + pl fragments in a groundmass of q + pl + bi (f.o.v.4.64 mm); (b) a close up of several autoclasts (f.o.v. 1.16 mm) (Isoka 1:100000 map sheet).	69
Figure 2-50:	photomicrographs of (a) a thin section (xpl) of sample IS22 (Kachinga tuff) showing relict autoclastic fabric (f.o.v. 2.32 mm); (b) a thin section (xpl) of sample IS19 showing a strain shadow, developed either side of a relict devitrified vesicle filled in with quartz (f.o.v 1.16mm)(Isoka 1:100000 map sheet).	69
Figure 2-51:	(a) thin section (xpl) of the Mutangoshi Gneissic Granite (sample MTGG1) showing a coarse assemblage of q + pl + ksp + bi ± mu (f.o.v.=4.64 mm); (b) migmatitic aspect of the Mutangoshi Gneissic Granite.	73
Figure 2-52:	ptygmatic quartz veins in the Musalango Gneiss (sample LW10; Luswa River 1:100000 map sheet).	74
Figure 2-53:	(a) thin section of the Musalango Gneiss (sample LW10), showing sub-equigranular q + ksp + pl + bi (f.o.v 4.64 mm); (b) undeformed gabbroic dyke intruding into the Musalango Gneiss (Luswa River 1:100000 map sheet)	74
Figure 2-54:	(a) panoramic view over pre- syn- and late-tectonic granitoids in the Serenje 1:100000 map sheet; (b) type locality of the Lukamfwa Hill Granite Gneiss (Serenje 1:100000 map sheet).	75
Figure 2-55:	photomicrographs of thin sections (xpl) of the Lukamfwa Hill Granite Gneiss; (a) coarse-grained inequigranular (porphyritic) variety with q + pl +	

	ksp + bi + mu (sample SER6-2; f.o.v. 4.64 mm); (b) fine-grained variety with q + pl + ksp + bi (sample SER6-3; f.o.v. 2.32 mm) (both from the 1:100000 map sheet of Serenje).	75
Figure 2-56:	thin section (xpl) of the Bemba batholith (Lufila Granite). Porphyritic microcline crystals, set in a coarse groundmass of q + pl + ksp + bi ± mu (f.o.v. 4.64 mm) (sample SH8, Shiwa N'Gandu 1:100000 map sheet).	77
Figure 2-57:	(a) outcrop of the Chilubanama Granite in the Chinsali 1:100000 map sheet (Drs. Francis Tembo and Benjamin Mapani); (b) close up view of the Chilubanama Granite, showing a cluster of garnet, possibly a partly resorbed xenolith (Chinsali 1:100000 map sheet).	79
Figure 2-58:	(a) photomicrograph of a thin section (xpl) of the Chilubanama Granite (sample MTG3) showing a coarse q + pl + ksp + bi + mu assemblage (Chinsali 1:100000 map sheet) (f.o.v. 4.64 mm); (b) photomicrograph of a thin section (xpl) of the Chilubanama Granite (sample MTG4) showing garnet (black), q + pl + ksp + bi and alteration of plagioclase (Chinsali 1:100000 map sheet) (f.o.v. 4.64 mm).	79
Figure 2-59:	(a) small xenolith of interpreted metasedimentary parentage in porphyritic granite (Serenje 1:100000 map sheet); (b) mafic enclaves in porphyritic granite interpreted as a broken up and partially resorbed mafic dyke (Kanona 1:100000 map sheet).	80
Figure 2-60:	(a) meter size raft of metasedimentary parentage in porphyritic granite (Serenje 1:100000 map sheet); (b) photomicrograph of a thin section (xpl) of porphyritic granite (sample SER 6-4, Serenje 1:100000 map sheet) showing phenocrysts of plagioclase (right), a quartz veinlet (center) and K-feldspar + quartz (upper left) in a medium grained groundmass of q + pl + ksp + bi (f.o.v. 4.64 mm).	81
Figure 2-61:	(a) photomicrograph of a thin section (xpl) of porphyritic granite (sample MUN, Mununga Quarry, 1:100000 Mupamadzi River sheet) showing phenocrysts of perthitic K-feldspar (top and bottom) in a medium-grained groundmass of q + pl + ksp + bi (f.o.v. 4.64 mm); (b) photomicrograph of a thin section (xpl) of porphyritic granite (sample KN2a, Kanona 1:100000 map sheet) showing phenocrystic microcline (top right and left) in a medium grained groundmass of q + pl + ksp + bi + mu (f.o.v. 4.64 mm).	81
Figure 3-1:	Simplified structural map of northern Zambia showing tectonic transport directions and major shear zones. A-A' and B'B show the approximate location of the sections in Figure 3-2.	90
Figure 3-2:	Simplified cross-sections through the northeastern (A-A') and southwestern (B-B') Irumide belt. The locations of these sections are shown in Figure 3-1. Sections were constructed based on 1:100000 map sheets of the Geological Survey Department of Zambia (the diagrams are not to scale).	91
Figure 3-3:	Simplified metamorphic map of Zambia after Ramsay and Ridgway (1977) ..	94
Figure 4-1:	Location of samples and obtained zircon U-Pb SHRIMP igneous crystallisation ages for the area around Mkushi (includes Kapiri Mposhi, Kakulu (Mulungushi), Mita Hills, Mkushi, Musofu River, Fiwila and Ndabala map sheets and parts of Serenje, Chin'gombe, Luano and Bwana Mkubwa sheets). The Mulungushi Gneiss was dated by Rainaud et al. (2002).	105
Figure 4-2:	Location of samples and obtained zircon U-Pb SHRIMP igneous crystallisation ages for the area around Kanona (includes Kasanka (mapped from satellite imagery), Serenje, Kanona, Chitambo, and	

	Mupamadzi sheets). Two crystallisation ages of low Th/U metamorphic zircon rims are indicated with *.....	106
Figure 4-3:	Location of samples and obtained zircon U-Pb SHRIMP igneous crystallisation ages for the area around Mpika (includes Chilonga Mission and Katibunga Mission map sheets and parts of Mtofwe and Mupamadzi River map sheets)	107
Figure 4-4:	Location of samples and obtained zircon U-Pb SHRIMP igneous crystallisation ages for the area around Chinsali (includes Shiwa N'gandu, Ilondola Mission, Luswa River and Chinsali map sheets). A=Chilubanama Granite; B=Mutangoshi Gneissic Granite (location of samples MTGG-1 and MTGG-2); C=Lubu Granite Gneiss; D=Musalango Gneiss; E=Lufila Granite (Bemba Batholith). Whole-rock Rb-Sr date by Daly (1986b) for the Mutangoshi Gneissic Granite and Lufila Granite are indicated.....	108
Figure 4-5:	Location of samples and obtained zircon U-Pb SHRIMP igneous crystallisation ages for the area around Isoka (includes Malole, Mulilansolo Mission, and Mututa Hills map sheets, and parts of Isoka and Kalungu sheets).	109
Figure 4-6:	Location of samples and obtained zircon U-Pb SHRIMP crystallisation ages for the area around Mansa (includes the 1:100000 Mansa and Musonda Falls map sheets after Thieme (1970; 1971)).	110
Figure 4-7:	(a) photomicrograph of zircons from sample KMP-1 (xpl) showing magmatic zoning in clear zircons (f.o.v. = 600 μm); (b) Cathodoluminescence image of zircon from sample KMP-1 showing the location of analysed spots. Note the complex zircon (analyses 1 and 1r), with a core and rim, which yielded $^{207}\text{Pb}/^{206}\text{Pb}$ ages of 2700 ± 5 Ma and 2686 ± 13 Ma respectively (f.o.v. = 600 μm).	111
Figure 4-8:	U-Pb concordia plot for zircon analyses of sample KMP-1 (Kapiri-Mposhi map sheet). Error ellipses are at 1σ confidence level.	112
Figure 4-9:	(a) photomicrograph of zircons from sample MK-3 (Mkushi map sheet) (xpl) showing clear subhedral to euhedral zircons with minor cracks and inclusions (f.o.v. = 500 μm); (b) CL image of zircon from sample MK-3 showing the location of two analysed spots. Note the analysed zircon rim (analysis 2r), and the well-defined oscillatory zoning in the zircons (f.o.v.= 600 μm).	114
Figure 4-10:	CL image of zircon MK3-4 showing the location of two analysed spots. Note the oscillatory zoning in both zircon rim and core (f.o.v.= 250 μm).	115
Figure 4-11:	U-Pb concordia plot for zircon analyses of sample MK-3. Error ellipses are at 1σ confidence level.	115
Figure 4-12:	(a) photomicrograph of zircons from sample MK-5 (Mkushi map sheet) (xpl) showing clear sub- euhedral zircons with minor cracks and inclusions (f.o.v. = 1000 μm); (b) CL image of zircon from sample MK-5 showing the location of three analysed spots. Note the analysed magmatic zircon rim (analysis 5r), and the broad concentric zoning on the zircons (f.o.v.= 600 μm).	116
Figure 4-13:	U-Pb concordia plot for zircon analyses of sample MK-5. Error ellipses are at 1σ confidence level.	117
Figure 4-14:	(a) photomicrograph of zircons from sample CC10 (xpl) showing clear euhedral zircons with minor cracks and very few inclusions (f.o.v. = 700 μm); (b) CL image of zircon from sample CC10 showing the location of	

	three analysed spots. Note the concentric zoning of the crystals (f.o.v.= 500 μm).	118
Figure 4-15:	U-Pb concordia plot for zircon analyses of sample CC10. Error ellipses are at 1 σ confidence level. Dashed ellipse is analysis CC10-2.1, excluded from calculation of a concordia age.	119
Figure 4-16:	(a) photomicrograph of zircons from sample KN1 (Kanona sheet) (xpl) showing clear euhedral zircons with minor cracks and few inclusions (f.o.v. = 700 μm); (b) CL image of zircon from sample KN1 showing the location of four analysed spots. Note the concentric zoning of the crystals (f.o.v.= 900 μm).	120
Figure 4-17:	U-Pb concordia plot for zircon analyses of sample KN1. Error ellipses are at 1 σ confidence level. Dashed ellipse is analysis KN1-1, excluded from calculation of the age.....	120
Figure 4-18:	(a) photomicrograph of zircon (analysis SER66-19) from sample SER6-6 (xpl) showing a euhedral crystal with rounded core surrounded by a prominent rim (f.o.v. = ~400 μm); (b) CL image of zircon SER66-19 showing the location of analysed spots. Note the dark CL rim, and zoned core (f.o.v.= 300 μm). The $^{207}\text{Pb}/^{206}\text{Pb}$ ages for the core and rim were 2059 \pm 8 and 1012 \pm 8 Ma respectively.	124
Figure 4-19:	(a) photomicrograph of zircon SER67-10 from sample SER6-7 (xpl) showing a subhedral crystal (f.o.v. = ~350 μm); (b) CL image of the analysed zircon SER67-10 showing the location of analysed spots. Note the dark CL rim and the zoned core (f.o.v.= 200 μm). The $^{207}\text{Pb}/^{206}\text{Pb}$ ages for the core and rim were 2020 \pm 12 and 993 \pm 22 Ma respectively.	124
Figure 4-20:	U-Pb concordia plot for zircon core analyses of samples SER 6-6 and SER6-7. Error ellipses are at 1 σ confidence level.	125
Figure 4-21:	U-Pb concordia plot for zircon rim analyses of sample SER6-6. Error crosses are at 1 σ confidence level.	125
Figure 4-22:	U-Pb concordia plot for zircon rim analyses of sample SER6-7. Error crosses are at 1 σ confidence level.	126
Figure 4-23:	CL images of zircons SER67-13 (a), SER67-15 (b), and SER67-24 (c) showing approximate location of analysed spots. Note a subtle change in CL response across a boundary between what may be the outer metamorphic rim, and an older rim or core component. The analysis spots sample both zones, possibly giving a mixed age.	126
Figure 4-24:	(a) CL image of zircons from sample ISK1 (Isoka sheet) showing the location of two analysed spots (f.o.v. = 500 μm); (b) CL image of zircon from sample ISK2 (Isoka sheet) showing the location of three analysed spots (f.o.v.= 900 μm). Note the generally dark aspect and relatively homogenous luminescence of the crystals.	128
Figure 4-25:	U-Pb concordia plot for zircon analyses of sample ISK1. Error ellipses are at 1 σ confidence level. Dashed ellipses are analyses 2 and 3, excluded from calculation of the age. Inset shows CL image of low Th/U zircon analysis ISK1-2, which yielded a $^{207}\text{Pb}/^{206}\text{Pb}$ age of 1926 \pm 8 Ma (f.o.v.=300 μm).	128
Figure 4-26:	U-Pb concordia plot for zircon analyses of sample ISK2. Error ellipses are at 1 σ confidence level. Dashed ellipse is analysis ISK2-2, excluded from calculation of the age. Inset shows CL image of low Th/U zircon analysis ISK2-4, which yielded a $^{207}\text{Pb}/^{206}\text{Pb}$ age of 1944 \pm 20 Ma (f.o.v.=300 μm). .	130

Figure 4-27:	(a) photomicrograph of zircons from sample ML2 (xpl) showing sub-euhedral crystals with numerous cracks and inclusions (f.o.v. = ~1400 μm); (b) CL image of zircons from sample ML2 showing three analysed spots. Note the disrupted concentric zoning and dark recrystallised areas (f.o.v.= 1300 μm).	131
Figure 4-28:	U-Pb concordia plot for zircon analyses of sample ML2. Error ellipses are at 1 σ confidence level.	132
Figure 4-29:	CL image of zircons from sample MA1, showing the location of two analysed spots (f.o.v. = 500 μm).	133
Figure 4-30:	U-Pb concordia plot for zircon analyses of sample MA1. Error ellipses are at 1 σ confidence level.	134
Figure 4-31:	(a) photomicrograph of zircons from sample MA2 (Mansa sheet) (xpl) showing clear euhedral zircons with minor cracks and few inclusions (f.o.v. = ~1500 μm); (b) CL image of zircon from sample MA2 showing the location of three analysed spots. Note the concentric and sector zoning of the crystals (f.o.v.= 600 μm).	135
Figure 4-32:	U-Pb concordia plot for zircon analyses of sample MA2. Error ellipses are at 1 σ confidence level.	135
Figure 4-33:	(a) photomicrograph of zircons from sample MA3 (Mansa sheet) (xpl) showing clear sub-euhedral zircons with minor cracks and few inclusions (f.o.v. = ~1600 μm); (b) CL image of zircon from sample MA3 showing the location of three analysed spots. Note the concentric and sector zoning of the crystals (f.o.v.= 800 μm).	136
Figure 4-34:	U-Pb concordia plot for zircon analyses of sample MA3. Error ellipses are at 1 σ confidence level. Inset shows concordant data points.	137
Figure 4-35:	(a) photomicrograph of zircons from sample MA5 (xpl) showing clear subhedral zircons with minor cracks and few inclusions (f.o.v. = ~1000 μm); (b) CL image of zircon from sample MA5 showing the location of two analysed spots. Note the concentric and sector zoning of the crystals (f.o.v.= 1000 μm).	138
Figure 4-36:	U-Pb concordia plot for zircon analyses of sample MA5. Error ellipses are at 1 σ confidence level.	138
Figure 4-37:	U-Pb concordia plot for zircon analyses of sample MA9. Error ellipses are at 1 σ confidence level. Dashed ellipses are analyses MA9-4, 7 and 9, excluded from the calculation of the concordia age.	139
Figure 4-38:	CL image of zircon from sample MA6 showing the location of analysed spots. Note the rounded character and variable CL response of the crystals (f.o.v.= 1500 μm). Most zircons show concentric zoning consistent with their erosion from magmatic source rocks.	141
Figure 4-39:	U-Pb concordia plot for zircon analyses of sample MA6. Error ellipses are at 1 σ confidence level. Note the concordant nature of most analyses.	142
Figure 4-40:	Probability density plot of detrital zircon from a quartzite near the base of the Kabweluma Formation (Mporokoso Group, northern Zambia). The histogram indicates the number of 100 \pm 5% concordant analyses for each bin of 20 M.y. (right axis), while the curves show the relative probability density of the analyses. The light grey curve denotes 95-105% concordant analyses, while the dark grey curve behind it shows all analyses.	142
Figure 4-41:	CL image of zircon from sample KAS showing the location of analysed spots. Note the well-rounded character and variable CL response of the crystals (f.o.v.= 1400 μm). Most zircons show concentric zoning consistent	

	with magmatic source rocks. Analysis 5 yielded the youngest concordant $^{207}\text{Pb}/^{206}\text{Pb}$ age of 1434 ± 14 Ma.....	144
Figure 4-42:	U-Pb concordia plot for zircon analyses of sample KAS. Error ellipses are at 1σ confidence level. Note the concordant nature of most analyses.....	144
Figure 4-43:	Probability density plot of detrital zircon from the Mwela Quartzite (Kasama Formation, northern Zambia). The histogram indicates the number of $100\pm 5\%$ concordant analyses for each bin of 20 M.y. (right axis), while the curves show the relative probability density of the analyses. The light grey curve denotes 95-105% concordant analyses, while the dark grey curve behind it shows all analyses.	145
Figure 4-44:	(a) photomicrograph of zircons from sample IL14 (xpl) showing clear rounded zircons with minor cracks and inclusions (f.o.v. = $\sim 1600 \mu\text{m}$). Note the variable length to width ratios; (b) CL image of zircon from sample IL14. Note the concentric zoning of the crystals (f.o.v.= $1000 \mu\text{m}$)...	146
Figure 4-45:	U-Pb concordia plot for zircon analyses of sample IL14. Error ellipses are at 1σ confidence level. Note the concordant nature of the majority of analyses.	147
Figure 4-46:	Probability density plot of detrital zircon from the Chembewesu Quartzite (Manshya River Group, northern Zambia). The histogram indicates the number of $100\pm 5\%$ concordant analyses for each bin of 20 M.y. (right axis), while the curves show the relative probability density of the analyses. The light grey curve denotes 95-105% concordant analyses, while the dark grey curve shows all analyses.	147
Figure 4-47:	(a) photomicrograph of zircons from sample MK8 (xpl) showing clear zircons with minor cracks and inclusions (f.o.v. = $\sim 1600 \mu\text{m}$); (b) CL image of zircon from sample MK8. Note the concentric zoning of the crystals (f.o.v.= $1300 \mu\text{m}$).	149
Figure 4-48:	U-Pb concordia plot for zircon analyses of sample MK8. Error ellipses are at 1σ confidence level. The inset shows the probability density plot of the detrital zircons. The histogram indicates the number of $100\pm 5\%$ concordant analyses for each bin of 25 M.y. (right axis), while the curves show the relative probability density of the analyses. The light grey curve denotes 95-105% concordant analyses, while the dark grey curve shows all analyses.....	149
Figure 4-49:	(a) photomicrograph of zircons from sample ZM31 (xpl) showing clear euhedral zircons with minor cracks and inclusions (f.o.v. = $\sim 1400 \mu\text{m}$); (b) CL image of zircons from sample ZM31 showing analysed spots (f.o.v.= $1800 \mu\text{m}$).	150
Figure 4-50:	U-Pb concordia plot for zircon analyses of the Luswa River Volcanic. Error ellipses are at 1σ confidence level.	151
Figure 4-51:	(a) photomicrograph of zircons from sample IS20 (xpl) showing clear euhedral zircons with some cracks and inclusions (f.o.v. = $\sim 250 \mu\text{m}$); (b) CL image of zircons from sample IS20. Note the concentric zoning of the crystals (f.o.v.= $800 \mu\text{m}$).	152
Figure 4-52:	U-Pb concordia plot for zircon analyses of the Kachinga Tuff. Error ellipses are at 1σ confidence level.	152
Figure 4-53:	(a) photomicrograph of zircons from sample KB5 (xpl) showing clear sub-euhedral zircons with minor cracks and inclusions (f.o.v. = $\sim 1500 \mu\text{m}$); (b) CL image of zircons from sample KB5. Note the concentric zoning of the	

	crystals (f.o.v.= 450 μm). Analysis KB5-2 yielded an age of 2551 ± 36 Ma and is interpreted as a xenocryst.....	153
Figure 4-54:	U-Pb concordia plot for zircon analyses of the Katibunga Volcanic. Error ellipses are at 1σ confidence level.	154
Figure 4-55:	(a) photomicrograph of zircon (analysis numbers 3c and 3r) from sample MTGG1 (xpl) showing euhedral habit with minor cracks and inclusions (f.o.v. = ~ 1500 μm); (b) CL image of zircons from sample MTGG1 indicating analysed spots 2, 3c and 3r. Note the concentric zoning of the crystals (f.o.v.= 800 μm). Analysis 2 yielded a $^{207}\text{Pb}/^{206}\text{Pb}$ age of 1015 ± 12 Ma, while 3c and 3r yielded 1961 ± 15 and 1008 ± 8 Ma respectively.....	156
Figure 4-56:	U-Pb concordia plot for zircon analyses of sample MTGG1. Error ellipses are at 1σ confidence level. The box refers to the detailed plot in Figure 4-57.....	157
Figure 4-57:	U-Pb concordia plot for zircon analyses of sample MTGG1. Error ellipses are at 1σ confidence level.	157
Figure 4-58:	(a) photomicrograph of zircon (analysis number MTGG1-1) from sample MTGG1 (xpl) showing euhedral elongate habit with minor cracks and inclusions (f.o.v. = ~ 200 μm). Even in transmitted light, the complex nature of the zircon is evident; (b) CL image of the same zircon indicating the analysed spot (analysis 1). Note that the spot samples outside the core, but across what may be two separate dark CL rims (f.o.v.= 250 μm). This analysis yielded a $^{207}\text{Pb}/^{206}\text{Pb}$ age of 979 ± 6 Ma.	158
Figure 4-59:	(a) photomicrograph of zircon (analysis number 4) from sample MTGG2 (xpl) showing euhedral elongate habit with cracks and minor inclusions (f.o.v. = ~ 250 μm); (b) CL image of the same zircon indicating the analysed spot (analysis 4). Note the concentric zoning consistent with magmatic growth (f.o.v.= 400 μm). This analysis yielded a $^{207}\text{Pb}/^{206}\text{Pb}$ age of 1062 ± 12 Ma.	159
Figure 4-60:	U-Pb concordia plot for zircon analyses of sample MTGG2. Error ellipses are at 1σ confidence level. The box refers to a detailed plot in Figure 4-61..	159
Figure 4-61:	U-Pb concordia plot for zircon analyses of sample MTGG2. Error ellipses are at 1σ confidence level.	160
Figure 4-62:	(a) photomicrograph of zircon (analysis number 2) from sample LW10 (xpl) showing euhedral habit with numerous cracks and minor inclusions (f.o.v. = ~ 300 μm); (b) CL image of the same zircon indicating the analysed spot (analysis 2). Note the faint concentric zoning consistent with magmatic growth and the dark recrystallised areas (f.o.v.= 200 μm). This analysis yielded a $^{207}\text{Pb}/^{206}\text{Pb}$ age of 1615 ± 22 Ma.	161
Figure 4-63:	U-Pb concordia plot for zircon analyses of sample LW10. Error ellipses are at 1σ confidence level.	162
Figure 4-64:	(a) photomicrograph of a zircon (analysis SER62-41) from sample SER6-2c (xpl) showing euhedral habit with minor cracks and inclusions (f.o.v. = ~ 300 μm); (b) CL image of the same zircon showing the location of analysed spots in the core and magmatic rim. Note the concentric zoning on the rim, and very dark luminescence of the core (f.o.v.= 300 μm). $^{207}\text{Pb}/^{206}\text{Pb}$ ages obtained were 1660 ± 145 and 1625 ± 37 Ma respectively.	164
Figure 4-65:	U-Pb concordia plot for zircon analyses of sample SER6-2c. Error ellipses are at 1σ confidence level.	164

Figure 4-66:	(a) photomicrograph of a zircon (analysis SER63-29) from sample SER6-3 (xpl) showing euhedral habit with cracks and minor inclusions (f.o.v. = ~200 μm); (b) CL image of the same zircon showing the location of the analysed spot. Note the concentric zoning (f.o.v.= 300 μm). This spot yielded a $^{207}\text{Pb}/^{206}\text{Pb}$ age of 1632 ± 13 Ma.	166
Figure 4-67:	U-Pb concordia plot for zircon analyses of sample SER6-3. Error ellipses are at 1σ confidence level.	166
Figure 4-68:	CL image of zircons from sample SR12 showing the location of seven analysed spots. (f.o.v.= 1500 μm).....	168
Figure 4-69:	U-Pb concordia plot for zircon analyses of sample SR12. Error ellipses are at 1σ confidence level.	168
Figure 4-70:	(a) photomicrograph of zircons from sample ND2 (xpl) showing euhedral crystals with minor cracks and inclusions (f.o.v. = ~1200 μm); (b) CL image of zircons from sample ND2 showing three analysed spots. Note the concentric zoning (f.o.v.= 800 μm).....	169
Figure 4-71:	U-Pb concordia plot for zircon analyses of sample ND2. Error ellipses are at 1σ confidence level.	170
Figure 4-72:	(a) photomicrograph of zircons from sample SH8 (xpl) showing sub-euhedral habit with cracks and minor inclusions (f.o.v. = ~800 μm); (b) CL image of zircons from sample SH8 showing the location of analysis SH8-2. Note the faint concentric zoning (f.o.v.= 500 μm).	171
Figure 4-73:	U-Pb concordia plot for analyses of SH8. Error ellipses are at 1σ confidence level.....	172
Figure 4-74:	(a) typical zircons from sample LW2 (xpl) showing subhedral habit with cracks and minor inclusions (f.o.v. = ~200 μm); (b) CL image of zircons of sample LW2 showing the location of analyses. Note the faint concentric zoning, disrupted by recrystallisation (f.o.v.= 500 μm).....	173
Figure 4-75:	U-Pb concordia plot (Tera-Wasserburg) for zircon analyses of sample LW2. Error ellipses are at 1σ confidence level. Data is corrected for common Pb.	173
Figure 4-76:	(a) photomicrograph of zircons from sample ZM32 (xpl) showing sub-euhedral habit with cracks and minor inclusions (f.o.v. = ~1500 μm); box indicates the area of next photograph (b) detail of zircon ZM32-1.1 (center), which was analysed twice, once on the core (1859 ± 20 Ma), and once on the rim (abandoned due to high ^{204}Pb counts)(f.o.v.=~400 μm). Note the highly variable morphology and clarity of the crystals, suggesting multiple sources.....	175
Figure 4-77:	U-Pb concordia plot for zircon analyses of sample ZM32. Error ellipses are at 1σ confidence level. $^{207}\text{Pb}/^{206}\text{Pb}$ ages and concordance are indicated. ...	176
Figure 4-78:	(a) photomicrograph of zircon from sample MTG4 (xpl) showing subhedral habit with cracks and minor inclusions (f.o.v. = 250 μm); (b) CL image of zircons from sample MTG4 showing analysed spots. Note the complex character of most zircons, and the dark CL rims, most of which are interpreted to have grown during a metamorphic event. Note analyses 8c and 8r, which yielded $^{207}\text{Pb}/^{206}\text{Pb}$ ages of 1425 ± 47 and 1013 ± 9 Ma respectively.....	178
Figure 4-79:	U-Pb concordia plot for zircon analyses of sample MTG4. Error ellipses are at 1σ confidence level.	178
Figure 4-80:	U-Pb concordia plot for concordant zircon (rim) analyses of sample MTG4. Error ellipses are at 1σ confidence level.....	179

Figure 4-81:	(a) photomicrograph of zircon LW1-5 (xpl) showing subhedral habit with cracks and inclusions (f.o.v. = ~400 μm); (b) CL image of the same zircon showing the location of analysis LW1-5. Note the faint concentric zoning (f.o.v.= 250 μm).	180
Figure 4-82:	(a) photomicrograph of zircon LW1-7 (xpl) showing euhedral habit with cracks and inclusions (f.o.v. = ~300 μm); (b) CL image of the same zircon showing the location of analysis LW1-7. Note the concentric zoning and low CL response (f.o.v.= 400 μm).	180
Figure 4-83:	U-Pb concordia plot for zircon analyses of sample LW1. Error ellipses are at 1 σ confidence level. Dashed ellipses denote analyses excluded from age calculations.....	181
Figure 4-84:	(a) photomicrograph of zircon from sample KK1 (xpl) showing euhedral crystals with minor cracks and inclusions (f.o.v. = ~1600 μm); (b) CL image of zircons from sample KK1 showing the location of analysis KK1-6. Note the prominent concentric zoning (f.o.v.= 1500 μm).....	183
Figure 4-85:	U-Pb concordia plot for zircon analyses of sample KK1. Error ellipses are at 1 σ confidence level. Dashed ellipse denotes analysis excluded from age calculation.	183
Figure 4-86:	(a) photomicrograph of zircon from sample MH4 (xpl) showing euhedral crystals with minor cracks and inclusions (f.o.v. = ~1600 μm); (b) CL image of zircons from sample MH4 showing the location of analysed spots. Note the prominent concentric zoning (f.o.v.= 1500 μm).....	185
Figure 4-87:	U-Pb concordia plot for zircon analyses of sample MH4. Error ellipses are at 1 σ confidence level.	185
Figure 4-88:	(a) photomicrograph of zircon from sample MH9c (xpl) showing euhedral crystals with minor cracks and inclusions (f.o.v. = ~1000 μm); (b) CL image of zircons from sample MH9c showing the location of analysed spots. Note the prominent concentric zoning (f.o.v.= 800 μm).	187
Figure 4-89:	U-Pb concordia plot for zircon analyses of sample MH9c. Error ellipses are at 1 σ confidence level.	187
Figure 4-90:	CL image of zircons from sample CC5 showing analysed spots.	188
Figure 4-91:	U-Pb concordia plot for zircon analyses of sample CC5. Error ellipses are at 1 σ confidence level.	189
Figure 4-92:	(a) photomicrograph of zircons from sample CC8 (xpl) showing euhedral crystals with minor cracks and inclusions (f.o.v. = ~1000 μm); (b) CL image of zircons from sample CC8 showing the location of analysed spots. Note the prominent concentric zoning (f.o.v.= 1200 μm).....	190
Figure 4-93:	U-Pb concordia plot for zircon analyses of sample CC8. Error ellipses are at 1 σ confidence level.	190
Figure 4-94:	(a) photomicrograph of zircons from sample MK7 (xpl) showing euhedral crystals with numerous cracks and inclusions (f.o.v. = ~1600 μm); (b) CL image of zircons from sample MK7 showing the location of analysed spots MK7-2 and 2r. Note the prominent concentric zoning in the core, and dark CL aspect of the rim (f.o.v.= 600 μm).	192
Figure 4-95:	U-Pb concordia plot for zircon analyses of sample MK7. Error ellipses are at 1 σ confidence level.	192
Figure 4-96:	(a) photomicrograph of zircons from sample FW1 (xpl) showing a wide variety of crystals (f.o.v. = ~1500 μm); (b) CL image of zircons from sample FW1 showing the location of analysed spots. Note the prominent concentric zoning at the analysed sites (f.o.v.= 750 μm).....	194

Figure 4-97:	U-Pb concordia plot for zircon analyses of sample FW1. Error ellipses are at 1 σ confidence level.	194
Figure 4-98:	(a) photomicrograph of zircons from sample FW2 (xpl) showing variably sized and shaped crystals (f.o.v. = ~1000 μ m); (b) CL image of zircons from sample FW2 showing the location of analysed spots. Note the wide range of CL response and morphologies (f.o.v.= 1500 μ m).....	196
Figure 4-99:	U-Pb concordia plot for zircon analyses of sample FW2. Error ellipses are at 1 σ confidence level. Inset shows a concordant age group defining an age of 2033 \pm 14 Ma.	196
Figure 4-100:	Probability density diagram and histogram showing the 100 \pm 5% concordant age populations in zircon from sample FW2. The dark grey curve denotes data within 5% of concordia, while the light grey curve shows all data. The bin-size for the histogram is 25 M.y.	197
Figure 4-101:	(a) photomicrograph of zircons from sample CHT6 (xpl) showing euhedral crystals (f.o.v. = ~1500 μ m); (b) CL image of zircons from sample CHT6 showing the location of analysed spots. Note the wide range of CL response and oscillatory zoning patterns (f.o.v.= 1000 μ m).	198
Figure 4-102:	U-Pb concordia plot for zircon analyses of sample CHT6. Error ellipses are at 1 σ confidence level.	198
Figure 4-103:	(a) photomicrograph of zircons from sample KN2A (xpl) showing euhedral crystals (f.o.v. = ~1200 μ m); (b) CL image of zircons from sample KN2A showing the location of analysed spots. Note the oscillatory zoning patterns (f.o.v.= 1200 μ m).	199
Figure 4-104:	U-Pb concordia plot for zircon analyses of sample KN2A. Error ellipses are at 1 σ confidence level. Note the drift away from concordia due to incorrect common Pb correction based on measured ²⁰⁴ Pb.....	200
Figure 4-105:	U-Pb concordia plot (Tera-Wasserburg) for zircon analyses of sample KN2A. The data are uncorrected for common Pb. Error crosses are at 1 σ confidence level. The regression (dashed line) is made towards common Pb, calculated for an age of 1050 Ma after Stacey and Kramers (1975).	200
Figure 4-106:	(a) photomicrograph of zircons from sample KN5 (xpl) showing euhedral crystals (f.o.v. = ~1200 μ m); (b) CL image of zircons from sample KN5 showing the location of analysed spots. Note the oscillatory zoning patterns (f.o.v.= 1200 μ m).	202
Figure 4-107:	U-Pb concordia plot for zircon analyses of sample KN5. Error ellipses are at 1 σ confidence level. Note the drift away from concordia due to incorrect common Pb correction based on measured ²⁰⁴ Pb.....	202
Figure 4-108:	U-Pb concordia plot (Tera-Wasserburg) for zircon analyses of sample KN5. The data are uncorrected for common Pb. Error crosses are at 1 σ confidence level. The dashed regression (dashed line) is made towards common Pb, calculated for an age of 1050 Ma after Stacey and Kramers (1975).	203
Figure 4-109:	(a) photomicrograph of zircons from sample KN7 (xpl) showing anhedral, subhedral and euhedral crystals (f.o.v. = ~1000 μ m); (b) CL image of zircons from sample KN7 showing the location of analysed spots. Note the variability on CL response and oscillatory zoning patterns (f.o.v.= 1200 μ m).	204
Figure 4-110:	Tera-Wasserburg U-Pb concordia plot for zircon analyses of sample KN7. Error ellipses are at 1 σ confidence level. Insets show enlargements	

	(Wetherill U-Pb concordia plots) of a coherent age group at ~2010 Ma and a concordant analysis (KN7-7) at 1048 ± 10 Ma.	205
Figure 4-111:	(a) photomicrograph of zircons from sample KN8 (xpl) showing euhedral crystals (f.o.v. = ~1000 μm); (b) CL image of zircons from sample KN8 showing the location of analysed spots. Note the variability on CL response, oscillatory zoning patterns and complex internal fabrics of the zircons (f.o.v.= 1200 μm).	206
Figure 4-112:	U-Pb concordia plot for all zircon analyses of sample KN8. Error ellipses are at 1σ confidence level. Note the drift away from concordia in the younger age group due to incorrect common Pb correction based on measured ^{204}Pb	207
Figure 4-113:	U-Pb concordia plot (Tera-Wasserburg) for selected zircon analyses of sample KN8. The data are uncorrected for common Pb. Error crosses are at 1σ confidence level. The regression is made towards common Pb, calculated for an age of 1050 Ma after Stacey and Kramers (1975).	207
Figure 4-114:	(a) photomicrograph of zircons from sample ND1 (xpl) showing sub-euhedral crystals (f.o.v. = ~1200 μm); (b) CL image of zircons from sample ND1 showing the location of analysed spots. Note the variability on CL response. High luminescence crystals show oscillatory zoning patterns while dark CL crystals show very faint concentric zoning (f.o.v.= 1000 μm).	209
Figure 4-115:	U-Pb concordia plot for zircon analyses of sample ND1. Error ellipses are at 1σ confidence level. Note the large errors on three data points and two discordant analyses (dashed ellipses). The box shows the area enlarged in Figure 4-116.	209
Figure 4-116:	U-Pb concordia plot for concordant zircon analyses of sample ND1. Error ellipses are at 1σ confidence level.	210
Figure 4-117:	(a) photomicrograph of zircons from sample ND4 (xpl) showing sub-euhedral crystals (f.o.v. = ~1600 μm); (b) CL image of zircons from sample ND4 showing the location of analysed spots. Note the oscillatory zoning patterns (f.o.v.= 700 μm).	211
Figure 4-118:	U-Pb concordia plot for zircon analyses of sample ND4. Error ellipses are at 1σ confidence level.	211
Figure 4-119:	(a) photomicrograph of zircons from sample ND5 (xpl) showing sub-euhedral crystals (f.o.v. = ~1600 μm); (b) CL image of zircons from sample ND5 showing the location of analysed spots. Note the oscillatory zoning patterns (f.o.v.= 1700 μm).	213
Figure 4-120:	U-Pb concordia plot for zircon analyses of sample ND5. Error ellipses are at 1σ confidence level.	213
Figure 4-121:	(a) photomicrograph of zircons from sample SASA2 (xpl) showing anhedral and euhedral crystals (f.o.v. = ~800 μm); (b) inset shows zircon SASA2-12 on which a core and rim can be distinguished; (c) CL image of zircon SASA2-12 showing the location of analysed spots. Note the oscillatory zoning patterns on both core and two rims (f.o.v.= 150 μm).	215
Figure 4-122:	U-Pb concordia plot for zircon analyses of sample SASA2. Error ellipses are at 1σ confidence level.	216
Figure 4-123:	(a) photomicrograph of zircons from sample SER5-3 (xpl) showing euhedral crystals (f.o.v. = ~800 μm); (b) CL image of zircons from SER5-3 showing the location of analysed spots. Note the oscillatory zoning patterns (f.o.v.= 800 μm).	217

Figure 4-124:	U-Pb concordia plot for zircon analyses of sample SER5-3. Error ellipses are at 1 σ confidence level.	217
Figure 4-125:	(a) photomicrograph of zircons from sample SER6-4 (xpl) showing euhedral crystals (f.o.v. = ~500 μ m); (b) CL image of zircons from SER6-4 showing the location of analysed spots. Note the oscillatory zoning patterns (f.o.v.= 800 μ m).	219
Figure 4-126:	(a) photomicrograph of an analysed zircon (analysis SER64-9.1) from sample SER6-4 (xpl) showing a euhedral crystal, with narrow rim (f.o.v. = ~200 μ m); (b) CL image of the same zircon showing the location of the analysed spot. Note the dark CL rim (f.o.v.= 200 μ m).	219
Figure 4-127:	U-Pb concordia plot for zircon analyses of sample SER6-4. Inset shows a concordia plot for all 10 data points. Error ellipses are at 1 σ confidence level.	220
Figure 4-128:	(a) photomicrograph of an analysed zircon (analysis SQG-7) from sample SQG (xpl) showing a euhedral crystal, with narrow rim (f.o.v. = ~300 μ m); (b) CL image of the same zircon showing the location of the analysed spot. Note the oscillatory zoning (f.o.v.= 300 μ m).	221
Figure 4-129:	U-Pb concordia plot (Tera-Wasserburg) for zircon analyses of sample SQG. Error ellipses are at 1 σ confidence level. Dashed ellipse represents analysis SQG-70 with high δ^{206} (1.20%) yielding an age of 1099 ± 30 Ma. Grey ellipses are two data points possibly defining a ~1065 Ma xenocrystic component.	222
Figure 4-130:	(a) photomicrograph of zircons from sample ZM36 (xpl) showing euhedral crystals (f.o.v. = ~700 μ m); (b) CL image of analysed zircons from sample ZM36 showing the location of analysed spots. Note the oscillatory zoning (f.o.v.= 1000 μ m).	223
Figure 4-131:	U-Pb concordia plot for zircon analyses of sample ZM36. Error ellipses are at 1 σ confidence level.	223
Figure 4-132:	(a) photomicrograph of zircons from sample CHL5 (xpl) showing euhedral crystals (f.o.v. = ~1200 μ m); (b) CL image of analysed zircons from sample CHL5 showing the location of analysed spots. Note the oscillatory zoning (f.o.v.= 1200 μ m).	225
Figure 4-133:	U-Pb concordia plot for zircon analyses of sample CHL5. Error ellipses are at 1 σ confidence level. Dashed ellipses represent two analyses that may represent an older xenocrystic component.	225
Figure 4-134:	Probability density plot of detrital zircon from the Mufulira Quartzite (Kanona Group, Copperbelt (data after Rainaud et al. (2003))). The histogram indicates the number of 100 \pm 5% concordant analyses for each bin of 20 M.y. (right axis), while the curves show the relative probability density of the analyses. The light grey curve denotes 95-105% concordant analyses, while the dark grey curve shows all analyses.	233
Figure 4-135:	Probability density plot (light grey curve) of xenocrystic zircon extracted from igneous lithologies in the Irumide belt. The histogram indicates the number of analyses for each bin of 25 M.y. (right axis). Only 100 \pm 10% concordant analyses are included.	237
Figure 4-136:	Combined probability density/histogram diagram showing emplacement ages of magmatic rocks in the Irumide belt and the Bangweulu block of northern Zambia, obtained in this study.	240

Figure 5-1	(a) QAP diagram indicating a granodioritic composition for the Kapiri Mposhi granite gneiss; (b) Diagram after Maniar and Picolli (1989), characterising the Kapiri Mposhi Granodiorite Gneiss as peraluminous251
Figure 5-2:	(a) binary diagram plotting the K ₂ O content versus Na ₂ O content of the Kapiri Mposhi Granodiorite Gneiss showing its sodic character; (b) Plot of SiO ₂ vs. ASI after Clarke (1992) suggesting S-type character of the Kapiri Mposhi Granodiorite Gneiss.....252
Figure 5-3:	Discrimination diagram after Whalen et al. (1987).....252
Figure 5-4:	Tectonic discrimination diagrams after Pearce (1996a) and Pearce et al. (1984a) suggesting a Volcanic Arc signature for the Kapiri Mposhi granite gneiss.....253
Figure 5-5	Chondrite normalised rare earth element distribution pattern for the Kapiri Mposhi granite gneiss (normalisation values after McDonough and Sun (1995)).....254
Figure 5-6	Primordial Mantle (P-mantle) normalised multi-element cationic distribution diagram (spidergram) for the Kapiri Mposhi granite gneiss (normalisation values after Sun and McDonough (1989)).....254
Figure 5-7	(a) QAP diagram indicating monzo-granitic composition of the Mkushi Gneiss and the Luwalizi Granite Gneiss; (b) Diagram after Maniar and Picolli (1989), characterising the Mkushi Gneiss and Luwalizi Granite Gneiss as peraluminous (symbols as in Figure 5-7 (a)).257
Figure 5-8	(a) Binary diagram plotting the K ₂ O content versus Na ₂ O for the Mkushi Gneiss and Luwalizi Granite Gneiss; (b) ASI versus SiO ₂ plot for the Mkushi Gneiss and Luwalizi Granite Gneiss. The plot shows that the granite gneisses have predominant S-type characteristics (symbols as in Figure 5-7 (a)).258
Figure 5-9	(a) Plot after Whalen et al. (1987), showing the Mkushi Gneiss in the Orogenic granite type and fractionated granite fields and the Luwalizi Granite Gneiss in the A-type field. Sample CC10, which is the youngest granite gneiss mapped as part of the Mkushi Gneiss (~1.95 Ga), also plots in the A-type field; (b) Plot of Y/Nb versus Yb/Ta after Eby (1990).....259
Figure 5-10	(a) Tectonic discrimination diagram after Pearce et al. (1984), depicting the Mkushi Gneiss with predominant volcanic arc / syn-collisional characteristics, and the Luwalizi Granite Gneiss towards the within plate field; (b) tectonic discrimination diagram after Pearce (1996) showing the Mkushi Gneiss and Luwalizi Granite Gneiss straddling syn-collisional, within plate, post-collisional and volcanic arc fields.....259
Figure 5-11	Chondrite normalised rare earth element distribution pattern for the Mkushi Gneiss and the Luwalizi Granite Gneiss (normalisation values after McDonough and Sun (1995)).....260
Figure 5-12	P-mantle normalised multi-element cationic plot for the Mkushi Gneiss and Luwalizi Granite Gneiss (normalisation values after Sun and McDonough (1989)).....261
Figure 5-13:	(a) QAP diagram indicating monzogranitic composition of the Mansa Granitoids (after Le Maître, (1989)); (b) total alkalis versus silica classification diagram of the Mansa Volcanics after Cox et al. (1979).....264
Figure 5-14:	(a) Diagram after Maniar and Picolli (1989), characterising the Mansa Granite (circles) and Volcanic (triangles) as peraluminous to metaluminous; (b) binary diagram plotting the K ₂ O content versus Na ₂ O for the Mansa Granite (circles) and Volcanic (triangles).....265

Figure 5-15:	ASI versus SiO ₂ plot for the Mansa Granites. The granites plot close to the I-type and S-type fields.....	265
Figure 5-16:	(a) Plot after Whalen et al. (1987), showing sample MA9 in the fractionated felsic granite field and sample MA2 in the A-type granite field; (b) Tectonic discrimination diagram after Pearce et al. (1984) depicting the Mansa Granite in the within plate field.....	266
Figure 5-17:	(a) Zr/Ti vs. Nb/Y diagram for the Mansa Volcanics (Pearce, 1996b) modified after Winchester and Floyd (1977); (b) Th-Ta-Hf discrimination plot after Wood (1980), showing the volcanics to plot in the field of volcanic arc / within-plate basalt (grey ellipse).	267
Figure 5-18:	CI chondrite normalised rare earth element distribution pattern for the Mansa Granites (normalisation values after McDonough and Sun (1995)). .	268
Figure 5-19:	Primordial Mantle normalised multi-element cationic distribution diagram (spidergram) for the Mansa Granites (normalisation values after Sun and McDonough (1989)).....	268
Figure 5-20:	Primordial Mantle normalised multi-element cationic distribution diagram (spidergram) for the Mansa Volcanics (normalisation values after Sun and McDonough (1989)).....	269
Figure 5-21:	(a) Total alkalis versus silica (TAS) diagram of the Irumide volcanics showing the classification fields proposed by Cox et al. (1979); (b) Normative Q'(F')-ANOR diagram after Streckeisen and Le Maitre (1979) for the Irumide volcanics.....	274
Figure 5-22:	(a) Ternary diagram of Al ₂ O ₃ – FeO _{tot} + TiO ₂ and MgO, with classifications fields after Jensen (1976), showing the Irumide volcanics; (b) AFM diagram of the Irumide volcanics showing the boundary between calc-alkaline and tholeiitic series after Kuno (1968)(dotted line) and Irvine and Baragar (1971)(dashed line)(symbols as in Figure 5-21).....	275
Figure 5-23:	(a) Diagram after Maniar and Picolli (1989), characterising the acid end-members of the Irumide volcanics as peraluminous, and the basic members as metaluminous; (b) binary diagram plotting the K ₂ O content versus Na ₂ O for the Irumide volcanics, clearly distinguishing the Katibunga basalts as sodic, and the Luswa River and Kachinga Tuff as predominantly potassic (symbols as in Figure 5-21).	276
Figure 5-24:	(a) Zr/Ti vs. Nb/Y diagram after Winchester and Floyd (1977), with revised fields after Pearce (1996b) showing the Irumide volcanics; (b) Ternary diagram of Th-Hf/3-Ta after Wood (1980) (VAB=Volcanic Arc Basalt; WPB=Within Plate Basalt; MM=MORB Mantle source, LC=Lower Crust; symbols as in Figure 5-21).	278
Figure 5-25:	(a) Binary plot of Th/Yb vs. Ta/Yb after Pearce (1983), showing proposed fields for ocean island arc (OIA), active continental margin (ACM), enriched mantle (EM), intraplate basalt (IPB), depleted mantle (DM) and mid-ocean ridge basalts (MORB); (b) Binary plot of Ce/Pb vs. Ce showing the fields of volcanic arc basalt and MORB + ocean island basalt + east African rift basalt (fields after Hoffman (1986) and Kampunzu and Mohr (1991)).....	279
Figure 5-26:	(a) Binary diagram of La vs. Th after Gill (1981), classifying the Katibunga Volcanics as predominantly orogenic andesites; (b) Binary diagram of V vs. Ti/1000 after Shervais (1982) demonstrating relatively high Ti/V ratios for the Katibunga Volcanics.	280

Figure 5-27:	Chondrite normalised rare earth element distribution pattern for the Katibunga Volcanics (normalisation values after McDonough and Sun (1995)). Light grey patterns are samples KV1 and KB2, excluded from interpretations.	281
Figure 5-28:	Chondrite normalised rare earth element distribution pattern for the Ilondola Volcanics (normalisation values after McDonough and Sun (1995)).....	281
Figure 5-29:	Chondrite normalised rare earth element distribution pattern for the Kachinga Tuffs (normalisation values after McDonough and Sun (1995)).....	282
Figure 5-30:	Chondrite normalised rare earth element distribution pattern for the Luswa Volcanics (normalisation values after McDonough and Sun (1995)).	282
Figure 5-31:	MORB normalised rare earth element distribution pattern for the Katibunga Volcanics (normalisation values after Pearce (1996b)).	283
Figure 5-32:	Primordial mantle normalised multi-element cationic plot for the Katibunga Volcanics (normalisation values after Sun and McDonough (1989)).	283
Figure 5-33:	Primordial mantle normalised multi-element cationic plot for the Ilondola Volcanics (normalisation values after Sun and McDonough (1989)).	284
Figure 5-34:	Primordial mantle normalised multi-element cationic plot for the Kachinga Tuff (normalisation values after Sun and McDonough (1989)).	284
Figure 5-35:	Primordial mantle normalised multi-element cationic plot for the Luswa River Volcanics (normalisation values after Sun and McDonough (1989))....	285
Figure 5-36:	QAP diagram indicating a monzo-granitic composition for the Lukamfwa Hill Gneisses (diamond), the Lubu Granite Gneiss (square) and the Musalango Gneiss (triangle).	290
Figure 5-37:	(a) Diagram after Maniar and Picolli (1989), characterising Group IV Granitoids as peraluminous to metaluminous; (b) binary diagram plotting the K ₂ O content versus Na ₂ O content for Group IV granite gneisses, showing the potassic character of the suite. Symbols as in Figure 5-36.	290
Figure 5-38:	(a) Aluminium Saturation Index versus SiO ₂ diagram showing Group IV Granite Gneisses to range from A-, I- to S-type granitoids (Clarke, 1992); (b) Plot after Batchelor and Bowden (1985) suggesting syn- to post-collisional setting for Group IV granitoids. Symbols as in Figure 5-36.....	291
Figure 5-39:	(a) binary plot of Zr+Nb+Ce+Y versus FeO*/MgO after Whalen et al. (1987) showing the A-type affinity of Group IV granitoids; (b) Triangular plot of Y-Nb-Ce after Eby (1992), suggesting that the majority of Group IV granite gneisses are orogeny-related A-type granitoids. Sample ML2 (triangle) plots well into the anorogenic granitoid field, having significantly higher Nb content. Symbols as in Figure 5-36.....	292
Figure 5-40:	Plot of Y/Nb versus Ce/Nb after Eby (1990), suggesting crustal magma sources for Group IV granitoids. Note that the Lubu Granite Gneiss plots closer to an ocean island basalt source commonly associated with anorogenic granitoids. Symbols as in Figure 5-36.....	292
Figure 5-41:	Tectonic discrimination diagrams after Pearce (1996a) and Pearce et al. (1984a) suggesting within-plate and post-collisional signatures for Group IV granite gneisses. Symbols as in Figure 5-36.	293
Figure 5-42:	Chondrite normalised rare earth element distribution pattern for Group IV granite gneisses (normalisation values after McDonough and Sun (1995)). Light grey samples are samples SI/98/2A and SI/98/2B, which show extremely high fractionation trends.....	294

Figure 5-43:	Primordial Mantle normalised multi-element cationic distribution diagram (spidergram) for Group IV granite gneisses (normalisation values after Sun and McDonough (1989)).	295
Figure 5-44:	Ocean Ridge Granite normalised multi-element plot for Group IV granite gneisses (normalisation values after Pearce et al. (1984)).	295
Figure 5-45:	QAP diagram for Group V granitoids in the Irumide belt.	302
Figure 5-46:	(a) Diagram after Maniar and Picolli (1989), characterising Group V granitoids as peraluminous to metaluminous; (b) binary diagram plotting the K ₂ O content versus Na ₂ O content for Group V granitoids, showing the potassic character of the suite.	303
Figure 5-47:	(a) Aluminium Saturation Index versus SiO ₂ diagram showing Group V granitoids to range from A-, I- to S-type granitoids (Clarke, 1992); (b) Plot after Batchelor and Bowden (1985) suggesting syn- to post-collisional setting for Group V granitoids.	303
Figure 5-48:	(a) binary plot of Ga*10000/Al versus Zr after Whalen et al. (1987) showing the A-type affinity of a large fraction of Group V granitoids; (b) Triangular plot of Y-Nb-Ce after Eby (1992), suggesting that the majority of Group V Granite Gneisses are orogeny-related A-type granitoids (filled diamonds are data points classified as I- and S-type in the plot of Whalen et al. (1987), open circles are those classified as A-type).	304
Figure 5-49:	Plot of Y/Nb versus Yb/Ta after Eby (1990), suggesting various crustal magma sources for Group V granitoids.	305
Figure 5-50:	Tectonic discrimination diagrams after Pearce (1996a) and Pearce et al. (1984a) suggesting syn- and post-collisional setting for Group V granitoids.	306
Figure 5-51:	Trace element – SiO ₂ variation diagram for Group V granitoids	306
Figure 5-52:	REE plot for Group V granitoids (normalisation values after McDonough and Sun (1995)).	307
Figure 5-53:	Multi-cationic SPIDER plot for Group V granitoids (normalisation values after Sun and McDonough (1989)).	308
Figure 5-54:	Ocean Ridge Granite normalised multi-element plot for Group V granitoids (normalisation values after Pearce et al. (1984)).	309
Figure 5-55:	Differentiation trends (Harker diagrams) for Group II, Group IV and Group V granitoids in the Irumide belt.	311
Figure 5-56:	Differentiation trends (Harker diagrams) for Group II, Group IV and Group V granitoids in the Irumide belt.	312
Figure 5-57:	Differentiation trends (Harker diagrams) for Group II, Group IV and Group V granitoids in the Irumide belt and log scale diagram showing the relationship between Zr and Hf. The lines on the Zr vs. SiO ₂ diagram are trends through the maximum Zr for each suite. The grey zone defines the silica-content range corresponding to the maximum Zr values.	313
Figure 5-58:	Relationships between Ba and Eu and Sr and Eu in Group II, Group IV and Group V granitoids.	315
Figure 6-1:	T _{chur} model age versus crystallisation age for granitoids and volcanics in the Irumide belt and Bangweulu block, showing the predominantly reworked character of all igneous suites (t=U-Pb SHRIMP emplacement age).	329
Figure 6-2:	Plot of initial ε _{Nd} isotopic compositions, relative to that of CHUR (Wasserburg et al., 1981) versus U-Pb SHRIMP zircon crystallisation age. The grey area is the inferred growth envelope modelled on the basis of	

	present day ϵ_{Nd} values for the most juvenile and most ancient end-members.	330
Figure 7-1:	Mesoproterozoic tectonic provinces of central and southern Africa. (CK=Choma-Kalomo block; IRUMIDE=Irumide belt; KIBARAN=Kibaran belt; LURIO=foreland to the Lurio belt; NaB=Natal belt; NB=Namaqua belt; NW=northwest Botswana rift; SS=Sinclair sequence; RI=Rehoboth inlier. Question marks indicate uncertain position or continuation of inferred boundaries or suture.	332
Figure 7-2:	Overview of Mesoproterozoic terrains in Zambia. Small squares denote the location of the Serenje map sheet, and the Muyombe map sheet discussed in text. BB=Bangweulu block CI=Chewore Inliers; CT=Chipata Terrane; IB=Irumide belt; LT=Luangwa Terrane; NT=Nyimba Terrane; PST=Petauke-Sinda Terrane; RG=Rushinga Group; UG=Umkondo Group. Box indicates area of Figure 7-3.	333
Figure 7-3:	Simplified geological map of the southeastern part of the Irumide belt in eastern Zambia, indicating tectonic terranes (black lettering) discussed in the text: ST=Serenje Terrane, LT=Luangwa Terrane, NT=Nyimba Terrane, PST=Petauke-Sinda Terrane, CT=Chipata Terrane. Towns indicated with white lettering: R=Rufunsa, S=Serenje, L=Luangwa, N=Nyimba, P=Petauke and C=Chipata. Possible correlatives of the Muva Supergroup are labelled.	346
Figure 7-4:	One possible configuration of the Rodinia continent at ca. 1.02 Ga, showing the number of palaeomagnetic poles per landmass, which satisfy at least four of the seven criteria of reliability of Van der Voo (1990). The relative position of the continental blocks is taken after Pisarevski et al. (2003) and Pisarevski and Natapov (2003). In=India; Ka=Kalahari; Ma=Mawson; Aus=Australia; T=Tarim; Sc=South China; Si=Siberia; Lau=Laurentia; Rp=Rio de la Plata; P=Pampean terrane; Am=South American cratons; Gr=Greenland; R=Rockall; B=Barentsia; O=Oaxaquia; Ba=Baltica; WA=West Africa; Co=Congo; Sf=Saõ-Francisco.	353
Figure 7-5:	Various simplified schematic models for Rodinia, after assembly. The approximate position of the Irumide and Grenville belt are shown in black (M=Madagascar; other abbreviations as in Figure 7-4)(Hoffman, 1991; Dalziel, 1997; Weil et al., 1998; Li et al., 2004).	354
Figure 9-1	Setup for LST heavy liquid separation (a similar setup is used for any heavy liquid separation)	365
Figure 10-1	Simplified diagram of the SHRIMP II (adapted from Australian Scientific Instruments documentation)	370
Figure 10-2	Geometry of a typical SHRIMP spot. Note the sharply defined crater edge and the flat bottom of the pit (picture taken from Australian Scientific Instruments documentation).	371
Figure 11-1	Diagram of a Quadrupole Induced Coupled Plasma Mass Spectrometer (ICP-MS) system.	384
Figure 12-1	Schematic representation of the sample holder and casing for digestion of the sample in hydrofluoric acid (HF).	401
Figure 12-2:	Schematic representation of the calibration of cation exchange columns used to separate Rb, Sr and REE in this study. Rb is collected in 2ml after 7ml wash in 2M HCl. Sr is collected in 7ml after 5ml wash in 4M HCl. REE are collected in 5ml of 6M HCl straight after the Sr peak.	403

Figure 12-3:	Schematic representation of the calibration of Kel-F / HDPEP column # 1 used in the study to separate Nd from Sm.....	404
Figure 12-4:	Schematic representation of the calibration of Kel-F / HDPEP columns # 2, #3 and #4 used in the study to separate Nd from Sm.....	404
Figure 12-5	Triple Rhenium filament configuration used for Sm, Nd and Rb Thermal Ionisation mass Spectrometry (TIMS)	405
Figure 12-6	Single Tantalum (1Ta) filament configuration used for TIMS analysis of Sr.	405

1 CHAPTER 1: Introduction

1.1 Regional geological setting of the study area

The regional geology of the African continent is traditionally subdivided into three main Proterozoic orogenic cycles (Holmes, 1951), which are expressed in a series of mobile belts enclosing stable Archaean and Palaeoproterozoic crustal blocks. In sub-Saharan Africa, Archaean cratonic nuclei include the Angola-Kasai craton, the Tanzania craton and the Zimbabwe and Kaapvaal cratons welded along the Archaean Limpopo belt (Clifford et al., 1970; Petters, 1991)(Figure 1-1). These Archaean nuclei were further enlarged and amalgamated following Palaeo- and Mesoproterozoic tectonism into two stable blocks called the Congo craton in the north, including the Angola-Kasai craton, the Tanzania craton and the Palaeoproterozoic Bangweulu block of Zambia, and the Kalahari craton in the south, including the Zimbabwe and Kaapvaal cratons. The three orogenic cycles that link these cratons in sub-Saharan Africa are termed the Eburnian, Kibaran and Pan-African. The Eburnian is the oldest cycle and comprises orogenic activity between 2.2 and 1.8 Ga, and in the south-central region of Africa includes the Ubendian-Usagaran belts of Zambia and Tanzania and the Kheis and Magondi belts of Namibia, South Africa, Botswana and Zimbabwe (Hanson, 2003). This event is recognised globally, and may have contributed to the amalgamation of continental blocks to form the proposed supercontinent of Hudsonland or Columbia (Meert, 2002; Zhao et al., 2002; Pesonen et al., 2003). The Kibaran cycle is named after the central African Kibaran belt and spans orogenic activity between 1.4 and 1.0 Ga. It is reflected in a series of orogenic belts, which include the Kibaran belt of the Democratic Republic of Congo (DRC), Uganda, Burundi, Rwanda and Tanzania, the Irumide belt of Zambia and Malawi, the Choma-Kalomo block of Zambia, the Mesoproterozoic basement to the northwest Botswana rift of Botswana, the Rehoboth inliers and Sinclair sequence of Namibia, the Namaqua belt of Namibia and South Africa, the Natal belt of South Africa, the foreland of the Lurio belt of Mozambique (also termed proto-Lurio (Sacchi et al., 2000) or Nampula (Pinna et al., 1993) to denote the Mesoproterozoic part) and rocks in the northwestern part of

Mozambique. This peak in orogenic activity is recognised worldwide, often referred to as the Grenvillian, and has been linked to the possible amalgamation of the Rodinia supercontinent (McMenamin and McMenamin, 1990; Hoffman, 1991). The last phase of major Precambrian orogenic activity is known as the Pan-African (Kennedy, 1964; Hoffman, 1991), and includes orogenic belts of the East African Orogen (Stern, 1994) and Damara-Lufilian-Zambezi Orogen (Johnson et al., in press). In the East, the East African Orogen runs from Sudan southwards to South Africa, and is believed to continue further into Antarctica (Stern, 1994; Jacobs et al., 1998). In the West, the Damara-Lufilian-Zambezi Orogen traverses the continent between the Congo and Kalahari cratons and comprises the Zambezi belt of Zimbabwe and Zambia, the Lufilian belt of Zambia and DRC, and the Damara belt of Botswana and Namibia. These belts host some of the world's largest base-metal provinces, including the central African Copperbelt. In Zambia, the sedimentary successions of the Copperbelt form the Katanga Supergroup, which was deposited between 0.88 – 0.57 Ga. The supracrustals within the Damara-Lufilian-Zambezi Orogen, together with those within the Neoproterozoic Saldania belt of South Africa, were previously connected to supracrustal sequences within the Brasiliano belt of South America, and formed the succession overlying the West Africa – Amazonia – Rio de la Plata mega-continent of Trompette (1994).

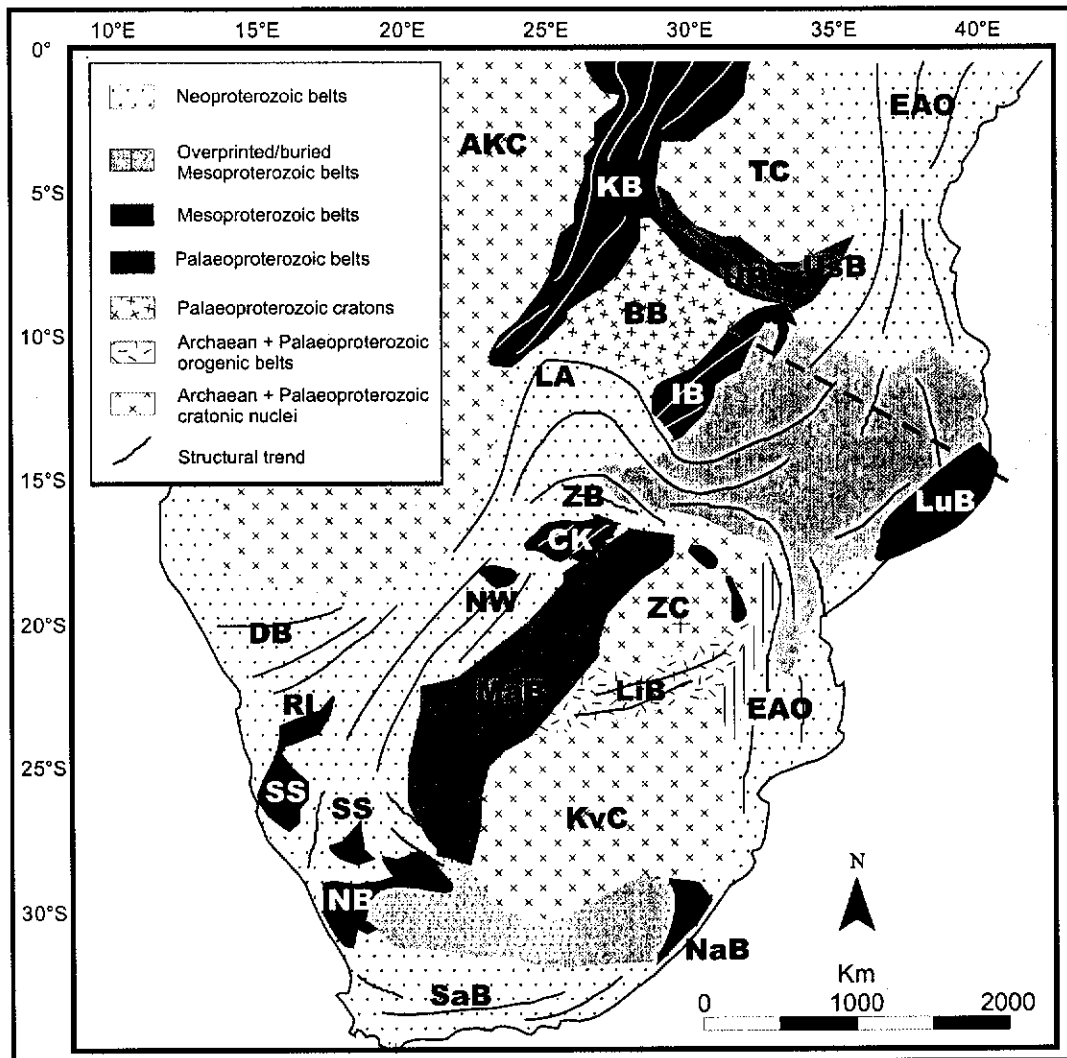


Figure 1-1: The tectonic provinces of central and southern Africa. (AKC=Angola-Kasai craton; BB=Bangweulu block; CK=Choma-Kalomo block; DB=Damara belt; EAO=East African Orogen; IB=Irumide belt; KB=Kibaran belt; KVC=Kaapvaal craton; LA=Lufilian belt; LiB=Limpopo belt; LuB=foreland to the Lurio belt; MaB=Magondi belt; NaB=Natal belt; NB=Namaqua belt; NW=northwest Botswana rift; SS=Sinclair sequence; RI=Rehoboth inlier; SaB=Saldania belt; TC=Tanzania craton; UB=Ubendian belt; UsB=Usagaran belt; ZB=Zambezi belt; ZC=Zimbabwe craton. Dashed line indicates the approximate position of the cross section by Daly (1986b)(Figure 1-3)

1.2 A summary of previous work on the Irumide belt

The Irumide belt is a northeast-southwest trending orogenic belt bound to the north by the Palaeoproterozoic Bangweulu block, to the northeast by Pan-African shear zones within the Palaeoproterozoic Ubendian belt, to the southwest by the Neoproterozoic Zambezi belt, and to the west by the Neoproterozoic Lufilian belt (Figure 1-2). To the east and southeast, the Irumide belt is overprinted by Neoproterozoic tectonism related to the EAO and the Zambezi belt. The Irumide belt comprises basement gneisses, overlain by a metasedimentary cover sequence, both of which were folded along northeast-trends during a main tectonic event (the Irumide orogeny). Irumide tectonism displaced the sequence onto the Palaeoproterozoic foreland of the Bangweulu block and reworked basement lithologies. The basement and cover sequences are intruded by various generations of granitoids, ranging from deformed pre-Irumide, to Irumide-aged syntectonic and post-Irumide early Neoproterozoic granitoids.

The Irumide belt was first recognised as a separate tectonic entity by Ackermann (1936; 1960) and Ackermann and Forster (1960), who described the Irumide belt as a northeast trending terrain of granites and gneisses, overlain by a sequence of quartzites and pelites they termed the Muva system. The basement to the Irumide belt was called the Mkushi Gneiss, a polymetamorphic granitic complex of presumed Palaeoproterozoic age. Stillman (1965c) divided the Muva into two series of metasedimentary rocks, the older Musofu Formation and younger Kalonga Formation. He retained the definition of the Mkushi Gneiss of Ackermann (1936; 1950) and ascribed all granitoids and gneisses to the Mkushi Gneiss complex. Stillman (1965c) made the subdivision into two metasedimentary series predominantly because of observed differences in metamorphic grade, and his recognition of older north-south trending structures exclusively in the older Musofu series and underlying Mkushi Gneiss. He therefore introduced an older Tumbeide event, recognised in north-south trending folds within the Musofu Formation, and the younger Irumide event, imparting the dominant northeast-southwest grain of the belt. Subtle lithological differences between the metasedimentary sequences were noted by Stillman (1965c) to be in support of his subdivision, and include the observation

that the Musofu Formation comprises very pure quartzites with little or no heavy minerals, while the younger Kalonga Formation contains quartzites with tourmaline, muscovite and biotite. A whole rock Rb-Sr date of 1693 ± 50 Ma on an undeformed aplite cutting the Mkushi Gneiss in the Mkushi map sheet (box 1 on Figure 1-2) was interpreted to represent a lower age limit to relict northerly (Tumbide) structures that affected the Mkushi Gneiss and the Musofu Formation (Ng'ambi et al., 1986). Note that in this thesis, the term “date” is used where geological significance, attributed or not, is tenuous at best, where “age” is used in cases where clear geological significance can be attached to the date. The gneisses themselves were dated (whole rock Rb-Sr) by Ng'ambi et al. (1986) at 1777 ± 89 Ma, but this date has been superseded by a zircon U-Pb Sensitive High mass Resolution Ion MicroProbe (SHRIMP) crystallisation age of 2049 ± 6 Ma (Rainaud et al., 2002). Zircons from undeformed aplite dykes intruding the Mkushi Gneiss, such as the one dated by Ng'ambi et al. (1986), have yielded U-Pb SHRIMP crystallisation ages on cores of 2036 ± 22 Ma and rim ages of 1088 ± 159 Ma (Rainaud et al., 2002). The validity and geological meaning of the reported Rb-Sr date of Ng'ambi et al. (1986) is therefore highly questionable. The ages of 1088 ± 159 Ma were interpreted by Rainaud et al. (2002) to indicate a magmatic episode at that time, rather than peak metamorphic conditions. The Musofu-Kalonga division was adopted by geologists of the Zambian Geological Survey (Smith, 1965; Moore, 1967b), but later discarded as it was largely based on differences in metamorphic grade, with no significant lithostratigraphic differences (Mapani, 1992; De Waele and Mapani, 1998; 2002). Daly et al. (1984) reinterpreted the “older” north-south fabrics in the succession ascribed to the Musofu Formation as lateral ramps developed during Irumide deformation.

Fitches conducted PhD work in the far northeast section of the belt (Fitches, 1968b), known as the Mafingi Hills area (box 3, Figure 1-2). This region is located at the intersection of three orogenic belts, namely the Palaeoproterozoic Ubendian belt, the Mesoproterozoic Irumide belt, and the Neoproterozoic EAO. Fitches (1968b) demonstrated that the Mafingi Group metasedimentary rocks recognised in the far northeast of the Irumide belt could be correlated with metasedimentary sequences farther southwest in the Irumide belt, based on general lithostratigraphic similarities, and deformation styles. In the Mafingi Hills area, Fitches (1968b) reported K/Ar

dates of 1330 ± 60 Ma on hornblende from an amphibolite belonging to the Ubendian belt underlying the Mafingi Group, 1145 ± 60 Ma for arfvedsonite from a lamprophyre dyke intruding and deformed with the Mafingi Group, and 1120 ± 30 Ma for a biotite from the Nthonga granite which intrudes the Ubendian basement and is unconformably overlain by the Mafingi Group. All these lithologies were affected by Irumide tectonism, and Fitches interpreted the apparent ages between 1.33 and 1.12 Ga to bracket the timing of the Irumide event (Fitches, 1971).

A comprehensive study was conducted by Daly (1986a, b), focusing on the tectonic and thermal evolution of the Irumide belt. His work was centered on the northeastern 1:100,000 map sheets of Chinsali, Mutangoshi Hills, Isoka and Mulilansolo, but included structural traverses west of Chinsali, the Luongo fold-and-thrust zone east of Mansa, the Serenje and Mkushi areas in the southwest and the far northeast termination of the belt near the border with Tanzania (Figure 1-2). Daly (1986b) considered the Irumide belt a zone where intracontinental rifting, accompanied by the deposition of 10 kilometers of shallow water sediments, was followed by a contractional episode between 1.10 and 1.05 Ga causing northwest-directed thrusting and high-temperature (HT)-medium-pressure (MP) regional metamorphism. Crustal melting and the emplacement of syn- and late-tectonic granitoids accompanied peak metamorphic conditions. Despite the limited geochronological data, Daly (1986b) believed the entire Irumide belt to be underlain by older basement, and interpreted the large-scale horizontal displacements, which he estimated to total 110 kilometers, to be the result of thin-skinned thrust tectonics above a regional scale basal detachment. Daly (1986b) argued that this substantial contraction was bound to the north by the Mugesse shear zone, believed to have accommodated the strain by northwest-southeast transcurrent movement (Figure 1-2). Mesoproterozoic activity along the Mugesse shear zone has since been supported by $^{207}\text{Pb}/^{206}\text{Pb}$ zircon evaporation ages between 1.12 and 1.09 Ga for syntectonic granitoids within strike-slip shear zones of the Ubendian belt (Ring, 1999) and the occurrence of Mesoproterozoic pull-apart basins within the Ubendian belt (Klerkx et al., 1998).

Similarities in northwest/southeast tectonic transport direction and the age of deformation (~ 1100 Ma) in northwest Mozambique and southern Malawi were used

to propose that rocks in southern Malawi and northwestern Mozambique (Mozambican cycle of Pinna et al. (1993)) and the Irumide belt could be part of a single orogenic system (Daly, 1986b). In Daly's model (Daly, 1986b), the proposed Lurio and Niassa microplates were caught up in a continental collision between the "Indo-Malagash Plate" and the "Proto-Africa Plate" (Figure 1-3). The bimodality in tectonic transport directions along a transect from the Irumide belt in the northwest to the Lurio belt in the southeast (for location see Figure 1-1) fits well with the different thrust directions envisaged to result from this complex collision zone (Figure 1-3). The ultimate driving force for deformation in the Irumide belt was interpreted to be a far field effect of a plate tectonic collision some distance away to the southeast. It must be noted that it is unlikely that the Indo-Malagash Plate was the colliding continental block as suggested in Daly's model, as it is generally believed that the Indian and African plates collided at ca. 600-500 Ma along the EAO (Meert and Van der Voo, 1995; Rogers et al., 1995; Shackleton, 1996; Meert et al., 1997; 1997; Paquette and Nédélec, 1998; Bauer and Jacobs, 2001; Meert, 2003).

The thermotectonic history of the northeastern section of the Irumide belt was studied using limited bulk zircon U-Pb work, a series of whole-rock Rb-Sr analyses and some K-Ar and Ar-Ar work on selected minerals and rock types throughout the northeastern region, and near the sheared contact of the Luongo fold-and-thrust zone. In the northeastern section of the Irumide belt (box 2, Figure 1-2), Daly (1986b) recognised the existence of several igneous suites, intruding both the basement and the cover sequences. A sample of the basement (the Mwambwa River Gneiss) yielded a poorly constrained Rb-Sr whole-rock errorchron date of 1804 ± 170 Ma, based on regression of 9 datapoints. A regression of the 7 data points with the highest $^{87}\text{Rb}/^{86}\text{Sr}$ ratios, however, yielded a date of 1100 ± 252 Ma, which Daly (1986b) interpreted to reflect isotopic resetting at around 1100 Ma, related to Irumide tectonism. Daly (1986b) reported a 12-point whole-rock Rb-Sr date of 1407 ± 34 Ma for the Mutangoshi Gneissic Granite near Chinsali, and interpreted this granite gneiss to form part of a bimodal magmatic suite, signalling crustal thinning during an early extensional event. A nine point whole-rock Rb-Sr date of 1005 ± 71 Ma for a post-Irumide granite, a less reliable whole-rock Rb-Sr date of 947 ± 89 Ma and a U-Pb bulk zircon crystallisation age on the Lufila Granite of 970 ± 5 Ma were inferred to constrain a post-tectonic magmatic phase (Daly, 1986b). Daly (1986b) also reported

four $^{40}\text{Ar}/^{39}\text{Ar}$ plateau ages for hornblende collected from amphibolites. The ages are reported without errors and range from 1040 to 935 Ma; they were interpreted to date post-tectonic cooling below $\sim 500 \pm 50^\circ\text{C}$ after the Irumide orogeny. The data also indicate that Irumide rocks were largely unaffected by any post-Irumide thermal event exceeding the closure temperature of $\sim 500 \pm 50^\circ\text{C}$ for hornblende (McDougall and Harrison, 1999). K/Ar data reported by Vail (1968) for the area around Serenje do however indicate a post-Irumide thermal overprint above $280 \pm 40^\circ\text{C}$, with biotite K/Ar cooling ages ranging from 567 ± 24 to 495 ± 20 Ma, and partial thermal overprints above $350 \pm 50^\circ\text{C}$, with muscovite dates ranging from 886 ± 36 to 755 ± 30 Ma.

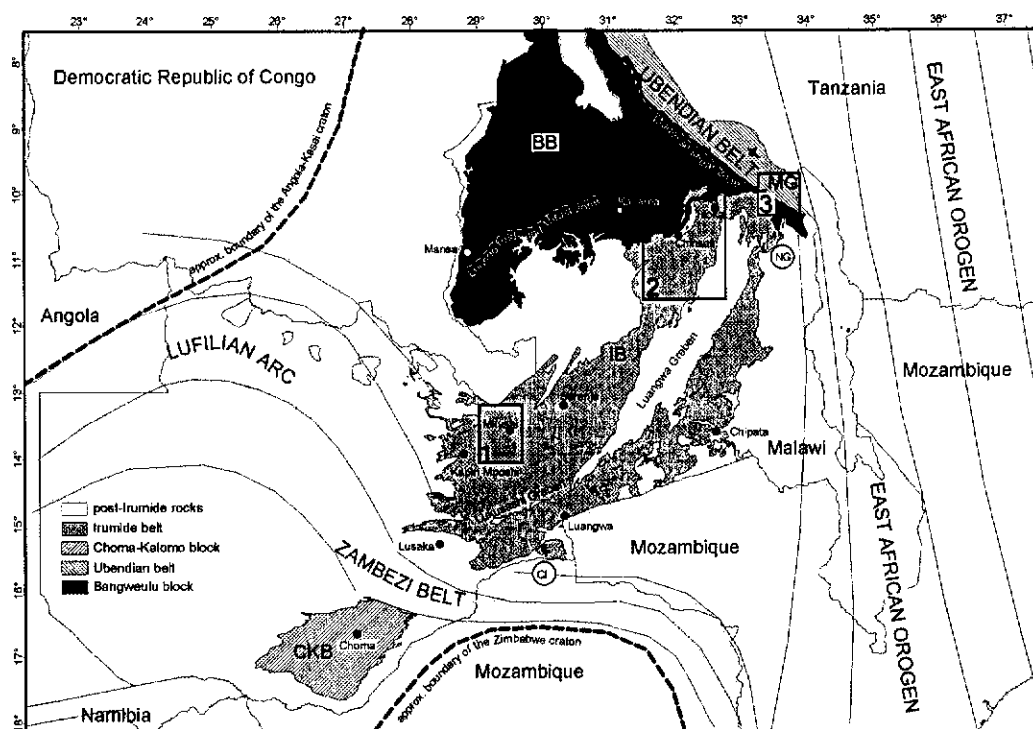


Figure 1-2: Overview map showing the location of the Irumide belt (IB) with respect to the Bangweulu block (BB), Choma-Kalomo block (CKB) and various orogenic belts in the region (MG=Mafingi Group; CI=Chewore Inliers; NG=Nyika Granite; boxes indicate the map sheets mapped by Stillman (1965c, box 1), Daly (1995b; 1995a, box 2) and Fitches (1971, box 3)).

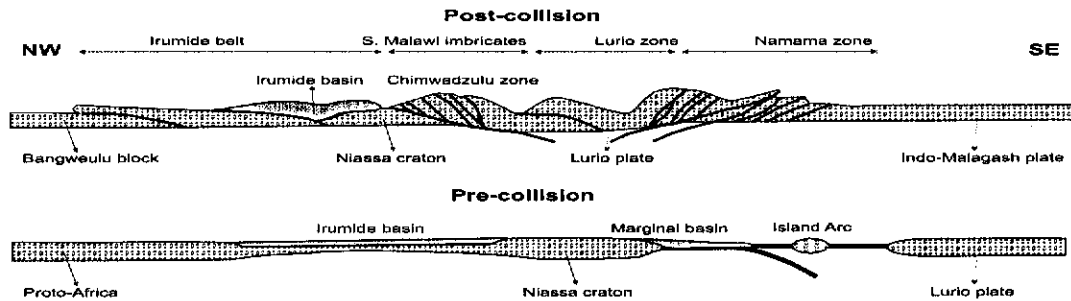


Figure 1-3: Schematic crustal cross-section through the Irumide belt into southern Malawi and northwestern – central Mozambique (after Daly, 1986b). The approximate position of the section is indicated on Figure 1-1.

1.3 Aims of this study

In this study, an attempt is made to resolve a series of longstanding and important questions regarding the Irumide belt. These questions include:

- What is the timing of events in the Irumide belt and in particular, what is the age and extent of the basement, the age of sedimentation, the age of magmatism and the age of peak metamorphism?
- What is the tectonic setting of the Irumide belt?
- How does the Irumide belt fit into the regional Mesoproterozoic tectonic framework?

In order to correctly address these questions, there was a need to collect data from a wide area, in contrast to many previous studies that focused on small sections of the Irumide belt alone. Samples were therefore collected along the entire strike length of the Irumide belt to check for along-strike consistency. Fieldwork during the second year was directed to some degree towards constraining the extent of units identified by geochronology of sample suites collected in the first season.

This thesis deals in particular with the most contentious issue enshrouding our knowledge of the Irumide belt, namely its geochronological history. Previous geochronological studies were largely based on the whole-rock Rb-Sr technique, which often produces results that are difficult to interpret, especially in high-grade metamorphic terranes where partial open-system behaviour of the Rb-Sr isotope

system is widely documented (Dickin, 1995). The dating technique employed is based on the U-Th-Pb decay system, as applied to the mineral zircon. Because of the fact that zircon from polymetamorphic terranes can contain complex growth zones of differing age, thereby providing a record of the geological history of the area, the Sensitive High mass Resolution Ion Microprobe (SHRIMP) technique was applied, which allows the analysis of small volumes of zircon sampled from within single growth zones. The rationale for this approach is further discussed at the beginning of Chapter 4.

1.4 Methodology

During the course of this research, a range of techniques have been employed to obtain the data presented. The following sections describe the methodologies applied, starting from the fieldwork carried out in Zambia, down to the various laboratory analyses conducted as part of this study. These methods are only briefly described here, with a detailed account of methodologies presented in Appendices as indicated in the text.

1.4.1 Fieldwork planning

The area covered in this study is the area of the Irumide belt to the northwest of the Luangwa and Lukusashi grabens (Figure 1-2), and as such does not include the southeastward continuation of the belt in eastern Zambia and in Mozambique, where Pan-African structures overprint the Irumide grain. Two field seasons were planned based on existing 1:100000 scale geological maps covering the Irumide belt of Zambia. Traverses were prepared along motorable tracks to gain access to areas of interest, and, where necessary, foot-traverses were planned to reach remote locations not accessible by car. In many cases, sample localities were selected from the 1:100,000 geological maps, using structural measurements on the maps as an indication of outcrop. In areas of good exposure, especially along stratigraphic successions, or across geological or structural contacts, sections were traversed on foot. All observations were recorded in a field notebook, and cross-referenced to

sample and observation localities on the geological base maps. No attempt was made to map specific areas in detail, but modifications to the existing maps at 1:100,000 scale were implemented where necessary.

1.4.2 Sampling method

This study of the Irumide belt was accompanied by sampling of key lithologies of all different magmatic suites recognised based on field relations. Samples from the main metasedimentary groups of the region, including undeformed sediments on the Bangweulu block and deformed metasedimentary rocks in the Irumide belt, were also included in the study. Depending on the anticipated analyses to be conducted on each given sample, sampling volume and methodology were adapted for each locality. All samples were extracted from fresh outcrop, using a large hammer and brute force. The resultant blocks were shaped using a geological hammer, labelled and bagged. The sample locality, taken from a handheld Global Positioning System (GPS) unit, was recorded in the notebook and plotted on the geological map. A list of samples collected during this study is given in Appendix A. Some samples were oriented before extraction, using a Brunton geological compass. In cases where only a thin section was expected, the extracted sample weighed anything between 0.2 to 1.0 kg. For magmatic rocks, on which geochronology, geochemistry and possible isotope analyses were anticipated, the weight of rock taken ranged between 1 and 10 kg. In general, the size of the sample increased with the grain size of the rock. For sedimentary rocks, for which a detrital provenance study was planned, a sample of at least 5 kg was taken.

1.4.3 Sample preparation

In the first year (2001), a portion of the collected samples was cut for thin section preparation, while the remainder was crushed and washed prior to shipping, with any further preparations being conducted in Perth. For samples collected in 2002, more substantial preparations were done in Lusaka to minimise shipping fees. Preparations conducted in Lusaka included crushing, washing, pulverising, and

mineral separation. Although several stages of sample preparation were done in different laboratories (Perth and Lusaka), using slightly different instrumentation, the methodologies employed were identical. The following sections briefly describe the methodologies employed, while the reader is referred to various Appendices (as indicated in the text) for a more complete description of the techniques.

1.4.3.1 Preliminary crushing

Upon return from the field, all samples were crushed in a large jaw-crusher at the School of Mines in Lusaka. Prior to each sample, the crusher and receptacles were cleaned with compressed air. The crushing system was set to a size of roughly 20 mm. To avoid contaminants and dust resulting from the crushing operation, the resulting chips were blown with compressed air and washed over a 2 mm mesh using tap water, and then rinsed with deionised water. Only chips larger than 2 mm were kept for further processing. The washed chips were air dried on a clean piece of paper. For samples collected in the first field season (2001), the chips were packed in plastic bags, labelled, and shipped in cardboard boxes to Perth. For samples collected in the second field season (2002), the dried samples were further personally prepared in the laboratories of the School of Mines in Lusaka. Full details on the crushing and washing of samples are given in Appendix B.

1.4.3.2 Mineral separation

During the course of this study, geochronological work was carried out on zircon extracted from bulk rock samples. In order to extract the zircon from the samples, traditional mineral separation techniques were employed, including heavy liquid (density) and magnetic separation. The reader is referred to Appendix B for detailed descriptions of the procedures.

1.4.3.3 Preparation of whole rock powder

To minimize sampling effects, the washed rock chips were first crushed and sieved over 300 μm mesh and a representative fraction of the rock sample collected from this powder. The mill was cleaned using acetone and lint free paper towels, and then pre-contaminated with 50 grammes of sample. The mill was then cleaned using paper towels and a final 50 grammes ground to a fine powder for 3 minutes. From this fine powder, a representative fraction was extracted and placed in a sample bottle. For the purpose of whole-rock geochemistry, the finely ground powder was used directly. For Isotope Dilution-Thermal Ionisation Mass-Spectrometry (ID-TIMS or TIMS), 20 grammes of whole-rock powder was placed in an agate mortar and pestle, mixed with 100% pure ethanol, and manually ground fine prior to digestion in Teflon bombs (see Appendix E).

1.4.4 SHRIMP dating

U-Pb zircon geochronology makes up the primary dataset collected for this study. Data collection was aimed at constraining the geological history of the Irumide belt including the timing of emplacement of various plutonic rocks, timing of metamorphism and the age of detrital zircon in sedimentary rocks. Throughout this study, the U-Th-Pb isotopic system was used for dating of zircons extracted from rock samples. Isotopic compositions were measured on the Perth Consortium SHRIMP II at Curtin University of Technology. A brief overview of SHRIMP II instrumentation is given in Appendix C, along with an overview of the analytical procedures followed during data collection and data reduction. Critical points of zircon U-Th-Pb geochronology, pertaining to the methodologies followed during this study, are discussed at the start of Chapter 4.

1.4.5 Major and trace element geochemistry

In an attempt to help characterise the various magmatic suites in the Irumide belt, whole-rock geochemistry was conducted on samples from all igneous suites. The geochemical data also help constrain possible geotectonic settings and petrological processes active during emplacement. The geochemical data were complemented with Sm-Nd isotopic studies on a small subset of the samples, to help constrain the extent of crustal reworking in the generation of the magmatic suites.

Crushed powders were processed for whole rock chemistry using an oven (overnight at $\sim 105^{\circ}\text{C}$) to determine unbound H_2O and a furnace (overnight at $\sim 1050^{\circ}\text{C}$) to determine total loss on ignition (LOI = carbonates and organic matter). Hydrofluoric acid based solution followed by inductively coupled plasma – mass spectrometry (ICP-MS) analysis was applied for trace elements, and lithium tetraborate fusion followed by ICP-optical emission spectrometry (OES) for major element analysis. Details on the methodologies are given in Appendix D.

1.4.6 Isotope geochemistry

During this study, several samples, which had yielded a reliable zircon U-Pb crystallisation age, were selected for further isotope work. Using the ID-TIMS method, samarium and neodymium isotopic ratios were determined for those selected samples. The reader is referred to Appendix E for details on the procedures followed.

1.5 Structure of this thesis

Chapters 2 and 3 give a broad overview of the lithostratigraphy, structure and metamorphism of the Irumide belt, largely building on previous work, but combined with new mapping, field visits and sampling exercises conducted as part of this study, and in the years preceding this work.

In Chapter 4, which forms the main part of this thesis, a geochronological framework is established, based on an extensive set of SHRIMP U-Pb data on zircons from a wide variety of samples both from magmatic and metasedimentary rocks within the Irumide belt, and from the Bangweulu block to the north. Five SHRIMP U-Pb zircon dates on three granitoids and two volcanics near Mansa refine earlier age constraints for magmatism in the Bangweulu block of Zambia. Two SHRIMP U-Pb extrusion ages from volcanic tuff layers and one age on a pillow-lava sequence occurring within the metasedimentary sequence in the northeastern part of the belt place constraints on the timing of sedimentation. Three SHRIMP U-Pb datasets on detrital zircon from quartzites of northern Zambia further constrain the depositional age and sources of the metasedimentary sequences, and allow for the first time a direct comparison with one another and with metasedimentary sequences outside Zambia. One sample from the basal conglomerate of the Manshya River Group in the southeast (Mkushi map sheet) provides further constraints on the nature of the basement on which the sequence was deposited. Finally, 41 emplacement ages for various deformed and undeformed granitoids and orthogneisses are presented, firmly placing detailed constraints on the various magmatic events that shaped the belt. Three samples yielded complex zircons, from which four ages were extracted of low Th/U metamorphic zircon rims, placing direct age constraints on peak metamorphic conditions in the belt.

Chapter 5 focuses on the geochemistry of granitoids and volcanic sequences in the Irumide belt, presenting whole-rock geochemical data on 108 rocks. An attempt is made to use whole-rock geochemistry to elucidate the petrogenesis of the various magmatic suites, and determine possible petrogenetic processes involved in the generation of these suites. Based on the geochemical data, assumptions are

presented as to the geotectonic environment governing the emplacement of the various magmatic suites.

The petrology and geochemical character of the various magmatic suites in the Irumide belt are further studied in Chapter 6, where a limited set of whole rock Sm-Nd data are presented. These data, in conjunction with independently obtained emplacement ages for these lithologies, allow the calculation of $\epsilon_{\text{Nd}}(T)$ values and T_{CHUR} and T_{DM} ages, giving insight into the possible source materials and average crustal residence time of Irumide granitoids and volcanics.

In Chapter 7, all data are used in combination to propose a testable hypothesis on the evolution and tectonic setting of the Irumide belt, outlining remaining contentious issues regarding the belt, and the regional geological picture for central and southern Africa.

2 CHAPTER 2: Lithostratigraphy

2.1 *Introduction*

The Irumide belt comprises a complex of granitoids and gneisses, which can be subdivided into pre-tectonic and syn- to late-tectonic suites with respect to the Irumide orogeny, and a metasedimentary sequence called the Muva Supergroup. During fieldwork, an attempt was made to investigate the various lithologies described in the Irumide belt, work out their relative age relationships and construct a working tectono-stratigraphy for the Irumide belt. Due to time constraints and logistical limitations, the work concentrated on the area of the Irumide belt northwest of the Luangwa graben, between Kapiri Mposhi in the southwest and Isoka in the northeast (Figure 1-2) and excludes lithologies described within or directly adjacent to the Ubendian belt in the northeast.

Limited work was carried out near Mansa and Kasama (Figure 1-2) to provide some understanding of lithologies within the Bangweulu block to the north of the Irumide belt. The description of lithologies near Mansa is largely based on data collected in this study, but also builds upon mapping by Thieme (1970; 1971). The detailed stratigraphic work on the Mporokoso Group is largely based on Andersen and Unrug (1984), as the basal two formations defined in the Mporokoso Group are locally absent near Mansa. The stratigraphy presented for the Kasama Formation is entirely based on Unrug (1982).

For completeness, lithologies of the far northeastern part of the Irumide belt, including those of the Chozi, Nakonde, Mututa, Kalungu, Mafingi and Muyombe 1:100,000 map sheets, are briefly described based on published reports and literature (Fitches, 1966, 1967, 1968a, 1968b, 1970, 1971; Ray, 1974; Thatcher, 1974; Ray and Crow, 1975; Priem et al., 1979; Schandelmeier, 1980, 1981, 1983; Namateba, 1994; Van Tuijl and Verhoog, 1995c; Verhoog and Van Tuijl, 1995a, 1995b, 1995c; Ring et al., 1997; 1999; Vrána et al., 2004).

The following sections give an overview of the lithologies encountered during this study. Figure 2-1 shows an overview map of Zambia, indicating the position of the various metasedimentary successions of northern Zambia. Figure 2-2 shows a simplified geological map of the Bangweulu block and, Figure 2-3 and Figure 2-4 an overview of the southwestern and northeastern part of the Irumide belt respectively, indicating the map sheets completed by geologists of the Zambian Geological Survey at a scale of 1:100,000. Wherever used in this thesis, the term “southwestern Irumide belt” refers to the area of the Irumide belt to the southwest of Mpika, likewise “northeastern Irumide belt” refers to the area of the belt to the northeast of Mpika (Figure 2-1). Figure 2-5 shows an overview of previously published Proterozoic age data for Zambia discussed in the text. The age data are tabulated in Table 2-2. Mineral abbreviations used in the text are as follows: q=quartz; chl=chlorite; st=staurolite; cd=cordierite; g=garnet; opx=orthopyroxene; bi=biotite; mu=muscovite; ksp=K-feldspar s.l.; pl=plagioclase and hb=hornblende s.l.

2.2 Previous work

Early work was mainly concentrated in the southwestern parts of the Irumide belt, where previous workers believed that the crystalline rocks of the belt collectively formed a Palaeoproterozoic basement complex, termed the Mkushi Gneiss (Ackermann, 1936; 1950; 1960; Ackermann and Forster, 1960; Smith, 1965; Stillman, 1965c; Cvetcovic, 1973), which was reworked during the Irumide event. Later investigations distinguished intrusive units within what was termed the Mkushi Gneiss, which are clearly syn- to post-orogenic granitoids with respect to Irumide tectonism (Daly, 1986b; Mapani, 1992; De Waele, 1997; De Waele and Mapani, 2002). Based on field relations and structural differences and to a certain extent previously published age data, magmatism can be subdivided into four generations (Table 2-1). Please note that the dates indicated by [#] are based on whole-rock Rb-Sr geochronology, a dating technique regarded as contentious for the estimation of emplacement ages because of potential open-system Rb-Sr systematics in numerous environments (Dickin, 1995).

Table 2-1: Different magmatic suites recognised in the Irumide belt, Bangweulu block and adjacent Lufilian belt

Southwest	Northeast
GROUP Ia	GROUP Ia
2.05 – 1.97 Ga	2.09 - 1.93 Ga
Mkushi Gneiss, Mulungushi Gneiss, Samba Porphyry, Chambishi Granite, Mufulira Granite (Rainaud et al., 1999; 2002; 2003)	Ubendian gneisses including the Rumpi, Luromo and Chelinda Granites (Ring et al., 1997), the Nyika Granite (Dodson et al., 1975; Ring et al., 1997) and a biotite-metatonalite in the Muyombe area (Vrána et al., 2004)
GROUP Ib	GROUP Ib
1.83 – 1.81 Ga *	1.87 * – 1.83 Ga *
Granitoids and volcanics on the Bangweulu block (Brewer et al., 1979)	Granitoids along the southwestern margin of the Ubendian belt in the Bangweulu block of northern Zambia (Schandelmeier, 1980); Mwambwa Gneiss (Daly, 1986b)
1.88 – 1.85 Ga	
Granitoids and volcanics in the Copperbelt (Ngoyi et al., 1991; Rainaud et al., 1999; John, 2001; Rainaud et al., 2002)	
GROUP II	GROUP II
No previous age constraints	~1.41 Ga *
Biotite granite gneisses intruding the metasedimentary sequence and pre-kinematic intrusions termed the Lukamfwa Hill Granite Gneiss.	The Mutangoshi Gneissic Granite and Musalango Gneiss (Daly, 1986b)
	GROUP III
	1.36 – 1.34 Ga *
	The Mivula syenite (Tembo, 1986; Vrána et al., 2004) and the Ntendeke metatonalite (Vrána et al., 2004)
GROUP IV	GROUP IV
No previous age constraints	1.01 * – 0.97 Ga
Irumide granitoids, mainly weakly deformed porphyritic biotite granites	The Kaunga and Lufila Granites (Daly, 1986b)

Overlying the basement units, an extensive metasedimentary sequence comprising quartzites and pelites occurs within the Irumide belt, which was termed the “Muva”. The “Muva” was first described by Gray (1930) in the Copperbelt of Zambia, to distinguish an older series of metasediments (called the Lufubu Series) from the younger pre-Katangan Muva Series. The term Muva was later adopted by Jackson (1932) for the Nchanga sheet to the south of Mufulira, and was elevated to higher stratigraphic status in Mendelsohn’s comprehensive discourse on the Northern Rhodesian Copperbelt (Mendelsohn, 1961). The term “Muva” was first used in the Irumide belt by Ackermann (1950) in the Mkushi-Serenje area, and the unit was described in extensive detail by Stillman (1965c) in the Mkushi 1:100,000 map sheet. In Stillman’s definition, the Muva comprises two metasedimentary sequences of quartzites and meta-pelites termed the Musofu and Kalonga Formations. The term “Muva Supergroup” was introduced by Daly and Unrug (1982) and encompasses the

pre-Katangan sequences of the Bangweulu block and in the Irumide belt. In Daly and Unrug's definition, the Muva Supergroup supercedes and includes a number of previously named units including the Plateau Series of Guernsey (1951), Phillips (1955) and Searle (1972), the Abercorn Sandstone of McConnell (1950), Halligan (1963) and Page (1962), the Mafingi Group of Fitches (1968b) and Thatcher (1974) and the Manshya River Group of Marten (1968). Daly and Unrug (1982) proposed a four-fold division for the Muva Supergroup and distinguished from north to south the Mporokoso Group, Kasama Formation and Mitoba River and Manshya River Groups. The Mporokoso Group unconformably overlies Palaeoproterozoic granitic and volcanic rocks of the Bangweulu block, and comprises largely undeformed sediments of predominantly fluvial affinity. The Kasama Formation comprises undeformed sediments found in several small basins in the eastern part of the Bangweulu block and consists largely of supermature fluvial sandstones, which were interpreted to be derived by sedimentary reworking of the Mporokoso Group to the west (Andersen and Unrug, 1984). In the Irumide belt, Daly and Unrug (1982) divided the metasedimentary package into a lower fluvial and an upper shallow marine part. The lower part, which they termed the Mitoba River Group, passes upwards into the Manshya River Group with no discernable break, and the entire package is affected by Irumide tectonism (Daly and Unrug, 1982). Based on the similar fluvial character of the Kasama Formation and the Mitoba River Group, these two sequences were believed by Daly and Unrug (1982) to be lateral correlatives. The geological reports and maps published by the Geological Survey Department of Zambia, however, do not distinguish the Mitoba River Group and include it within the Manshya River Group. In its new definition, the Manshya River Group thus comprises the thick, folded and deformed metasedimentary lithologies of the northern Irumide belt, and includes a basal fluvial succession, previously named the Mitoba River Group, which passes into the upper, shallow marine sequences of the originally defined Manshya River Group of Marten (1968).

The Mafingi Group described near the border with Malawi (Fitches, 1968b; Van Tuijl and Verhoog, 1995c) is considered by Fitches (1971) to be the equivalent of the Manshya River Group, as it can be traced laterally into the former Mitoba River Group. Throughout the Irumide belt, the sedimentary sequence is given a variety of local names, which have been redefined into the Kanona Group in the

southwest, and the Manshya River Group in the northeast (De Waele and Mapani, 2002). The distinction between the Kanona and Manshya River Groups was initially made purely on the fact that the two sequences cannot be traced laterally into each other, as there is an exposure gap across the Chitambo Mission sheet (Figure 2-4), precluding direct formation-to-formation correlation (De Waele and Mapani, 2002). The Kanona and Manshya River Groups are in fact the same succession as will be shown in Chapter 4.

Rainaud et al. (2003) reported a geochronological study on detrital zircon from a quartzite collected from the Kanona Group near Mufulira. The data show a prominent age population between 2.05 and 1.95 Ga, with another significant population between 2.25 and 2.10 Ga and small populations with ages of 2.40 Ga, 2.50 Ga, 2.70 Ga, 3.03 Ga and 3.20 Ga. Rainaud et al. (2003) also reported 3.20 Ga xenocrysts in lavas in the Congolese Copperbelt and explained the 3.20 Ga component in the quartzite and these xenocrysts by postulating a cryptic Mesoarchaean terrane beneath the Copperbelt. The youngest concordant analysis of 1941 ± 40 Ma places a maximum age constraint on the deposition of the quartzite.

In summary, the metasedimentary sequences of northern Zambia consist of five regionally separated and distinct stratigraphic packages (Daly and Unrug, 1982)(Figure 2-1). An extensive package of quartzites and pelites, with intercalated tuff layers, occurs on the Bangweulu block (Andersen and Unrug, 1984; Unrug, 1984; Andrews-Speed, 1989) and forms the Mporokoso Group. Between the Mporokoso basin and the Irumide belt, a series of undeformed quartzites and pelites occur in a series of small basins, the largest of which lies east of the town of Kasama. Based on the supermature nature of the quartzites and the sedimentary transport indicating derivation from the west and northwest (i.e. from the Mporokoso Group), these sediments were interpreted as a younger sequence, which is called the Kasama Formation (Daly and Unrug, 1982; Unrug, 1982; 1984). Within the Irumide belt itself, the deformed sedimentary successions consist of three laterally equivalent sedimentary packages: the Kanona Group in the southwest, the Manshya River Group in the northeast and the Mafingi Group in the far northeast near the Zambia-Malawi border (Fitches, 1968b; Marten, 1968; De Waele and Mapani, 2002)(Figure

2-1). Because of the fact that exposure gaps between these three successions preclude direct formation-to-formation correlation, they are described separately in this thesis.

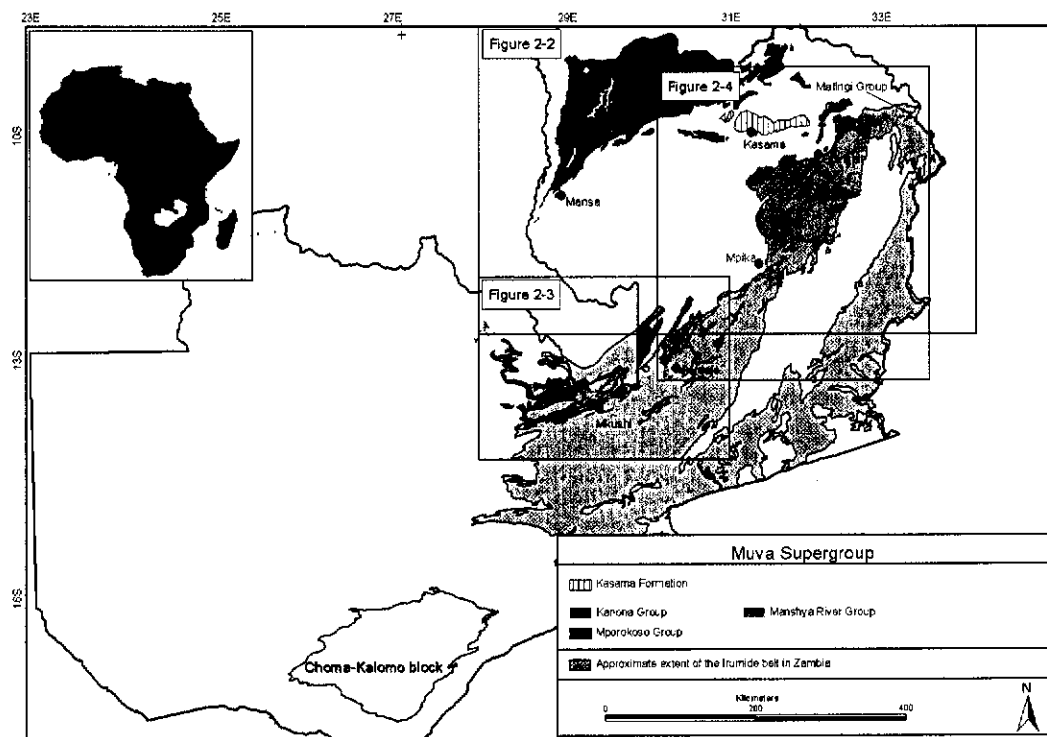


Figure 2-1: Overview of the Muva Supergroup of Zambia. The inset shows the location of Zambia (white) in Africa (black). The boxes indicate the areas shown in Figure 2-2, Figure 2-3 and Figure 2-4.

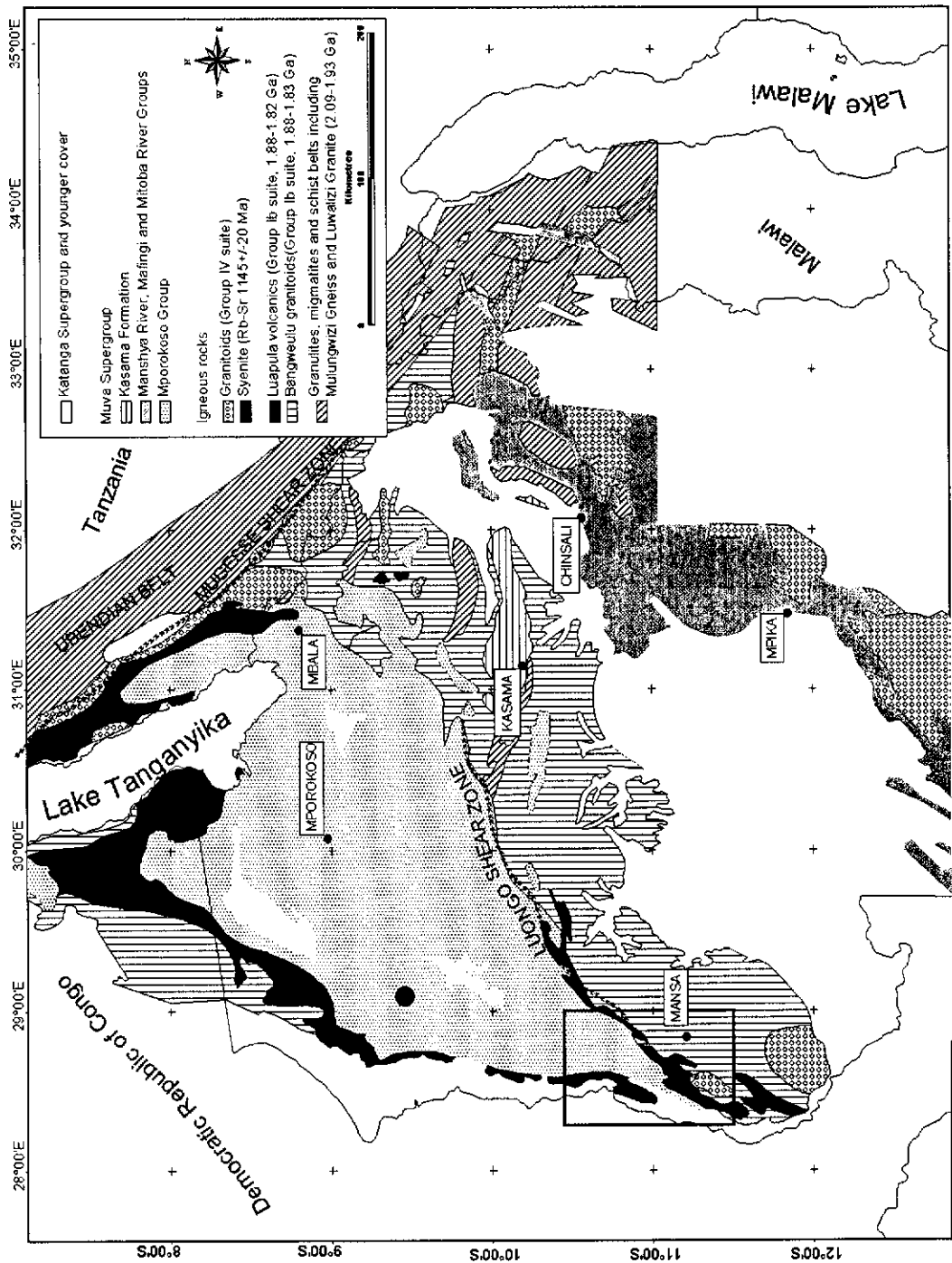


Figure 2-2: Simplified geological map of the Bangweulu block. The box indicates the two quarter degree geological sheets (1:100,000) of Mansa and Musonda Falls (shown in detail in Figure 2-6). The map is adapted from the geological map of Zambia (Thieme and Johnson, 1981) and from Andersen and Unrug (1984).

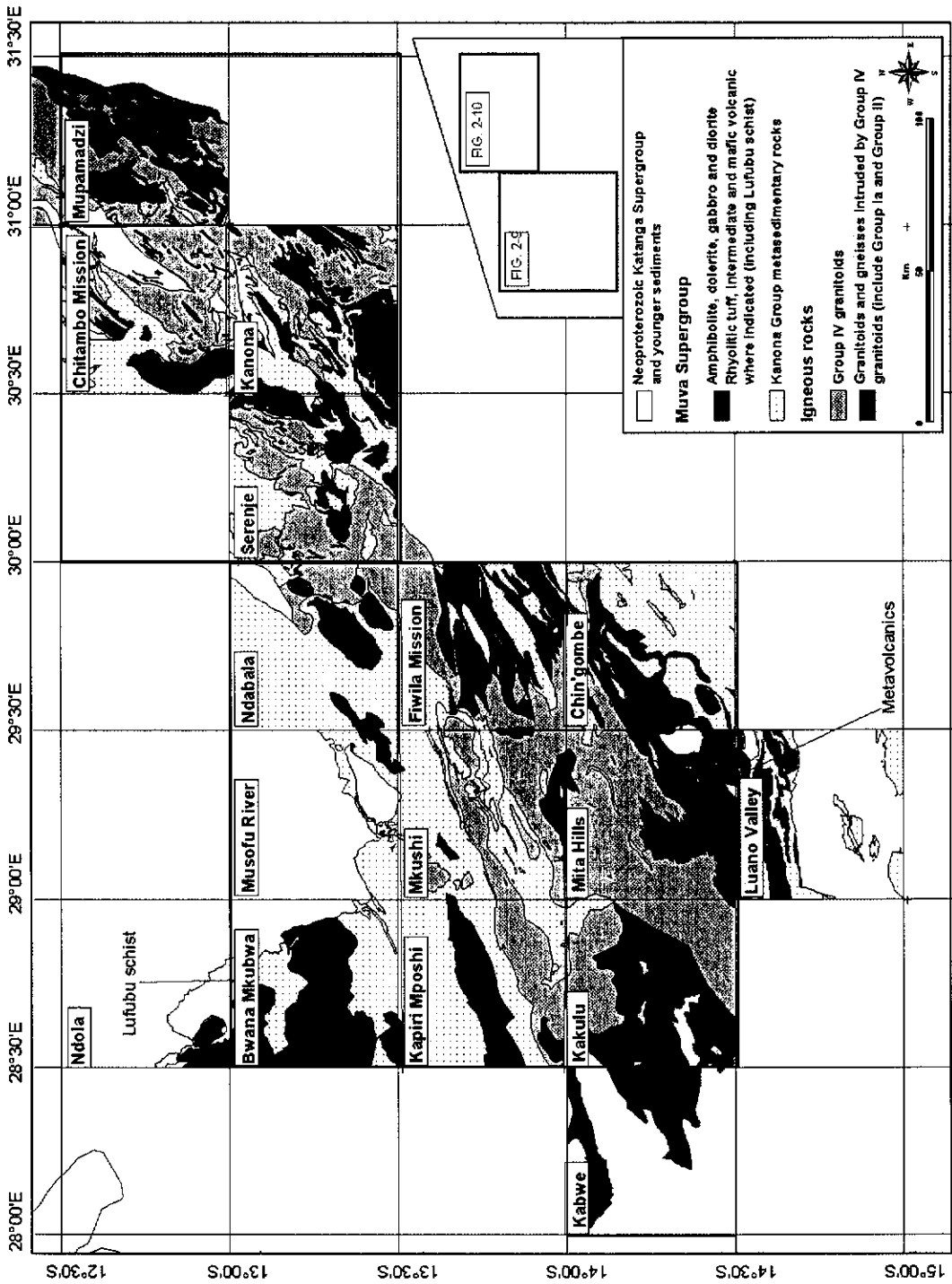


Figure 2-3: Overview map of the southwestern Irumide belt, showing simplified geology and the location of mapped quarter degree sheets. Simplified geology is adapted from the 1:1,000,000 geological map of Zambia (Thieme and Johnson, 1981). The inset and boxes indicate the areas shown in detail in Figure 2-9 and Figure 2-10.

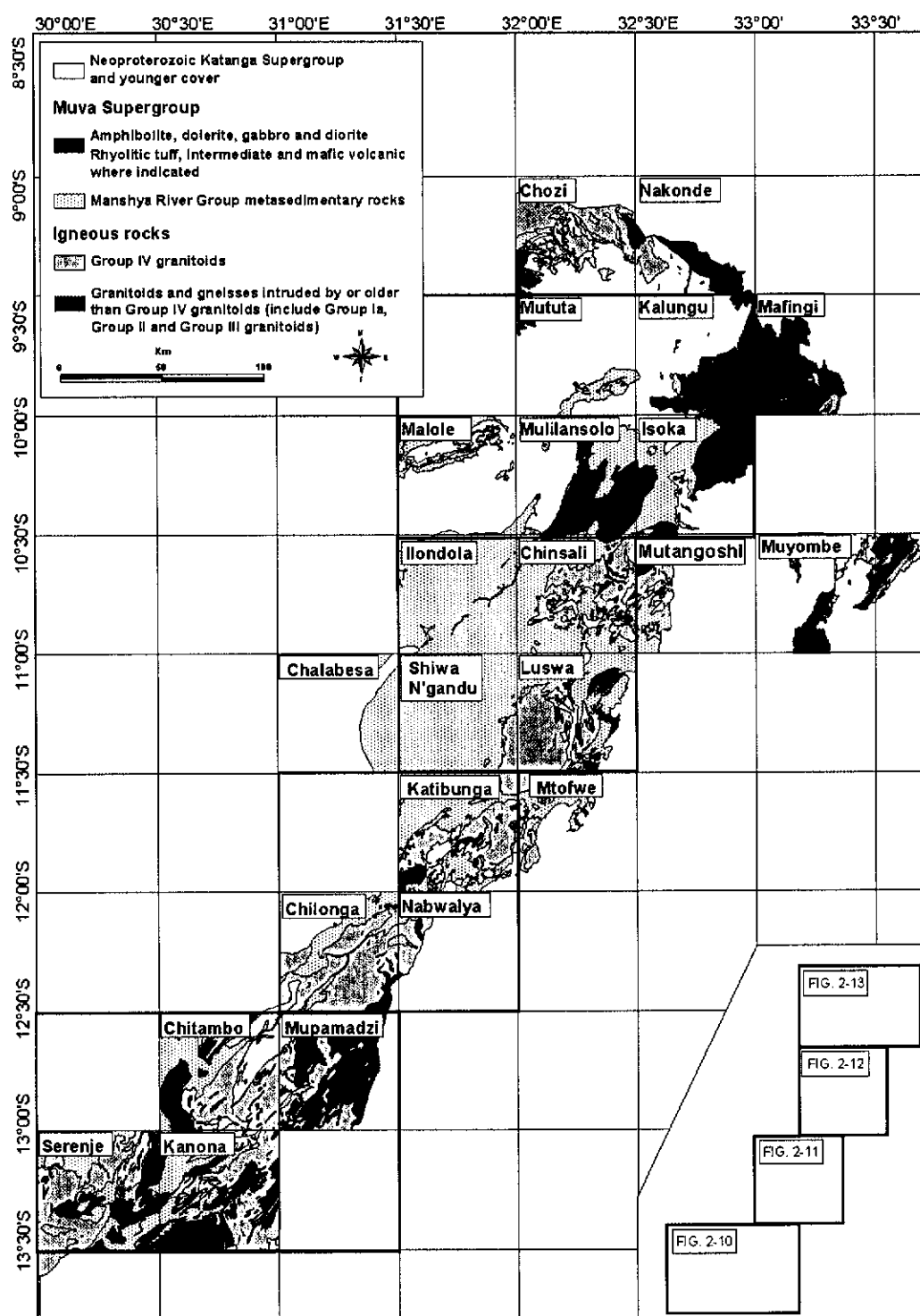


Figure 2-4: Overview map of the northeastern Irumide belt, showing simplified geology and the location of mapped quarter degree sheets. Simplified geology is adapted from the 1:1,000,000 geological map of Zambia (Thieme and Johnson, 1981). The inset and boxes indicate areas shown in detail in Figure 2-10, Figure 2-11, Figure 2-12 and Figure 2-13.

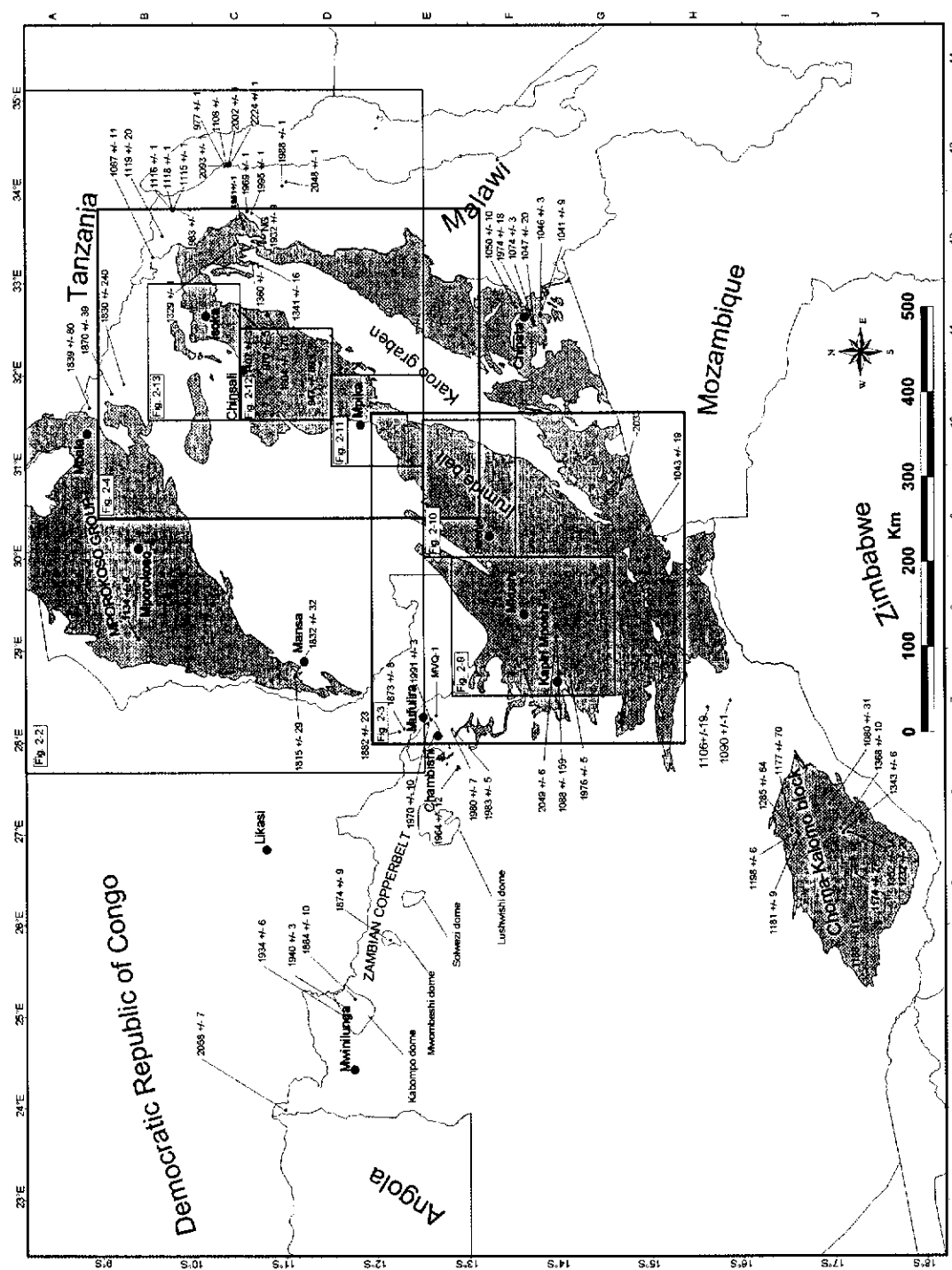


Table 2-2: Previously published and unpublished Proterozoic age data (> ca. 950 Ma) for Zambia (refer to Figure 2-5 using grid square for locations). *Italics* date growth of metamorphic zircon

Sample ID	Age \pm error (Ma)	*Grid square	Method	Source
Lufila Granite	947 \pm 89	D11	Whole-rock Rb-Sr	Daly, 1986
Kaunga Granite	970 \pm 5	C11	U-Pb TIMS bulk zircon	Daly, 1986
Aplite (Luromo Granite)	977 \pm 1	C13	Pb evaporation single zircon	Ring et al., 1999
Aplite (Willilo Granite)	983 \pm 1	B12	Pb evaporation single zircon	Ring et al., 1997
Porphyritic granite (ZAM5)	1041 \pm 9	F11	U-Pb SHRIMP zircon	De Waele et al. in prep.
Luangwa gneiss	1043 \pm 19	G9	LA-ICP-MS	Cox et al., 2002
Chipata granulite	1046 \pm 3	F11	U-Pb TIMS single monazite	Schenk and Appel, 2001
Madzimoyo Gneiss (ZAM1)	1047 \pm 20	F11	U-Pb SHRIMP zircon	De Waele et al. in prep.
Porphyritic granite (ZAM4)	1050 \pm 10	F11	U-Pb SHRIMP zircon	De Waele et al. in prep.
Porphyritic granite (ZAM3)	1074 \pm 3	F11	U-Pb SHRIMP zircon	De Waele et al. in prep.
Phoenix Mine mica	1080 \pm 31	I6	Rb-Sr mica	Cahen et al., 1984
lwakwa Granite	1087 \pm 11	B12	U-Pb TIMS single zircon	Ring et al., 1999
Mkushi Gneiss	1088 \pm 159	F8	U-Pb SHRIMP zircon	Rainaud et al., 2002
Munali Granite	1090 \pm 1	H8	U-Pb TIMS single zircons	Katongo et al. submitted
Mpande Gneiss	1106 \pm 19	H7	U-Pb TIMS bulk zircon	Hanson, 1988a
Luromo Granite	1108 \pm 1	C13	Pb evaporation single zircon	Ring et al., 1999
Willilo Granite	1115 \pm 1	B12	Pb evaporation single zircon	Ring et al., 1999
Willilo Granite	1116 \pm 1	B12	Pb evaporation single zircon	Ring et al., 1999
Willilo Granite	1118 \pm 1	B12	Pb evaporation single zircon	Ring et al., 1999
Mwenga Granite	1119 \pm 20	B12	U-Pb TIMS single zircon	Ring et al., 1999
Lusenga Syenite	1134 \pm 8	A8	Whole-rock Rb-Sr	Brewer et al. 1979
Granite (Choma-Kalomo block)	1174 \pm 27	J5	U-Pb SHRIMP zircon	Bulambo et al., 2004
Granite (Choma-Kalomo block)	1177 \pm 70	I6	U-Pb SHRIMP zircon	Bulambo et al., 2004
Granite (Choma-Kalomo block)	1181 \pm 9	I6	U-Pb SHRIMP zircon	Bulambo et al., 2004
Granite (Choma-Kalomo block)	1188 \pm 11	J5	U-Pb SHRIMP zircon	Bulambo et al., 2004
Semahwa Gneiss	1198 \pm 6	I6	U-Pb TIMS bulk zircon	Hanson et al., 1988a
Siasikabole Granite	1232 \pm 20	J6	Whole-rock Rb-Sr	Hanson et al., 1988a
Chilala Gneiss	1285 \pm 64	I6	U-Pb TIMS bulk zircon	Hanson et al., 1988a
Ntendeles metatonalite	1329 \pm 1	C12	Pb evaporation single zircon	Vrána et al., 2004
Mivula Syenite	1341 \pm 16	C12	Whole-rock Rb-Sr	Tembo, 1986
Zongwe Gneiss	1343 \pm 6	J6	U-Pb TIMS bulk zircon	Hanson et al., 1988a
Siasikabole Granite	1352 \pm 14	J6	U-Pb TIMS bulk zircon	Hanson et al., 1988a
Mivula Syenite	1360 \pm 1	C12	Pb evaporation single zircon	Vrána et al., 2004
Granite (Choma-Kalomo block)	1368 \pm 10	J6	U-Pb SHRIMP zircon	Bulambo et al., 2004
Mutangoshi Gneissic Granite	1407 \pm 33	C11	Whole-rock Rb-Sr	Daly, 1986b
Mwambwa River Gneiss	1804 \pm 170	C11	Whole-rock Rb-Sr	Daly, 1986b
Luchewe Granite	1830 \pm 240	B11	Whole-rock Rb-Sr	Schandelmeier, 1980
Mansa Volcanic	1815 \pm 29	D8	Whole-rock Rb-Sr	Brewer et al. 1979
Mansa Granite	1832 \pm 32	D8	Whole-rock Rb-Sr	Brewer et al. 1979
Kate Granite	1839 \pm 80	A10	Whole-rock Rb-Sr	Schandelmeier, 1980
Kinsenda Lufubu Schist	1873 \pm 8	E7	U-Pb SHRIMP zircon	Rainaud et al., 2002
Solwezi Granite	1874 \pm 9	E4	U-Pb TIMS single zircon	John, 2001
Mambwe Gneiss	1870 \pm 39	B10	Whole-rock Rb-Sr	Schandelmeier, 1980
Kinsenda Granite (Luina dome)	1882 \pm 23	E7	U-Pb TIMS single zircon	Ngoyi et al., 1991
Kabompo Granite	1884 \pm 10	D4	U-Pb TIMS single zircon	John, 2001
Nyika Granite	1932 \pm 9	C12	U-Pb TIMS bulk zircon	Dodson et al., 1975
Kabompo Dome granite	1934 \pm 6	D4	U-Pb zircon	Key et al. 2001
Kabompo Dome granite	1940 \pm 3	D4	U-Pb zircon	Key et al. 2001
Biotite metatonalite	1961 \pm 1	C12	Pb evaporation single zircon	Vrána et al., 2004
Samba porphyry	1964 \pm 12	E6	U-Pb SHRIMP zircon	Rainaud et al., 2002
Nyika Granite	1969 \pm 1	C12	Pb evaporation single zircon	Ring et al., 1997
Lufubu Schist	1970 \pm 10	E7	U-Pb SHRIMP zircon	Rainaud et al., 2002
Mafic enclave in Gneiss (ZAM2)	1974 \pm 18	F11	U-Pb SHRIMP zircon	De Waele et al. in prep.
Mulungushi Gneiss	1976 \pm 5	G7	U-Pb SHRIMP zircon	Rainaud et al., 2002
Chambishi Granite	1980 \pm 7	E7	U-Pb SHRIMP zircon	Rainaud et al., 2002
Chambishi Granite	1983 \pm 5	E7	U-Pb SHRIMP zircon	Rainaud et al., 2002
Rumphi Granite	1988 \pm 1	C13	Pb evaporation single zircon	Ring et al., 1997
Mufulira Granite	1991 \pm 3	E7	U-Pb SHRIMP zircon	Rainaud et al., 2002
Chelinda Granite	1995 \pm 1	C12	Pb evaporation single zircon	Ring et al., 1997
Luromo Granite	2002 \pm 1	C13	Pb evaporation single zircon	Ring et al., 1997
Luangwa gneiss	~2033	G9	LA-ICP-MS	Cox et al., 2002
Rumphi Granite	2048 \pm 1	D13	Pb evaporation single zircon	Ring et al., 1997
Mkushi Gneiss	2049 \pm 6	F8	U-Pb SHRIMP zircon	Rainaud et al., 2002
Mwinilunga granite	2058 \pm 7	D3	U-Pb SHRIMP zircon	Key et al., 2001
Luromo Granite	2093 \pm 1	C13	Pb evaporation single zircon	Ring et al., 1997
Luromo Granite	2224 \pm 1	C13	Pb evaporation single zircon	Ring et al., 1997
Mufulira quartzite	Detrital	E7	U-Pb SHRIMP zircon	Rainaud et al., 2002

*Square refers to grid square in Fig. 2-5; ** error on the age not provided by the author(s)

2.3 Basement rocks

2.3.1 Archaean granitoids

The known occurrence of Archaean lithologies in Zambia is limited to the far northwestern corner of the country, where Key et al. (2001a; 2001b) reported U-Pb SHRIMP zircon ages of 2543 ± 5 Ma, 2561 ± 10 Ma and 2538 ± 10 Ma for various granite gneisses near Mwinilunga (see Table 2-2 and Figure 2-5). Indications of Neoarchaeon crust below the Lufilian belt have recently been reported by Rainaud et al. (2003), who dated numerous xenocrystic zircons at between 3.22 and 3.03 Ga in a lapilli tuff collected near Likasi (DRC). They obtained similar ages from detrital zircons in a quartzite from the Muva Supergroup (sample MVQ-1, Figure 2-5) collected near Mufulira. Even for the Bangweulu block, which is thought to be underlain by granite gneisses predating Ubendian tectonism at ~ 2.0 Ga (Andersen and Unrug, 1984), no ages have been reported older than 1.87 (Schandelmeyer, 1980). Within that part of the Irumide belt of concern here, no lithologies are reported to belong to the Archaean (cf. Figure 2-5).

2.3.2 Undeformed basement of the Bangweulu block

Palaeoproterozoic magmatism emplaced granitoids and coeval volcanic rocks in the Bangweulu block between 1.88 and 1.83 Ga (Brewer et al., 1979; Schandelmeyer, 1980; 1981). Similarly aged granitoids have been described further west underlying the Copperbelt (Figure 2-5). Bangweulu granitoids and coeval acid volcanic rocks studied in the course of this work occur near Mansa in northern Zambia, and form a typical part of the Bangweulu block crystalline basement (Figure 2-6). The granites are typically reddish, medium grained and contain quartz + K-feldspar + plagioclase + biotite (samples MA1, MA2 and MA9; Figure 2-7 (a) and (b)). Accessory minerals include hornblende, sphene and epidote. The granites contain fine-grained xenoliths of metavolcanic rock and are interpreted to intrude the volcanic rocks and the basal part of the Mporokoso Group (Thieme, 1970; 1971;

Verhoog and Van Tuijl, 1995b). The granite is generally unfoliated, but in places, a weakly developed biotite foliation is defined along east-dipping northerly trends.

The volcanic rocks on the Bangweulu block are known as the Luapula Volcanics. The Luapula Volcanics are widespread along the western and northern margin of the block. They underlie the sedimentary successions on the Bangweulu block (the Mporokoso Group), but are also reported to occur within the lowermost part of the Mporokoso Group. The Luapula Volcanics have previously been dated by Brewer et al. (1979) at 1815 ± 29 Ma (Figure 2-5). Several samples of the Luapula Volcanics were collected in this study near Mansa (samples MA3, MA4, MA4B and MA5; Figure 2-6). The Luapula Volcanics of the Mansa and Musonda Falls sheets were described by Thieme (1970; 1971). They are dark grey to green, fine grained rhyolitic and rhyodacitic tuffs, either found to be intruded by granitoids (Figure 2-8 (a)), or interlayered with siltstone and laminated quartzite of the basal part of the Mporokoso Group sedimentary rocks. The volcanic rocks are altered and devitrified, but show remnant lithic fragments, coarse agglomerates and a vague vitroclastic structure, which attest to their pyroclastic origin. In places, flow banding, flow folds, and eutaxitic structure, mainly in volcanics of more dacitic to andesitic composition, indicate possible emplacement as ash-flows or lava flows. Most volcanics are porphyritic, with feldspar, quartz and (chloritised) biotite phenocrysts set in an aphanitic groundmass of quartz, feldspar, epidote, sericite, chlorite and iron oxides. Accessory phases include sphene, apatite and zircon. Plagioclase dominates over microcline, and microcline is absent in dacitic end members of the volcanic series, which are also characterised by the presence of hornblende.

Rainaud et al. (2002) reported a U-Pb SHRIMP age of 1873 ± 8 Ma on a volcanic schist north of Mufulira in the Congolese part of the copperbelt (Figure 2-5). The adjacent granite yielded a U-Pb TIMS age of 1882 ± 20 Ma, confirming the coeval nature of granite magmatism and volcanism (Table 2-2, Fig. 2-5, Ngoyi et al., 1991). Two other granite domes farther west in the Copperbelt yielded U-Pb TIMS emplacement ages of 1874 ± 9 Ma and 1884 ± 10 Ma (Fig. 2-5, John, 2001) suggesting that the 1.88-1.82 Ga magmatic province of the Bangweulu block extends westwards and underlies much of the Neoproterozoic Lufilian belt.

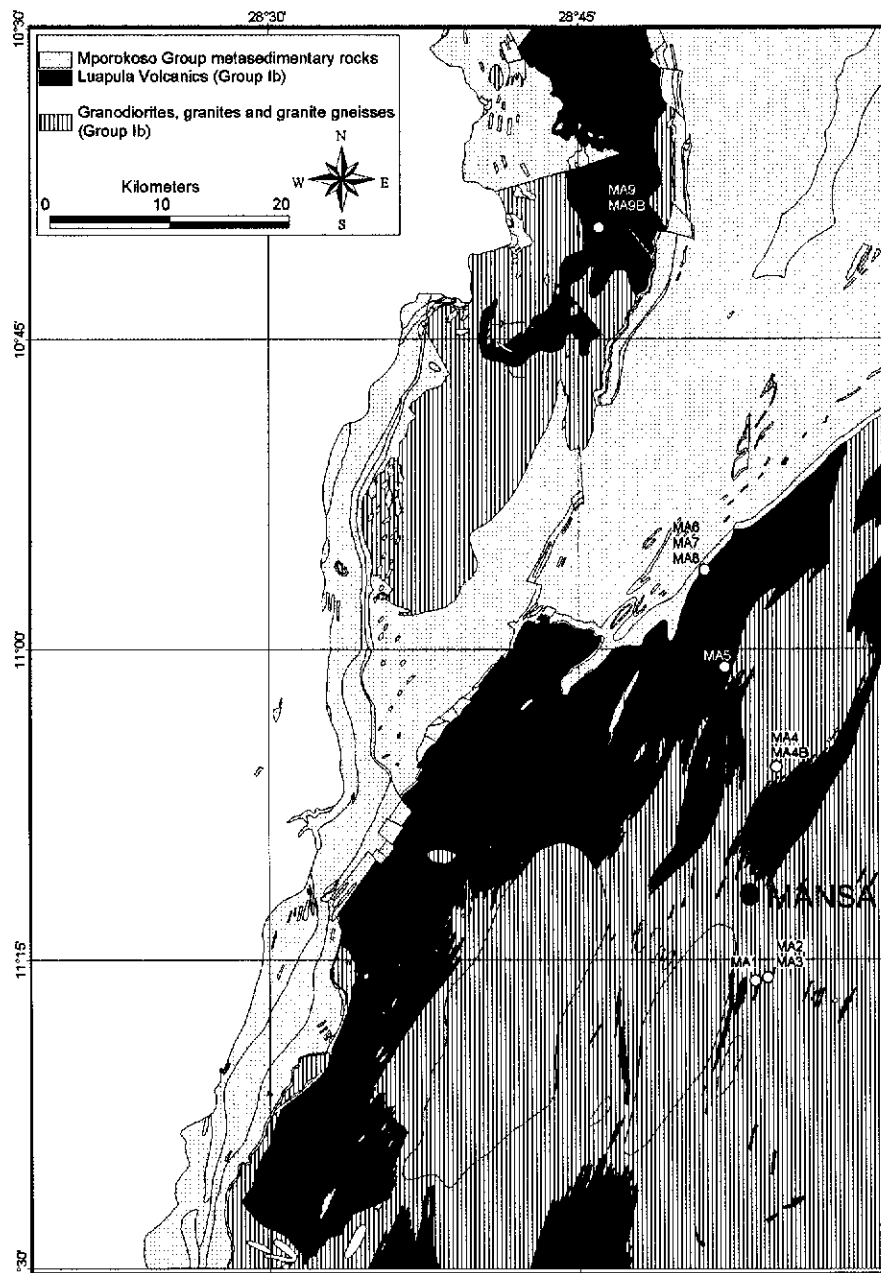


Figure 2-6: Simplified geological map of the Mansa and Musonda Falls map sheets indicating location of samples (regional location indicated on Figure 2-2). Adapted from 1:100,000 geological maps of Mansa and Musonda Falls after Thieme (1970; 1971).

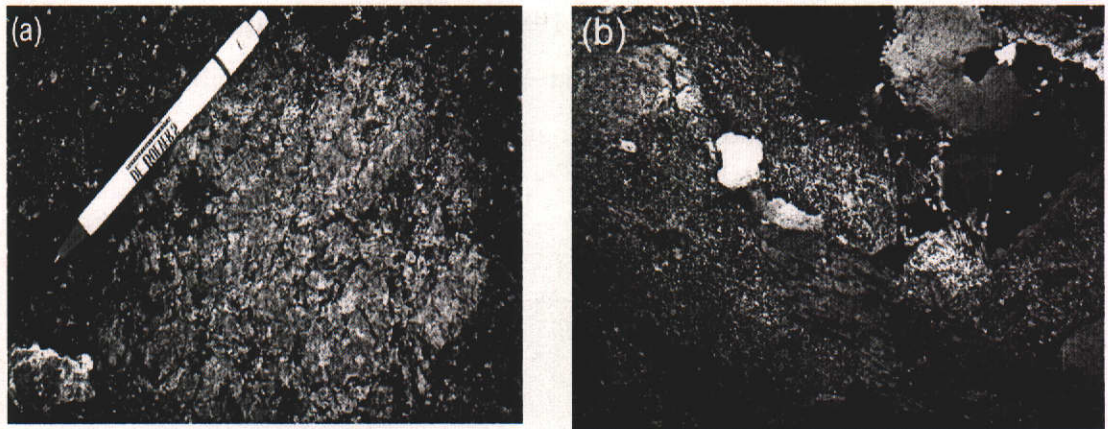


Figure 2-7: (a) the Mansa Granite, showing porphyritic K-feldspar in a matrix of q-ksp-pl-chl-bi; (b) photomicrograph of a thin section (crossed polars (xpl)) of sample MA1 (Mansa Granite) showing a coarse-grained q-pl-bi assemblage with minor K-feldspar (field of view (f.o.v.) 4.64 mm). The plagioclase is extensively saussuritised. Biotite is variably altered to chlorite. The quartz shows undulose extinction.

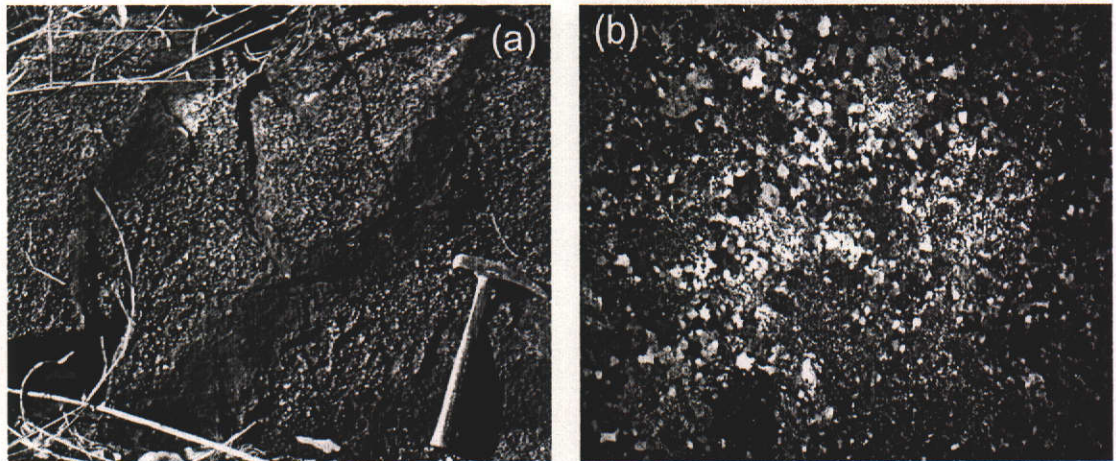


Figure 2-8: (a) Fine grained enclaves of volcanic rock within coarse granite. Age data indicate that intrusion of the granite and volcanic rocks was penecontemporaneous; (b) photomicrograph of a thin section (xpl) of sample MA3 showing equigranular quartz and feldspar, in a microcrystalline groundmass of q + ksp + epidote + iron oxides and chl. Rounded microcrystalline zones surrounded by equigranular quartz may represent relict vesicles (f.o.v. 4.64 mm).

2.3.3 Deformed basement of the Irumide belt

Deformed basement granitoids of the Irumide belt comprise a suite of granite gneisses in the southwest called the Mkushi Gneiss, and several suites of gneisses in the northeast, referred to as the Mulungwizi Gneiss, Mwambwa River Gneiss, Luwalizi Granite Gneiss and the Lubu Granite Gneiss. Of these, only the Mkushi Gneiss, Luwalizi Granite Gneiss and Lubu Granite Gneiss were investigated during this study. Brief discussions on the Mulungwizi and Mwambwa River Gneiss given

here are based on published work (Daly, 1986b; Namateba, 1994; Daly, 1995a; Van Tuijl and Verhoog, 1995c; Verhoog and Van Tuijl, 1995a; 1995b; 1995c). The distribution of deformed basement lithologies is shown in Figures 2-9, 2-10, 2-11, 2-12 and 2-13.

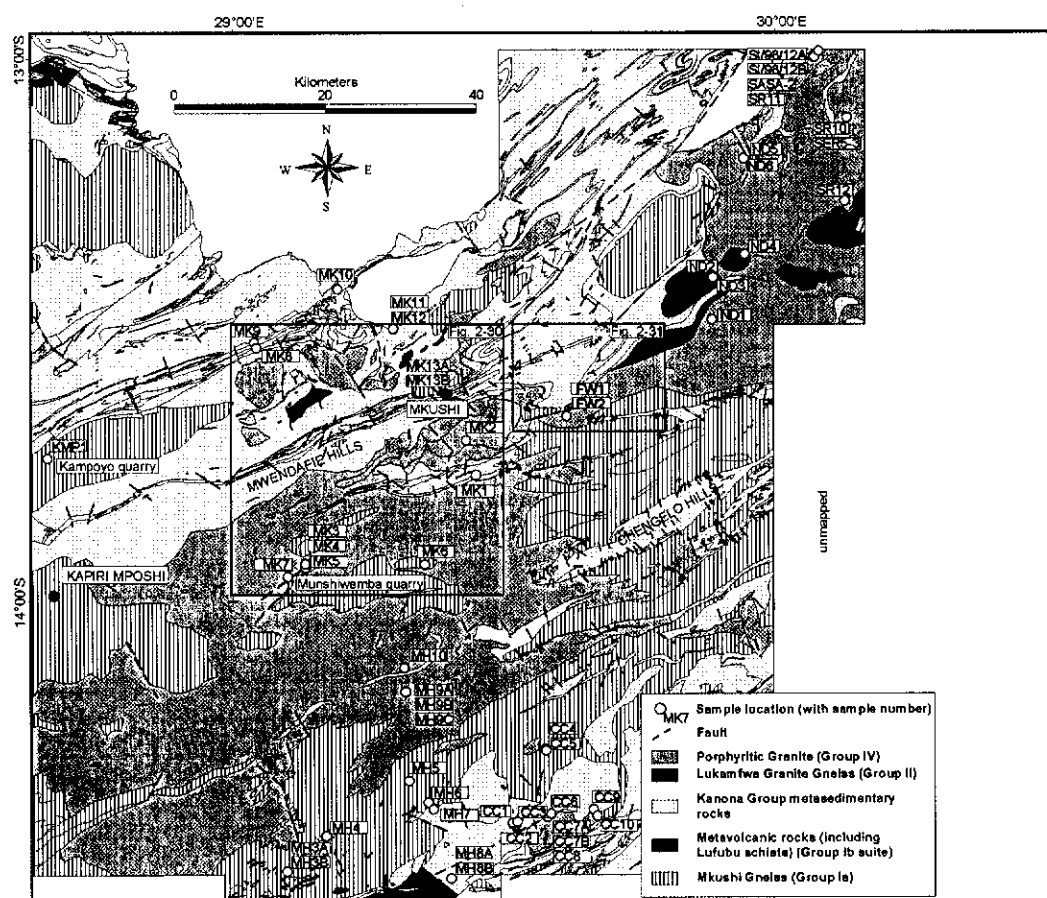


Figure 2-9: Simplified geological map of the area around Mkushi showing sample locations for this study, based on published 1:100,000 scale geological maps (includes Kapiri Mposhi, Kakulu (Mulungushi), Mita Hills, Mkushi, Musofu River, Fiwila and Ndabala map sheets and parts of Serenje, Chin'gombe, Luano and Bwana Mkubwa sheets)(Smith, 1965; Stillman, 1965a; 1965b; Moore, 1967a; Cvetcovic, 1992; Reichwalder and Brandon, 1992; Kerr, 1994; Mapani and Moore, 1995a; Carruthers, 2000; Smith, 2000; Chisela, in press). The boxes indicate the approximate position of Figure 2-30 and Figure 2-31. Outlines of quartzite ridges are traced in the Manshya River Group.

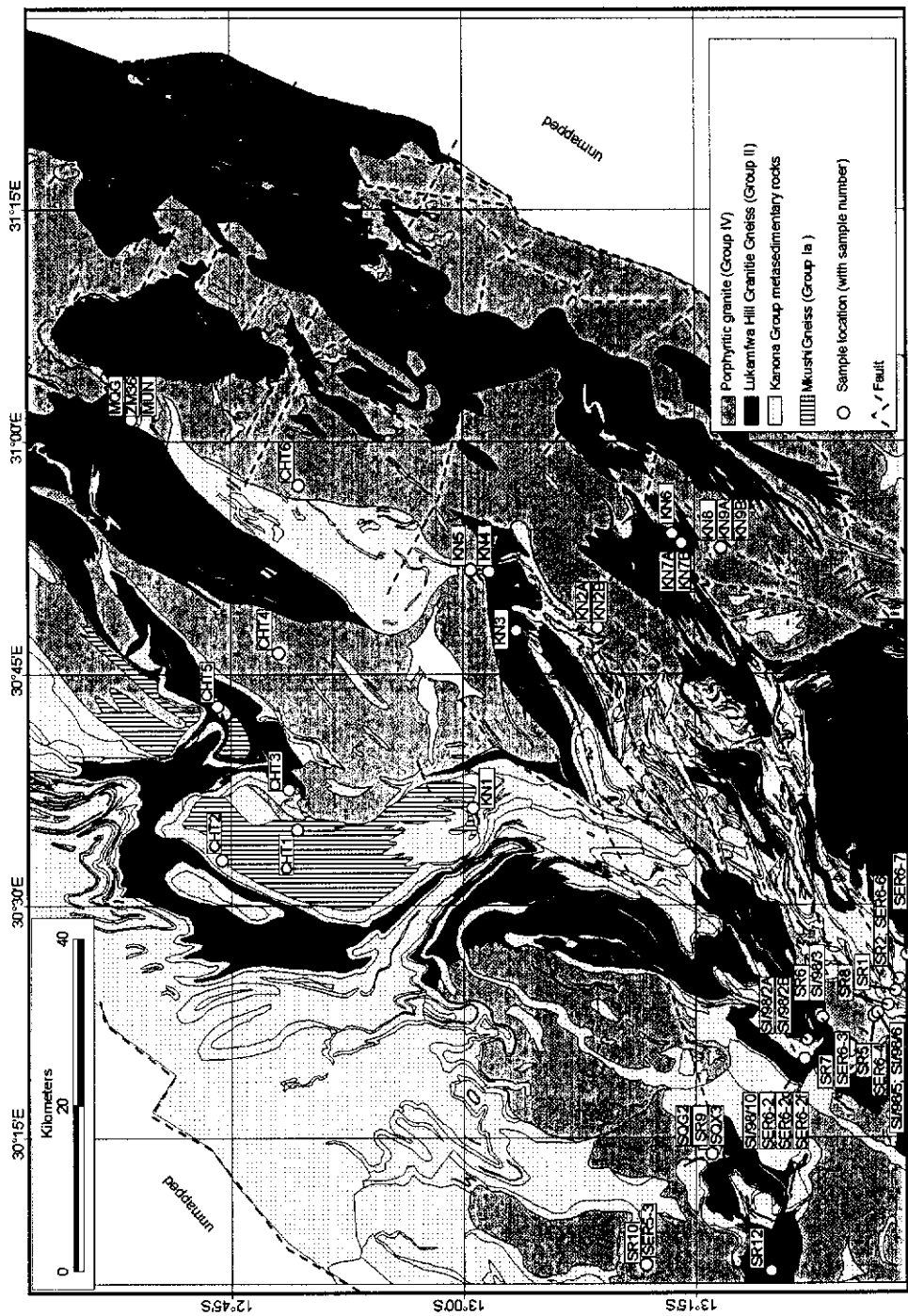


Figure 2-10: Simplified geological map of the region around Kanona showing sample locations for this study, adapted from published 1:100,000 scale geological maps (includes Kasanka (mapped from satellite imagery), Serenje, Kanona, Chitambo, and Mupamadzi sheets) (Cordiner, 1994; Mapani and Moore, 1995a; Van de Velde and De Waele, 1997; Cordiner, 2000). Outlines of quartzite ridges are traced in the Manshya River Group.

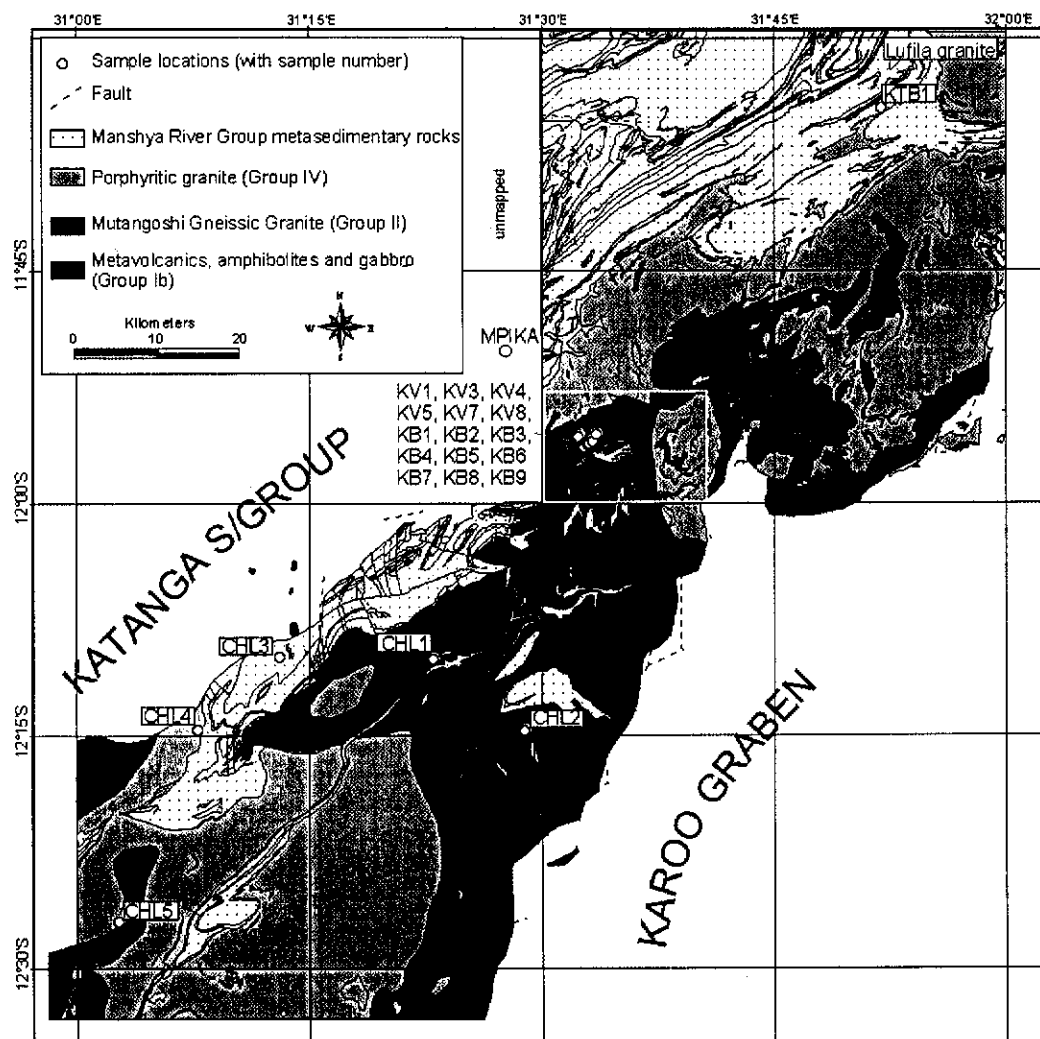


Figure 2-11: Simplified geological map of the region around Mpika showing sample locations for this study, adapted from published 1:100,000 scale geological maps (includes Chilonga Mission and Katibunga Mission sheets and parts of Mtofwe and Mupamadzi River sheets)(Cordiner, 1994; Mosley, 1994; Mosley and Marten, 1994; Van de Velde and De Waele, 1997). The white rectangle shows the area of the detailed map in Figure 2-37. Outlines of quartzite ridges are traced in the Manshya River Group.

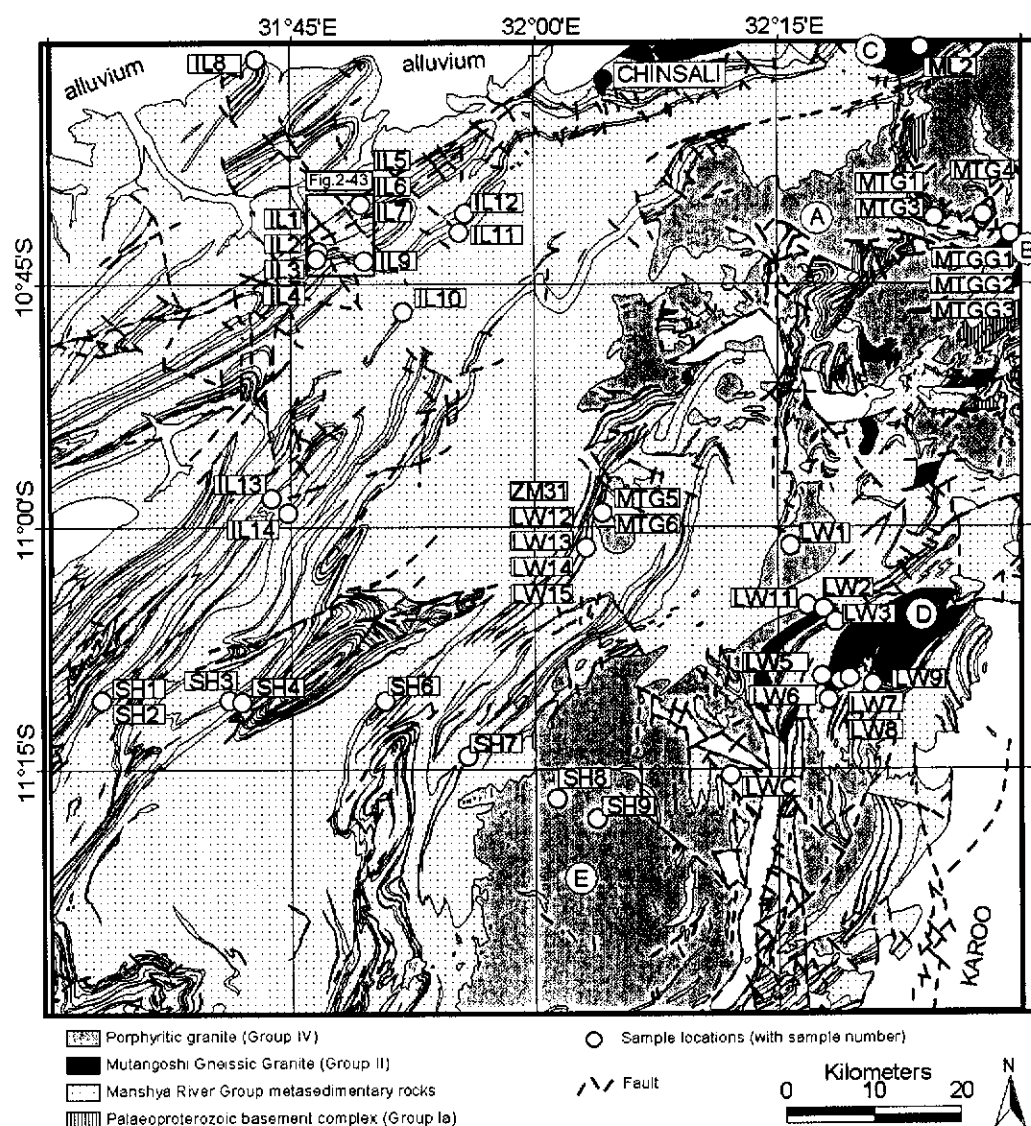


Figure 2-12: Simplified geological map of the region around Chinsali showing sample localities for this study, adapted from published 1:100,000 scale geological maps (includes Shiwa N'gandu, Ilondola Mission, Luswa River and Chinsali map sheets)(Daly, 1994a; Sykes, 1994; Ayres, 1998; Lucacik, 1998a). Specific units referred to in the text are: A=Chilubanama Granite; B=Mutangoshi Gneissic Granite; C=Lubu Granite Gneiss; D=Musalango Gneiss; E=Lufila Granite (Bemba Batholith). Outlines of quartzite ridges are traced in the Manshya River Group.

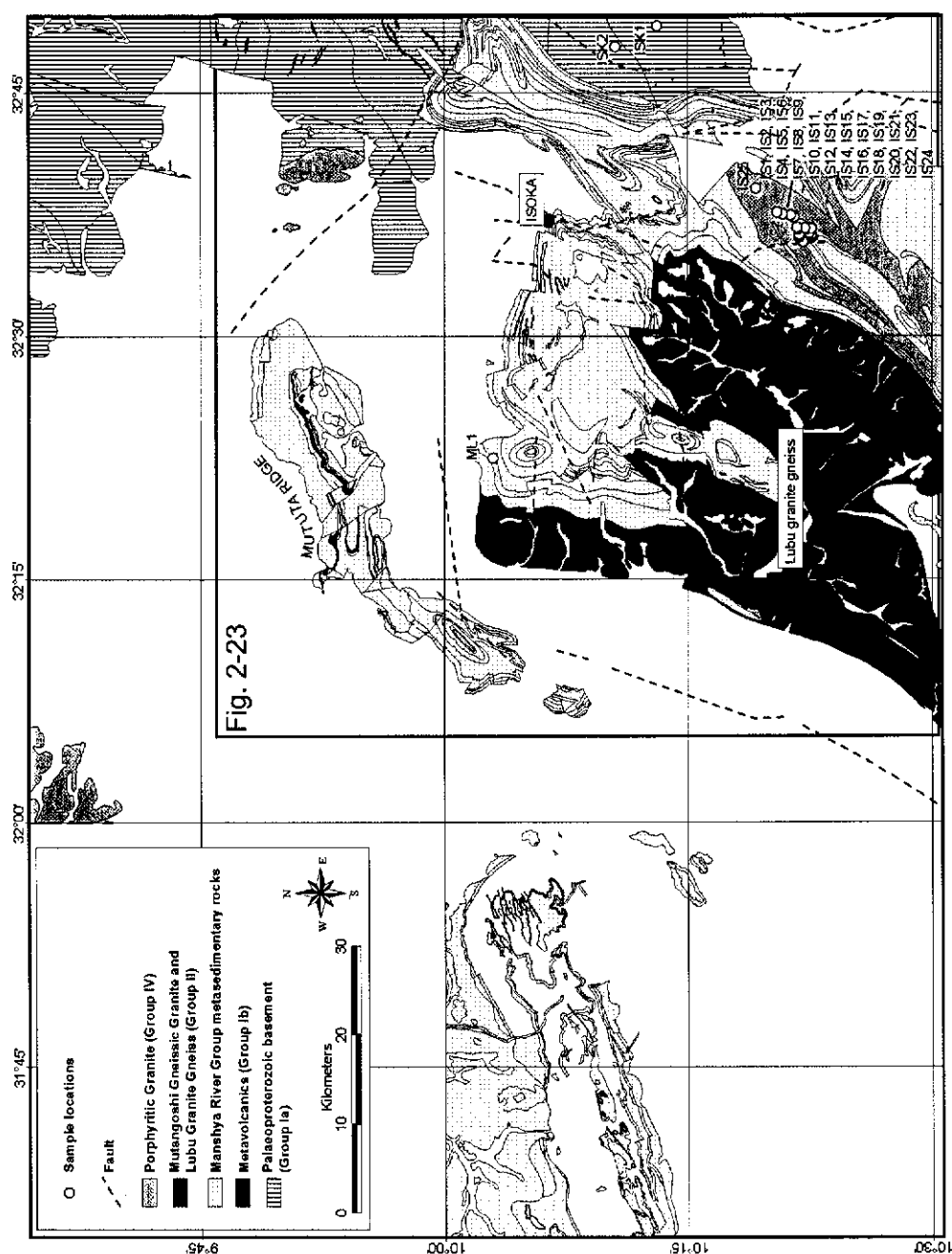


Figure 2-13: Simplified geological map of the region around Isoka showing sample localities for this study, based on published 1:100,000 scale geological maps (includes Malole, Mullansolo Mission, and Mututa Hills map sheets, and parts of Isoka and Kalungu sheets)(1994c; Daly, 1994b; Van Tuijl and Verhoog, 1995a; 1995b). The rectangle indicates the area of Figure 2-23. Outlines of quartzite ridges are traced in the Manshya River Group.

2.3.3.1 The Palaeoproterozoic Mkushi Gneiss

The Mkushi Gneiss has been previously defined as comprising all granitic and gneissic lithologies in the southwestern Irumide belt, and was regarded as a polymetamorphic basement to the folded Muva cover sequences (Ackermann, 1936; 1950; 1960; Ackermann and Forster, 1960; Stillman, 1965c; Smith, 1966; Moore, 1967b; Cvetcovic, 1973; Kerr, 1975; Smith and Kerr, 1975; Legg, 1976; Ng'ambi et al., 1986). Recent work has redefined the Mkushi Gneiss to comprise an older complex of gneisses and deformed granitoids, intruded by various suites of younger granitoids and associated aplites and pegmatites (Mapani, 1999; De Waele and Mapani, 2002). The Mkushi Gneiss commonly has a pervasive foliation defined by oriented biotite in a matrix of stretched and flattened quartz and feldspar. Deformed as well as undeformed small pegmatites occur within the gneiss (Figures 2-14 (a) and (b)), and some have gradational contacts with weakly deformed, or undeformed coarse porphyritic varieties of the gneiss. Because of the strongly heterogeneous fabrics of the gneiss, the distinction of the Mkushi Gneiss from younger granitoids is not always possible based on field evidence alone.

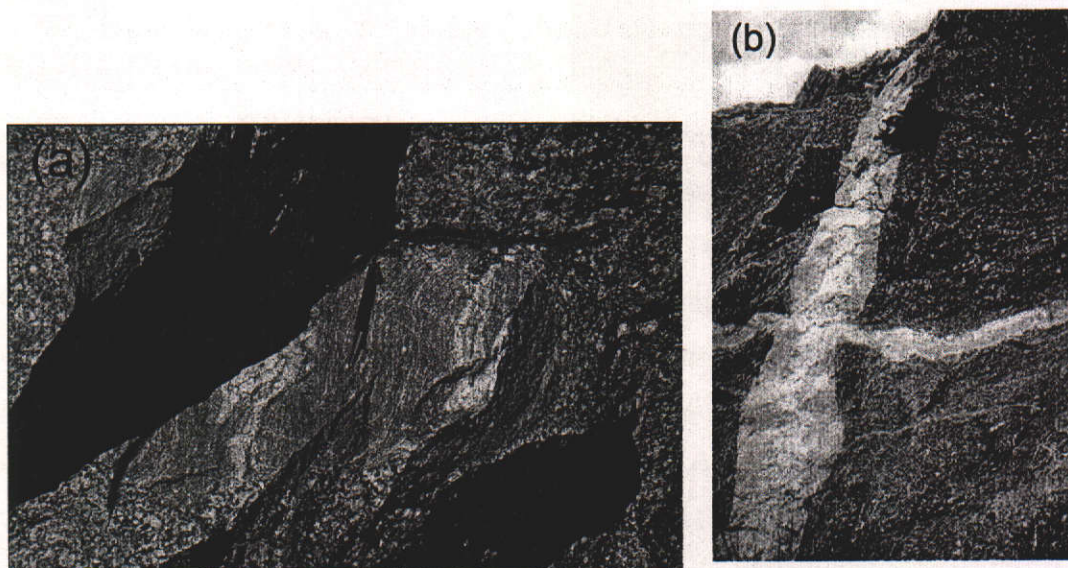


Figure 2-14: (a) strongly deformed Mkushi Gneiss (Munshiwebemba mine), intruded by various generations of chalcopyrite-bearing pegmatites (b).

During the present study, the most westerly occurrence of the Mkushi Gneiss studied was at Kampoyo Quarry near Kapiri Mposhi (sample KMP-1, Fig. 2-9). In this quarry, the granite gneiss is well exposed and consists of strongly foliated quartz + plagioclase + biotite with minor muscovite and sphene (Figure 2-15(a)). The granite gneiss is intruded by various generations of quartz veins and undeformed small pegmatites (Figure 2-15(b)). In the quarry, the foliation, defined by aligned biotite and feldspar, is oriented along a northeast direction, dipping steeply southeast. A strong lineation is defined by stretched feldspar with a shallow to steep northeasterly plunge. At various locations in the quarry, the granite gneiss is strongly sheared, deflecting the foliation trend to east-southeast along shear planes dipping steeply to the north.



Figure 2-15: (a) photomicrograph of thin section (xpl) of sample KMP1 (Mkushi Gneiss, Kampoyo Quarry) showing q-pl-ksp-bi-mu assemblage (f.o.v. 2.32 mm); (b) Strongly foliated biotite granite gneiss in Kampoyo quarry. An aplitic melt pocket truncates the foliation.

The Mkushi Gneiss is best exposed in its type locality, the abandoned open cut Munshiwemba Copper Mine (Munshiwemba Quarry on Figure 2-9). The gneiss was described by Stillman (1965c) as a complex of poorly exposed banded gneisses and porphyroblastic gneisses. A unit of strongly sheared schists and quartzites, which Stillman interpreted to have been produced through extensive shearing of the gneisses, was attributed to the Irumi Formation. In Munshiwemba Quarry, the characteristic Mkushi Gneiss occurs both as a strongly sheared, biotite-rich variety (e.g. sample MK3), and as a pristine porphyritic variety (e.g. sample MK5). Munshiwemba Quarry was exploited for copper, which occurs disseminated in the gneiss, along the shear zones, and within large undeformed aplites that cut the gneiss.

The typical Mkushi Gneiss is a coarse biotite gneiss, with large porphyroclasts of microcline in a groundmass of quartz + plagioclase + biotite (Figure 2-16 (a)). Away from the shearzones, the Mkushi Gneiss is a pink biotite + K-feldspar + plagioclase + quartz gneiss, with a foliation defined by flattened feldspar and aligned biotite (sample MK5, Figure 2-16 (b)). Accessories include magnetite, sphene, apatite and epidote. In the shear zones, the biotite flakes become very large, wrapping around quartz-feldspar augen, and developing a strong L-fabric (sample MK3). The lineation plunges to the east, and is defined in northeast-oriented foliation planes dipping steeply to the north. The gneiss mainly remains porphyritic but locally grain size reduction leads to a mylonitic aspect. The Mkushi Gneiss is cut by large aplitic dykes and small pegmatites, which show no evidence of deformation. A series of minor older pegmatites can be distinguished, which are folded isoclinally. All generations of pegmatite and aplite contain chalcopyrite.

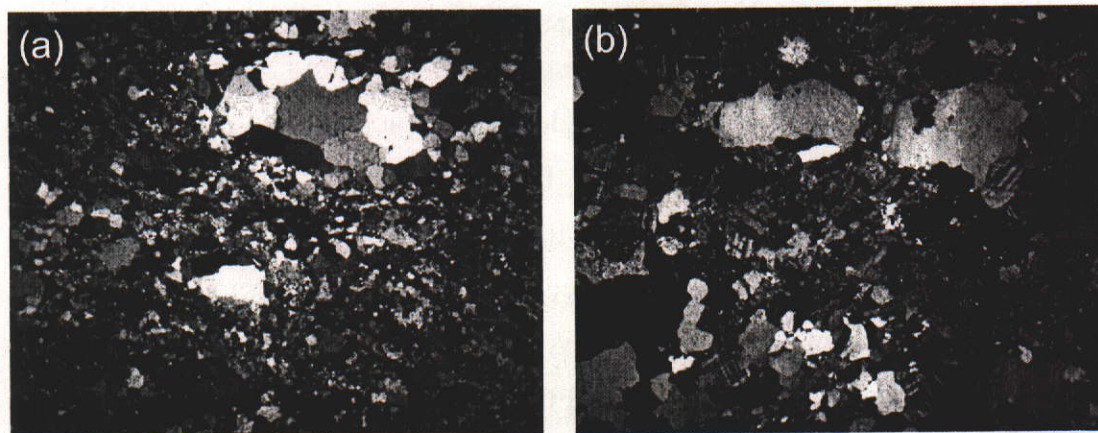


Figure 2-16: (a) photomicrograph of thin section (xpl) of sample MK3 (Mkushi Gneiss, Munshiwemba Quarry) showing q-pl-(ksp)-bi assemblage, with sericitised matrix and relict coarse q-pl crystals. Biotite defines a strong foliation (f.o.v. 4.64 mm); (b) photomicrograph of thin section (xpl) of sample MK5 (Mkushi Gneiss, Munshiwemba Quarry) showing the less deformed coarse granite gneiss variety, with q-pl-ksp-bi (f.o.v. 4.64 mm).

In the far southeastern corner of the 1:100,000 map sheet of Serenje, a unit of strongly deformed nebulitic migmatites is ascribed to the Mkushi Gneiss. The migmatites are best exposed along the Lukusashi and the Fukwe Rivers, where they occur together with interspersed rafts of metasedimentary rocks, comprising mainly sillimanite-biotite-garnet schist, and mafic dykes. The migmatites themselves consist of interspersed bands of mafic and felsic minerals. The felsic minerals are mainly

quartz, microcline, orthoclase and plagioclase, and the mafic mineral is biotite. Sillimanite and garnet are observed within the leucosomes.

2.3.3.2 *The Mulungwizi and Mwambwa River Gneiss*

In the northeastern part of the Irumide belt and adjacent parts of the Bangweulu block, the basement complex occurs in a series of east-west-oriented schist belts, which pass into coeval lithologies of the Ubendian belt. The schist belts are collectively termed the Mulungwizi Gneiss (Figure 2-2). Banded migmatitic biotite gneisses of the Mwambwa River Gneiss occur further southwest in the Irumide belt, and were correlated with the Mulungwizi Gneiss (Daly, 1995a). Daly (1986b) reported a nine-point whole-rock Rb-Sr date of 1804 ± 170 Ma for the Mwambwa River Gneiss (Figure 2-5) but considered this a highly unreliable approximation of the emplacement age because of excessive scatter around the regression line. The Mulungwizi and Mwambwa River Gneiss were not included in this study, but will be briefly discussed below, based on published geological reports (Daly, 1986b; Namateba, 1994; Daly, 1995a; Van Tuijl and Verhoog, 1995c; Verhoog and Van Tuijl, 1995b; 1995c; 1995a). The Mwambwa Gneiss (Daly, 1995a) comprises banded migmatitic biotite gneiss interleaved with large quartzite sheets believed to be part of the Manshya River Group. A strong pre-Irumide gneissic banding is truncated by mafic dykes and then folded along northeast-oriented axial planes during Irumide tectonism. The Mulungwizi Gneiss was described by Verhoog and Van Tuijl (1995a; 1995b; 1995c), Van Tuijl and Verhoog (1995c) and Namateba (1994) as a sequence of compositionally banded, steeply dipping paragneisses striking west-northwest–east-southeast. The sequence includes migmatitic biotite gneisses, biotite-epidote gneisses, muscovite gneisses and schists, hornblende gneisses and amphibolites. Thin bands of quartzite attest to the original sedimentary protoliths. These rocks are strongly deformed and occur in three west-northwest–east-southeast trending belts within the granites of the Bangweulu block. This strong deformation obliterated any pre-existing stratigraphy within the schist belts, and left only remnant resistant quartzite lenses. The Mulungwizi Gneiss within the belts is deformed, unlike the granitoids in which it resides, indicating that the belts predate intrusion of the granites of the Bangweulu block. A Rb-Sr date of 1830 ± 240 Ma for

an undeformed granite immediately south of the Mambwe schist belt and a Rb-Sr date of 1870 ± 39 Ma for the Mambwe Gneiss within the schist belt in northern Zambia (Schandelmeier, 1980; 1983)(Figure 2-17) constrain a minimum age for the Mulungwizi Gneiss.

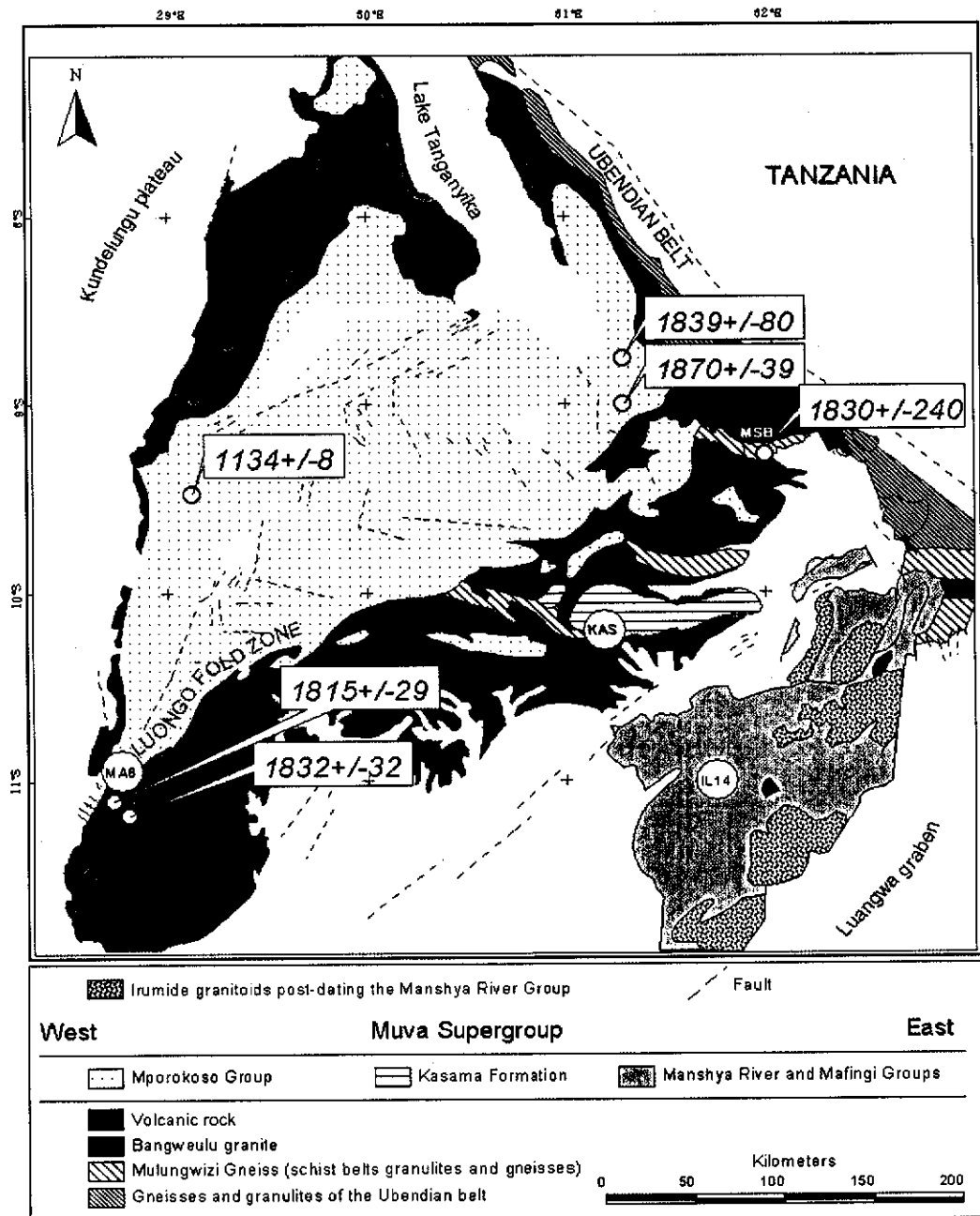


Figure 2-17: Geological map of northern Zambia, showing published whole rock Rb-Sr dates and localities sampled in this study for detrital provenance (see Chapter 4). MSB=Mambwe schist belt (adapted after Andersen and Unrug, 1984).

2.3.3.3 *The Luwalizi and Lubu Granite Gneiss*

The Luwalizi Granite Gneiss was sampled east of Isoka (samples ISK1 and ISK2, Figure 2-13). At the sampling locality, the unit is a weakly-foliated coarse quartz + K-feldspar + plagioclase + biotite + hornblende granite, which displays a remnant primary igneous fabric of aligned K-feldspar phenocrysts (Figure 2-18). Locally, a structural fabric is expressed through stretched K-feldspar and alignment of biotite along northeasterly trends dipping steeply to the northwest. Xenoliths of melanocratic fine-grained material are similarly affected by the foliation.

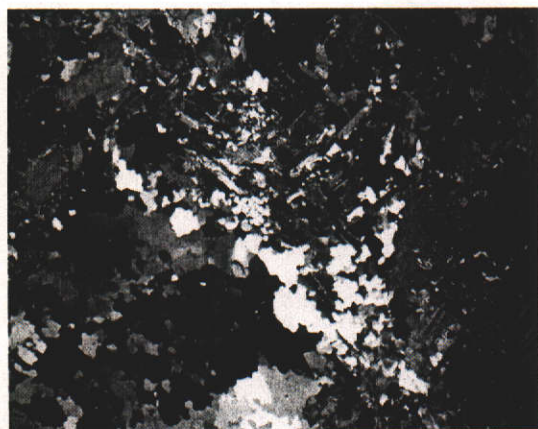


Figure 2-18: photomicrograph of thin section (xpl) of sample ISK1 (Luwalizi Granite Gneiss, Isoka area) showing q-pl-(ksp)-bi-ms assemblage (f.o.v. 4.64 mm).

The Lubu Granite Gneiss crops out to the north of the 1:100,000 Chinsali sheet and in the Mulilansolo Mission sheet, and has been described in detail by Daly (1995a)(Figure 2-4, Figure 2-12 and Figure 2-13). It is a pinkish and greenish biotite granite gneiss with a weakly to strongly developed biotite foliation along northeasterly trends dipping to the south. The feldspars occur as rounded to stretched augen and as subhedral laths cross-cutting the deformation fabric. Myrmekitic texture is commonly found within plagioclase where in contact with the K-feldspar phenocrysts (Figure 2-19). The granite gneiss locally has biotite schlieren aligned near parallel to the regional fabric and contains xenoliths of mafic material, and is cut by various generations of pegmatites. One sample (sample ML2, Figure 2-12 and Figure 2-13) was collected from the gneiss for geochemistry and U-Pb SHRIMP dating.

Both the Luwalizi and Lubu Granite Gneiss were considered by Daly (1986b) to be the deformed equivalents of the granites of the Bangweulu block in the Irumide belt. Daly (1986b) distinguished these weakly to moderately deformed granitoids from the much more strongly deformed Mulungwizi and Mwambwa River Gneisses and suggested that the latter two units form remnants within the Irumide belt of basement affected by Ubendian tectonism. In Daly's view, the less deformed granitoids in the Bangweulu block, together with the Lubu and Luwalizi Granite Gneiss, form part of the post-Ubendian magmatic development of the Bangweulu block (Daly, 1986b).

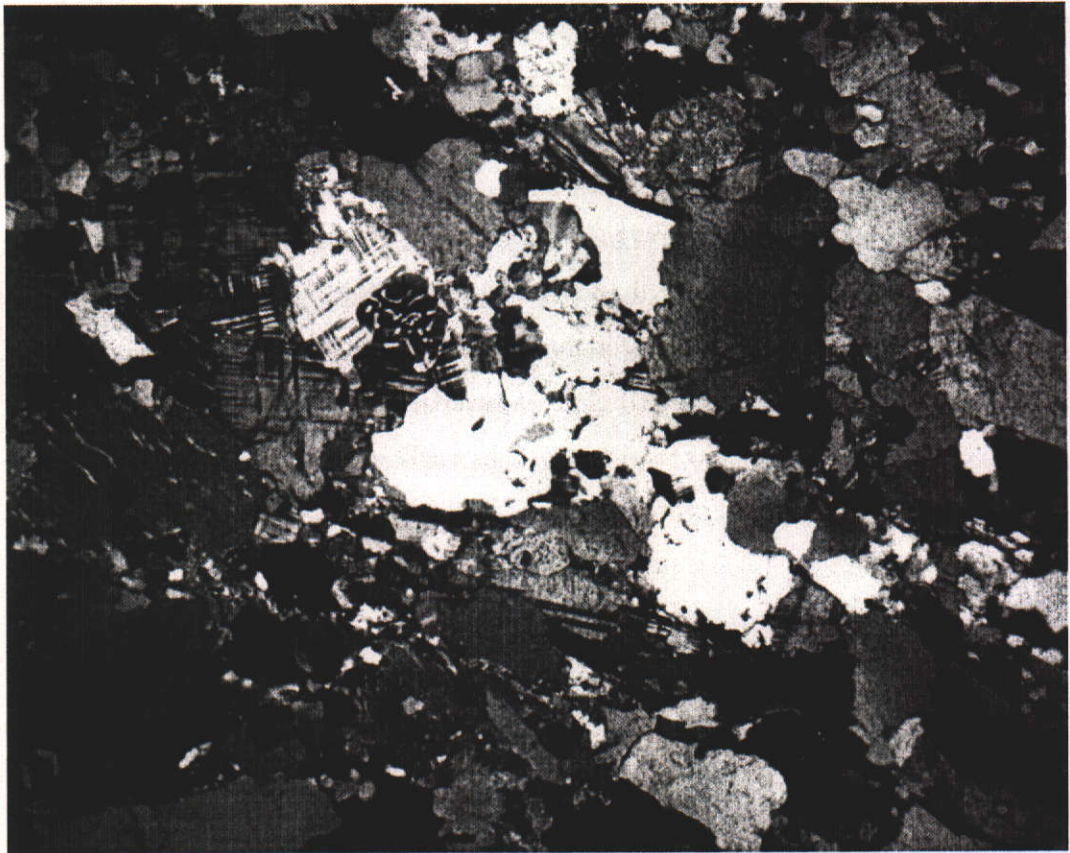


Figure 2-19: photomicrograph of thin section of sample ML2 (Lubu Granite Gneiss) showing coarse grained quartz, plagioclase and microcline, with biotite and minor muscovite. Note the myrmekitic intergrowth commonly found in the Lubu Granite Gneiss (f.o.v. 4.64 mm).

2.4 The Muva Supergroup

A five-fold division of the Muva Supergroup is adopted in this thesis. The Mporokoso Group comprises the pre-Katangan successions resting on the ca. 1.8 Ga granitic and volcanic rocks of the Bangweulu block, as defined by Unrug (1984). The Kasama Formation is considered as a separate unit to the southeast of the Mporokoso Group, and occurs in an east-west oriented basin east of Kasama. The Kanona, Manshya River and Mafingi Groups comprise the deformed metasedimentary successions in the Irumide belt itself. Even though the deformed successions of the Irumide belt are essentially the same along strike, they are described separately because lateral breaks preclude unequivocal correlation. Although Unrug (1982) included the Mututa Ridge sedimentary successions to the east of the Chambeshi River with the Kasama Formation, based on their common fluviatile character, I follow Van Tuijl and Verhoog (1995c) in correlating the Mututa Ridge successions with the Mafingi Group rather than with the undeformed Kasama Formation. Although the Mafingi Group was not included in this study, a short description based on published literature is included below. Simplified stratigraphic columns of the Mporokoso Group, Kasama Formation, Manshya River Group, Kanona Group and Mafingi Group are shown in Figure 2-20.

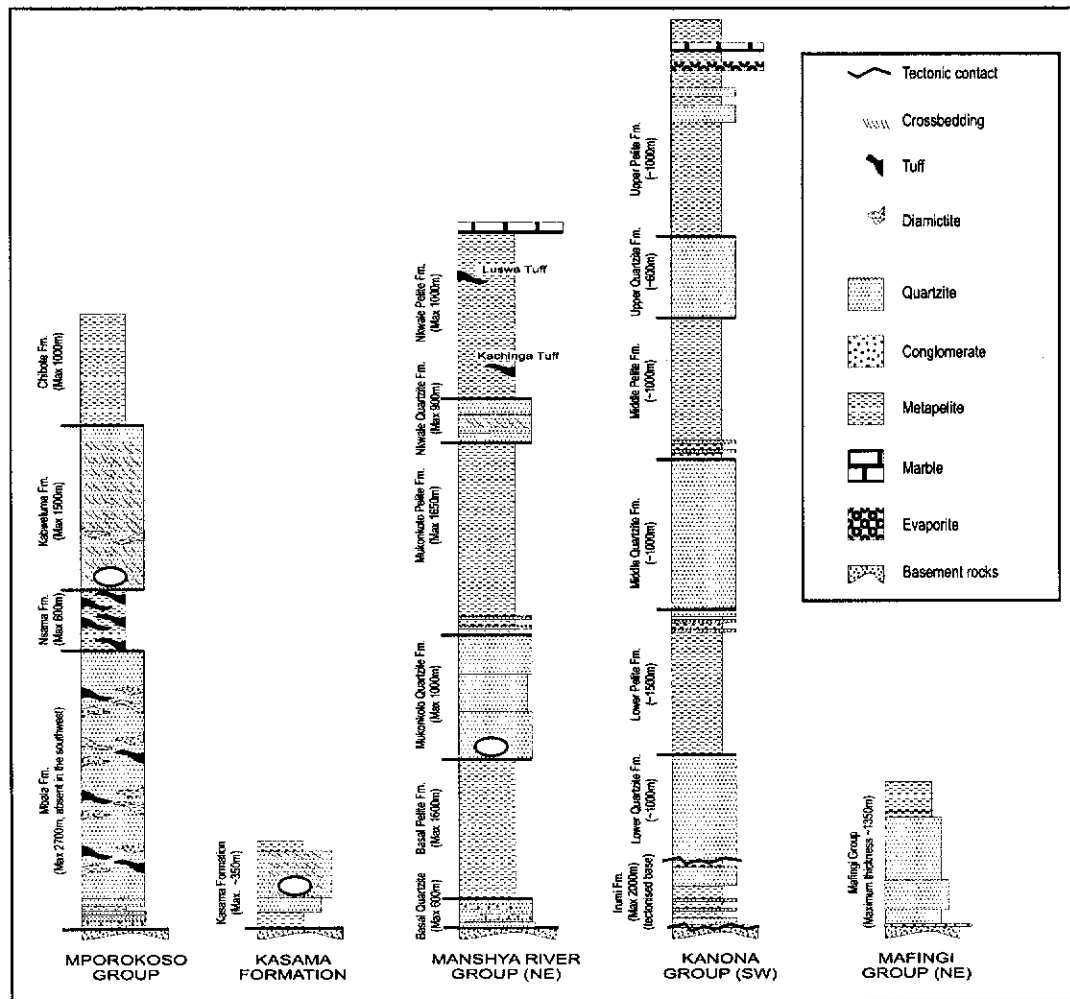


Figure 2-20: Simplified stratigraphic columns for the (meta)sedimentary sequences of the Muva Supergroup. The stratigraphic locations of samples collected for a detrital provenance study (see Chapter 4) are indicated with ellipses. Thicknesses are estimated maxima; actual thickness varies strongly along strike.

2.4.1 Mporokoso Group

The Mporokoso Group (Andersen and Unrug, 1984) is subdivided into four lithostratigraphic packages, from bottom to top the Mbala Formation, Nsama Formation, Kabweluma Formation and Chibote Formation (Figure 2-20 and Figure 2-21). The work presented in this thesis is limited to a reconnaissance traverse in the Mansa and Musonda Falls map sheets (see box on Figure 2-2 and detailed map in Figure 2-6), where the two lowermost formations (Mbala and Nsama Formations) are very thin or absent. Detailed accounts of the Mporokoso Group were presented by Unrug (1984), Andrews-Speed and Unrug (1982) and Andrews-Speed (1986), from which the salient points are reported here.

Coarse, immature sandstones and pebble beds, with abundant trough crossbeds, channels, alluvial fan deposits and interfingering pebble conglomerates, dominate the Mbala Formation. The pebble conglomerates are reported to be polymictic with predominant quartzite clasts, red chert and subordinate granite, granodiorite and rhyolite, possibly derived from the basement they overlie. Minor occurrences of jaspillite pebbles have been reported (Andrews-Speed and Unrug, 1982; Unrug, 1984), for which no (local) source is known. Sedimentary structures in the sandstones are defined by minor amounts of opaque minerals, mainly hematite, along bedding planes. The sequence gradually becomes red towards the top, indicating an increasingly arid environment. The occurrence of intercalated felsic tuffs and ignimbrites in the lower quartzites of the Mbala Formation suggests no time gap between Bangweulu block magmatism and the onset of sedimentation of the Mporokoso Group. The overall thickness of the Mbala Formation is estimated at 250 m in the south, increasing to a maximum of 2700 m in the north near Mbala. In the Mansa 1:100,000 map sheet, Thieme (1971) described the Mbala Formation (his "Lower Quartzites") as a 150-250 m thick series of coarse quartzites, resting unconformably on the granitic-volcanic basement. The Mbala Formation gradually becomes finer grained towards the top and grades into the Nsama Formation, which consists of reddish shales with a considerable component of silicic tuffs, ignimbrites, and fine-grained volcanoclastic deposits. The Nsama Formation is locally absent in the south and increases in thickness to some 600 m in the north. In the Mansa and Musonda 1:100,000 map sheets, where the Nsama Formation is absent, the Mbala Formation gradually coarsens upwards into the Kabweluma Formation, which consists of fluvial, poorly sorted quartzites, with abundant trough cross bedding, channels, and interfingering shales, thought to represent fluvial and floodplain sequences (Figure 2-22 (a)). The maximum thickness of the Kabweluma Formation is estimated at 1500 m and it comprises the bulk of the sedimentary sequence near Mansa. The Chibote Formation was not recognised in the Mansa area but was described further north by Andrews-Speed and Unrug (1989) as a sequence of siliceous mudstones of lacustrine origin, with a maximum thickness of 1000 m.

Andersen and Unrug (1984) reported palaeocurrent data showing a decrease in pebble size towards the north indicating that the sediments of the Mbala Formation were derived from terranes to the present south. The pebble size and thickness of conglomerates in the Mbala Formation increases from the west to the central part near Mporokoso, and then decreases towards the east, indicating that the main drainage channels were located near the present centre of the basin. Towards the eastern part of the basin, some palaeocurrent directions in the Mbala Formation indicate a source area to the east. This may represent a portion of the fluvial system transporting sediments into the main basin from the east. The Mporokoso Group and Bangweulu basement are unconformably overlain by Neoproterozoic basal conglomerate of the Kundelungu Group (Katanga Supergroup), locally called the Luapula beds (Figure 2-22 (b)).

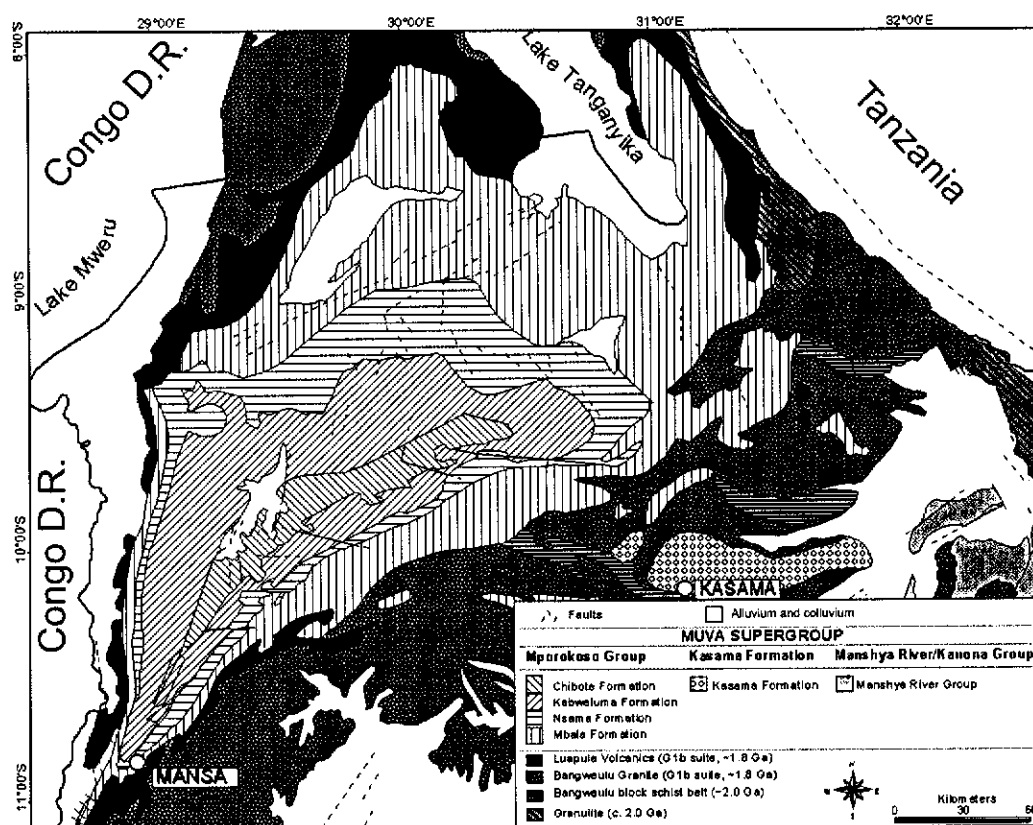


Figure 2-21: Geological map of northern Zambia, adapted from Andersen and Unrug (1984), showing the subdivision of the Palaeoproterozoic Mporokoso Group into four formations.

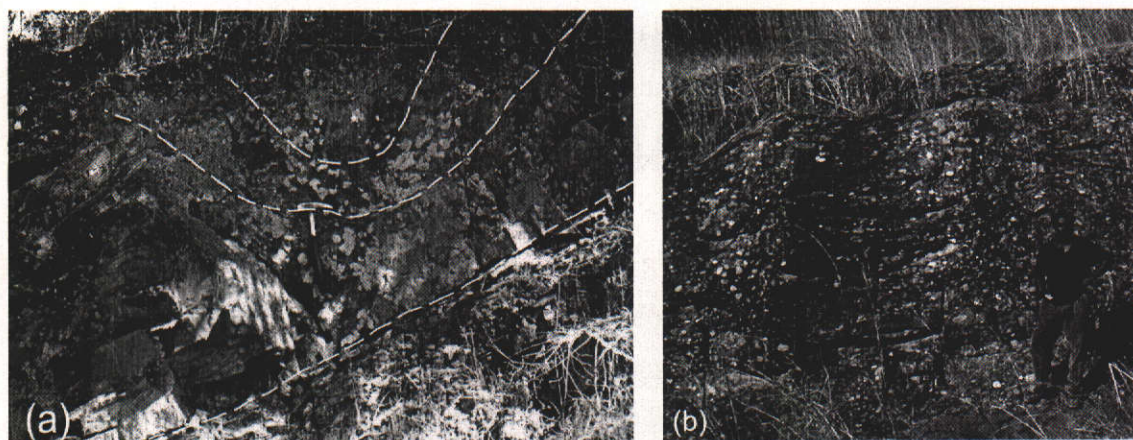


Figure 2-22: (a) typical thick bedded quartzite of the Kabweluma Formation (locality of sample MA6 in the Mansa 1:100,000 map sheet). Note the alternating thick and thin beds, a prominent channel-fill structure and the planar bedding (below the dashed line); (b) coarse pebble conglomerate of the Neoproterozoic Luapula beds unconformably overlying the Bangweulu block and Mporokoso Group (Musonda Falls 1:100,000 map sheet; Mr. Willy Nundwe for scale).

2.4.2 Kasama Formation

The Kasama Formation was first described by Unrug (1982) from sedimentary rocks cropping out in an east-west oriented basin near Kasama, and is described from its type locality 12 km east of Kasama (Figure 2-2). At the type-section, Unrug (1982) described a fine-grained, very well-sorted white quartzite, accompanied by reddish sandstones and subordinate red mudstones, directly overlying the crystalline basement of the Bangweulu block. Within the Kasama Formation, Unrug (1982) recognised four lithostratigraphic units, from bottom to top: the Mabula Mudstone, Chansamina Sandstone, Makumba Sandstone and Misamfu Mudstone. The Mabula Mudstone directly overlies the granites of the Bangweulu block, and is a 40-meter-thick reddish mudstone, with lenses of coarse white sandstone. It is overlain with gradational contact by 20 m of poorly-sorted medium- to coarse-grained micaceous sandstone of the Chansamina Formation. This in turn gradually passes into the well-sorted pinkish-white Makumba Sandstone, which forms the main outcrop near Kasama and in the present study was sampled from a quarry near the Mwela rock paintings national monument (sample KAS-1, Figure 2-17 and Figure 2-20). The Makumba Sandstone shows well-developed cross-stratification, small-scale climbing ripples and graded bedding, and numerous large-scale trough crossbeds, indicating fluvial deposition. The uppermost Misamfu

Mudstone occurs on top, interfingering laterally with the Makumba Sandstone, and represents a floodplain deposit. Daly and Unrug (1982) reported palaeocurrent directions indicating a sediment source lying to the west. The preserved thickness of the formation increases from 100 m west of Kasama to 300 m in the east of the basin. Based on the supermature character and palaeocurrent information, the Kasama Formation has been interpreted as a reworked deposit of the Mporokoso Group (Daly and Unrug, 1982; Unrug, 1982; Andersen and Unrug, 1984;).

2.4.3 Mafingi Group

In the Mafingi Hills area (see Figure 2-4), Fitches (1971) recognised a basal conglomerate, followed by a succession of quartzites, which fine upwards into a sequence of green argillaceous rocks (Figure 2-20). The sequence in places rests unconformably on the crystalline basement, while in some cases the basement-cover contact is tectonic. The thickness of the Mafingi Group is estimated not to exceed 1350 m. Herringbone crossbedding and planar laminations are thought to indicate a shallow marine depositional environment, while the alternating nature of the sequence further suggests a migrating shoreline environment. Palaeocurrent analyses confirm dominant bimodal currents along north-south axes. Considering the interpretation that the Mafingi Group represents a shallow marine, coastal sediment, Fitches postulated the palaeo-coastlines to have been along east-west axes (Fitches, 1971).

2.4.4 Manshya River Group s.s. (northeastern Irumide belt)

The Manshya River Group is described here based on a complete section in the Chimbwe syncline (Figure 2-23 and Figure 2-24), rather than from its type section in the Chalabesa Mission area (Marten, 1968), which lacks the lowermost and topmost units.

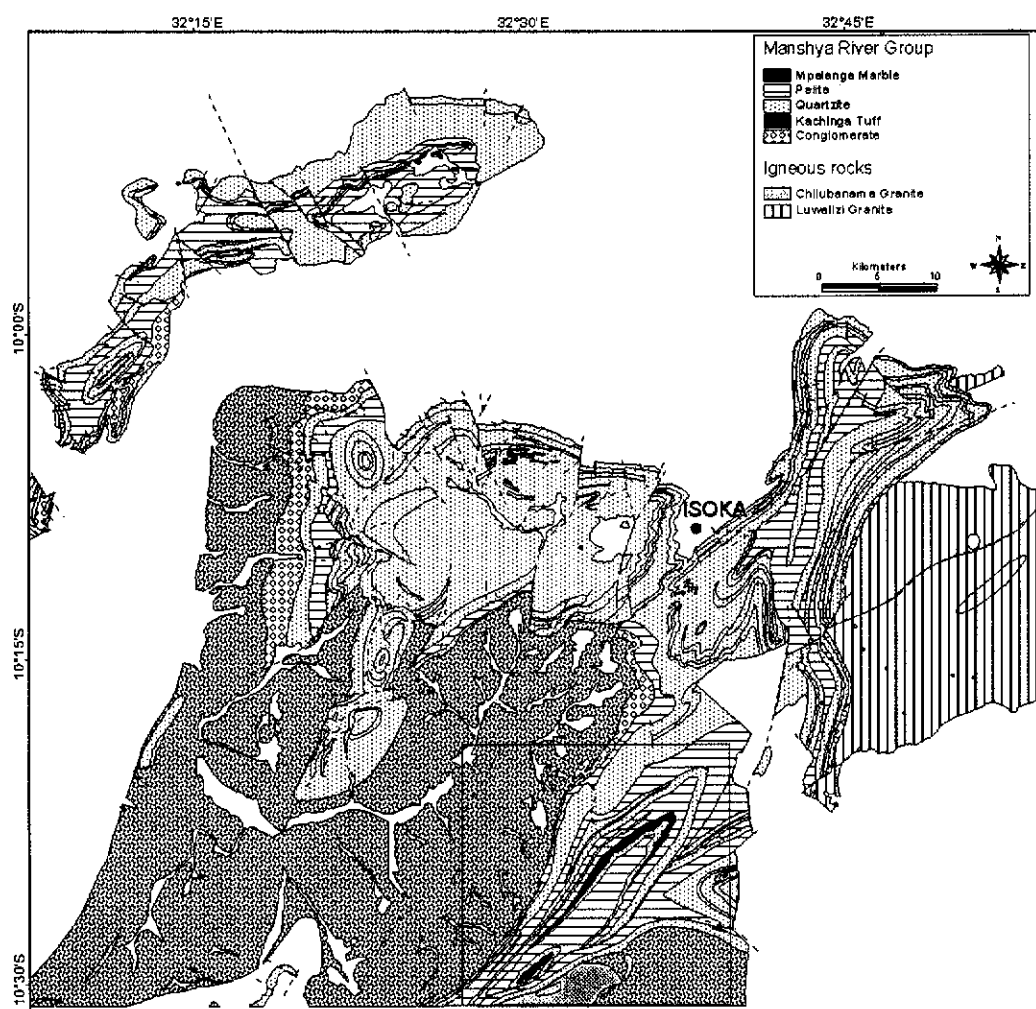


Figure 2-23: Geological map adapted from the published Isoka, Mulilansolo Mission and part of Mututa ridge 1:100,000 map sheets (Daly, 1994b; 1994c; Van Tuijl and Verhoog, 1995b). The outlined box shows the area of Figure 2-24.

The basal quartzite consists of ripple-marked grits, conglomerates, cobble beds, and coarse poorly-sorted quartzites with an estimated thickness of 600 m. The basal contact with the granitoids and volcanics of the Bangweulu block is not exposed, but believed to be tectonic (Daly, 1995b). This unit grades into a poorly exposed sequence of metapelites, comprising mainly phyllites, slates and laminated siltstones with a maximum thickness of 1600 m. Towards the top of this sequence, a gradational unit of interbedded siltstones and thin quartzites leads into the Mukonkoto Quartzite Formation. This prominent quartzite has a basal well-sorted member, passing into a poorly sorted coarse micaceous quartzite and finally another well-sorted, pure white quartzite. The thickness of the Mukonkoto Quartzite Formation is estimated at 1000 m.

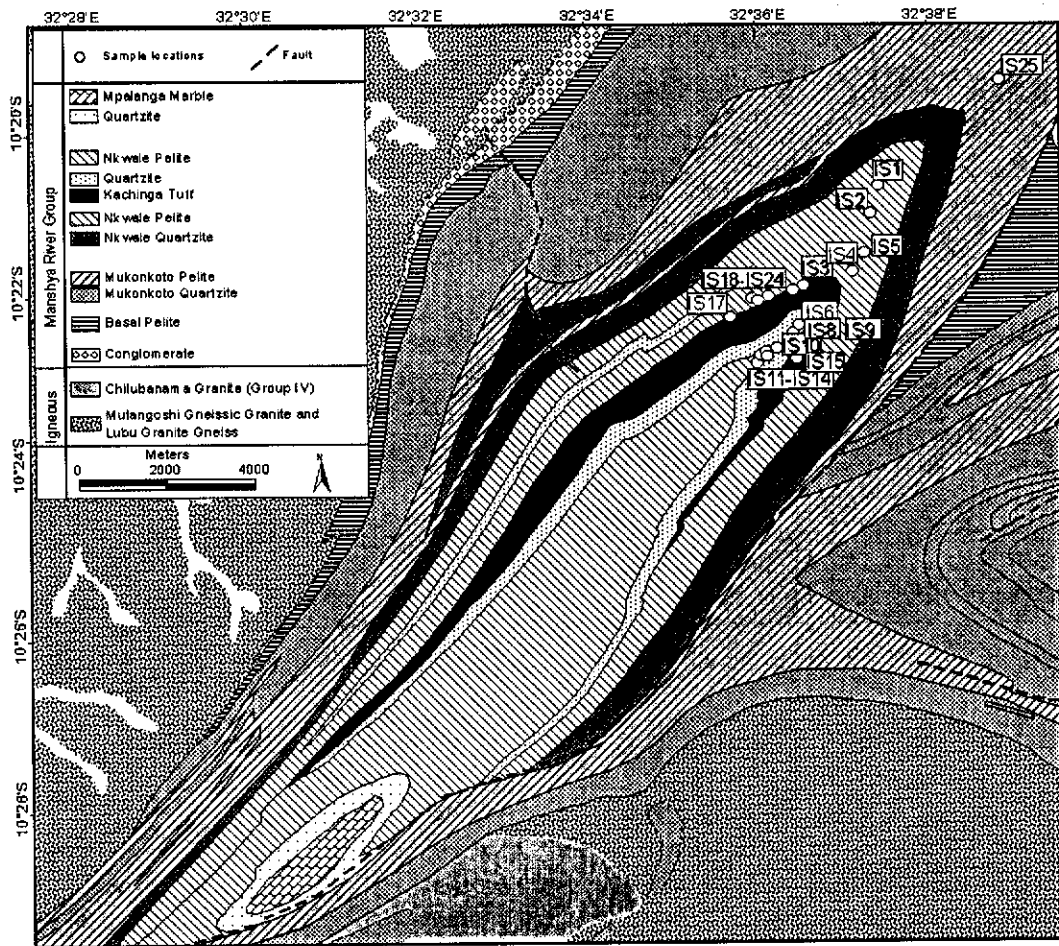


Figure 2-24: Geological map of the Chimbwe syncline, showing the location of the Kachinga Tuff and localities of samples. The map is adapted after Daly (1994b).

A gradational contact at the top of the Mukonkoto Quartzite Formation leads into the Mukonkoto Pelite Formation, which is poorly exposed and has an estimated thickness of 1650 m. The Nkwale Quartzite Formation follows this, with an estimated thickness of 900 m. Three members have been distinguished in the Nkwale Formation, starting with a basal, coarsening-upward quartzite. This grades into a pinkish, extensively cross-bedded middle quartzite unit, finally leading into poorly sorted and impure quartzites. The Nkwale Quartzite Formation is overlain by the ~1000-m-thick Nkwale Pelite Formation comprising metapelites, with interbedded quartzites and, in the Chimbwe syncline, a tuff member (Kachinga Tuff) up to 300 m in thickness. At the top of the Nkwale Pelite Formation, a thin unit of marble has been described (Daly, 1995b), in which stromatolites have been recognised, indicating low energy conditions during deposition of the uppermost part of the

Manshya River Group. The carbonates were not observed during this study. The Manshya River Group quartzites commonly display metre-scale, low-angle crossbeds, typical for shallow-water palaeoenvironments (Figure 2-25). The entire Manshya River sequence has been intensely folded, resulting in kilometre scale isoclinal folds such as the Chimbwe syncline (Figure 2-24), and small-scale tight to isoclinal folds (Figure 2-26).

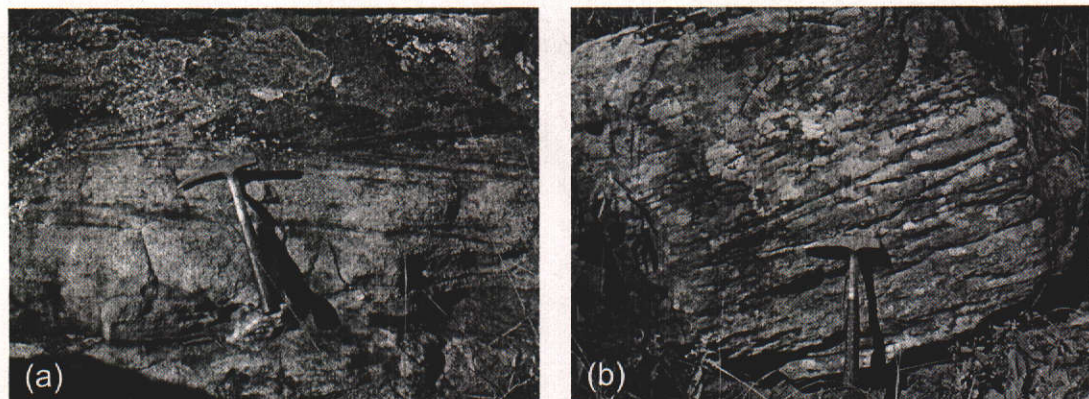


Figure 2-25: Cross bedding structures in quartzites of the Manshya River Group; (a) Luswa River sheet; (b) Chembewesu Hill, Ilondola Mission 1:100,000 map sheet (near location of sample IL14).

In thin section, the quartzites show an interlocking patchwork of quartz, often with undulose extinction (Figure 2-27). The pelitic members are often highly altered, ferruginous schist. With increasing metamorphic grade they may contain andalusite, sillimanite, garnet (Figure 2-28 (a)), or kyanite (Figure 2-28 (b)).

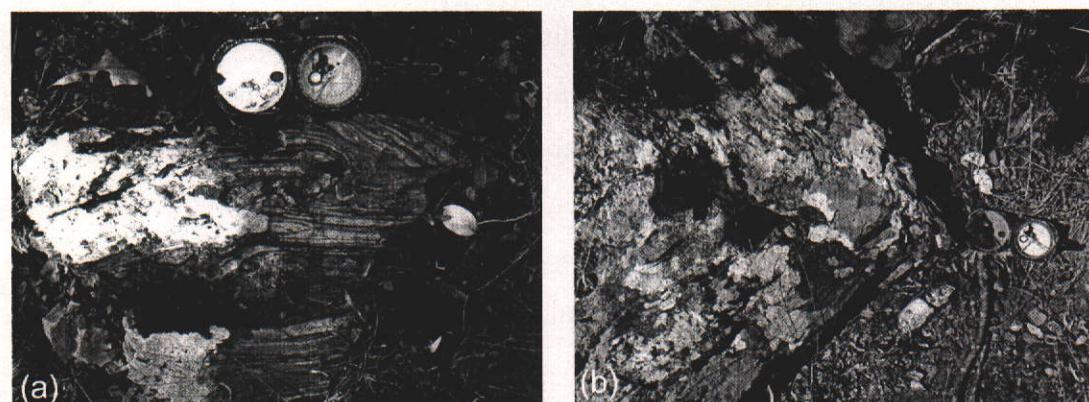


Figure 2-26 (a) tight folding in a fine laminated quartzite-pelite unit of the Manshya River Group (Ilondola Mission 1:100,000 map sheet); (b) fold nose in quartzite of the Manshya River Group (Shiwa N'gandu 1:100,000 map sheet, Figure 2-4)

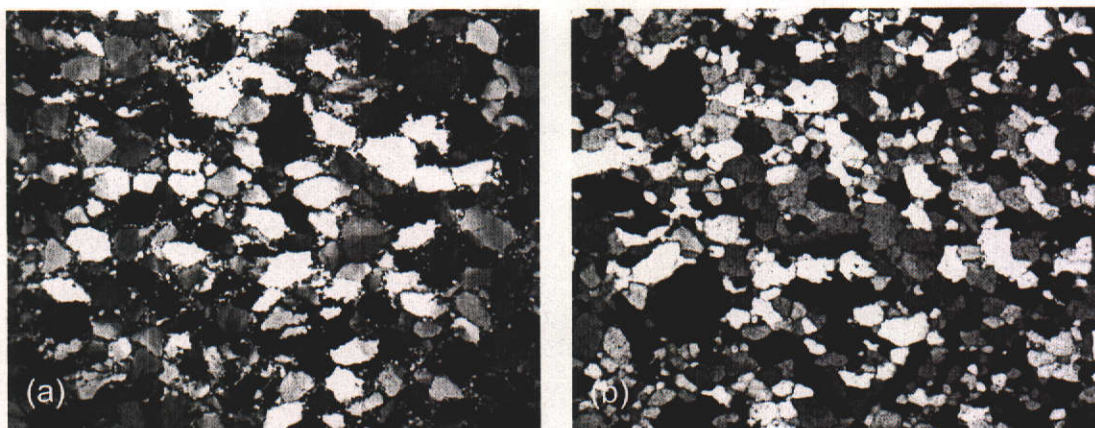


Figure 2-27: photomicrograph of thin sections (xpl) of quartzites from the Manshya River Group ((a) a mild grain flattening fabric in sample IL8 (Ilondola Mission 1:100,000 map sheet)(f.o.v. 4.64 mm); (b) photomicrograph of a thin section of sample IS25 (Chimbwe syncline, Isoka 1:100,000 map sheet)(f.o.v. 4.64 mm).

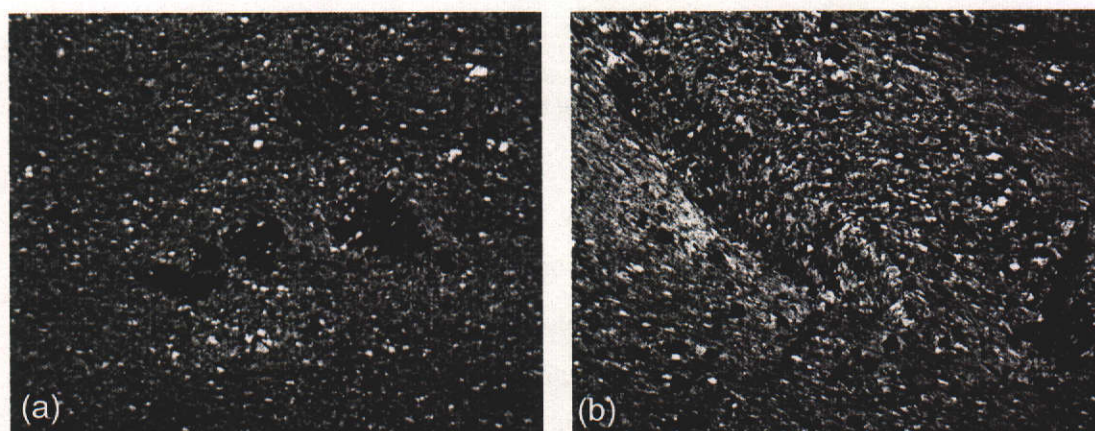


Figure 2-28: (a) photomicrograph of thin section (xpl) of sample IS15 (Isoka 1:100,000 map sheet), showing garnetiferous biotite schist of the Manshya River Group (f.o.v. 2.32 mm); (b) photomicrograph of thin section (xpl) of kyanite schist in the Manshya River Group (sample IS2, Chimbwe syncline, Isoka 1:100,000 map sheet)(f.o.v. 2.32 mm).

2.4.5 Kanona Group (Manshya River Group, southwestern Irumide belt)

The Kanona Group is spectacularly exposed in a series of northeast oriented ridges, comprising resistant quartzite and minor pelite (Figure 2-29 (a)). The Kanona Group is described from the Mwendafie Ridge in the Mkushi 1:100000 map sheet, where the lower part of the sequence can be observed (Figure 2-30). The description is completed with the top of the sequence along the Chengelo Ridge (Fiwila Mission 1:100000 map sheet, Figure 2-9), where the upper pelite-quartzite sequence occurs, and where stromatolitic limestone has been reported (Figure 2-31).



Figure 2-29: (a) panoramic view of dominant quartzite ridges in the Kanona map sheet, southwestern Irumide belt; (b) Crenulated garnet-sillimanite schist near Kamena school, Serenje map sheet.

At Mwendafie Hill, the sequence starts with a mylonitic schist unit, with subordinate quartzite units called the Irumi Formation. Metapelites of the Irumi Formation are garnet-andalusite, garnet-biotite, garnet-sillimanite (such as in Figure 2-29 (b)) or kyanite schists, while the quartzite members are ferruginous muscovite quartzite, locally containing kyanite. The sequence was described by Stillman (1965c) to have either gradational or sheared contacts with underlying granite gneisses. During this study, no direct contact relationships between basement lithologies and the Irumi Formation have been observed, but the absence of a regionally defined clear conglomeratic horizon suggests that most of the sequence is allochthonous or parautochthonous, and in structural contact with the basement gneisses. No direct thicknesses could be measured in the field, but estimates from geological maps indicate that the Irumi Formation reaches a thickness of up to 2000 m. The Irumi Formation is overlain by about 1000 m of coarse quartzite (Lower Quartzite Formation), in which local conglomeratic lags can be distinguished (Figure 2-32 (a)). The quartzites show current bedding and large-scale crossbedding and are interbedded with ferruginous schists (Figure 2-32 (b)). This sequence grades upwards into roughly 1650 m of flaggy metasilstone, with slates and phyllites (Lower Pelite Formation), which passes into a micaceous, sugary quartzite member about 1000 m thick, with minor pelitic schists (Middle Quartzite Formation). A second pelite unit,

about 1000 m thick, consisting of slate and phyllite occurs further up (Middle Pelite Formation), and grades into a prominent quartzite sequence about 600 m thick (Upper Quartzite Formation). This quartzite is recrystallised and pure, and practically no primary structure is preserved. A poorly exposed pelitic unit, the Upper Pelite Formation, overlies the quartzite, and gradually coarsens upwards into a single or double quartzite horizon, in which ripple marks and small-scale cross bedding are common. The top of the Kanona Group consists of a poorly exposed metasiltstone unit in which silicified evaporites and algal stromatolites have been observed (Kerr, 1975; Smith and Kerr, 1975). Attempts to locate these evaporate and algal units during this research have not been successful. An identical stratigraphic succession can be observed, in part, south of the border with Congo, west of Mkushi (Figure 2-9). There, a conglomerate directly overlies the Mkushi Gneiss (sample MK8) and consists of a coarse monomictic pebble conglomerate, with pebbles derived from gneisses and granite gneisses similar to those of the Mkushi Gneiss. The conglomerate is overlain by alternating quartzites and coarse to conglomeratic quartzites, grading into metapelites, and is ascribed to the Lower Quartzite Formation. Higher up, the succession continues with the Lower Pelite Formation, which occurs as far as the border between Zambia and the Democratic Republic of Congo. The conglomerate is here considered the stratigraphic base of the Kanona Group, while the Irumi Formation represents the tectonised interface between the Kanona Group and its basement rather than a true stratigraphic unit in sedimentological terms. The localised occurrence of the basal conglomerate and absence of the tectonised Irumi Formation north of Mkushi indicates that at least some parts of the sequence are autochthonous.

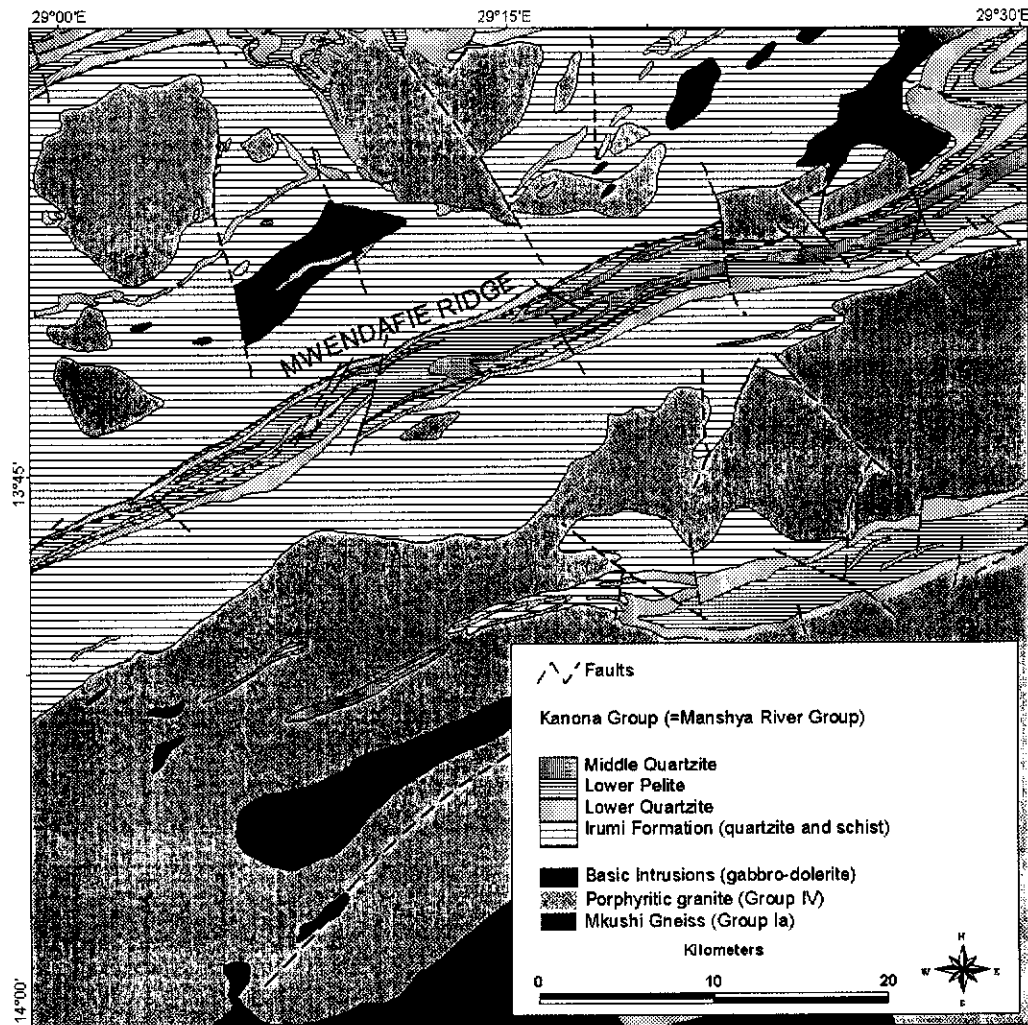


Figure 2-30: Geological map of the region around Mwendaie ridge and Munshiwebba Quarry (adapted after Stillman (1965a)). Location is shown on Figure 2-9.

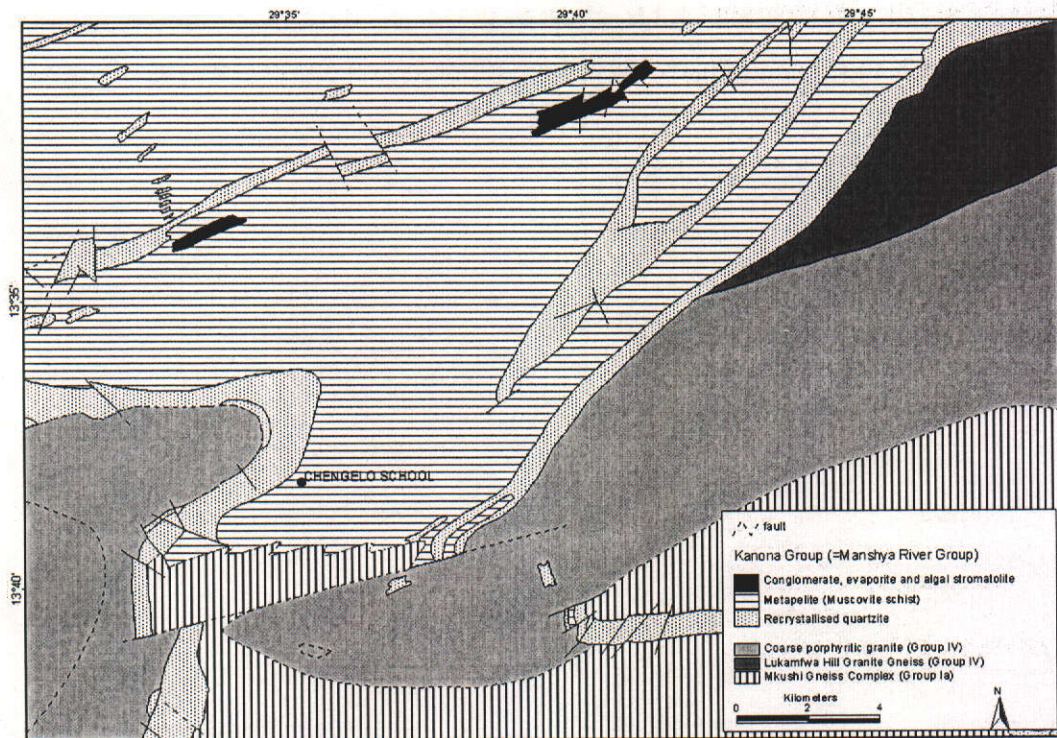


Figure 2-31: Geological map of the area around Chengelo school, showing the evaporites and stromatolitic limestones mapped by Kerr (1994). Location is shown on Figure 2-9.



Figure 2-32: (a) strongly deformed conglomerate at the base of the Kanona Group (Kakulu 1:100000 map sheet); (b) alternating thick and thin-bedded quartzites with minor schists in the Kanona Group

The Kanona Group, as well as the Manshya River Group sequences, have been intensely deformed and folded during Irumide tectonism. On a large scale, deformation resulted in regional-scale isoclinal folds, such as those from the Shiwa N'gandu area (Figure 2-12) and Isoka area (Figure 2-13 and Figure 2-24). Such large structures are predominantly recumbent, but when upright, they can be observed in the field, such as is the case at Kundalila Falls near Serenje (Figure 2-33 (a) and (b)).

In outcrop, small, often parallel folds, attest to the strong deformation of the Kanona Group (Figure 2-34 (a) and (b)).

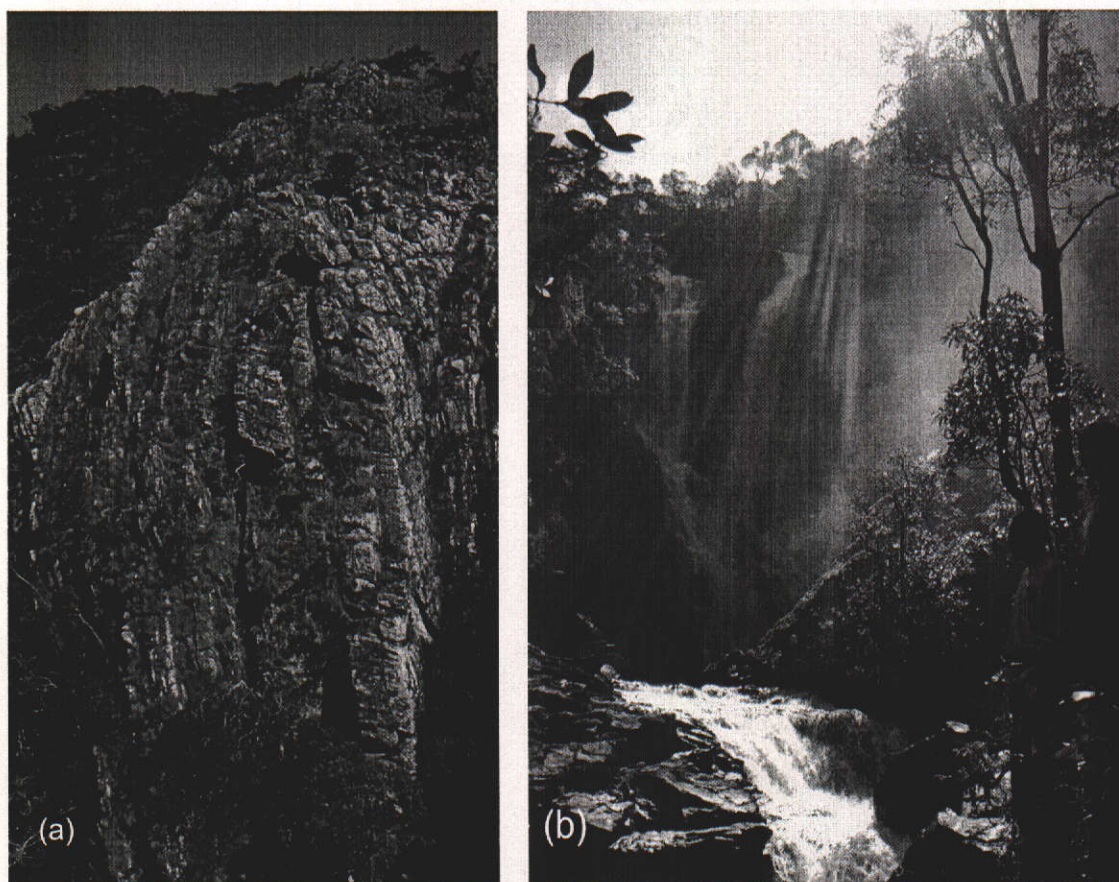


Figure 2-33: (a) large-scale upright isoclinal parallel fold in quartzite at Kundalila Falls national monument near Serenje; (b) Kundalila Falls drop spectacularly from the quartzite ridge (Mr. Willy Nundwe and Otis Nyirenda for scale).



Figure 2-34: (a) strongly folded quartzite-pelite sequence of the Kanona Group (Kanona 1:100000 map sheet); (b) parallel folding in quartzite-pelite sequences of the Kanona Group (Kanona 1:100000 map sheet).

In thin section, the Kanona Group quartzites show undulose extinction, while the metapelites are often crenulated (Figure 2-35) and contain mica fish or other deformed mineral grains (Figure 2-36) attesting to a complex deformational history.

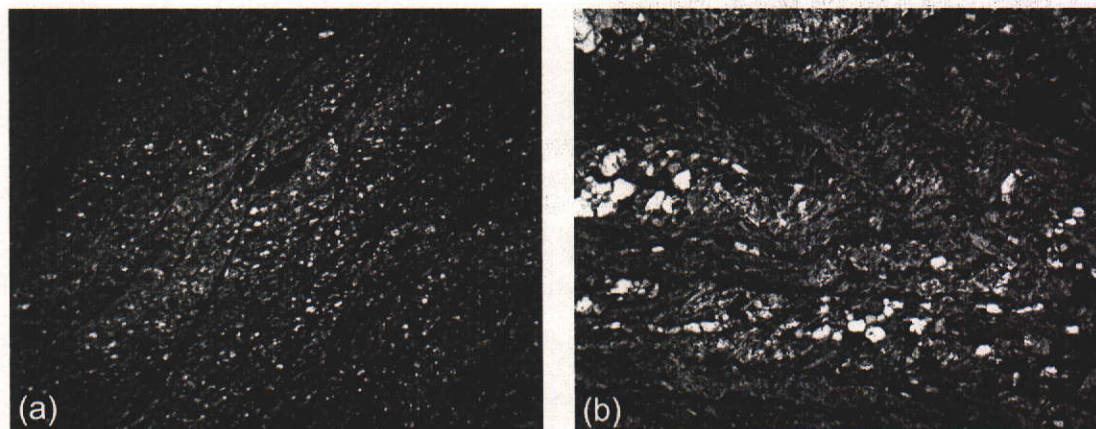


Figure 2-35: photomicrographs of thin sections showing strongly crenulated biotite schist in the Kanona Group (a) sample CHL3 (Chilonga Mission 1:100000 sheet); (b) sample MK11 (Mkushi 1:100000 sheet)(f.o.v. 4.64 mm).

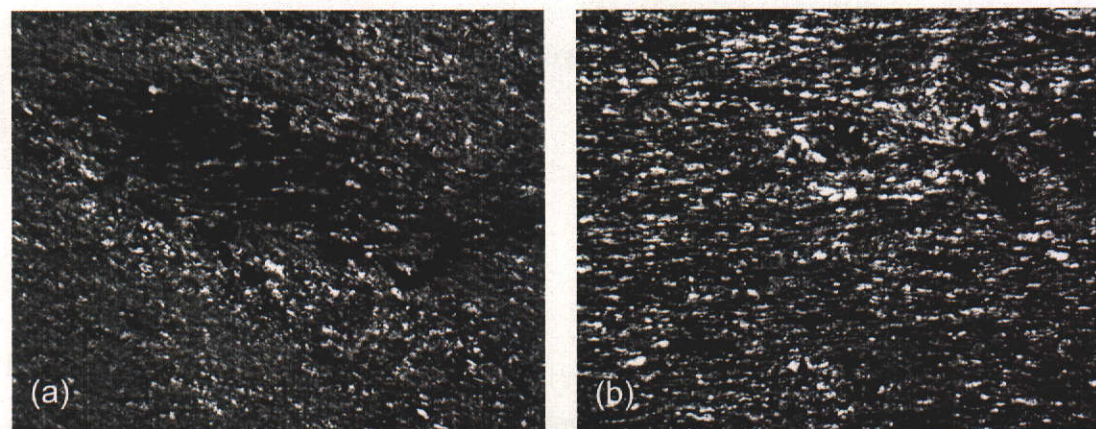


Figure 2-36: (a) photomicrograph of thin section showing relict andalusite porphyroblast in biotite schist of the Kanona Group, altered to a shimmer aggregate of biotite, muscovite and iron oxides. Sample CHT5 (Chitambo Mission 1:100000 map sheet), (b) photomicrograph of thin section showing andalusite-sillimanite schist of the Kanona Group (sample MK13; f.o.v. 2.32 mm) showing preserved andalusite and sillimanite aggregate in a foliated groundmass of $q + pl + ksp + bi$ (Mkushi 1:100000 map sheet).

2.4.6 Volcanic rocks in the Muva Supergroup

In the Irumide belt, volcanic rocks occur locally in five areas within the basal parts of the Manshya River Group (refer to Figure 2-4 for the location of map sheets):

- Katibunga Volcanics (Katibunga Mission 1:100000 map sheet)
- Luswa River Volcanics (Luswa River 1:100000 map sheet)
- Ilondola Volcanics (Ilondola Mission 1:100000 map sheet)
- Kachinga Tuffs (Chimbwe syncline, Isoka 1:100000 map sheet)
- Mututa Volcanics (Mututa Hills 1:100000 map sheet)

These volcanic or volcanoclastic sequences are up to a few hundreds of meters thick and occur conformably within the lower parts of the Manshya River Group in the northeastern Irumide belt. To date, no metavolcanic units have been recognised in the southwestern Irumide belt that can unequivocally be assigned to the metasedimentary sequence.

2.4.6.1 The Katibunga Volcanics

Mosley and Marten (1979) described a series of metavolcanic rocks and quartzites in the southwest of the Katibunga Mission 1:100000 map sheet, some 15 kilometers southeast of Mpika (Figure 2-4 and Figure 2-37). The volcanic rocks consist mainly of deformed pillow lavas, with minor agglomerates and tuffaceous rhyolitic deposits. The sequence is underlain by a pelitic package with subordinate quartzite, and overlain by a massive thick quartzite, and has been defined as the Ibangwe Group (Mosley and Marten, 1979). The exposure of the Ibangwe Group metasedimentary-volcanic sequence is structurally bound by faults to the east and west, while contacts with the gneisses to the north and south are also inferred to be faults. Mosley and Marten (1979) equated the Ibangwe Group with the base of the Manshya River Group. Pillow lavas are well exposed at Nakalya Hill, and consist of deformed, lensoid pillows, with cusped, interpillow masses of chalcedonic silica,

jasper and chert (Figure 2-38 (a) and (b)). The pillows range from 20 cm to 1 meter in diameter. The pillow margins show pits formed by weathering of vesicles up to 4 mm in size, now filled by epidote, hornblende and plagioclase. Massive basic rocks range from aphanitic dark grey basalts to dark grey, coarse, doleritic to gabbroic rocks that probably represent hypabyssal units. In places, the basic volcanic rocks are riddled with numerous fine quartz veinlets, possibly indicating quenching of the basaltic magma in subaqueous conditions. Interbedded with the basaltic pillow lavas are schists, agglomerates and tuffaceous deposits. The rhyolitic tuffs are typically composed of quartz, plagioclase, microcline, epidote, chlorite and minor hornblende and are often mixed with schistose material and minor quartz layers (Figure 2-39 (a) and (b)). The schists are blastose, reddish weathered rocks, which show tight to isoclinal folding along northeast-trending axial planes. A very clear crenulation cleavage has developed along a north-south trend, dipping steeply to the east, with a crenulation lineation plunging steeply to the south, attesting to at least two deformation events.

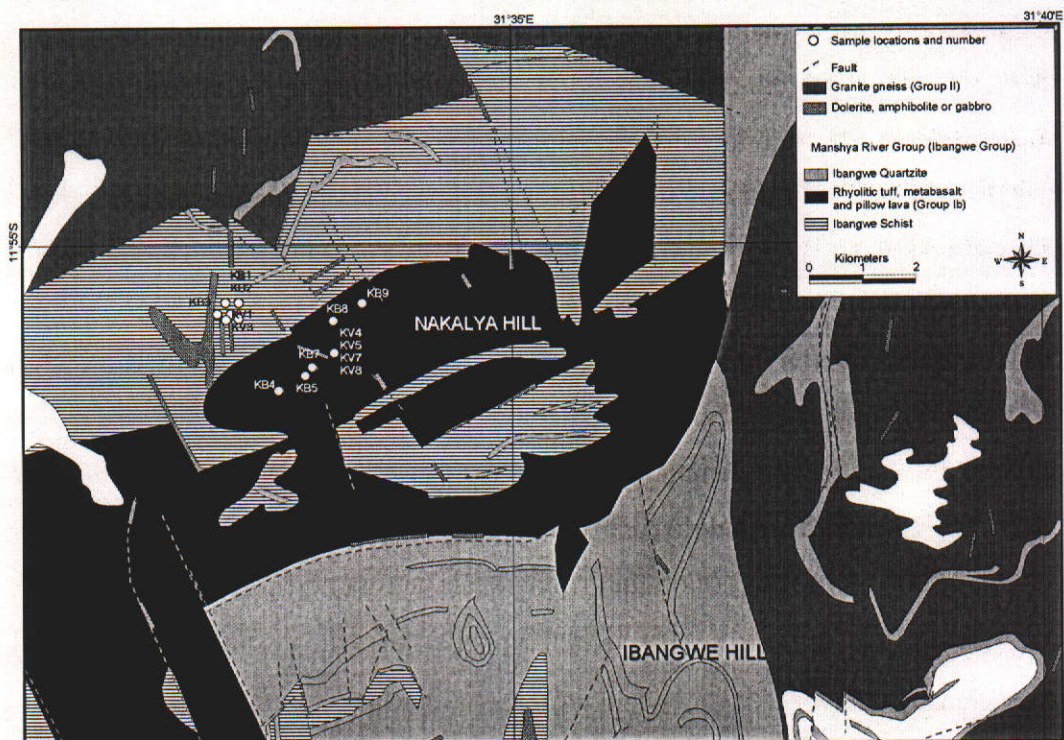


Figure 2-37: Geological map of the Ibangwe Hill area near Mpika showing the location of samples (Katibunga Mission 1:100000 map sheet, see Figure 2-11 for location), adapted from Mosley and Marten (1994).

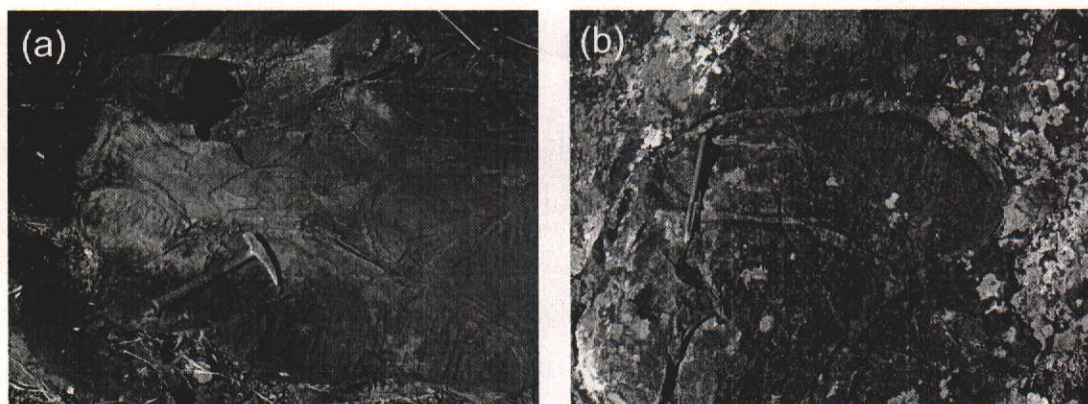


Figure 2-38: (a) Pillow structures in (meta)basaltic lavas at Nakalya Hill south of Mpika (see Figure 2-37 for location); (b) detail of a single pillow, outlined by a corona of chalcedonic silica.

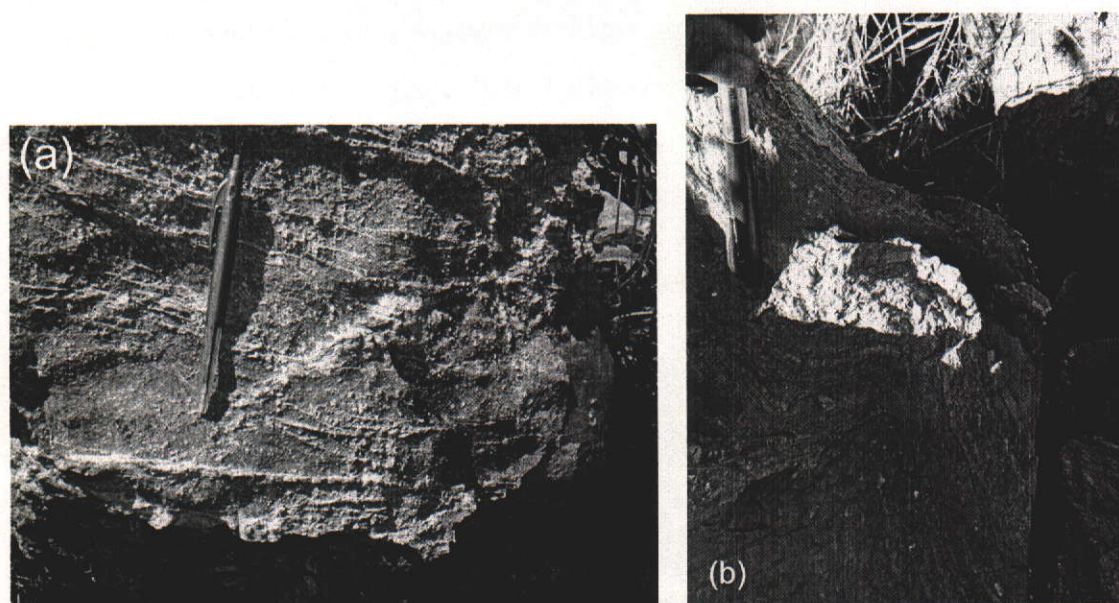


Figure 2-39: (a) Katibunga rhyolite tuff (sample KB1, Figure 2-37); (b) tight, crenulated folding in the Katibunga rhyolite tuff suggesting at least two deformation events (sample KV1; Nakalya Hill, south of Mpika, Figure 2-37).

2.4.6.2 The Luswa River Volcanics

A felsic volcanic member, running parallel to the quartzite-pelite sequences of the Manshya River Group, occurs in the Luswa River 1:100000 map sheet (samples ZM31, LW12, 13, 14 and 15, Figure 2-12)(Sykes, 1995). The metavolcanic is typically a grey, hard, fine-grained rock, consisting of quartz, feldspar, fine biotite and subordinate muscovite. On weathered surfaces, microphenocrysts of quartz and feldspar, as well as alternating coarse and fine flow layers and some flow folding are

clear (Figures 2-40 (a) and (b) and 2-41 (a) and (b)). Cross bedding is common, indicating that at least some of the volcanic material was deposited or reworked under water. In thin section, the rhyolitic tuff consists of quartz + K-feldspar + plagioclase + biotite \pm muscovite (Figure 2-42 (a) and (b)). Accessory phases include zircon and sphene.

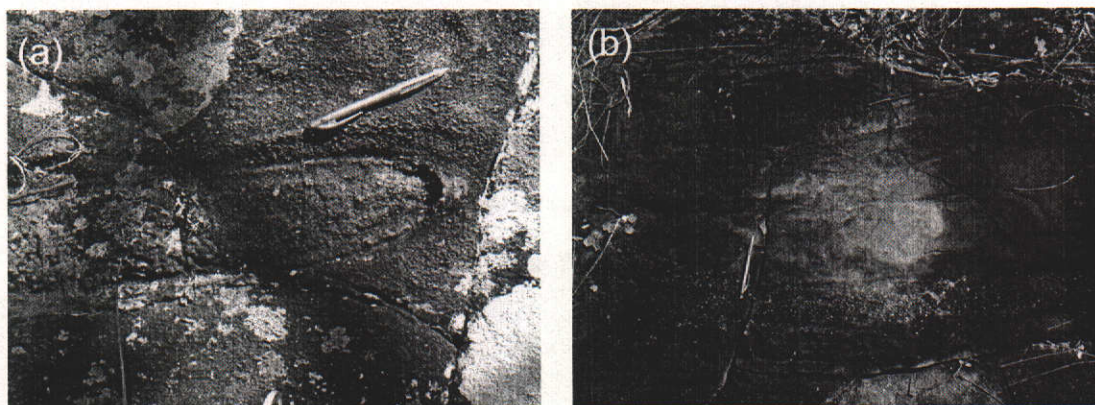


Figure 2-40: (a) a small flow fold in a rhyolitic lava flow in the Luswa River 1:100000 map sheet; (b) a coarse phenocrystic flow layer (below) overlain by a finer grained flow layer (Luswa River 1:100000 map sheet).

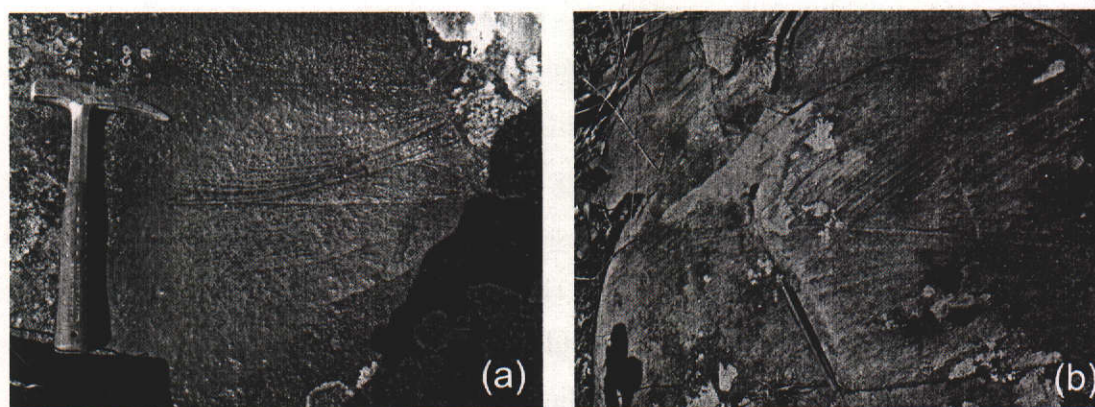


Figure 2-41: cross-bedding structures in pyroclastic volcanics in the Luswa River 1:100000 map sheet implying subaqueous deposition or reworking.

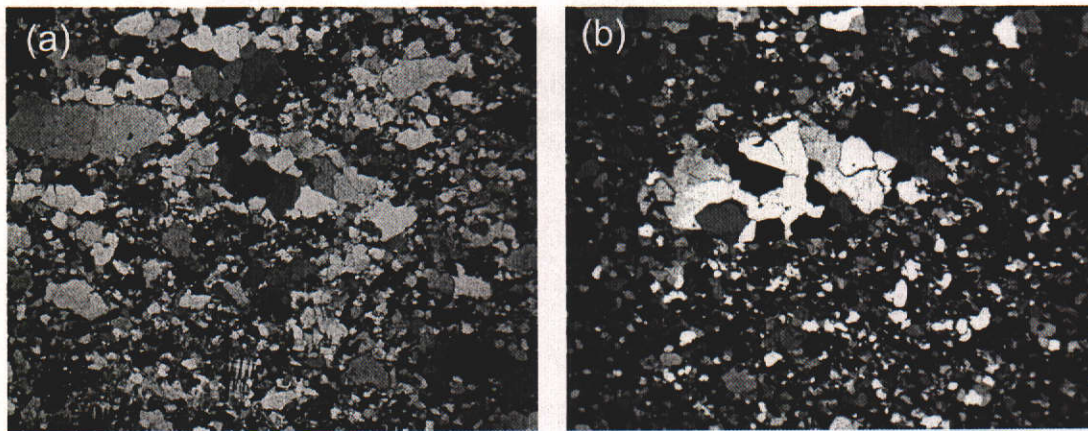


Figure 2-42: photomicrographs of (a) a thin section of sample LW12 (xpl) showing q-pl-ksp-bi±mu (Luswa River 1:100000 map sheet)(f.o.v. 4.64 mm); (b) a thin section (xpl) of sample LW14 showing phenocrysts or clasts of q-pl (Luswa River 1:100000 map sheet)(f.o.v. 2.32 mm).

2.4.6.3 *The Ilondola Volcanics*

Lucacik (1998b) described a minor occurrence of volcanic rocks near Ilondola Mission (Figure 2-43). The volcanics are very weathered, and appear as pinkish, orange and violet schist in the field (Figure 2-44). In thin section, the rocks show a matrix of quartz and sericite, with minor feldspar crystals. Lucacik (1998b) interpreted these rocks to have originally been rhyolitic or andesitic tuffs. In thin section, the weathered rocks show small-scale layering and intense crenulation, and significant amounts of iron oxides (Figure 2-45 (a)). Mineralogically the metavolcanic rocks contain quartz + K-feldspar + plagioclase + muscovite + biotite + sericite + iron oxides and minor tourmaline. One sample (IL3) contains some large corroded kyanite crystals, interpreted to be detrital, suggesting that the volcanic material is mixed with a sedimentary component (Figure 2-45 (b)).

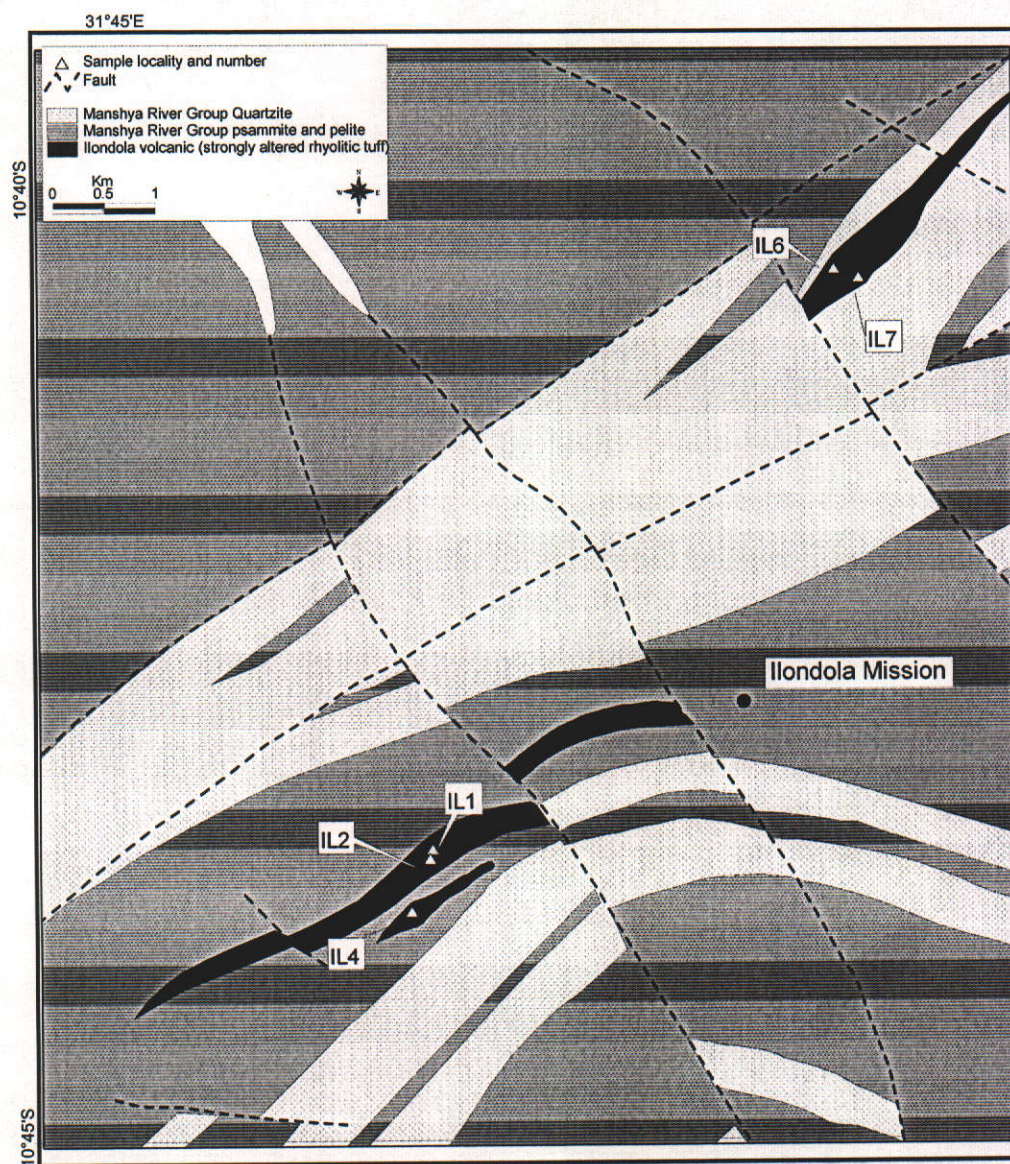


Figure 2-43: Geological map of the area around Ilondola Mission (Ilondola 1:100000 map sheet), adapted from Lucacik (1998a), showing the location of samples collected from the Ilondola Volcanics. White areas represent recent deposits (alluvium/colluvium). See Figure 2-12 for location.



Figure 2-44: (a) the Ilondola Volcanic. Note the small crenulation of fine layering; (b) weathered and stained crossbedded quartzite northeast of Ilondola Mission, interpreted to contain significant volcanic input (Ilondola Mission 1:100000 map sheet).

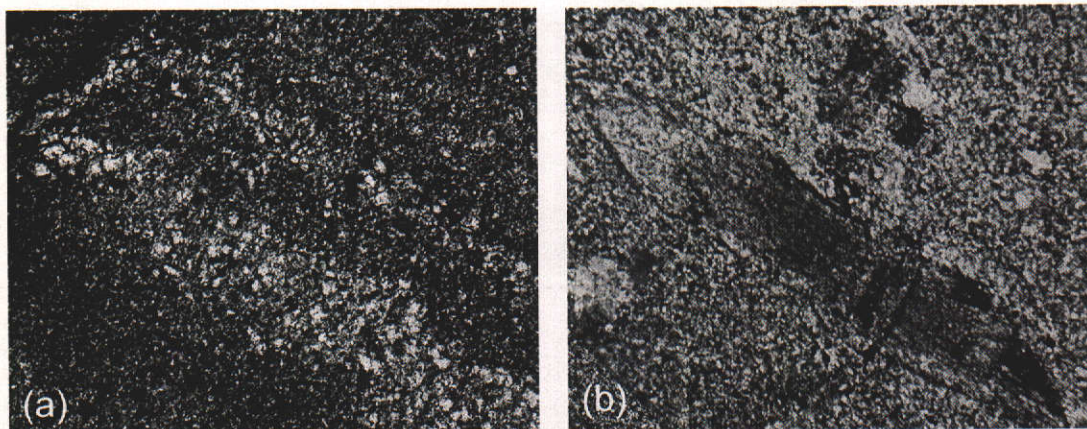


Figure 2-45: (a) thin section of sample IL2 showing q-pl-ksp-mu-bi-Feox. Note the Fe-oxide vein in the upper left corner, and the fine crenulation of primary layering (f.o.v. 2.32 mm); (b) detrital kyanite in sample IL3. Note that the kyanite crystal is aligned parallel to the primary layering (both samples from Ilondola Mission 1:100000 map sheet) (f.o.v. 2.32 mm).

2.4.6.4 The Kachinga Tuffs

A ~300-meter-thick layer of rhyolitic tuff plus intercalated lava flows has been described from the Isoka area (Daly, 1995b)(Figure 2-23 and Figure 2-24). The Kachinga Tuff occurs as a thick unit in the Chimbwe syncline (Daly, 1986b), some 20 kilometers south of Isoka. The volcanic unit overlies a pelitic member (Figure 2-46 (a)), and passes upwards into a white, pure quartzite, which forms a high ridge. The sequence is tightly folded along a northeast-southwest trending isocline, with shallow plunge to the southwest (Figure 2-24). A strong axial-planar foliation penetrates the sequence, imparting a strong schistosity on the pelitic members. The contact with the underlying pelitic schist is gradational, with alternating pelitic and rhyolitic layers, and with the volcanic component steadily increasing in abundance up sequence until the unit consists entirely of bedded rhyolitic tuff and thin lava flows. The unit includes crystal tuffs with graded bedding, and intercalated thin lavas. Some tuff layers show evidence of reworking by currents and display flow folds (Figures 2-46, 2-47 and 2-48). On weathered surfaces, relict amygdalae are observed (Figure 2-48 (b)), while in thin section, evidence of autobrecciation indicates the emplacement of at least some of the rhyolites as lava flows (Figure 2-49). The rhyolites consist of quartz + plagioclase + K-feldspar + biotite + muscovite, with accessory iron oxides, zircon and tourmaline (Figure 2-50). The rocks are deformed, recrystallised and devitrified, and only relict primary fabrics, such as primary layering, volcanic flows, vesicles and amygdalae, can be observed. At the top of the sequence, the volcanic component gradually gives way to a pure white quartzite.

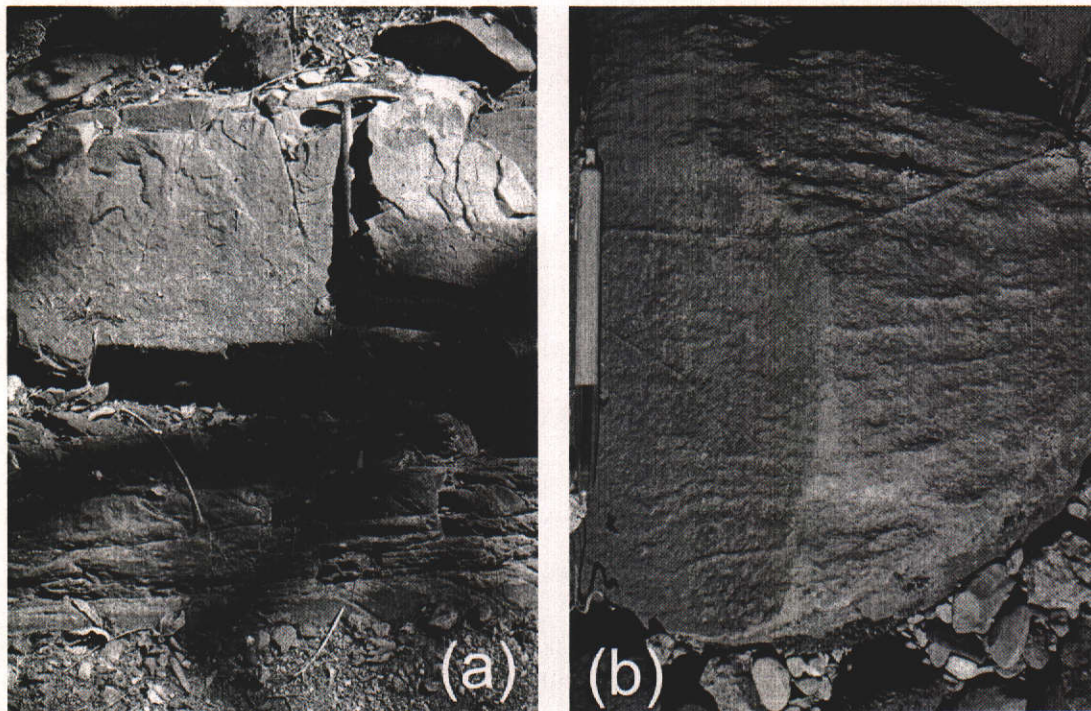


Figure 2-46: (a) contact between pelitic sequences of the Kachinga Pelite (below) and a massive rhyolitic tuff flow of the Kachinga Tuff; (b) close-up view of the rhyolitic tuff, showing fine layering (Isoka 1:100000 map sheet).

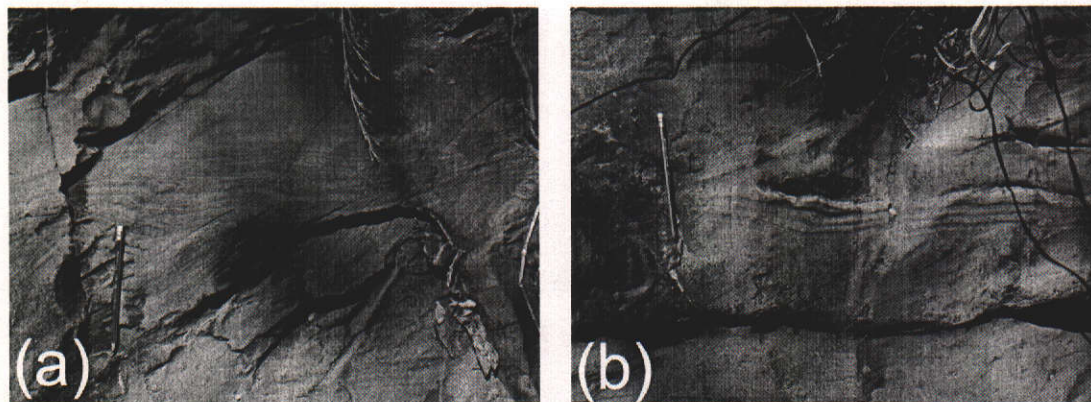


Figure 2-47: (a) fine layering in the Kachinga Tuff; (b) truncation of the fine layering in the Kachinga Tuff indicating sedimentary processes during deposition (Isoka 1:100000 map sheet).

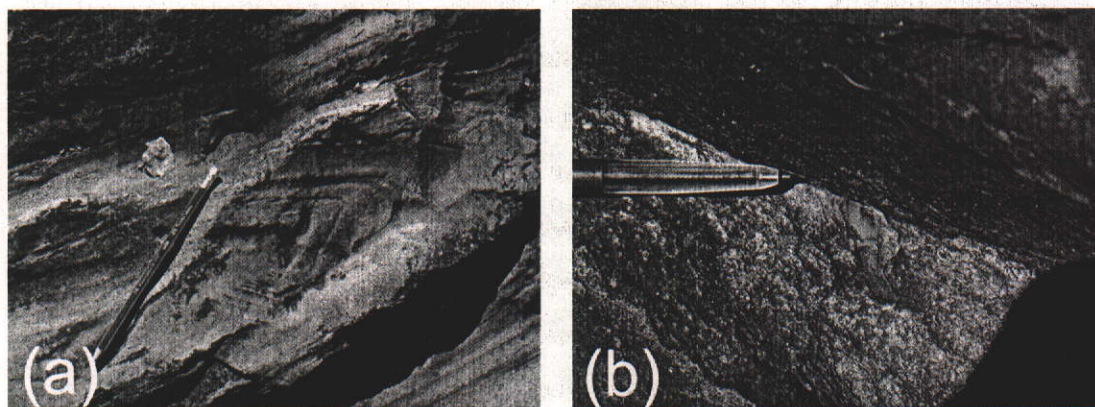


Figure 2-48: (a) flow fold in the Kachinga Tuff; (b) relict amygdale, filled in by chert (Isoka 1:100000 map sheet).

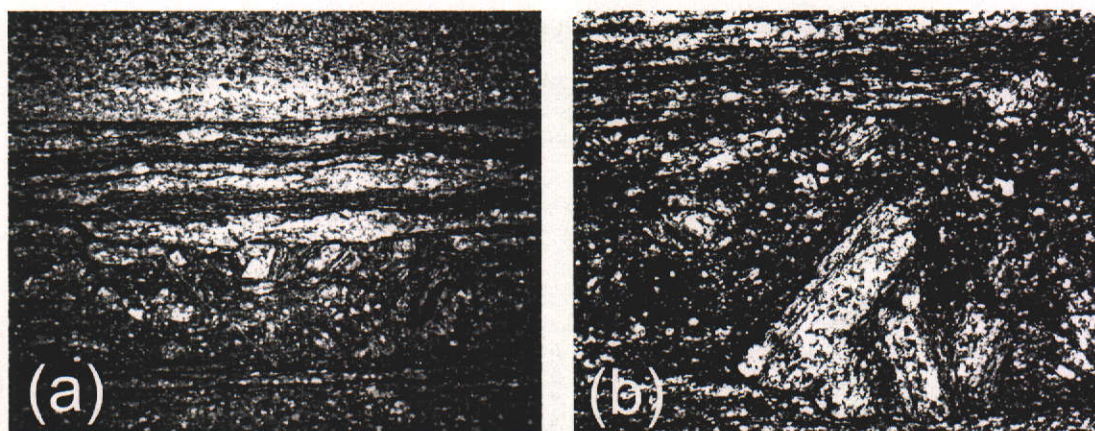


Figure 2-49: photomicrographs of (a) a thin section (xpl) of sample IS18 showing primary layering defined by opaque minerals (iron oxides). Autoclastic fabrics can be observed, with broken q + pl fragments in a groundmass of q + pl + bi (f.o.v.4.64 mm); (b) a close up of several autoclasts (f.o.v. 1.16 mm) (Isoka 1:100000 map sheet).

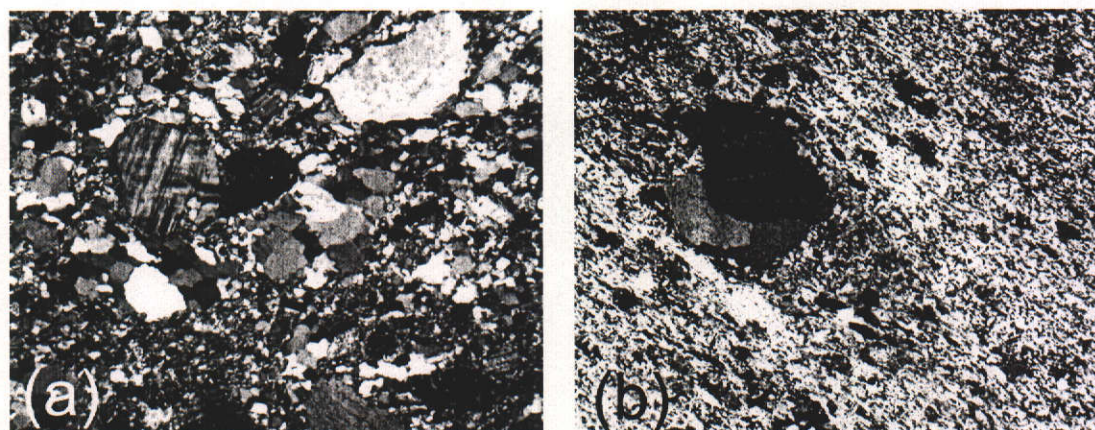


Figure 2-50: photomicrographs of (a) a thin section (xpl) of sample IS22 (Kachinga tuff) showing relict autoclastic fabric (f.o.v. 2.32 mm); (b) a thin section (xpl) of sample IS19 showing a strain shadow, developed either side of a relict devitrified vesicle filled in with quartz (f.o.v 1.16mm)(Isoka 1:100000 map sheet).

2.4.6.5 *The Mututa Ridge volcanics*

Several thin felsic volcanic or hypabyssal units have been recognised in the Mututa Hills area (Figure 2-13). Van Tuijl and Verhoog (1995c) interpreted these units as porphyry sills and crystal tuffs, which were intruded (extruded) during the waning stages of widespread magmatism associated with the Bangweulu block. They occur conformably in the folded metasedimentary succession that Van Tuijl and Verhoog (1995c) termed the Mututa Group and correlated with the Mafingi and the Manshya River Groups. Van Tuijl and Verhoog (1995c) observed the felsic rocks both in direct intrusive contact with the quartzite, and in gradational depositional contact, indicating that the rock was both emplaced at shallow depth as concordant sills and deposited as a crystal tuff together with the quartzite. The felsic rocks consist of coarse feldspar and quartz phenocrysts in a sericitised matrix of quartz, microcline, minor biotite and iron oxides.

2.5 Irumide granitoids

2.5.1 Strongly deformed Irumide granitoids

Strongly deformed Irumide granitoids exposed in the northeastern Irumide belt are gneissic and foliated granitoids, interpreted as having been emplaced during Irumide tectonism, and known as the Mutangoshi Gneissic Granite, Musalango Gneiss and Chituli-Lufila Gneiss, the latter of which was not included in this study. In the southwest, strongly deformed granitoids post-dating the Mkushi Gneiss have been termed the Lukamfwa Hill Granite Gneiss after a prominent hill in the Serenje area (De Waele and Mapani, 2002; De Waele et al., 2003). Some syn-Irumide granitoids described below were previously believed to belong to a (Palaeoproterozoic) basement complex, but are here described separately as they contain xenoliths of sedimentary origin ascribed to the Muva Supergroup, and contain a pervasive northeast-southwest oriented fabric related to Irumide tectonism, while lacking any evidence of earlier deformation. The Mkushi Gneiss itself, even though it does not appear to contain an unequivocal pre-Irumide fabric, does contain numerous generations of small and large pegmatites and aplites, one of which was dated at ~1080 Ma (Rainaud et al., 2002).

2.5.1.1 Mutangoshi Gneissic Granite and Musalango Gneiss

The Mutangoshi Gneissic Granite and its equivalents occur in the Chinsali area, where they form large bodies of grey biotite gneiss (Figure 2-12). In outcrop, the gneiss is deformed by east-west discrete shear zones and in thin section it is composed of an irregular patchwork of quartz + plagioclase + K-feldspar + biotite + muscovite, with accessory hornblende, sphene and zircon (Figure 2-51 (a)). The Mutangoshi Gneissic Granite is mesocratic, and contains abundant biotite + amphibole or biotite, locally converted into chlorite (Figure 2-51 (a) and (b)). The gneiss shows evidence of polyphase deformation, with a northeast-southwest gneissic fabric cut by steep east-west shear zones accompanied by C-S fabrics, steep

lineations plunging towards southeast and intrusion of numerous melt veins displaying ptigmatic folding along east-west axes. Daly (1986b) interpreted these gneisses as pre-kinematic intrusions, deformed together with the supracrustal sequence. He pointed out that the deformed granitoids are closely associated with amphibolites and suggested that they both belong to a pre-kinematic extensional bimodal magmatic event. The Mutangoshi Gneissic Granite occurs together with a compositionally very similar suite of granites, which Daly called the “Grey Granite”, “Chilubanama Granite” or the “Mutangoshi Granite” (Daly, 1986b; 1995b; 1995a), and which will henceforth be referred to as the “Chilubanama Granite”. Extensive shearing and mylonitisation obscure the original contact between the Mutangoshi Gneissic Granite and the younger Chilubanama Granite, producing a gradual transition from one body to the other. However, grain size variation and the presence of migmatitic granite pods within the Chilubanama Granite suggest that the Mutangoshi Gneissic Granite and the unfoliated Chilubanama Granite are two distinct bodies. In fact, near the location where Daly (1986b) collected his samples for whole rock Rb-Sr dating, both gradational and intrusive contacts were observed between what was mapped as the foliated Mutangoshi Gneissic Granite, and the largely unfoliated Chilubanama Granite. The whole rock Rb-Sr analyses yielded a Rb-Sr date of 1407 ± 33 Ma with an MSWD value of 4.7 and an initial $^{87}\text{Sr}/^{86}\text{Sr}$ ratio of 0.724 (Daly, 1986b). Daly (1986b) interpreted this date as a good estimate of the emplacement of the precursor granite, while the high initial ratio was interpreted to indicate significant crustal reworking. In addition, the Mutangoshi Gneissic Granite contains xenoliths of partially resorbed quartzite and pelite, leading to the interpretation that the gneiss is derived from anatexis of the Manshya River Group (Daly, 1995a). Rafts of the Mutangoshi Granite Gneiss are described in the Chilubanama Granite (Daly, 1995a) and in the Bemba batholith (Sykes, 1995) indicating that it predates these intrusions. In this study, two samples of strongly foliated migmatitic Mutangoshi Gneissic Granite (samples MTGG-1 and MTGG-2) were collected for geochemistry and U-Pb SHRIMP dating, from near the location where Daly sampled the gneiss. The samples were collected only meters away from the gradational (granitised) contact with the Chilubanama Granite.



Figure 2-51: (a) thin section (xpl) of the Mutangoshi Gneissic Granite (sample MTGG1) showing a coarse assemblage of $q + pl + ksp + bi \pm mu$ (f.o.v.=4.64 mm); (b) migmatitic aspect of the Mutangoshi Gneissic Granite.

The Musalango Gneiss occurs in the Luswa River map sheet, and was described in detail by Sykes (1995). Typically, it is a strongly foliated grey and pinkish biotite gneiss. The strong northeast-trending foliation is defined by aligned biotite. Numerous small pegmatite veins cut the gneissic foliation, and small ptygmatically folded veinlets of quartz are abundant (Figure 2-52). In thin section, the gneiss consists of quartz, plagioclase and microcline, with abundant biotite (Figure 2-53 (a)). The plagioclase is commonly sericitised. The quartz shows undulose extinction, and is elongated parallel to the foliation. Accessory mineral phases include iron oxide, apatite and zircon. Similar gneisses have been described to the east of the Musalango Gneiss (Chituli-Lufila Gneiss (Sykes, 1995)) and range from granitic, leucocratic gneisses to dark, porphyritic biotite gneisses. In this study, one sample was collected from the main Musalango Gneiss outcrop for geochemistry and dating (sample LW10). The gneiss is intruded in various places by undeformed (post-Irumide) gabbroic dykes (Figure 2-53 (b)). Although during this study no xenoliths were observed within the Musalango Gneiss, Sykes (1995) reported the occurrence of xenoliths of metasedimentary origin within the gneiss.

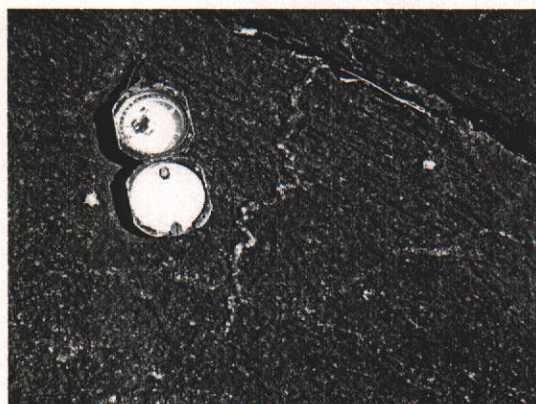


Figure 2-52: ptymatic quartz veins in the Musalango Gneiss (sample LW10; Luswa River 1:100000 map sheet).

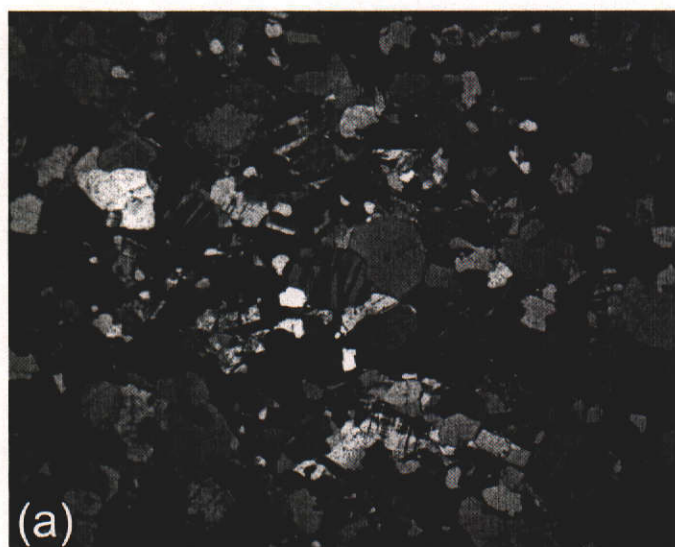


Figure 2-53: (a) thin section of the Musalango Gneiss (sample LW10), showing sub-equigranular q + ksp + pl + bi (f.o.v 4.64 mm); (b) undeformed gabbroic dyke intruding into the Musalango Gneiss (Luswa River 1:100000 map sheet)

2.5.1.2 *Lukamfwa Hill Granite Gneiss*

The Lukamfwa Hill Granite Gneiss in the southwestern part of the Irumide belt comprises coarse K-feldspar-phyric biotite granite gneiss, and fine-grained biotite gneiss. These rocks often occur as large domal kopjes or as flat-lying whaleback outcrops (Figure 2-54 (a) and (b)). In the type locality at Lukamfwa Hill in the Serenje area, the granite gneiss bodies consist of coarse-grained, K-feldspar phyric granite gneiss, with a strong northeast-trending foliation defined by biotite, which wraps around stretched microcline porphyroclasts, imparting an augen texture

to the rock (Figure 2-55 (a) and (b)). This lithology is in contact with poorly defined dykes of fine-grained biotite gneiss, which also carry the penetrative northeast-trending fabric. The gneiss is intensely folded, with isoclinally folded quartz veins and S_1 biotite foliation defining a first deformation event, and a crenulation of the biotite foliation along a northeast-trending S_2 foliation defining a second event. The two deformation events are recorded in both the coarse- and the fine-grained gneisses. The Lukamfwa Hill Granite Gneiss contains large rafts of quartzite and pelite ascribed to the Kanona Group (Mapani and Moore, 1995b).

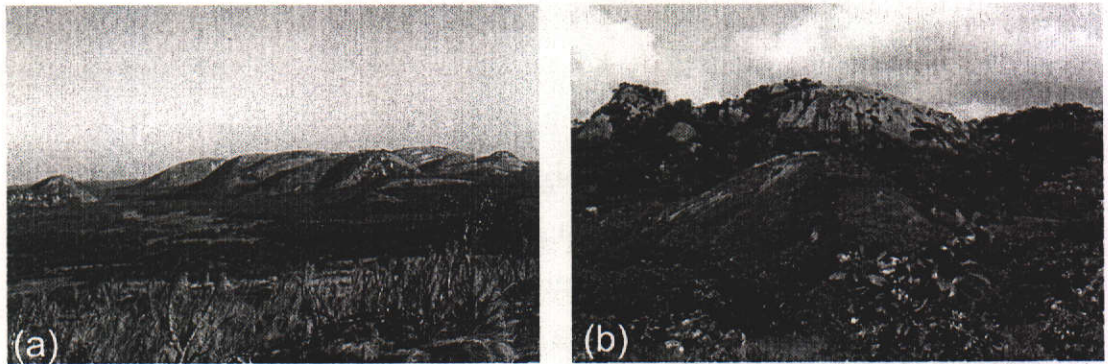


Figure 2-54: (a) panoramic view over pre- syn- and late-tectonic granitoids in the Serenje 1:100000 map sheet; (b) type locality of the Lukamfwa Hill Granite Gneiss (Serenje 1:100000 map sheet).

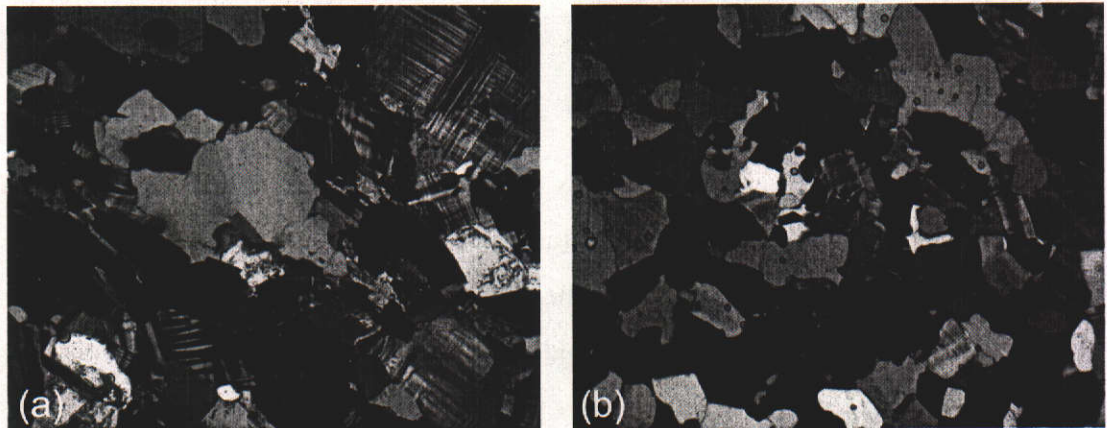


Figure 2-55: photomicrographs of thin sections (xpl) of the Lukamfwa Hill Granite Gneiss; (a) coarse-grained inequigranular (porphyritic) variety with q + pl + ksp + bi + mu (sample SER6-2; f.o.v. 4.64 mm); (b) fine-grained variety with q + pl + ksp + bi (sample SER6-3; f.o.v. 2.32 mm) (both from the 1:100000 map sheet of Serenje).

2.5.1.3 The Mivula Syenite and Ntendele metatonalite

Two ca. 1.3 Ga intrusive bodies are known only from the far northeastern part of the Irumide belt in the Muyombe Mission 1:100000 map sheet (Figure 2-4) and consist of the Mivula Hill nepheline syenite and a deformed biotite metatonalite. The nepheline syenite of Mivula Hill covers ~1 by 4 km (Newton, 1959; Tembo, 1986; Vrána et al., 2004) and is located ~70 km south-southeast of Isoka. It is a medium-grained, locally porphyritic, nepheline-rich intrusion, with sodalite veinlets. Minor aegirine syenite and a sheared to mylonitic biotite syenite occur in this complex. The Ntendele biotite granite exposed 50 km northeast of Mivula Hill is foliated, with stretched K-feldspar augen. The pluton possibly extends into Malawi where it is called the Kalopo biotite granite previously linked to the ca. 1930 Ma Nyika Granite suite by Ring et al. (1997). The Mivula Syenite has yielded a whole-rock Rb-Sr isochron date of 1341 ± 16 Ma (Tembo, 1986). The same syenite yielded a $^{207}\text{Pb}/^{206}\text{Pb}$ zircon evaporation age of 1360 ± 1 Ma (Vrána et al., 2004). The Ntendele biotite granite yielded a $^{207}\text{Pb}/^{206}\text{Pb}$ zircon evaporation age of 1329 ± 1 Ma (Vrána et al., 2004).

2.5.2 Late-Irumide granitoids

Late-kinematic Irumide granitoids form the Bemba batholith (or Lufila Granite) and the Chilubanama Granite (also called Mutangoshi and Grey Granite (Daly, 1986b)) complexes in the northeastern part of the Irumide belt. In the southwestern part, late-Irumide granitoids include large volumes of porphyritic granites and granite gneisses, which were previously ascribed to the Mkushi Gneiss basement complex (Figure 2-3 and Figure 2-4). The clear intrusive character of these granitoids into the Mkushi Gneiss, together with their relatively unfoliated character, however, set them apart from the basement.

2.5.2.1 *The Bemba batholith (Lufila Granite)*

A large intrusion occurs in the northeastern part of the Irumide belt, straddling the Shiwa N'Gandu and Luswa River 1:100000 map sheets, and was described in detail by Ayres (1974), Sykes (1995) and Daly (1986b) (Figure 2-4, Figure 2-11 and Figure 2-12). Typically, the granite is pink, white or grey, coarsely crystalline and porphyritic. Subhedral to euhedral feldspar phenocrysts have well-developed carlsbad twinning and are often aligned along a primary magmatic foliation. The phenocrysts are up to 4 cm long and are set in an even-grained quartz-feldspar groundmass (Figure 2-56). The groundmass is commonly rich in biotite, but also contains minor muscovite. Accessories are apatite, sphene and zircon, with some iron oxide minerals and a few garnet grains. The granite body contains numerous large (kilometer scale) enclaves and rafts. Most of these are quartzites, with minor pelites. The quartzites are generally recrystallised, and contain randomly oriented muscovite flakes. The pelitic enclaves consist of schists, in which sillimanite can be found. In the northern part of the granite body, the unfoliated granite is cut by discrete east-west trending shear zones, which locally reduce the coarse granite into a mylonite. The shear zones are reported to continue into the surrounding metasediments of the Manshya River Group (Sykes, 1995).

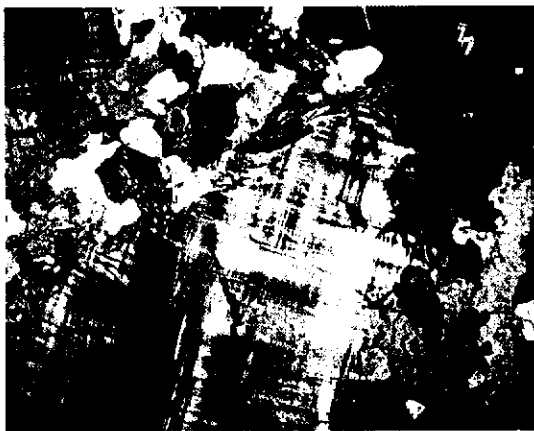


Figure 2-56: thin section (xpl) of the Bemba batholith (Lufila Granite). Porphyritic microcline crystals, set in a coarse groundmass of q + pl + ksp + bi ± mu (f.o.v. 4.64 mm) (sample SH8, Shiwa N'Gandu 1:100000 map sheet).

2.5.2.2 *Chilubanama Granite*

The Chilubanama Granite comprises an extensive series of granite plutons in the northeastern part of the Irumide belt (Figure 2-12). The granite was described by Daly (1986b; 1995b; 1995a). The Chilubanama Granite is typically a mesocratic pinkish grey biotite granite (Figure 2-57), which often contains partially resorbed xenoliths rich in garnet (Figure 2-57 (b)). Mineralogically the granite consists of quartz, microcline, plagioclase and biotite, with varying amounts of muscovite, garnet, hornblende, chlorite and epidote (Figure 2-58 (a) and (b)). In places the granite is equigranular and medium grained, but may grade into porphyritic types. The biotite flakes are aligned along a weak foliation, while alignment of feldspar phenocrysts parallel to the margins of the intrusions is interpreted as a primary magmatic fabric. The intrusion of these granitoids appears to have triggered anatexis of especially the pelitic part of the Manshya River Group, as indicated by the occurrence of interbedded sheets of granite within the quartzites, and abundant partially resorbed xenoliths of presumed metasedimentary origin within the Chilubanama Granite. Transitions have been reported, in which metapelites of the Manshya River Group are observed to progressively become “granitised” into the Chilubanama Granite (Daly, 1986b). Likewise, gradual transitions from coarse Chilubanama Granite into strongly foliated, nebulitic Mutangoshi Gneissic Granite were observed in the field, suggesting that the Chilubanama Granite was at least locally derived from remelting of the older Mutangoshi Gneissic Granite.

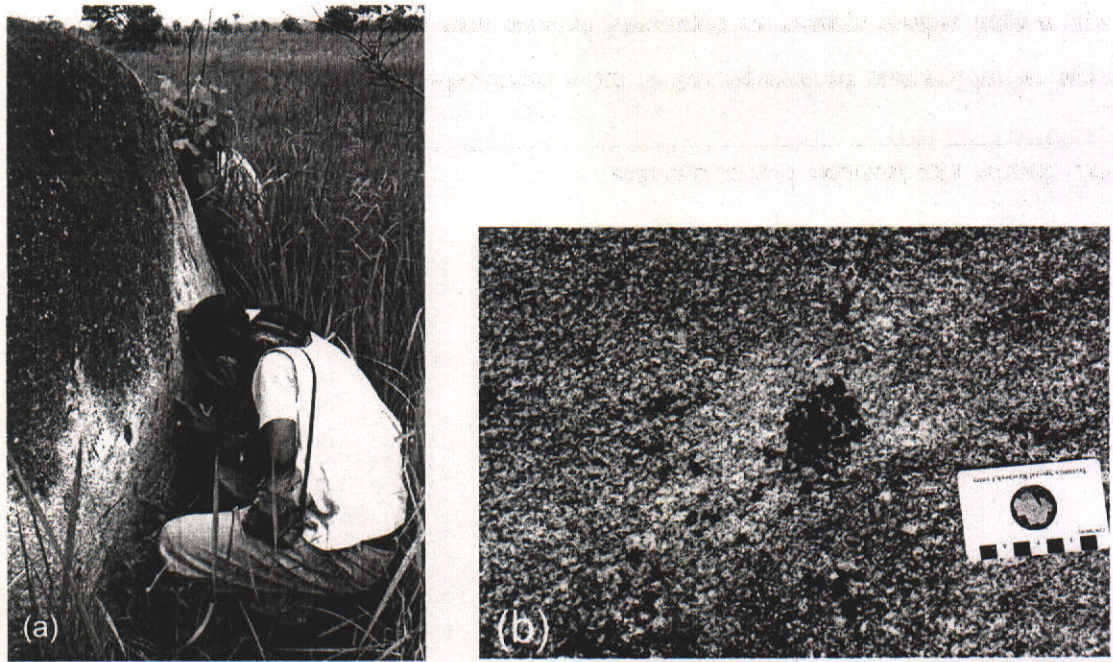


Figure 2-57: (a) outcrop of the Chilubanama Granite in the Chinsali 1:100000 map sheet (Drs. Francis Tembo and Benjamin Mapani); (b) close up view of the Chilubanama Granite, showing a cluster of garnet, possibly a partly resorbed xenolith (Chinsali 1:100000 map sheet).

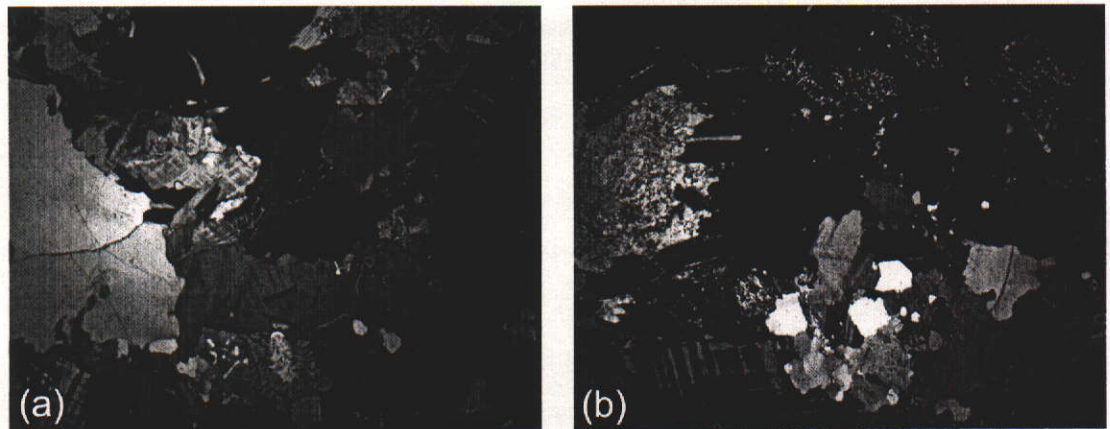


Figure 2-58: (a) photomicrograph of a thin section (xpl) of the Chilubanama Granite (sample MTG3) showing a coarse q + pl + ksp + bi + mu assemblage (Chinsali 1:100000 map sheet) (f.o.v. 4.64 mm); (b) photomicrograph of a thin section (xpl) of the Chilubanama Granite (sample MTG4) showing garnet (black), q + pl + ksp + bi and alteration of plagioclase (Chinsali 1:100000 map sheet) (f.o.v. 4.64 mm).

2.5.2.3 Porphyritic granites

In the southwestern part of the Irumide belt, porphyritic granites make up the majority of granitoid lithologies (see Figure 2-3 and Figure 2-4). They commonly form massive inselbergs and tors, characterised by well-developed exfoliation caused by sheet jointing. The granites contain numerous xenoliths of mafic composition,

some of which can be interpreted to have metasedimentary parentage (Figure 2-59 (a)), whilst others appear to represent broken and partially resorbed mafic dykes (Figure 2-59 (b)).

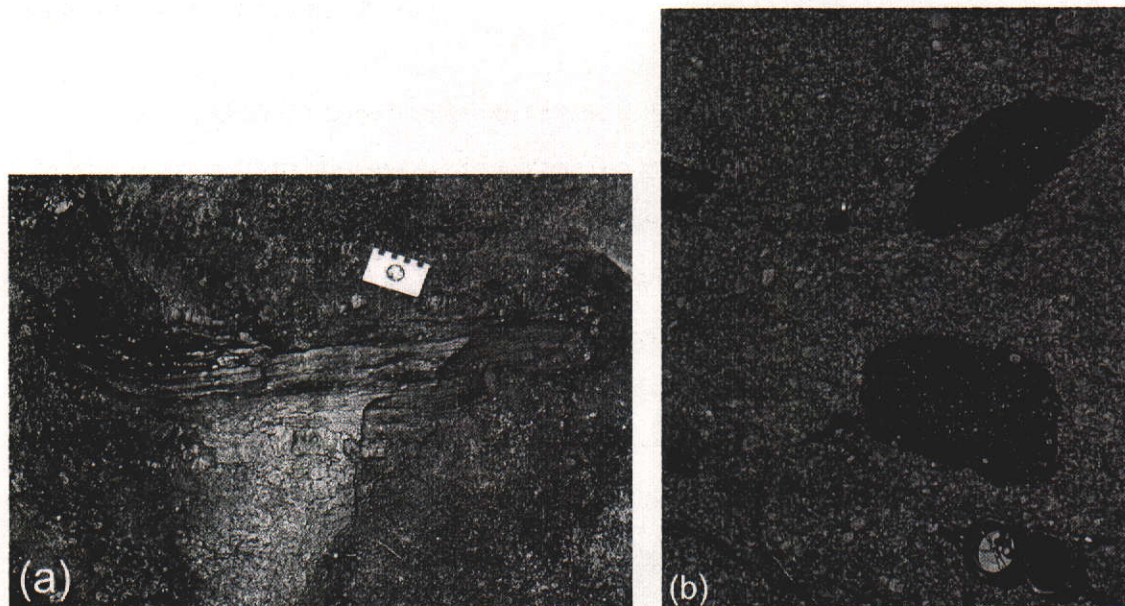


Figure 2-59: (a) small xenolith of interpreted metasedimentary parentage in porphyritic granite (Serenje 1:100000 map sheet); (b) mafic enclaves in porphyritic granite interpreted as a broken up and partially resorbed mafic dyke (Kanona 1:100000 map sheet).

The porphyritic granites range from foliated to unfoliated and meso- to leucocratic, but invariably have large microcline megacrysts up to 7 cm in size, set in a groundmass of coarse quartz, biotite, plagioclase and K-feldspar. In foliated granite, large biotite laths wrap the megacrysts, which can be oriented parallel to the foliation, but more often show random orientation or a primary fabric oblique to the foliation. The porphyritic granites often engulf large metasedimentary pods, which form meter size rafts with partially resorbed edges (Figure 2-60 (a)). In thin section, the granite has a porphyritic texture, with poikilitic K-feldspar in a medium grained groundmass of plagioclase and quartz. Brown biotite is well developed, generally enclosing zircon grains, while muscovite is a minor phase (Figure 2-60 (b) and Figure 2-61 (a) and (b)).

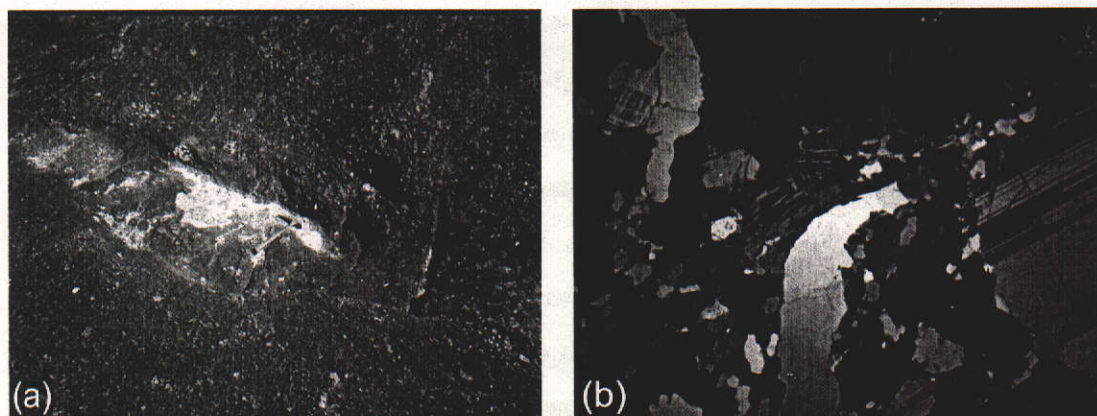


Figure 2-60: (a) meter size raft of metasedimentary parentage in porphyritic granite (Serenje 1:100000 map sheet); (b) photomicrograph of a thin section (xpl) of porphyritic granite (sample SER 6-4, Serenje 1:100000 map sheet) showing phenocrysts of plagioclase (right), a quartz veinlet (center) and K-feldspar + quartz (upper left) in a medium grained groundmass of q + pl + ksp + bi (f.o.v. 4.64 mm).

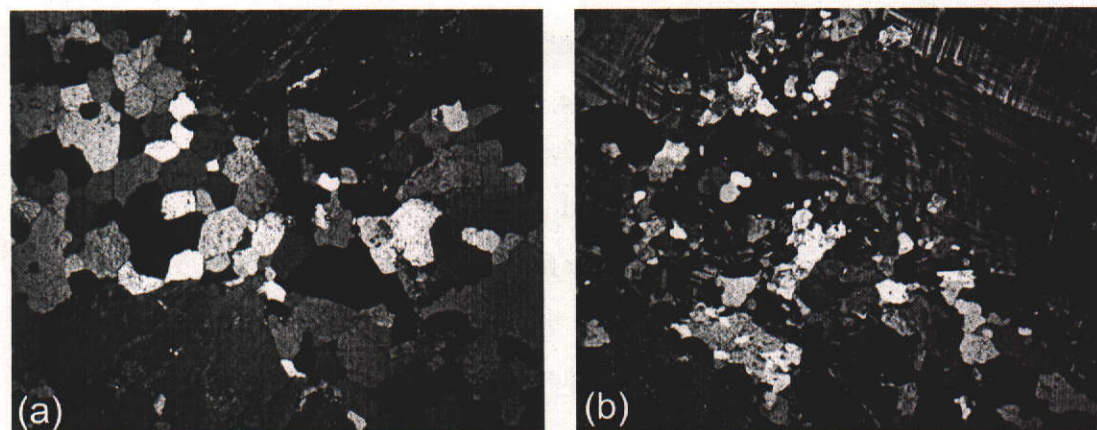


Figure 2-61: (a) photomicrograph of a thin section (xpl) of porphyritic granite (sample MUN, Mununga Quarry, 1:100000 Mupamadzi River sheet) showing phenocrysts of perthitic K-feldspar (top and bottom) in a medium-grained groundmass of q + pl + ksp + bi (f.o.v. 4.64 mm); (b) photomicrograph of a thin section (xpl) of porphyritic granite (sample KN2a, Kanona 1:100000 map sheet) showing phenocrystic microcline (top right and left) in a medium grained groundmass of q + pl + ksp + bi + mu (f.o.v. 4.64 mm).

2.6 Discussion

The following lithostratigraphic units have been recognised within the Bangweulu block and the Irumide belt in northern Zambia:

1. Palaeoproterozoic high-grade meta-granites and schists belonging to the Ubendian belt, and termed the Mulungwizi Gneiss. These gneisses underlie the Irumide belt and the adjacent parts of the Bangweulu block in the far northeast. Granitoids and gneisses of the Ubendian belt in Malawi have yielded $^{207}\text{Pb}/^{206}\text{Pb}$ zircon ages between 2093 ± 1 Ma and 1932 ± 9 Ma (Dodson et al., 1975; Ring et al., 1997; Vrána et al., 2004).
2. Palaeoproterozoic granite-gneisses of the Bangweulu block, and the Lubu Granite Gneiss and Luwalizi Granite Gneiss in the northeastern Irumide belt. These lithologies are in places notably less deformed than their presumed time-correlatives in the Ubendian belt, and underlie parts of the northeastern Irumide belt. No precise age data are available for these lithologies.
3. Palaeoproterozoic granite gneisses in the southwestern Irumide belt, collectively termed the Mkushi Gneiss, which underlie parts of the southwestern Irumide belt and appear to continue westwards, where they underlie parts of the Lufilian arc (Congolese and Zambian Copperbelt). The Mkushi Gneiss has yielded a U-Pb SHRIMP zircon age of 2049 ± 6 Ma, while basement lithologies in the Zambian and Congolese Copperbelt yielded U-Pb SHRIMP zircon ages between 1991 ± 3 Ma and 1964 ± 12 Ma (Rainaud et al., 1999; Key et al., 2001b; 2002; 2003).
4. Palaeoproterozoic plutono-volcanic rocks of the Bangweulu block, including the Luapula Volcanics and the Bangweulu Granitoids, which make up the larger portion of the Bangweulu block, underlying the Mporokoso Group, and extending southwestwards, where they underlie parts of the Katangan sequence in the Congolese and Zambian Copperbelt. These lithologies yielded Rb-Sr whole-rock dates of 1877 ± 55 Ma to 1815 ± 29 Ma on the Bangweulu block (Brewer et al., 1979; Schandelmeier, 1981, 1983) and U-Pb zircon ages between 1884 ± 10 Ma and 1873 ± 8 Ma in the Congolese and Zambian Copperbelt (Ngoyi et al., 1991; John, 2001; Rainaud et al., 2002).

5. The Muva Supergroup (meta) sedimentary cover, which includes three main sequences defined on the basis of spatial arrangement, sedimentary character, and deformation:
 - a. The Mporokoso Group of northern Zambia. A shallow water sequence of quartzites and pelites, with volcanic contribution in the lower units. The Mporokoso Group unconformably overlies older rocks of the Bangweulu block.
 - b. The Kasama Formation on the Bangweulu block, mainly confined to a small east-west-oriented basin near Kasama and comprising a supermature quartzite-pelite sequence derived from sedimentary reworking of the Mporokoso Group to the (north)west.
 - c. The quartzite-pelite successions occurring in the Irumide belt and strongly deformed during the Irumide orogeny. These sequences can be collectively called the Manshya River Group, but comprise three regionally defined, but correlated groups, including the Kanona Group in the southwestern Irumide belt, the Manshya River Group in the northeastern Irumide belt, and the Mafingi Group in the far northeastern Irumide belt straddling the border between Zambia and Malawi.

Direct age constraints are unavailable for the Muva Supergroup, but deposition is constrained by the dates of the underlying Bangweulu Granitoids (1815 ± 29 Ma, Brewer et al., 1979) and the intrusion of the Lusenga syenite (1134 ± 8 Ma, Brewer et al., 1979) into the sedimentary sequence.

6. Strongly deformed Irumide granitoids within the Irumide belt, characterised by strong deformation and containing xenoliths of mafic rocks as well as metasedimentary rocks. These granitoids intrude the supracrustals and thus post-date the deposition of the Manshya River Group and pre-date the Irumide orogeny, and comprise the Mutangoshi Gneissic Granite and Musalango Gneiss in the northeastern Irumide belt, and the Lukamfwa Hill Granite Gneiss in the southwestern Irumide belt. The only age constraint available is an unreliable whole-rock Rb-Sr errorchron date reported by Daly (1986b) for the Mutangoshi Gneissic Granite of 1407 ± 33 Ma. A nepheline syenite (the Mivula syenite) and a metatonalite intrusion in the northeastern Irumide belt, dated at 1360 ± 1 Ma and 1329 ± 1 Ma respectively (Vrána et al., 2004), also belong to the pre-Irumide

granitoid suites, although they occur outside the Irumide belt *sensu strictu* and are adjacent to lithologies that form part of the Ubendian belt.

7. Syn- and late-Irumide granitoids form an extensive magmatic suite dominated by coarse, phenocrystic granitoids. These granitoids include the Bemba batholith (Lufila Granite) and Chilubanama Granite in the northeastern Irumide belt, and numerous unnamed porphyritic biotite granitoids in the rest of the Irumide belt. Syn-kinematic granitoids are characterised by a weak to strong tectonic foliation, and a remnant margin-parallel magmatic foliation, heterogeneously distributed through the plutons, while post-kinematic granitoids are largely undeformed and coarse, with well-defined margin-parallel magmatic fabrics. Daly (1986b) reported a Rb-Sr whole-rock date of 947 ± 89 Ma for the post-tectonic Lufila Granite and a TIMS U-Pb age of 970 ± 5 Ma for four multigrain zircon fractions from the post-kinematic Kaunga Granite in the northeastern Irumide belt, providing the only age constraints for post-Irumide granitoid magmatism in the belt.

3 CHAPTER 3: Structure and metamorphism

3.1 Introduction

This chapter provides an overview of the present understanding of the structure and kinematics of the Irumide belt and the metamorphic evolution associated with it. In essence, few new data are presented in this chapter, which builds largely on previous published work, complemented by observations made in this study in the field and from thin sections.

3.2 Structure

3.2.1 Introduction

The study area covered in this thesis comprises a large part of the Irumide belt and parts of its foreland, stretching from central Zambia to the Zambia-Tanzania border (600+ kilometers). The far northeastern part of the belt, where the Irumide trends are reported to terminate in post-Irumide shear zones within the Ubendian belt (Daly, 1986b; Ring, 1993; 1999; Ring et al., 1999), as well as the small part of the Irumide belt within Malawi (Padget, 1959; Fitches, 1966; 1967; 1968a; 1968b; 1970; 1971; Ray, 1974; Ray and Crow, 1975) and the strongly overprinted southeastern extent of the Irumide belt in eastern Zambia, were not included in this thesis, and the reader is referred to the literature for those areas.

Over 80% of the Irumide belt has been mapped at a scale of 1:100000 by the Geological Survey Department of Zambia. As such, in depth structural analysis and regional mapping of the Irumide belt were considered outside the scope of this thesis. This thesis instead focuses on key areas, contacts, and lithologies, selected using existing geological maps. Since many of these maps date back to the 1960's, an effort was made to re-evaluate and re-interpret the

geology on these maps in order to provide a more up-to-date geological picture of the Irumide belt. The structural geology conducted as part of this thesis is limited to observations at sampling localities and limited traverse mapping. Based on these field observations and analytical data, especially geochronological constraints obtained as part of this thesis (see chapter 4), the existing maps were critically reviewed and adapted where necessary.

3.2.2 Previous work

The earliest structural investigations established the northeast structural grain of the Irumide belt (Ackermann, 1936; 1950; 1960; Ackermann and Forster, 1960) and compared the Irumide belt to an “Alpine-type” orogen. The strongly contorted metasedimentary sequence, which Ackermann called the “Muva”, was divided into a recrystallised and higher grade sequence, later called the Musofu Formation (Stillman, 1965c), and a heavy-mineral-depleted, lower grade “Kalonga series” (Forster, 1965), which occur in two parallel ridges north and south of Mkushi. The recognition of these two different sequences was used to support a pre-Irumide tectonic event called the Tumbide orogeny. As Irumide tectonism affected both the metasedimentary sequence and the crystalline rocks, resulting in the virtual obliteration of any pre-Irumide fabrics and reorientation of all structures into the southwest-northeast Irumide grain (Forster, 1965), this earlier event remained obscure and poorly documented, and was finally refuted on the basis of renewed mapping in the Irumide belt (Daly et al., 1984; Mapani and Moore, 1995b; De Waele and Mapani, 1998; Mapani, 1999). Recent work has shown that: (a) the sedimentary record in the earlier defined Musofu and Kalonga Formations is identical (Mapani, 1992; De Waele and Mapani, 2002); (b) the base of the Kalonga Formation is not observed. Instead, a tectonic unit is observed, interpreted to lie above a thrust interface with the Mkushi Gneiss (Stillman, 1965c; Mapani, 1992; De Waele and Mapani, 2002). The Musofu Formation rests unconformably on the Mkushi Gneiss basement. The higher grade of the base of the Musofu Formation (the part of the sequence that lies in Zambia) is interpreted to reflect its deeper stratigraphic level with respect to the Kalonga succession.

Daly (1986b) proposed a four stage tectonic evolution for the Irumide belt:

- 1/ Minor rifting event (formation of the Mporokoso basin)
- 2/ More regional and profound rifting event (formation of the Irumide basin)
- 3/ Contractual orogeny affecting both basins
- 4/ Post-Irumide strike-slip deformation

The structural model proposed by Daly (1986b) has remained unchallenged to date. Daly (1986b) believed that the southwestern part of the Irumide belt was dominated by pre-Irumide gneisses and recognised an axis of structural divergence defining a “pop-up” structure. Although basement “pop-up” is still possible, field relations show that a large amount of essentially undeformed granitoids intrude the Mkushi Gneiss, indicating that the extent of the pre-Irumide lithologies in the southwestern part of the Irumide belt has previously been grossly overstated (Stillman, 1965c; Cvetcovic, 1973; Mapani, 1992).

On a more regional scale, Daly considered the Irumide belt and the Luongo fold belt in northern Zambia as part of a thick-skinned fold-and-thrust belt with tectonic transport to the northwest (Daly, 1986b). Furthermore, he linked the Mesoproterozoic events in the foreland of the Lurio belt of northern Mozambique to the structural development of the Irumide belt. On this ground, Daly (1986b) postulated the existence of a pre-Mesoproterozoic microcraton (the Niassa craton) in southern Malawi to explain the variation of structural vergence along a section running from the Irumide belt, across southeastern Zambia, southern Malawi and into northern Mozambique. It is important to note that the timing of the deformation events that produced the structures in the different orogenic provinces used to construct the above model was not constrained.

Post-Irumide events are only recognised in the southwestern part of the belt, where effects of the Lufilian arc and Zambezi belt become apparent. The effects of “Pan-African” tectonism appear to be restricted to the east of the study area (in Malawi), as neither Daly (1986b) nor Vrána et al. (2004) reported significant Neoproterozoic disturbance of the ^{40}Ar - ^{39}Ar isotopic systems for hornblende and muscovite respectively. Near Serenje, Vail et al. (1968) reported

K-Ar ages on biotite between 567 ± 24 and 495 ± 20 Ma and on muscovite at 885 ± 36 Ma possibly indicating complete resetting of the K/Ar system in biotite and partial resetting in muscovite during the Pan-African event.

3.2.3 Irumide structures

Deformation in the Irumide orogeny was pervasive, largely obliterating pre-Irumide structural imprints on the rocks. At the same time, tectonism appears to be strongly heterogeneous within large Irumide-age plutons, which can have strong foliations in one place and appear largely undeformed elsewhere.

In the Irumide belt, two episodes of ductile deformation are reported to affect the rocks of the Manshya River/Kanona Groups (Daly, 1986b). The earliest D_1 event, which is responsible for the dominant grain of the Irumide belt, is evident from the large resistant quartzite ridges, and the dominant foliation trending southwest-northeast. D_1 developed open to isoclinal, upright to recumbent F_1 folds with northeast- to north-northeast-trending axial planes. In metasedimentary rocks, folding is accompanied by a cleavage or schistosity developed axial planar to the folds and thus often parallel or at low angle to the primary layering. The schistosity is defined by aligned mica and, in pure quartzites, grain flattening. In gneisses and granite-gneisses, the foliation is developed unevenly in coarse-grained lithologies, defined by alignment of mica and/or elongate minerals, and in more extreme cases, by neocrystallisation of quartz-feldspar aggregates, flattening and stretching of feldspar in augen structures and partial recrystallisation and flattening of the groundmass. Doubly-plunging fold axes are interpreted by Daly (1986b) to indicate an F_2 refolding event. D_2 is expressed on a regional scale through attenuation of F_1 folds, their limbs separated from their noses, which Daly (1986b) interpreted to indicate a period of extension after F_1 fold formation. A strong L_2 lineation, defined by sillimanite laths in metapelites, is well developed in the southwestern part of the Irumide belt and is parallel to F_2 fold axes with shallow plunges to the northeast. In the northeast of the belt, Daly (1986b) reported fold axes related to D_2 to trend north-northeast and L_2 lineations to plunge steeply to the southeast. The relations

between S_0 and S_1 in the northwestern part of the Irumide belt are clear, but further southeast, where the metamorphic grade increases, S_1 and S_2 fabrics become dominant. According to Daly (1986b), crustal shortening in the northeastern part of the Irumide belt was accommodated by large transverse shear zones, e.g. the reactivated Mugesse shear zone in the Ubendian belt. Contractional deformation in the Irumide belt induced northwesterly thrusting of nappes onto the Bangweulu block (Figure 3-1)(Daly, 1986b). It is estimated that a minimum shortening of 11 km occurred in the Mporokoso Group near Mansa (Luongo fold zone, Figure 3-1) and that up to 60 km shortening occurred in the Manshya River Group (Shiwa N'gandu zone, Figure 3-1) in the northeastern Irumide belt (Daly, 1986b). Thrusts within the supracrustal sequence and ductile deformation at the basement-cover contact in the southwestern part of the Irumide belt suggest that the Kanona Group was detached from its basement, while shallow plunging lineations confirm a dominant northwest-directed tectonic transport (Daly, 1986b). Locally, tectonic transport verging to the southeast can be seen, interpreted to indicate the presence of minor backthrusts (Daly, 1986b). Two structural sections from the northeastern southwestern parts of the Irumide belt are presented in Figure 3-2.

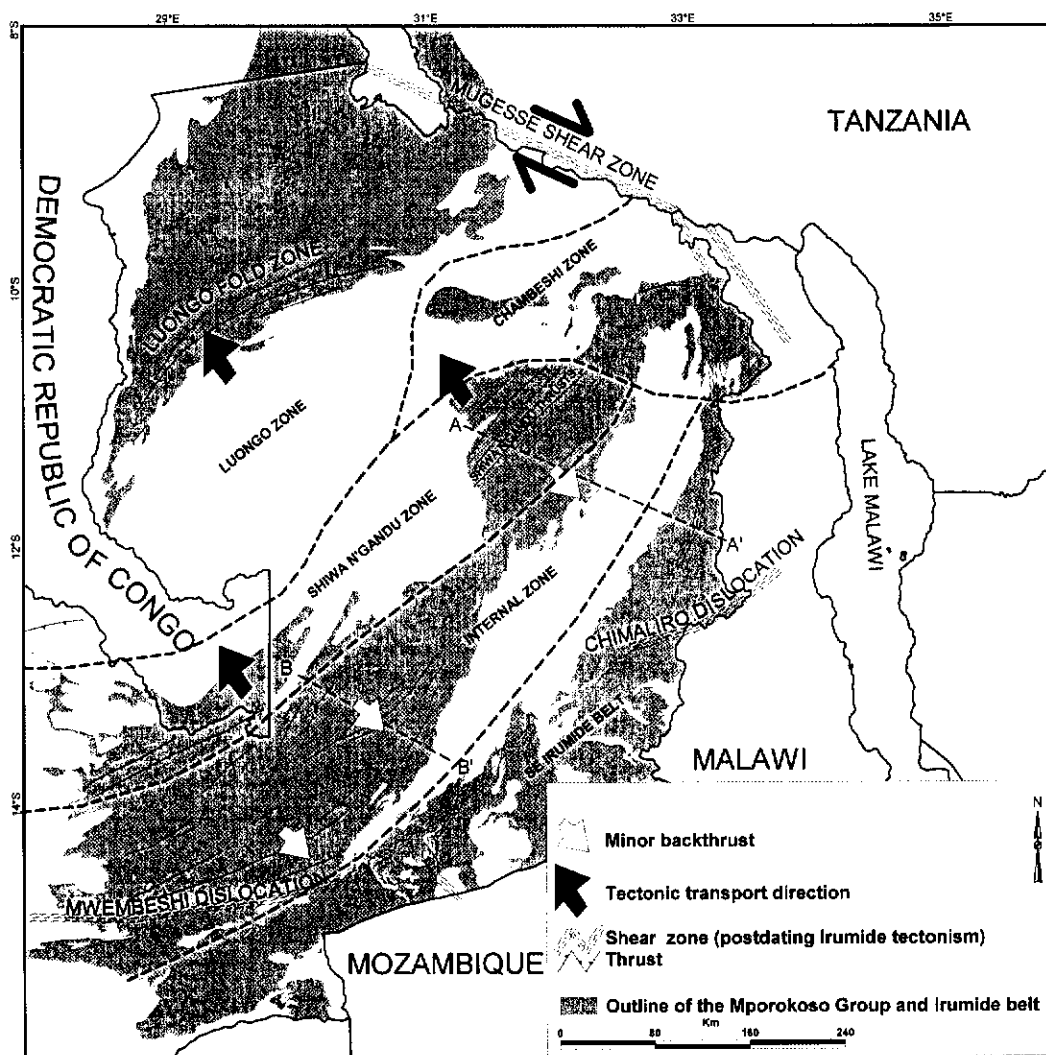


Figure 3-1: Simplified structural map of northern Zambia showing tectonic transport directions and major shear zones. A-A' and B-B' show the approximate location of the sections in Figure 3-2.

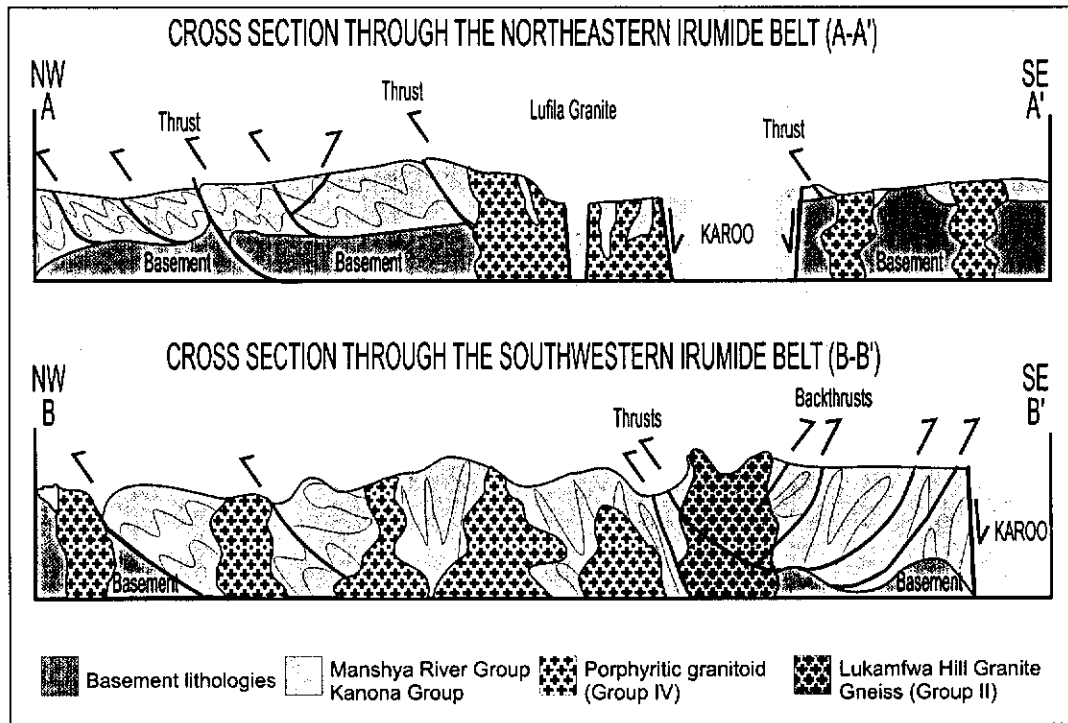


Figure 3-2: Simplified cross-sections through the northeastern (A-A') and southwestern (B-B') Irumide belt. The locations of these sections are shown in Figure 3-1. Sections were constructed based on 1:100000 map sheets of the Geological Survey Department of Zambia (the diagrams are not to scale).

3.2.4 Late- to post-Irumide doming

Due to the voluminous intrusion of syntectonic granitoids in the Irumide belt, large extensional faults formed, accompanied by localised deformation and mylonitisation (Daly, 1986b; Sykes, 1995). Diapiric rise of domal granitoid bodies resulted in the reorientation of Irumide structures into parallelism with the intrusion margins, as well as the development of a margin-parallel primary fabric within the granitoids (Mapani and Moore, 1995b; Van de Velde and De Waele, 1998). Aligned feldspar phenocrysts are a common feature in late- to post-tectonic granitoids, and are interpreted as a primary magmatic fabric.

3.2.5 Lufilian and Zambezi structures

In the area of concern here, post-Irumide deformation is limited to the southwestern intersection of the Irumide belt with the Lufilian and Zambezi belts, where the Irumide belt and its basement underlie the thick Katangan Supergroup of the Copperbelt. Lufilian deformation imposed prominent northwest-southeast-trending fabrics, often obliterating the northeast-southwest-trending Irumide grain (Porada and Berhorst, 2000). This deformation strongly affected the Palaeoproterozoic basement of the Copperbelt, but is not discernable in the Mkushi Gneiss within the Irumide belt. Extensive reorientation of structural trends from northeast to northwest within the Kanona Group produced a sub-parallel alignment of Kanona units and the Neoproterozoic Katangan Supergroup (Daly et al., 1984). The higher metamorphic grade preserved in the Kanona Group metasedimentary succession is, however, in stark contrast with the greenschist-facies Katangan rocks and makes these different units easy to distinguish. Occasionally, thrust imbrication of basement and sometimes overlying Kanona Group places Katangan strata in structural contact with either Kanona Group metasedimentary rocks or the Mkushi Gneiss basement.

Lufilian tectonism was terminated by a period of late-Lufilian doming, rotating earlier structures and producing complex fold patterns. Daly et al. (1984) interpreted rotated northwest-trending structures and complex folds at the margin of basement domes as lateral culmination structures produced during northwest-directed thrusting (Daly et al., 1984).

3.3 Metamorphism

The vast majority of outcrop in the Irumide belt comprises relatively pure quartzites and voluminous granitoids, which poorly record metamorphic facies. The pelitic members of the Kanona/Manshya River Group are commonly extensively weathered and unsuitable for petrographic work, while the Irumide belt has a distinct lack of mafic igneous lithologies, which may adequately record

metamorphic assemblages. As a result, metamorphic facies boundaries within the Irumide belt are difficult to define due to the scarcity of diagnostic assemblages.

The general distribution of metamorphic facies in Zambia was described by Ramsay and Ridgway (1977) and Ridgway and Ramsay (1986)(Figure 3-3). The Irumide belt lies entirely in the Luangwa-Kariba metamorphic zone defined by these authors and is characterised by an increase of metamorphic grade, from sub-greenschist to greenschist facies in the northwest, up to the amphibolite and localised granulite facies in the southeast part of the Irumide belt.

The highest metamorphic grade in the Mporokoso Group is in the lower greenschist facies, with the assemblages chlorite + muscovite + albite \pm epidote. The Manshya River/Kanona Groups are in the lower greenschist facies in the northwest, increasing to upper amphibolite and locally granulite grade in the southeast. The change in metamorphic assemblages is best exemplified in the Serenje 1:100000 map sheet. In the northwest, metapelites consistently record the metamorphic assemblages muscovite + chlorite + quartz + albite + talc \pm epidote or muscovite + biotite + albite + quartz. Towards the southeast, staurolite + muscovite + garnet and cordierite + andalusite appear, and in the extreme southeastern corner of the Serenje 1:100000 map sheet, sillimanite + garnet + amphibole and sillimanite + garnet + biotite are recorded in migmatites and metapelites, indicating medium-pressure/high-temperature conditions (Mapani, 1999). In the Mkushi 1:100000 map sheet, Stillman (1965c) reported muscovite-kyanite-quartz assemblages in pelitic schists, supporting regional Barrovian-type rather than low-pressure Buchan-type conditions in the Irumide belt. Similar kyanite-bearing quartzites were observed during this study in the Kanona 1:100000 map sheet, and kyanite-andalusite schists are reported in association with quartzites in the Mkushi 1:100000 map sheet (Stillman, 1965c). In the Serenje 1:100000 map sheet (Figure 2-10), Mapani (1999) recorded the following metamorphic zones from the northwest to the southeast: biotite \pm garnet \rightarrow staurolite \rightarrow kyanite \rightarrow sillimanite. The presence of biotite + sillimanite + garnet + K-feldspar in schists in the southeastern corner of the 1:100000 Serenje map sheet indicates that granulite facies conditions prevailed in the southeast. In the northeastern part of the belt, the lithologies are more feldspathic and poorly record

the grade of metamorphism. Throughout the Irumide belt, recrystallisation of quartzite is widespread (Stillman, 1965c; Daly, 1986b; Mapani and Moore, 1995b). The transition from andalusite to sillimanite along with coexisting kyanite and sillimanite and reports of kyanite locally replacing cordierite (Mapani, 1999) suggest increasing temperatures and pressures. This crustal thickening event was followed by exhumation and was accompanied by reheating coinciding with the emplacement of late- to post-Irumide granite bodies. This heating is recorded in the static growth of chloritoid, cordierite, biotite and feldspar in various rock types.

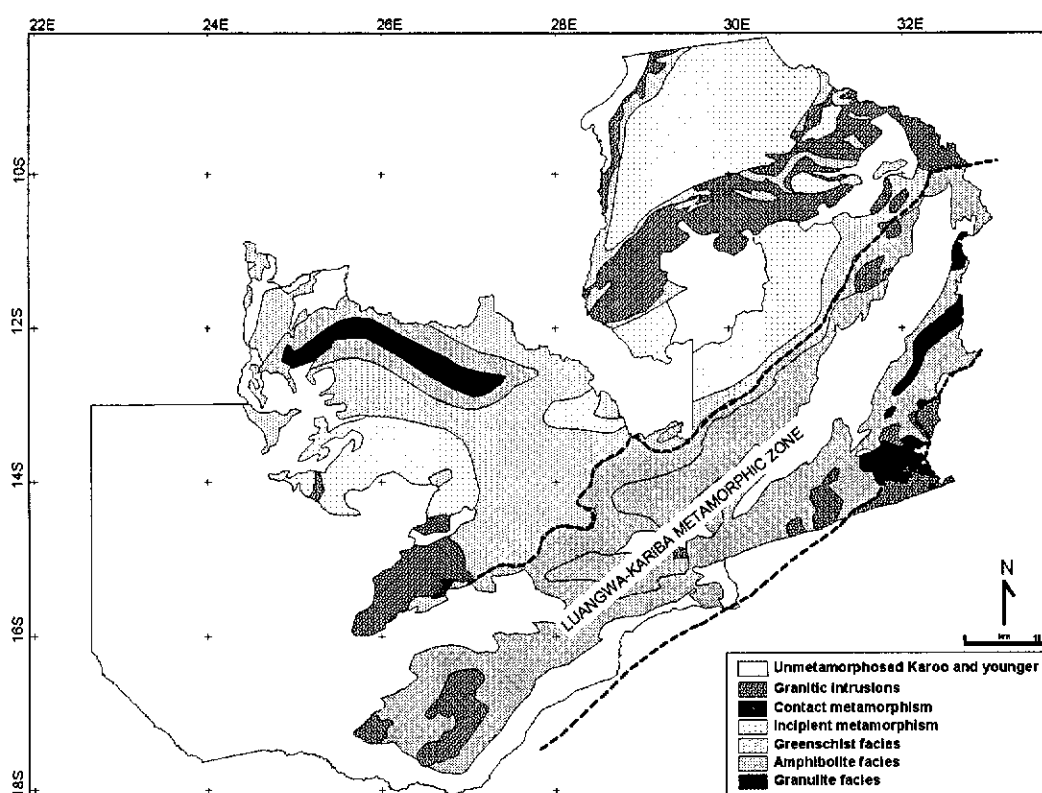


Figure 3-3: Simplified metamorphic map of Zambia after Ramsay and Ridgway (1977)

3.4 Summary

The structure of the Irumide belt indicates overall northwest-directed tectonic transport as demonstrated by upright to recumbent northwest-verging folds, shallow southeastward plunge of mineral lineations, general top-to-the-northwest shear-sense indicators and regional northeast-southwest structural grain indicating

crustal shortening along a northwest-southeast direction. These features are predominant in the northwestern part of the Irumide belt, especially in the Shiwa N'gandu fold zone and in the northwest of the Serenje area. Towards the southeast, small backthrusts are locally defined by steepening of foliation planes, locally dipping to the northwest, and carrying shear-sense indicators showing a southeast vergence (Daly, 1986b). These structures are best defined in the southwestern Irumide belt, where Daly (1986b) ascribed the change from northwest-vergent to vertical and southeast-vergent structures to a regional "pop-up" structure within a progressive deformation sequence related to northwest-directed subhorizontal displacement during Irumide tectonism.

Metamorphic grade in the Irumide belt increases from greenschist facies in the northwest to granulite facies in the southeast, with chlorite-albite-muscovite in the metapelites in the northwest and widespread presence of sillimanite-biotite-garnet and sillimanite-garnet-amphibole in metapelites in the southeast (Mapani, 1999). The highest metamorphic grades occur in the southeastern part of the belt, where sillimanite-garnet and kyanite-sillimanite are recorded in high-grade gneisses and migmatites (Mapani, 1999). The metamorphic assemblages recorded in the Irumide belt indicate regional medium pressure / medium to high temperature conditions.

4 CHAPTER 4: Zircon U-Pb SHRIMP Geochronology

4.1 Introduction

The geochronology presented in this thesis is based on the U-Th-Pb isotopic system as applied to zircon dating (refer to Appendix C for details and to standard textbooks such as Dickin (1995) and Faure (1997)). Zircon was chosen because of its abundance in the predominant granitic lithologies sampled during the study, its resistance to weathering, metamorphism and alteration, its well-established ability to preserve various growth zones related to successive periods of crystallisation, and the fact it can grow during magmatic crystallisation as well as metamorphism (Vavra, 1990; Hanchar and Miller, 1993; Vavra, 1993; 1994; Vavra et al., 1996; Kempe et al., 2000; Rubatto and Gebauer, 2000; Möller et al., 2002). Because of the potential complexity of zircon, various imaging techniques were used prior to dating, in order to select suitable analysis spots, as well as make inferences on the nature and composition of the zircon. Interpretations on the nature of zircon based on morphology and cathodoluminescence (CL) response followed Rubatto and Gebauer (2000)(Table 4-1). According to those authors, the quenching effect of some incompatible elements, including uranium, which are concentrated in metamorphic fluids, results in a diagnostic dark aspect in CL-images of metamorphic zircon. In fact, low CL response is commonly equated to high uranium content of the zircon.

Table 4-1: Typical characteristics of zircons from different sources (Rubatto and Gebauer, 2000).

Zircon type	CL	Chemistry
Granitic	Narrow, planar, banded, oscillatory zoning	$0.1 < \text{Th/U} < 16$; variable across zoning; U ranges from 1ppm to >1000ppm
Gabbroic	Narrow to broad, banded, oscillatory zoning	$0.1 < \text{Th/U} < 16$; U is variable across zoning from 1ppm to >100ppm
Metamorphic	Homogeneous U content, no zoning.	$\text{Th/U} < 0.1$; $\text{U} > 200$ ppm
Metasomatic	Zoning near core fades towards the rim.	Low U at rim, increasing towards core

In this chapter, a brief introduction to the instrumentation (SHRIMP II) and methodologies followed for U-Th-Pb geochronology is given, followed by a brief introduction to zircon geochronology as applied to the various types of rocks and problems discussed in this study. This is followed by a summary of the questions that will be addressed in this chapter, and finally the data are presented and interpreted.

4.2 Instrumentation and methodologies

The instrument used to collect the U-Th-Pb data presented in this study is a particular type of Secondary Ion Mass Spectrometer (SIMS) housed at Curtin University of Technology, namely the Sensitive High-mass Resolution Ion Microprobe (SHRIMP) produced by Australian Scientific Instruments at the Australian National University in Canberra (Compston et al., 1984; Williams, 1998). The SHRIMP allows micro-analysis of zircons at a scale of 10-30 μm and is therefore particularly well-suited for the dating of complex zircons, as often found in metamorphic terrains such as the Irumide belt.

In the SHRIMP, a beam of “primary” ions (O_2^+) is collimated and accelerated towards the target, and used to sputter “secondary” ions from the sample. These “secondary” ions are accelerated along the instrument where the various isotopes of uranium, lead and thorium are measured successively, along with reference peaks for Zr_2O^+ , ThO^+ and UO^+ . Since the sputtering yield differs between ion species and relative sputtering yield increases or decreases with time depending on the ion species (due to increasing crater depth, charging effects and other factors), the measured relative isotopic abundances do not relate to the real relative isotopic abundances in the target. Corrections are determined by analysing unknowns and standard material (gem quality zircon of known age and isotopic composition; during this study CZ3 standard was used), and determining a calibration factor following procedures described in detail by Claoué-Long et al. (1995)(refer to Appendix C for detailed description of these procedures).

Because of the high sensitivity of the SHRIMP instrumentation, it is possible to detect and analyse the non-radiogenic isotope ^{204}Pb with adequate precision to use its abundance to estimate the contribution of common Pb (i.e. Pb not related to the decay of uranium and thorium incorporated during zircon growth) to the total analysed Pb. This common Pb correction method relies on the fact that the isotopic abundance of ^{204}Pb is fixed in time and thus provides a direct estimate of the amount of non-radiogenic Pb in the analysis. Because of the fact that in nature, the relative abundance of Pb isotopes changes over time, and because it is impossible to distinguish whether measured ^{204}Pb was incorporated during crystallisation of the zircon, or represents present day contamination with common Pb, the isotopic composition chosen for common Pb (either present day or an assumed composition appropriate for the age of the zircon) is a contentious issue. During this study, present-day contamination with common Pb through the conductive gold coat and surface contaminants was minimised through a rigorous cleaning procedure of the mount, and the use of ultra-pure gold. Pb-contamination was further minimised through careful selection of analysis spots, away from surface defects, cracks and inclusions. As a result of these procedures, proportions of common Pb in total Pb (throughout this thesis expressed as the proportion $^{206}\text{Pb}_{\text{common}}$ in measured ^{206}Pb , or denoted as f_{206} in %) were found to be low, and common Pb was assumed to be related to Pb incorporated in the zircon lattice during zircon crystallisation. The assumed isotopic composition of common Pb was taken from the model of Stacey and Kramers (1975) at the calculated $^{207}\text{Pb}/^{206}\text{Pb}$ age of the zircon, and the estimated amounts of common ^{206}Pb , ^{207}Pb and ^{208}Pb , based on the measured ^{204}Pb as outlined above, removed from the total measured amounts prior to the final age calculation. Because of the low proportions of common Pb encountered during this study (mean of $f_{206}=0.507\%$), the corrections applied were relatively insensitive to the choice of isotopic composition. For more details on the preparations preceding SHRIMP analysis, a detailed description of methodologies followed for analysis, and data reduction strategies, the reader is referred to Appendix C.

4.3 *U-Pb SHRIMP zircon geochronology*

4.3.1 Magmatic zircon

Zircon is an important accessory phase in a wide variety of silica-saturated or silica-oversaturated igneous rocks, and crystallises directly from the magma. Its average closure temperature for the U-Th-Pb decay system is reported to be 900°C, making zircon an excellent mineral to date the original crystallisation of magmatic rocks because it is unlikely to be reset by later metamorphic events (Cherniak and Watson, 2000). However, because zircon is a refractory mineral, and relatively resistant to alteration and chemical abrasion, it can also be preserved as xenocrysts in magmatic rocks. Significant differences in zircon morphology (size, length to width ratio, habit) or CL response may help distinguish primary from xenocrystic zircon. Unfortunately, in most cases, neither can unequivocally be used to determine whether a zircon is primary or xenocrystic. During this study, the majority of dated lithologies are granitoids, which generally contain significant amounts of primary zircon, crystallised directly from the magma. Nevertheless, because xenocrystic zircons can (and are likely to) be incorporated in the rock, every attempt is made during this study to date a reasonable number of magmatic zircons from igneous rocks. Since crystallisation from the melt is assumed to take place in a relatively short period of time (a few million years for granitoids at most)(Pitcher, 1997), the primary magmatic zircons (which generally make up the majority of all zircons) are expected to define a coherent age group. Xenocrystic zircons on the other hand can be derived from a wide variety of country rock with a range of ages, and in most cases will show poorly defined age groups predating the crystallisation age of the magmatic rock. During this study, the youngest, dominant and coherent age population of magmatic zircon in a sample of igneous rock is interpreted to date the magmatic crystallisation of the rock. In a few cases, the xenocrystic zircon component in an igneous rock can, however, outweigh the primary zircon population (e.g. S-type granite). For those rocks, the youngest coherent age group can be regarded the maximum age of crystallisation.

For magmatic rocks, a typical SHRIMP II dataset consists of U-Th-Pb isotopic analyses on several (typically no less than 6) zircons from the same sample. In the case that each of these measurements agree internally to within error, and that the distribution is approximately symmetrical, it is appropriate to calculate either an arithmetic mean or a mean weighted by the inverse of the variances (Bevington and Robinson, 1992). In this study, weighted mean values at 95% confidence are reported. Data reduction was done using the program Isoplot (Ludwig, 2001a), which calculates the 95% confidence errors for the weighted mean as:

$$\pm 95\% = \sigma(\text{mean}) \times \sqrt{\text{MSWD}} \times \text{Student} - t$$

where σ = standard deviation; MSWD = Mean Square of Weighted Deviates and Student-t = Student-t's factor for the actual degrees of freedom (N-1) at 95% confidence level.

For the age ranges encountered during this study, and for concordant data groupings, the weighted mean $^{207}\text{Pb}/^{206}\text{Pb}$ age was taken to represent the most reliable result in most cases. In cases of recent Pb-loss, typified by a linear regression of the data with lower intercept within error of 0 Ma, a calculated weighted mean $^{207}\text{Pb}/^{206}\text{Pb}$ age still provided a reliable result, but in cases where a well-defined linear regression could be constructed (MSWD < 2), preference was given to an upper intercept age. For concordant data, Isoplot allows the calculation of a "concordia" age (Ludwig, 1998), which was used in preference to either upper intercept age or weighted mean $^{207}\text{Pb}/^{206}\text{Pb}$ age only if its age was within error of these, had an acceptable MSWD value comparable or smaller than the values for either of the other ages, and was calculated from a sufficient number of concordant data points.

4.3.2 Detrital zircon

Because zircon is a common accessory phase in a wide range of rocks, and because of its robust nature, detrital zircon grains are commonly accumulated in sediments (Morton, 1985; Johnsson, 1993). The chemical and physical resistance of zircon varies according to uranium content as well as age. High-uranium zircon can suffer radiation damage, resulting in metamictisation, and will be less resistant to weathering and sedimentary transport than low-uranium zircon (Morton, 1985; Johnsson, 1993). On the other hand, very old low-uranium zircon would also have suffered cumulative radiation damage, making it susceptible to chemical or physical weathering. Other factors that have a bearing on relative zircon population in a sediment are the volume of source rock, the initial amount, morphology and size of zircon in the source rock, the distance from source to depocentre, and the sedimentary environment and transport conditions. The use of detrital zircon ages in an attempt to link zircons to possible source rocks has been successfully used in numerous studies (Rainbird et al., 1992; Kampunzu et al., 2000; Cawood et al., 2003). Even where direct correlation of detrital zircons with possible source rocks is difficult, detrital age patterns (or fingerprints) may help match the sediment to potential source regions (Ross et al., 1992; Sircombe et al., 2001; Collins et al., 2003; Cox, submitted) or allow comparison of different sedimentary units (Sircombe, 2002). Detrital provenance analysis relies on the calculation of a crystallisation age for each individual zircon. Because of this, only concordant zircon analyses are considered ($100 \pm 5\%$ concordant). During this study, $^{207}\text{Pb}/^{206}\text{Pb}$ ages are reported for all detrital zircons, as they are older than 1400 Ma and have sufficient ^{207}Pb to yield precise $^{207}\text{Pb}/^{206}\text{Pb}$ ages (Cox, submitted).

4.3.3 Metamorphic zircon

The growth of zircon during metamorphism is a widely documented phenomenon (Vavra, 1990, 1993, 1994; Vavra et al., 1996; 1999; Hoskin and Black, 2000; Nemchin et al., 2001; Möller et al., 2002). Metamorphic zircon can

grow directly from metamorphic melts, or can grow onto pre-existing zircon during solid-state crystallisation, forming complex zircons with core and rim domains (Vavra et al., 1996; Roberts and Finger, 1997; Hoskin and Black, 2000). Metamorphic zircon is reported to be characterised by very low Th/U ratios (Hoskin and Black, 2000), although there are exceptions (e.g. Möller et al., 2003). At the same time, incompatible elements are significantly enriched in metamorphic fluids, leading to growth of relatively high-uranium zircon growth during high-grade metamorphic events. During this study, several high-uranium and low-thorium zircon rims were analysed and interpreted to date peak metamorphic conditions in the Irumide belt.

4.4 Rocks dated in this study

The geochronological work presented in this chapter is aimed at solving a series of longstanding questions regarding the Irumide belt:

Firstly, SHRIMP dating was used to constrain the emplacement age of a range of orthogneisses from the Irumide belt and undeformed plutono-volcanic rocks from the Mansa area on the Bangweulu block to test proposed correlation between basement rocks in the Irumide belt and those of the Bangweulu foreland (Figure 2-3, Figure 2-4 and Figure 2-17). The Irumide basement lithologies dated in this study include the Mkushi Gneiss, the Luwalizi Granite Gneiss and the Lubu Granite Gneiss.

In order to help characterise the various metasedimentary sequences of northern Zambia, one sample each was analysed from quartzites of the Kabweluma Formation (Mporokoso Group), Kasama Formation and the Manshya River Group. Additionally, a limited study was conducted on the basal conglomerate of the Kanona Group near Mkushi.

Three volcanic members interlayered with the Manshya River Group sequence of the northeastern part of the Irumide belt were dated, providing direct constraints on the depositional age of this sequence.

In order to gain a better understanding of the timing of granitoid magmatism during the Irumide event, samples were collected from both deformed and undeformed granitoids from across the belt, assumed to be pre-, syn- and post-tectonic respectively. The age data obtained from these samples show that previous interpretations of granitoids as pre-tectonic or syn-tectonic are not always correct.

High-grade migmatitic gneisses, believed to reflect partial melting of the Mkushi Gneiss during the Irumide event in the Serenje area (samples SER6-6 and SER6-7), were collected to directly constrain peak metamorphism in the Irumide belt. Metamorphic rims on zircon were analysed from the Chinsali area (sample MTG4, Chilubanama Granite) in the northeastern part of the belt to allow comparison of the timing of peak conditions across the entire strike length.

For the most part, the data in this chapter are presented in subsections according to their measured age grouping, rather than according to their assumed relative age before dating. The location and ages of analysed samples are shown on Figure 4-1, Figure 4-2, Figure 4-3, Figure 4-4, Figure 4-5 and Figure 4-6.

105

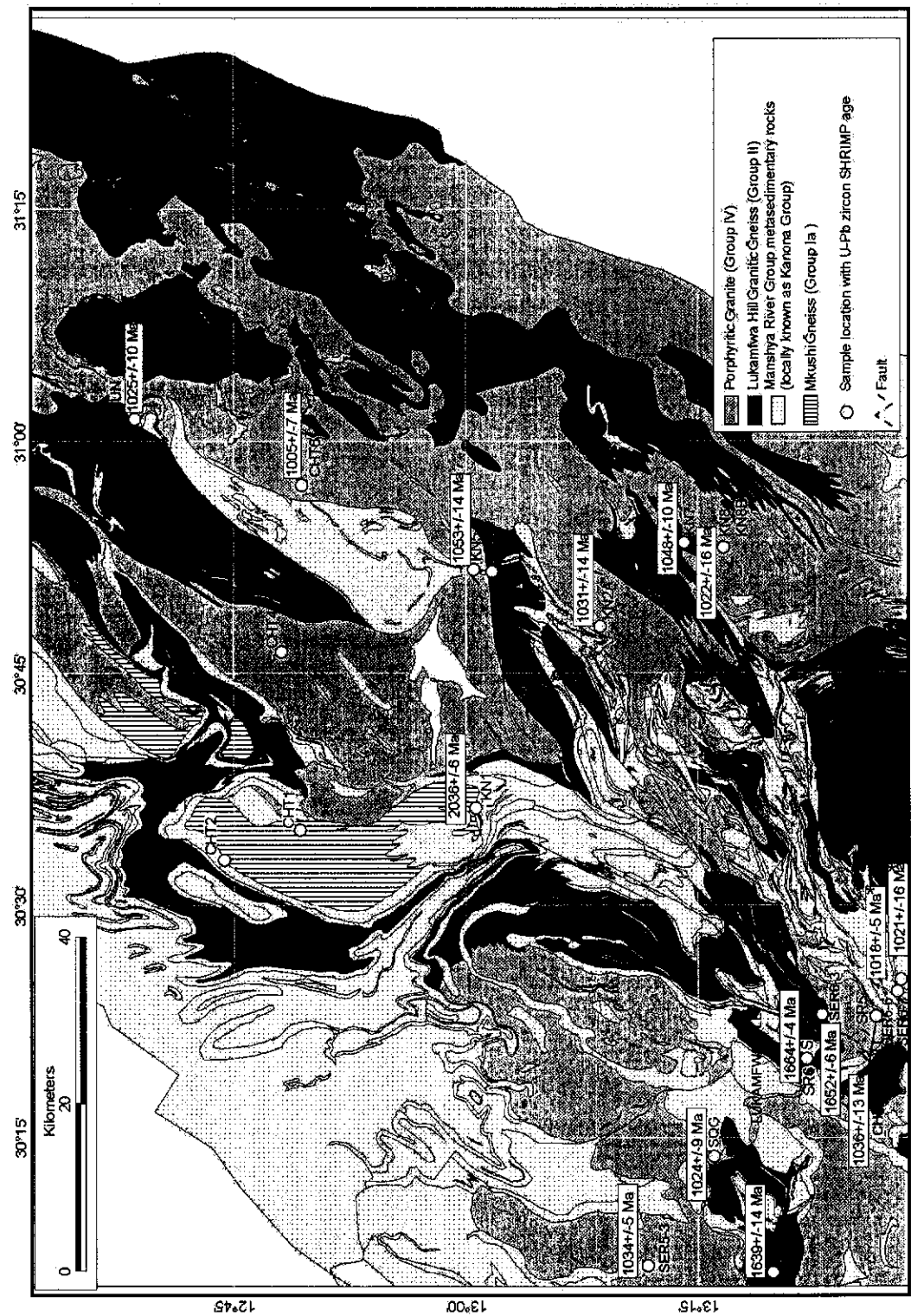


Figure 4-2: Location of samples and obtained zircon U-Pb SHRIMP igneous crystallisation ages for the area around Kanona (includes Kasanka (mapped from satellite imagery), Serenje, Kanona, Chitambo, and Mupamadzi sheets). Two crystallisation ages of low Th/U metamorphic zircon rims are indicated with *.

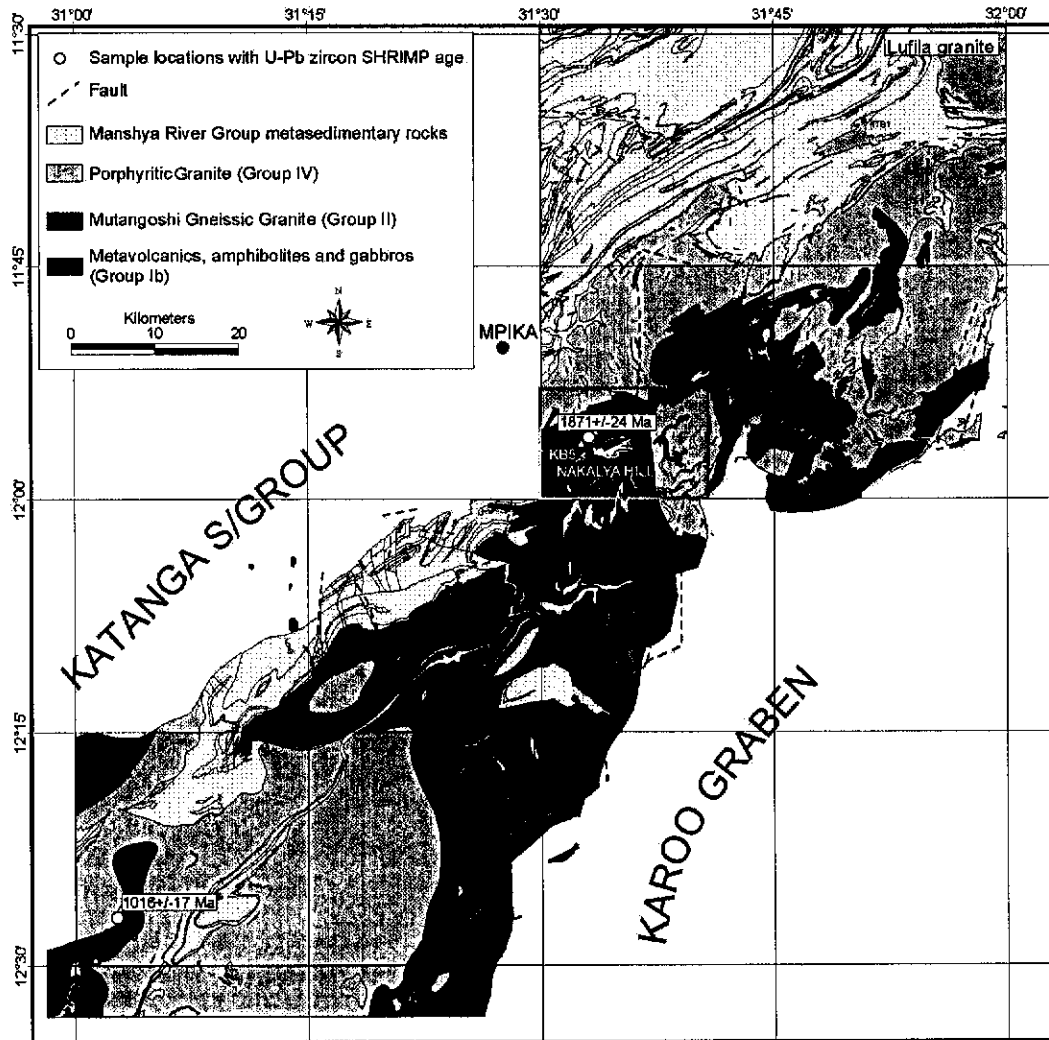


Figure 4-3: Location of samples and obtained zircon U-Pb SHRIMP igneous crystallisation ages for the area around Mpika (includes Chilonga Mission and Katibunga Mission map sheets and parts of Mtofwe and Mupamadzi River map sheets)

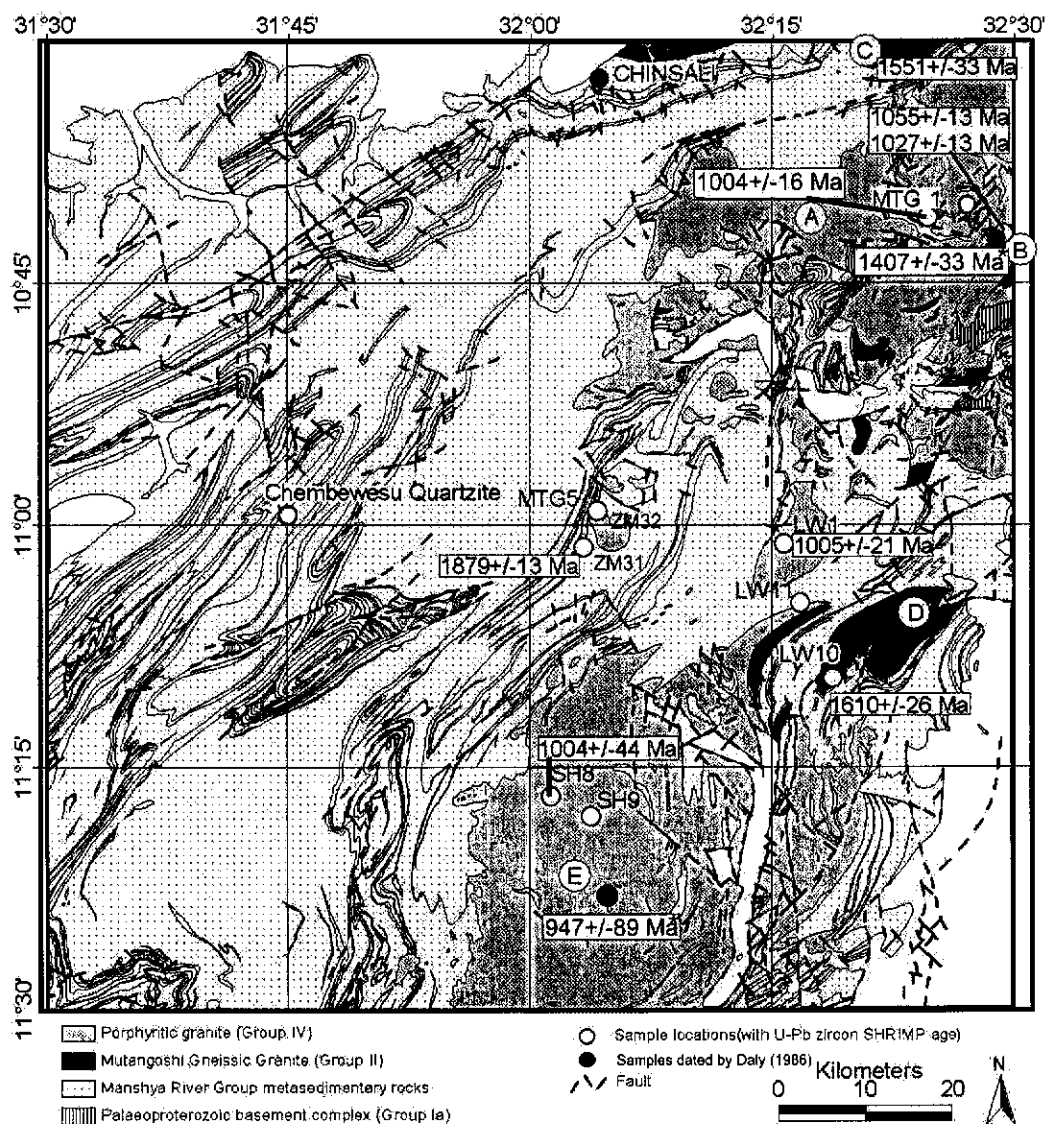


Figure 4-4: Location of samples and obtained zircon U-Pb SHRIMP igneous crystallisation ages for the area around Chinsali (includes Shiwa N'gandu, Ilondola Mission, Luswa River and Chinsali map sheets). A=Chilubanama Granite; B=Mutangoshi Gneissic Granite (location of samples MTGG-1 and MTGG-2); C=Lubu Granite Gneiss; D=Musalango Gneiss; E=Lufila Granite (Bemba Batholith). Whole-rock Rb-Sr date by Daly (1986b) for the Mutangoshi Gneissic Granite and Lufila Granite are indicated.

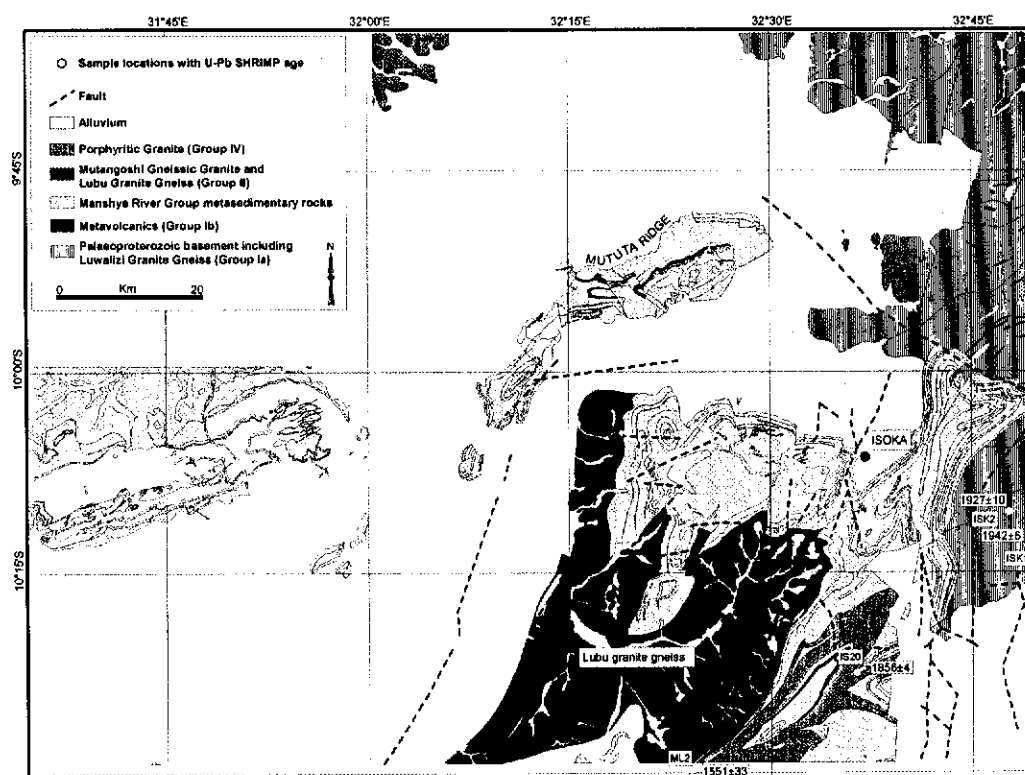


Figure 4-5: Location of samples and obtained zircon U-Pb SHRIMP igneous crystallisation ages for the area around Isoka (includes Malole, Mulilansolo Mission, and Mututa Hills map sheets, and parts of Isoka and Kalungu sheets).



Figure 4-6: Location of samples and obtained zircon U-Pb SHRIMP crystallisation ages for the area around Mansa (includes the 1:100000 Mansa and Musonda Falls map sheets after Thieme (1970; 1971)).

4.5 *Archaean and Palaeoproterozoic basement*

4.5.1 Kapiro Mposhi granite gneiss

One sample was collected (sample KMP-1) from strongly foliated biotite granite gneiss in the Kapiro Mposhi area (Figure 4-1). Although previously regarded as part of the Mkushi Gneiss, the age data presented here show it to be significantly older, and for this reason it is treated separately from the Mkushi Gneiss and referred to as the Kapiro Mposhi Granite Gneiss. The sample was collected from a part of the granite gneiss that was free of quartz veins and away from pegmatites, and yielded a small amount of zircon ranging in size from 100 to 250 μm . The length-to-width ratio of the zircons ranges from 2:1 up to 4:1. The zircons are euhedral, and show well-formed bipyramidal terminations. In transmitted light, the zircons are clear, pale yellow, and contain only minor amounts of inclusions and cracks (Figure 4-7(a)).

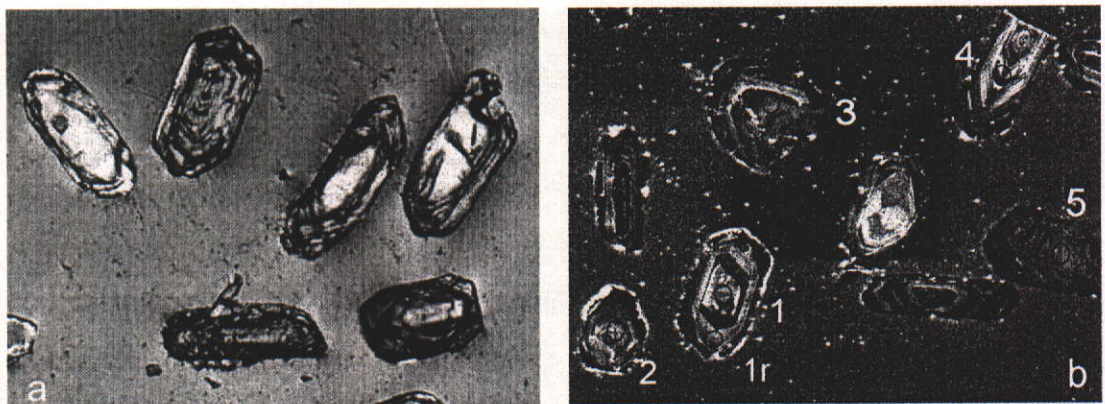


Figure 4-7: (a) photomicrograph of zircons from sample KMP-1 (xpl) showing magmatic zoning in clear zircons (f.o.v. = 600 μm); (b) Cathodoluminescence image of zircon from sample KMP-1 showing the location of analysed spots. Note the complex zircon (analyses 1 and 1r), with a core and rim, which yielded $^{207}\text{Pb}/^{206}\text{Pb}$ ages of 2700 ± 5 Ma and 2686 ± 13 Ma respectively (f.o.v. = 600 μm).

CL imaging shows concentric zoning patterns, consistent with magmatic growth (Figure 4-7(b)). Narrow, high-response rims were below the spatial resolution of the microprobe. Six analyses were conducted on five zircons (Figure 4-7(b)), yielding f_{206} values ranging from 0.087 to 5.328% (Table 13-1). U and Th range from 300 to 714 ppm and 109 to 440 ppm respectively, giving Th/U

ratios between 0.31 and 0.72. The data range from 80 to 100% concordant (Figure 4-8). One pair of analyses on core and rim yielded broadly similar $^{207}\text{Pb}/^{206}\text{Pb}$ ages of 2700 ± 5 Ma for the core and 2686 ± 13 Ma for the rim. One analysis (KMP1-2) yielded a $^{207}\text{Pb}/^{206}\text{Pb}$ age of 3105 ± 143 Ma, and displays the largest common Pb ($f_{206}=5.328\%$). This zircon is near concordant (97.9% concordant) and is interpreted as a xenocryst possibly derived from the source of the granite. The remaining data points appear to have suffered a combination of recent and ancient isotopic disturbance and a regression on five data points yielded an upper intercept of 2726 ± 36 Ma (Figure 4-8). The high MSWD value of 13 for this fit shows that the analytical errors on the data cannot account for the excessive scatter of the data points. The most concordant data point yielded a $^{207}\text{Pb}/^{206}\text{Pb}$ age of 2738 ± 4 Ma (100.6% concordant), and supports the interpretation that the Kapiri Mposhi granite gneiss was emplaced at ca. 2730 Ma. The upper intercept age of 2726 ± 36 Ma can be considered a reasonable estimate of the igneous crystallisation of zircons in the precursor granite of the Kapiri Mposhi granite gneiss.

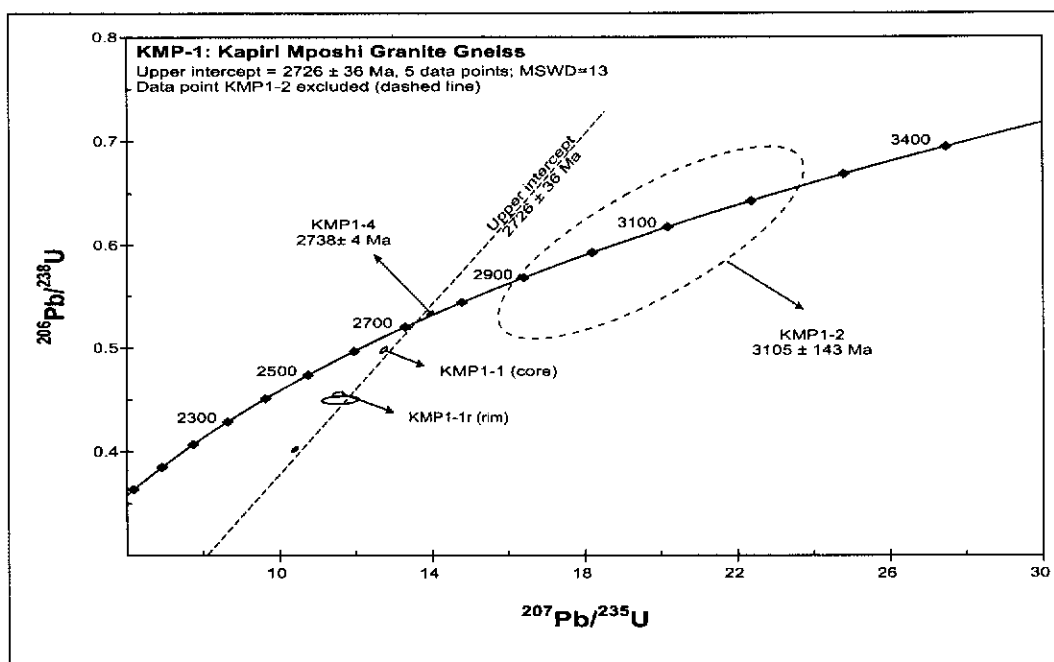


Figure 4-8: U-Pb concordia plot for zircon analyses of sample KMP-1 (Kapiri-Mposhi map sheet). Error ellipses are at 1σ confidence level.

4.5.2 Mkushi Gneiss

Four samples of the Mkushi Gneiss were collected in total for geochronology, two from its type locality at Munshiwemba Quarry south of Mkushi (samples MK3 and MK5), one in the Chin'gombe Mission area (sample CC10) and one in the Kanona area (sample KN1) (Figure 4-1 and Figure 4-2). Two additional samples were collected from migmatites in the Serenje 1:100000 map sheet which, although not mapped as the Mkushi Gneiss (Mapani and Moore, 1995b), represent parts of strongly reworked basement units farther northeast. The age data reported here for these migmatites suggest a close affinity with the Mkushi Gneiss and they are therefore discussed in this section. At Munshiwemba quarry, sample MK3 was collected from the strongly foliated dark grey Mkushi Gneiss in the north of the quarry, while sample MK5 was collected from a weakly foliated pink granite gneiss in the southern part of the quarry. Sample CC10 was collected from a flat outcrop of strongly foliated biotite granite gneiss. Sample KN1 was collected from strongly foliated biotite gneiss in the Kanona area. In all sampled outcrops, the Mkushi Gneiss is cut by aplites and pegmatites, which lack any foliation, and by small folded pegmatites and quartz veins. All samples were collected from fresh outcrop, away from the aplites and pegmatites to avoid contamination by the younger intrusives.

4.5.2.1 *Sample MK3*

Zircons from sample MK3 range in size from 200 to 350 μm and have length to width ratios of 2:1 to 4:1. The crystals are euhedral, with sharp terminations, and are pale yellow to colourless, containing only minor inclusions (Figure 4-9 (a)). CL imaging reveals well developed concentric zoning, and the zircons are interpreted to be of magmatic origin (Figure 4-9 (b)).

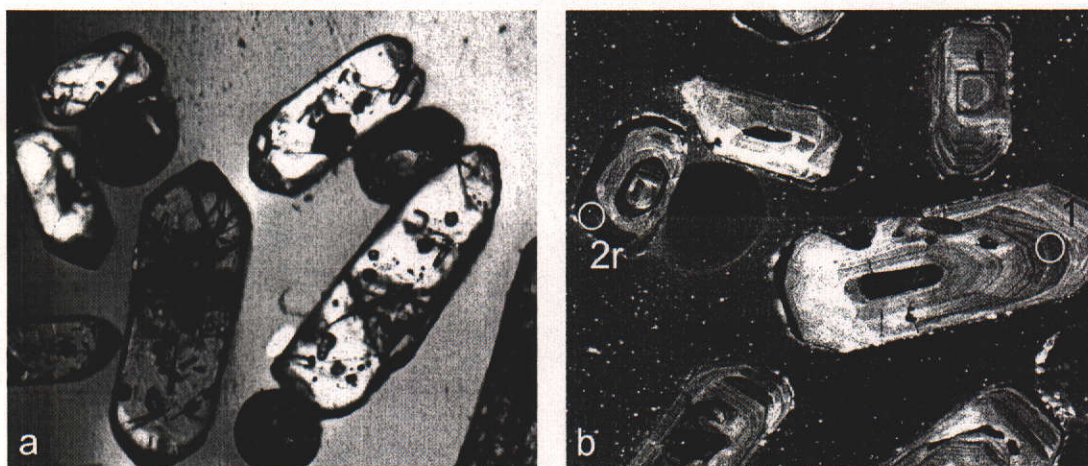


Figure 4-9: (a) photomicrograph of zircons from sample MK-3 (Mkushi map sheet) (xpl) showing clear subhedral to euhedral zircons with minor cracks and inclusions (f.o.v. = 500 µm); (b) CL image of zircon from sample MK-3 showing the location of two analysed spots. Note the analysed zircon rim (analysis 2r), and the well-defined oscillatory zoning in the zircons (f.o.v.= 600 µm).

Five analyses were conducted on four zircons. Three analyses were located on rims, one analysis was conducted on a single-domain zircon interpreted to be of magmatic origin because of well-developed oscillatory zoning, and one analysis sampled a zircon core. f^{206} values are low, reaching up to 0.089%, and U ranges from 137 to 891 ppm (Table 13-2). Th/U ratios range from 0.08 to 0.91, with lowest values for rim analyses MK3-2r and 3r (0.08 and 0.10 respectively). Analysis MK3-4r and 4c (Figure 4-10) display identical Th/U ratios of 0.91 and yielded $^{207}\text{Pb}/^{206}\text{Pb}$ crystallisation ages of 2044 ± 12 and 2037 ± 8 Ma respectively. Two low-Th/U rim analyses have the lowest $^{207}\text{Pb}/^{206}\text{Pb}$ ages of 2015 ± 22 and 2031 ± 22 Ma, and can be resolved from the other analyses. The rims, which have a low CL response and a low Th/U ratio may have grown during a metamorphic event (Hoskin and Black, 2000), which appears to have occurred soon after the emplacement recorded by the magmatic zircons. All five data points yield a weighted mean $^{207}\text{Pb}/^{206}\text{Pb}$ age of 2032 ± 15 Ma (MSWD=2.8). The relatively high MSWD indicates that these data comprise multiple populations. Excluding the two low-Th/U rim analyses, on the basis that they represent a slightly younger metamorphic zircon growth, a weighted mean $^{207}\text{Pb}/^{206}\text{Pb}$ age of 2042 ± 10 Ma (MSWD=0.51) can be calculated. A regression on the same three points indicates a lower intercept at 184 ± 360 Ma and an upper intercept at 2050 ± 19 Ma (MSWD=0.092)(Figure 4-11). The calculated lower intercept is consistent with recent Pb-loss, and the weighted mean $^{207}\text{Pb}/^{206}\text{Pb}$ age of $2042 \pm$

10 Ma is taken to be the best estimate for the crystallisation of the precursor to the Mkushi Gneiss. The slightly younger low Th/U rims could indicate that this emplacement was directly followed by zircon growth during a metamorphic episode between 2031 ± 22 and 2015 ± 22 Ma, although ancient Pb-loss may also account for their apparent younger $^{207}\text{Pb}/^{206}\text{Pb}$ age.

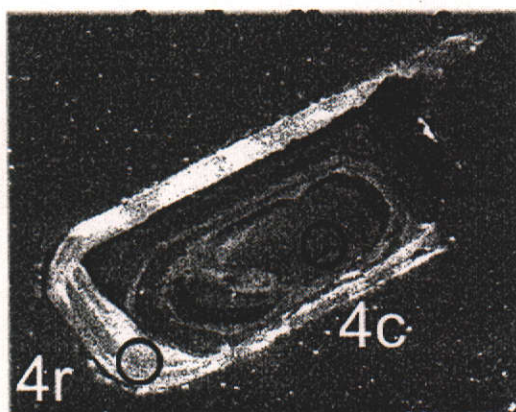


Figure 4-10: CL image of zircon MK3-4 showing the location of two analysed spots. Note the oscillatory zoning in both zircon rim and core (f.o.v. = 250 μm).

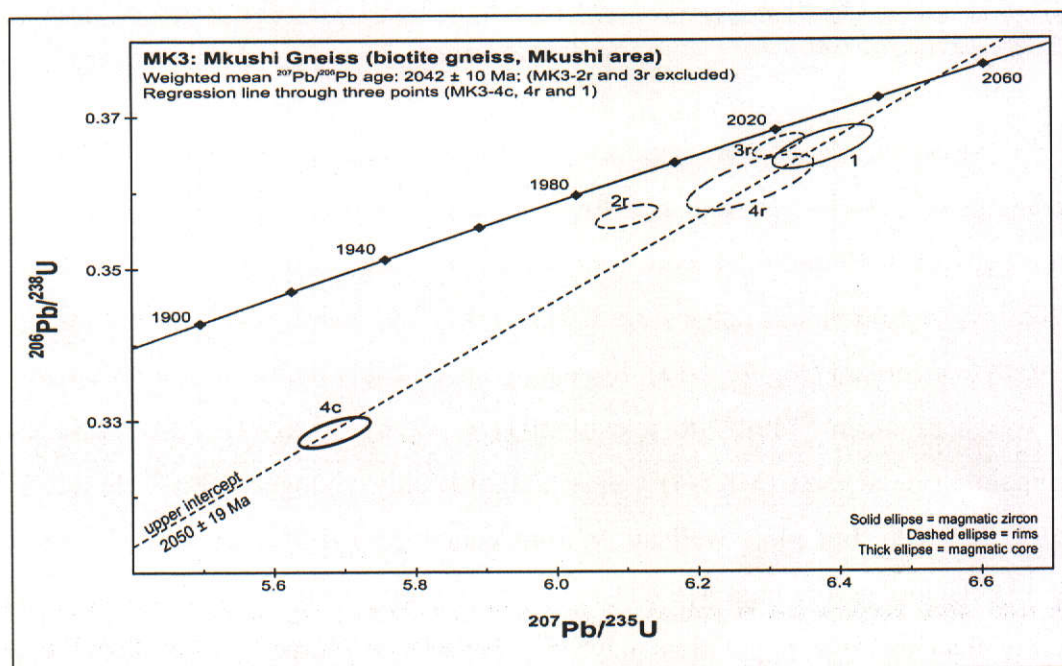


Figure 4-11: U-Pb concordia plot for zircon analyses of sample MK-3. Error ellipses are at 1 σ confidence level.

4.5.2.2 Sample MK5

Sample MK5 yielded zircons ranging in size from 50 to 300 μm . Length to width ratios range from equant to 3:1 and the zircons are generally euhedral in shape (Figure 4-12).

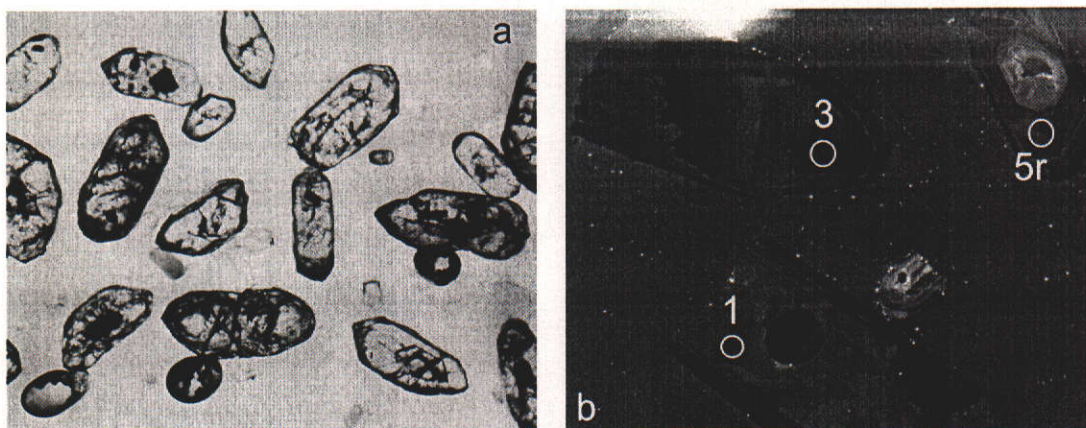


Figure 4-12: (a) photomicrograph of zircons from sample MK-5 (Mkushi map sheet) (xpl) showing clear sub-euhedral zircons with minor cracks and inclusions (f.o.v. = 1000 μm); (b) CL image of zircon from sample MK-5 showing the location of three analysed spots. Note the analysed magmatic zircon rim (analysis 5r), and the broad concentric zoning on the zircons (f.o.v. = 600 μm).

Seven analyses were conducted on as many zircons and yielded U and Th contents of 224-804 ppm and 139-409 ppm respectively (Table 13-3). Th/U ratios are between 0.47 and 0.84, consistent with magmatic zircon (Hoskin and Black, 2000). The f_{206} values range from 0.013 to 0.712%, and the analyses are 86.8 to 99.9% concordant (Figure 4-13). Six data points loosely define an age group with a weighted mean $^{207}\text{Pb}/^{206}\text{Pb}$ age of 2037 ± 12 Ma (MSWD=2.7), while the remaining data point (MK5-4) yields a significantly younger $^{207}\text{Pb}/^{206}\text{Pb}$ age of 1973 ± 7 Ma, but plots well away from concordia (91.9% concordant, Figure 4-13). The relatively high MSWD value for the former six zircons indicates that more than one age population may be present in this group, or could indicate intermediate Pb-loss. Analyses MK5-2 and 3 from this group have $^{207}\text{Pb}/^{206}\text{Pb}$ ages of 2030 ± 4 Ma and 2026 ± 9 Ma, which combine to a weighted mean $^{207}\text{Pb}/^{206}\text{Pb}$ age of 2029 ± 7 Ma (MSWD=0.15) (Figure 4-13). The remaining four data points, MK5-1, 5r, 6 and 7 define a weighted mean $^{207}\text{Pb}/^{206}\text{Pb}$ age of 2050 ± 9 Ma (MSWD=0.35). In conclusion, the igneous protolith to the pink Mkushi

Gneiss is either the result of a multistage intrusion or of multistage crystallisation of a single intrusion, with an earlier phase at 2050 ± 9 Ma, and a later phase at 2029 ± 7 Ma, or was emplaced at 2050 ± 9 Ma as given by the four concordant data points MK5-6, 5r, 1 and 7. The youngest zircon, though discordant, may indicate late stage crystallisation at 1973 ± 7 Ma, but not much weight is given to this analysis because of its high discordance (8%). Further work is needed to confirm the emplacement age of this phase of the Mkushi Gneiss.

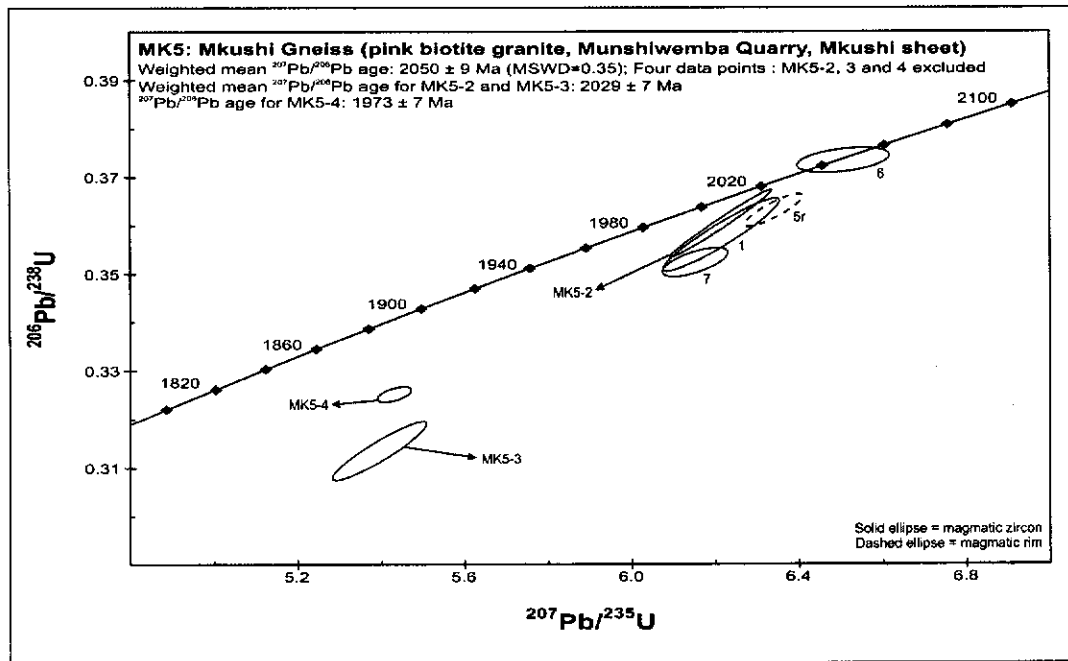


Figure 4-13: U-Pb concordia plot for zircon analyses of sample MK-5. Error ellipses are at 1 σ confidence level.

4.5.2.3 Sample CC10

Zircons from sample CC10 range in size from 100 to 300 μm and are euhedral in shape (Figure 4-14). The crystals have well-developed crystal faces and length to width ratios generally greater than 2:1. In transmitted light, the crystals are pale yellow in colour, while CL imaging shows concentric zoning patterns consistent with magmatic growth.

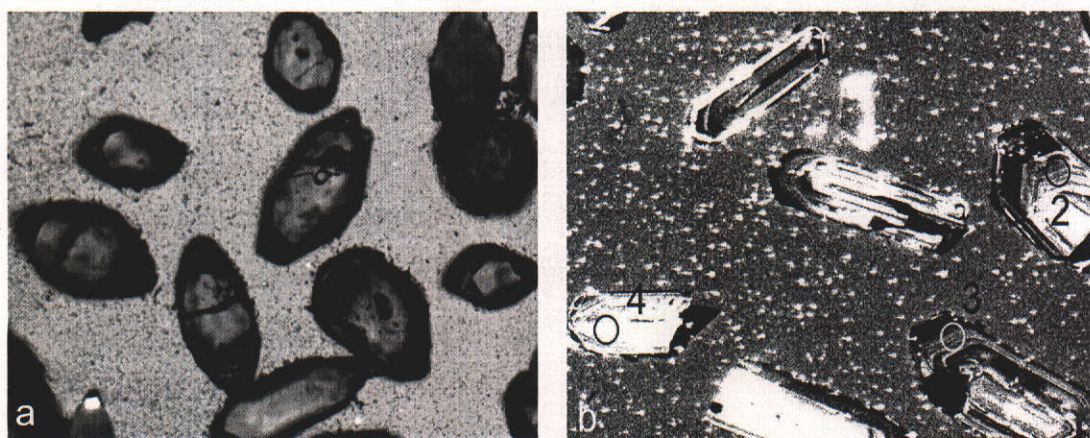


Figure 4-14: (a) photomicrograph of zircons from sample CC10 (xpl) showing clear euhedral zircons with minor cracks and very few inclusions (f.o.v. = 700 µm); (b) CL image of zircon from sample CC10 showing the location of three analysed spots. Note the concentric zoning of the crystals (f.o.v.= 500 µm).

Six zircons were analysed, and have low f_{206} values up to 0.85% (Table 13-4). U contents range from 167 to 693 ppm, and Th from 121 to 612 ppm, with Th/U ratios between 0.60 and 0.91. The data range from 91.7 to 103.9% concordant and yield a weighted mean $^{207}\text{Pb}/^{206}\text{Pb}$ age of 1953 ± 6 Ma with MSWD of 2.19 for all data points (Figure 4-15). A concordia age of 1952 ± 6 Ma (MSWD=1.8) can be calculated from the five most concordant points, excluding analysis CC10-2.1. The concordia age does not significantly differ from the weighted mean $^{207}\text{Pb}/^{206}\text{Pb}$ age, and is considered the best estimate for the crystallisation of the granite precursor.

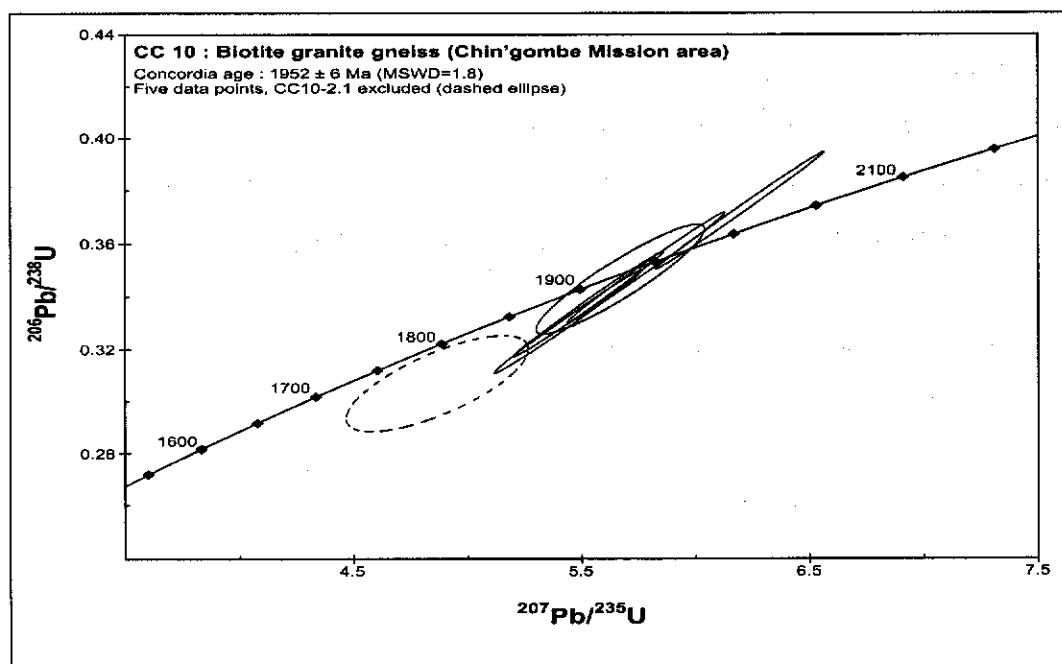


Figure 4-15: U-Pb concordia plot for zircon analyses of sample CC10. Error ellipses are at 1 σ confidence level. Dashed ellipse is analysis CC10-2.1, excluded from calculation of a concordia age.

4.5.2.4 Sample KN1

Sample KN1 yielded zircon ranging in size from 100 to 400 μm , with length to width ratios ranging from 1:1 to 3:1. The zircons are pale yellow to light brown and contain variable amounts of small inclusions and cracks (Figure 4-16). Most zircons are well formed, with well-developed facets. In CL, broad concentric zoning is observed and a small number of zircons display a high-response inner core, surrounded by zoned magmatic zircon. Six analyses were conducted on six zircons, and are characterised by low f_{206} values of up to 0.041% (Table 13-5). U and Th contents range from 268-440 ppm and 68-223 ppm respectively, yielding Th/U ratios of 0.26-0.61. The data range from 82.7 to 100% concordant (Figure 4-17). The five most concordant analyses yield a weighted mean $^{207}\text{Pb}/^{206}\text{Pb}$ age of 2036 ± 6 Ma (MSWD=1.0). Analysis KN1-1 is excluded from the calculation, as it appears to plot off a general regression trend of the five more concordant data points. This discordant analysis yields a $^{207}\text{Pb}/^{206}\text{Pb}$ age of 2089 ± 9 Ma, suggesting this zircon may be a xenocryst. Note that due to the high discordance of this analysis (17.3%), and the inability to determine whether recent and/or ancient Pb-loss is responsible for the

discordance, no great weight can be given to this age. We take the weighted mean $^{207}\text{Pb}/^{206}\text{Pb}$ age of 2036 ± 6 Ma for the other five analyses as the best estimate for the crystallisation age of the intrusion.

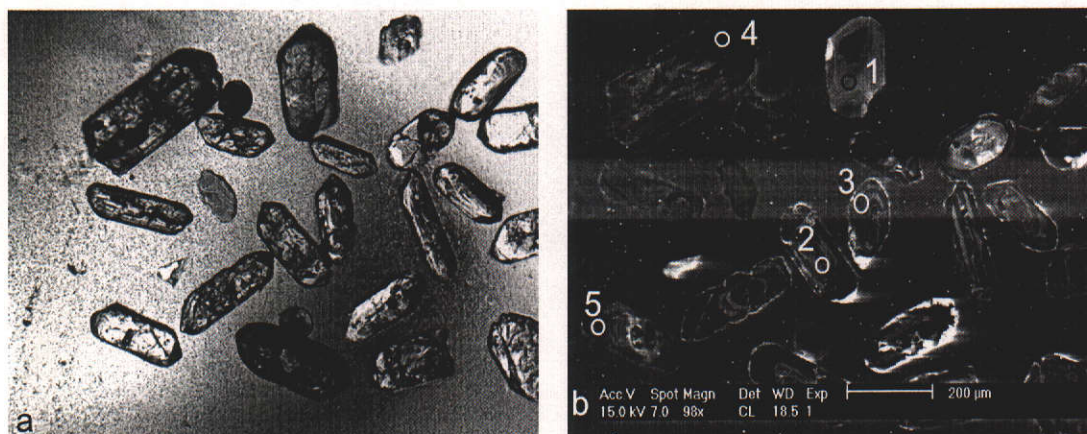


Figure 4-16: (a) photomicrograph of zircons from sample KN1 (Kanona sheet) (xpl) showing clear euhedral zircons with minor cracks and few inclusions (f.o.v. = 700 µm); (b) CL image of zircon from sample KN1 showing the location of four analysed spots. Note the concentric zoning of the crystals (f.o.v.= 900 µm).

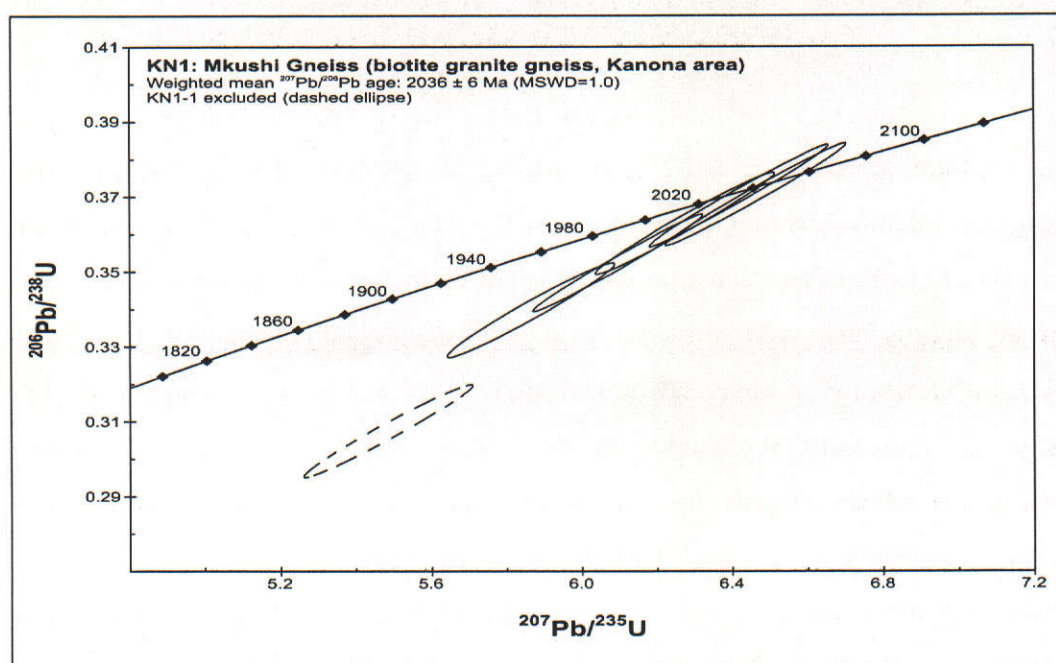


Figure 4-17: U-Pb concordia plot for zircon analyses of sample KN1. Error ellipses are at 1σ confidence level. Dashed ellipse is analysis KN1-1, excluded from calculation of the age.

4.5.2.5 *Samples SER 6-6 and SER 6-7 (migmatitic gneiss)*

Samples SER 6-6 and SER 6-7 were collected along the Lukusashi and Fukwe River crossings respectively (Figure 4-2), where a large flat outcrop exposes strongly deformed and folded migmatitic gneiss. The migmatite consists of darker units of quartz-feldspar-biotite, with accessory apatite and garnet, and felsic units with quartz-microcline-plagioclase, and accessory sillimanite-garnet. The segregated banding is defined by strong nebulitic and stromatic structures, cut by ptlygmatically folded quartz-feldspar veins. The melt fractions commonly form in situ pegmatitic pockets, often containing beryl and tourmaline. A strong linear fabric is pervasive throughout the unit, defining a northeast-directed crenulation lineation. The Fukwe Migmatite contains a very prominent garnet-sillimanite assemblage in the melanosomes. Where stromatic and nebulitic patterns are less strongly developed, the rocks show tight irregular folding along northeasterly trends.

Zircons collected from both the Lukusashi and Fukwe Migmatite samples are complex in structure, and contain a core, often broken, but sometimes with a euhedral outline, surrounded by up to two successive overgrowths. The cores display well-developed concentric zoning, and some are surrounded by a narrow overgrowth of high-CL zircon. The high response of this first rim indicates growth from low-uranium fluids (Figures 4-18 and 4-19). These minor low uranium rims do not exceed a few microns in thickness, and their analysis was not within the capabilities of SHRIMP. A prominent, poorly zoned low-response outer rim overgrows the narrow high-CL-response rim in the majority of zircons, indicating a significant crystallisation event involving melts or metamorphic fluids with high uranium content. The f_{206} values for the cores as well as the high-uranium rims are quite low, and range from 0.06 to 0.84% (cores) and 0.04 to 0.50% (rims) in zircon from SER6-6, and from 0.05 to 0.38% (cores) and 0.05 to 0.32% (rims) in SER6-7 (Table 13-55 and Table 13-56). Taken together, Th/U ratios range from 0.07 to 0.84 for the cores, and are very low (0.03 or smaller) for the rims. The consistent extremely low Th/U ratios, coupled with the absence of

concentric zoning, strongly support the interpretation that the thick high-uranium rims have formed during metamorphism.

A total of six cores were analysed from the Lukusashi Migmatite, five of which are within 5% of concordia and form a coherent age group with an upper intercept at 2053 ± 11 Ma and a lower intercept at -154 ± 320 Ma (MSWD=0.90). A weighted mean $^{207}\text{Pb}/^{206}\text{Pb}$ age of 2050 ± 8 Ma (MSWD=0.89) can be calculated on all six data points. Eight analyses were conducted on cores from the Fukwe gneiss, six of which yield an upper intercept age of 2023 ± 11 Ma with lower intercept 0 ± 140 Ma (MSWD=0.86). The same points yielded a weighted mean $^{207}\text{Pb}/^{206}\text{Pb}$ age of 2023 ± 9 Ma (MSWD=0.69). Taken together, 10 of the 12 analyses appear to define a broadly coherent age group from which an upper intercept age of 2040 ± 14 Ma (MSWD=2.50) can be calculated (Figure 4-20). The two rejected data points of the Fukwe gneiss are SER 67-15c (high U) and SER67c-1 (low U and Th, and relative high f_{206}). Analysis SER67c-1 is 93.3% concordant, and yielded a minimum $^{207}\text{Pb}/^{206}\text{Pb}$ age of 2250 ± 13 Ma, while SER67-15c is 85.6% concordant and yielded a $^{207}\text{Pb}/^{206}\text{Pb}$ age of 1907 ± 39 Ma. It can be concluded that the age of the protolith of both the Lukusashi and Fukwe Migmatites is between 2050 and 2020 Ma, and that a minor older xenocrystic component with an age of 2.25 Ga may be present.

Ten analyses were made of wide rim overgrowths in zircon from the Lukusashi Migmatite (Table 13-55, page 431). Common Pb content is generally low, ranging up to 0.50%. U is high, between 1486 and 3138 ppm, while Th is low, ranging from 12 to 37 ppm. The rims exhibit extremely low Th/U ratios of less than 0.01, consistent with metamorphic growth. The data plot within 5% of concordia and have a weighted mean $^{207}\text{Pb}/^{206}\text{Pb}$ age of 1018 ± 5 Ma (MSWD=0.69)(Figure 4-21), taken as the best estimate for the timing of growth of the metamorphic rims.

Twelve rims were analysed for the Fukwe migmatite. The data are characterised by low f_{206} values of up to 0.18% (Table 13-56). U content is high, between 913 and 1632 ppm, and Th very low, between 7 and 48 ppm, yielding low Th/U ratios less than 0.03, typical for metamorphic rims. One data point plots

about 10% away from the concordia, and defines a $^{207}\text{Pb}/^{206}\text{Pb}$ age of 554 ± 20 Ma (SER67-3r). The analysis exhibits an extremely low Th/U value and represents the first constraint on a Pan African metamorphic overprint in the region. Eight rims plot in a cluster close to concordia (Figure 4-22). Of those, the six most concordant points (SER67-1, 2r, 4, 4r, 11 and 19) define a concordia age of 1007 ± 16 Ma (MSWD=13). Because of the close clustering of the data, no reliable trend line can be calculated, but all eight near-concordant data points yield a weighted mean $^{207}\text{Pb}/^{206}\text{Pb}$ age of 1021 ± 16 Ma (MSWD=1.2). The lower MSWD value for this age indicates the coherence of this dataset, and the age can be considered to represent the timing of metamorphic rim growth during Irumide tectonism. The three remaining analyses of the Fukwe Migmatite zircon rims (SER67-13, 15 and 24) appear to define a separate trend below concordia, with an upper intercept at 1225 ± 79 Ma and a lower intercept at 319 ± 330 Ma (MSWD=0.035). A weighted mean $^{207}\text{Pb}/^{206}\text{Pb}$ age of 1174 ± 37 Ma (MSWD=1.50) can be calculated for the same three points. These three data points show slightly higher Th/U ratios than the younger metamorphic rims, which may indicate that these spots penetrate very small parts of older core material. Close inspection of the analysed spots on CL imagery shows the proximity of the analysed spots to the zircon core, and it cannot be ruled out that sampling of both older core material and younger metamorphic rim occurred (Figure 4-23). Should this have been the case, the ~ 1170 Ma ages are rendered geologically meaningless, and could represent mixed ages derived from ~ 1.02 Ga metamorphic rims and ~ 2.0 Ga cores.

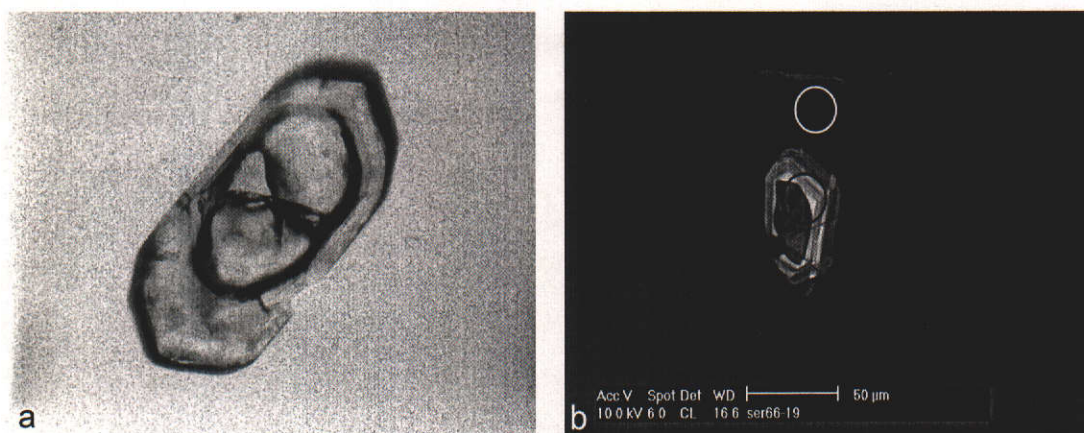


Figure 4-18: (a) photomicrograph of zircon (analysis SER66-19) from sample SER6-6 (xpl) showing a euhedral crystal with rounded core surrounded by a prominent rim (f.o.v. = ~400 µm); (b) CL image of zircon SER66-19 showing the location of analysed spots. Note the dark CL rim, and zoned core (f.o.v.= 300 µm). The $^{207}\text{Pb}/^{206}\text{Pb}$ ages for the core and rim were 2059 ± 8 and 1012 ± 8 Ma respectively.

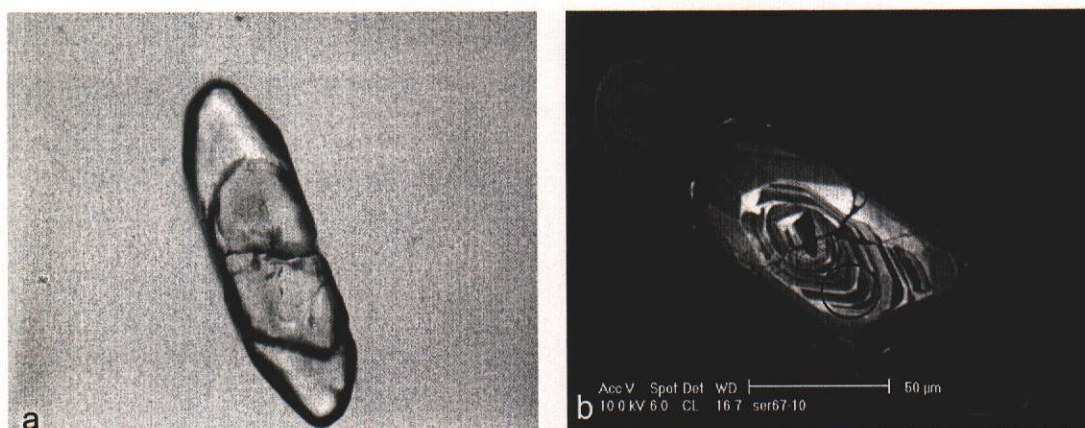


Figure 4-19: (a) photomicrograph of zircon SER67-10 from sample SER6-7 (xpl) showing a subhedral crystal (f.o.v. = ~350 µm); (b) CL image of the analysed zircon SER67-10 showing the location of analysed spots. Note the dark CL rim and the zoned core (f.o.v.= 200 µm). The $^{207}\text{Pb}/^{206}\text{Pb}$ ages for the core and rim were 2020 ± 12 and 993 ± 22 Ma respectively.

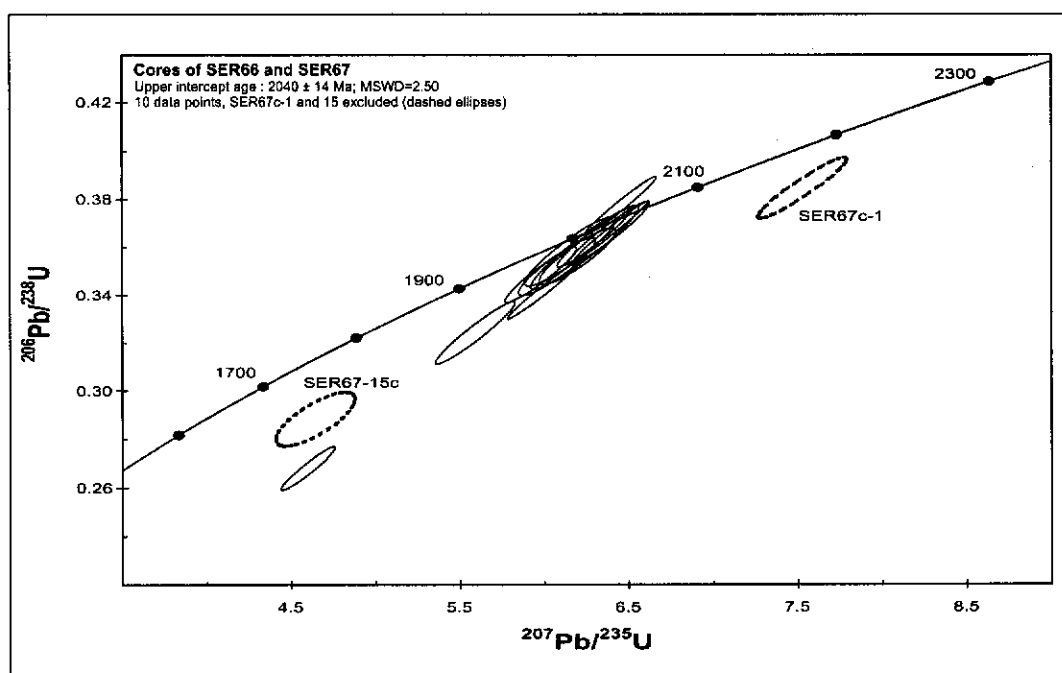


Figure 4-20: U-Pb concordia plot for zircon core analyses of samples SER 6-6 and SER6-7. Error ellipses are at 1σ confidence level.

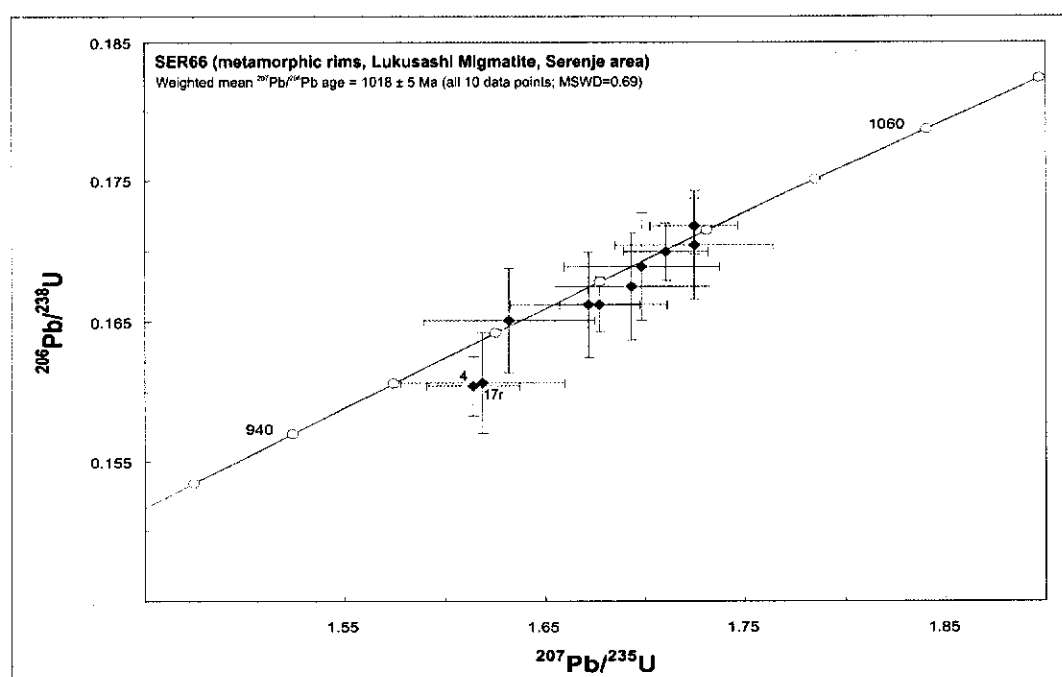


Figure 4-21: U-Pb concordia plot for zircon rim analyses of sample SER6-6. Error crosses are at 1σ confidence level.

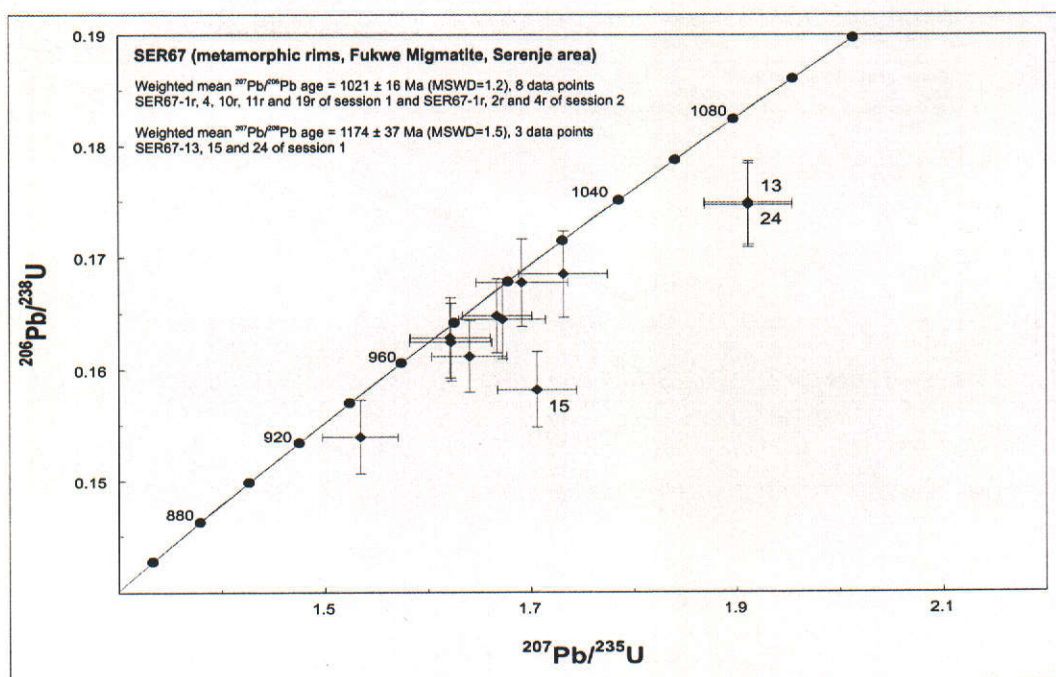


Figure 4-22: U-Pb concordia plot for zircon rim analyses of sample SER6-7. Error crosses are at 1σ confidence level.

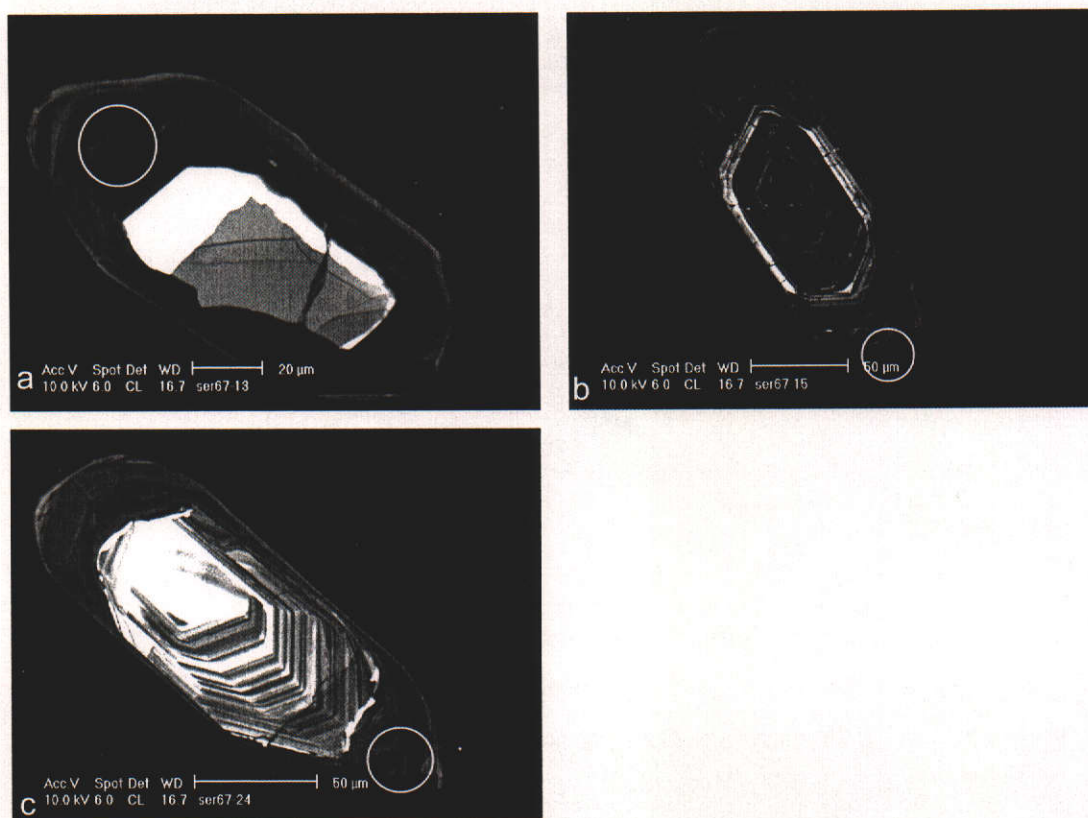


Figure 4-23: CL images of zircons SER67-13 (a), SER67-15 (b), and SER67-24 (c) showing approximate location of analysed spots. Note a subtle change in CL response across a boundary between what may be the outer metamorphic rim, and an older rim or core component. The analysis spots sample both zones, possibly giving a mixed age.

4.5.3 Luwalizi Granite Gneiss

The Luwalizi Granite Gneiss is a large body of foliated coarse biotite granite extending from Chinsali northwards into the Bangweulu block (Palaeoproterozoic basement in Figure 2-13). The granite gneisses form the basement to the Irumide sequences in the northeast, and are correlated with the widespread Bangweulu granitoids of northern Zambia (Daly, 1986b). Two samples were taken from the Luwalizi Granite Gneiss in the Isoka area, where it appears relatively weakly foliated and is best described as a granite (Figure 4-5).

4.5.3.1 Sample ISK1

Zircons from sample ISK1 range from 100 to 500 μm in length, with length to width ratios up to 5:1, and are sub- to euhedral in shape. They appear pale to dark brown under the microscope and often contain large inclusions. CL imaging reveals relatively homogenous low to medium luminescence (Figure 4-24 (a)). Nine analyses were conducted on as many zircons. Th/U ranges from 0.04 to 1.93 and f_{206} up to 0.855% (Table 13-6). Two analyses, ISK1-2 and ISK1-3, are excluded from calculations: analysis ISK1-2 displays an unusually high concentration of U (2669 ppm), while analysis ISK1-3 yielded high f_{206} (0.855%), low U (93 ppm) and high Th/U (1.93). The low Th/U ratio of the former (0.04) is more consistent with growth from metamorphic or metasomatic fluids than with crystallisation from a magmatic melt. The zircon, however, displays a euhedral habit and has a length to width ratio of close to 3:1, consistent with a magmatic origin. The analysis is 103.3 % concordant, and yielded a $^{207}\text{Pb}/^{206}\text{Pb}$ age of 1926 ± 8 Ma. The seven remaining analyses plot close to concordia and define a linear array with an upper intercept of 1945 ± 13 Ma and a lower intercept of 242 ± 620 Ma (Figure 4-25). A weighted mean $^{207}\text{Pb}/^{206}\text{Pb}$ age of 1942 ± 6 Ma (MSWD=0.25) can be calculated on the same seven data points and is taken to be the best estimate for the crystallisation age of the Luwalizi Granite. The crystallisation age of the low Th/U zircon indicates that the Luwalizi Granite Gneiss may have undergone a metamorphic/metasomatic event at $1926 \pm$

8 Ma, soon after its original emplacement, although more work is needed to fully substantiate this.

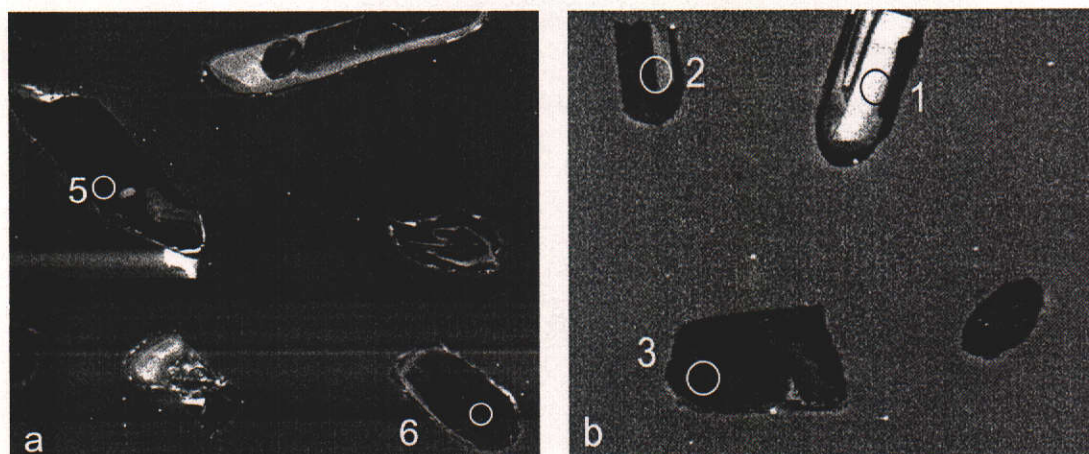


Figure 4-24: (a) CL image of zircons from sample ISK1 (Isoka sheet) showing the location of two analysed spots (f.o.v. = 500 µm); (b) CL image of zircon from sample ISK2 (Isoka sheet) showing the location of three analysed spots (f.o.v.= 900 µm). Note the generally dark aspect and relatively homogenous luminescence of the crystals.

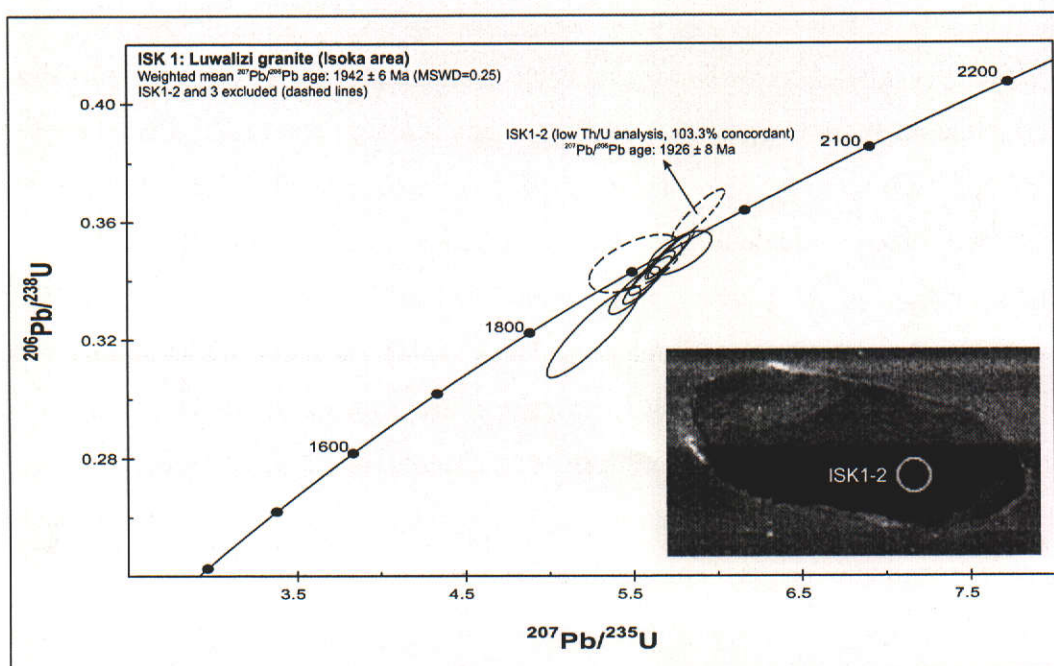


Figure 4-25: U-Pb concordia plot for zircon analyses of sample ISK1. Error ellipses are at 1 σ confidence level. Dashed ellipses are analyses 2 and 3, excluded from calculation of the age. Inset shows CL image of low Th/U zircon analysis ISK1-2, which yielded a $^{207}\text{Pb}/^{206}\text{Pb}$ age of 1926 ± 8 Ma (f.o.v.=300 µm).

4.5.3.2 Sample ISK2

Zircons from sample ISK2 range from 100 to 300 μm long and are pale brown to colourless, euhedral, and variably cracked. Length to width ratios range up to 4:1, and most zircons have been broken perpendicular to their long axis (Figure 4-24 (b)). CL response is generally low and reveals broad oscillatory zoning patterns consistent with magmatic growth (Figure 4-24 (b)). Five analyses were conducted on five zircon grains, four of which group in a tight cluster close to concordia (Figure 4-26). f_{206} ranges up to 0.688%, while U and Th content is quite variable ranging from 103-949 ppm and 29-391 ppm respectively. Th/U ranges from 0.03 to 1.34, similar to the range observed for sample ISK1. $^{207}\text{Pb}/^{206}\text{Pb}$ ratios are tightly defined, yielding a weighted mean $^{207}\text{Pb}/^{206}\text{Pb}$ age of 1931 ± 9 Ma (MSWD=1.39). Using only the four near concordant data points, an age of 1927 ± 10 Ma can be calculated (MSWD=0.92). The weighted mean of the four concordant points can be taken as a reasonable estimate for the age of the precursor granite to the Luwalizi Granite Gneiss. The significance of a small number of zircons with low Th/U ratios in both samples of the Luwalizi Granite Gneiss remains unclear. Such low ratios are commonly associated with zircon growth during metamorphism, but the elongate and euhedral habit of the zircons is more consistent with a magmatic origin. Increasing uranium content from rim to core, and broad, poorly defined concentric zoning are commonly associated with metasomatic alteration in zircon (Rubatto and Gebauer, 2000). The zoning in zircon from the Luwalizi Granite Gneiss is poorly defined, which could indicate metasomatic alteration, but more work is needed on these zircons to assess whether an increase of uranium towards the core supports this model.

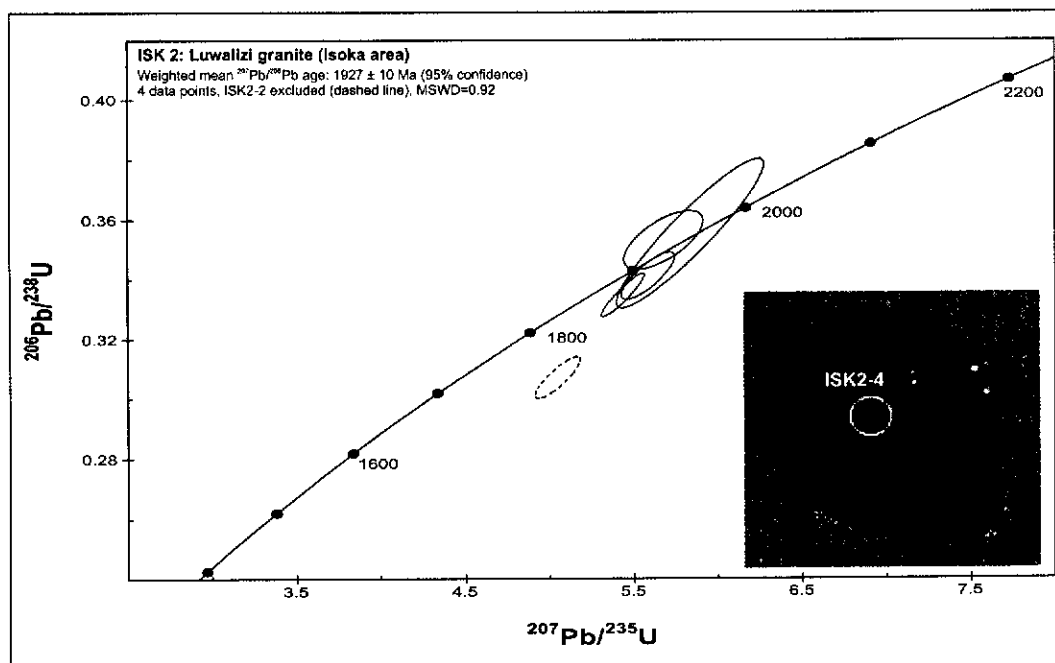


Figure 4-26: U-Pb concordia plot for zircon analyses of sample ISK2. Error ellipses are at 1σ confidence level. Dashed ellipse is analysis ISK2-2, excluded from calculation of the age. Inset shows CL image of low Th/U zircon analysis ISK2-4, which yielded a $^{207}\text{Pb}/^{206}\text{Pb}$ age of 1944 ± 20 Ma (f.o.v.=300 μm).

4.5.4 Lubu Granite Gneiss (sample ML2)

The Lubu Granite Gneiss was sampled in the north of the Chinsali map sheet (sample ML2 indicated with C on Figure 4-4) and was interpreted by Daly (1986b; 1995a; 1995b) to form the basement to the Manshya River Group. Although he presented no age data, Daly (1986b; 1995a; 1995b) ascribed the Lubu Granite Gneiss to the Palaeoproterozoic Bangweulu block granitoids. The Lubu granite gneiss is an equigranular, strongly foliated pink biotite granite gneiss, which in places is cut by numerous small pegmatites along the foliation. The pegmatites in the granite are tightly folded, with axial planes parallel to the foliation striking along an east-northeast direction. Zircons from sample ML2 range from colourless to yellow-brown, are variably cracked and some are dark brown owing to small inclusions. Most zircons are sub- to euhedral, and range in length from 100 μm to 300 μm . Their length to width ratio is variable, ranging from equant to 3:1 (Figure 4-27 (a)). The crystals appear to have undergone some subsolidus recrystallisation, but concentric zoning still shows up in CL imagery (Figure 4-27 (b)). The zircons are characterised by generally low CL response,

with faint oscillatory zoning, crosscut by mottled rehomogenised zones with high U (dark CL). Eleven clear, uncracked portions of eleven zircons were analysed during two separate sessions. The zircons have low to high f_{206} , ranging from 0.07 to 4.67%. U and Th vary from 171–415 ppm and 279–687 ppm respectively, giving high Th/U ratios ranging from 1.68 to 2.04 (Table 13-23, page 419). Two points (ML2-5 and 22) are excluded from calculations based on high common Pb and low precision, and plot off a regression line defined by the remaining 9 data points (Figure 4-28). The trend line through the nine points defines an upper intercept of 1551 ± 33 Ma and lower intercept of 537 ± 440 Ma (MSWD=0.48). The poor precision of the age is a result of the relatively high proportions of common Pb in the analyses. A weighted $^{207}\text{Pb}/^{206}\text{Pb}$ age on the same nine data points yields an age of 1532 ± 14 Ma with an MSWD value of 0.96. Based on the lower MSWD value, and the fact that the data display a discordia trend, the upper intercept age of 1551 ± 33 Ma is taken as the best estimate for the crystallisation age of the Lubu Granite Gneiss.

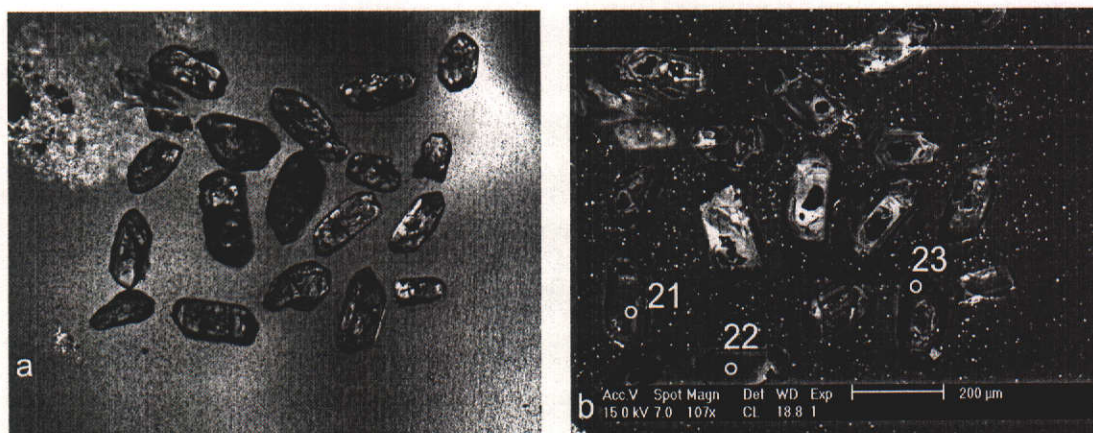


Figure 4-27: (a) photomicrograph of zircons from sample ML2 (xpl) showing sub-euhedral crystals with numerous cracks and inclusions (f.o.v. = ~1400 µm); (b) CL image of zircons from sample ML2 showing three analysed spots. Note the disrupted concentric zoning and dark recrystallised areas (f.o.v. = 1300 µm).

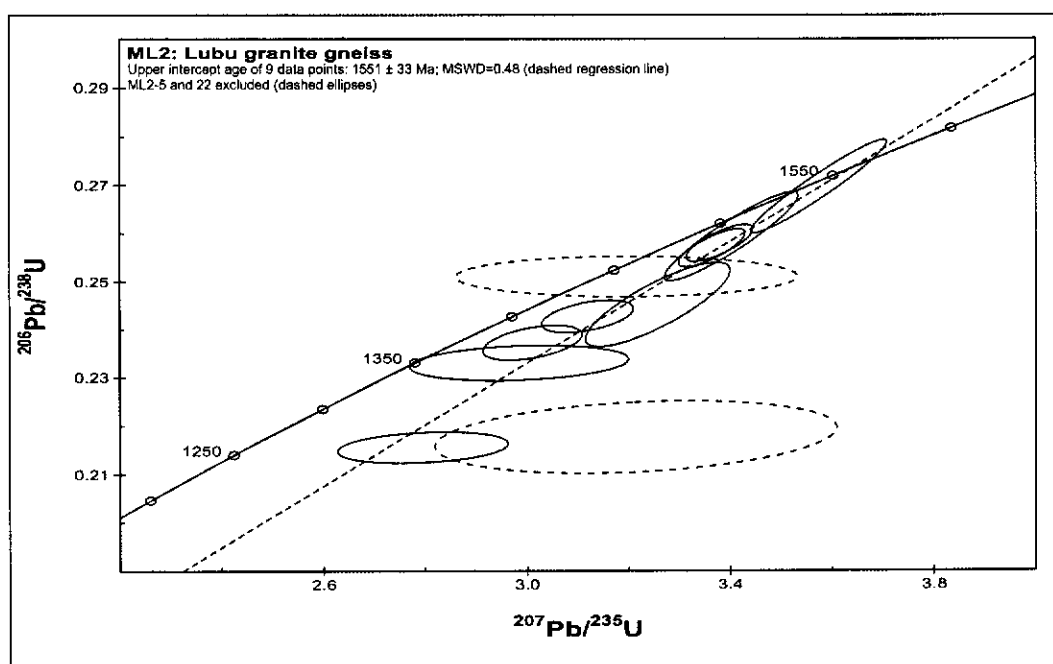


Figure 4-28: U-Pb concordia plot for zircon analyses of sample ML2. Error ellipses are at 1σ confidence level.

4.5.5 Bangweulu Granitoids and Luapula Volcanics

In the western part of the Bangweulu block near Mansa, three samples were collected for dating from the Mansa Granite and two from the Mansa Volcanics (Figure 4-6). Sample MA1 was collected from a large outcrop some 10 km south of Mansa and consists of coarse biotite granite, which contains xenoliths of dark fine-grained rock (possibly metavolcanic). Samples MA2 and MA3 were collected from a flat-lying outcrop some two kilometers east of MA1, where the granite (sample MA2) is seen to intrude the metavolcanic sequence (sample MA3). Both granites (MA1 and MA2) are undeformed, have a coarse porphyritic texture and contain about 5% biotite. The coarse phenocrysts in each case are euhedral microcline up to 4 cm in length. The metavolcanic (MA3) is a fine-grained rhyolite, which is devitrified and recrystallised. At the sample locality of MA2 and MA3, the granite, which makes up the bulk of the outcrop, is in sharp contact with the volcanic. Sample MA5 was collected some 20 km north-northwest of Mansa, and consists of dark greyish green bedded metavolcanic. The rock is rhyolitic in composition, with amygdaloidal texture and vesicles filled by epidote. The rhyolite appears to be mixed with a sedimentary component of silty

material, indicating that the volcanism overlaps with sedimentation in the Mporokoso Group. Sample MA9 was collected in the Musonda Falls map sheet and consists of medium-grained granite, which is cut by aplitic dykes. The granite is leucocratic, containing only minor amounts of biotite.

4.5.5.1 Sample MA1

Zircons from sample MA1 are pale yellow in colour and have euhedral shapes. Their size ranges from below 100 up to 300 μm , with length to width ratios as high as 4:1. CL reveals concentric zoning patterns, with some zircons showing high-response inclusions (Figure 4-29). Four analyses were conducted on four zircon grains (Table 13-8). U ranges from 161 to 481 ppm and Th from 219 to 447 ppm, yielding Th/U ratios between 0.96 and 1.42. f_{206} is low, varying from 0.010 to 0.446 %. The data vary from near concordant to 89.5% concordant (Figure 4-30) and define a regression line with an upper intercept at 1860 ± 13 Ma and lower intercept at 100 ± 580 Ma (MSWD=1.04). Because of the poor constraints, the lower intercept cannot be assigned geological meaning other than that it indicates recent lead loss. The upper intercept age of 1860 ± 13 Ma is taken to represent the crystallisation age of the granite.

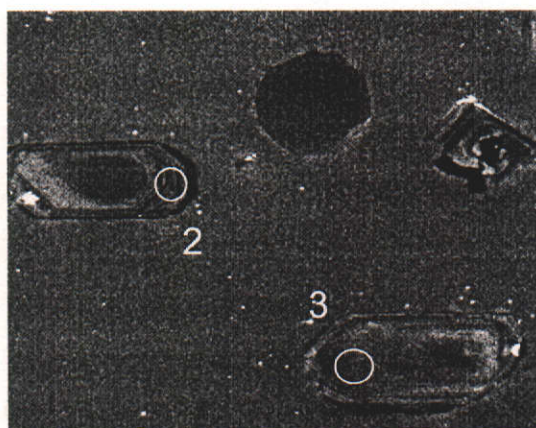


Figure 4-29: CL image of zircons from sample MA1, showing the location of two analysed spots (f.o.v. = 500 μm).

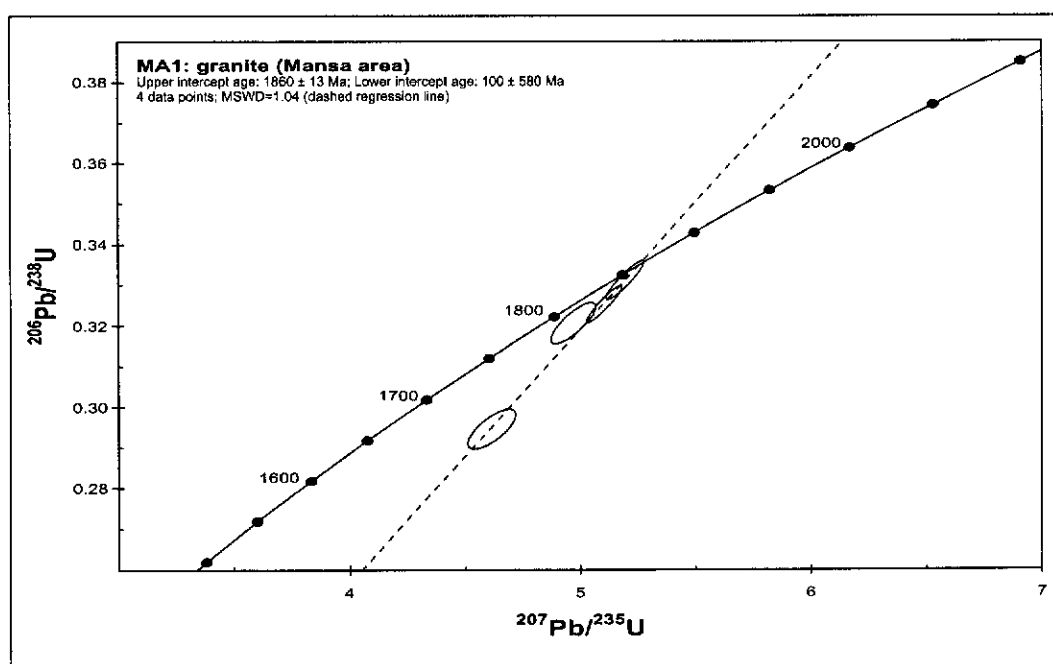


Figure 4-30: U-Pb concordia plot for zircon analyses of sample MA1. Error ellipses are at 1σ confidence level.

4.5.5.2 Sample MA2

Zircons separated from sample MA2 range from 100 to 300 μm in size, are euhedral, light yellow in colour and reasonably clear of inclusions (Figure 4-31 (a)). The grains are variably cracked and show sharp-tipped bipyramidal terminations. CL imaging reveals patterns of broad concentric and sector zoning (Figure 4-31 (b)). Nine analyses were conducted on nine different zircons and yield U and Th contents ranging from 151-365 ppm and 133-278 ppm respectively (Table 13-9). Th/U ratios range from 0.73 to 1.16. f^{206} is low, ranging up to 0.34 %. The nine data points plot within 5% of concordia and define a single age group with a weighted mean $^{207}\text{Pb}/^{206}\text{Pb}$ age of 1862 ± 7 Ma (MSWD=0.4)(Figure 4-32). The tight clustering of the data allows the calculation of a concordia age of 1862 ± 8 Ma (MSWD=1.4), which can be taken as the best estimate for the crystallisation age of the granite.

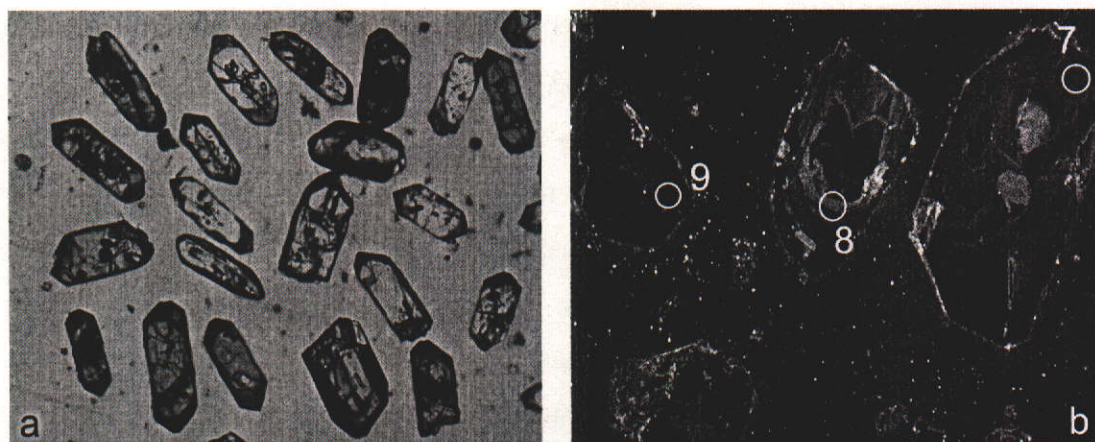


Figure 4-31: (a) photomicrograph of zircons from sample MA2 (Mansa sheet) (xpl) showing clear euhedral zircons with minor cracks and few inclusions (f.o.v. = ~1500 µm); (b) CL image of zircon from sample MA2 showing the location of three analysed spots. Note the concentric and sector zoning of the crystals (f.o.v. = 600 µm).

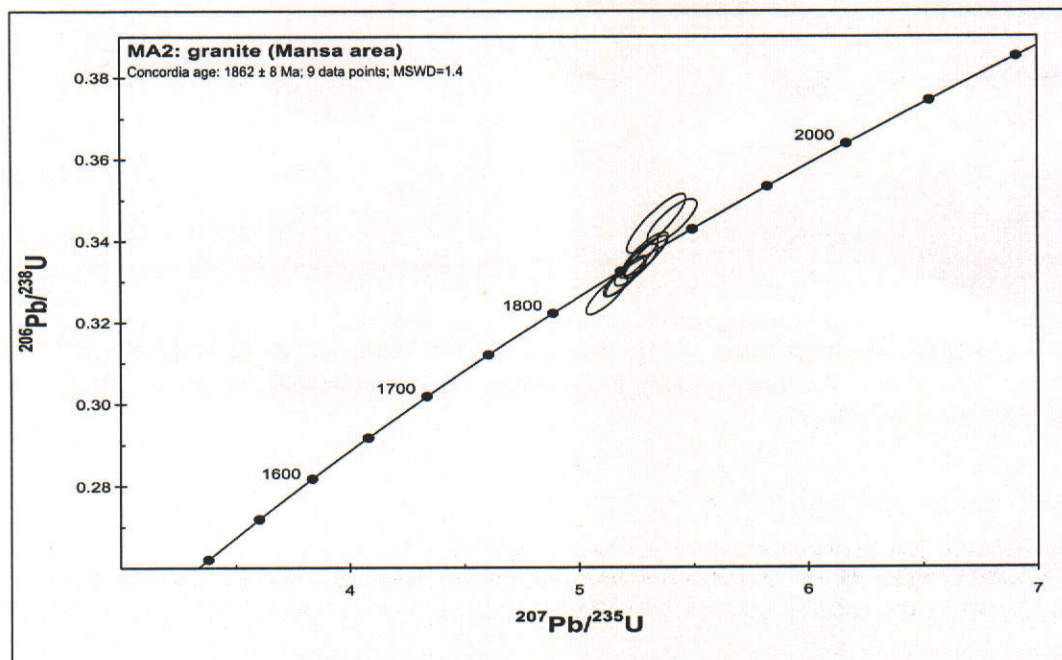


Figure 4-32: U-Pb concordia plot for zircon analyses of sample MA2. Error ellipses are at 1 σ confidence level.

4.5.5.3 Sample MA3

Zircons from sample MA3 range from 100 to 200 µm in size, are elongated with length to width ratios of 2:1 and have sharp terminations. The zircons are light yellow, clear, and practically free of inclusions (Figure 4-33 (a)). CL imagery shows broad oscillatory and sector zoning patterns resulting from a

single crystallisation event (Figure 4-33 (b)). Nine spots were analysed from nine different zircons. f_{206} ranges from 0.057 to 0.258%. U content ranges from 71 to 453 ppm while Th ranges from 68 to 398 ppm (Table 13-10). Th/U ratios are between 0.85 and 1.57, and typical for magmatic zircon. The data are near concordant, with the exception of analysis MA3-1 (93.2% concordant)(Figure 4-34). The eight concordant data points define a concordia age of 1868 ± 7 Ma (MSWD=1.15). The concordia age, constrained from eight data points, represents the best age estimate for the crystallisation of the volcanic rock.

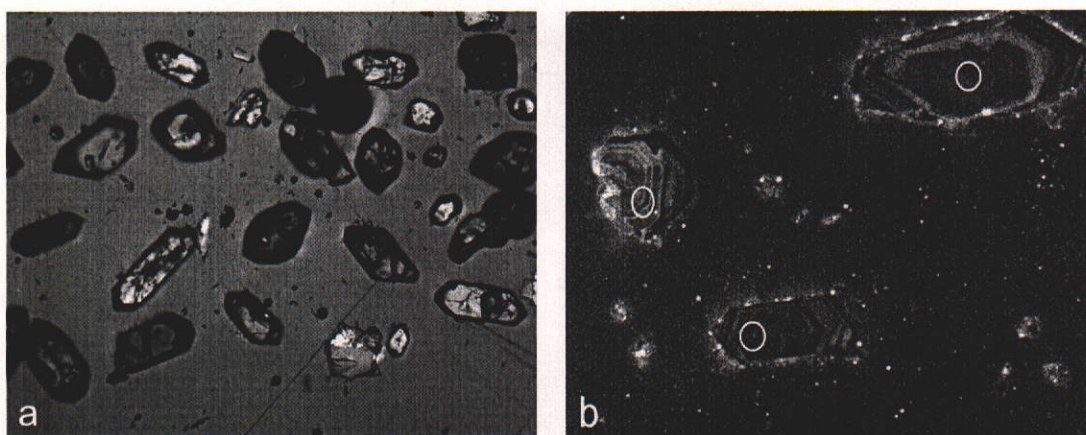


Figure 4-33: (a) photomicrograph of zircons from sample MA3 (Mansa sheet) (xpl) showing clear sub-euhedral zircons with minor cracks and few inclusions (f.o.v. = ~1600 μ m); (b) CL image of zircon from sample MA3 showing the location of three analysed spots. Note the concentric and sector zoning of the crystals (f.o.v.= 800 μ m).

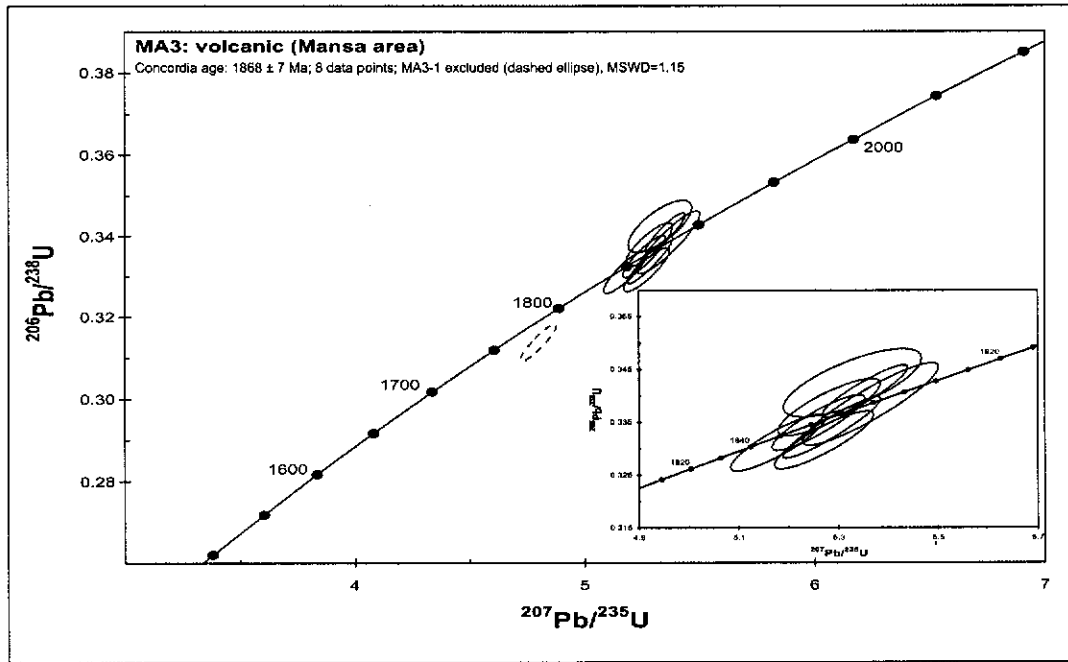


Figure 4-34: U-Pb concordia plot for zircon analyses of sample MA3. Error ellipses are at 1 σ confidence level. Inset shows concordant data points.

4.5.5.4 Sample MA5

Zircons from sample MA5 are small (~ 100 μm) and have length to width ratios between 1:1 and 2:1. Most are subhedral, with bipyramidal terminations and are dark brown to yellow, due to numerous inclusions (Figure 4-35 (a)). CL imaging reveals low luminescence and oscillatory zoning patterns (Figure 4-35 (b)). Four analyses were conducted on four zircons and show low proportions of common Pb ranging from 0.02 to 0.45 % (Table 13-11). U and Th are high in two analyses (620-667 ppm and 679-739 ppm) and quite low in the other two (57-72 ppm and 63-77 ppm). Th/U ratios are between 0.91 and 1.39. The data range from 90 to 102% concordant (Figure 4-36), defining a regression line with upper intercept 1862 ± 19 Ma and lower intercept 719 ± 440 Ma (MSWD=0.18). A weighted mean of the three most concordant points yields a $^{207}\text{Pb}/^{206}\text{Pb}$ age of 1876 ± 10 Ma (MSWD=0.5) taken as the best estimate of the crystallisation age of the volcanic.

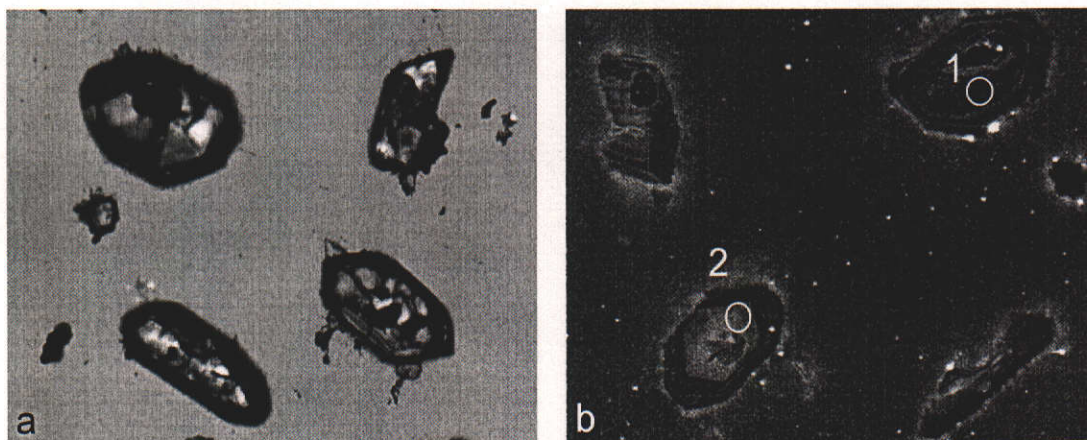


Figure 4-35: (a) photomicrograph of zircons from sample MA5 (xpl) showing clear subhedral zircons with minor cracks and few inclusions (f.o.v. = ~1000 µm); (b) CL image of zircon from sample MA5 showing the location of two analysed spots. Note the concentric and sector zoning of the crystals (f.o.v.= 1000 µm).

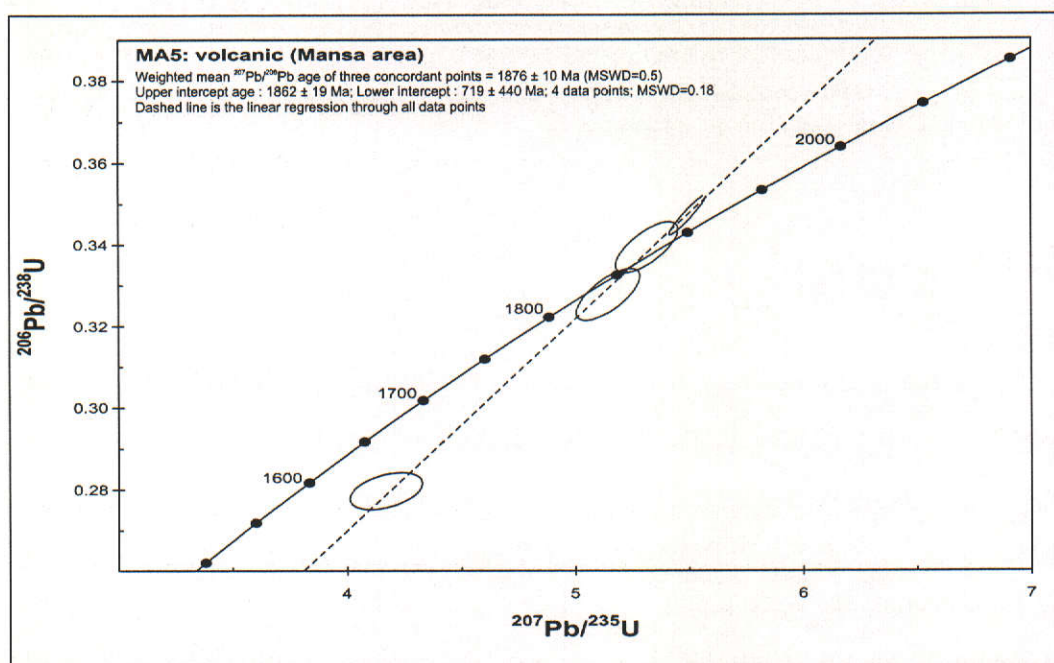


Figure 4-36: U-Pb concordia plot for zircon analyses of sample MA5. Error ellipses are at 1σ confidence level.

4.5.5.5 Sample MA9

Zircons collected from sample MA9 are between 100 and 200 μm in size and have length to width ratios up to 2:1. The zircons are light yellow to colourless and contain few or no inclusions. CL imagery shows variable response and concentric zoning patterns. Nine spots were analysed on nine zircons and yielded f^{206} values reaching up to 0.99 % (Table 13-12). U ranges from 93 to 298 ppm, while Th ranges from 94 to 311 ppm, yielding Th/U ratios between 0.71 and 1.40. The data plot from 86.6 to 102.1% concordant, with seven analyses more than 95% concordant (Figure 4-37). A regression through all points yields an upper intercept age of 1867 ± 9 Ma with lower intercept at 105 ± 340 Ma (MSWD=0.94). A concordia age can be calculated for six near concordant points and yields a virtually identical age of 1866 ± 9 Ma (MSWD=1.12). This concordia age represents the best estimate for the age of crystallisation of the granite.

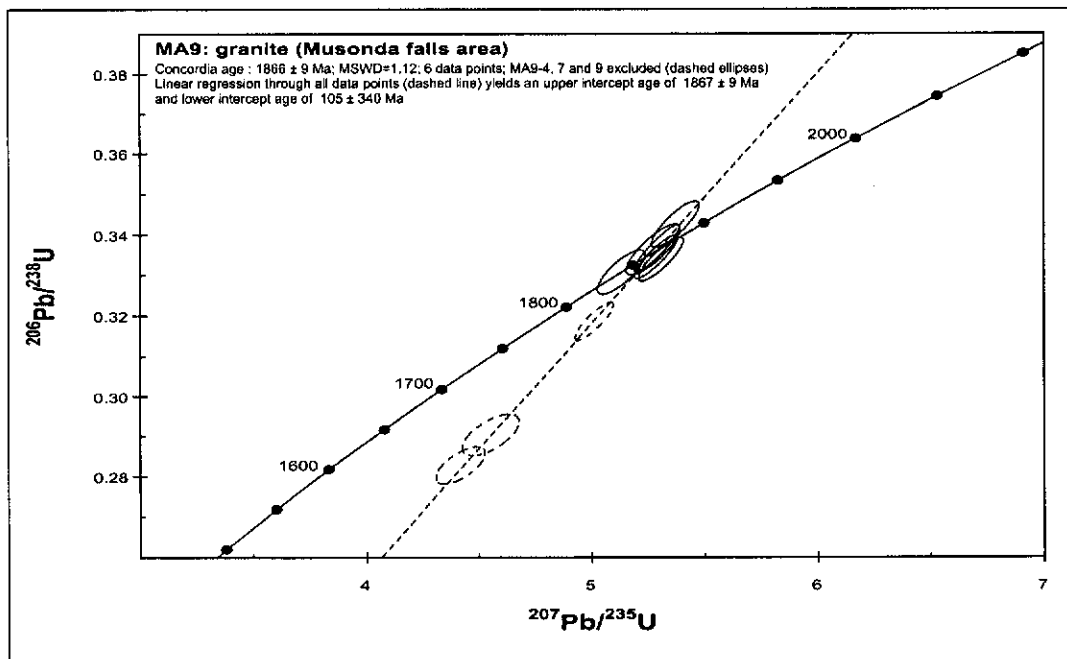


Figure 4-37: U-Pb concordia plot for zircon analyses of sample MA9. Error ellipses are at 1 σ confidence level. Dashed ellipses are analyses MA9-4, 7 and 9, excluded from the calculation of the concordia age.

4.6 *Muva Supergroup*

4.6.1 Detrital provenance of the Mporokoso Group (sample MA6)

A prominent quartzite ridge was sampled (sample MA6) some 40 km north of Mansa, and forms part of the base of the Kabweluma Formation of the Mporokoso Group (Figure 2-6, Figure 2-17, Figure 2-20 and Figure 4-6). In the Mansa map sheet, the basal Nsama Formation is missing, while the Mbala Formation consists of a thin unit of coarse sandstone and conglomerate, which passes gradually into the Kabweluma Formation. The quartzite is poorly sorted, ferruginous and displays thick, massive bedding. The beds dip gently to the east and are cut by a weak southeast-dipping cleavage oriented northeast. Up sequence, various conglomeratic horizons are recognised, which are oligomictic, containing only well-rounded chert pebbles, and are often overlain by a small layer of fine, laminated mudstone. The poorly sorted nature of the formation and the interfingering conglomeratic-siltstone layers are indicative of a fluvial depositional environment. Zircons from sample MA6 range from 100 to 250 μm in size, and have length to width ratios up to 3:1. Morphology ranges from sub-angular to well rounded, indicating a mixture of proximal and distal sources (Figure 4-38). CL imaging shows that nearly all zircons display concentric zoning patterns, consistent with a dominance of magmatic source rocks. CL response ranges from high to low, indicating varying contents of trace elements and uranium in the zircons, possibly reflecting a variety of magmatic source rocks.

Thirty-one zircons were analysed during two separate sessions (Table 13-13). Twenty-seven analyses on unknowns yielded more than 95% concordant results (Figure 4-39). f_{206} varies from 0.03 to 0.42%, while uranium content varies between 27 and 441 ppm, with Th/U ratios ranging from 0.35 to 1.89. Two populations of similar abundance can be distinguished that together make up 80% of the total analyses. Neither of these age populations correlate with zircon morphology, indicating that both age populations have proximal as well as distal sources (Figs. 4-39 and 4-40). 40% of the total population ranges in age from

1800 to 1900 Ma, while another 40% of the zircons range in age from 1950 to 2050 Ma. These two populations are clearly distinguishable, with a prominent lack of ages between 1900 and 1950 Ma (Figure 4-40). The remaining 20% of analyses have near concordant $^{207}\text{Pb}/^{206}\text{Pb}$ ages of 2160 ± 17 , 2174 ± 22 , 2214 ± 16 , 2422 ± 8 and 2710 ± 13 Ma (Table 13-13) and indicate minor input from older Palaeoproterozoic and Archaean basement lithologies. The youngest concordant analysis provides a maximum limit on the age of deposition for the Kabweluma Formation at 1824 ± 19 Ma (0.2% reversely discordant analysis).

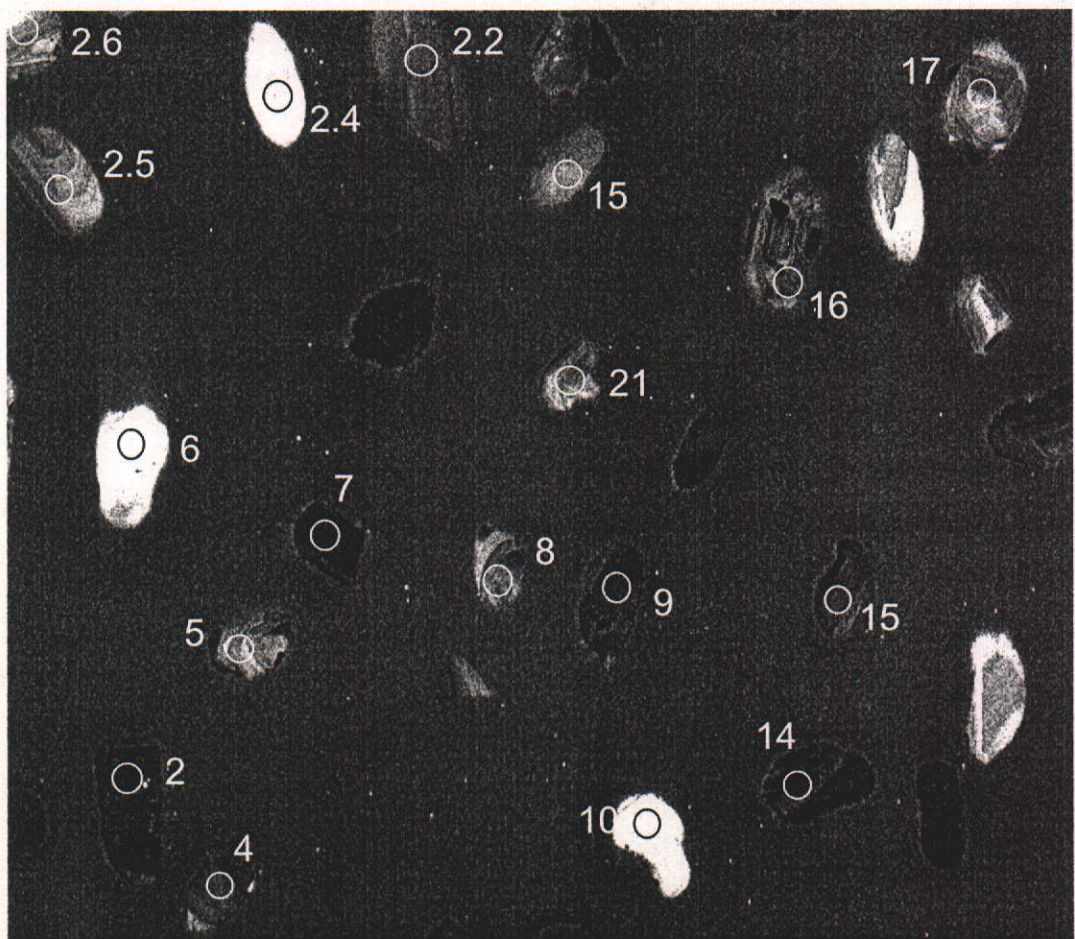


Figure 4-38: CL image of zircon from sample MA6 showing the location of analysed spots. Note the rounded character and variable CL response of the crystals (f.o.v. = 1500 μm). Most zircons show concentric zoning consistent with their erosion from magmatic source rocks.

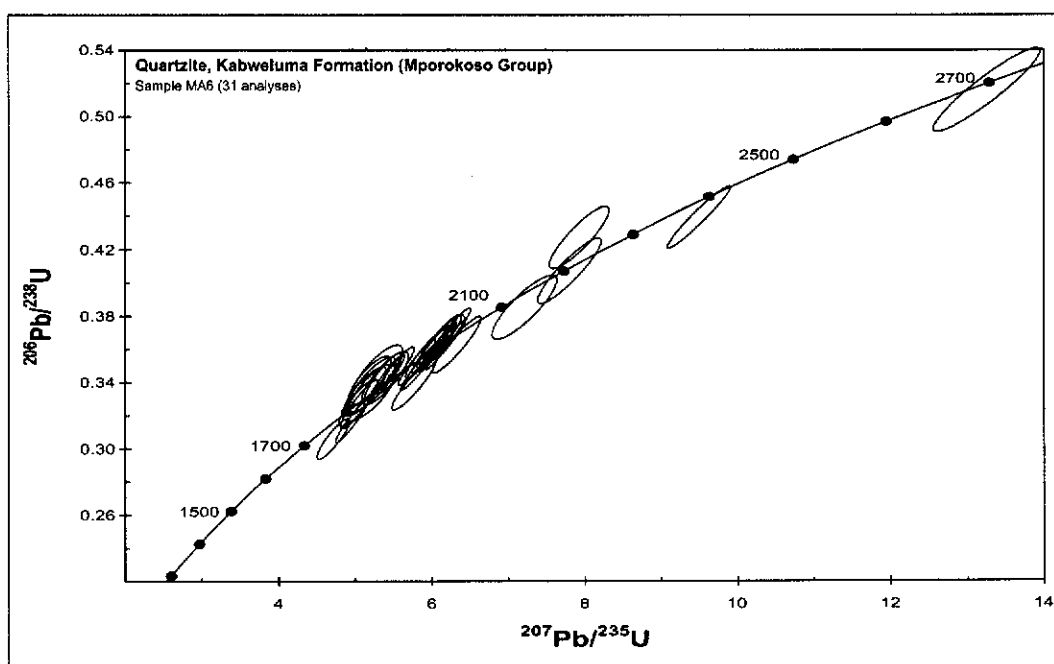


Figure 4-39: U-Pb concordia plot for zircon analyses of sample MA6. Error ellipses are at 1σ confidence level. Note the concordant nature of most analyses.

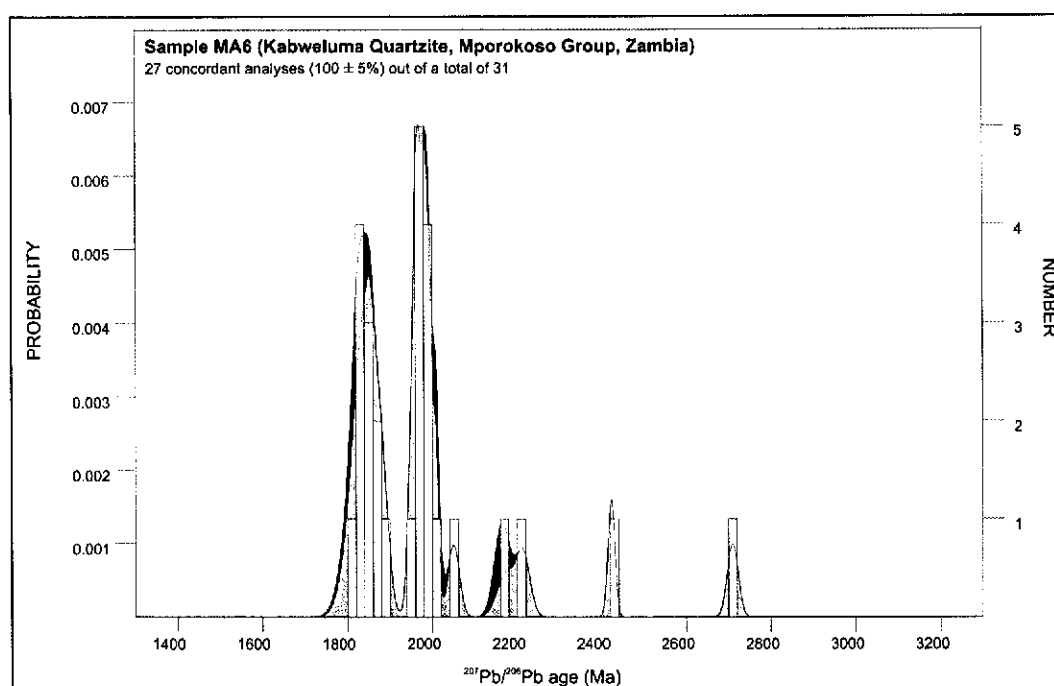


Figure 4-40: Probability density plot of detrital zircon from a quartzite near the base of the Kabweluma Formation (Mporokoso Group, northern Zambia). The histogram indicates the number of $100\pm 5\%$ concordant analyses for each bin of 20 M.y. (right axis), while the curves show the relative probability density of the analyses. The light grey curve denotes 95-105% concordant analyses, while the dark grey curve behind it shows all analyses.

4.6.2 Detrital provenance of the Kasama Formation (sample KAS)

A large sample of supermature, crossbedded quartzite was collected near the Mwela Rock painting national monument east of Kasama (Figure 2-2). The quartzite forms part of the Kasama Formation, and occurs extensively in a small basin to the north of the Irumide belt. The supermature character of the quartzite is evident from the well-rounded grains and extremely well-sorted nature of the rock. Zircons from the sample are rounded and have length to width ratios up to 2:1. CL imaging indicates predominantly magmatic zircon, characterised by concentric zoning patterns. Luminescence ranges from low to high, indicating various sources of magmatic rocks with varying uranium content (Figure 4-41). Thirty-three analyses were conducted on different zircons, during two separate sessions (Table 13-14). Only 5 of the 33 analyses are less than 95% concordant (Figure 4-42). f_{206} ranges up to 0.507 %, but is generally below 0.2%. Uranium content ranges from 49 to 483 ppm, and Th/U ratios from 0.35 to 2.42, consistent with a magmatic source. 90% of the analysed zircons have $^{207}\text{Pb}/^{206}\text{Pb}$ ages between 1900 and 2050 Ma, while one single analysis yields a younger age of 1434 ± 14 Ma (96% concordant) and two analyses indicate a minor contribution of older populations at 2168 ± 17 Ma and 2593 ± 5 Ma ($^{207}\text{Pb}/^{206}\text{Pb}$ ages)(Figure 4-43). The youngest grain of 1434 ± 14 Ma places a maximum limit on the age for the deposition of the Kasama Formation, which is significantly younger than that of the Mporokoso Group.

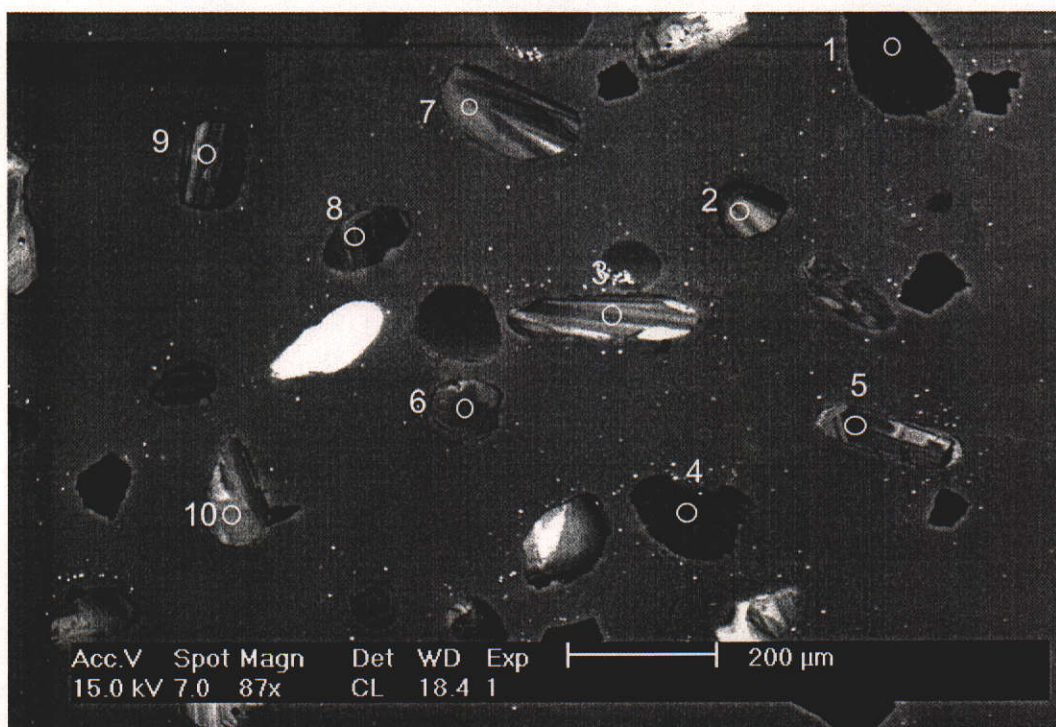


Figure 4-41: CL image of zircon from sample KAS showing the location of analysed spots. Note the well-rounded character and variable CL response of the crystals (f.o.v.= 1400 μm). Most zircons show concentric zoning consistent with magmatic source rocks. Analysis 5 yielded the youngest concordant $^{207}\text{Pb}/^{206}\text{Pb}$ age of 1434 ± 14 Ma.

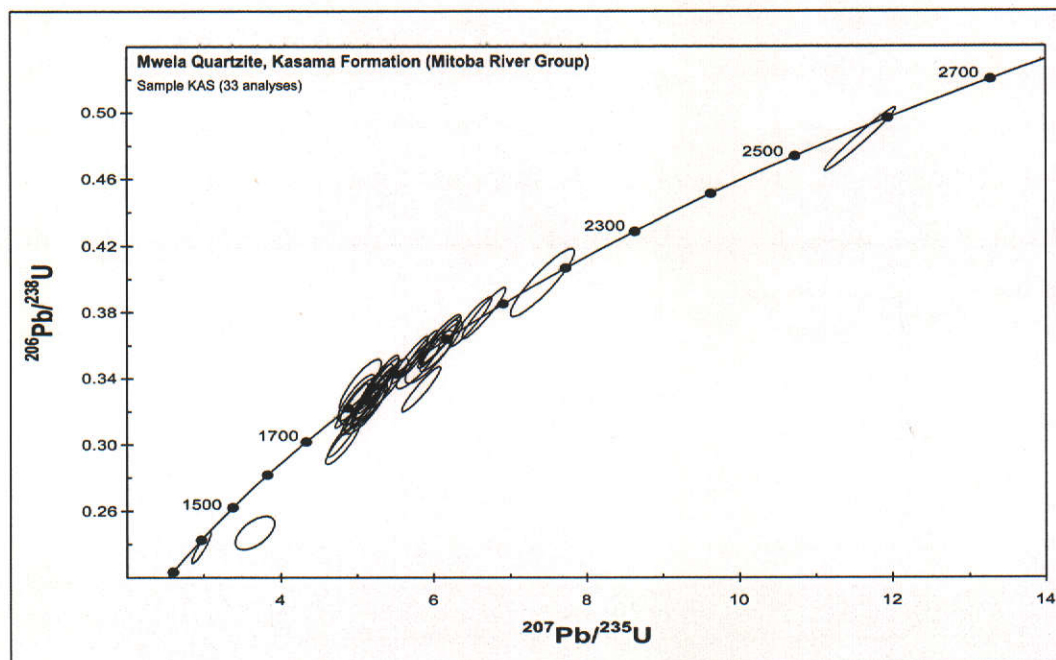


Figure 4-42: U-Pb concordia plot for zircon analyses of sample KAS. Error ellipses are at 1σ confidence level. Note the concordant nature of most analyses.

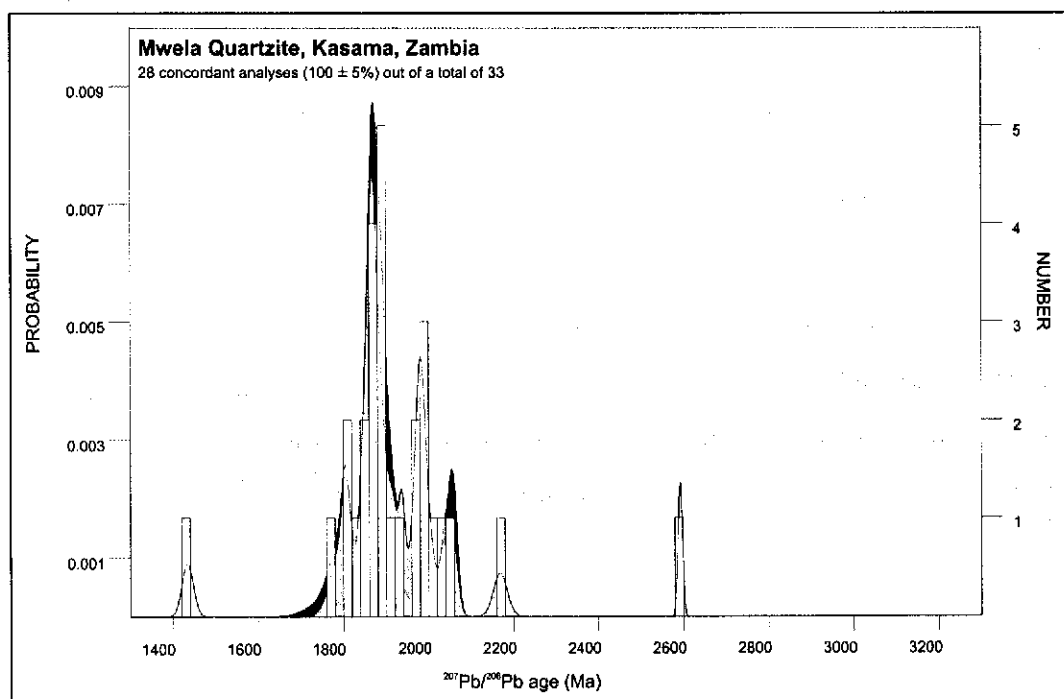


Figure 4-43: Probability density plot of detrital zircon from the Mwela Quartzite (Kasama Formation, northern Zambia). The histogram indicates the number of $100 \pm 5\%$ concordant analyses for each bin of 20 M.y. (right axis), while the curves show the relative probability density of the analyses. The light grey curve denotes 95-105% concordant analyses, while the dark grey curve behind it shows all analyses.

4.6.3 Detrital provenance of the Manshya River Group (sample IL14)

Chembewesu Hill forms a large outcrop of white, micaceous quartzite of the Manshya River Group to the north of the Great North Road between Isoka and Mpika (Figure 2-12). Massive, thick beds of white recrystallised micaceous quartzite, which display large scale, shallow-angle cross bedding, underlie the hill. The quartzite is relatively poorly sorted, and the zircon grains are subangular to subrounded (Figure 4-44 (a)). Zircons collected from the sample have length to width ratios of up to 3:1 and can be subdivided into two main populations based on morphology alone. One population, making up about 30% of all grains, consists of euhedral zircons, often with bipyramidal terminations, indicating a proximal source. A second population is represented by subrounded to rounded grains, which may have been sampled from a more distal source. CL imaging indicates oscillatory zoning patterns for nearly all zircons, with luminescence ranging from extremely low to extremely high (Figure 4-44 (b)).

Forty-seven analyses were conducted during one single analytical session. Thirty-two analyses plot within 5% of concordia, while the remaining 15 analyses are from 5 to 14% discordant (Figure 4-45). f_{206} is generally low, ranging up to 0.622% (Table 13-15). Uranium content is generally above 100 ppm, and ranges from 38 to 425 ppm. Th/U ratios vary from 0.17 to 2.19. The detrital population appears to be largely unimodal with 70% of the analyses having $^{207}\text{Pb}/^{206}\text{Pb}$ ages between 2.05 and 2.00 Ga. This dominant group covers all morphological types, indicating little or no age differences between distal and proximal sources. Five analyses are younger, with the youngest concordant grain yielding a $^{207}\text{Pb}/^{206}\text{Pb}$ age of 1882 ± 30 Ma (2% reversely discordant). Of these grains, four appear to form a population around 1880 Ma, with ages ranging from 1860 to 1889 Ma, while one zircon has a $^{207}\text{Pb}/^{206}\text{Pb}$ age of 1918 ± 20 Ma. Several older grains are identified, three of which define a small population between 2200 and 2130 Ma, while single grains have $^{207}\text{Pb}/^{206}\text{Pb}$ ages of 2426 ± 18 Ma, 2665 ± 14 Ma, 2851 ± 7 Ma and 3011 ± 16 Ma.

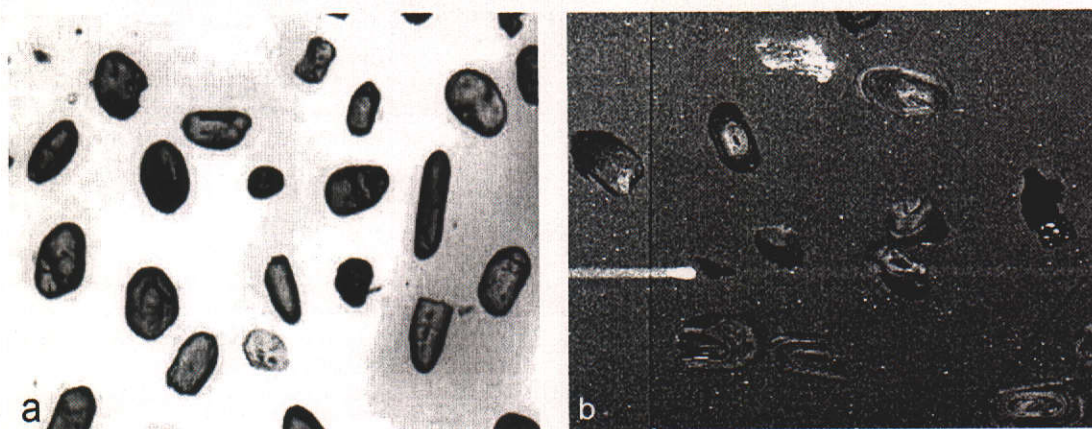


Figure 4-44: (a) photomicrograph of zircons from sample IL14 (xpl) showing clear rounded zircons with minor cracks and inclusions (f.o.v. = ~1600 μm). Note the variable length to width ratios; (b) CL image of zircon from sample IL14. Note the concentric zoning of the crystals (f.o.v. = 1000 μm).

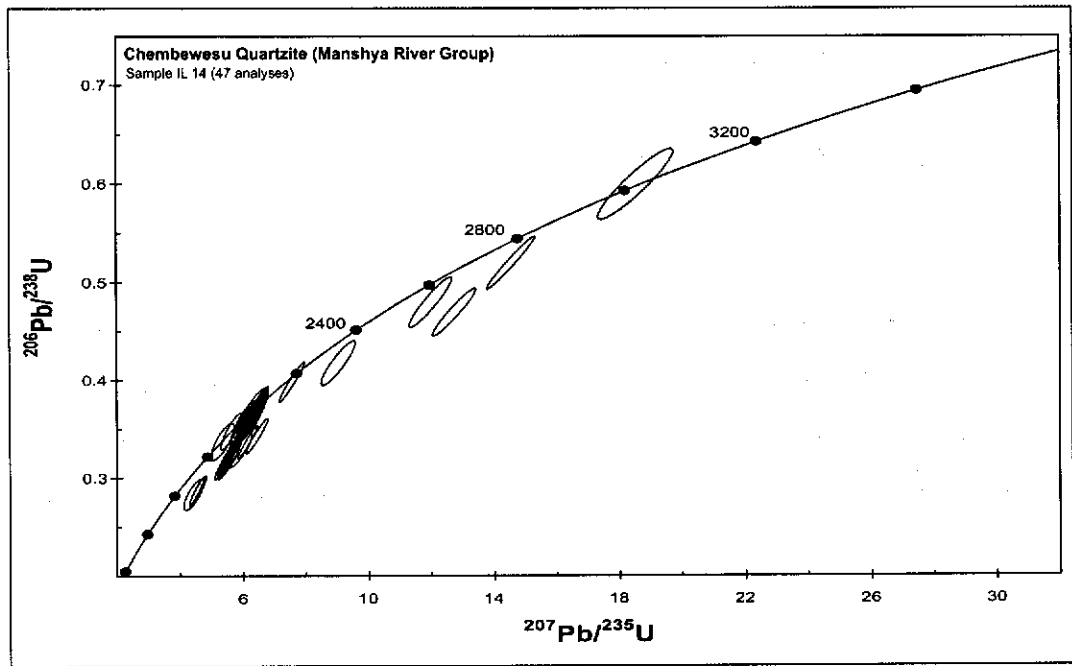


Figure 4-45: U-Pb concordia plot for zircon analyses of sample IL14. Error ellipses are at 1 σ confidence level. Note the concordant nature of the majority of analyses.

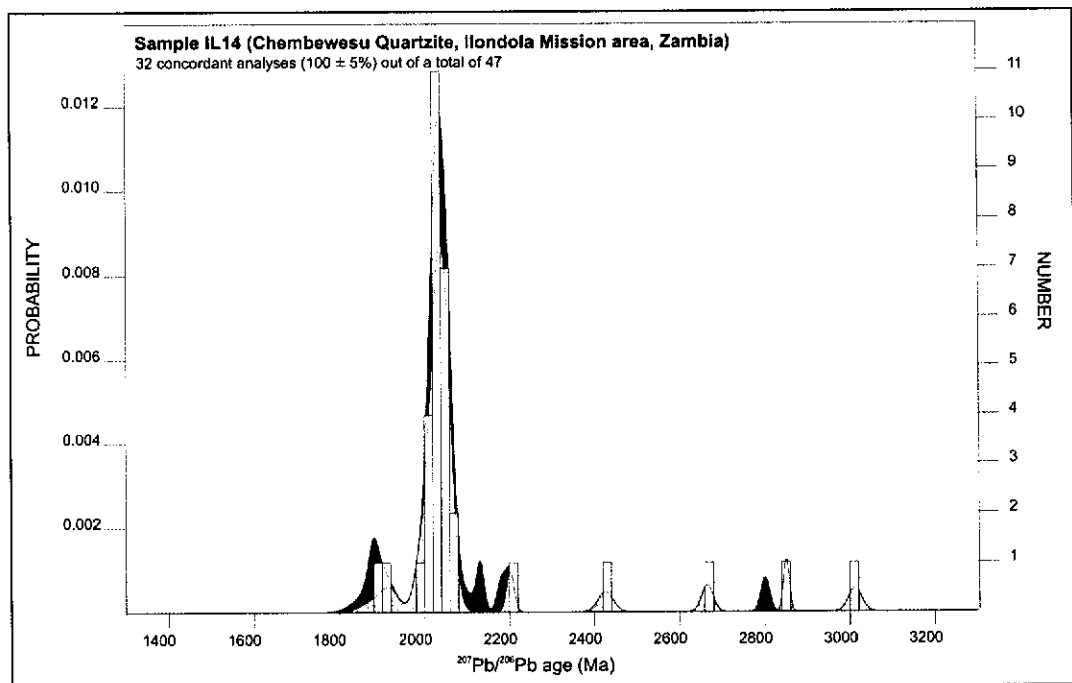


Figure 4-46: Probability density plot of detrital zircon from the Chembewesu Quartzite (Manshya River Group, northern Zambia). The histogram indicates the number of 100 \pm 5% concordant analyses for each bin of 20 M.y. (right axis), while the curves show the relative probability density of the analyses. The light grey curve denotes 95-105% concordant analyses, while the dark grey curve shows all analyses.

4.6.4 The basal conglomerate of the Kanona Group (sample MK8)

A conglomerate occurs at the base of the Kanona Group in the southwestern portion of the Irumide belt, where local shearing and tectonism have not obliterated the contact between the Kanona Group metasedimentary sequence and Mkushi Gneiss basement. The conglomerate, which occurs only at the base of the former Musofu Formation near the Zambia-DRC border (Figure 4-1), forms lensoid bodies within gritty quartzite, interpreted to have been deposited in a deltaic environment (Stillman, 1965c). The sampled conglomerate is largely oligomictic, with a predominance of large, rounded and flattened quartz-rich clasts. The sequence is hematitic near the base, and gradually becomes less iron-stained towards the top. Individual conglomeratic horizons range from a few meters to several tens of meters thick. As the entire sequence is folded, the apparent thinning and attenuation of the conglomeratic units may be a structural feature rather than an original sedimentary characteristic, but the occurrence of festoon and trough crossbeds supports shallow water deposition. One large sample (sample MK8) was collected from a conglomeratic horizon, which contains cm-sized clasts in a psammitic matrix of quartz-feldspar-hematite-sericite. Zircons extracted from the conglomerate are rounded, and range in length to width ratio between equant and 3:1 (Figure 4-47). The zircons are clear, and contain minor cracks and inclusions. In CL imaging, the zircons show clear concentric zoning patterns, consistent with a provenance from magmatic source rocks. The zircons are generally non-complex in nature. Seven analyses were conducted on seven zircons, and yielded low f_{206} values up to 0.456% (Table 13-16). U and Th range from 80 to 250 ppm and 22 to 98 ppm respectively, yielding Th/U ratios between 0.21 and 0.86. Apart from one analysis (MK8-7), the data plot within 5% of concordia (Figure 4-48). Five near-concordant data points appear to reflect a uniform source for which a weighted mean $^{207}\text{Pb}/^{206}\text{Pb}$ age of 2034 ± 16 Ma can be calculated (MSWD=1.06). Analysis MK8-3 yields a $^{207}\text{Pb}/^{206}\text{Pb}$ age of 1953 ± 15 Ma and reflects a slightly younger component, which corresponds in age with the younger phases of the Mkushi Gneiss. It must be stressed that due to the limited number of analyses, these data cannot be regarded representative for the detrital populations present in the sample.

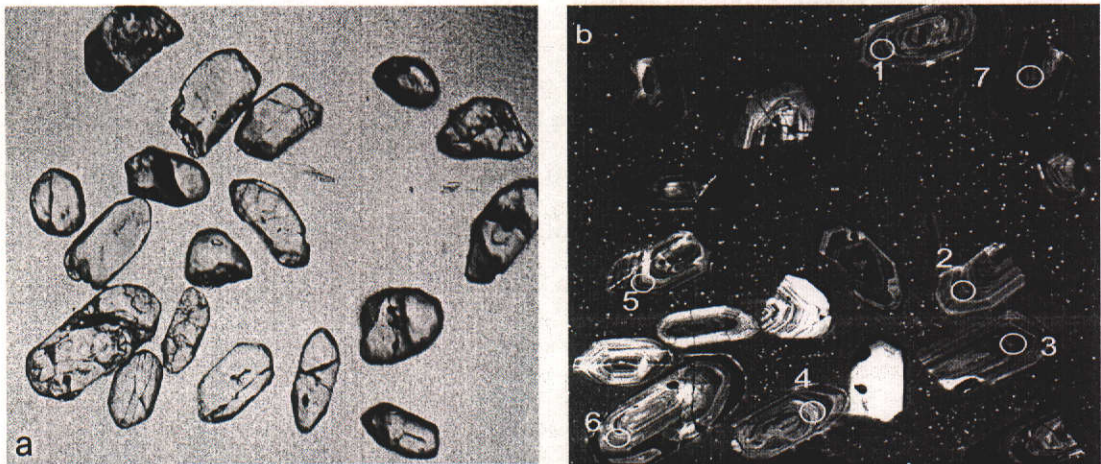


Figure 4-47: (a) photomicrograph of zircons from sample MK8 (xpl) showing clear zircons with minor cracks and inclusions (f.o.v. = ~1600 μm); (b) CL image of zircon from sample MK8. Note the concentric zoning of the crystals (f.o.v.= 1300 μm).

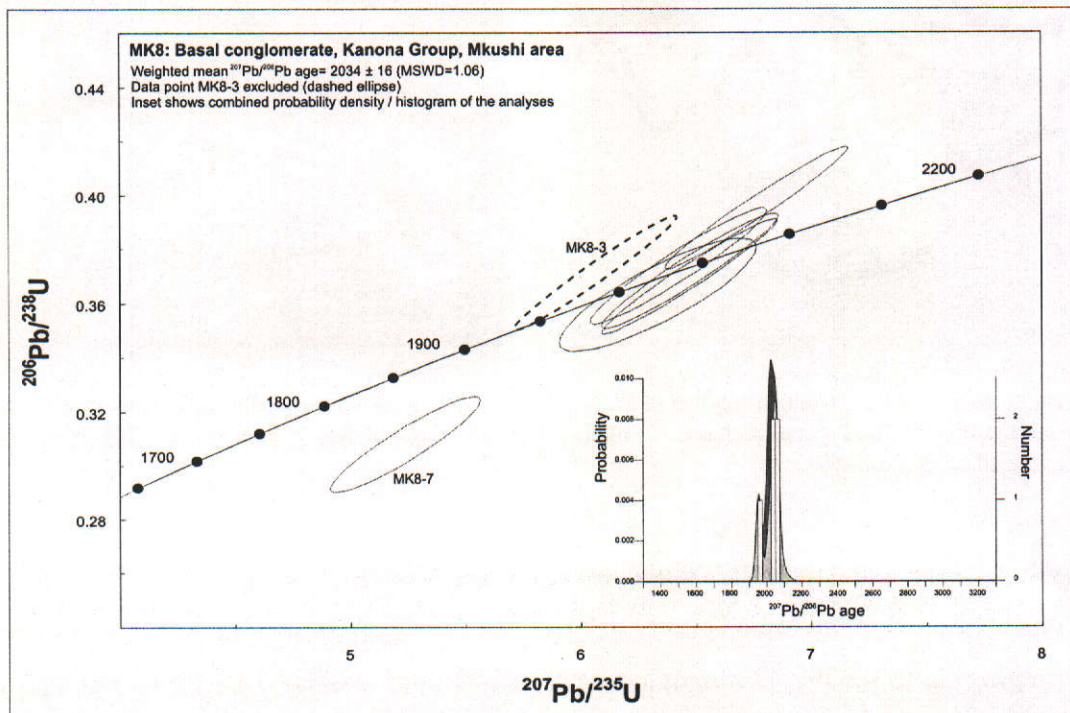


Figure 4-48: U-Pb concordia plot for zircon analyses of sample MK8. Error ellipses are at 1 σ confidence level. The inset shows the probability density plot of the detrital zircons. The histogram indicates the number of 100 \pm 5% concordant analyses for each bin of 25 M.y. (right axis), while the curves show the relative probability density of the analyses. The light grey curve denotes 95-105% concordant analyses, while the dark grey curve shows all analyses.

4.6.5 Luswa River Volcanic (sample ZM31)

Sample ZM31 was taken from a thin layer of rhyolitic tuff of the Manshya River Group in the area of the 1:100000 Luswa River map sheet (Figure 4-4). The tuff has well preserved graded bedding shown by small crystals, indicating pyroclastic deposition. Zircons extracted from sample ZM31 are euhedral, ranging in length from 50 to 200 μm and have length to width ratios up to 3:1 (Figure 4-49). The crystals are clear and pale yellow in colour. CL imaging reveals concentric zoning patterns of high and low CL response, consistent with crystallisation from magma.

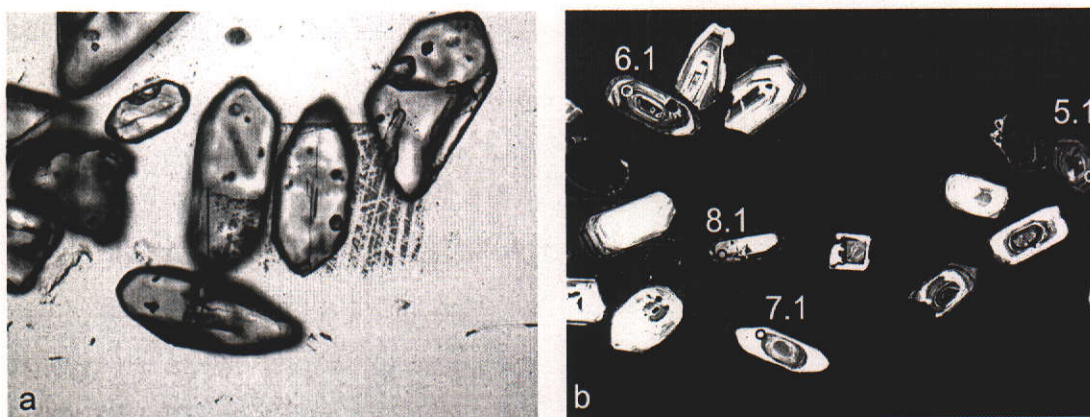


Figure 4-49: (a) photomicrograph of zircons from sample ZM31 (xpl) showing clear euhedral zircons with minor cracks and inclusions (f.o.v. = ~1400 μm); (b) CL image of zircons from sample ZM31 showing analysed spots (f.o.v.=1800 μm).

Ten analyses were conducted on different zircon grains and yield a tight cluster close to concordia (Figure 4-50). f_{206} values are relatively low with values ranging up to 0.33%. U ranges from 70 to 272 ppm and Th from 59 to 361 ppm, yielding Th/U ratios between 0.64 and 1.37. The data range from 94.5 to 103.3% concordant. A linear regression of the data yields an upper intercept of 1884 ± 15 Ma and a lower intercept of 465 ± 840 Ma (MSWD=0.36). A weighted mean $^{207}\text{Pb}/^{206}\text{Pb}$ age of 1883 ± 10 Ma (MSWD=0.58) can be calculated from all data points. The calculated lower intercept indicates recent lead loss, and with all data points near concordia, a concordia age can be calculated of 1879 ± 13 Ma (MSWD=1.02). Based on its lower MSWD value, the weighted mean $^{207}\text{Pb}/^{206}\text{Pb}$

age is taken to be the best estimate for the crystallisation of the Luswa River Volcanic.

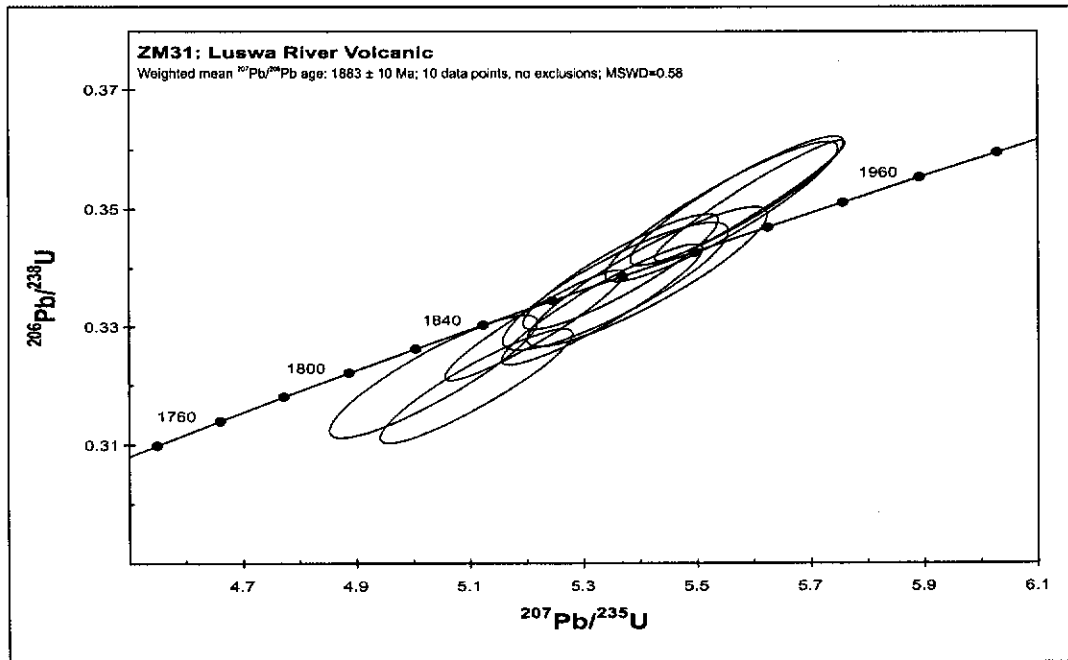


Figure 4-50: U-Pb concordia plot for zircon analyses of the Luswa River Volcanic. Error ellipses are at 1 σ confidence level.

4.6.6 Kachinga Tuff (sample IS20)

Sample IS20 was taken from a prominent 300 m thick unit of rhyolitic tuffs and intercalated lava flows (the Kachinga Tuff), which has been isoclinally folded in the Chimbwe syncline (Figure 4-5). The Kachinga Tuff has an irregular contact with the underlying pelite and grades upwards into a well-bedded crystal tuff. Much of the unit is interpreted as a water-lain tuff (Daly, 1995b). Zircons from sample IS20 are euhedral, clear to pale yellow, free of inclusions and variably cracked. Their size ranges from 100 to 200 μm , with length to width ratios of up to 2:1 (Figure 4-51 (a)). The crystals have sharp ends, and show oscillatory zoning patterns in CL response (Figure 4-51 (b)). Seven analyses were conducted on seven different zircon grains (Table 13-18). Common lead is very low (0.33%). The zircons contain moderate amounts of U and Th, with Th/U ranging from 0.75 to 1.38. The analyses plot within 2% of concordia (Figure 4-52), and define an age group with a weighted mean $^{207}\text{Pb}/^{206}\text{Pb}$ age of 1859 ± 11

Ma (MSWD=2.06). Because of the high concordance of the data, a concordia age of 1856 ± 4 Ma can be calculated on all seven points (MSWD of 1.05). Based on the lower MSWD value for the latter, the concordia age provides the best estimate for the crystallisation age of the Kachinga Tuff.

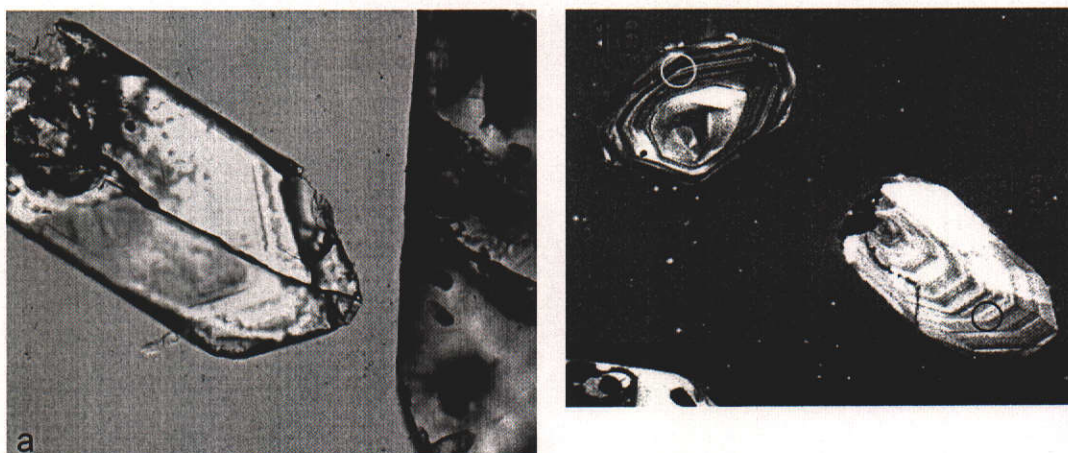


Figure 4-51: (a) photomicrograph of zircons from sample IS20 (xpl) showing clear euhedral zircons with some cracks and inclusions (f.o.v. = ~ 250 μm); (b) CL image of zircons from sample IS20. Note the concentric zoning of the crystals (f.o.v.= 800 μm).

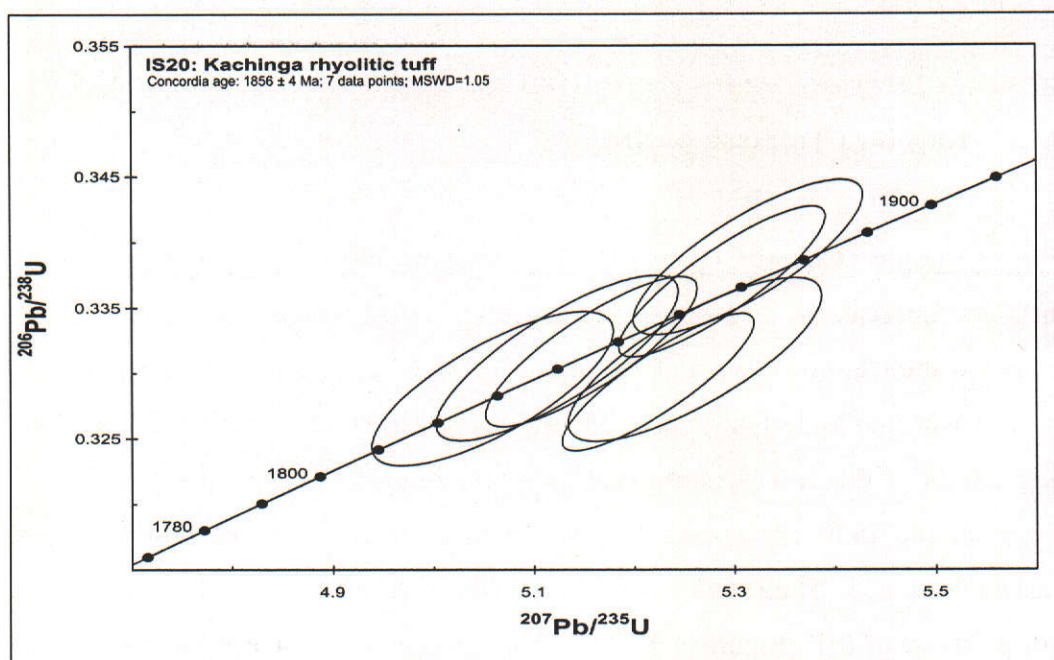


Figure 4-52: U-Pb concordia plot for zircon analyses of the Kachinga Tuff. Error ellipses are at 1σ confidence level.

4.6.7 Katibunga Volcanic (sample KB5)

Sample KB5 was taken from a medium-grained portion of dolerite 5 kilometers north of Ibangwe Hill (Figure 4-3), interpreted as a hypabyssal feeder to the volcanic units. Only a few zircons were separated, and range from sub- to euhedral. In transmitted light they are clear, containing only minor inclusions (Figure 4-53 (a)). In CL response, the zircons display variable luminescence and concentric zoning patterns. Some zircons do, however, appear corroded and overgrown by narrow, zoned zircon rims, and the cores may possibly represent xenocrysts (e.g. analysis KB5-2, Figure 4-53 (b)).

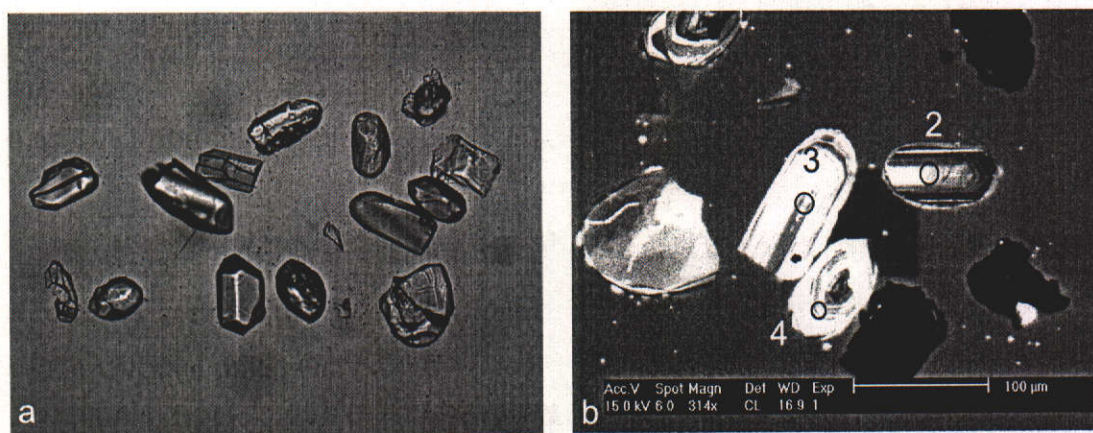


Figure 4-53: (a) photomicrograph of zircons from sample KB5 (xpl) showing clear sub-euhedral zircons with minor cracks and inclusions (f.o.v. = ~1500 µm); (b) CL image of zircons from sample KB5. Note the concentric zoning of the crystals (f.o.v.= 450 µm). Analysis KB5-2 yielded an age of 2551 ± 36 Ma and is interpreted as a xenocryst.

Seven zircons were analysed during two separate sessions, and yield variable proportions of f_{206} ranging from 0.11 to 1.72%. U and Th vary from 59 to 165 ppm and 65 to 364 ppm respectively, yielding Th/U ratios between 0.50 and 2.37 (Table 13-19). One discordant analysis yields a $^{207}\text{Pb}/^{206}\text{Pb}$ age of 2551 ± 36 Ma and is interpreted to be a xenocryst. The remaining six analyses range from 93.1 to 99.2% concordant, and define a coherent age group with a weighted mean $^{207}\text{Pb}/^{206}\text{Pb}$ age 1871 ± 24 Ma (MSWD=1.06), which can be considered a reasonable estimate of the crystallisation age of the zircons. Given the limited number of zircons analysed and their corroded nature, it cannot be ruled out that all zircons are xenocrysts, derived from the quartzites that the Katibunga

Volcanics were emplaced through. Unfortunately no badelleyite was recovered from the sample to directly confirm the emplacement age.

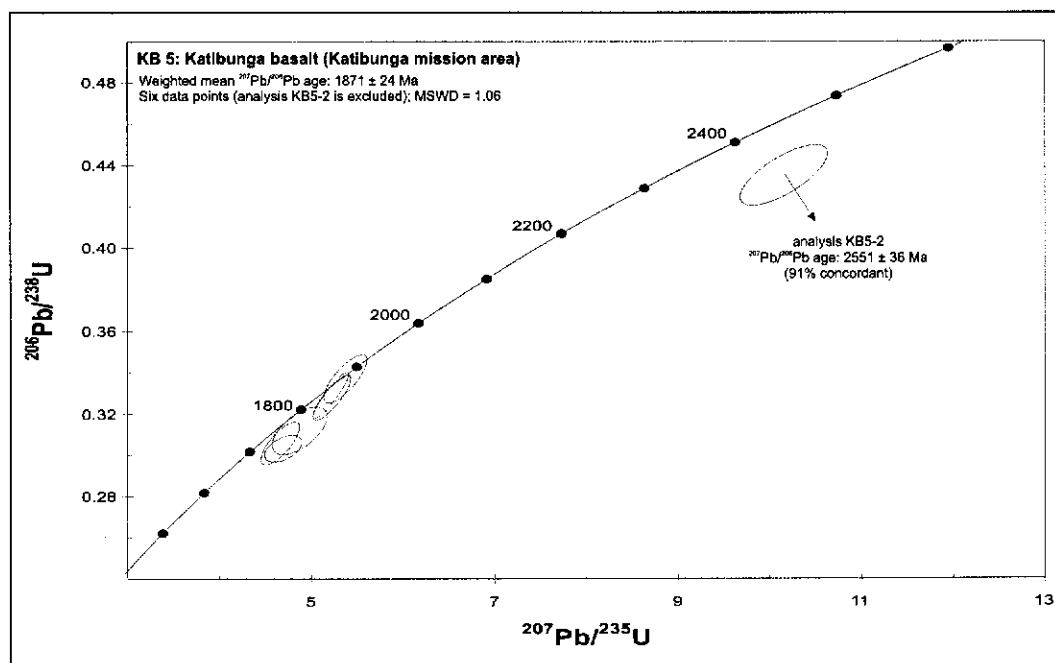


Figure 4-54: U-Pb concordia plot for zircon analyses of the Katibunga Volcanic. Error ellipses are at 1 σ confidence level.

4.7 Strongly deformed Irumide granitoids

4.7.1 The Mutangoshi Gneissic Granite

The Mutangoshi Gneissic Granite of Daly (1986b) was sampled from one location in the eastern part of the Chinsali area (Figure 4-4), near its contact with the younger Chilubanama Granite where it takes on a migmatitic aspect with biotite-amphibole schlieren and a uniform felsic component. Away from the contact, the gneiss gains a more uniform character and is locally affected by mylonitic zones. At the sampled outcrop, a gradational contact was observed between the Mutangoshi Gneissic Granite and the Chilubanama Granite. At the contact, the grain size of the Chilubanama Granite decreases, giving way to the nebulitic and strongly foliated and migmatitic Mutangoshi Gneissic Granite. This relationship is taken to indicate that the Chilubanama Granite is derived from

partial melting of the Mutangoshi Gneissic Granite. Both samples were collected several meters away from the gradual contact, within what was interpreted as the Mutangoshi Gneissic Granite. Sample MTGG1 was taken from a medium-grained felsic variety of the gneiss, while sample MTGG2 was collected from a coarse melt pocket in the Mutangoshi Gneissic Granite.

4.7.1.1 Sample MTGG1

Zircons from sample MTGG1 measure between 100 and 500 μm in size, are prismatic in shape and have length to width ratios of up to 5:1 (Figure 4-55). All zircons are yellow to light brown in colour, variably cracked, and contain a minor amount of small inclusions. A considerable proportion of the grains have a rounded core surrounded by an extensive rim, both showing concentric zoning in CL, consistent with a magmatic origin (Figure 4-55). Thirteen analyses were conducted on ten different zircons (Table 13-20), including analyses of core-rim pairs in three different zircon grains (MTGG1-3, MTGG1-6 and MTGG1-7). Several analyses on rims and cores were aborted after the first few minutes of analysis time due to high ^{204}Pb counts and are not included in the data table. Th/U ranges from 0.18 to 0.74, with one core having elevated Th content (MTGG1-12; Th/U=1.95)(Table 13-20). Values for f_{206} are generally small, ranging up to 0.068%, but three analyses have relatively high f_{206} (MTGG1-3c (0.643%), MTGG1-5 (0.445%) and MTGG1-6c (1.178%)). Core analysis MTGG1-3c yielded a $^{207}\text{Pb}/^{206}\text{Pb}$ age of 1961 ± 15 Ma (98.6% concordant), whilst rim analysis MTGG1-3r has a $^{207}\text{Pb}/^{206}\text{Pb}$ age of 1008 ± 8 Ma (99.7% concordant)(Figure 4-56). The age of the core compares well with core analysis MTGG1-12c, which yielded a $^{207}\text{Pb}/^{206}\text{Pb}$ age of 1955 ± 6 Ma (98.6% concordant). Both cores are interpreted to be part of the protolith of the Mutangoshi Gneissic Granite and define a concordia age of 1954 ± 11 Ma (MSWD=1.6). Eleven analyses, including core and rim analyses of zircons MTGG1-6 and MTGG1-7, one analysis on a core (MTGG1-4c), and two analyses on rims (MTGG1-1r and MTGG1-3r), define a cluster on the concordia diagram that yields a regression line with upper intercept age of 1029 ± 21 Ma (MSWD=1.8). Excluding MTGG1-6c on the basis of its high proportion of

common Pb (1.178%), low uranium (109 ppm) and low thorium (78 ppm) and excluding two rim analyses (MTGG1-1r and MTGG1-3r) on the basis of high uranium (>1000 ppm) and low Th/U (0.18-0.25) (Figure 4-57), an upper intercept age of 1029 ± 9 Ma and lower intercept age of 152 ± 340 Ma (MSWD=1.16) can be calculated. The latter upper intercept is taken to be the best estimate of the crystallisation age of magmatic zircon in the Mutangoshi Gneissic Granite. The low Th/U analyses on rims MTGG1-1r and MTGG1-3r, which have $^{207}\text{Pb}/^{206}\text{Pb}$ ages of 979 ± 6 Ma (97.0% concordant) and 1008 ± 8 Ma (99.7% concordant), sampled across the tip of elongate zircon crystals (Figure 4-55 (a) and Figure 4-58), are interpreted to date zircon crystallisation postdating the emplacement of the precursor granite. The relatively low Th/U ratio that characterises these analyses indicates that these rims may have developed from low Th/U metamorphic or metasomatic fluids. Taken together, analyses MTGG1-3r and MTGG1-1 could bracket late stage metamorphism/metasomatism between 1008 ± 8 and 979 ± 6 Ma. An alternative interpretation for these apparent younger $^{207}\text{Pb}/^{206}\text{Pb}$ ages lies in intermediate Pb-loss. The data are insufficient to discriminate between these two possibilities, and not much weight is given to the apparently younger zircons.

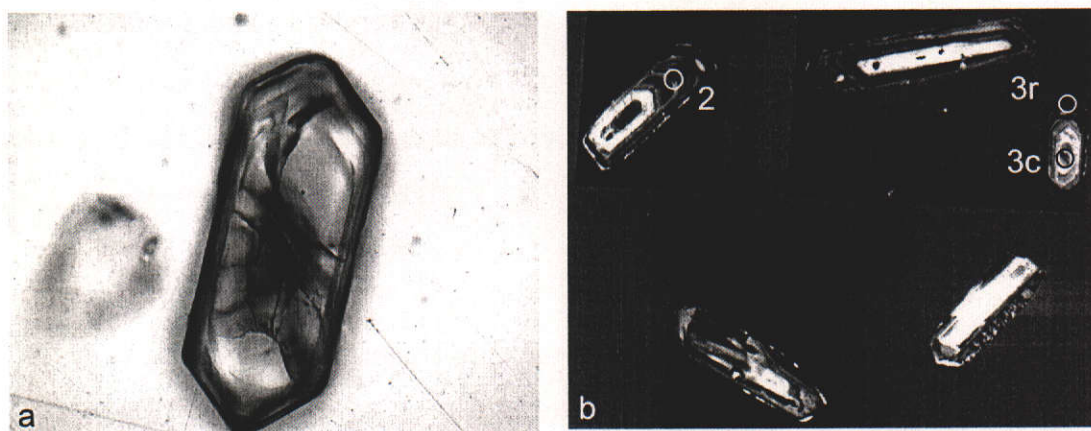


Figure 4-55: (a) photomicrograph of zircon (analysis numbers 3c and 3r) from sample MTGG1 (xpl) showing euhedral habit with minor cracks and inclusions (f.o.v. = ~ 1500 μm); (b) CL image of zircons from sample MTGG1 indicating analysed spots 2, 3c and 3r. Note the concentric zoning of the crystals (f.o.v.= 800 μm). Analysis 2 yielded a $^{207}\text{Pb}/^{206}\text{Pb}$ age of 1015 ± 12 Ma, while 3c and 3r yielded 1961 ± 15 and 1008 ± 8 Ma respectively.

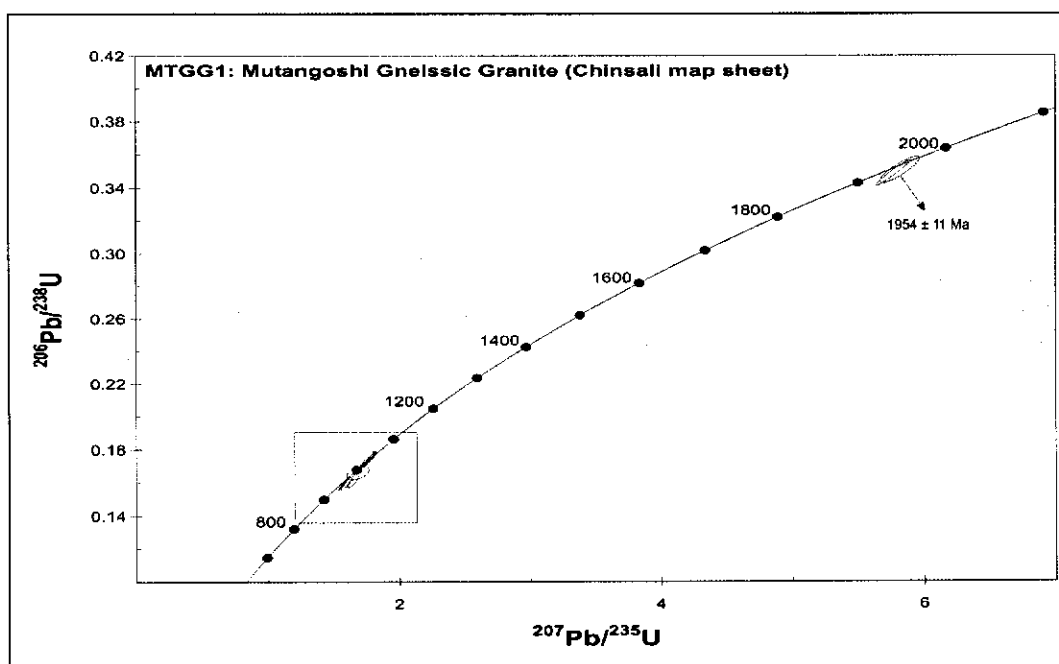


Figure 4-56: U-Pb concordia plot for zircon analyses of sample MTGG1. Error ellipses are at 1σ confidence level. The box refers to the detailed plot in Figure 4-57.

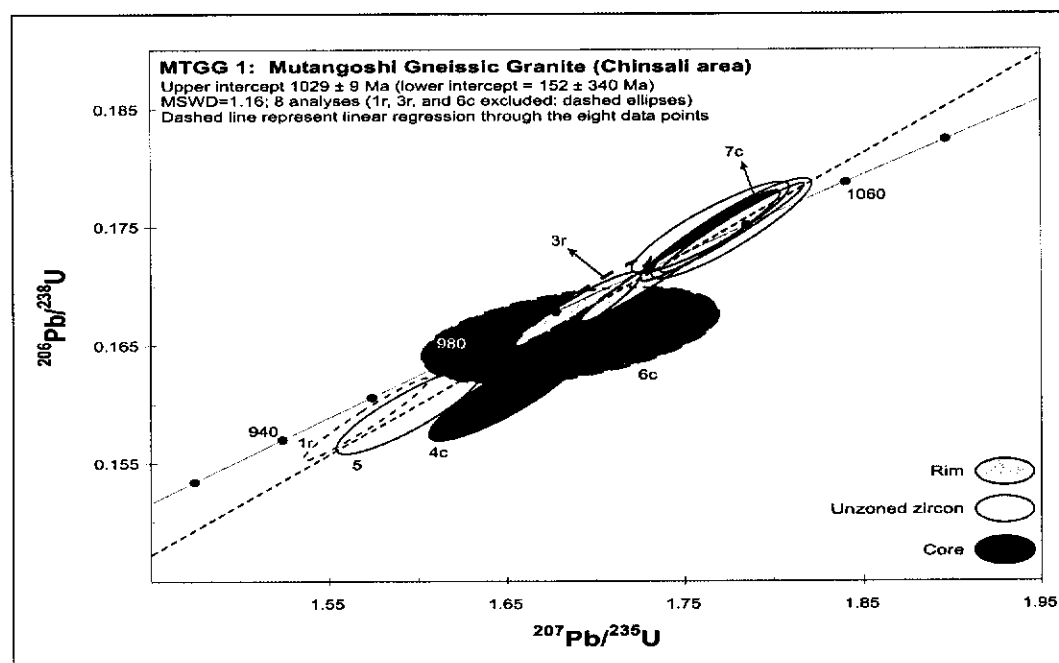


Figure 4-57: U-Pb concordia plot for zircon analyses of sample MTGG1. Error ellipses are at 1σ confidence level.

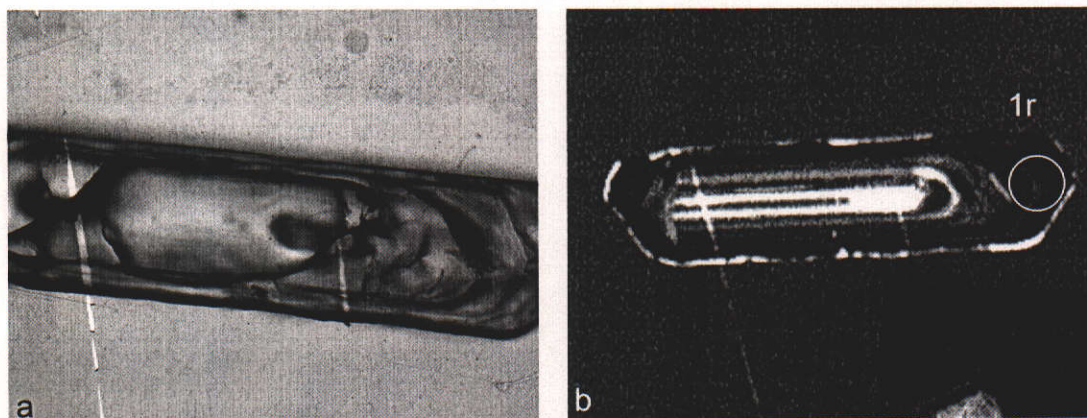


Figure 4-58: (a) photomicrograph of zircon (analysis number MTGG1-1) from sample MTGG1 (xpl) showing euhedral elongate habit with minor cracks and inclusions (f.o.v. = ~200 µm). Even in transmitted light, the complex nature of the zircon is evident; (b) CL image of the same zircon indicating the analysed spot (analysis 1). Note that the spot samples outside the core, but across what may be two separate dark CL rims (f.o.v.= 250 µm). This analysis yielded a $^{207}\text{Pb}/^{206}\text{Pb}$ age of 979 ± 6 Ma.

4.7.1.2 Sample MTGG2

Zircons from sample MTGG2 are quite large, ranging from 200 to 500 µm in size, and are dark brown in colour. Length to width ratios range from 2:1 to 5:1 and crystals are sub- to euhedral, with conical tips (Figure 4-59). In CL, the zircons appear very dark, but often contain a high-CL, concentrically zoned irregular core. Six analyses were made on different zircons, including two cores and four unzoned zircons, with numerous analyses aborted due to high counts of ^{204}Pb . Two cores analysed from sample MTGG2 yield $^{207}\text{Pb}/^{206}\text{Pb}$ ages of 1989 ± 39 (99.3% concordant; MTGG2-16c) and 1978 ± 18 Ma (100.4% concordant; MTGG2-10c), combining to give a concordia age of 1980 ± 25 Ma, which is comparable to the cores analysed from sample MTGG1 (see above). The concordia age is interpreted to date the crystallisation age of the Palaeoproterozoic granite that was melted to form the Mutangoshi Gneissic Granite. f_{206} values on the remaining four analyses are highly variable, ranging up to 8.24%, while Th/U ranges from 0.01 to 0.55 (Table 13-21). All data plot close to concordia, but with progressively lower Pb/U ratios with increasing proportion of common Pb (Figure 4-60). Data point MTGG2-19 plots at a significantly younger age than the other three analyses, having experienced substantial Pb-loss, and is also the least precise analysis. The other three points plot within 6% of concordia, and yield a concordia age of 1055 ± 13 Ma (MSWD=1.11) and weighted mean $^{207}\text{Pb}/^{206}\text{Pb}$ age of 1047

± 75 Ma (MSWD=3)(Figure 4-61). This latter age can be considered a reasonable estimate for the crystallisation age of magmatic zircons in the melt pocket.

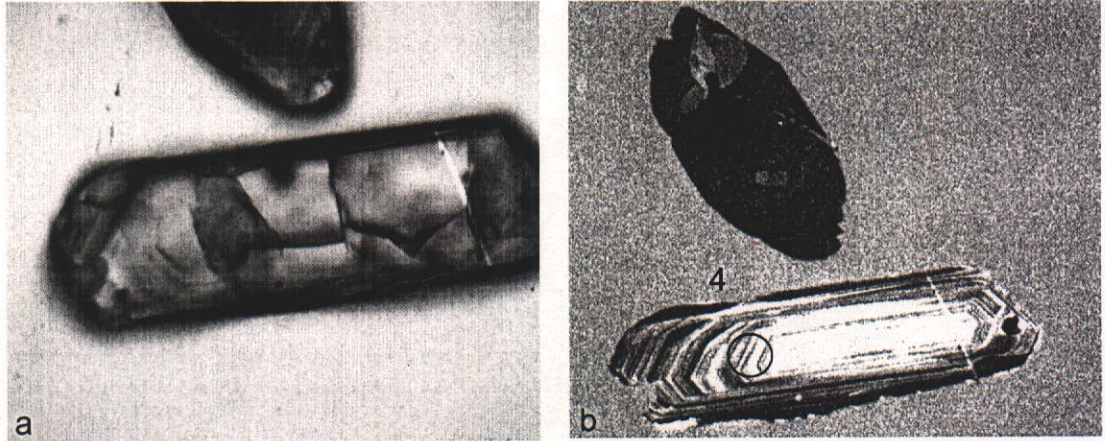


Figure 4-59: (a) photomicrograph of zircon (analysis number 4) from sample MTGG2 (xpl) showing euhedral elongate habit with cracks and minor inclusions (f.o.v. = ~ 250 μm); (b) CL image of the same zircon indicating the analysed spot (analysis 4). Note the concentric zoning consistent with magmatic growth (f.o.v.= 400 μm). This analysis yielded a $^{207}\text{Pb}/^{206}\text{Pb}$ age of 1062 ± 12 Ma.

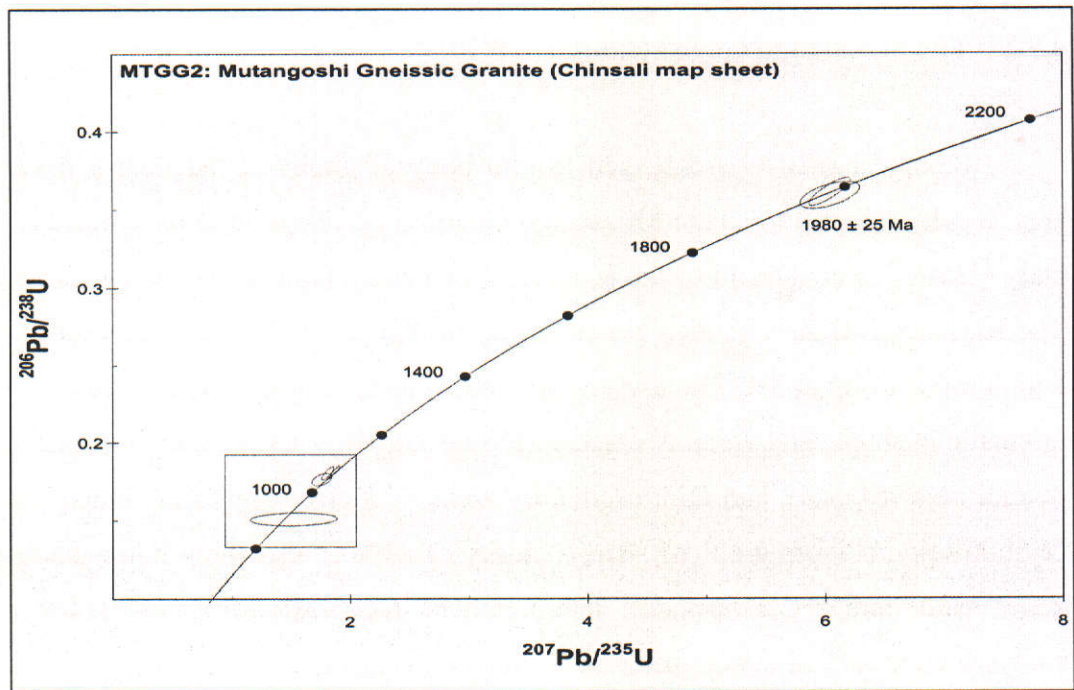


Figure 4-60: U-Pb concordia plot for zircon analyses of sample MTGG2. Error ellipses are at 1 σ confidence level. The box refers to a detailed plot in Figure 4-61.

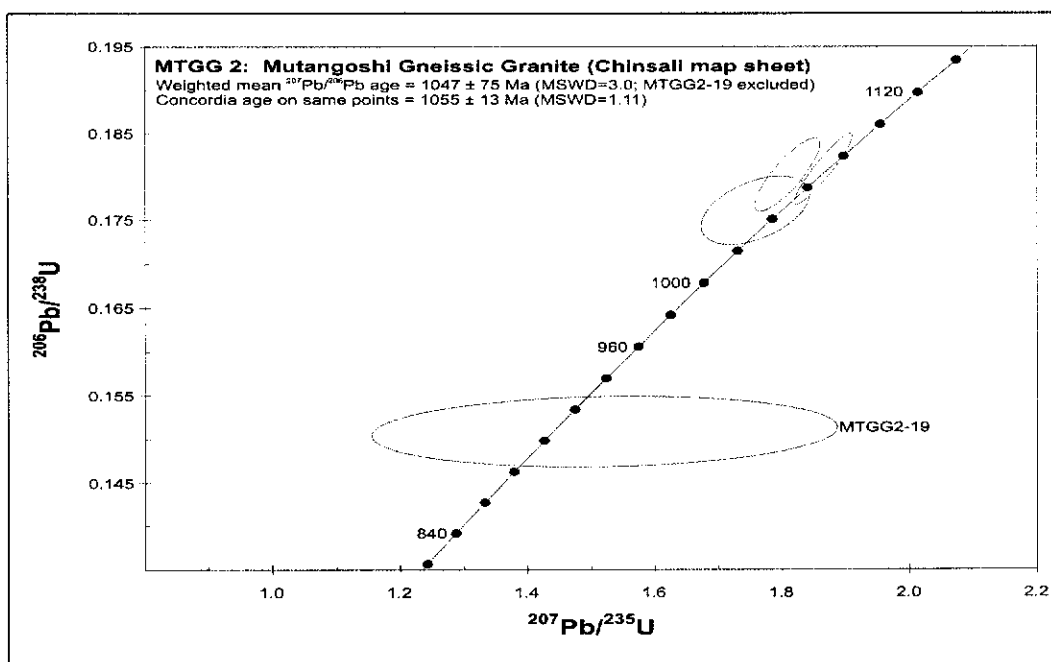


Figure 4-61: U-Pb concordia plot for zircon analyses of sample MTGG2. Error ellipses are at 1 σ confidence level.

4.7.2 The Musalango Gneiss (sample LW10)

Sample LW10 was collected from a body of gneiss in the Luswa River area, locally referred to as the Musalango Gneiss (Figure 4-4) and interpreted by Daly (1986b) as equivalent to the Mutangoshi Gneissic Granite further northeast. The Musalango Gneiss yielded zircons of up to 200 μm in length, with width to length ratios of up to 3:1. The crystals are yellow to light brown, sub- to euhedral prismatic in shape, and variably cracked (Figure 4-62 (a)). CL imaging reveals an overall high response, and faint oscillatory zoning patterns, suggesting magmatic crystallisation (Figure 4-62 (b)). The majority of zircons also show homogenous zones with darker CL response, interpreted as recrystallised zones. Thirteen analyses were carried out on different zircon grains during two analytical sessions and are characterised by low U (50-164 ppm) and Th (35-96 ppm), with Th/U ranging from 0.67 to 0.89 (Table 13-22). The zircons have variable f^{206} ranging up to 0.43% in most cases, but higher values for analyses LW10-7 (1.84%) and LW10-10 (1.60%). The low contents of U and Th result in a low precision for the analyses, which scatter around concordia and define a weighted mean $^{207}\text{Pb}/^{206}\text{Pb}$ age of 1594 ± 30 Ma (MSWD=2.9)(Figure 4-63). The high MSWD value of 2.9

reflects the wide scatter of the data and suggests poor data quality or that the data contain more than one age group. Calculating a weighted mean $^{207}\text{Pb}/^{206}\text{Pb}$ age for eight data points with f_{206} values below 0.25% yields an age of 1610 ± 26 Ma with MSWD of 1.5. The data cluster around the concordia and yield a concordia age of 1589 ± 15 Ma, with MSWD value 9.3. The weighted mean $^{207}\text{Pb}/^{206}\text{Pb}$ age of 1610 ± 26 Ma, which has the lowest MSWD value, is considered to represent the best estimate for the crystallisation age of the precursor to the Musalango Gneiss.

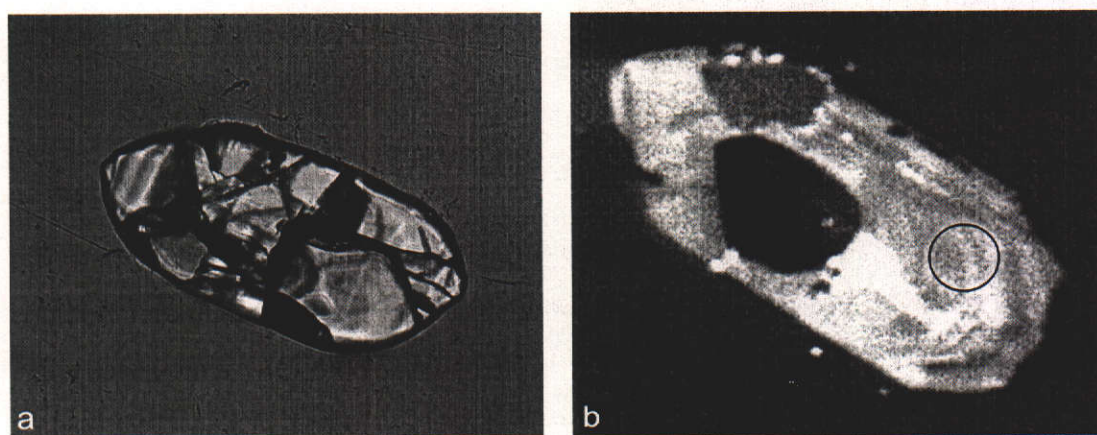


Figure 4-62: (a) photomicrograph of zircon (analysis number 2) from sample LW10 (xpl) showing euhedral habit with numerous cracks and minor inclusions (f.o.v. = $\sim 300 \mu\text{m}$); (b) CL image of the same zircon indicating the analysed spot (analysis 2). Note the faint concentric zoning consistent with magmatic growth and the dark recrystallised areas (f.o.v. = $200 \mu\text{m}$). This analysis yielded a $^{207}\text{Pb}/^{206}\text{Pb}$ age of 1615 ± 22 Ma.

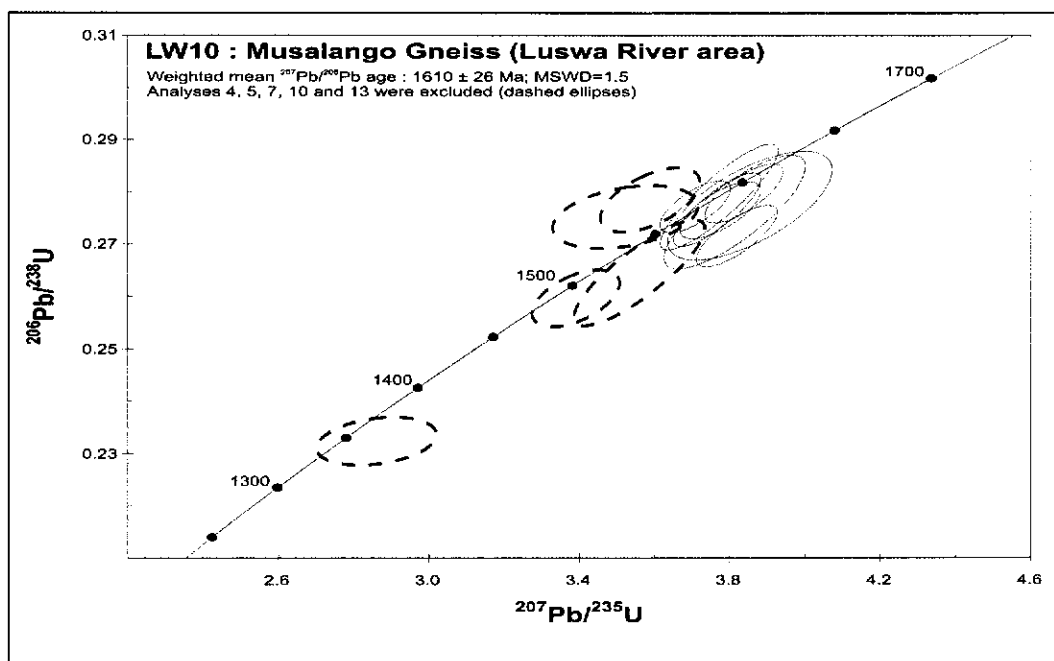


Figure 4-63: U-Pb concordia plot for zircon analyses of sample LW10. Error ellipses are at 1σ confidence level.

4.7.3 Lukamfwa Hill Granite Gneiss

The Lukamfwa Hill Granite Gneiss comprises leuco- to mesocratic biotite granites, with a strong foliation defined by aligned biotite flakes. The granite gneiss is locally sheared, displaying proto-mylonitic fabrics, and commonly contains two deformation fabrics. Four samples were collected from the Lukamfwa Hill Granite Gneiss, three from the Serenje 1:100000 map sheet (Figure 4-2, samples SER6-2c, SER6-3 and SR12) and one from the Ndabala sheet (Figure 4-1, sample ND2).

4.7.3.1 Sample SER6-2c

Sample SER 6-2c was collected a few kilometers south of Lukamfwa Hill (Figure 4-2). The outcrop consists of pink biotite granite gneiss, with a clear S_1 foliation defined by biotite along northerly trends, dipping shallow to the east. In places a strong crenulation occurs, defining a steep S_2 crenulation cleavage along northeasterly trends. Microcline phenocrysts are affected by the D_2 event and

show alignment along S_2 . Discrete shear zones along a northeast direction have resulted in grain reduction and proto-mylonitisation. Zircons from SER 6-2c can be subdivided into three main types. A limited number of zircons contain an igneous core, with oscillatory zonation typical for igneous crystallisation, surrounded by a substantial zone recording a second phase of igneous crystallisation (Figure 4-64). The majority of zircons have an apparently simple primary igneous nature with well defined concentric zoning. A third zircon population has very low CL response, poorly developed zonation and consists of quite small (~50 micron) grains. Eleven analyses were performed on nine separate zircons covering the first two morphological types. Th/U varies from 0.38 to 1.16 and f_{206} ranges from 0.04 to 0.61%, with high values for two cores (SER62-41c (14.98%) and SER62-26c (0.99%))(Table 13-24). U and Th values are quite low for analyses 26c, 28 and 29 (< 100 ppm) and extremely high for analyses SER62-32 and 41c. The high U content of 41c, coupled with the high f_{206} value of 14.49%, indicates substantial disturbance of the isotopic ratios in this core, which plots well away from concordia (Figure 4-65). In both analysed complex zircons, core and rim yielded statistically indistinguishable $^{207}\text{Pb}/^{206}\text{Pb}$ ages. Regression of all data points yields an upper intercept of 1660 ± 12 Ma and a lower intercept of 73 ± 150 Ma (MSWD=2.9). A weighted mean $^{207}\text{Pb}/^{206}\text{Pb}$ age on all data points yields 1659 ± 11 Ma (MSWD=2.86). Using only the eight near concordant (>95%) points, a concordia age of 1664 ± 6 Ma with MSWD of 0.01 is obtained. All calculated ages are within error of each other, and the concordia age of 1664 ± 6 Ma is taken as the best estimate for the crystallisation age of the precursor granite of the Lukamfwa Hill Granite Gneiss recorded by sample SER 6-2c.

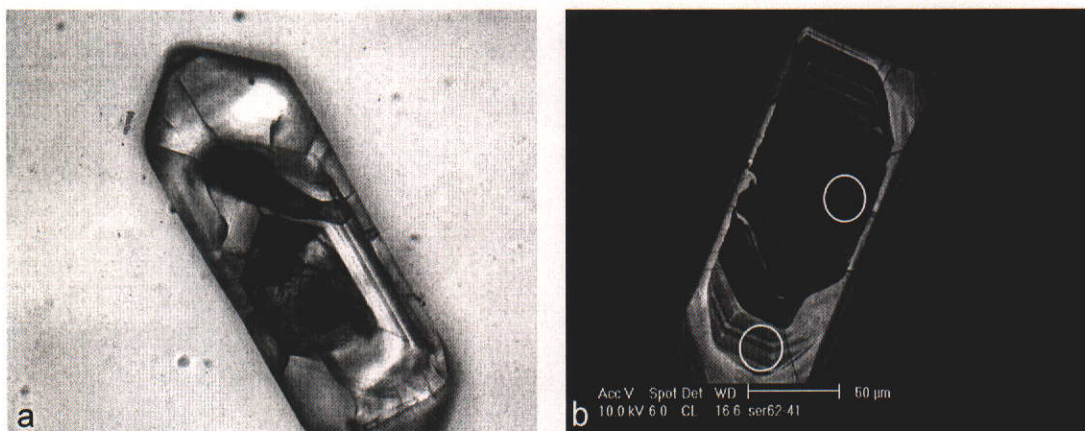


Figure 4-64: (a) photomicrograph of a zircon (analysis SER62-41) from sample SER6-2c (xpl) showing euhedral habit with minor cracks and inclusions (f.o.v. = ~300 μm); (b) CL image of the same zircon showing the location of analysed spots in the core and magmatic rim. Note the concentric zoning on the rim, and very dark luminescence of the core (f.o.v.= 300 μm). $^{207}\text{Pb}/^{206}\text{Pb}$ ages obtained were 1660 ± 145 and 1625 ± 37 Ma respectively.

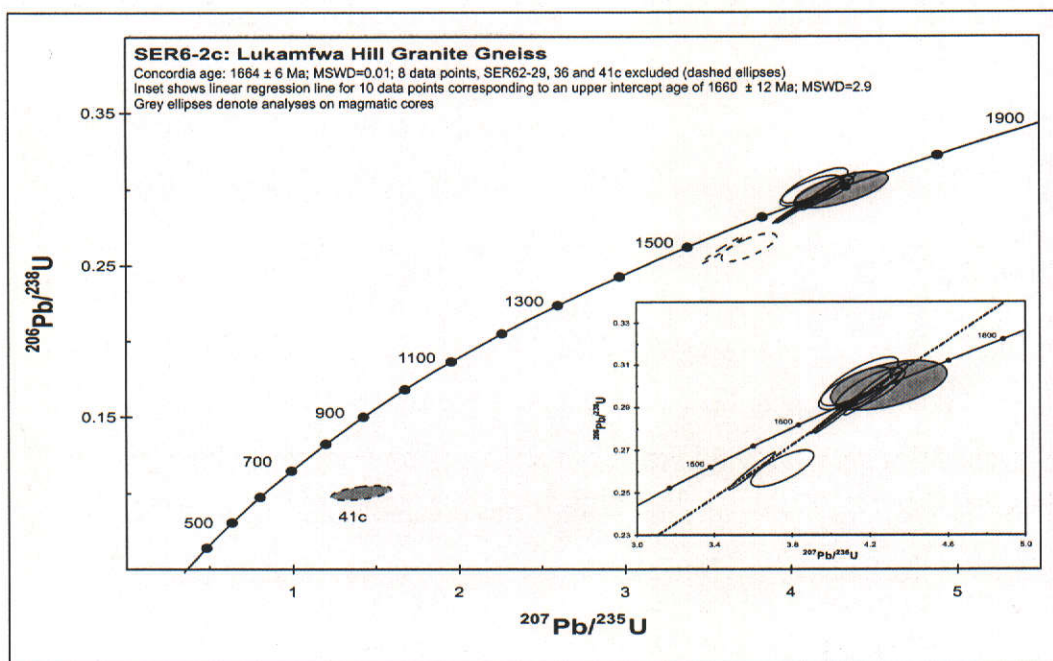


Figure 4-65: U-Pb concordia plot for zircon analyses of sample SER6-2c. Error ellipses are at 1σ confidence level.

4.7.3.2 Sample 6-3

Sample 6-3 was collected from Lukamfwa Hill, which forms an inselberg rising thirty meters above the plateau (Figure 2-10 and Figure 2-54) and consists of a coarse-grained quartz-microcline-plagioclase-biotite granite gneiss, with the main foliation crenulated by an S_2 cleavage. The bulk of Lukamfwa Hill consists of porphyroclastic granite gneiss, with large cm-size porphyroclasts of K-feldspar set in a strongly deformed biotite-plagioclase-quartz matrix. Locally, high-strain shear zones cut the granite, giving rise to mylonitic zones of fine-grained feldspathic gneiss, in which pegmatitic quartz veins have developed. Two main types of zircon grains were separated from sample SER 6-3. A large fraction of zircons has quite small grain sizes (~ 100 micron), and has a very low CL response. In transmitted light, this population is brownish in colour and in places appears slightly metamict, suggesting high uranium content. A faint oscillatory zoning suggests these zircons are of primary (magmatic) origin. A second zircon population consists of larger prismatic grains (~ 200 micron in length), with well-developed oscillatory alternation of high-CL and low-CL zones (Figure 4-66). Part of this population displays localised recrystallisation and homogenisation. Ten analyses were conducted on ten zircon grains showing oscillatory zoning. The proportion of common Pb is generally quite low, ranging from 0.06 to 0.36% (Table 13-25). U and Th contents are between 200 and 500 ppm, with Th/U ranging from 0.59 to 1.11. The data form a tight age cluster (Figure 4-67) for which a weighted mean $^{207}\text{Pb}/^{206}\text{Pb}$ age of 1653 ± 7 Ma is calculated (MSWD=1.23). With all data points at least 97% concordant, a concordia age of 1652 ± 6 Ma can be calculated with an MSWD of 1.3. This concordia age is considered the best estimate for the igneous crystallisation age of the precursor granite of the Lukamfwa Hill Granite Gneiss at the sample locality.

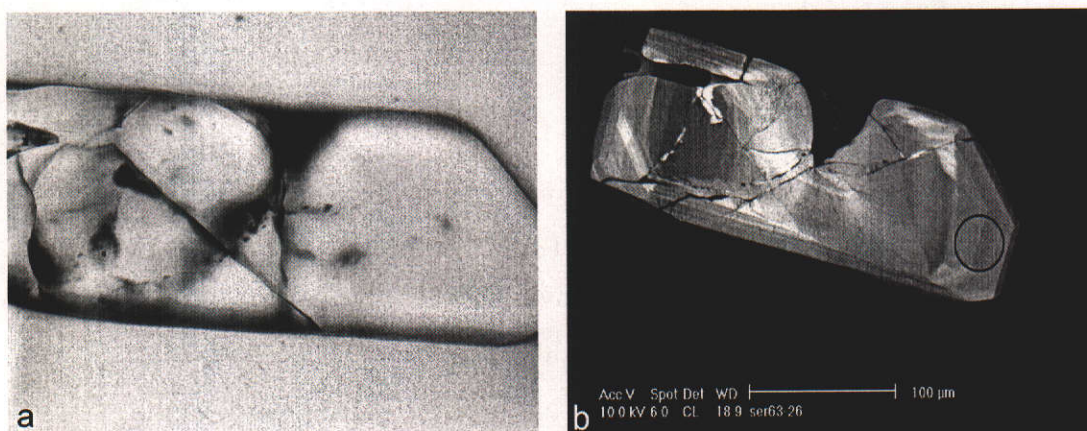


Figure 4-66: (a) photomicrograph of a zircon (analysis SER63-29) from sample SER6-3 (xpl) showing euhedral habit with cracks and minor inclusions (f.o.v. = ~200 µm); (b) CL image of the same zircon showing the location of the analysed spot. Note the concentric zoning (f.o.v.= 300 µm). This spot yielded a $^{207}\text{Pb}/^{206}\text{Pb}$ age of 1632 ± 13 Ma.

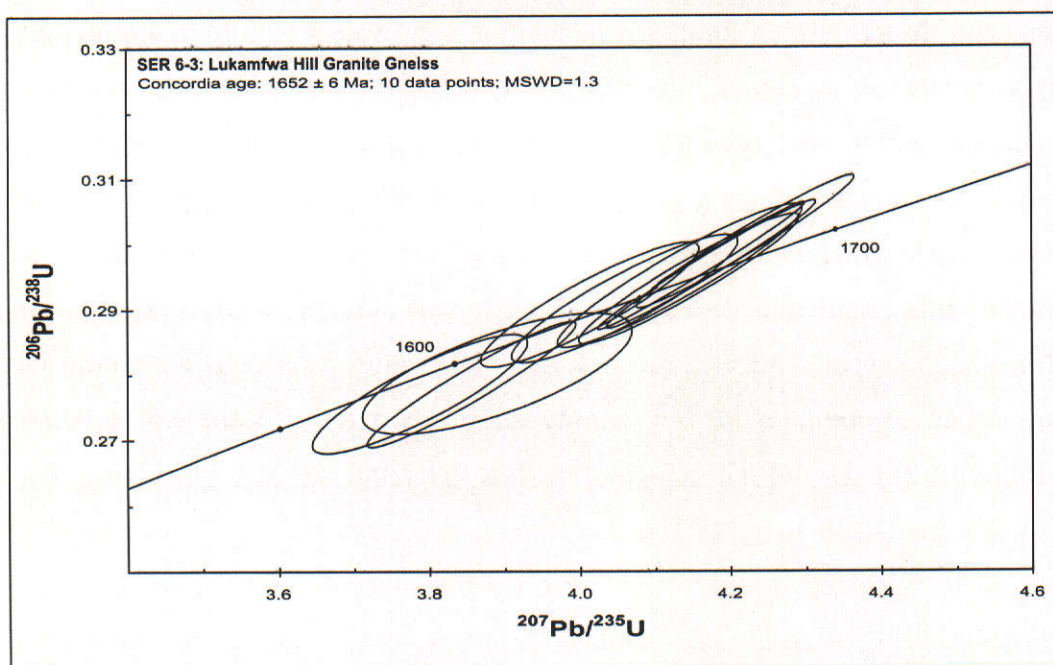


Figure 4-67: U-Pb concordia plot for zircon analyses of sample SER6-3. Error ellipses are at 1 σ confidence level.

4.7.3.3 *Sample SR12*

Sample SR12 was collected some 15 km west of Lukamfwa Hill, from a small isolated outcrop consisting of strongly foliated, pinkish grey biotite granite gneiss (Figure 4-1 and Figure 4-2). Zircons from sample SR12 are elongate, prismatic, and measure up to 350 μm in length, with length to width ratios of up to 5:1. The crystals are clear to pale yellow, have few inclusions and are variably cracked. CL imaging shows simple concentric zoning patterns, with very narrow low CL rims (Figure 4-68). Seven analyses were conducted on seven different zircons. Th/U ratios range from 0.63 to 1.19 and f_{206} is quite low ($\leq 0.82\%$) (Table 13-26). All data are near concordant ($>97\%$ concordant) and define a well-constrained weighted mean $^{207}\text{Pb}/^{206}\text{Pb}$ age of 1639 ± 14 Ma (MSWD=0.91)(Figure 4-69). Pb-loss has displaced three analyses (SR12-2, 3 and 8) away from concordia and allows a linear regression, which yields an upper intercept age of 1639 ± 26 Ma and lower intercept of 903 ± 660 Ma (MSWD=0.019). Both the upper intercept and weighted mean $^{207}\text{Pb}/^{206}\text{Pb}$ age are within error of each other, but the regression has a larger error due to limited spread of data and relatively poor precision of each analysis. The weighted mean $^{207}\text{Pb}/^{206}\text{Pb}$ age is therefore taken as the best estimate for the crystallisation age of the precursor granite of the Lukamfwa Hill Granite Gneiss recorded by sample SR12.

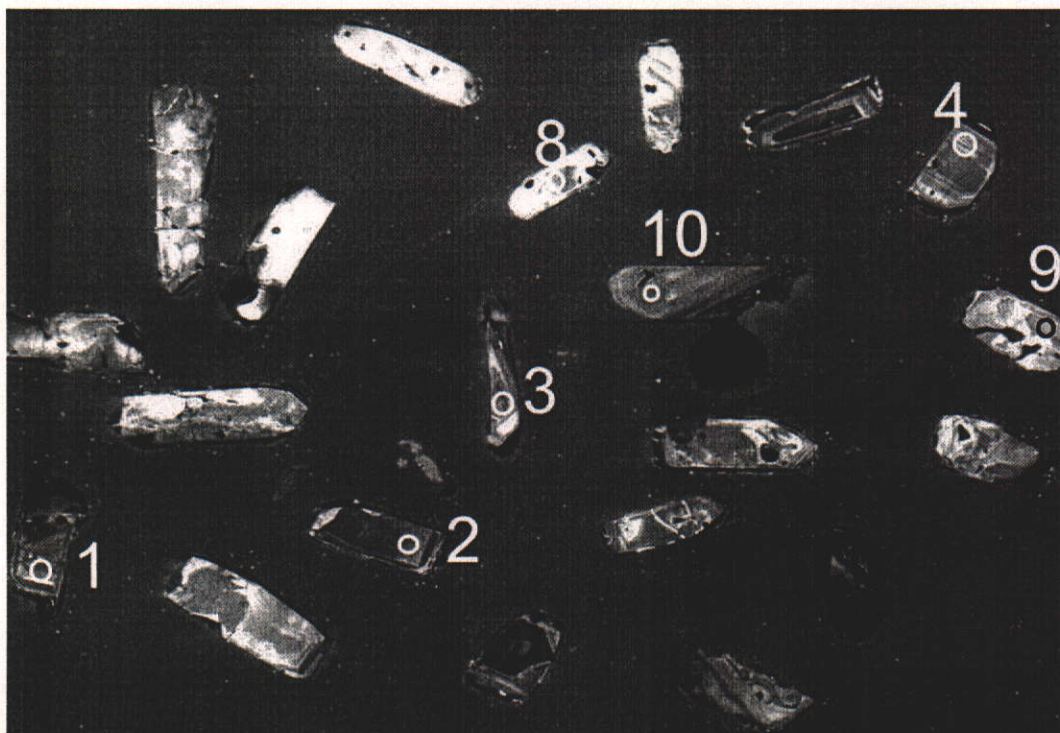


Figure 4-68: CL image of zircons from sample SR12 showing the location of seven analysed spots. (f.o.v.= 1500 μm).

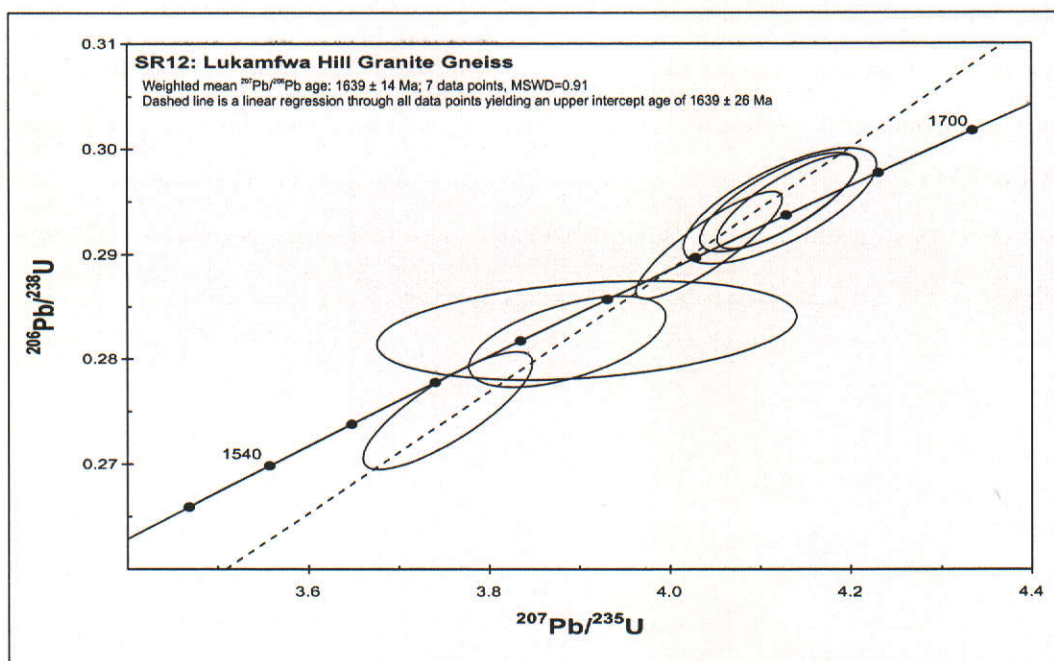


Figure 4-69: U-Pb concordia plot for zircon analyses of sample SR12. Error ellipses are at 1 σ confidence level.

4.7.3.4 *Sample ND2*

Sample ND2 was taken from a small quarry in the Ndabala 1:100000 map sheet where the granite gneiss is dark grey, strongly foliated, and consists of plagioclase, microcline, quartz and biotite. Various aplitic dykes and small pegmatites cut the gneiss along discrete shear zones. The dykes contain minor amounts of chalcopyrite and are undeformed. The gneiss is strongly deformed, with K-feldspar drawn into an augen texture, and biotite defining a strong foliation along northeasterly trends. Zircons from sample ND2 are between 100 and 300 μm in size and euhedral in shape (Figure 4-70). Bipyramidal terminations and concentric zoning patterns under CL attest to a probable magmatic origin. The length to width ratios of the zircons reach up to 5:1, and the crystals range from clear and colourless to cracked and dark yellow (Figure 4-70). Most zircons have small inclusions. Four analyses were conducted on different zircon grains (Table 13-27). The proportion of common Pb is very low, ranging up to 0.091%, and U and Th range from 103 to 229 ppm and 82 to 196 ppm respectively, giving Th/U ratios between 0.80 and 0.88. The data are near concordant, and define an age group with a weighted mean $^{207}\text{Pb}/^{206}\text{Pb}$ age of 1631 ± 15 Ma (MSWD=0.30)(Figure 4-71). A concordia age of 1627 ± 12 Ma with an MSWD value of 0.73 can be calculated on the data points, and is taken as a reliable estimate for the igneous crystallisation age of the protolith granite.

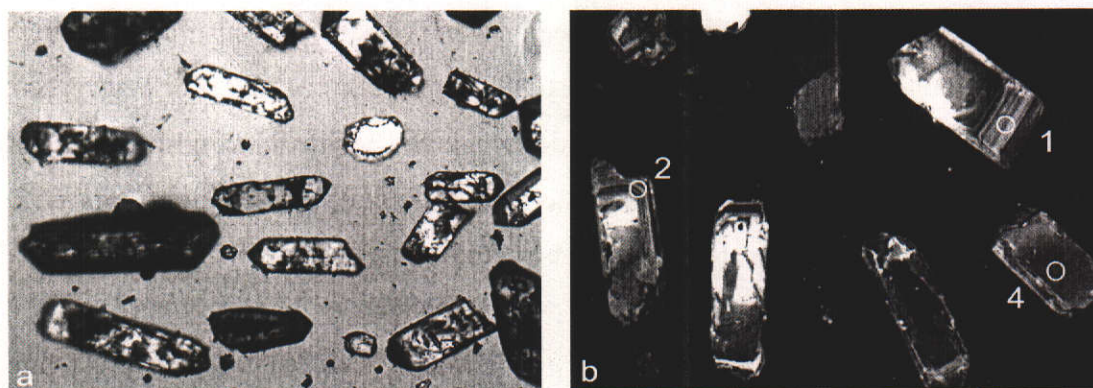


Figure 4-70: (a) photomicrograph of zircons from sample ND2 (xpl) showing euhedral crystals with minor cracks and inclusions (f.o.v. = ~1200 μm); (b) CL image of zircons from sample ND2 showing three analysed spots. Note the concentric zoning (f.o.v.= 800 μm).

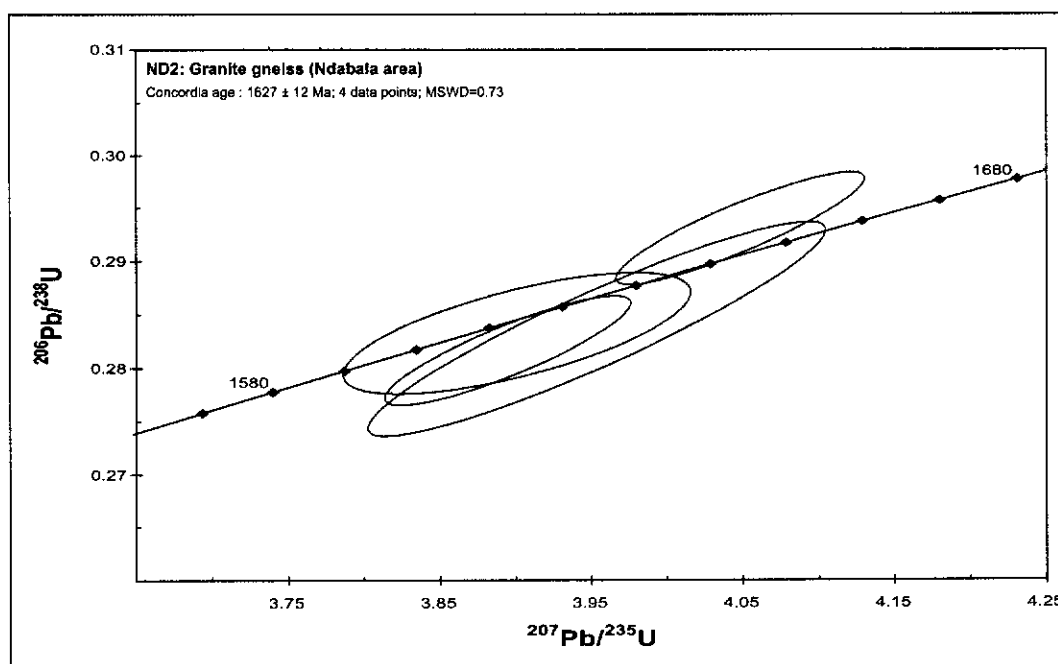


Figure 4-71: U-Pb concordia plot for zircon analyses of sample ND2. Error ellipses are at 1σ confidence level.

4.8 Mildly deformed to undeformed Irumide granitoids

The majority of granitoids exposed in the Irumide belt form large, often interconnected batholiths, consisting of coarse-grained, K-feldspar-phyric biotite granites, which remain remarkably similar along strike in the belt. Because extensive mapping in the northeastern Irumide belt was conducted by Daly (1995b; 1995a), who mapped four 1:100000 geological map sheets, granitoid bodies in that part of the belt have been given formal names, whereas no such nomenclature has been applied to the southwestern Irumide belt. For that reason, the porphyritic granites of the Irumide belt are discussed below according to formal nomenclature for the northeastern Irumide belt, whereas the porphyritic granitoids in the southwestern Irumide belt are discussed in separate sections.

4.8.1 The Lufila Granite (Bemba batholith, sample SH8)

The Lufila Granite was sampled (sample SH8) from one locality to the west of Chinsali (Figure 4-4). At the sampling site, the Lufila Granite consists of reddish unfoliated biotite granite, which crops out as rounded boulders. The K-feldspar phenocrysts define a crude primary flow fabric. Very few zircons were extracted from the granite and range in size from 50 to 100 μm (Figure 4-72 (a)). The length to width ratio ranges from 3:1 to 2:1 and the zircons are generally clear and pale yellow, with minor cracks and inclusions. In CL, the crystals show low response indicative of relatively high U content (Figure 4-72 (b)). Only two analyses were conducted, and yield relatively high f_{206} values of 0.95 and 1.25%. U and Th range from 269-689 ppm and 219-235 ppm respectively, giving Th/U ratios between 0.35 and 0.84 (Table 13-28). The two analyses are 6 and 20% discordant and define a weighted mean $^{207}\text{Pb}/^{206}\text{Pb}$ age of 1001 ± 44 Ma (MSWD=0.88)(Figure 4-73). The same granite was dated using nine whole-rock Rb-Sr analyses and yielded an age of 947 ± 89 Ma with an MSWD of 2.0 (Daly, 1986b). Taken together, these data appear to support a crystallisation age of the Lufila Granite of around 1000 Ma. A more rigorous age estimate awaits additional work.

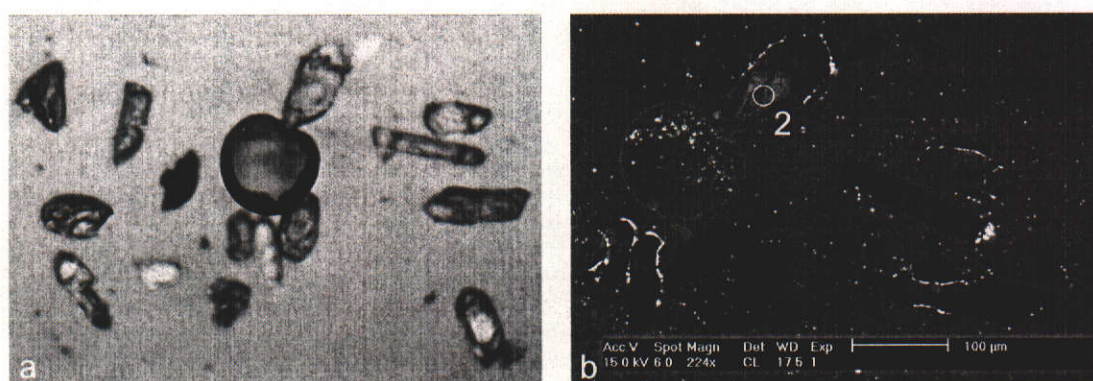


Figure 4-72: (a) photomicrograph of zircons from sample SH8 (xpl) showing sub-euhedral habit with cracks and minor inclusions (f.o.v. = ~800 μm); (b) CL image of zircons from sample SH8 showing the location of analysis SH8-2. Note the faint concentric zoning (f.o.v.= 500 μm).

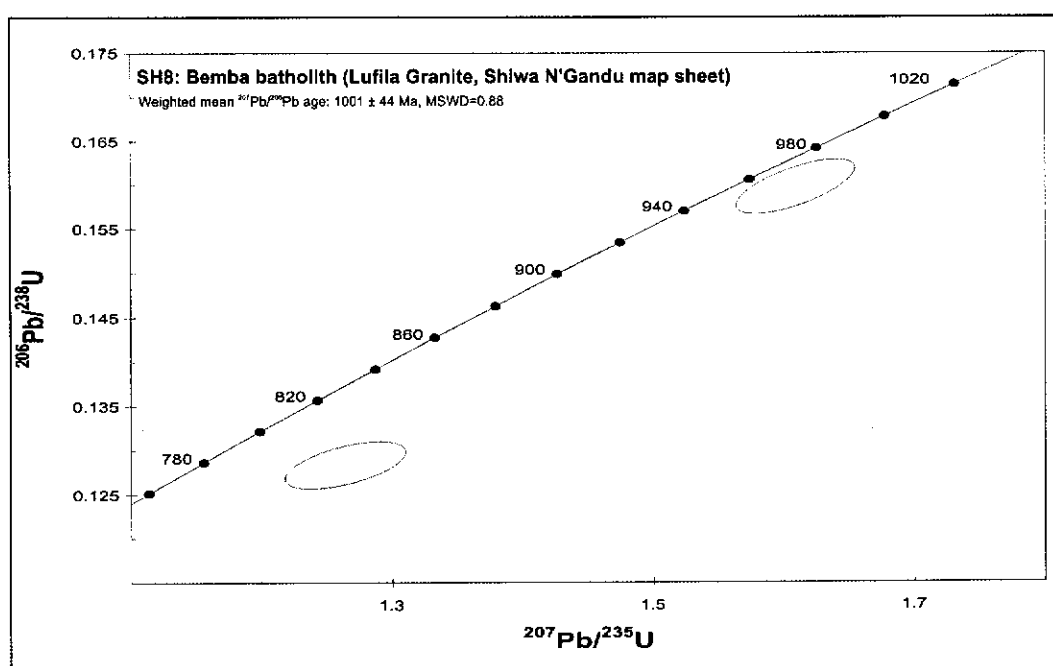


Figure 4-73: U-Pb concordia plot for analyses of SH8. Error ellipses are at 1 σ confidence level.

4.8.2 Luswa River leuco-syenite gneiss (sample LW2)

Sample LW2 was collected from a leuco-syenite gneiss in the Luswa River area (Figure 4-4). The gneiss forms a kilometre-sized lens-shaped body and occurs adjacent to strongly foliated granite mapped as part of the Musalango Gneiss. The leuco-syenite gneiss is very rich in feldspar and characterised by spectacular perthite development. Zircons collected from sample LW2 are yellow to brown, sub- to euhedral, and have length to width ratios of up to 3:1 (Figure 4-74 (a)). Because their original size often exceeded 500 μm , most zircons were cracked and broken into pieces that could pass through 300 μm mesh. Some of the crystals contain abundant small inclusions, imparting a cloudy look. CL response is variable and reveals portions with concentric zoning, consistent with magmatic growth (Figure 4-74 (b)). Analyses were conducted on clear, uncracked sections of the crystals, exhibiting oscillatory zoning patterns. Eight analyses were done on different zircon grains and indicate variable common lead (f_{206} values of 0.03 to 1.29%) and Th/U (0.18 to 3.36) (Table 13-29). Analysis LW2-2 yielded very low U (68 ppm) and relatively high f_{206} (0.84%). For these reasons it was excluded from the calculations. The data plot close to concordia (with the exception of

LW2-2) and yield a weighted mean $^{207}\text{Pb}/^{206}\text{Pb}$ age of 953 ± 19 Ma (MSWD=0.62)(Figure 4-75). A linear regression of seven data points results in an upper intercept age of 951 ± 27 Ma, and a lower intercept age of 289 ± 720 Ma (MSWD=0.63). A concordia age of 943 ± 5 Ma (MSWD=0.23) can be calculated for three near concordant points (LW2-5, 5 and 6). The latter result is taken as the best estimate for the crystallisation age of the Luswa River leuco-syenite gneiss.

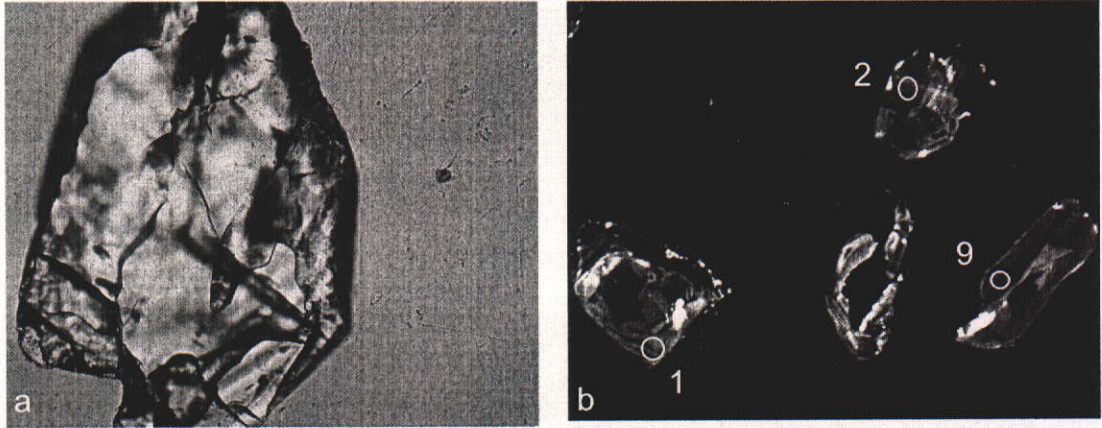


Figure 4-74: (a) typical zircons from sample LW2 (xpl) showing subhedral habit with cracks and minor inclusions (f.o.v. = ~200 µm); (b) CL image of zircons of sample LW2 showing the location of analyses. Note the faint concentric zoning, disrupted by recrystallisation (f.o.v.= 500 µm).

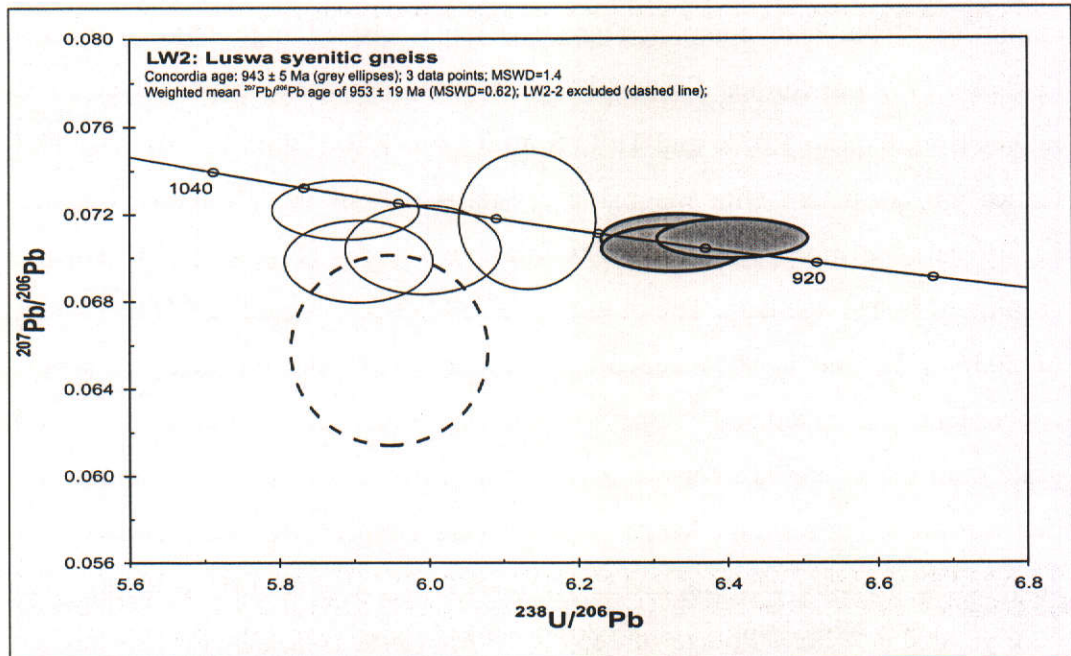


Figure 4-75: U-Pb concordia plot (Tera-Wasserburg) for zircon analyses of sample LW2. Error ellipses are at 1σ confidence level. Data are corrected for common Pb.

4.8.3 The Chilubanama (grey) Granite

The Chilubanama Granite (Daly's "Grey" granite (1986b)) was sampled from three different localities in the Chinsali and Luswa River sheets (samples ZM32, MTG4 and LW1; Figure 2-12 and Figure 4-4). In all localities, the unit consists of grey, biotite granite, with minor garnet in the case of MTG4. The Chilubanama Granite is commonly unfoliated and in places shows primary igneous fabrics.

4.8.3.1 Sample ZM32

Zircons extracted from sample ZM32 were few and of varying morphology. One type of grain is large, rounded, and pale brown in colour due to numerous inclusions, while a second type is elongate, prismatic and very clear, with no inclusions (Figure 4-76). A total of five analyses were conducted on different grains, and an additional analysis (ZM32-1.1) was done on a core of a complex grain, while a rim analysis on the same grain was aborted due to high counts on ^{204}Pb . One completed analysis that recorded high f_{206} of 23.88% (ZM32-4.1) is not further discussed here. For the remaining five analyses, f_{206} ranges from 0.04 to 1.02% and Th/U from 0.52 to 1.10 (Table 13-30). The Th/U values are consistent with magmatic crystallisation of these zircons, but their highly variable morphology suggests multiple sources (Figure 4-76), which is confirmed by the age data. The oldest grain (ZM32-5.1) records a $^{207}\text{Pb}/^{206}\text{Pb}$ age of 2036 ± 30 and is 95% concordant (Figure 4-77). As the analysis is 95% concordant, the calculated $^{207}\text{Pb}/^{206}\text{Pb}$ age represents the minimum age of this grain, and the zircon is interpreted as a xenocryst derived from the source rock that was melted to form the Mutangoshi Gneissic Granite. The second oldest grain analysed is the core analysis ZM32-1.1 discussed above (Figure 4-76 (b)). This core yielded a $^{207}\text{Pb}/^{206}\text{Pb}$ age of 1859 ± 19 Ma (94% concordant). This analysis has a relatively high f_{206} of 0.32%, resulting in a relatively large correction for common Pb, and this age is taken as the minimum age of crystallisation of this zircon, which is interpreted as a xenocrystic core. A third analysis of a xenocrystic

zircon was conducted on ZM32-2.1 and yielded a $^{207}\text{Pb}/^{206}\text{Pb}$ age of 1649 ± 23 Ma (98% concordant). With a low f_{206} and high concordance, this age is taken to closely approximate the crystallisation of this zircon. The two other zircons are significantly younger and record poorly constrained $^{207}\text{Pb}/^{206}\text{Pb}$ ages of 946 ± 50 Ma and 853 ± 85 Ma. Both display elevated f_{206} values (1.02 and 0.75% respectively), and are slightly reversely discordant (104% and 108% concordant). The large uncertainties on these data mean that the analyses are difficult to interpret, but suggest that the Chilubanama Granite was emplaced at ~ 1.0 Ga. The data on three xenocrysts indicate that the Chilubanama Granite sampled at least three different sources in its ascent. The oldest sources can be ascribed to the original source rock of the Mutangoshi Gneissic Granite and to felsic units in the Bangweulu block, generally bracketed between 2050 and 1850 Ma. The 1859 ± 19 Ma grain corresponds closely to the age of volcanics reported in this study. The age of 1649 ± 23 Ma obtained on ZM32-2.1 corresponds to the protolith age of the Musalango Gneiss, dated at 1610 ± 26 Ma in the Luswa River 1:100000 map sheet to the west. It may be noted that in an alternative interpretation the Chilubanama Granite could have been derived from partial melting of a single sedimentary source containing detritus of various ages.



Figure 4-76: (a) photomicrograph of zircons from sample ZM32 (xpl) showing sub-euhedral habit with cracks and minor inclusions (f.o.v. = ~ 1500 μm); box indicates the area of next photograph (b) detail of zircon ZM32-1.1 (center), which was analysed twice, once on the core (1859 ± 20 Ma), and once on the rim (abandoned due to high ^{204}Pb counts)(f.o.v.= ~ 400 μm). Note the highly variable morphology and clarity of the crystals, suggesting multiple sources.

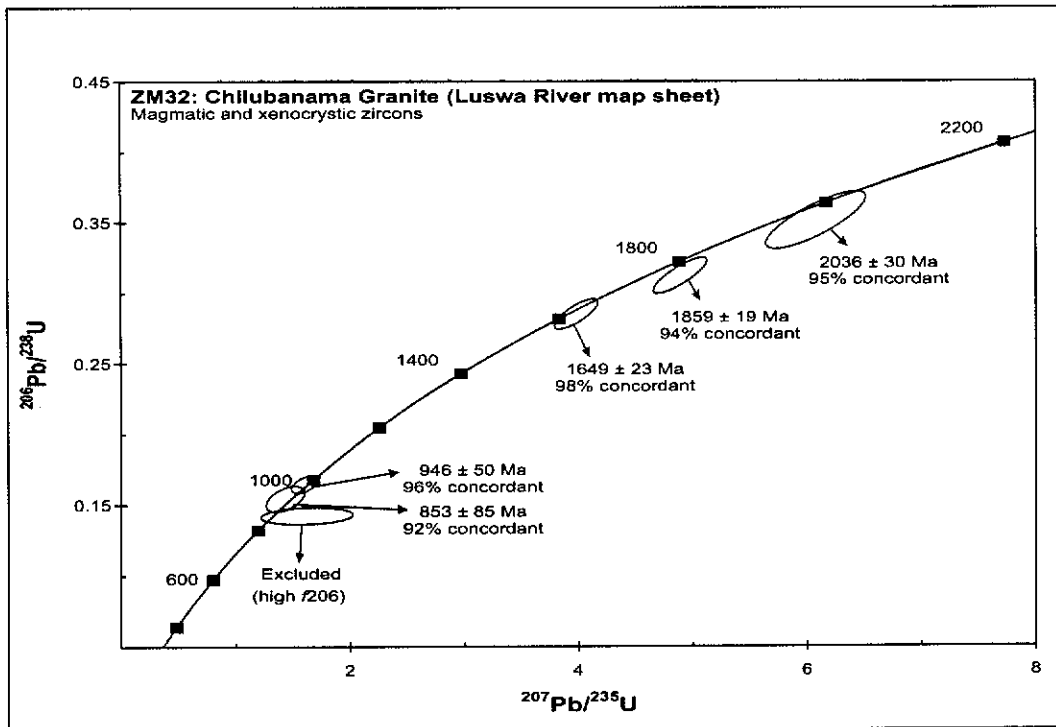


Figure 4-77: U-Pb concordia plot for zircon analyses of sample ZM32. Error ellipses are at 1 σ confidence level. $^{207}\text{Pb}/^{206}\text{Pb}$ ages and concordance are indicated.

4.8.3.2 Sample MTG4

Zircons from MTG4 are equant to elongate, euhedral and concentrically zoned. They range from colourless and transparent to light yellowish in colour and are predominantly clear and relatively free of inclusions (Figure 4-78). Length to width ratios vary up to 4:1, with crystals ranging in size from 100 to 400 μm . CL imaging reveals rounded and irregular, zoned and unzoned cores in about 75% of the grains, surrounded by rims with low CL response (Figure 4-78). High ^{204}Pb counts resulted in the termination of many analyses, and only five core/rim pairs, together with one core and two rims from three different grains were analysed. f_{206} ranges up to 4.33%, but does not exceed 1% for ten out of thirteen analyses. Uranium and thorium range from 124 to 1201 ppm and 9 to 820 ppm respectively, with Th/U ratios ranging from 0.02 to 1.34. Th/U ratios for analyses MTG4-4r, 8r, 9r and 10r are below 0.1, suggesting these zircon rims developed during metamorphism. The equally low Th/U ratio of core MTG4-10c may reflect solid-state recrystallisation of this zircon during the metamorphic event that created the rims. The oldest cores analysed (MTG4-7c, MTG4-4c and MTG4-1c) yielded

$^{207}\text{Pb}/^{206}\text{Pb}$ ages of 2045 ± 11 Ma (106% concordant), 2017 ± 17 Ma (97% concordant) and 2010 ± 8 Ma (98% concordant)(Figure 4-79). The f_{206} for these analyses ranges from 0.03 to 0.66% and the calculated ages are interpreted as approximating the original crystallisation ages of these zircons. Another core (MTG4-8c) yielded a $^{207}\text{Pb}/^{206}\text{Pb}$ age of 1425 ± 47 Ma (98 % concordant), but has a high f_{206} value of 2.48%. The Chilubanama Granite thus appears to have sampled sources with estimated ages of ~2050-2000 Ma (cores MTG4-1c, 4c and 7c) and 1425 ± 47 Ma (core MTG4-8c). The remaining nine data points, which comprise four cores (MTG4-5c, 6c, 9c and 10c) and five rims (MTG4-1r, 4r, 8r, 9r and 10r) are over 90% concordant and define a coherent age group with weighted mean $^{207}\text{Pb}/^{206}\text{Pb}$ age of 1019 ± 13 Ma (MSWD=1.6). Excluding analysis MTG4-5c based on its high f_{206} value of 4.33%, a concordia age of 1010 ± 11 Ma can be calculated (MSWD=1.4). The low MSWD of both $^{207}\text{Pb}/^{206}\text{Pb}$ and concordia ages, which include analyses on magmatic cores and metamorphic rims, indicates that the low Th/U rims developed very soon after crystallisation of the magmatic zircon and that the ages of igneous crystallisation and metamorphism are statistically indistinguishable. Three analyses (MTG4-1r, 6c and 9c), from zircon with Th/U ratios ranging from 0.12 to 1.22 and interpreted as magmatic, yield a concordia age of 1010 ± 22 Ma (MSWD=0.19). The low Th/U zircon rims (MTG4-4r, 8r, 9r and 10r), which could have formed during metamorphism, define a concordia age of 1004 ± 16 Ma (MSWD=0.81)(Figure 4-80), within error of the age on magmatic zircon in the Chilubanama Granite. The granite thus could have been emplaced during a metamorphic event dated at 1004 ± 16 Ma, with the concordia age of the three magmatic zircons recording crystallisation of the Chilubanama Granite at 1010 ± 22 Ma.

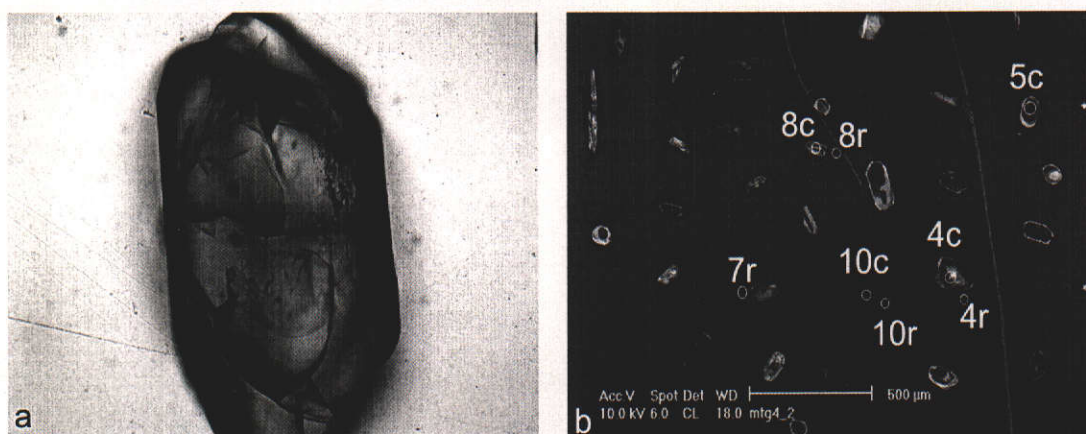


Figure 4-78: (a) photomicrograph of zircon from sample MTG4 (xpl) showing subhedral habit with cracks and minor inclusions (f.o.v. = 250 µm); (b) CL image of zircons from sample MTG4 showing analysed spots. Note the complex character of most zircons, and the dark CL rims, most of which are interpreted to have grown during a metamorphic event. Note analyses 8c and 8r, which yielded $^{207}\text{Pb}/^{206}\text{Pb}$ ages of 1425 ± 47 and 1013 ± 9 Ma respectively.

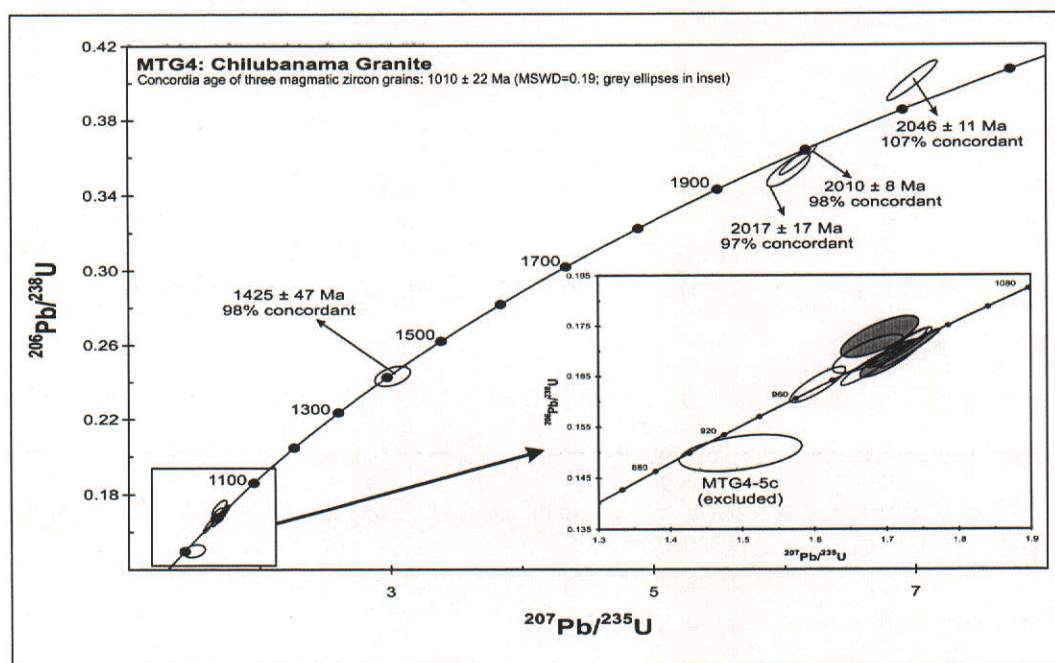


Figure 4-79: U-Pb concordia plot for zircon analyses of sample MTG4. Error ellipses are at 1σ confidence level.

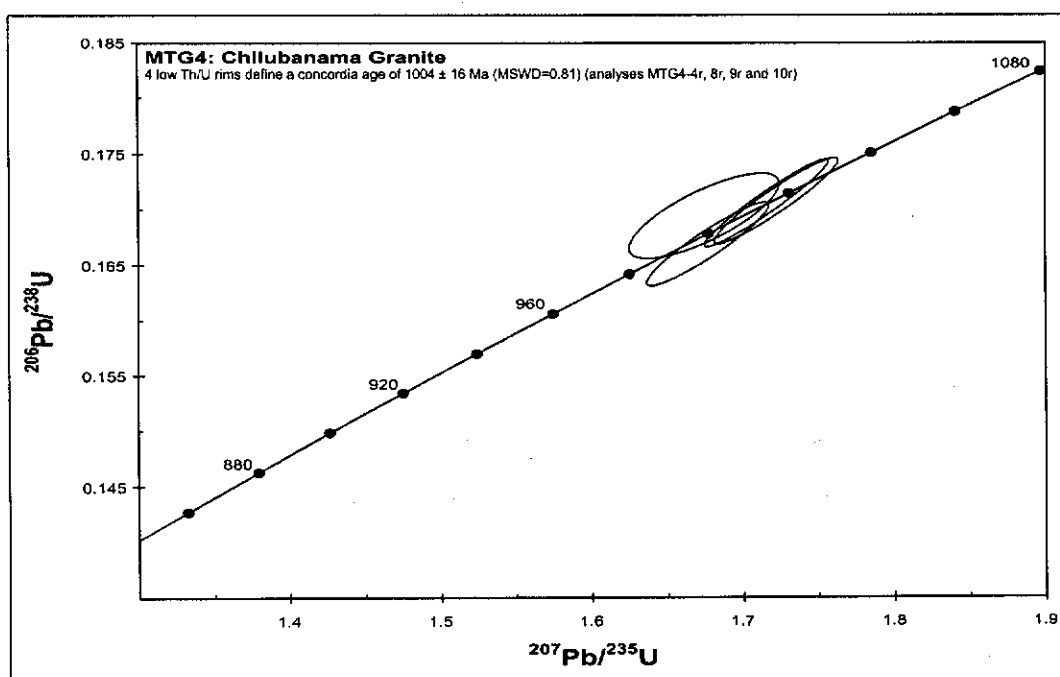


Figure 4-80: U-Pb concordia plot for concordant zircon (rim) analyses of sample MTG4. Error ellipses are at 1 σ confidence level.

4.8.3.3 Sample LW1

Zircons from sample LW1 are of widely varying morphology, from euhedral to anhedral, and range in size from 200 to 500 μm , with length to width ratios from 1:1 to 3:1. Their colour is generally light brown due to numerous inclusions and the zircons are invariably cracked. CL imagery reveals a very wide range of response from very high CL to very low CL (Figure 4-81 and Figure 4-82). Six analyses were conducted on six grains and yielded f^{206} values ranging from 0.28 to 0.97%, and Th/U ratios of 0.97 to 2.08 (Table 13-32). Analysis LW1-2 displays high Th (1001 ppm), while LW1-4 has low U and Th (57 and 83 ppm respectively), resulting in poor precision. These two points plot more than 5% away from concordia and are excluded from age calculations. One analysis (LW1-5) yields a $^{207}\text{Pb}/^{206}\text{Pb}$ age of 1005 ± 21 Ma (99.6% concordant). This zircon is subhedral, has a length to width ratio of 3:1 and has very low CL response with faint concentric zoning (Figure 4-81). Its high Th/U ratio of 1.72, together with the zoning, suggests a magmatic origin. A group of three near concordant analyses (LW1-1, LW1-6 and LW1-7) yield a concordia age of 1526 ± 12 (MSWD=0.07). These zircons are over 200 μm in size, and have low CL

response with faint oscillatory zoning (Figure 4-82). Based on the available data, no unequivocal crystallisation age can be suggested for sample MTG4 of the Chilubanama Granite. The apparent magmatic nature of the youngest zircon, however, suggests that the granite crystallised at 1005 ± 21 Ma. Whether the 1526 ± 12 Ma age for three magmatic zircons recorded in the sample reflects the protolith age of an older granite that was partially melted to form the ~ 1.0 Ga Chilubanama intrusion, or xenocrystic inheritance from country rock remains unclear. In either interpretation, the Lubu Granite Gneiss (see sample ML2) could represent the source for these zircons.

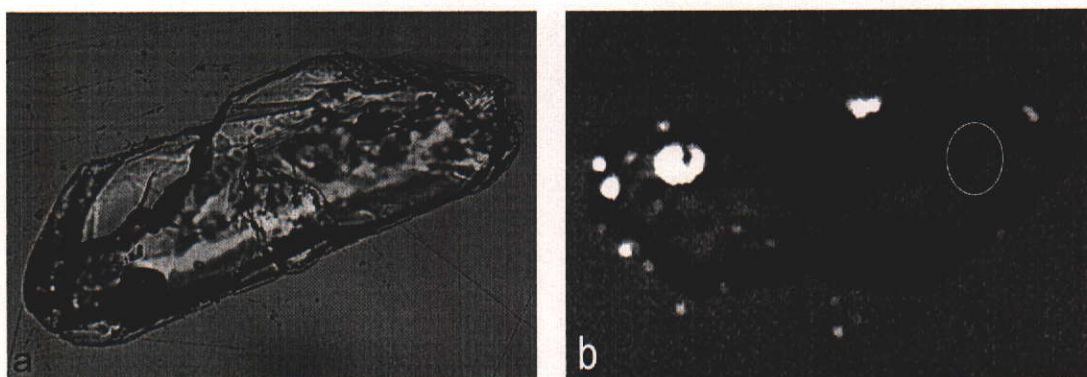


Figure 4-81: (a) photomicrograph of zircon LW1-5 (xpl) showing subhedral habit with cracks and inclusions (f.o.v. = ~ 400 μm); (b) CL image of the same zircon showing the location of analysis LW1-5. Note the faint concentric zoning (f.o.v.= 250 μm).

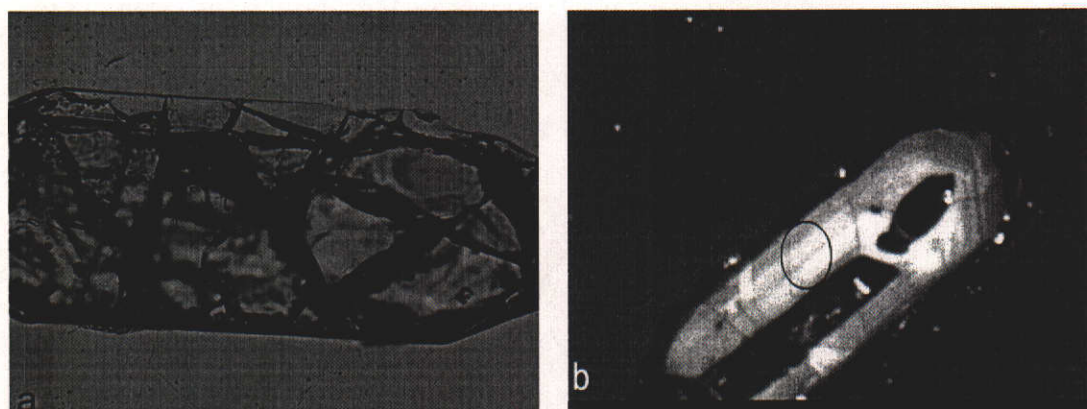


Figure 4-82: (a) photomicrograph of zircon LW1-7 (xpl) showing euhedral habit with cracks and inclusions (f.o.v. = ~ 300 μm); (b) CL image of the same zircon showing the location of analysis LW1-7. Note the concentric zoning and low CL response (f.o.v.= 400 μm).

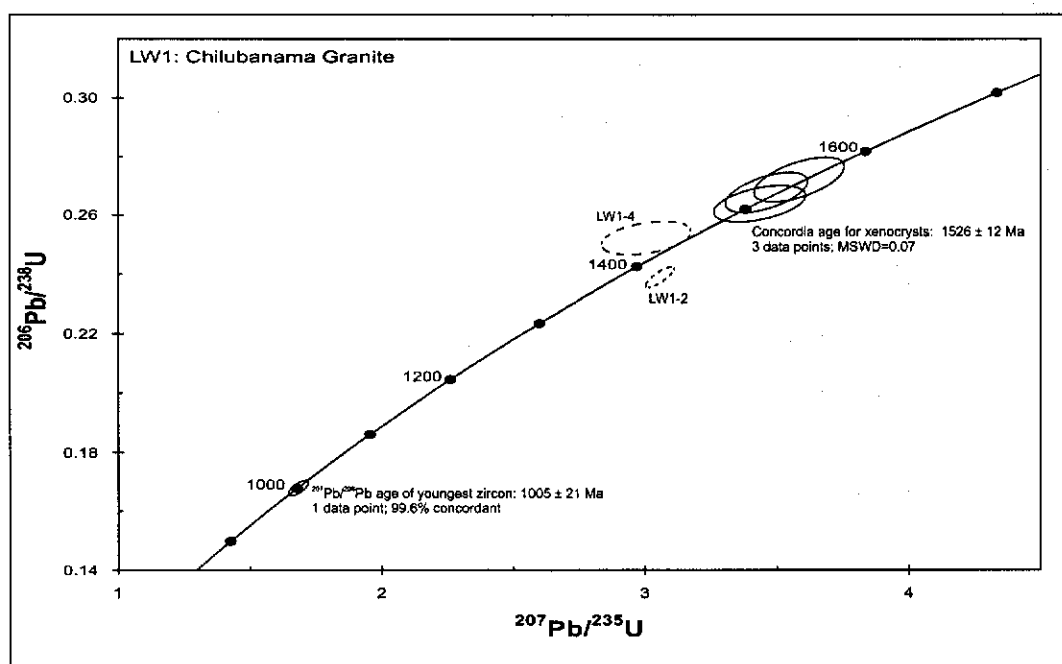


Figure 4-83: U-Pb concordia plot for zircon analyses of sample LW1. Error ellipses are at 1 σ confidence level. Dashed ellipses denote analyses excluded from age calculations.

4.8.4 Porphyritic granites

Samples KK1, MH4, MH9c, CC5, CC8, FW1, FW2, CHT6, KN2a, KN5, KN7, KN8, ND1, ND4, ND5, SASA2, SER 5-3, SER 6-4, SQG, ZM36 and CHL5 are porphyritic granitoids, some foliated, some not, with quartz – plagioclase – biotite making up the matrix, and microcline megacrysts that are often aligned along a magmatic foliation (Figure 4-1, Figure 4-2 and Figure 4-3). Sample ND4 was taken from a porphyritic diorite and represents the most basic end member of the suite. The weak foliation, sub- to euhedral shape of the K-feldspar phenocrysts and strong magmatic fabrics observed in these granites suggest that they represent syn-, late- and post-orogenic intrusions.

4.8.4.1 Sample KK1

Sample KK1 was taken from a flat lying outcrop along the sealed road between Kabwe and Kapiri Mposhi and consists of foliated porphyritic biotite granite. The granite contains elongate fine-grained angular xenoliths of mafic

material, possibly broken-up mafic dykes. A steep south-dipping foliation with an easterly trend is defined by strongly aligned biotite, wrapping around euhedral large microcline phenocrysts. Zircons from sample KK1 are large, between 200 and 500 μm in size, and euhedral in shape. Their length to width ratio varies from 4:1 to 1:1, and the crystals are colourless to pale yellow in transmitted light (Figure 4-84). Most zircons contain a small number of large inclusions and some limited cracks, but have large zones that are essentially free of inclusions and cracks. CL imaging brings out distinct oscillatory zoning and, in a few cases, a small rounded core surrounded by a wide concentrically zoned (magmatic) rim (Figure 4-84). Six analyses were conducted on six unzoned zircons and yield common f^{206} values of up to 0.92% (Table 13-33). U and Th are low, ranging from 56 to 262 ppm and 74 to 208 ppm respectively, with Th/U ratios between 0.50 and 1.35. The data vary from 4% reversely discordant to 6% normally discordant and yield a weighted mean $^{207}\text{Pb}/^{206}\text{Pb}$ age of 1021 ± 25 Ma with an MSWD value of 1.10 (Figure 4-85). The low U content results in relatively imprecise isotopic ratios and a corresponding poor precision of $^{207}\text{Pb}/^{206}\text{Pb}$ ages. Excluding the most discordant data point (KK1-6) improves the MSWD value on the weighted mean and yields an age of 1003 ± 31 Ma (MSWD=0.46). This result provides the best estimate for the igneous crystallisation age of the granite.

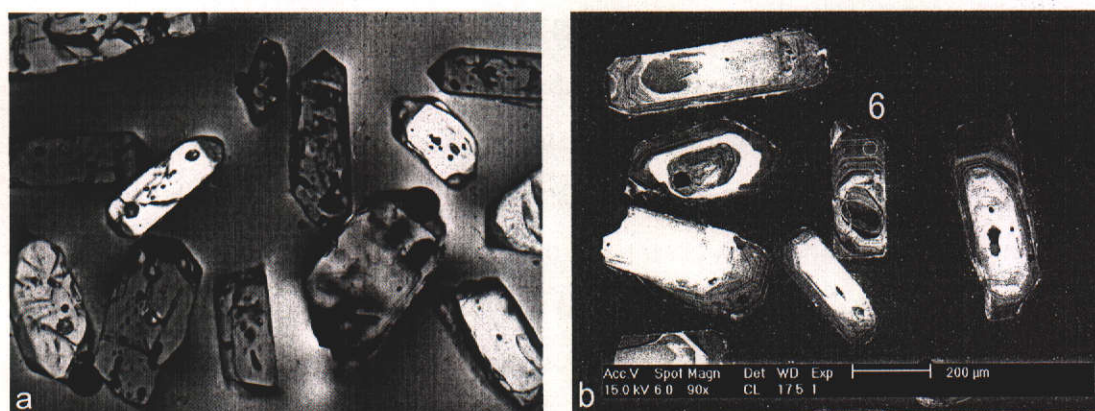


Figure 4-84: (a) photomicrograph of zircon from sample KK1 (xpl) showing euhedral crystals with minor cracks and inclusions (f.o.v. = ~1600 μm); (b) CL image of zircons from sample KK1 showing the location of analysis KK1-6. Note the prominent concentric zoning (f.o.v.= 1500 μm).

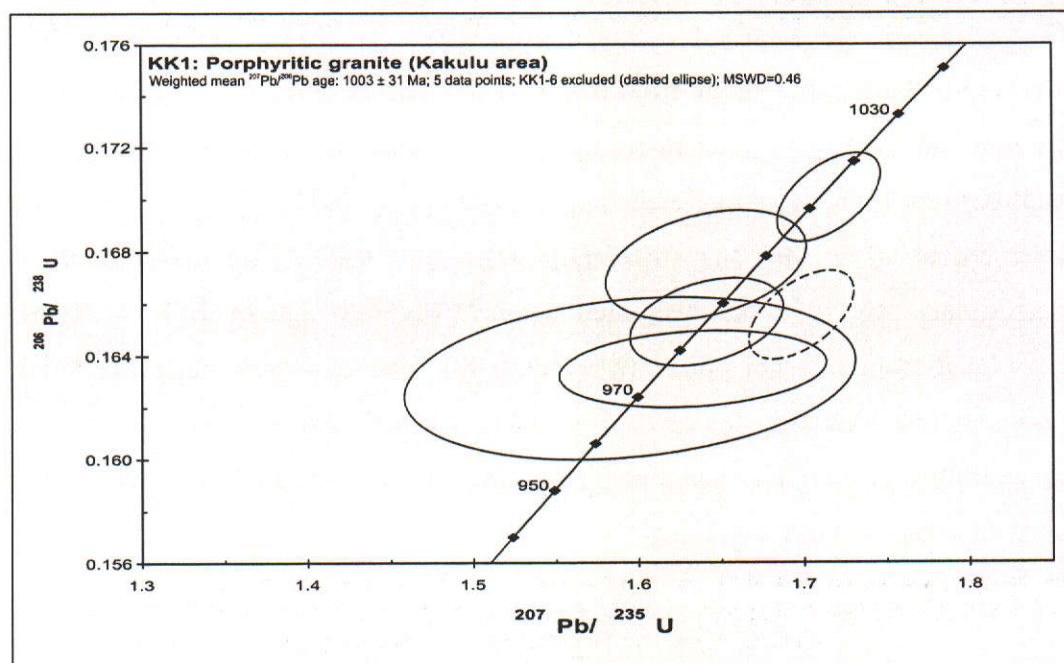


Figure 4-85: U-Pb concordia plot for zircon analyses of sample KK1. Error ellipses are at 1 σ confidence level. Dashed ellipse denotes analysis excluded from age calculation.

4.8.4.2 Sample MH4

Sample MH4 was collected from a flat outcrop of foliated porphyritic granite, cut by various aplite dykes, which are folded along axes plunging shallowly to the north. Microcline phenocrysts are euhedral and aligned along an east-west direction, defining a shallow northerly-dipping fabric interpreted as a

primary magmatic foliation. In size, the zircons vary from 200 to 300 μm and have length to width ratios of up to 3:1. In transmitted light, they are clear, pale yellow, variably cracked and some contain minor inclusions (Figure 4-86 (a)). CL imaging brings out well-defined oscillatory zoning patterns and a minority of the zircons appear to be composite in nature (Figure 4-86 (b)). In the composite grains, a semi-rounded, but essentially euhedral, core can be distinguished, which is surrounded by a concentrically zoned wide rim. The majority of complex zircon grains show abrupt changes from cores with high CL response to overgrowths with low CL response, both displaying well-defined oscillatory zoning patterns, indicating rapid fluctuations of trace elements in the melt as crystallisation progressed (Figure 4-86 (b)). Six unzoned zircons were analysed during two sessions, yielding two near concordant and four increasingly discordant analyses (Table 13-34). The f_{206} values range from 0.089 to 2.762% and U from 88 to 1418 ppm. Th/U ratios range from 0.32 to 1.67 consistent with magmatic growth. Because of the large spread in isotopic composition, the six data points yield a well-defined regression line with upper intercept at 1031 ± 31 Ma and lower intercept at 41 ± 300 Ma (MSWD=1.09)(Figure 4-87). The upper intercept corresponds well with the weighted mean $^{207}\text{Pb}/^{206}\text{Pb}$ age of 1030 ± 30 Ma calculated from all data points (MSWD=0.88). The two most concordant data points yield a concordia age of 1017 ± 19 Ma (MSWD=0.053), within error of the upper intercept age. The latter result provides the best estimate for the igneous crystallisation age of the granite.

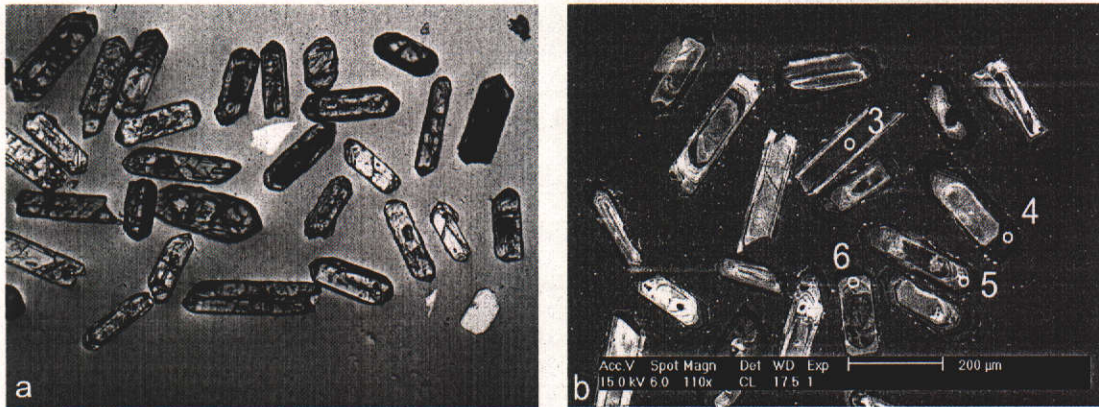


Figure 4-86: (a) photomicrograph of zircon from sample MH4 (xpl) showing euhedral crystals with minor cracks and inclusions (f.o.v. = ~1600 μm); (b) CL image of zircons from sample MH4 showing the location of analysed spots. Note the prominent concentric zoning (f.o.v. = 1500 μm).

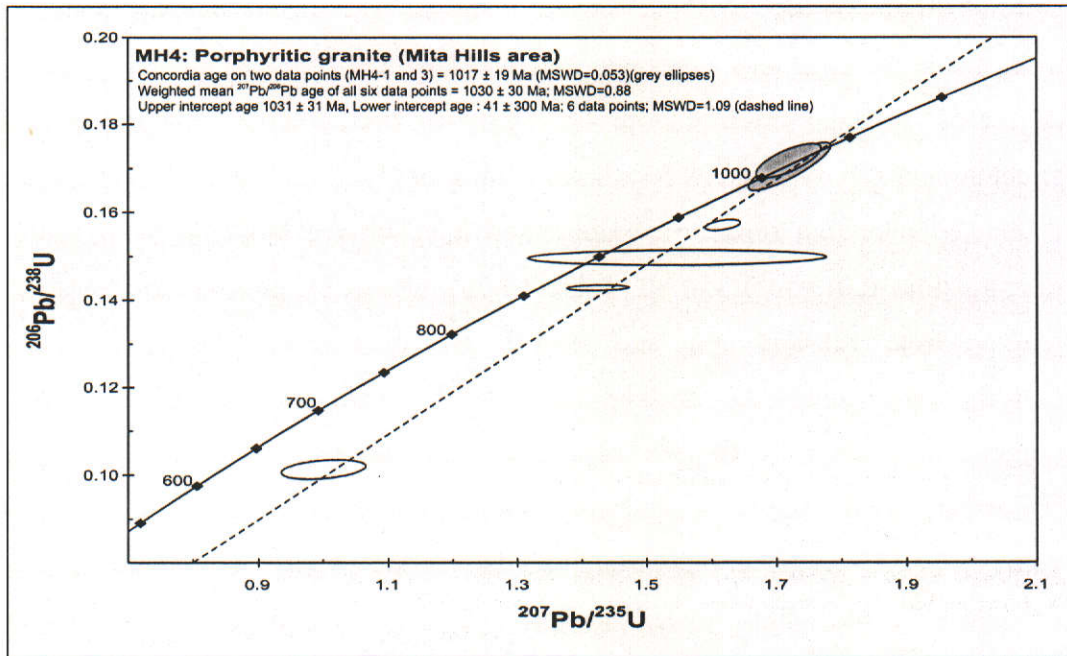


Figure 4-87: U-Pb concordia plot for zircon analyses of sample MH4. Error ellipses are at 1σ confidence level.

4.8.4.3 Sample MH9c

Sample MH9c is taken from a large whaleback outcrop of megacrystic granite, with abundant megacrysts of microcline of up to 5 cm in length. The granite is cut by numerous shallow-dipping aplitic dykes, which appear to follow a flat-lying primary magmatic fabric defined by aligned megacrysts. A shallow foliation, oriented east-northeast and dipping north, is defined by alignment of biotite flakes and cuts the magmatic fabric. Zircons from MH9c range in size from 150 to 300 μm and have length to width ratios between 3:1 and 2:1. Most crystals are euhedral, with sharp terminations and minor cracks. Small inclusions are common, but all zircons are reasonably clear, varying from colourless to pale yellow (Figure 4-88 (a)). CL imaging reveals oscillatory zoning patterns, truncated by homogenous zones with relatively low CL-response, indicating some degree of recrystallisation (Figure 4-88 (b)). All zircons have a simple internal structure and appear to have crystallised from a single event. Seven analyses were conducted over two separate sessions, and have low to moderate f_{206} values ranging from 0.019 to 1.354 % (Table 13-35). U and Th contents are variable, ranging from 120-808 ppm and 79-632 ppm respectively, giving relatively uniform Th/U ratios between 0.68 and 0.84. The data plot close to concordia, ranging from 95.3 to 101.9% concordant (Figure 4-89). A weighted mean $^{207}\text{Pb}/^{206}\text{Pb}$ age of 1029 ± 14 Ma can be calculated for all data, with a low MSWD value of 0.2. A regression line through all data points gives an upper intercept age of 1036 ± 12 Ma, with a lower intercept age of 159 ± 630 Ma (MSWD=0.63). This upper intercept age is within error of the calculated weighted mean $^{207}\text{Pb}/^{206}\text{Pb}$ age of all data points, which, based on its lower MSWD value, is taken to be the best estimate of the crystallisation age of the megacrystic granite.

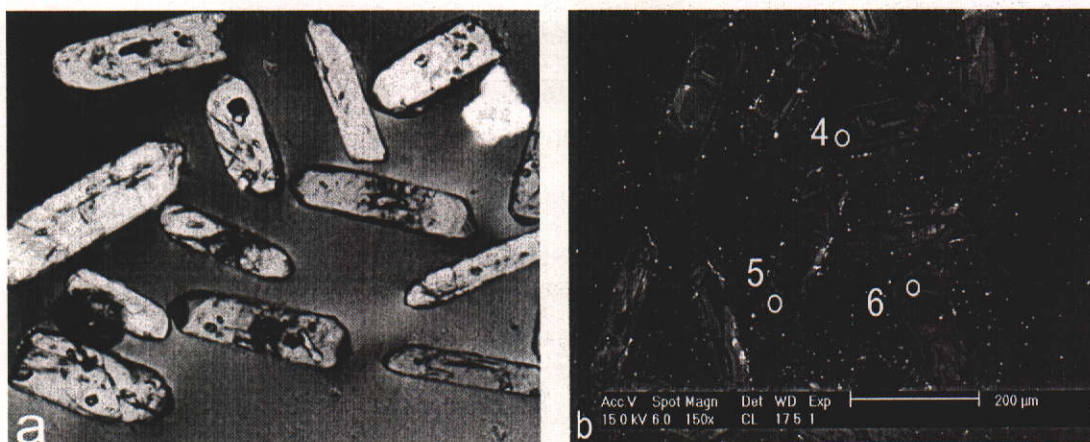


Figure 4-88: (a) photomicrograph of zircon from sample MH9c (xpl) showing euhedral crystals with minor cracks and inclusions (f.o.v. = ~1000 μm); (b) CL image of zircons from sample MH9c showing the location of analysed spots. Note the prominent concentric zoning (f.o.v.= 800 μm).

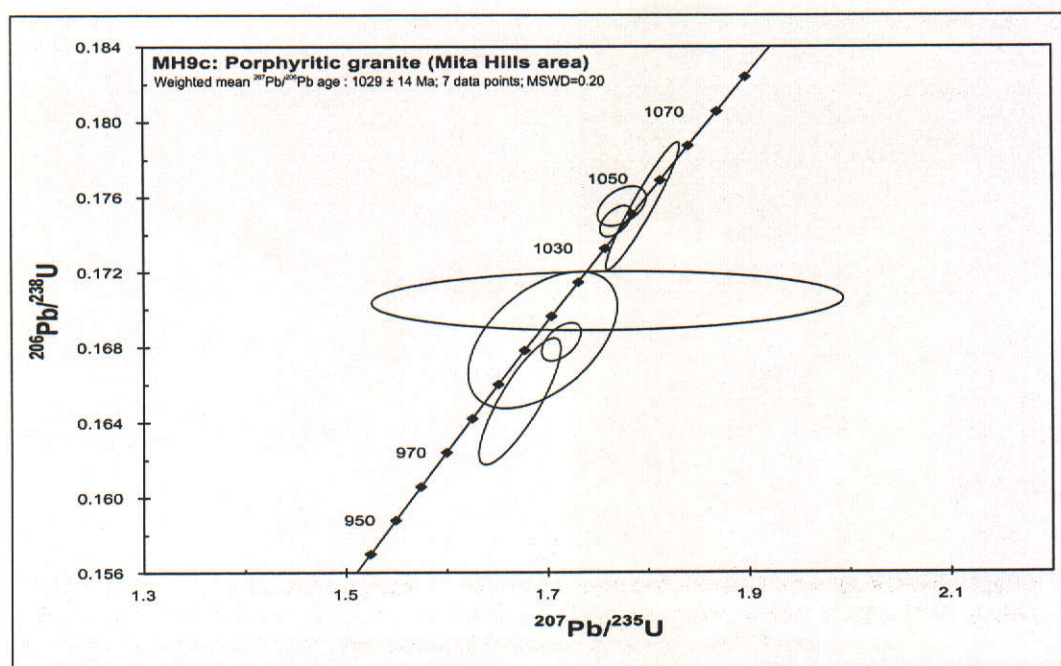


Figure 4-89: U-Pb concordia plot for zircon analyses of sample MH9c. Error ellipses are at 1σ confidence level.

4.8.4.4 Sample CC5

Sample CC5 was collected from a large flat outcrop of porphyritic granite, intruded by various aplite dykes. The granite also contains small, late melt veins, in which abundant garnet was observed. Zircons from the granite are pale yellow to colourless and range in size from 100 to 400 μm. Their length to width ratios

are greater than 3:1. In CL images, they reveal concentric zoning patterns and homogenous zones of possible late-stage magmatic zircon growth. CL response ranges from high to low (Figure 4-90). Six analyses were conducted on five zircons. The f_{206} values range up to 0.68%, while U and Th contents vary from 145 to 338 ppm and 57 to 207 ppm respectively. A pair of analyses on core and rim (CC5-3.1 and 3.2) yielded $^{207}\text{Pb}/^{206}\text{Pb}$ ages of 996 ± 52 and 1114 ± 29 Ma. Th/U ratios are between 0.40 and 0.62, consistent with magmatic zircon (Table 13-36). A concordia age of 1038 ± 17 Ma (MSWD=0.58) can be calculated on all data points (including the core), which provides a reliable estimate for the crystallisation age of the granite.

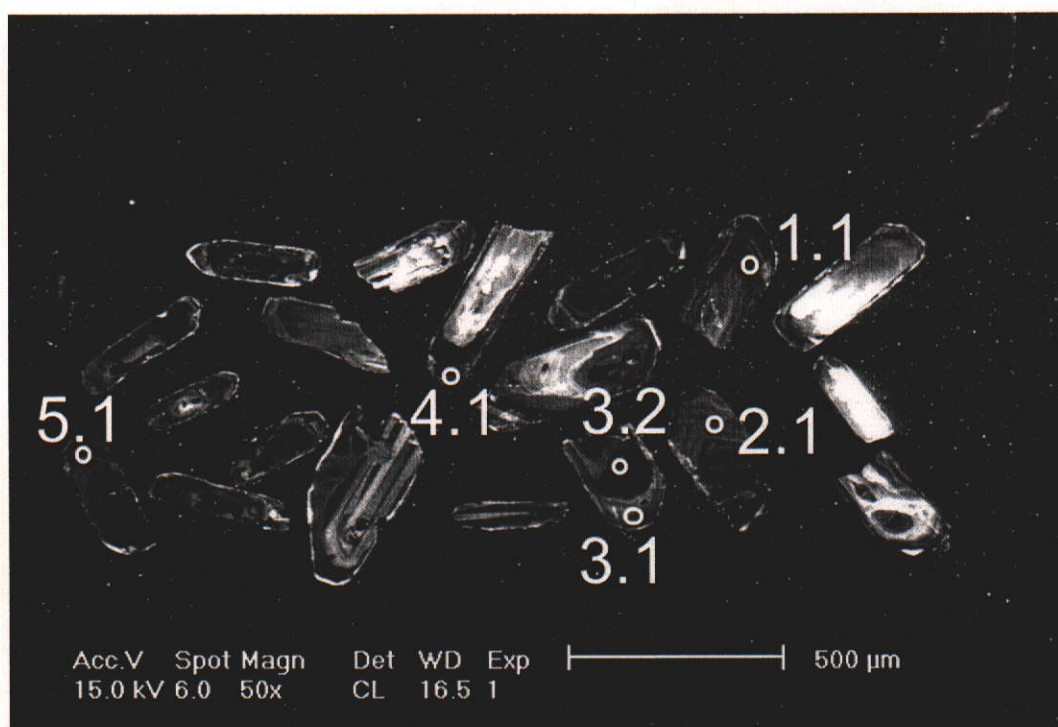


Figure 4-90: CL image of zircons from sample CC5 showing analysed spots.

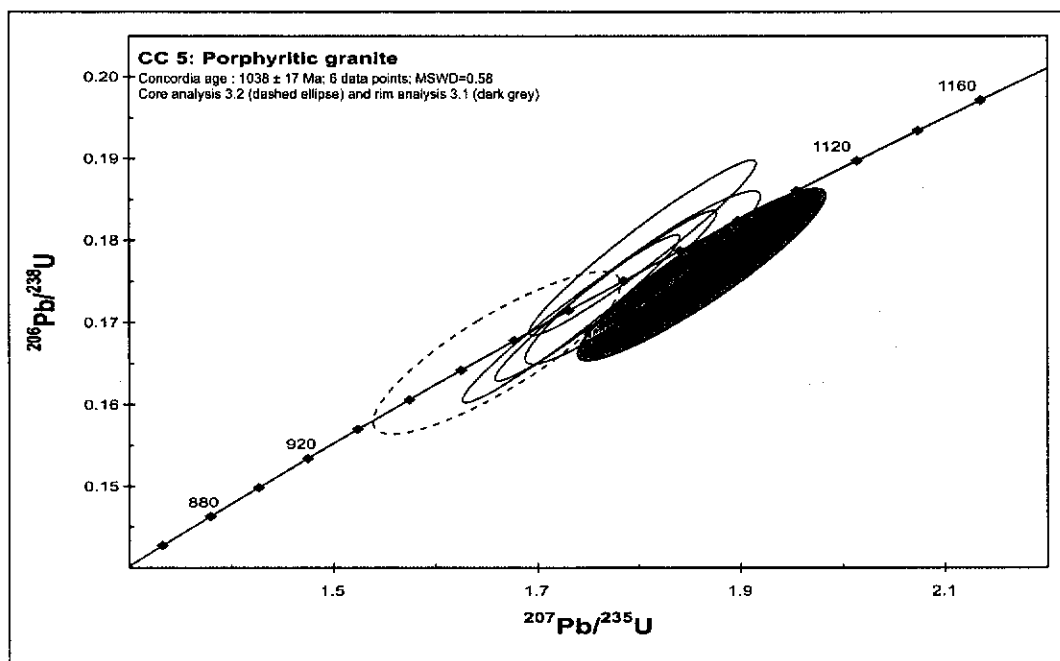


Figure 4-91: U-Pb concordia plot for zircon analyses of sample CC5. Error ellipses are at 1 σ confidence level.

4.8.4.5 Sample CC8

Sample CC8 was collected from a flat outcrop of foliated porphyritic biotite granite. Zircons from the granite are large, ranging in size from 200 to 400 μm . The crystals are prismatic, with length to width ratios larger than 3:1. The zircons are pale yellow to brownish and contain abundant inclusions and some cracks (Figure 4-92 (a)). Some zircons consist of a magmatic core, rimmed by a large magmatic rim, with both displaying concentric zoning in CL (Figure 4-92 (b)). Six analyses were conducted on six clear zircons (Table 13-37). Five data points display low f_{206} values from zero to 0.06%, and one spot (CC8-5.1) shows an elevated common lead content of 0.65%. This data point plots slightly off concordia and is characterised by poor precision (Figure 4-93). The other five analyses range from 97.2 to 100.3 % concordant, and define a concordia age of 1035 ± 12 Ma (MSWD=0.67), which can be considered the best estimate for the age of crystallisation of the granite.

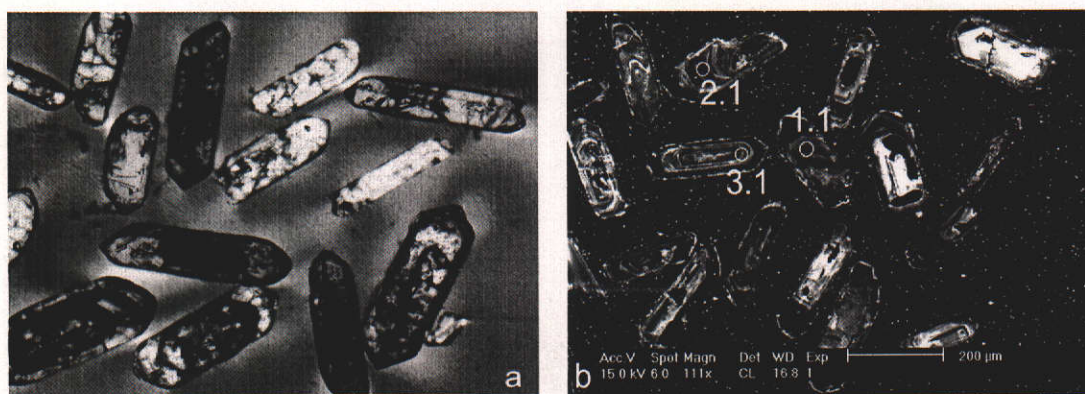


Figure 4-92: (a) photomicrograph of zircons from sample CC8 (xpl) showing euhedral crystals with minor cracks and inclusions (f.o.v. = ~1000 µm); (b) CL image of zircons from sample CC8 showing the location of analysed spots. Note the prominent concentric zoning (f.o.v.= 1200 µm).

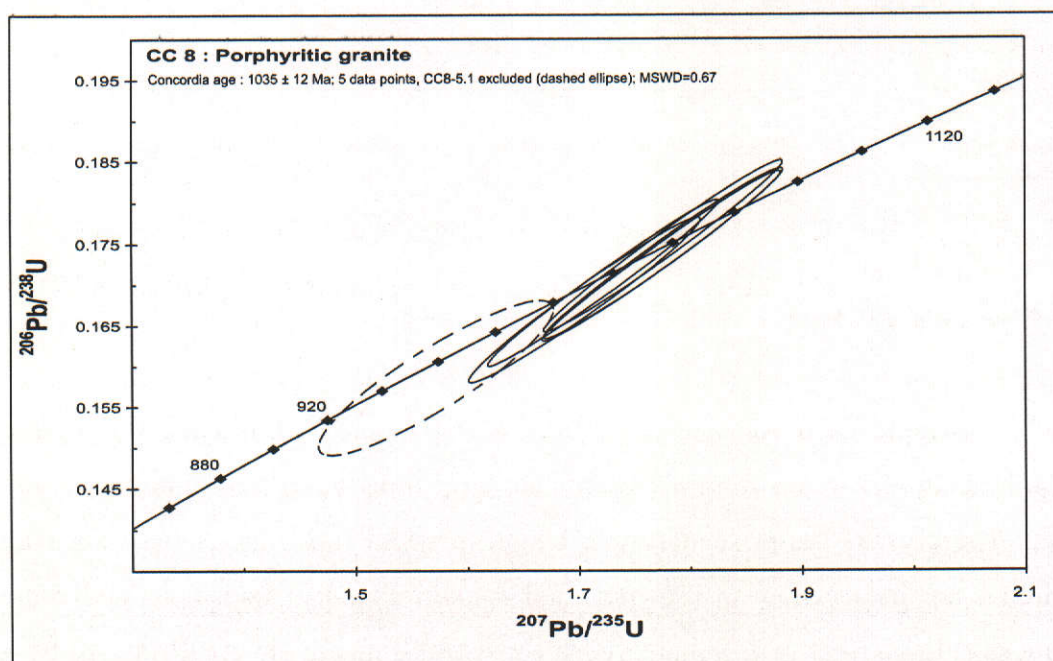


Figure 4-93: U-Pb concordia plot for zircon analyses of sample CC8. Error ellipses are at 1 σ confidence level.

4.8.4.6 *Sample MK7*

Sample MK7 was collected from foliated reddish biotite granite in the Mkushi map sheet (Figure 2-9). The granite is intruded by various cross-cutting small pegmatites. Both the granite and the pegmatites are deformed, and a series of mafic xenoliths occur along the foliation, which trends east-northeast, dipping steeply east. Few zircons were retrieved from the sample, and range in size from 200 to 300 μm (Figure 4-94). They appear dark brown due to numerous cracks and inclusions. CL imaging suggests that the zircons have elevated uranium and trace element content, as they are characterised by very low CL response (Figure 4-94 (b)). Six analyses were conducted on five zircons, and show high f_{206} values ranging from 0.53 to 1.09% (Table 13-38). U and Th range from 192-1815 ppm and 64-422 ppm respectively, giving a highly variable Th/U range between 0.04 and 2.16. The lowest Th/U ratio (0.04) was obtained from the analysis on a rim (MK7-2r), which also yields the lowest amount of common Pb and plots closest to the concordia (98.8% concordant). This rim analysis yielded a $^{207}\text{Pb}/^{206}\text{Pb}$ age of 893 ± 17 Ma and is interpreted to approximate the timing of a metamorphic and/or metasomatic event responsible for its growth. The remaining five analyses plot at least 5% away from concordia and do not appear to define a coherent age population (Figure 4-95). Analysis MK7-1 yielded a $^{207}\text{Pb}/^{206}\text{Pb}$ age of 1035 ± 32 Ma (94.1 % concordant) and possibly approaches the emplacement age of the granite. One data point defines an older $^{207}\text{Pb}/^{206}\text{Pb}$ age of 2003 ± 36 Ma. This zircon analysis was taken from a magmatic core and is inferred to be a xenocrystic component, possibly derived from the ~2.05-1.93 Ga Mkushi Gneiss. The remaining data points define poorly constrained ages between 891 ± 110 and 1193 ± 63 Ma, but plot at least 20% off concordia. Because of the discordance of these points, and their poor precision, no interpretation is made here for these data.

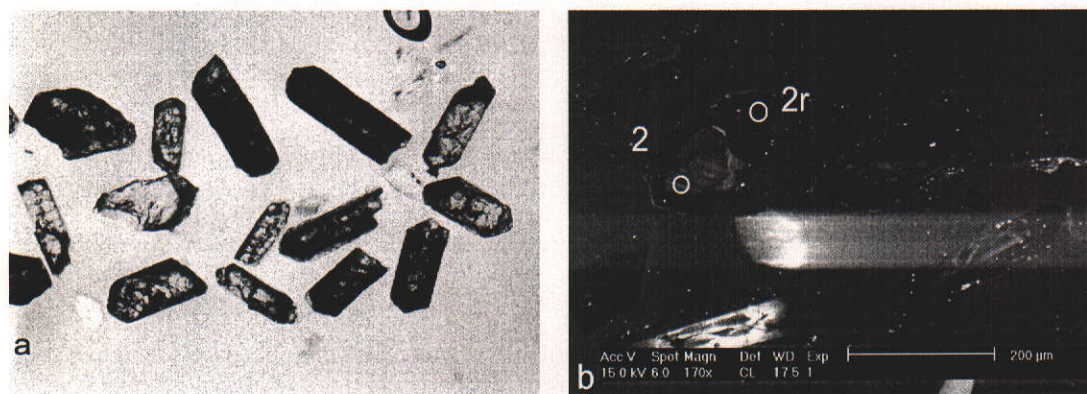


Figure 4-94: (a) photomicrograph of zircons from sample MK7 (xpl) showing euhedral crystals with numerous cracks and inclusions (f.o.v. = ~1600 µm); (b) CL image of zircons from sample MK7 showing the location of analysed spots MK7-2 and 2r. Note the prominent concentric zoning in the core, and dark CL aspect of the rim (f.o.v.= 600 µm).

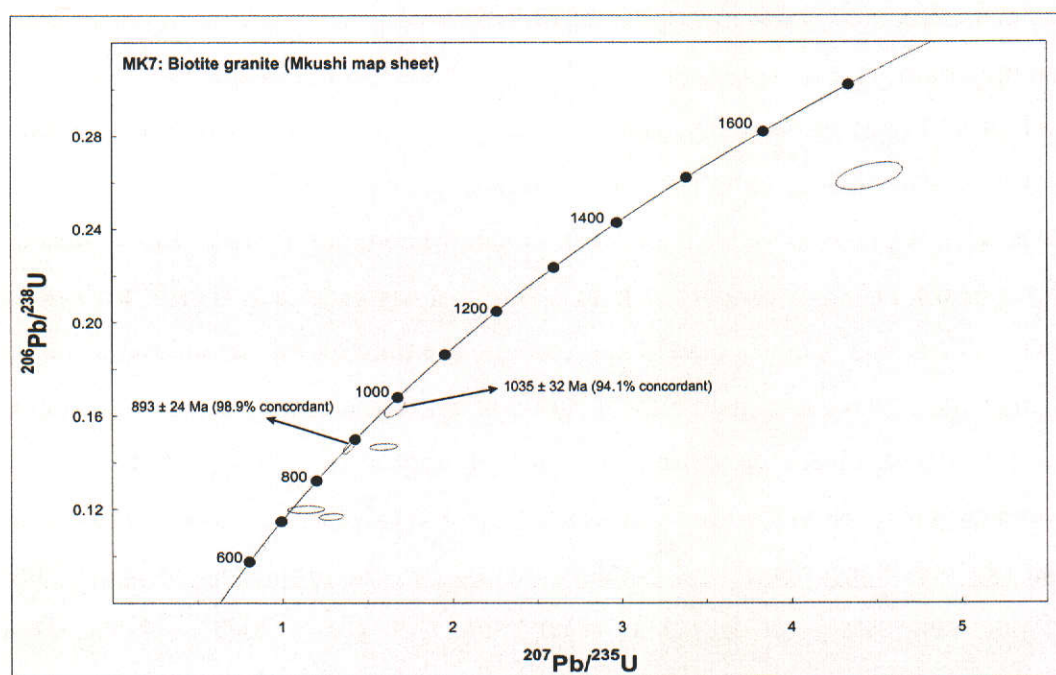


Figure 4-95: U-Pb concordia plot for zircon analyses of sample MK7. Error ellipses are at 1σ confidence level.

4.8.4.7 Sample FW1

Sample FW1 was collected from a flat outcrop of coarse porphyritic foliated granite. A biotite foliation in this rock is oblique to an older magmatic foliation defined by aligned microcline phenocrysts that are themselves undeformed. The granite is cut by aplite dykes (see sample FW2 below). Zircons from sample FW1 are light yellow to light brown, sub- to euhedral, and elongate in shape (Figure 4-96 (a)). Length to width ratio varies up to 3:1, and the size ranges from 100 to 250 μm . The zircons range from clear, with little or no inclusions, to heavily included and cloudy. CL imaging shows relatively low luminescence, with faint concentric zoning patterns (Figure 4-96 (b)). All zircons appear to have crystallised during a single magmatic event. Seven analyses were conducted on different zircons and yield variable U and Th contents of 203-2020 ppm and 148-499 ppm respectively (Table 13-39). Th/U ratios range from 0.12 to 1.82, and f^{206} values up to 1.112%. The analyses range from 9% reversely discordant to concordant, with four zircons within 5% of concordia (Figure 4-97). The three discordant data points (FW1-1, 3 and 7) yield a weighted mean $^{207}\text{Pb}/^{206}\text{Pb}$ age of 964 ± 29 Ma (MSWD=0.94). Because of the relatively large reverse discordance, it is unclear whether this age has geological meaning. The four concordant points align on a regression line with an upper intercept age at 1038 ± 58 Ma and a lower intercept age at 611 ± 850 Ma (MSWD=0.27). Their weighted mean $^{207}\text{Pb}/^{206}\text{Pb}$ age is 1052 ± 18 Ma (MSWD=0.75). Although the data do not allow for calculation of a well-constrained age, the upper intercept of 1038 ± 58 Ma is taken as the most reliable estimate of the age of emplacement of the porphyritic granite.

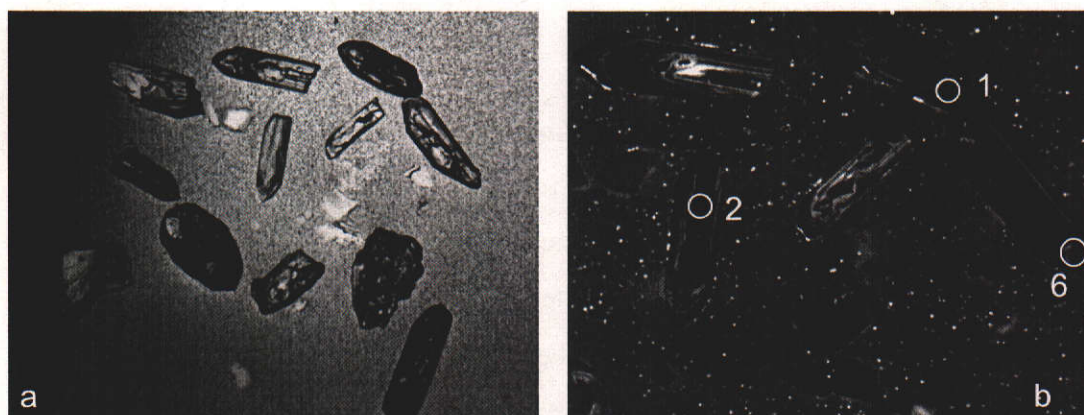


Figure 4-96: (a) photomicrograph of zircons from sample FW1 (xpl) showing a wide variety of crystals (f.o.v. = ~1500 µm); (b) CL image of zircons from sample FW1 showing the location of analysed spots. Note the prominent concentric zoning at the analysed sites (f.o.v.= 750 µm).

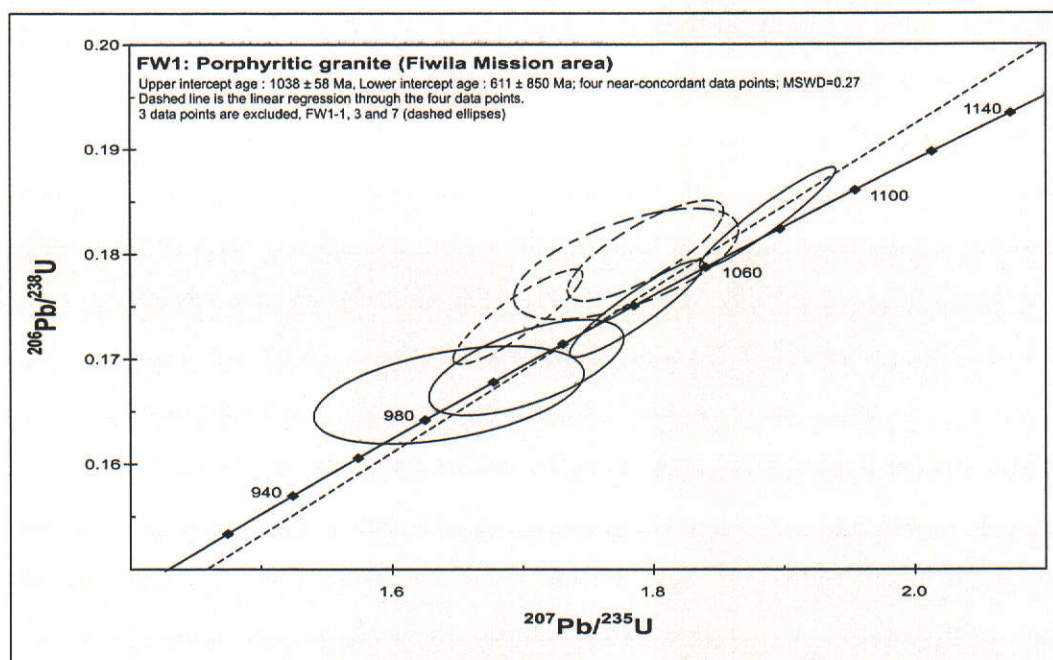


Figure 4-97: U-Pb concordia plot for zircon analyses of sample FW1. Error ellipses are at 1σ confidence level.

4.8.4.8 Sample FW2

Sample FW2 was taken from an aplite dyke cutting a porphyritic granite (see sample FW1 above). Zircons from the aplite (sample FW2) are sub- to euhedral and can be split into three populations based on morphology. The first population consists of large (300µm), semi-rounded zircons (Figure 4-98 (a)),

which are brown to reddish brown in colour. These zircons contain some minor inclusions and are variably cracked. Another population is small to large (100-400 μm), subhedral and rounded (Figure 4-98 (a)), but is colourless to pale yellow. This population contains only minor inclusions, and very few grains are cracked. The smallest population comprises small (100 μm), euhedral, clear grains, with length to width ratios up to 3:1, and may have crystallised directly from the melt that formed the aplite. None of this latter population of primary zircons was analysed. Under CL, the differences between the zircon populations are highlighted (Figure 4-98 (b)). The large brown zircons range from low to high CL, and show complicated internal structure, with core-rim relationships and abrupt changes in trace element content, resulting in sharp CL contrasts. The large colourless zircons are generally simple in structure, and show low CL response. The small, elongate crystals show oscillatory zoning patterns and are generally low in CL. Thirteen analyses were conducted on thirteen zircons (Table 13-40), while numerous analyses were aborted due to high counts on ^{204}Pb . The analyses yield U and Th contents of 77-1375 ppm and 22-237 ppm respectively. Th/U ratios range from 0.07 to 2.16 and f_{206} values from 0.056 to 1.017 %. Eight zircons appear to define a single age group, for which a concordia age of 2033 ± 14 Ma can be calculated (MSWD=0.43)(Figure 4-99). These zircons belong to the large, brownish population and are often characterised by a core, showing well-developed concentric zoning patterns, surrounded by a narrow darkish rim (not analysed). The age of 2033 ± 14 Ma is interpreted to reflect an underlying granitic basement, which was sampled by the aplite intrusions. Of the remaining five zircon analyses sampled from large, pale yellow to brown zircons, two are concordant (FW2-4 and 12) and define $^{207}\text{Pb}/^{206}\text{Pb}$ ages of 2774 ± 23 Ma and 1637 ± 46 Ma respectively. These two analyses reflect additional sources of xenocrystic zircon sampled by the aplites, and correspond with emplacement ages of granitoids reported in the region (Kapiri Mposhi Granite and Lukamfwa Hill Granitoid). The three remaining analyses (FW2-2, 5 and 13) are over 10% discordant, and define $^{207}\text{Pb}/^{206}\text{Pb}$ ages of 1258 ± 103 Ma (FW2-2; 82.9% concordant), 1837 ± 28 Ma (FW2-5; 90.7% concordant) and 2484 ± 8 Ma (FW2-13; 86.3% concordant). Due to the large discordance, not much weight is given to these data. The age populations sampled by this aplite are best shown in a combined probability distribution and histogram diagram, which shows a

predominant source of xenocrysts around 2050 Ma, with minor contributions of ~1600 and 2750 Ma (Figure 4-100).

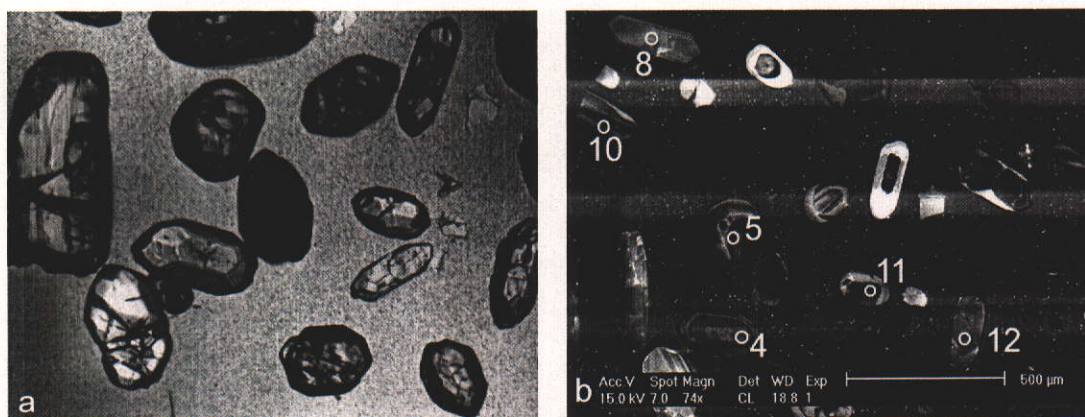


Figure 4-98: (a) photomicrograph of zircons from sample FW2 (xpl) showing variably sized and shaped crystals (f.o.v. = ~1000 µm); (b) CL image of zircons from sample FW2 showing the location of analysed spots. Note the wide range of CL response and morphologies (f.o.v.= 1500 µm).

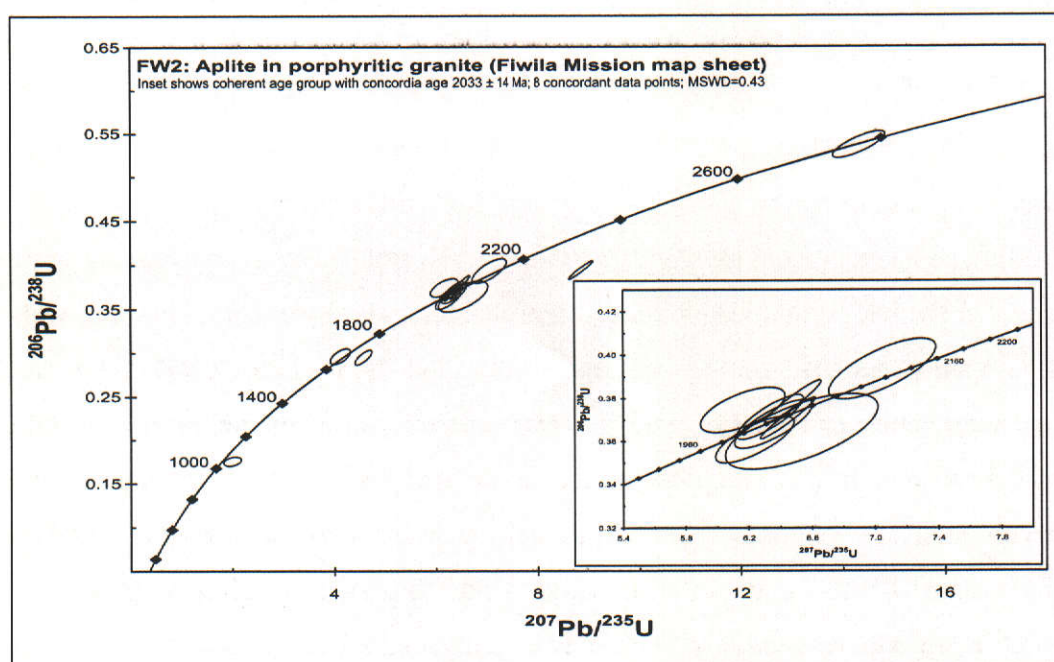


Figure 4-99: U-Pb concordia plot for zircon analyses of sample FW2. Error ellipses are at 1σ confidence level. Inset shows a concordant age group defining an age of 2033 ± 14 Ma.

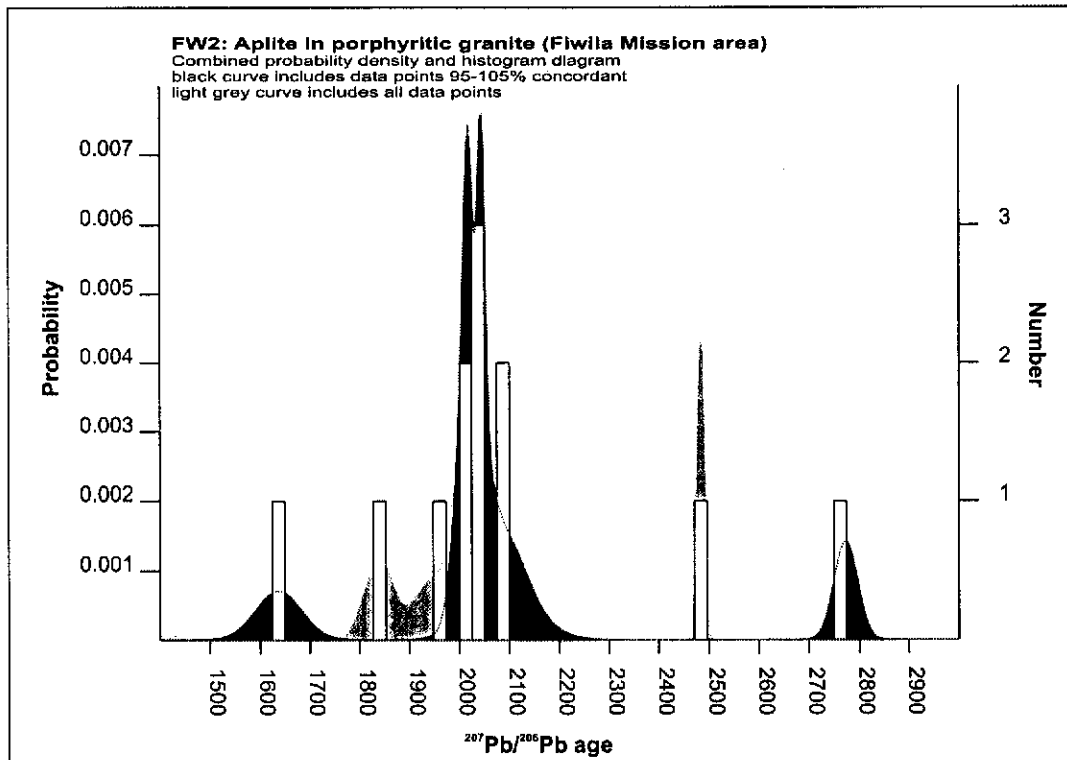


Figure 4-100: Probability density diagram and histogram showing the 100±5% concordant age populations in zircon from sample FW2. The dark grey curve denotes data within 5% of concordia, while the light grey curve shows all data. The bin-size for the histogram is 25 M.y.

4.8.4.9 Sample CHT6

Sample CHT6 comes from a flat-lying outcrop of coarse, foliated biotite granite, which contains abundant small dark xenoliths of metasedimentary origin. The granite is cut by a northeast-trending biotite foliation dipping steeply southeast. Zircons from CHT6 are clear and appear colourless in transmitted light (Figure 4-101 (a)). They contain some inclusions and are sometimes cracked. The crystals are euhedral, with well-defined bipyramidal terminations. The grain size ranges from 200 to 500 μm , with length to width ratios between 1:1 and 4:1. CL images indicate simple zircons, with broad concentric zoning patterns, often marred by zones of late-stage magmatic embayment. CL response ranges from high to medium (Figure 4-101 (b)). Nine analyses were conducted on nine zircons, and give f^{206} values ranging from 0.225 to 2.414 % (Table 13-41). U and Th are relatively low, ranging from 93 to 415 ppm and 99 to 282 ppm respectively. Th/U ratios vary from 0.70 to 1.38, consistent with magmatic crystallisation. A weighted mean $^{207}\text{Pb}/^{206}\text{Pb}$ age of 1015 ± 42 Ma with

MSWD=1.07 can be calculated for all analyses. The data vary from 27% inversely discordant to 8% normally discordant, with six points within 10% of concordia (Figure 4-102). Because of the relatively large errors on the isotopic ratios, a concordia age can be calculated based on all data points, and yields a more precise age estimate of 1005 ± 7 Ma (MSWD=0.19), which represents the best estimate of the crystallisation age of the granite.

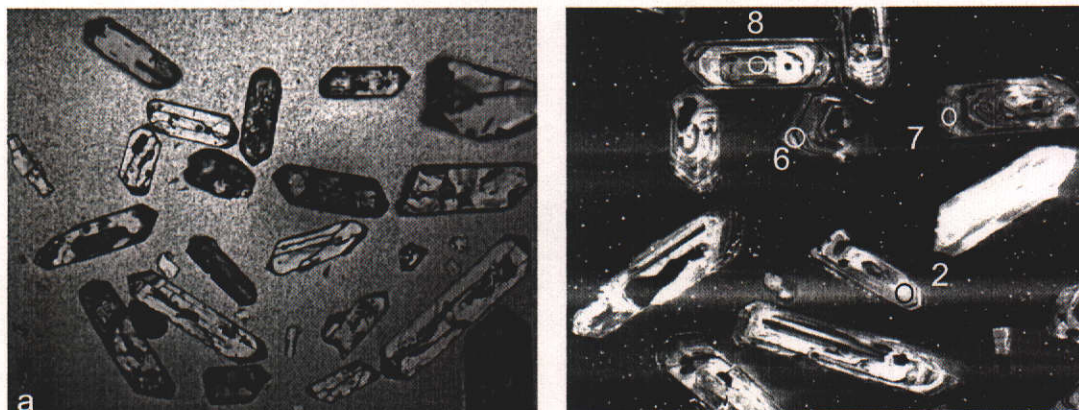


Figure 4-101: (a) photomicrograph of zircons from sample CHT6 (xpl) showing euhedral crystals (f.o.v. = ~1500 µm); (b) CL image of zircons from sample CHT6 showing the location of analysed spots. Note the wide range of CL response and oscillatory zoning patterns (f.o.v.= 1000 µm).

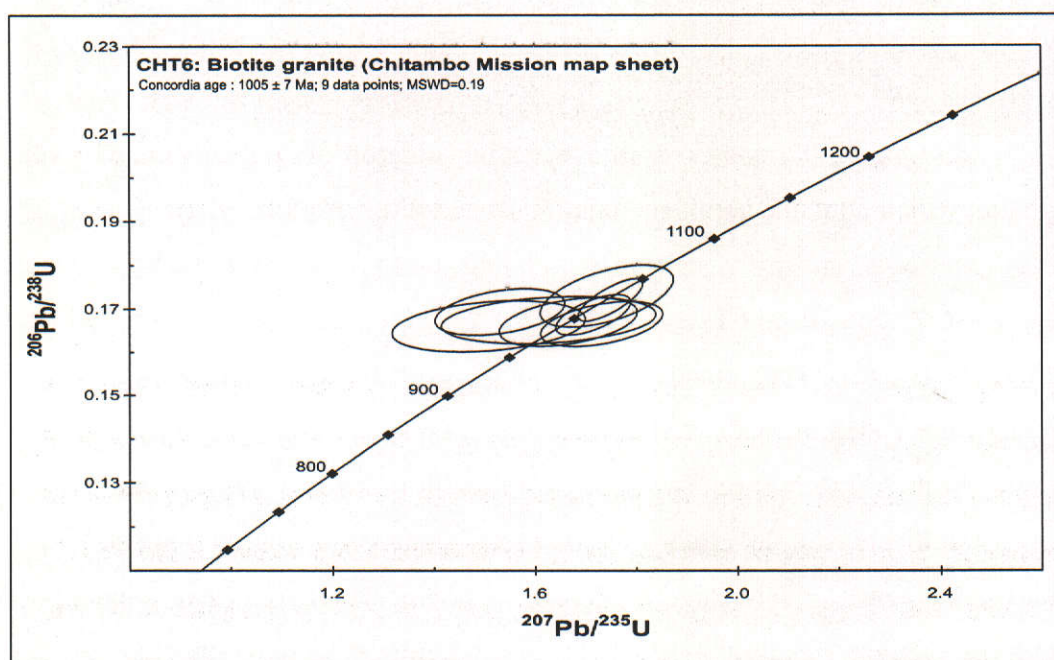


Figure 4-102: U-Pb concordia plot for zircon analyses of sample CHT6. Error ellipses are at 1σ confidence level.

4.8.4.10 Sample KN2A

Sample KN2A was sampled from foliated biotite gneiss with large K-feldspar phenocrysts. Fine-grained aplitic dykes that contain garnet cut the granite gneiss. Zircons from sample KN2A are large, ranging in size from 200 to 300 μm , have euhedral habit, and are light yellow to colourless. The crystals are relatively clear and uncracked, with only minor inclusions (Figure 4-103 (a)). CL response reveals oscillatory zoning patterns, and homogenous zones of recrystallisation. CL response ranges from low to medium indicating high to moderate U content (Figure 4-103 (b)). Eight analyses were conducted on eight different zircons and yielded low f_{206} values ranging up to 0.066% (Table 13-42). U ranges from 116 to 247 ppm for seven points, with analysis 5 yielding an anomalously high value of 1421 ppm. Likewise, Th ranges from 117 to 282 ppm for seven analyses, with analysis 5 anomalously high at 882 ppm. Th/U ratios range from 0.54 to 1.43, consistent with magmatic zircon. The data plot from 75.5 to 99.7% concordant, but the ^{204}Pb -corrected data display an erratic drift normal to the concordia (Figure 4-104) interpreted as reflecting a problem with the common Pb correction. The uncorrected data (Figure 4-105) show a clear trend towards common Pb, and a regression towards a common Pb composition appropriate for the age of the sample (1050 Ma; $(^{207}\text{Pb}/^{206}\text{Pb})_{\text{common}} = 0.913$ (Stacey and Kramers, 1975)) yields an intercept at 1031 ± 14 Ma (MSWD=0.81), which represents the best estimate for the crystallisation age of the granite.

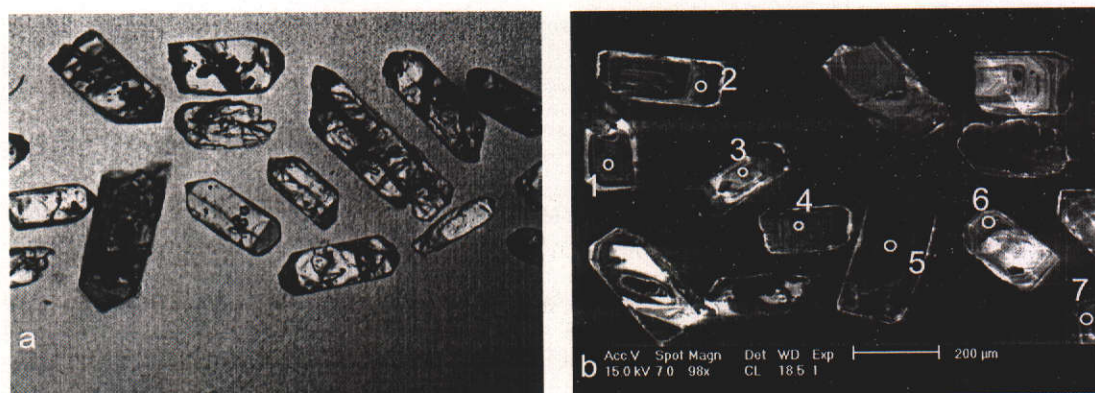


Figure 4-103: (a) photomicrograph of zircons from sample KN2A (xpl) showing euhedral crystals (f.o.v. = ~1200 μm); (b) CL image of zircons from sample KN2A showing the location of analysed spots. Note the oscillatory zoning patterns (f.o.v.= 1200 μm).

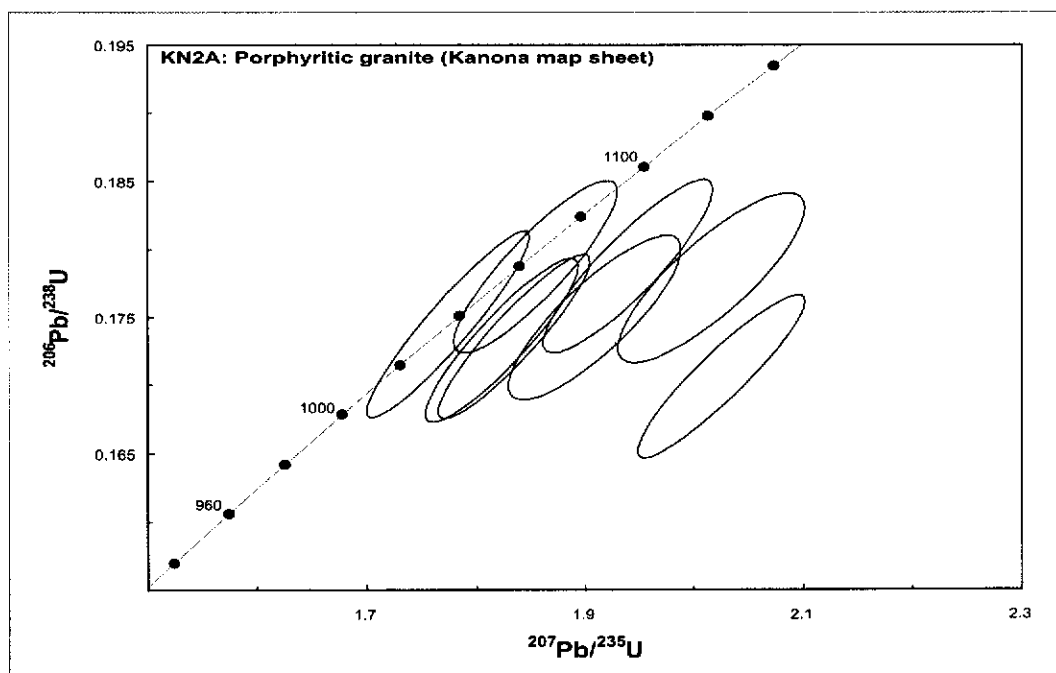


Figure 4-104: U-Pb concordia plot for zircon analyses of sample KN2A. Error ellipses are at 1σ confidence level. Note the drift away from concordia due to incorrect common Pb correction based on measured ^{204}Pb .

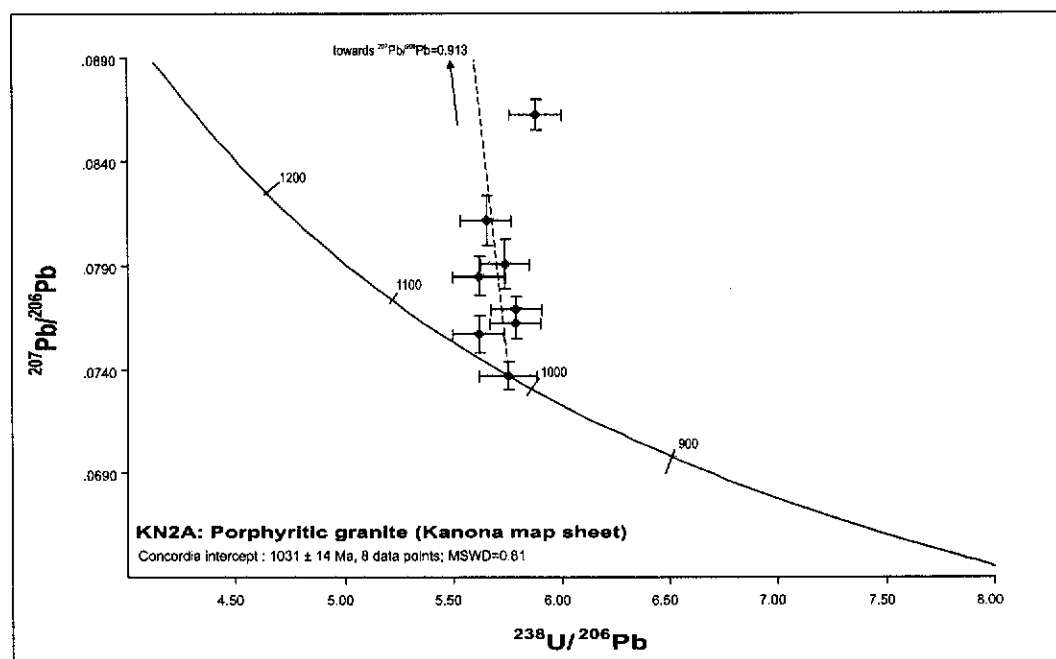


Figure 4-105: U-Pb concordia plot (Tera-Wasserburg) for zircon analyses of sample KN2A. The data are uncorrected for common Pb. Error crosses are at 1σ confidence level. The regression (dashed line) is made towards common Pb, calculated for an age of 1050 Ma after Stacey and Kramers (1975).

4.8.4.11 Sample KN5

Sample KN5 was collected from a flat outcrop of foliated porphyritic biotite granite in the Kanona area (Figure 2-10). The granite contains abundant xenoliths of mafic composition, as well as rafts of metasedimentary rocks, migmatitic material and fine-grained granite gneiss. The granite carries a penetrative S_1 foliation along a north-south direction, dipping steeply to the west. Zircons from KN5 are large, ranging in size between 200 and 350 μm , and are pale yellow in colour (Figure 4-106 (a)). The crystals are euhedral in shape and contain some cracks and minor inclusions. CL shows the crystals to be concentrically zoned, with medium to low response (Figure 4-106 (b)), and with the majority of grains showing an inner concentrically zoned magmatic core, surrounded by an extensive concentrically zoned magmatic rim. Seven analyses were conducted on different zircons, together with one pair of core and rim analyses of a complex zircon. The analysed rim contains a high amount of U (2299 ppm) and is radiogenically damaged as evidenced by the significant Pb-loss and discordance. For the other analyses, U ranges from 181 to 456 ppm and Th from 132 to 356 ppm (Table 13-43). Th/U ranges from 0.48 to 2.03 for the single zircon analyses, 0.55 for the core, and is relatively low for the analysed rim (0.10). The common Pb content is generally low, ranging from zero to 0.098%. The data range from 87.3 to 100.0% concordant, and show the same drift, normal to the concordia, as sample KN2A (Figure 4-107). The values are plotted uncorrected for common Pb in Figure 4-108, and can be regressed towards common Pb to yield an intercept at 1053 ± 14 Ma (MSWD=0.24). The analysed rim plots well away from the regression line, indicating significant disturbance of the isotopic system due to radiogenic damage. The intercept age from Figure 4-108 provides the best estimate for the crystallisation age of the granite.

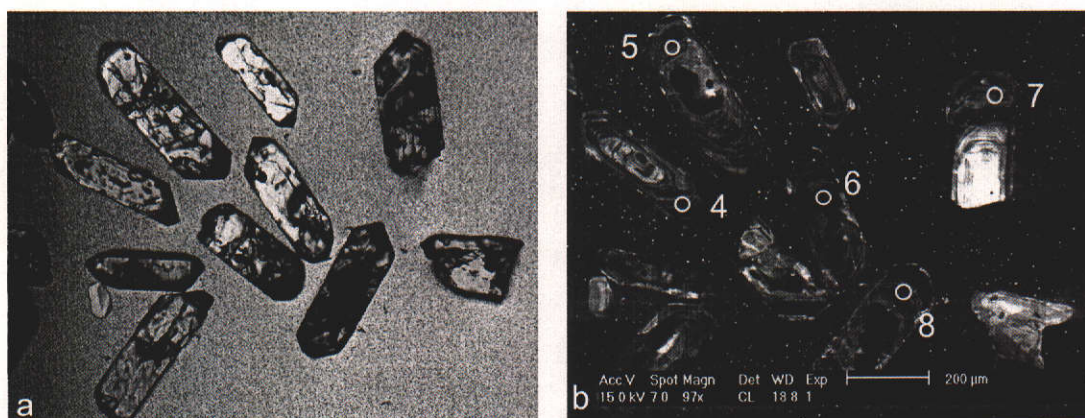


Figure 4-106: (a) photomicrograph of zircons from sample KN5 (xpl) showing euhedral crystals (f.o.v. = ~1200 µm); (b) CL image of zircons from sample KN5 showing the location of analysed spots. Note the oscillatory zoning patterns (f.o.v.= 1200 µm).

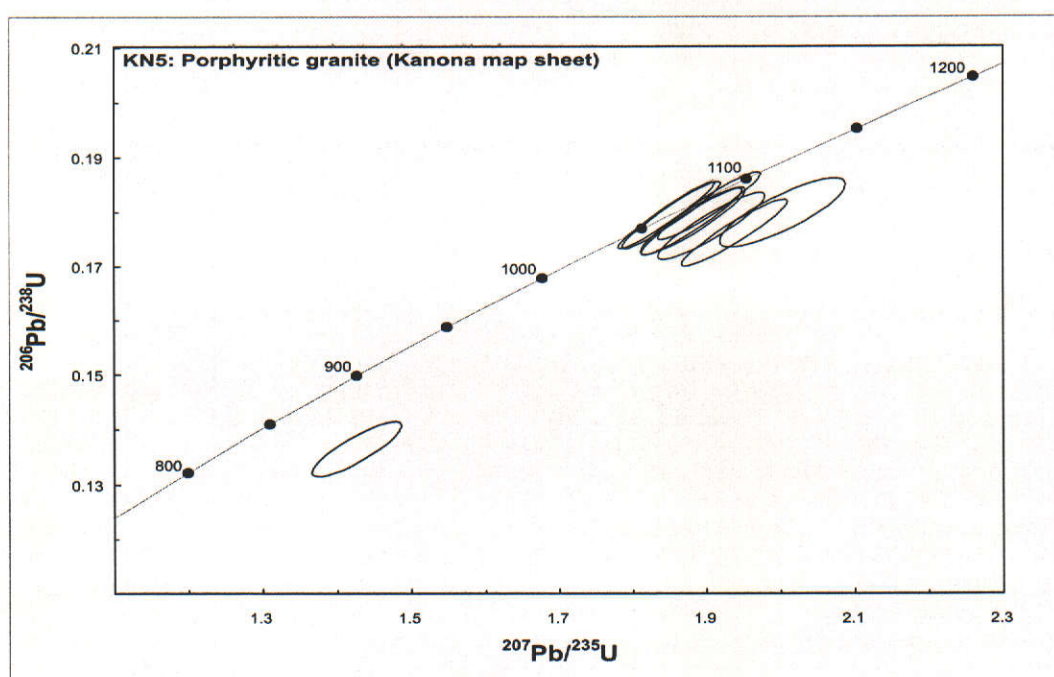


Figure 4-107: U-Pb concordia plot for zircon analyses of sample KN5. Error ellipses are at 1σ confidence level. Note the drift away from concordia due to incorrect common Pb correction based on measured ^{204}Pb .

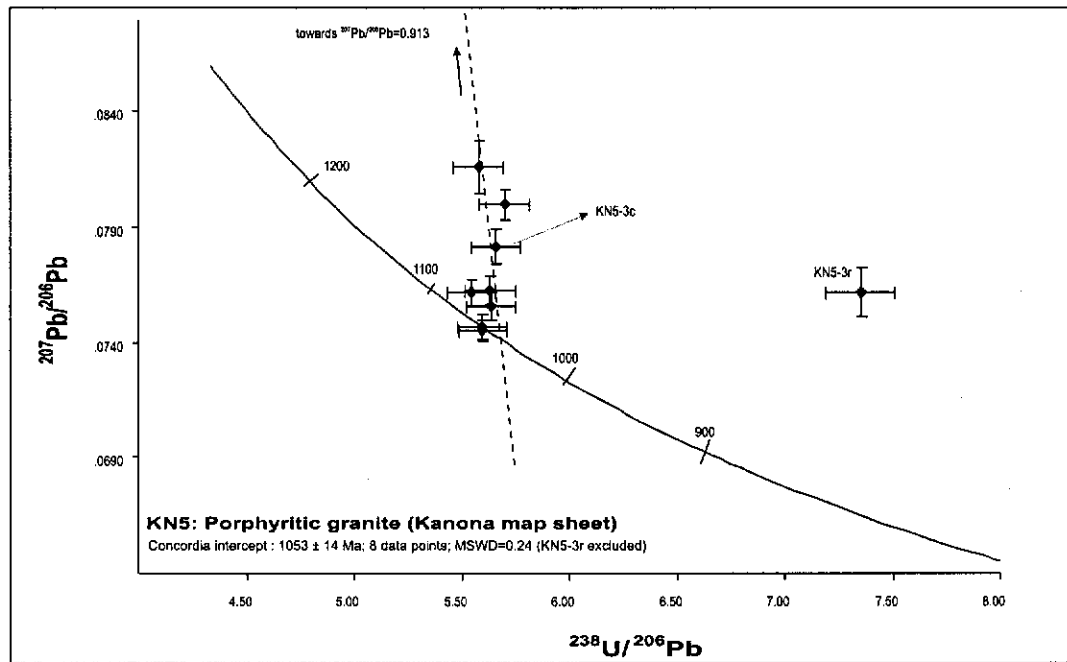


Figure 4-108: U-Pb concordia plot (Tera-Wasserburg) for zircon analyses of sample KN5. The data are uncorrected for common Pb. Error crosses are at 1σ confidence level. The dashed regression (dashed line) is made towards common Pb, calculated for an age of 1050 Ma after Stacey and Kramers (1975).

4.8.4.12 Sample KN7

Sample KN7 was collected from an inselberg in the Kanona map sheet, consisting entirely of foliated two-mica granite. Only a few zircons were retrieved from the granite and are quite variable in morphology (Figure 4-109). The zircons range from colourless and clear, to brownish and cloudy, and range in size from 100 to 400 μm . Variable response characterises the CL image, suggesting widely different sources for the zircons in the granite (Figure 4-109 (b)). Eight analyses were conducted on seven zircons. One core and rim pair from the same grain yielded no significant difference in $^{207}\text{Pb}/^{206}\text{Pb}$ age (Table 13-44, analyses KN7-3c and 3r). The analysis on the rim yielded anomalously high U and Th contents of 2878 and 39994 ppm respectively, and is extremely discordant (82% discordance). The core yielded U and Th of 184 and 258 ppm respectively, giving a Th/U ratio of 1.45, and plots 20.5% away from concordia, defining a $^{207}\text{Pb}/^{206}\text{Pb}$ age of 2793 ± 13 Ma. This zircon is interpreted as a xenocryst, while the $^{207}\text{Pb}/^{206}\text{Pb}$ age is interpreted as its minimum age. For the other six analyses, U and Th range from 209 to 973 ppm and 30 to 825 ppm respectively. Common Pb

is low, ranging from zero to 0.049%. Four of the analysed zircons define a broad age group, for which a weighted mean $^{207}\text{Pb}/^{206}\text{Pb}$ age of 2011 ± 24 Ma can be calculated. The data in this group range from 94.9 to 102.4% concordant. The high MSWD value for this age calculation (4.20) indicates that the scatter of the four points cannot be adequately explained by analytical errors. These xenocrysts are interpreted to reflect inheritance from multiple 1.95-2.02 Ga sources. Analysis KN7-6 plots 28.1% away from concordia, and yielded a $^{207}\text{Pb}/^{206}\text{Pb}$ age of 1277 ± 16 Ma. Because of the high discordance it is unclear whether this zircon represents a ca. 1.28 Ga xenocryst, or an older xenocryst that suffered complex Pb-loss. Analysis KN7-7 yielded a concordant age of 1048 ± 10 Ma. This zircon is colourless, has euhedral habit, and displays concentric zoning patterns in CL (Figure 4-109). This zircon is interpreted to have crystallised from the magma, and provides the best estimate for the crystallisation age of the granite.

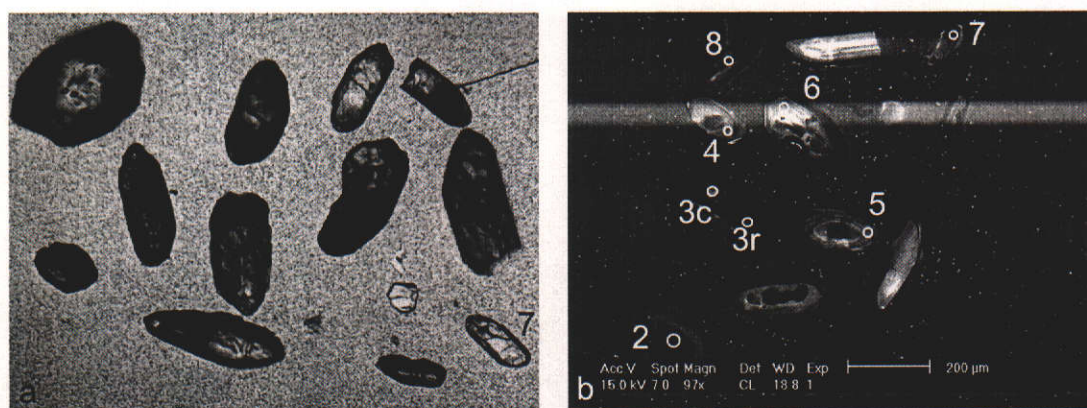


Figure 4-109: (a) photomicrograph of zircons from sample KN7 (xpl) showing anhedral, subhedral and euhedral crystals (f.o.v. = ~1000 μm); (b) CL image of zircons from sample KN7 showing the location of analysed spots. Note the variability on CL response and oscillatory zoning patterns (f.o.v.= 1200 μm).

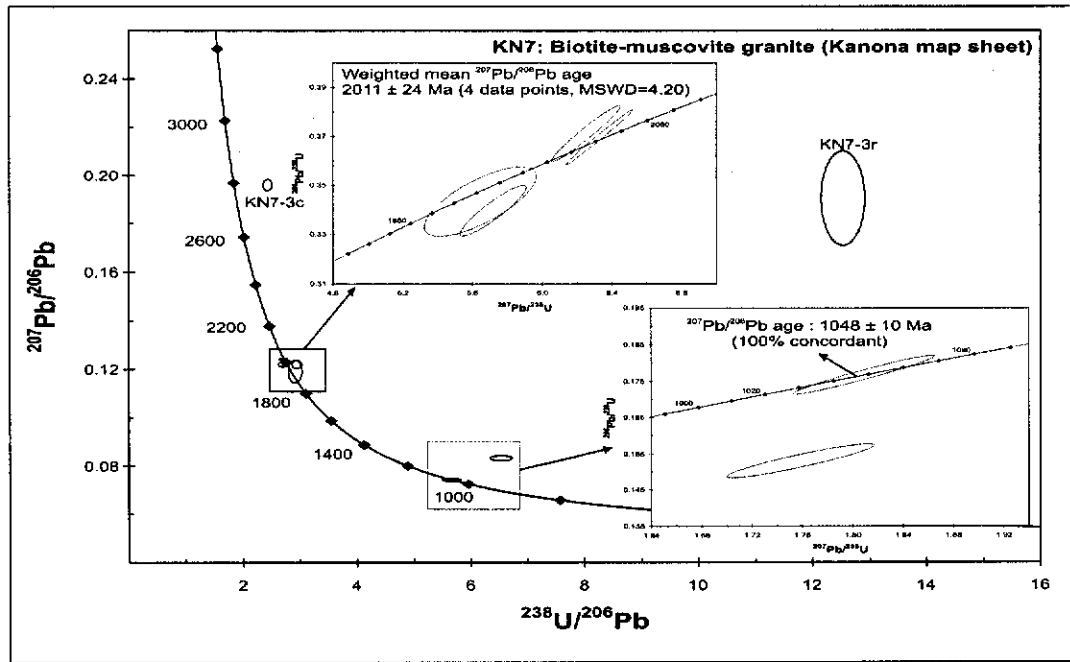


Figure 4-110: Tera-Wasserburg U-Pb concordia plot for zircon analyses of sample KN7. Error ellipses are at 1σ confidence level. Insets show enlargements (Wetherill U-Pb concordia plots) of a coherent age group at ~2010 Ma and a concordant analysis (KN7-7) at 1048 ± 10 Ma.

4.8.4.13 Sample KN8

Sample KN8 was collected from a foliated porphyritic granite in the Kanona area (Figure 2-10). The granite is foliated along northeasterly trends, dipping shallowly to steeply to the northwest. Euhedral K-feldspar phenocrysts define a north-south-trending primary magmatic fabric. Zircons from sample KN8 are large, varying from 200 to 350 μm in size. They appear yellow and colourless in transmitted light. A small proportion of the zircons consist of an internal core, surrounded by an extensive rim. CL response reveals an oscillatory zoning pattern for all zircons, including cores and rims, indicating a magmatic source (Figure 4-111). Nine single analyses were conducted on complex zircons, while core-rim pairs were analysed in two zircons. The data show low f_{206} values up to 0.091%, and plot up to 24% away from concordia (Table 13-45 and Figure 4-112). U and Th range from 107 to 725 ppm and 58 to 1171 ppm respectively, yielding a Th/U range between 0.23 and 2.44. Neither of the analysed rims have a low Th/U ratio, and both are interpreted to be magmatic. One analysis on a core (KN8-1c) yielded a 99.7% concordant age of 2052 ± 13 Ma and confirms the presence of a ca. 2.05

Ga xenocrystic component, potentially sourced from the Mkushi Gneiss. Nine data points are between 76 and 99.4% concordant, but display an erratic drift normal to the concordia curve, interpreted to reflect incorrect correction for common Pb. Uncorrected data, plotted on a Tera-Wasserburg concordia diagram, yield a regression towards common Pb, with an intercept at 1022 ± 16 Ma (MSWD=1.40)(Figure 4-113). This result is considered the best estimate for the emplacement age of the granite. Three strongly discordant data points yield $^{207}\text{Pb}/^{206}\text{Pb}$ ages of 1320 ± 16 Ma (KN8-1r, 86.2% concordant), 1626 ± 30 Ma (KN8-7, 85.4% concordant) and 2075 ± 35 Ma (KN8-4c, 87.9% concordant). Because of the high discordance of these data, none of these analyses can be given much weight. Analysis KN8-1r was conducted on a wide rim, which, based on a clear oscillatory zoning pattern in CL, is interpreted as a magmatic overgrowth. Since no other 1.3 Ga ages are reported in the area, other than poorly constrained whole rock Rb-Sr dates (Daly, 1986), confirmation of a 1.32 Ga magmatic event awaits additional work. Analysis KN8-4c was conducted on a core, and can be interpreted to reflect a xenocrystic component similar to that recorded in core analysis KN8-1c and corresponding to the Mkushi Gneiss. Zircon analysis KN8-7 suggests inheritance from source rocks similar in age to the Lukamfwa Hill Granite Gneiss.

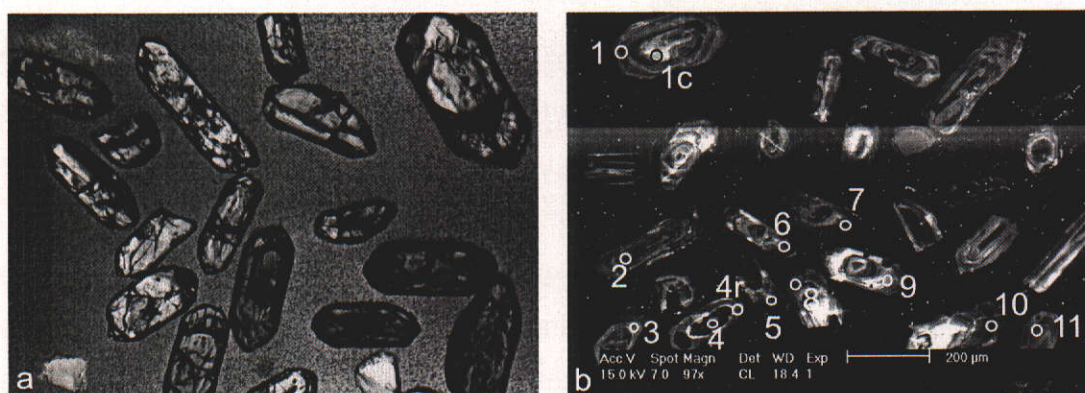


Figure 4-111: (a) photomicrograph of zircons from sample KN8 (xpl) showing euhedral crystals (f.o.v. = ~1000 µm); (b) CL image of zircons from sample KN8 showing the location of analysed spots. Note the variability on CL response, oscillatory zoning patterns and complex internal fabrics of the zircons (f.o.v.= 1200 µm).

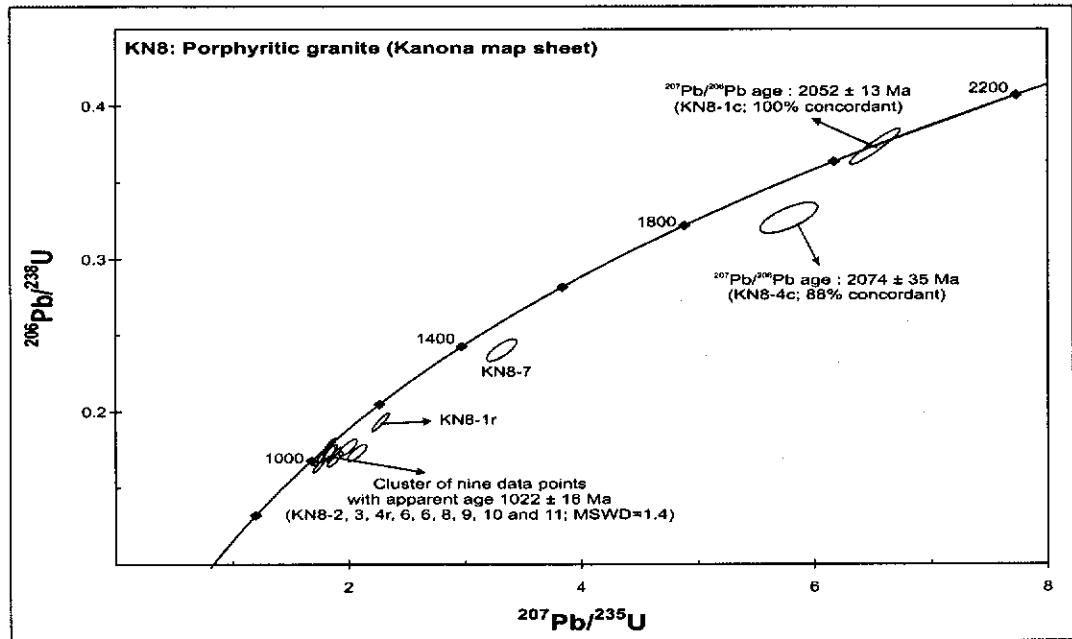


Figure 4-112: U-Pb concordia plot for all zircon analyses of sample KN8. Error ellipses are at 1σ confidence level. Note the drift away from concordia in the younger age group due to incorrect common Pb correction based on measured ^{204}Pb .

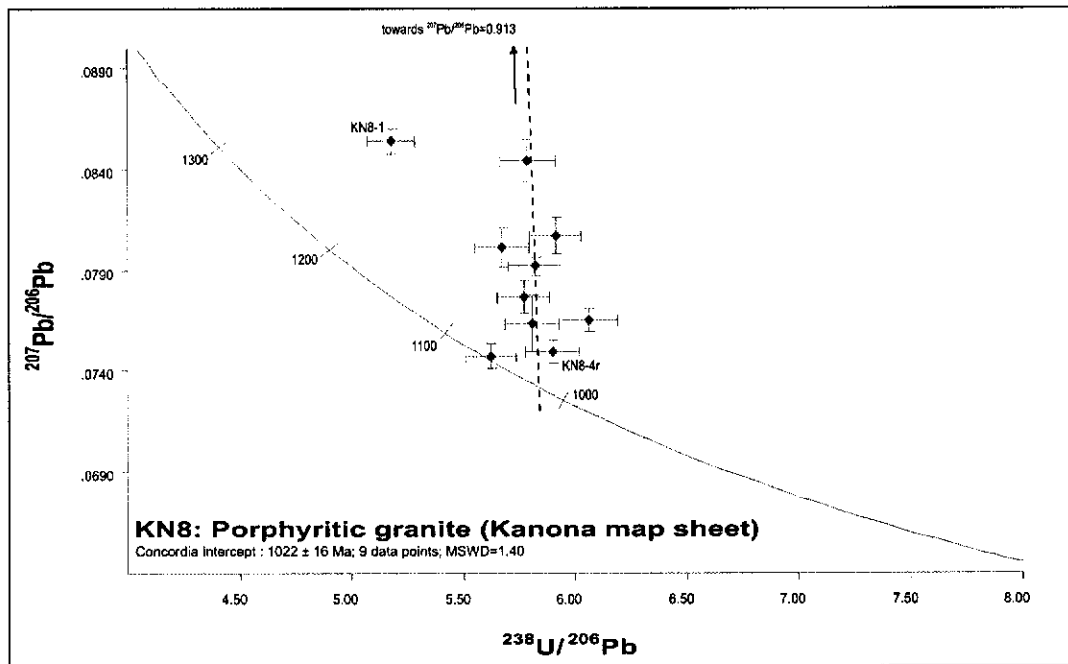


Figure 4-113: U-Pb concordia plot (Tera-Wasserburg) for selected zircon analyses of sample KN8. The data are uncorrected for common Pb. Error crosses are at 1σ confidence level. The regression is made towards common Pb, calculated for an age of 1050 Ma after Stacey and Kramers (1975).

4.8.4.14 Sample ND1

Sample ND1 was collected in the Ndabala map sheet (Figure 4-1). It consists of coarse porphyritic biotite granite, with a very weak biotite foliation that is oblique to a north-south-oriented magmatic foliation defined by large aligned microcline phenocrysts. The phenocrysts are euhedral and do not appear to be affected by the weak tectonic foliation. Zircons from the granite are large and euhedral, ranging from 200 to 500 μm in size. Most zircons have bipyramidal terminations, and have length to width ratios over 3:1. In transmitted light, the zircons range from dark yellow to dark brown in colour and are variably cracked (Figure 4-114 (a)). CL imaging shows a dominant proportion of the zircon to have very low response, with the smaller proportion of medium CL response grains showing broad oscillatory zoning patterns (Figure 4-114 (b)). Upon close inspection, the low CL zircons also show weakly developed concentric zoning, consistent with magmatic crystallisation, but are often characterised by truncating, uniformly low CL zones indicative of some degree of homogenisation. Ten analyses were conducted on six zircons, and confirm that most grains contain large amounts of uranium. Metamictisation allowed substantial disturbance of the U-Th-Pb system, and proportions of common ^{206}Pb in total ^{206}Pb range from zero to 6.37% (Table 13-46). U and Th range from 238 to 2459 ppm and 55 to 1017 ppm respectively, with Th/U ranging from 0.03 to 1.50. Significant disturbance of the U-Th-Pb isotopic system, possibly due to metamictisation, has displaced analyses ND1-1, 3, 7 and 8 and one analysis on a rim (MD1-5r) away from concordia. No meaningful intercepts can be calculated for these data points, and they are excluded from the age calculation (Figure 4-115). The remaining five points, including one analysis on a low Th/U core (ND1-5c) lie within 5% of concordia and define a weighted mean $^{207}\text{Pb}/^{206}\text{Pb}$ age of 1023 ± 7 Ma (MSWD=0.50)(Figure 4-116). This age is interpreted to date crystallisation of the porphyritic granite.

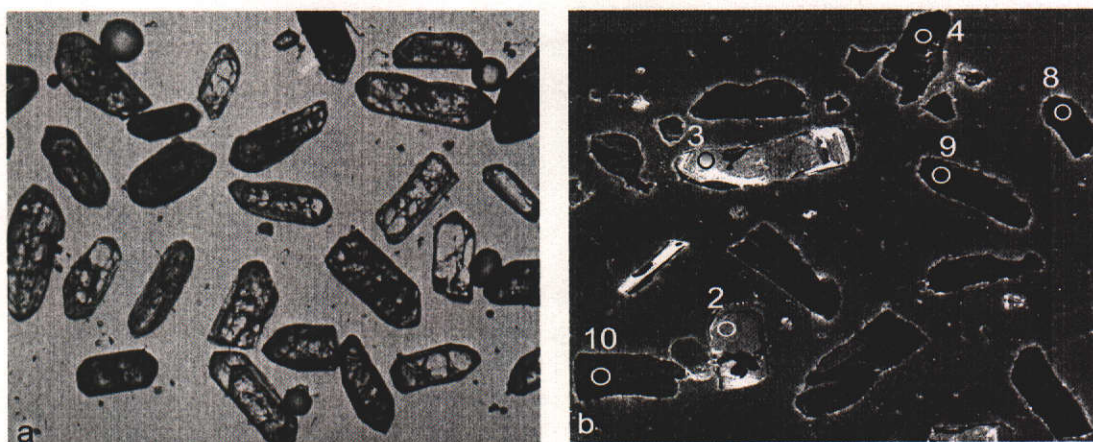


Figure 4-114: (a) photomicrograph of zircons from sample ND1 (xpl) showing sub-euhedral crystals (f.o.v. = ~1200 μm); (b) CL image of zircons from sample ND1 showing the location of analysed spots. Note the variability on CL response. High luminescence crystals show oscillatory zoning patterns while dark CL crystals show very faint concentric zoning (f.o.v. = 1000 μm).

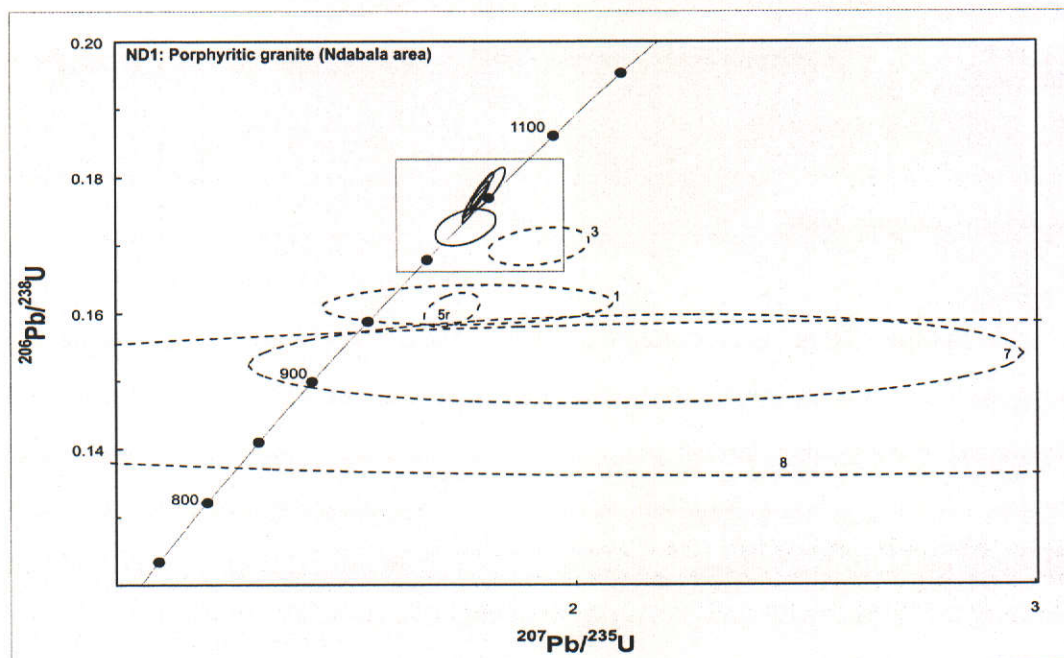


Figure 4-115: U-Pb concordia plot for zircon analyses of sample ND1. Error ellipses are at 1 σ confidence level. Note the large errors on three data points and two discordant analyses (dashed ellipses). The box shows the area enlarged in Figure 4-116.

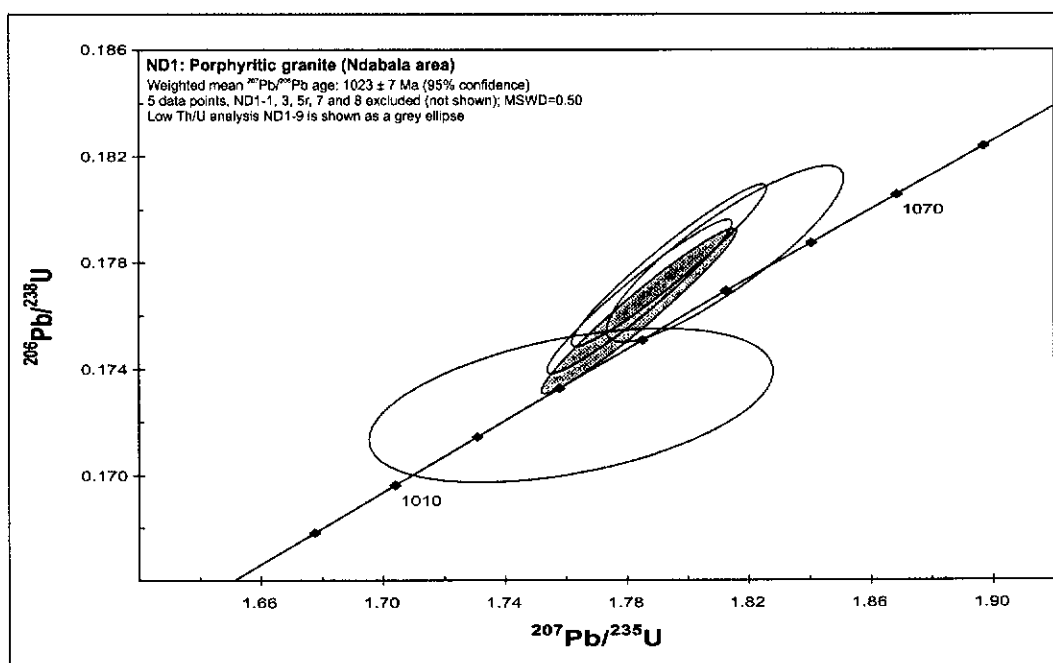


Figure 4-116: U-Pb concordia plot for concordant zircon analyses of sample ND1. Error ellipses are at 1 σ confidence level.

4.8.4.15 Sample ND4

Sample ND4 was collected from a small body of diorite some 20 kilometers northeast of Ndabala (Figure 2-9). The diorite is porphyritic and contains minor quartz, coarse plagioclase, abundant hornblende and subordinate biotite defining a weak foliation. Zircons from sample ND4 are large, between 200 and 600 μm , sub-euhedral, and brown-yellow in colour (Figure 4-117). Most zircons are clear, with few or no visible inclusions. The crystals are variably cracked, but in all cases large uncracked and clear areas could be selected for analysis. CL imaging shows the zircons to be of medium luminescence, with broadly defined concentric zoning patterns. Limited rehomogenisation has affected some grains, but the majority of crystals retain broad sector zoning. A very small proportion of zircon contains a very narrow rim overgrowth, too small to allow measurement with the ion microprobe. Four analyses were conducted on four zircons. f^{206} values are very low, ranging from zero to 0.071%. U and Th vary from 271 to 398 ppm and 288 to 650 ppm respectively (Table 13-47). Th/U ratios are between 1.10 and 1.69, indicative of magmatic zircon. The data plot within 4% of concordia and define a weighted mean $^{207}\text{Pb}/^{206}\text{Pb}$ age of 1037 ± 16

Ma (MSWD=0.61)(Figure 4-118). The four data points allow the calculation of a concordia age of 1031 ± 5 Ma with MSWD of 0.83. The latter age represents the best estimate for the crystallisation age of the diorite.

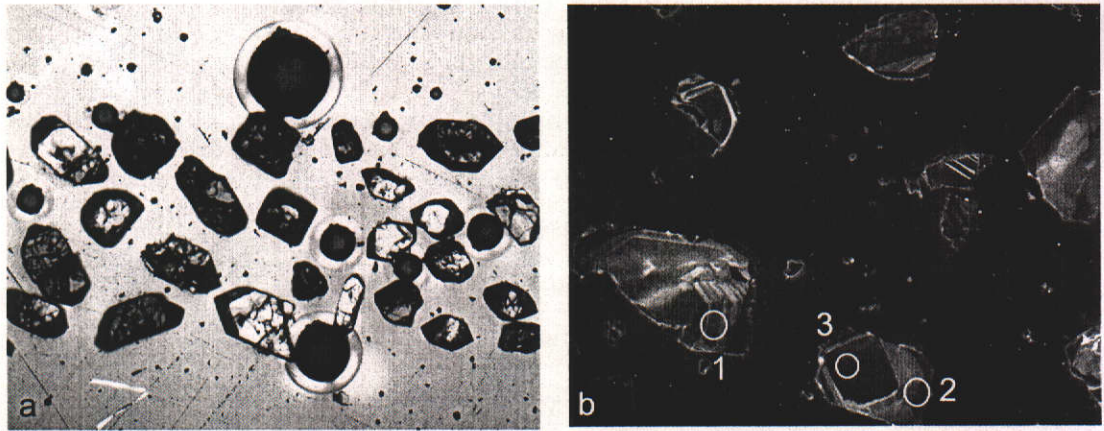


Figure 4-117: (a) photomicrograph of zircons from sample ND4 (xpl) showing sub-euhedral crystals (f.o.v. = ~1600 μm); (b) CL image of zircons from sample ND4 showing the location of analysed spots. Note the oscillatory zoning patterns (f.o.v.= 700 μm).

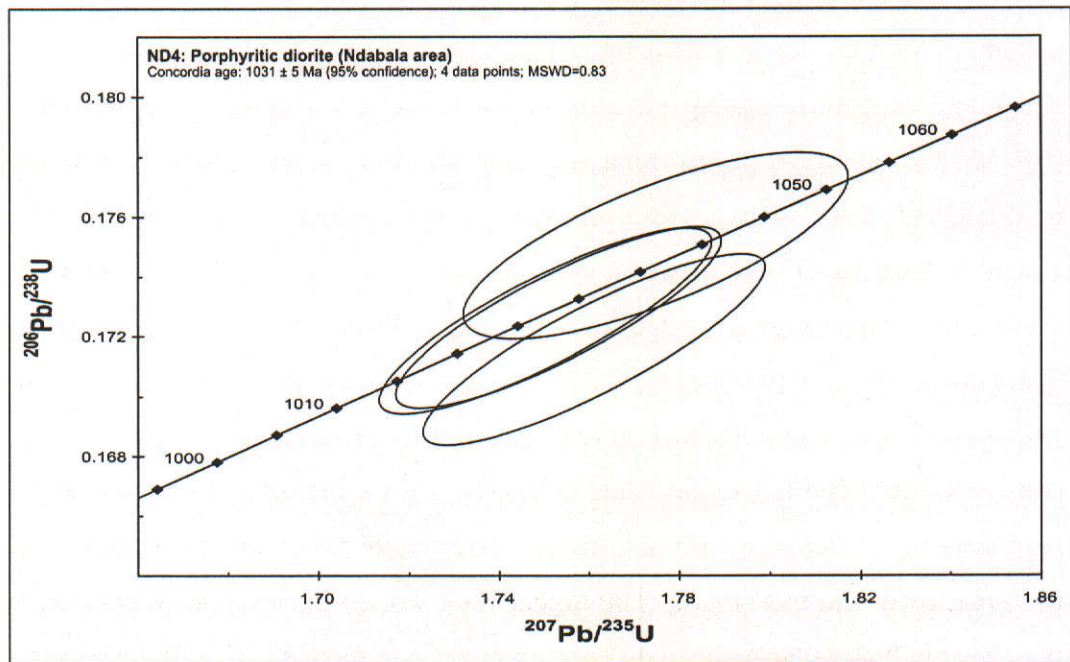


Figure 4-118: U-Pb concordia plot for zircon analyses of sample ND4. Error ellipses are at 1 σ confidence level.

4.8.4.16 Sample ND5

Sample ND5 was collected some 30 kilometers northeast of Ndabala from a small body of syenite within the porphyritic granites (Figure 4-1). Although the contact between the porphyritic granites and the syenite is not exposed, the weak deformation and similarities in fabric suggests the syenite was emplaced in the same time-frame as the granite. The syenite consists of abundant phenocrysts of microcline set in a matrix of plagioclase and microcline, with subordinate quartz and biotite. Various aplitic dykes cut the syenite and appear to display the same weak foliation as the host rock, indicating they were emplaced prior to the deformation that imparted the weak tectonic fabric. Zircons extracted from sample ND5 are generally sub-euhedral and range in size from 100 to 300 μm . The grains have length to width ratios up to 4:1 and show sharp terminations, indicative of magmatic growth. The crystals are clear, light yellow to light brown in colour and variably cracked (Figure 4-119 (a)). Some zircon appears to contain large central inclusions or may have grown on a metamict core. CL imaging shows well-developed concentric zoning patterns, and variable CL response (Figure 4-119 (b)). Most zircon has a narrow relatively high CL rim, too small to allow analysis on SHRIMP. Four zircons were analysed, two of which yield very low f_{206} values (0.04-0.10%), while two contain higher f_{206} values (0.62-0.72%) (Table 13-48). U and Th range from 230-263 ppm and 253-401 ppm respectively, giving Th/U ratios between 1.09 and 1.72. The two low common Pb analyses plot within 2% of concordia, while the two other points plot up to 14% away from concordia (Figure 4-120). The four data points do not appear to line up along a meaningful regression line, and there are insufficient data points to ascertain the reason for discordance of the two points. The higher f_{206} values for the discordant points, however, indicate that inadequate correction for common Pb may be responsible for the points plotting off a reasonable Pb-loss path. A weighted mean $^{207}\text{Pb}/^{206}\text{Pb}$ age of 1044 ± 28 Ma can be calculated on all points, but the high MSWD value of 2.40 indicates excessive scatter. Using only the two near concordant points, a weighted mean $^{207}\text{Pb}/^{206}\text{Pb}$ age of 1020 ± 34 Ma with MSWD=0.19 can be calculated. These two points also define a concordia age of 1028 ± 7 Ma

(MSWD=0.23), which represents the best estimate for the crystallisation age of the syenite.

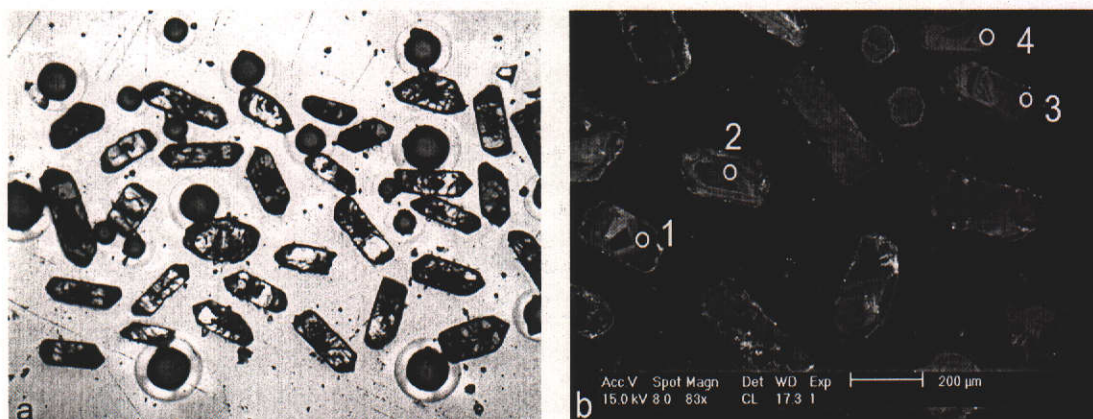


Figure 4-119: (a) photomicrograph of zircons from sample ND5 (xpl) showing sub-euhedral crystals (f.o.v. = ~1600 µm); (b) CL image of zircons from sample ND5 showing the location of analysed spots. Note the oscillatory zoning patterns (f.o.v.= 1700 µm).

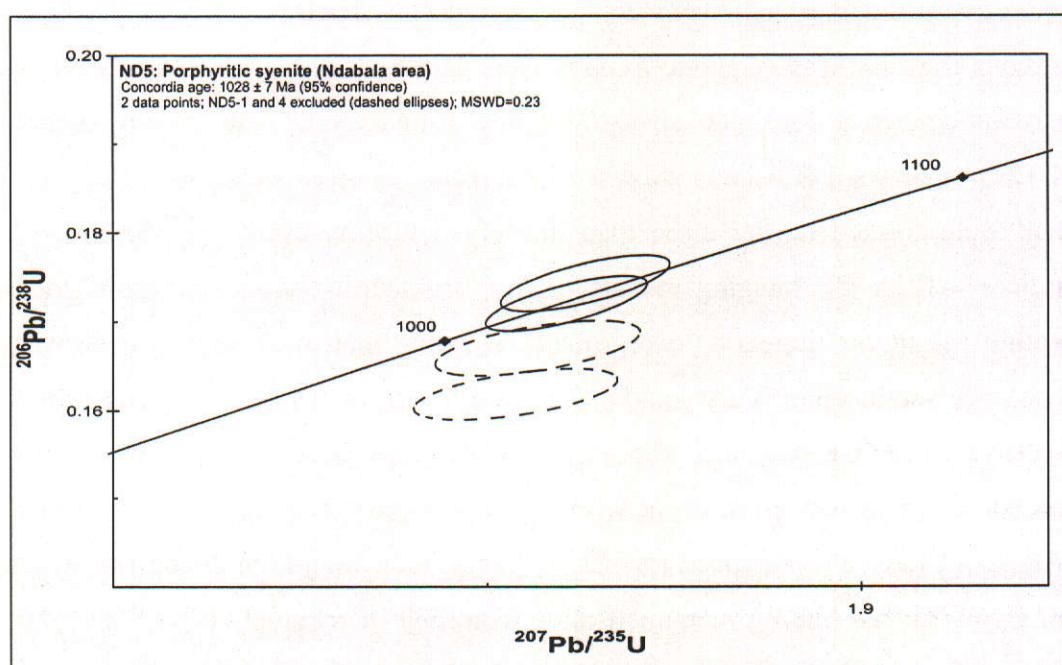


Figure 4-120: U-Pb concordia plot for zircon analyses of sample ND5. Error ellipses are at 1 σ confidence level.

4.8.4.17 Sample SASA2

Various samples were collected from the Sasa Foliated Granite in the northern part of the Serenje area, which consists of a medium-grained granitic gneiss containing quartz - calcic-plagioclase - microcline - biotite and accessory hornblende (Figure 4-2). The granite forms very poorly exposed, low-lying, flat outcrops, and occasionally loose boulder outcrops, especially along the course of the Sasa River and its tributaries. Regional outcrop forms a domal structure, surrounded by ridge-forming quartzites of the Kanona Group. Locally, shear zones have developed, along which mafic minerals are concentrated. Only one out of the three samples taken yielded an adequate amount of zircon for U-Pb dating (sample SASA2). A large proportion of zircons from this sample were found in the more magnetic fractions, appeared dark brown in colour, rich in inclusions and extensively cracked, and were not considered for SHRIMP analysis. Eighteen zircons from the less magnetic fraction were selected for analysis. Most of these zircons contain a core, and all show typical primary magmatic zoning (Figure 4-121). A very small number show a core surrounded by two wide magmatic rims that were formed during more than one crystallisation event (e.g. SASA2-12, Figure 4-121). CL imaging reveals patchy, crosscutting homogenisation zones within magmatic zircons or overgrowths, showing that most zircons underwent some recrystallisation. Very small (~1 micron) overgrowths occur on most grains, with very high CL response. These overgrowths may be related to post-orogenic recrystallisation during an event with minor introduction of low-uranium fluids. All grains have a pronounced low CL response, indicating high U content, which accounts for the intense metamictisation, resulting in relatively high ^{204}Pb . f_{206} ranges from 0.27 to 2.48%, while Th/U ratios vary from 0.03 to 2.38 (Table 13-49). Uranium exceeds 1000 ppm in four zircons, but varies from 48 to 1974 ppm overall. Analyses of rim-core and rim-rim pairs on two grains (SASA2-3 and SASA2-12) yield identical results (within error) to the unzoned zircon analyses. The Th/U ratios on these rims (0.25 and 0.36 respectively) also support a magmatic rather than metamorphic origin. A total of twelve analyses define a clear Pb-loss trend, yielding a regression line with upper intercept of 1015 ± 14 Ma and lower intercept of -677 ± 720 Ma (MSWD=0.59)(Figure 4-122).

Assuming that Pb-loss occurred recently (0 Ma), the upper intercept increases to 1023 ± 17 Ma. The increase of MSWD value (1.02) with respect to normal regression indicates that a model of recent Pb-loss, although possible, does not adequately explain the drift of the data points away from concordia. Using only the 6 most concordant data points (>95% concordant), a weighted mean $^{207}\text{Pb}/^{206}\text{Pb}$ age of 1012 ± 22 Ma (MSWD=0.55) is obtained and a concordia age can be calculated at 1016 ± 14 Ma (MSWD=0.63). This latter age can be regarded as the most reliable estimate for the crystallisation age of the Sasa Granite.

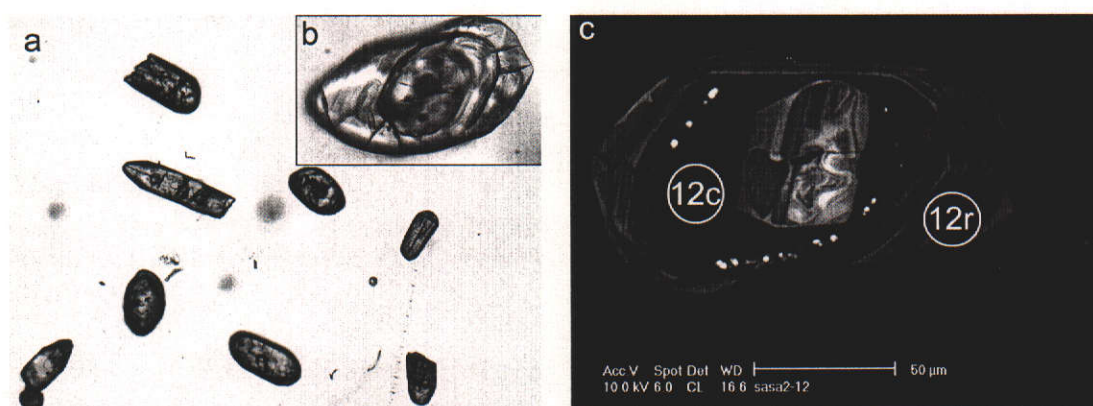


Figure 4-121: (a) photomicrograph of zircons from sample SASA2 (xpl) showing anhedral and euhedral crystals (f.o.v. = ~ 800 μm); (b) inset shows zircon SASA2-12 on which a core and rim can be distinguished; (c) CL image of zircon SASA2-12 showing the location of analysed spots. Note the oscillatory zoning patterns on both core and two rims (f.o.v. = 150 μm).

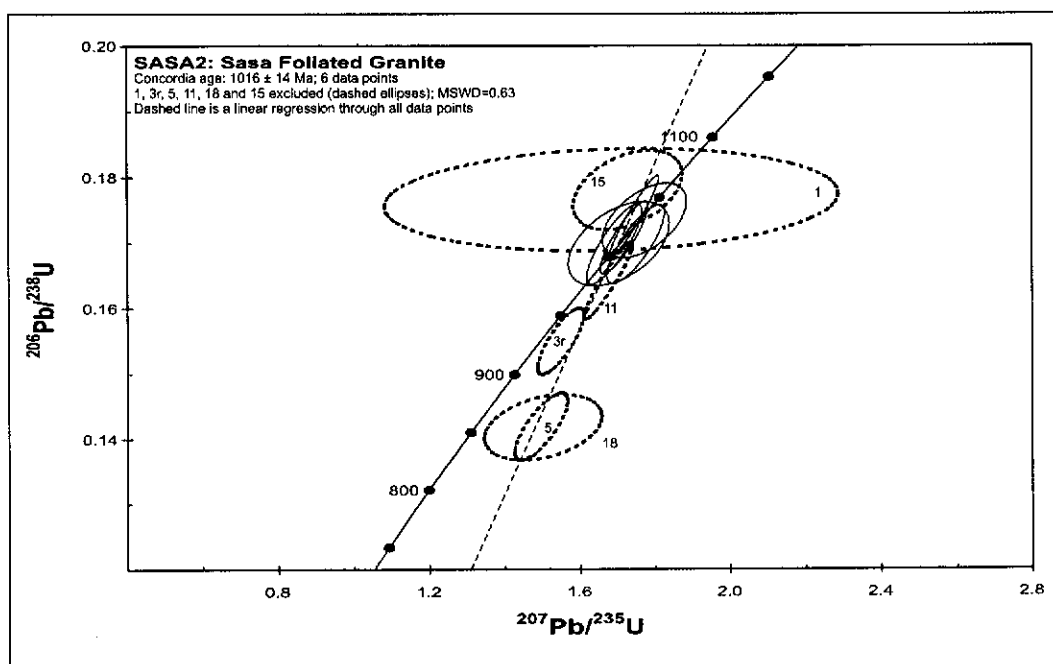


Figure 4-122: U-Pb concordia plot for zircon analyses of sample SASA2. Error ellipses are at 1 σ confidence level.

4.8.4.18 Sample SER 5-3

Sample SER 5-3 was collected from porphyritic granite exposed to the south of the Sasa dome (Figure 2-10) and shows a very weak biotite foliation trending northeast. The zircons separated from SER 5-3 are quite large, magmatic and often show complex patterns of oscillatory concentric mineral zoning (Figure 4-123 (a)). CL imaging reveals very well-developed oscillatory zoning patterns (Figure 4-123 (b)). Of the ten different zircons analysed, three show slightly elevated f_{206} values (SER53-10, 3 and 9), while f_{206} values for the remaining seven range up to 0.17% (Table 13-49). U and Th contents range from 117-813 ppm and 123-761 ppm respectively, and Th/U ratios range from 0.50 to 1.74. A few isolated grains show internal homogenisation due to recrystallisation. The data are all within 5% of concordia and yield a weighted mean $^{207}\text{Pb}/^{206}\text{Pb}$ age of 1029 ± 13 Ma (MSWD=1.44) and a concordia age of 1025 ± 12 Ma (MSWD=0.38)(Figure 4-124). Based on their high proportion of common lead, coupled with relatively low contents of U and Th leading to poor precision, analyses SER53-10.1 (4.93%), SER53-9.1 (0.42%) and SER53-3.1 (0.42%) can be excluded to yield a weighted mean $^{207}\text{Pb}/^{206}\text{Pb}$ age of 1032 ± 13 Ma

(MSWD=1.34) and concordia age of 1034 ± 5 Ma (MSWD=0.28). Based on the lower MSWD value for the latter, the age of 1034 ± 5 Ma is taken as the best estimate for the crystallisation age of sample SER5-3.

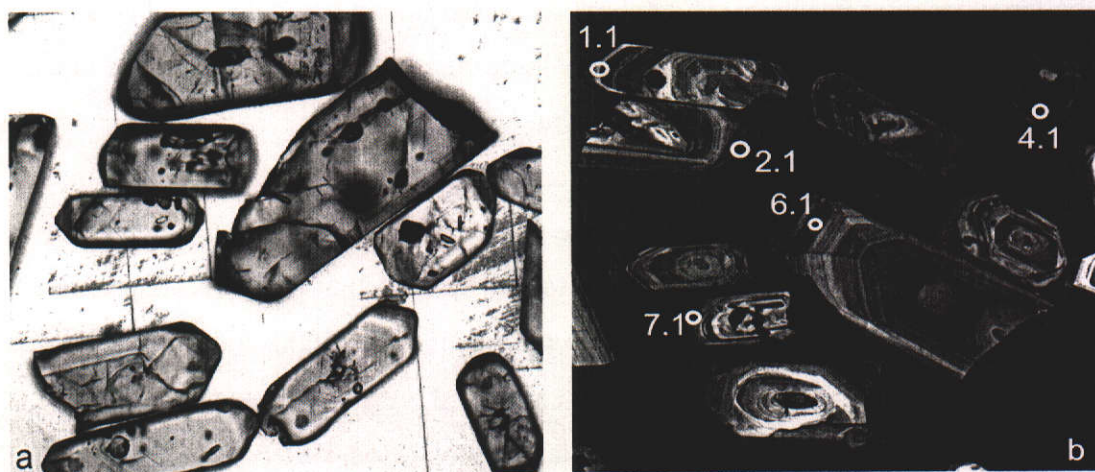


Figure 4-123: (a) photomicrograph of zircons from sample SER5-3 (xpl) showing euhedral crystals (f.o.v. = ~800 µm); (b) CL image of zircons from SER5-3 showing the location of analysed spots. Note the oscillatory zoning patterns (f.o.v.= 800 µm).

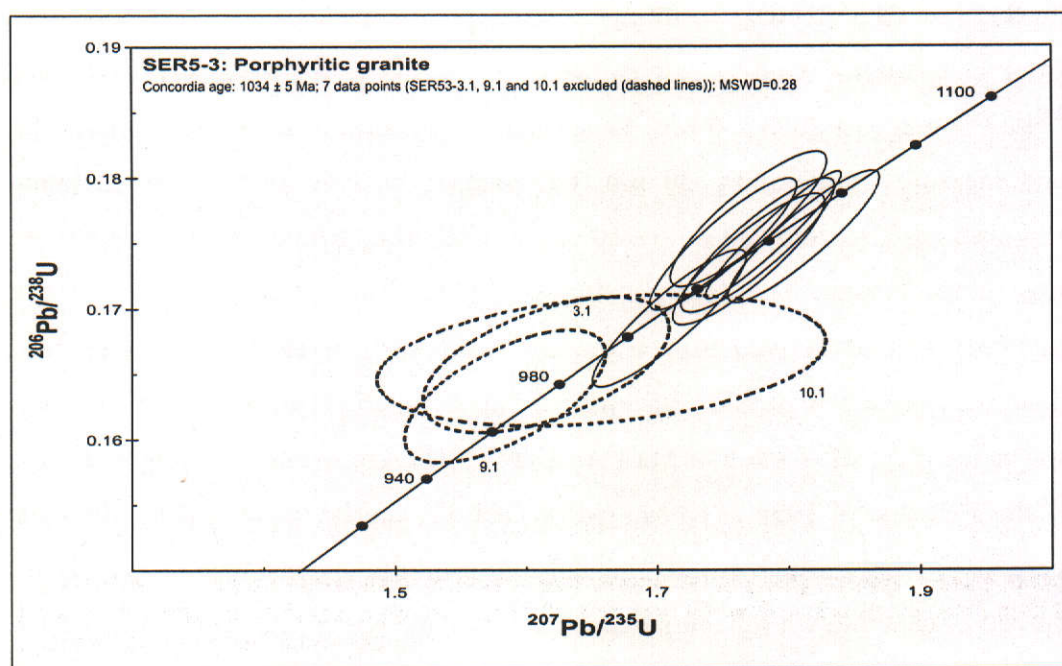


Figure 4-124: U-Pb concordia plot for zircon analyses of sample SER5-3. Error ellipses are at 1σ confidence level.

4.8.4.19 Sample SER 6-4

Sample SER 6-4 was collected from Chimuma Hill (Figure 4-2), which is a large irregular inselberg rising about 40 meters above the plateau and consisting entirely of coarse biotite granite with large microcline phenocrysts and clearly defined biotite foliation, with biotite wrapped around the microcline phenocrysts. The grains are generally non-complex and prismatic, but some have cores and are prismatic and sub- to euhedral in shape (Figure 4-125 (a)). Length to width ratios vary up to 4:1, with sizes ranging up to 300 μm . CL imaging reveals prominent concentric zoning patterns consistent with magmatic crystallisation of the zircons (Figure 4-125 (b)). Ten analyses were conducted on ten zircons. Common lead is extremely low for six analyses, but is larger for SER64-10.1 (0.29%), SER64-8.1 (0.60%), SER64-1.1 (0.63%) and SER64-6.1 (0.70%)(Table 13-51). U and Th contents are variable, ranging from 50 to 1252 ppm and 71 to 979 ppm respectively. Analysis SER64-6.1 shows very low U and Th (50 and 99 ppm) and the highest f_{206} (0.70%) resulting in an imprecise data point, and is excluded from calculations. One zircon (SER64-9.1) yields a 3% inversely discordant $^{207}\text{Pb}/^{206}\text{Pb}$ age of 2003 ± 6 Ma. This zircon is euhedral in shape, with sharp tips, and measures 250 μm by 50 μm . CL imaging reveals an elongate medium-response core, surrounded by a ~ 10 μm low CL rim, which widens towards the tips of the crystal. The spot penetrates only the core of the zircon, which is interpreted to be derived from a granitic precursor (Figure 4-126). Eight other analyses define a regression line with an upper intercept of 1036 ± 13 Ma and lower intercept of -53 ± 510 Ma (MSWD=1.5)(Figure 4-127). A weighted mean $^{207}\text{Pb}/^{206}\text{Pb}$ age of 1036 ± 12 Ma (MSWD=1.32) can be calculated for the eight consistent points, which is indistinguishable from the upper intercept age. As the spread of data allow a reliable linear regression, the upper intercept age of 1036 ± 13 Ma is regarded as the best estimate for the crystallisation age of the porphyritic granite of Chimuma Hill.

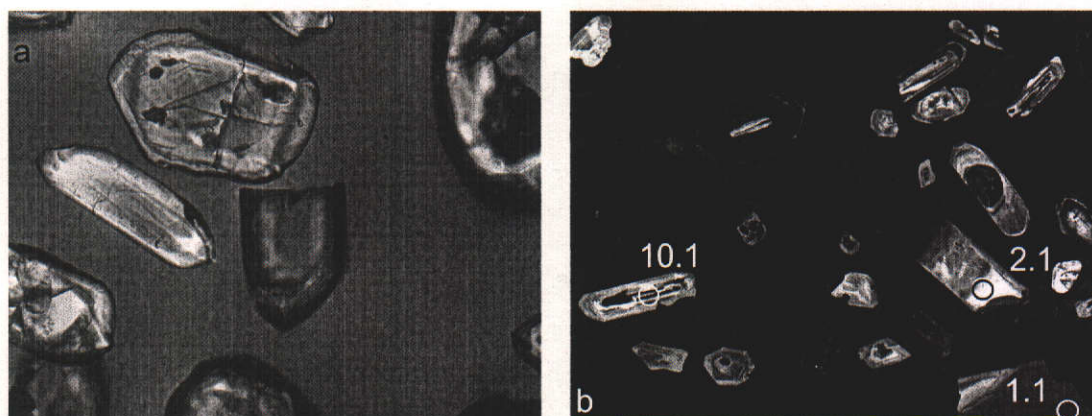


Figure 4-125: (a) photomicrograph of zircons from sample SER6-4 (xpl) showing euhedral crystals (f.o.v. = ~500 μm); (b) CL image of zircons from SER6-4 showing the location of analysed spots. Note the oscillatory zoning patterns (f.o.v.= 800 μm).

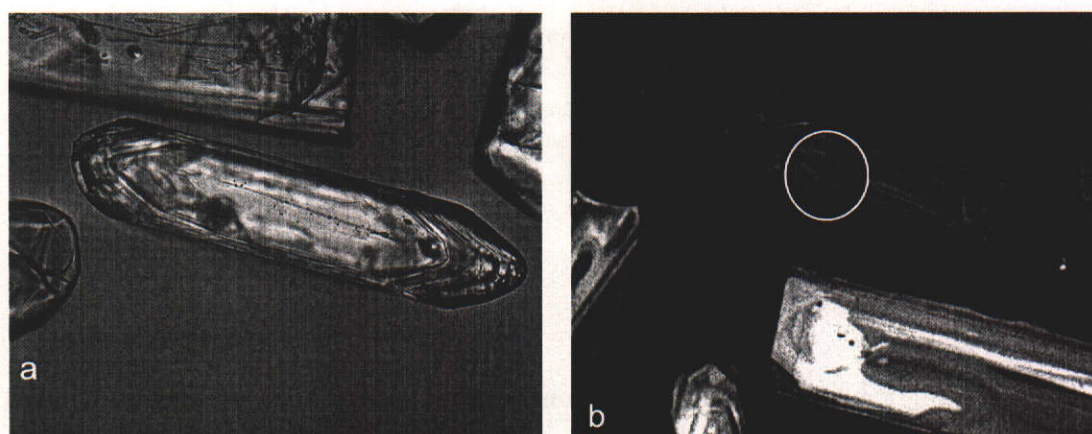


Figure 4-126: (a) photomicrograph of an analysed zircon (analysis SER64-9.1) from sample SER6-4 (xpl) showing a euhedral crystal, with narrow rim (f.o.v. = ~200 μm); (b) CL image of the same zircon showing the location of the analysed spot. Note the dark CL rim (f.o.v.= 200 μm).

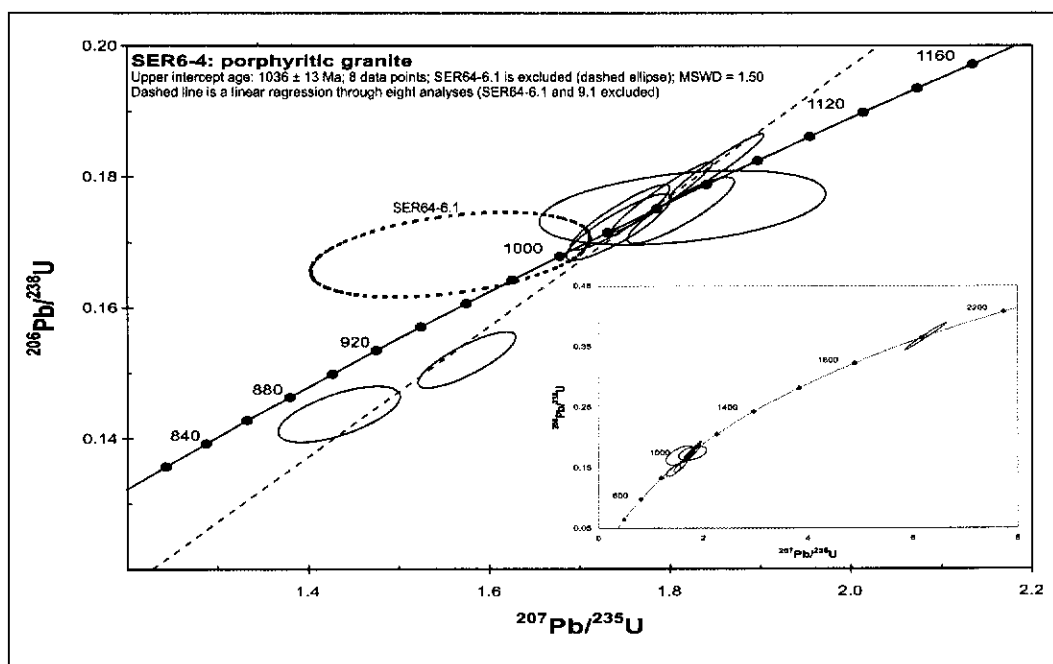


Figure 4-127: U-Pb concordia plot for zircon analyses of sample SER6-4. Inset shows a concordia plot for all 10 data points. Error ellipses are at 1σ confidence level.

4.8.4.20 Sample SQG

Sample SQG was collected from a small quarry west of Serenje (Figure 4-2). The quarry exposes grey porphyritic granite, containing a quartz-plagioclase-biotite matrix and microcline phenocrysts. A magmatic foliation is defined by weak alignment of microcline, and dark, lensoid mafic xenoliths of varying size are present. The granite is cut by numerous pegmatitic veins containing large quartz, plagioclase and biotite crystals. The pegmatites are undeformed and are interpreted to represent the latest phase of crystallisation from the melt. Zircons collected from SQG are euhedral magmatic grains, some of which have partially recrystallised as seen in homogenised zones in CL images. Most zircons have a ~ 1 -micron-wide outer rim with high CL response, which records late crystallisation from low-uranium fluids (Figure 4-128). Eleven analyses were conducted on eleven zircons. U and Th range from 133 to 702 ppm and 88 to 463 ppm respectively (Table 13-52). Th/U ratios range from 0.38 to 1.04, consistent with magmatic zircon. Common lead values are generally very low, ranging from zero to 0.09%, but are higher for SQG-14 (1.20%). The data define a broad cluster close to concordia for which no meaningful regression can be calculated (Figure

4-129). The spread of data, roughly parallel to concordia, could suggest limited Pb loss relatively soon after crystallisation of the granite. A weighted mean $^{207}\text{Pb}/^{206}\text{Pb}$ age of 1032 ± 15 Ma (MSWD=2.6) can be calculated from all data points, and provides only a rough estimate of the actual emplacement age of the Serenje Quarry Granite. Using only the six most concordant and coherent data points (SQG-7, 17, 20, 41, 48 and 60), but excluding three apparently older zircons (SQG-26, 70 and 72, see below), and analyses SQG-14 (high f_{206} of 1.201%) and 77 (low U and Th), a weighted mean $^{207}\text{Pb}/^{206}\text{Pb}$ age can be calculated at 1024 ± 9 Ma with an MSWD value of 1.07. The same points yield a concordia age of 1021 ± 8 Ma (MSWD=3.7). Three points with low amounts of common Pb and reasonable precision define older ages. One data point (SQG-70) plots 0.7% away from the concordia line and defines a $^{207}\text{Pb}/^{206}\text{Pb}$ age of 1099 ± 30 Ma. This data point has high f_{206} of 1.20% making the analysis relatively imprecise. Two data points (SQG-26 and 72) define a weighted mean $^{207}\text{Pb}/^{206}\text{Pb}$ age of 1062 ± 17 Ma (MSWD=0.0067). All three data points plot relatively close to concordia, and the ages may represent xenocrystic components of ~1065 and 1100 Ma, although more data are needed to confirm this. Based on its low MSWD value, the weighted mean $^{207}\text{Pb}/^{206}\text{Pb}$ age of 1024 ± 9 Ma provides the best estimate for the crystallisation age of the Serenje Quarry Granite.

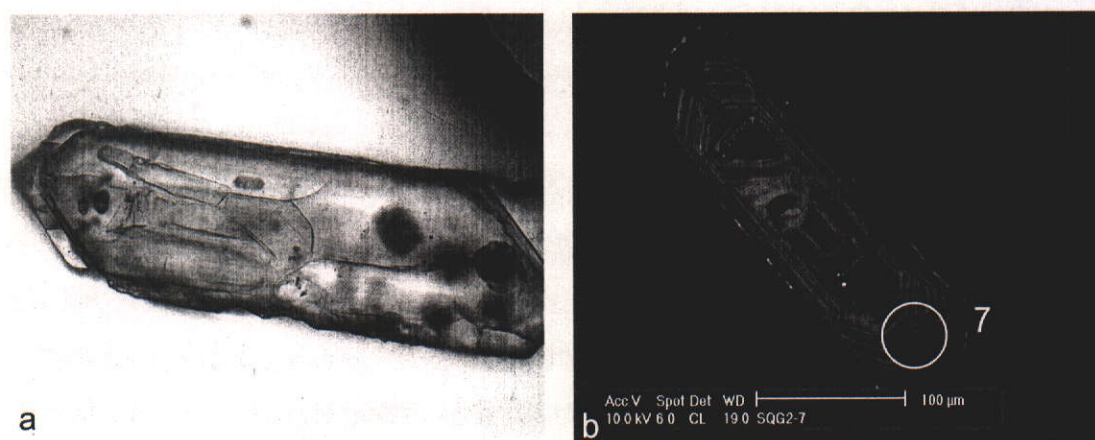


Figure 4-128: (a) photomicrograph of an analysed zircon (analysis SQG-7) from sample SQG (xpl) showing a euhedral crystal, with narrow rim (f.o.v. = ~300 µm); (b) CL image of the same zircon showing the location of the analysed spot. Note the oscillatory zoning (f.o.v. = 300 µm).

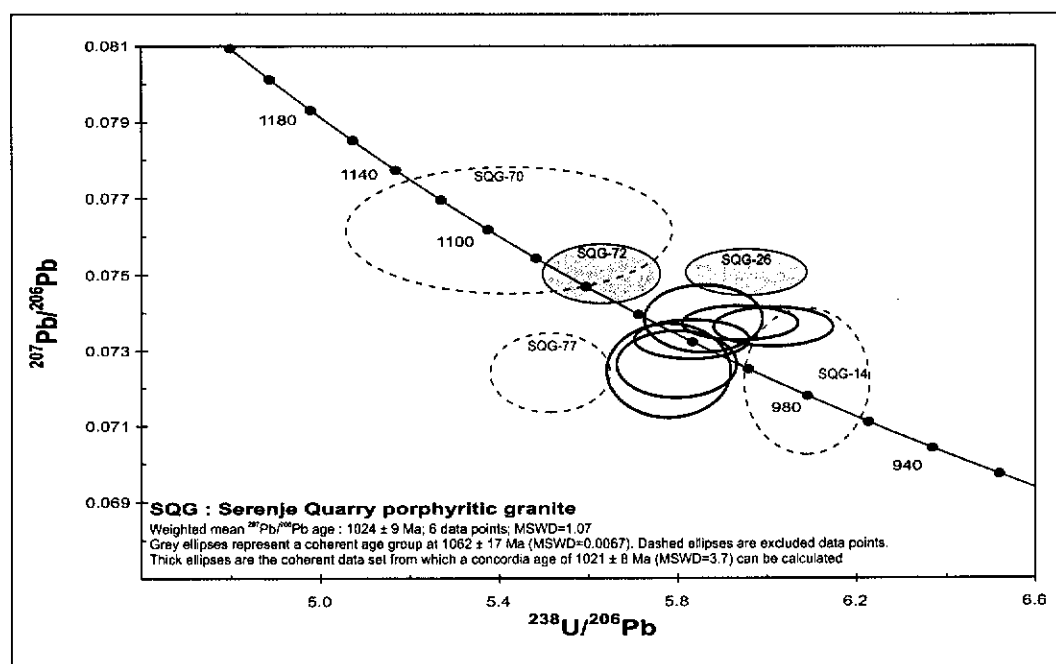


Figure 4-129: U-Pb concordia plot (Tera-Wasserburg) for zircon analyses of sample SQG. Error ellipses are at 1σ confidence level. Dashed ellipse represents analysis SQG-70 with high f_{206} (1.20%) yielding an age of 1099 ± 30 Ma. Grey ellipses are two data points possibly defining a ~ 1065 Ma xenocrystic component.

4.8.4.21 Sample ZM36

One sample was collected from the Mununga Quarry approximately midway along the sealed road between Serenje and Mpika (Figure 4-2). The rock is a coarse K-feldspar-phyric biotite granite. Zircons from the Mununga Granite (sample ZM36) are typically euhedral, and show clear oscillatory zoning patterns indicative of magmatic zircon (Figure 4-130). Length to width ratios range from equant to 5:1 and size varies from below 100 to over 300 μm . Ten zircons were analysed, three of which (ZM36-1.1, 3.1 and 6.1) yielded very low U and Th contents (Table 13-53) resulting in poor precision. The proportion of common ^{206}Pb in total ^{206}Pb is below 0.19% for the remaining seven analyses. A weighted mean $^{207}\text{Pb}/^{206}\text{Pb}$ age of 1030 ± 15 Ma (MSWD=1.24) can be calculated on all ten points (Figure 4-131) while a concordia age on all points gives 1025 ± 10 Ma (MSWD=0.44). Using only six concordant analyses, which have higher U, Th and lower f_{206} values, a concordia age of 1023 ± 11 Ma (MSWD=1.30) can be calculated, while a weighted mean $^{207}\text{Pb}/^{206}\text{Pb}$ age for the same points yields 1030 ± 15 Ma, with an MSWD value of 0.32. All calculated ages are statistically

indistinguishable, and the concordia age of 1025 ± 10 Ma calculated from all data points provides the best age estimate for the crystallisation of the Mununga Granite.

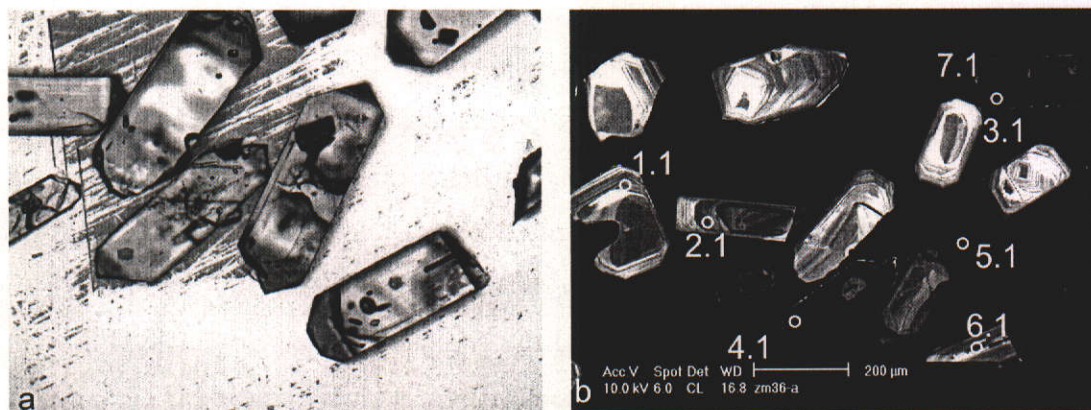


Figure 4-130: (a) photomicrograph of zircons from sample ZM36 (xpl) showing euhedral crystals (f.o.v. = $\sim 700 \mu\text{m}$); (b) CL image of analysed zircons from sample ZM36 showing the location of analysed spots. Note the oscillatory zoning (f.o.v.= $1000 \mu\text{m}$).

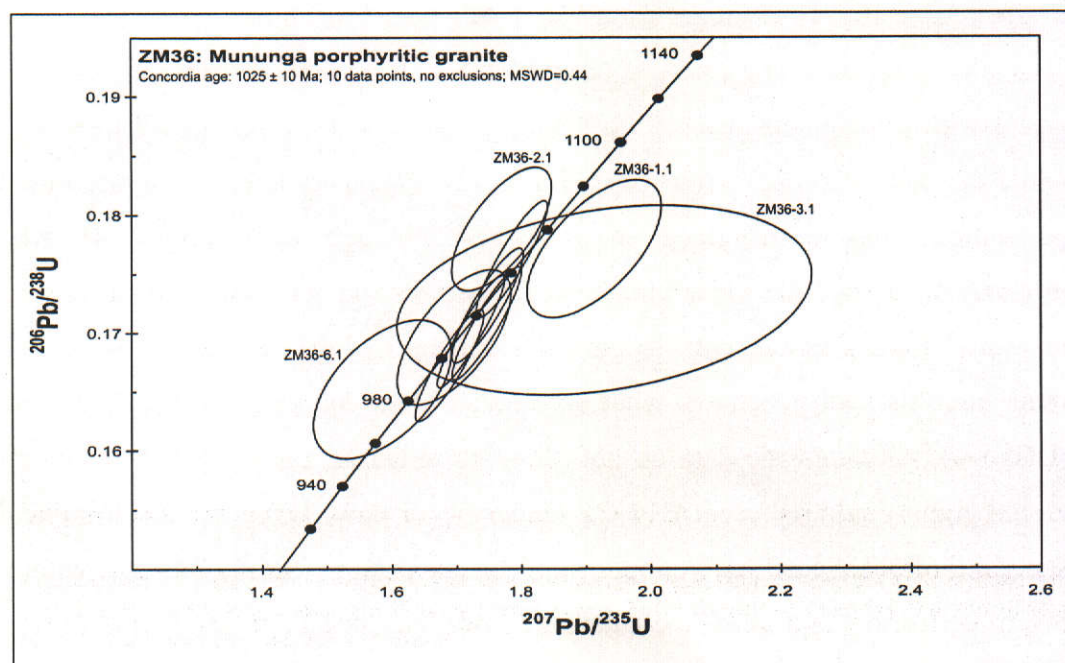


Figure 4-131: U-Pb concordia plot for zircon analyses of sample ZM36. Error ellipses are at 1σ confidence level.

4.8.4.22 Sample CHL5

Sample CHL5 was taken from a flat outcrop some 60 kilometers to the southwest of Mpika (Figure 4-2), where strongly foliated micaceous granite gneiss is intruded by numerous small pegmatites. The gneiss shows a marked biotite-muscovite foliation along east-southeasterly trends, dipping steeply to the north. It was mapped as the Mayenze Gneissose Granite (Page, 1973), which consists of porphyritic unfoliated granites and foliated gneisses. Zircons from sample CHL5 are euhedral, and range in size from 200 to 500 μm . Length to width ratios range from 4:1 to 2:1 and the crystals are clear and pale yellow in colour. They contain a range of inclusions and are variably cracked (Figure 4-132 (a)). CL imaging indicates concentric zoning patterns, with CL response ranging from extremely high to extremely low (Figure 4-132 (b)). Eight analyses were conducted on eight different zircons, and indicate f_{206} values between 0.07 and 0.72% (Table 13-54). U ranges from 130 to 421 ppm and Th from 44 to 586 ppm, giving Th/U ratios ranging from 0.18 to 2.78. Six data points form a coherent age group with a weighted mean $^{207}\text{Pb}/^{206}\text{Pb}$ age of 1014 ± 36 Ma (MSWD=0.44), while the other two data points (CHL5-4 and 5) appear to define a slightly older population with a weighted mean $^{207}\text{Pb}/^{206}\text{Pb}$ age of 1123 ± 41 Ma (MSWD=0.17). Of the older points, which are 96 and 94% concordant, one is measured from a zircon with length to width ratio of 4:1 (CHL5-5), while the other analysis spot penetrates what may be an older central portion of a zircon (CHL5-4). Although the data do not allow an unbiased assessment, these older zircon grains could represent 1.12 Ga xenocrysts or flawed analyses due to mixed sampling of older core and younger rim. The six younger data points plot within 5% of concordia, and allow the calculation of a concordia age of 1016 ± 17 Ma (MSWD=0.047)(Figure 4-133). This age represents the best estimate of the crystallisation age of the granite.

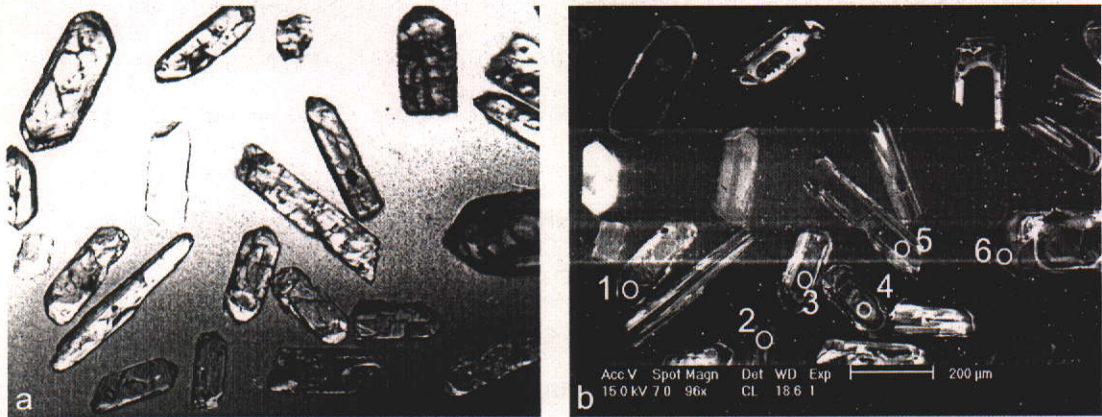


Figure 4-132: (a) photomicrograph of zircons from sample CHL5 (xpl) showing euhedral crystals (f.o.v. = ~1200 µm); (b) CL image of analysed zircons from sample CHL5 showing the location of analysed spots. Note the oscillatory zoning (f.o.v.= 1200 µm).

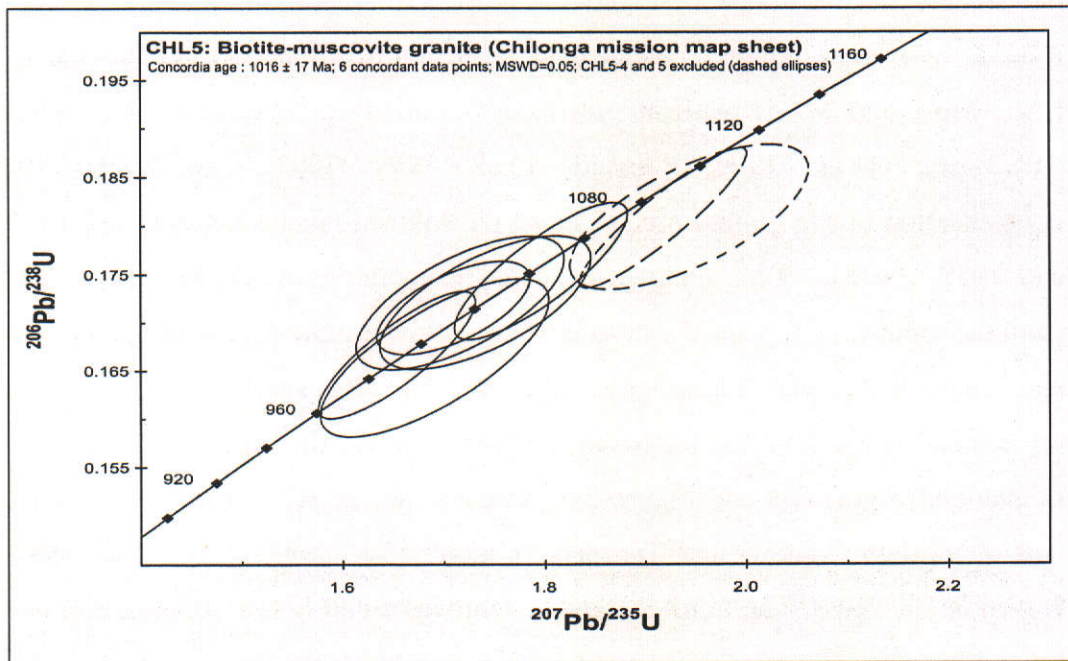


Figure 4-133: U-Pb concordia plot for zircon analyses of sample CHL5. Error ellipses are at 1σ confidence level. Dashed ellipses represent two analyses that may represent an older xenocrystic component.

4.9 Discussion

4.9.1 The basement of the Irumide belt and the Bangweulu block

Age data presented in this study confirm the presence of a basement to the Irumide belt, consisting of at least three different age components. The oldest component identified is the Kapiri Mposhi granite gneiss, which yielded a crystallisation age of 2726 ± 36 Ma and represents the oldest granitoid dated in the region. The second identified age component comprises the Mkushi Gneiss in the southwestern Irumide belt and the Luwalizi Granite in the northeastern Irumide belt. Four samples collected from the Mkushi Gneiss (samples CC10, KN1, MK3 and MK5) confirm previously reported age estimates of 2.05 Ga (Armstrong et al., 1999; Rainaud et al., 1999; 2002), and bracket the crystallisation of the granite precursors to the Mkushi Gneiss between 2050 ± 9 and 1952 ± 6 Ma. Two samples collected from the Luwalizi Granite Gneiss (samples ISK1 and 2) place the crystallisation of the granite precursor at 1942 ± 6 and 1927 ± 10 Ma. These latter ages are broadly similar to a 1.96 Ga crystallisation age reported for basement farther east in the Muyombe map sheet of Zambia (Figure 2-4 and Figure 2-5)(Vrána et al., 2004) and in the Ubendian belt of northern Malawi and Tanzania (Lenoir et al., 1994; Ring et al., 1997; Boven et al., 1999). The third age component was dated in two granites and two related lavas near Mansa on the western Bangweulu block (Figure 4-6), and was also identified in a rhyolitic unit in the Muva Supergroup of the northeastern Irumide belt (Figure 4-4 and Figure 4-5). The three granites near Mansa yielded crystallisation ages of 1866 ± 9 , 1862 ± 8 and 1860 ± 13 Ma (samples MA9, MA1 and 2), virtually identical to the crystallisation ages of 1868 ± 7 and 1862 ± 19 Ma for the lavas (samples MA3 and 9). Various granitoids and volcanics farther west in the Copperbelt have yielded similar crystallisation ages ranging from 1.88-1.87 Ga, suggesting that a 1.88-1.86 Ga plutono-volcanic province extends well into the Copperbelt (Figure 2-5). Two volcanic units, which occur conformably within the Manshya River Group metasedimentary succession of the northeastern Irumide belt (Kachinga Tuff and Luswa River Tuff), yielded igneous

crystallisation ages of 1879 ± 13 and 1856 ± 4 Ma, and provide direct evidence for the timing of deposition of the sequence. A pillow lava occurring within the Manshya River Group near Mpika (Katibunga Volcanic), in which zircons yielded an age of 1871 ± 24 Ma, provides further support for this age constraint.

4.9.2 The Muva Supergroup

During this study, detrital zircon grains were dated from one quartzite from each of the three different sedimentary sequences of northern Zambia (Figure 2-17). One sample (sample MA6) was analysed from quartzite of the Kabweluma Formation, which forms the basal part of the Mporokoso Group near Mansa, one from the main quartzite of the Kasama Formation east of Kasama (sample KAS), and one from a prominent folded quartzite ridge of the Manshya River Group in the Ilondola Mission 1:100000 map sheet (sample IL14). The following sections discuss these age data in terms of possible source terrains.

4.9.2.1 The Mporokoso Group

The probability density diagram for the ages of detrital zircon from quartzite of the Mporokoso Group defines two main peaks at 1.90-1.80 Ga, and at 2.05-1.95 Ga, accounting for 80% of the total population (Figure 4-40). Minor populations define peaks at 2.21-2.16 Ga, 2.42 Ga and 2.71 Ga. The granitoids and volcanics directly underlying the Mporokoso Group (samples MA1, MA2, MA3, MA5 and MA9 of this study) define a narrow age range of 1.87-1.86 Ga, which corresponds well with the younger of the dominant peaks defined in the probability density distribution diagram (Figure 4-40). Lithologies with ages corresponding to the older dominant peak at between 2.05-1.95 Ga are described to the south, southeast, east and west and include the Mkushi Gneiss (samples CC10, KN1, MK3 and MK5 of this study)(see also Armstrong et al., 1999; see also Rainaud et al., 2002; 2003), the Luwalizi Granite (samples ISK1 and 2 of this study), granitoids and gneisses of the Ubendian belt (Dodson et al., 1975; Lenoir et al., 1994; Ring et al., 1997; Vrána et al., 2004) and various granites and granite

gneisses in the Domes area of the Zambian and Congolese Copperbelt (Key et al., 2001b; Rainaud et al., 2002). Considering that clasts described in the basal conglomerate of the Mbala Formation, at the base of the Mporokoso Group, mainly comprise lithologies common in the underlying basement, and that no disconformities or unconformities have been identified further up in the Mporokoso Group, it is plausible that detritus in the entire group was derived from local sources of the underlying Bangweulu block basement. Andersen and Unrug (1984) used regional variations in pebble size gradient and directional information from cross stratification in the Mporokoso Group to indicate that palaeocurrents transported detritus from south to north. This would indicate a source area for the detritus to the south, which they proposed formed through uplift resulting from accretionary processes in the Ubendian belt. Largely because of the southern source area, rather than an eastern source from the Ubendian belt, Andersen and Unrug (1984) did not consider the Mporokoso Group to be a Ubendian molasse deposit.

The presence of volcanic tuffs in the base of the Mporokoso Group was interpreted by Andersen and Unrug (1984) to indicate significant overlap of sedimentation with plutono-volcanic activity responsible for the 1.87-1.86 Ga granites and volcanics that make up the Bangweulu block in the region. The maximum age of the Kabweluma Formation immediately above the volcanoclastic Nsama Formation is defined by the youngest concordant zircon with a $^{207}\text{Pb}/^{206}\text{Pb}$ age of 1824 ± 19 Ma, and is consistent with deposition immediately after the plutono-volcanic event at 1.87-1.86 Ga. The lack of any younger zircons supports this assumption, but does not constitute proof for the age of the sequence. No volcanic layer was dated from within the Mporokoso Group, which would have directly constrained the depositional age, and the interpretation that the Mporokoso Group constitutes a Palaeoproterozoic sequence deposited from 1.82 Ga onwards, awaits unequivocal confirmation in the future.

4.9.2.2 *The Kasama Formation*

Detrital zircons in the Kasama Formation define a dominant age distribution between 2.05 and 1.90 Ga, in which the following maxima can be distinguished: 1.81, 1.87, 1.94, 1.98, 2.04 and 2.06 Ma (Figure 4-43). Additionally, single zircon analyses define minor contributions of material with ages of 2.59, 2.17 and 1.43 Ga. For the majority of detrital zircons in the quartzite, potential source lithologies with identical ages have been reported in the region. Those include in this study the Mansa Volcanic and Granite (samples MA1, 2, 3 and 9), the Luswa Rhyolite (sample ZM31), the Kachinga Tuff (sample IS20), the Katibunga Volcanic (sample KB5), the Luwalizi Granite (samples ISK1 and 2) and the Mkushi Gneiss (samples CC10, KN1, MK3 and MK5)(see also Armstrong et al., 1999; see also Rainaud et al., 2002; 2003). Vrána (2004), Ring et al. (1997) and Lenoir (1994) reported numerous ages between 2.09-1.96 Ga within the Ubendian belt and northeasternmost part of the Irumide belt. As is the case with the Mporokoso Group, the detrital signature of the Mwela Quartzite is consistent with derivation from underlying basement sources, with the exception of two older zircons ($^{207}\text{Pb}/^{206}\text{Pb}$ ages of 2593 ± 5 and 2168 ± 17 Ma) and the youngest concordant zircon ($^{207}\text{Pb}/^{206}\text{Pb}$ age of 1434 ± 14 Ma), for which no local sources are known. Andersen and Unrug (1984) used the supermature character and palaeocurrent patterns of the Kasama Formation to argue that it was derived from a source to the west, which they suggested comprised the Mporokoso Group sedimentary rocks. In the view of Andersen and Unrug (1984), the Kasama Formation thus represents recycling of detritus from the Mporokoso Group. The detrital age data presented here support this idea, as age populations of the Mporokoso Group and Kasama Formation samples in this study are remarkably similar. Although this alone does not prove derivation from the Mporokoso Group, these age similarities, coupled with the transport directions reported by Andersen and Unrug (1984) and the supermature character of the Kasama Formation are all consistent with the latter unit representing recycling of Mporokoso Group sediments.

The most interesting feature of the Mwela Quartzite data is the youngest concordant zircon, which yielded an $^{207}\text{Pb}/^{206}\text{Pb}$ age of 1434 ± 14 Ma. This analysis was made on a zircon measuring 180 by 40 μm (analysis 5, Figure 4-41). This relatively high length to width ratio of over 4:1, coupled with the subrounded, as opposed to strongly rounded, morphology of the zircon suggests relatively minor sedimentary transport, and is not consistent with this zircon being a second-cycle product. About 10% of all zircons in the Mwela Quartzite have similar morphologies, with length to width ratios greater than 2:1, and subrounded to even subangular morphologies, indicating that a small fraction of the zircons may have been derived from more proximal, magmatic rather than sedimentary sources. Considering the sedimentary transport directions to have been from west to east, the ca. 1.43 Ga zircon would have been derived from a magmatic source of that age to the west of Kasama. To date, no such sources have been reported. However, given limitations imposed by a small dataset of only thirty-three analyses, and that it is not possible to rule out that the youngest zircon grain is a result of sample contamination (which I deem very unlikely), additional geochronological and possibly sedimentological work is needed to fully resolve the detrital provenance of the Kasama Formation.

4.9.2.3 The Manshya River Group (northeastern Irumide belt)

The depositional age of the deformed metasedimentary succession in the northeastern Irumide belt (Manshya River Group) has been directly constrained by the ages of two interlayered tuffs and a pillow lava in the sequence. The Kachinga tuff in the Isoka map sheet is dated at 1856 ± 4 Ma, while the Luswa River tuff in the Luswa River sheet is dated at 1879 ± 13 Ma. The mafic lavas of the Katibunga Volcanics yielded an age of 1871 ± 24 Ma. The youngest concordant zircon from a prominent quartzite in the Ilondola Mission sheet (Chembewesu Quartzite, northeastern Irumide belt) yielded a $^{207}\text{Pb}/^{206}\text{Pb}$ age of 1882 ± 30 Ma, placing a maximum age limit for sedimentation of this particular quartzite. Taken together, these data indicate that deposition of the Manshya River Group was ongoing from at least 1.88 Ga to 1.85 Ga. A minimum age for

sedimentation is provided by the oldest granitoid that intrudes the succession in the northeast, the Musalango Gneiss, dated in this study at 1610 ± 26 Ma.

The probability density diagram for detrital zircon ages from sample IL14 shows a major peak at 2.04 Ga making up 70% of the total population (Figure 4-46). At the lower end of the spectrum, a minor peak, accounting for 10% of the total number of analyses, is defined at around 1.91 Ga. At the higher end of the spectrum, the probability density curve defines peaks at 2.20, 2.43, 2.67, 2.86 and 3.01 Ga, each accounting for a few analyses. The main 2.04 Ga population is accounted for by local lithologies including the Mkushi Gneiss (samples CC10, KN1, MK3 and MK5 of this study)(see also Armstrong et al., 1999; see also Rainaud et al., 2002; 2003) and dated lithologies in the Ubendian belt and northeasternmost Irumide belt (Lenoir et al., 1994; Ring et al., 1997; Vrána et al., 2004). The younger population defined around 1.91 Ma, actually contains zircons dated at 1860 ± 33 , 1878 ± 11 , 1882 ± 30 and 1889 ± 16 Ma, all of which are indistinguishable from the ages obtained for the various volcanic lithologies dated in the Manshya River Group (samples ZM31, IS20 and KB5 of this study), as well as the granites and volcanics of the Bangweulu block (sample MA1, MA2, MA3, MA5 and MA9 of this study). No potential source lithologies are reported for the remaining, minor contributions in the quartzite. It can be concluded that 80% of the detritus in the Chembewesu Quartzite could have been locally derived from underlying basement lithologies or from the adjacent Bangweulu block, and may also have been derived from volcanic members within the lower part of the Manshya River Group. The older components reflect limited input from 2.20, 2.43, 2.66, 2.85 and 3.01 Ga sources, as yet unidentified in the area. It is important to note that no zircons younger than 1860 ± 33 Ma were detected in the Chembewesu Quartzite, adding weight to the notion that deposition of the Manshya River Group predates intrusion of the 1.61 – 1.55 Ga granitoids.

4.9.2.4 The Kanona Group (southwestern Irumide belt)

The limited analyses conducted on a conglomerate of the Kanona Group (sample MK8) appear to support derivation from the underlying Mkushi Gneiss

basement, as the coherent age population of 2034 ± 16 Ma as well as younger 1953 ± 15 Ma age is indistinguishable from ages obtained from the Mkushi Gneiss (samples CC10, KN1, MK3 and MK5 of this study)(see also Armstrong et al., 1999; see also Rainaud et al., 2002; 2003). The maximum age of deposition for the conglomerate is defined by the youngest concordant zircon at 1953 ± 15 Ma.

Farther west at Mufulira in the Zambian part of the Copperbelt, Rainaud et al. (2003) reported detrital age data for a quartzite of the Kanona Group. The quartzite records populations between 2.05 and 1.95 Ga, similar to those in the conglomerate (sample MK8) and most likely derived from the Mkushi Gneiss, but a large number of zircons defined a broad age population between 2.25 and 2.10 Ga and small populations of 2.40 Ga, 2.50 Ga, 2.70 Ga, 3.03 Ga and 3.20 Ga (Figure 4-134). The Kapiri Mposhi granite gneiss dated in this study provides a potential source for the 2.7 Ga population, but potential sources for the remaining minor contributions remain unidentified. Note that all peaks match with the detrital age peaks identified in the quartzites from this study. The youngest concordant analysis of 1941 ± 40 Ma places a maximum age constraint on the deposition of the quartzite, which is similar to that for the conglomerate.

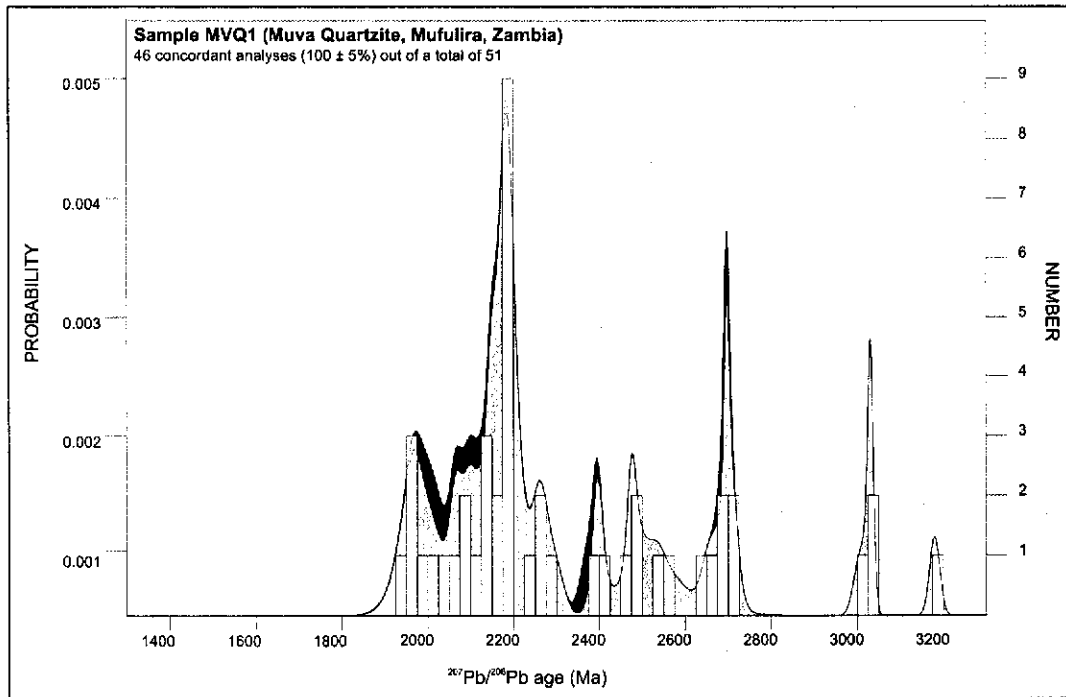


Figure 4-134: Probability density plot of detrital zircon from the Mufulira Quartzite (Kanona Group, Copperbelt (data after Rainaud et al. (2003))). The histogram indicates the number of 100±5% concordant analyses for each bin of 20 M.y. (right axis), while the curves show the relative probability density of the analyses. The light grey curve denotes 95-105% concordant analyses, while the dark grey curve shows all analyses.

4.9.3 Strongly deformed granitoids in the Irumide belt

A previously unrecognised magmatic event was identified in the Irumide belt, emplacing the precursor granites to the Lukamfwa Hill Granite Gneiss in the southwestern Irumide belt between 1.65-1.63 Ga, and the precursor granites to the Musalango Gneiss and Lubu Granite Gneiss in the northeastern Irumide belt between 1.61-1.55 Ga. In the southwestern Irumide belt, these granitoids include large rafts of metasedimentary rocks ascribed to the Manshya River Group (Mapani, 1992; De Waele, 1997; De Waele and Mapani, 2002). In the northeastern Irumide belt, metasedimentary rafts occurring in the Musalango Gneiss and Lubu Granite Gneiss were also interpreted to be derived from the Manshya River Group. The presence of another metasedimentary unit, the Mulungwizi and Mwambwa River Gneiss, in the northeastern Irumide belt and adjacent parts of the Bangweulu block, could however also account for these metasedimentary rafts. Evidence supporting derivation from the Manshya River Group rather than the Mulungwizi Gneiss relies on the preservation of a ghost

stratigraphy within the rafts, a feature not observed in the Mulungwizi Gneiss (Sykes, 1995). The presence of metasedimentary rafts ascribed to the Manshya River Group in the 1.65-1.55 Ga granitoids places a minimum age on the deposition of that group.

4.9.4 Weakly or undeformed Irumide granitoids

A significant magmatic pulse occurred during the Irumide orogeny and saw the emplacement of large volumes of porphyritic and megacrystic granitoids. Twenty-six ages have been obtained from various granitoid bodies across the Irumide belt, and bracket emplacement of syn- to post-orogenic granitoids between 1.05 and 0.94 Ga. Probability density analysis on the dates suggests that the peak magmatic activity was at around 1030 Ma.

4.9.5 Peak metamorphism in the Irumide belt

Metamorphic conditions are dated through low Th/U rims on zircon in migmatites from the southwestern Irumide belt (samples SER6-6 and SER6-7) and constrain peak Irumide tectonism between 1020 ± 16 Ma and 1018 ± 5 Ma. One low Th/U rim yielded an age of 554 ± 20 Ma and appears to reflect a second metamorphic event possibly related to the Damara-Lufilian-Zambezi orogen to the southwest and west. Metamorphic conditions are dated in the northeastern Irumide belt through low Th/U zircon overgrowths on zircon from the Chilubanama Granite at 1004 ± 16 Ma (sample MTG4).

4.9.6 Xenocrystic zircon

During this study, numerous xenocrystic zircons were dated from igneous lithologies in the Irumide belt, and provide an insight into the nature of the basement. Table 4-2 provides an overview of the $^{207}\text{Pb}/^{206}\text{Pb}$ ages obtained from these xenocrysts (only $100 \pm 10\%$ concordant data are shown). Firstly, it is noteworthy that no xenocrysts were recorded in the 1.65-1.55 Ga granitoids (Lukamfwa Hill Granite Gneiss, Musalango Gneiss and Lubu Granite Gneiss). The apparent lack of inheritance in these granitoids may be a result of the fact that xenocrystic zircons form too small a population and were not detected with the limited number of analyses, or that the 1.65-1.55 granitoid magmas were hot and undersaturated with respect to Zr, thus precluding the preservation of inherited zircon (Miller et al., 2003).

Only two xenocrysts were dated from pre-Irumide lithologies. One inherited zircon yielded a poorly constrained $^{207}\text{Pb}/^{206}\text{Pb}$ age of 3105 ± 143 Ma, and was dated from the 2.73 Ga Kapiri Mposhi granite gneiss. This zircon, together with detrital zircons reported by Rainaud et al (2003) in a quartzite of the Kanona Group near Mufulira, and xenocrystic zircons in a tuff further west (Likasi, DR Congo, see Figure 2-5), as well as a minor 3.2 Ga age component in the Manshya River Group of this study, provide evidence of a cryptic Mesoarchaean terrane. The other xenocrystic zircon was analysed from the Katibunga Volcanic, and has a $^{207}\text{Pb}/^{206}\text{Pb}$ age of 2551 ± 36 Ma. The Katibunga Volcanic forms a unit of pillow lava, and the xenocryst is most likely sampled from cryptic underlying basement lithologies of that age, or from sediments derived from such basement.

The majority of dated xenocrysts were extracted from the syn- and late-Irumide granitoids, and reflect sources ranging from 2.77 to 1.11 Ga (Table 4-2). A combined probability density and histogram diagram of all xenocrystic zircons shows a dominant peak between 2.05 and 2.00 Ga, and subordinate peaks at 2.7, 2.5, 1.85, 1.65, 1.48 and 1.11 Ga (Figure 4-135). The oldest 2.77 Ga xenocryst corresponds to the Kapiri Mposhi granite gneiss dated in this study. The main peak between 2.05 and 2.00 Ga corresponds closely to the ages defined for the

Mkushi Gneiss (samples CC10, KN1, MK3 and MK5)(Armstrong et al., 1999; Rainaud et al., 2002; 2003), while the ~1.85 Ga xenocrysts correspond to the ages defined for the volcanics in the Manshya River Group (samples ZM31, IS20 and KB5) and the plutono-volcanic rocks near Mansa (samples MA1, 2, 3 and 9). Several xenocrysts in the Chilubanama Granite (samples LW1 and MTG4) reflect sources ranging in age between the age of the Lubu Granite Gneiss (1.55 Ga) and ca. 1.40 Ga. The 1.4 Ga xenocrystic zircons in the Chilubanama Granite, although poorly constrained in age, provide evidence of the possible presence of source rocks of this age in the northeastern Irumide belt, similar in age to the youngest concordant detrital zircon identified in the Kasama Formation to the north.

Table 4-2: Crystallisation ages of xenocrystic zircon in the Irumide belt obtained as part of this study. *denotes % concordance of the zircon age; ** denotes the igneous crystallisation age of the host rock.

Sample	Name	$^{207}\text{Pb}/^{206}\text{Pb}$ age (Ma)	C* (%)	Age** (Ma)
CC5	Porphyritic granite	1114 ± 29	93.8	1038 ± 17
LW1	Porphyritic granite	1348 ± 66	107.6	1005 ± 21
MTG4	Chilubanama Granite	1425 ± 47	98.4	1010 ± 22
LW1	Porphyritic granite	1483 ± 12	93.2	1005 ± 21
LW1	Porphyritic granite	1503 ± 46	101.7	1005 ± 21
LW1	Chilubanama Granite	1516 ± 56	99.6	1005 ± 21
LW1	Porphyritic granite	1539 ± 48	100.8	1005 ± 21
FW2	Aplite in porphyritic granite	1637 ± 46	102.2	1038 ± 17
ZM32	Chilubanama Granite	1649 ± 23	101.5	~1000
FW2	Aplite in porphyritic granite	1837 ± 28	90.7	1038 ± 17
ZM32	Chilubanama Granite	1859 ± 20	95.8	~1000
KN7	Porphyritic granite	1944 ± 46	97.9	1048 ± 10
FW2	Aplite in porphyritic granite	1945 ± 39	105.4	1038 ± 17
KN7	Porphyritic granite	1987 ± 16	94.9	1048 ± 10
KN7	Porphyritic granite	1988 ± 9	102.4	1048 ± 10
SER6-4	Porphyritic granite	2000 ± 6	102.7	1036 ± 13
FW2	Aplite in porphyritic granite	2010 ± 21	101.3	1038 ± 17
MTG4	Chilubanama Granite	2010 ± 8	98.3	1010 ± 22
FW2	Aplite in porphyritic granite	2017 ± 10	102.6	1038 ± 17
MTG4	Chilubanama Granite	2017 ± 17	96.6	1010 ± 22
KN7	Porphyritic granite	2017 ± 4	100.5	1048 ± 10
FW2	Aplite in porphyritic granite	2032 ± 28	99.4	1038 ± 17
FW2	Aplite in porphyritic granite	2034 ± 31	97.7	1038 ± 17
ZM32	Chilubanama Granite	2036 ± 23	97.2	~1000
FW2	Aplite in porphyritic granite	2044 ± 8	99.5	1038 ± 17
MTG4	Chilubanama Granite	2046 ± 11	106.1	1010 ± 22
KN8	Porphyritic granite	2052 ± 13	99.7	1022 ± 16
FW2	Aplite in porphyritic granite	2096 ± 38	102.1	1038 ± 17
FW2	Aplite in porphyritic granite	2098 ± 65	95.5	1038 ± 17
KB5	Katibunga Volcanic	2551 ± 36	91.3	1871 ± 24
FW2	Aplite in porphyritic granite	2774 ± 23	99.8	1038 ± 17
KMP1	Kapiri Mposhi Granite Gneiss	3105 ± 143	97.9	2726 ± 36

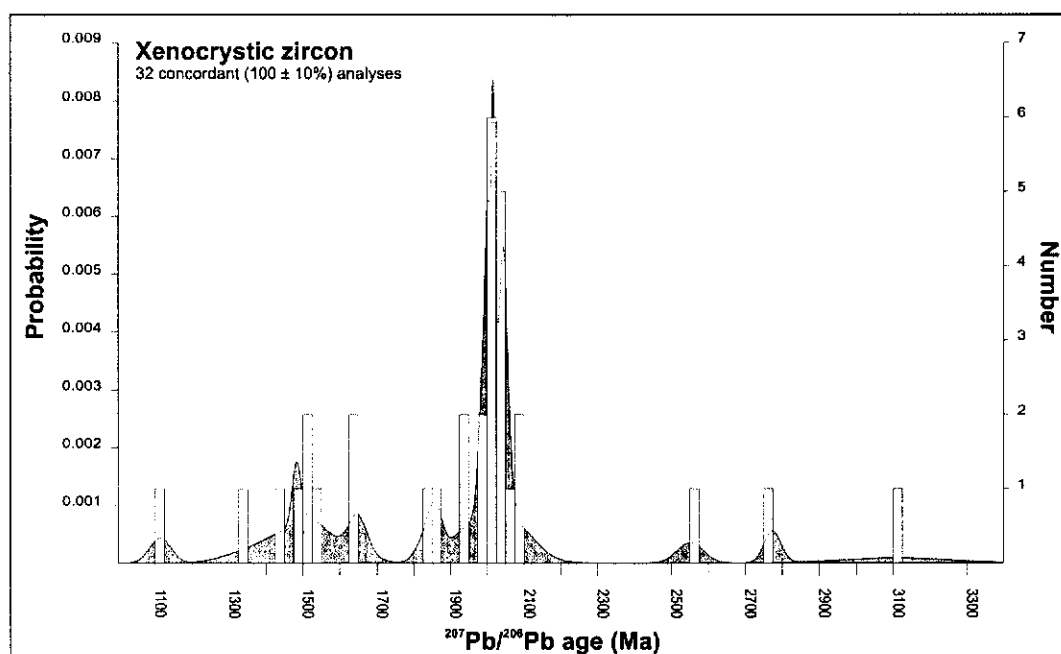


Figure 4-135: Probability density plot (light grey curve) of xenocrystic zircon extracted from igneous lithologies in the Irumide belt. The histogram indicates the number of analyses for each bin of 25 M.y. (right axis). Only $100 \pm 10\%$ concordant analyses are included.

4.9.7 Redefining the Bangweulu block

The age data presented above outline the presence of a basement, consisting of at least three age components, overlain by the Muva Supergroup. The detrital age data presented in this study for quartzites of the Muva Supergroup contain age populations reflecting each of those basement components, as well as minor detrital zircon populations with ages 3.20 Ga (sample MVQ-1, Kanona Group, Copperbelt (Rainaud et al., 2003)), 3.03 – 3.01 Ga (sample MVQ-1 (Rainaud et al., 2003) and sample IL14, Manshya River Group, northeastern Irumide belt (this study)), 2.85 Ga (sample IL14 (this study)), 2.71 – 2.66 Ga (samples MA6 and IL14 (this study)), 2.59 – 2.40 Ga (samples MVQ-1 (Rainaud et al., 2003), MA6, IL14 and KAS (this study)) and 2.25 – 2.10 Ga (samples MVQ-1 (Rainaud et al., 2003), MA6, IL14 and KAS (this study))). The presence of detrital zircon corresponding to all identified basement components in the Bangweulu block and within the Irumide belt (Mkushi Gneiss and Luwalizi Granite Gneiss) strongly suggests that these basement components (2.73, 2.05–1.93 and 1.88–1.85 Ga) were assembled to form a coherent unit prior to erosion and deposition of the Muva Supergroup after ca. 1.82 Ga. The minor contributions

within the Muva Supergroup that do not correspond to dated basement lithologies may reflect additional, as yet unidentified components within this composite basement, including the 3.2 Ga Likasi terrane proposed to underlie the Copperbelt to the west (Rainaud et al., 2003). The Bangweulu block s.s. is considered in this study to comprise only the crystalline basement to the northwest of the Irumide belt, i.e. 1.88-1.86 Ga plutono-volcanic rocks recognised to the west and southwest of the Palaeoproterozoic Ubendian belt, including the 1.88-1.87 Ga plutono-volcanic rocks identified in the Domes region of the Copperbelt. The Bangweulu block s.l. comprises a collage of basement rocks in the Irumide belt (2.73 Ga and 2.05-1.93 Ga) and 1.88-1.85 Ga plutono-volcanic rocks to the northwest and west of the Irumide belt in the Bangweulu block s.s.

4.9.8 Redefining the Muva Supergroup

A detrital provenance study of a quartzite from the Mporokoso Group on the Bangweulu block and the Chembewesu Quartzite of the Manshya River Group in the northeastern Irumide belt shows very similar age patterns for these units indicating derivation from the ca. 2.10-1.86 Ga Ubendian belt, and from the 1.88-1.86 Ga uplifted magmatic arc that underlies large parts of the Bangweulu block (Andersen and Unrug, 1984). The timing of deposition is directly constrained for the Manshya River Group through interlayered volcanic units dated at 1879 ± 13 Ma and at 1856 ± 4 Ma, i.e. very soon after, and actually overlapping with the 1.88 – 1.86 Ga magmatic event. Contrary to previously held beliefs, the 1.88-1.86 Ga Bangweulu block and the ~2.10-1.86 Ga Ubendian belt (Brewer et al., 1979; Schandelmeier, 1980; Ring et al., 1997) have been shown to extend southwards well into the Irumide belt (this study) and westwards, where similar aged lithologies are shown to underlie the Copperbelt (Ngoyi et al., 1991; John, 2001; Rainaud et al., 2002; 2003). As such, the argument of Andersen and Unrug (1984) that a southerly source precludes derivation from the Ubendian Orogen (i.e. that the Mporokoso Group could not represent a Ubendian molasse sequence), is invalidated. Based on the fact that detritus in the Mporokoso and Manshya River Groups appears to be derived from rocks which form part of the 2.10-1.86 Ga Ubendian Orogen, and was deposited immediately after the late Ubendian

magmatic event at 1.86 Ga, the Mporokoso, Manshya River and Kanona Groups can be regarded as Ubendian molasse deposits, and are related to the Palaeoproterozoic geological history of the Ubendian belt and associated Bangweulu block.

4.9.9 Summary

Based on the age data presented in this study, the magmatic evolution of the Bangweulu block and the Irumide belt is characterised by five different events (Table 4-3):

Table 4-3: Different magmatic suites recognised in the Bangweulu block and the Irumide belt, based on zircon U-Pb geochronological data presented in this study.

SUITE	Lithologies	Emplacement age
GROUP I	Kapiri Mposhi granite gneiss (southwestern Irumide belt)	2.73 Ga
GROUP II	Mkushi Gneiss (southwestern Irumide belt)	2.05 - 1.95 Ga
	Luwalizi Granite Gneiss (northeastern Irumide belt)	1.94 - 1.93 Ga
GROUP III	Mansa Granitoid (western Bangweulu block)	1.86 Ga
	Mansa Volcanic (western Bangweulu block)	1.87 – 1.86 Ga
	Kachinga Tuff (northeastern Irumide belt)	1.86 Ga
	Luswa Volcanic (northeastern Irumide belt)	1.88 Ga
	Katibunga Volcanic (northeastern Irumide belt)	1.87 Ga
GROUP IV	Lukamfwa Hill Granite Gneiss (southwestern Irumide belt)	1.66 - 1.64 Ga
	Musalango Gneiss (northeastern Irumide belt)	1.61 Ga
	Lubu Granite Gneiss (northeastern Irumide belt)	1.55 Ga
GROUP V	Bemba batholith (Lufila Granite) (northeastern Irumide belt)	~1.00 Ga
	Luswa River Leuco-Syenite Gneiss (northeastern Irumide belt)	0.94 Ga
	Chilubanama Granite (northeastern Irumide belt)	1.01 - 1.00 Ga
	Porphyritic granitoids (southwestern Irumide belt)	1.05 – 1.00 Ga

Therefore, for the remainder of this study, the various magmatic suites are referred to using this revised subdivision (Figure 4-136). A summary of ages obtained in this study is given in Table 4-4.

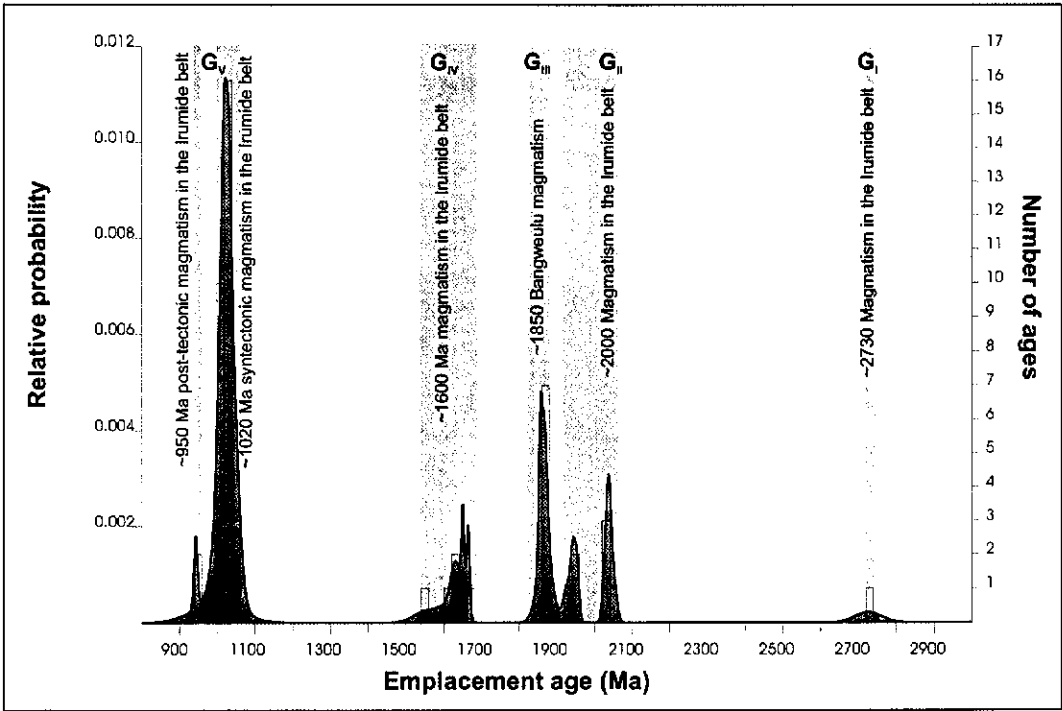


Figure 4-136: Combined probability density/histogram diagram showing emplacement ages of magmatic rocks in the Irumide belt and the Bangweulu block of northern Zambia, obtained in this study.

CHAPTER 4: Zircon U-Pb SHRIMP Geochronology

Table 4-4: Zircon U-Pb SHRIMP crystallisation ages for magmatic rocks obtained in this study (left: sorted alphabetically by sample name; right: sorted by age). ® denotes metamorphic zircon rims.

Sample	Rock-type	Age	Sample	Rock-type	Age
CC10	Porphyritic granite gneiss	1952+/-6	SER6-7 ®	Fukwe Migmatite	554+/-20
CC5	Porphyritic granite	1038+/-17	LW2	Luswa Syenite	943+/-5
CC8	Porphyritic granite	1035+/-12	ZM32	Chilubanama Granite	~946+/-50
CHL5	Granite gneiss	1016+/-17	SH8	Lufila Granite	1001+/-44
CHT6	Biotite granite gneiss	1005+/-7	KK1	Porphyritic granite	1003+/-31
FW1	Porphyritic granite	1038+/-58	MTG4 ®	Chilubanama Granite	1004+/-16
IS20	Kachinga Tuff	1856+/-4	LW1	Chilubanama Granite	1005+/-21
ISK1	Luwalizi Granite Gneiss	1942+/-6	CHT6	Biotite granite gneiss	1005+/-7
ISK2	Luwalizi Granite Gneiss	1927+/-10	MTG4	Chilubanama Granite	1010+/-22
KB5	Katibunga Basalt	1871+/-24	SASA2	Sasa Granite	1016+/-14
KK1	Porphyritic granite	1003+/-31	CHL5	Granite gneiss	1016+/-17
KMP1	Kapiri Mposhi Granite	2726+/-36	MH4	Porphyritic granite	1017+/-19
KN1	Mkushi Gneiss	2036+/-6	SER6-6 ®	Lukusashi migmatite	1018+/-5
KN2A	Porphyritic granite	1031+/-14	SER6-7 ®	Fukwe Migmatite	1021+/-16
KN5	Biotite granite gneiss	1053+/-14	KN8	Biotite granite gneiss	1022+/-16
KN7	Porphyritic granite	1048+/-10	ND1	Porphyritic granite	1023+/-7
KN8	Biotite granite gneiss	1022+/-16	SQG	Serenje Quarry Granite	1024+/-9
LW1	Chilubanama Granite	1005+/-21	ZM36	Mununga Quarry Granite	1025+/-10
LW10	Musalango Gneiss	1610+/-26	ND5	Syeno-granite	1028+/-7
LW2	Luswa Syenite	943+/-5	MH9C	Porphyritic granite	1029+/-14
MA1	Mansa Granite	1860+/-13	MTGG1	Mutangoshi Gneissic Granite	1029+/-9
MA2	Mansa granite	1862+/-8	KN2A	Porphyritic granite	1031+/-14
MA3	Mansa Volcanic	1868+/-7	ND4	Granodiorite	1031+/-5
MA5	Mansa Volcanic	1862+/-19	SER5-3	Porphyritic granite	1034+/-5
MA9	Musonda Falls Granite	1866+/-9	MK7	Porphyritic granite	~1035+/-32
MH4	Porphyritic granite	1017+/-19	CC8	Porphyritic granite	1035+/-12
MH9C	Porphyritic granite	1029+/-14	SER6-4	Porphyritic granite	1036+/-13
MK3	Mkushi Gneiss	2042+/-10	CC5	Porphyritic granite	1038+/-17
MK5	Mkushi Gneiss	2029+/-7	FW1	Porphyritic granite	1038+/-58
MK5	Mkushi Gneiss	2050+/-9	KN7	Porphyritic granite	1048+/-10
MK7	Porphyritic granite	~1035+/-32	KN5	Biotite granite gneiss	1053+/-14
ML2	Lubu Granite Gneiss	1551+/-33	MTGG-2	Mutangoshi Gneissic Granite	1055+/-13
MTG4	Chilubanama Granite	1010+/-22	ML2	Lubu Granite Gneiss	1551+/-33
MTG4 ®	Chilubanama Granite	1004+/-16	LW10	Musalango Gneiss	1610+/-26
MTGG1	Mutangoshi Gneissic Granite	1029+/-9	ND2	Granite gneiss	1627+/-12
MTGG-2	Mutangoshi Gneissic Granite	1055+/-13	SR12	Lukamfwa Hill Granite Gneiss	1639+/-14
ND1	Porphyritic granite	1023+/-7	SER6-3	Lukamfwa Hill Granite Gneiss	1652+/-6
ND2	Granite gneiss	1627+/-12	SER6-2c	Lukamfwa Hill Granite Gneiss	1664+/-6
ND4	Granodiorite	1031+/-5	IS20	Kachinga Tuff	1856+/-4
ND5	Syeno-granite	1028+/-7	MA1	Mansa Granite	1860+/-13
SASA2	Sasa Granite	1016+/-14	MA5	Mansa Volcanic	1862+/-19
SER5-3	Porphyritic granite	1034+/-5	MA2	Mansa granite	1862+/-8
SER6-2c	Lukamfwa Hill Granite Gneiss	1664+/-6	MA9	Musonda Falls Granite	1866+/-9
SER6-3	Lukamfwa Hill Granite Gneiss	1652+/-6	MA3	Mansa Volcanic	1868+/-7
SER6-4	Porphyritic granite	1036+/-13	KB5	Katibunga Basalt	1871+/-24
SER6-6 ®	Lukusashi migmatite	1018+/-5	ZM31	Luswa River Tuff	1879+/-13
SER6-7 ®	Fukwe Migmatite	554+/-20	ISK2	Luwalizi Granite Gneiss	1927+/-10
SER6-7 ®	Fukwe Migmatite	1021+/-16	ISK1	Luwalizi Granite Gneiss	1942+/-6
SH8	Lufila Granite	1001+/-44	CC10	Porphyritic granite gneiss	1952+/-6
SQG	Serenje Quarry Granite	1024+/-9	MK5	Mkushi Gneiss	2029+/-7
SR12	Lukamfwa Hill Granite Gneiss	1639+/-14	KN1	Mkushi Gneiss	2036+/-6
ZM31	Luswa River Tuff	1879+/-13	MK3	Mkushi Gneiss	2042+/-10
ZM32	Chilubanama Granite	~946+/-50	MK5	Mkushi Gneiss	2050+/-9
ZM36	Mununga Quarry Granite	1025+/-10	KMP1	Kapiri Mposhi Granite	2726+/-36

Taking into consideration data presented as part of this study and previously published data, the timing of Archaean and Proterozoic events associated with the evolution of the Bangweulu block s.l., Ubendian belt and the Irumide belt can be summarised as follows:

- | | |
|-------------------|--|
| 2.73 – 2.61 Ga | Emplacement of Group I granitoids, forming part of the early (Neoarchaean) history of the Bangweulu block s.l., namely the Kapiri Mposhi granite gneiss (this study) and possibly the Luangwa Gneiss (Cox et al., 2002). |
| 2.05 – 1.93 Ga | Emplacement of Group II granitoids of the Bangweulu block s.l. in the Irumide belt, namely the Mkushi Gneiss and Luwalizi Granite Gneiss (this study), and in the Zambian and Congolese Copperbelt, namely the Mufulira Granite, Chambishi Granite, Mulungushi Gneiss and Samba Porphyry (Rainaud et al., 1999; 2002; 2003). |
| 2.09 – 1.93 Ga | Tectonism in the Ubendian belt and related magmatism (Luromo, Rumphu, Chelinda and Nyika Granitoids)(Dodson et al., 1975; Ring et al., 1997; Vrána et al., 2004). |
| 1.88 – 1.86 Ga | Emplacement of Group III plutono-volcanic rocks of the Bangweulu block s.l. in the Zambian and Congolese Copperbelt (Ngoyi et al., 1991; John, 2001; Rainaud et al., 2002), in the Bangweulu block s.s. (Mansa Granite and Volcanic, this work) and extrusion of volcanic tuff and pillow lava in the Irumide basin along the southeastern margin of the Bangweulu block s.s. (Kachinga Tuff, Luswa Tuff and Katibunga Volcanic, this work). |
| 1.88 > - >1.66 Ga | Deposition of the Mporokoso, Manshya River and Kanona Groups on the assembled Bangweulu block (this work). |

1.66 – 1.55 Ga	Emplacement of Group IV granitoids in the Irumide belt, namely the Lukamfwa Hill Granite Gneiss, Musalango Gneiss and Lubu Granite Gneiss (this work).
1.43> - ? Ga	Deposition of the Kasama Formation (this work)
1.36 – 1.34 Ga	Limited anorogenic magmatism in the northeastern Irumide belt (Tembo, 1986; Vrána et al., 2004).
1.12 – 1.11 Ga	A-type magmatism in the Ubendian belt (Ring et al., 1999).
1.05 – 0.94 Ga	Emplacement of Group V syn- and post-Irumide plutons, comprising the Bemba batholith (Lufilia Granite), Chilubanama Granite, and widespread porphyritic granitoids in the Irumide belt (this study).
1.05 Ga	Peak metamorphic conditions in the southeastern Irumide belt (Schenk and Appel, 2001; Cox et al., 2002).
1.02 – 1.00 Ga	Peak metamorphic conditions in the Irumide belt s.s. (this work).
0.95 Ga	Post-Irumide cooling below the closing temperature for $^{40}\text{Ar}/^{39}\text{Ar}$ in hornblende in the northeastern Irumide belt (Daly, 1986b).
0.89 – 0.86 Ga	Post-Irumide cooling below the closing temperature for $^{40}\text{Ar}/^{39}\text{Ar}$ in muscovite in the northeastern Irumide belt (Vrána et al., 2004).
0.55 Ga	Metamorphic overprint of the Damara-Lufilian-Zambezi orogen in the southwestern Irumide belt (this study and (Vail et al., 1968).

5 CHAPTER 5: Major and trace element geochemistry

5.1 Introduction

During this study, 108 whole rock samples were analysed for geochemistry, covering the entire range of (meta-) igneous lithologies in the Irumide belt. The geochemistry comprises major elements and a range of trace elements and is aimed at addressing the following issues:

1. geochemical classification of each igneous rock sample using normative mineral content;
2. geochemical characterisation of the different igneous suites; and
3. proposing petrogenetic models for each suite and their geotectonic setting.

Although analyses were conducted over four different years (1998-2001), at three different laboratories (Chemex Canada Mississauga facility, Chemex Australia Sydney facility and Department of Applied Chemistry, Curtin University of Technology), the methodologies followed were nearly identical, and included standard digestion and/or fusion techniques followed by Inductively Coupled Plasma - Optical Emission Spectrometry (ICP-OES) for major elements and Inductively Coupled Plasma – Mass Spectrometry (ICP-MS) for trace elements. Details of these methodologies are reported in Appendix D. Minimum detection limits for analyses conducted by Chemex are identical to those reported for the instruments at Curtin University, and are given in Appendix C in Tables 11-7 and 11-8.

Quality control for the analyses conducted by Chemex included analysis of blanks, internal duplicates and internal standards, but the results of these were not returned with analyses, and are not reported here. Quality control for the batches analysed at the Curtin facilities consisted of analysis of blanks, which confirmed negligible background counts throughout, analysis of standards (see Tables 11-1, 11-2, 11-3 and 11-4) and duplicate analyses (see Tables 11-5 and 11-6). A

comparison of the values obtained on reference standard materials with officially quoted values for these international standards confirms that there are no significant discrepancies in either trace or major element analyses. Duplicates were run of ten samples for both major and trace elements at Chemex Australia and at the Curtin facilities. The results obtained indicate reproducibility of the ICP-MS and ICP-OES techniques (Tables 11-5 and 11-6). One duplicate (sample KB7, Table 11-6) was conducted for trace elements during two separate sessions at Curtin and yielded negligible differences between the two analytical runs.

In the treatment of geochemical data, a multitude of approaches can be used, dependent on individual cases. In this study, for reasons of consistency and space, only a limited number of parameters are calculated and diagrams used to characterise the rocks.

Even though, during this study, every effort was made to collect samples from fresh, unaltered rock, the chemical index of alteration (CIA) of Nesbitt and Young (1982) was calculated ($CIA = \text{molar } (100 * (Al_2O_3) / ((Al_2O_3) + (CaO^*) + (Na_2O) + (K_2O)))$; where CaO^* is the contribution of CaO from silicates only). According to Nesbitt and Young (1982), values of CIA for unaltered granite and basic rock are 50 and 42 respectively, while CIA values for any rock exceeding 60 indicate significant alteration. In addition to the CIA parameter, loss on ignition (LOI) is used to assess the level of alteration for the samples, with LOI values higher than 2% deemed to indicate significant alteration in carbonate-free samples. Throughout this study, samples with CIA values exceeding 60 and LOI values greater than 2% were considered suspect.

The plutonic rocks were classified using their calculated mesonormative composition. This method was preferred over point counting of constituent minerals as mesonormative compositions can be calculated for all types of magmatic and metamorphic rocks, ranging from aphanitic (as is the case for most volcanic rocks) to megacrystic (as is common in the porphyritic granite types). The mesonormative calculation therefore provided a uniform means of classifying magmatic rocks as part of this study. The particular norm calculated during this study is based on the accepted CIPW calculations (Johannsen, 1931; Best and

Christiansen, 2000) but has been simplified and is only suitable for the most common rocks, as many calculations necessary for rocks of uncommon composition (such as some silica-undersaturated rocks) have been omitted. The procedure also departs from the original CIPW norm in that all plagioclase components have been grouped together, while normative enstatite, ferrosilite and wollastonite have been recalculated into diopside and hypersthene end-members. Classification for the plutonic rocks is based on a ternary QAP diagram proposed by Le Maître (1989), plotting mesonormative composition of quartz, alkali feldspar and plagioclase at the apexes. For the volcanic rocks, a geochemical classification diagram proposed by Cox et al. (1979) was used, plotting total alkalis ($K_2O + Na_2O$) versus silica (SiO_2), and for the volcanic rocks in the Irumide belt a classification diagram proposed by Streckeisen and Le Maître (1979), plotting ANOR (anorthite / (anorthite + orthite) * 100) versus Q' ($Q/(Q + \text{anorthite} + \text{orthite} + \text{albite}) * 100$) was used.

The geochemical traits of the plutonic and volcanic rocks are demonstrated through several diagrams. A diagram proposed by Maniar and Picolli (1989) plots the aluminium saturation index ($ASI = A/CNK = \text{molar } (Al_2O_3 / ((CaO) + (Na_2O) + (K_2O)))$ (Zen, 1986) versus the algahtic index ($AI = \text{molar } (Al_2O_3 / ((Na_2O) + (K_2O)))$) and characterises the rocks as metaluminous ($ASI < 1$ and $AI > 1$), peraluminous ($ASI > 1$ and $AI > 1$) or peralkaline ($ASI < 1$ and $AI < 1$). A binary diagram of K_2O versus Na_2O further characterises the rock as potassic ($K_2O > Na_2O$) or sodic ($Na_2O > K_2O$). A diagram after Chappell and White (1974) and Clarke (1992) plots the ASI versus silica content (SiO_2) and helps distinguish I-, M-, A- and S-type granitoids. I-type granitoids result chiefly from the melting of source rocks of mafic to intermediate igneous composition, or infracrustal derivation; M-type are granitoids resulting from the melting of mantle sources, either indirectly through subducted oceanic crust, or directly; A-type are granitoids emplaced into non-orogenic settings and S-type are those granitoids chiefly derived from sources which have undergone at least one weathering cycle (i.e. sedimentary rocks) (Clarke, 1992). Of these, only the latter can be unequivocally recognised by their high ASI values of greater than 1.1 and the presence of more than 1% normative corundum, while considerable overlap exists in the I-, A- and M-types (Chappell and White, 1974, 1992; Chappell, 1999).

Because of the inability of this diagram to distinguish A-type from I-type granitoids, another diagram is used, either plotting $(Zr + Nb + Ce + Y)$ versus $(K_2O + Na_2O)/CaO$, or $(Zr + Nb + Ce + Y)$ versus $(total\ FeO/MgO)$ (Whalen et al., 1987). The diagrams by Whalen et al. (1987) clearly distinguish A-type granitoids from orogeny-related I-type and fractionated felsic granitoids because of the more elevated total REE content of the former. Eby (1990; 1992) further suggested that not all A-type granitoids are anorogenic, but can be subdivided into two types, namely orogeny-related A-type and anorogenic A-type. In order to distinguish these two sub-types, additional diagrams proposed by Eby (1990; 1992) are applied, including a ternary diagram with Y, Nb and Ce, and binary diagrams plotting (Y/Nb) versus (Ce/Nb) or (Y/Nb) versus (Yb/Ta) .

The tectonic discrimination of all granitoids relies strongly on the diagrams proposed by Pearce (1996a) and Pearce et al. (1984b), plotting Nb versus Y and $(Y + Nb)$ versus Rb. For the volcanic rocks discussed in this study, the approach proposed by Pearce (1996b) is followed. This includes the classification of the volcanic rocks on a binary diagram plotting (Nb/Y) versus (Zr/Ti) , proposed by Winchester and Floyd (1977), with revised fields after Pearce (1996b). Other than providing a classification of the volcanic rocks into basalt, andesite and rhyolite, the Nb/Y ratio also defines subalkaline, alkaline and ultra-alkaline fields. Pearce (1996b) proposed that samples plotting as basic or intermediate on this diagram are suitable for plotting on the ternary Th-Ta-Hf/3 classification diagram after Wood (1980), on the condition they do not comprise cumulates. Pearce (1996b) suggested that intermediate or felsic volcanics with $Al_2O_3\ wt\% < 20\%$, $Sc < 50\ ppm$, $Ni < 200\ ppm$, are unlikely to represent cumulates of feldspar, olivine or cpx respectively, and proposed that such rocks are suitable for discrimination on the diagram of Wood (1980).

The relative abundance of rare earth elements (REE) and a selection of trace elements are shown in REE diagrams and multi-element cationic distribution diagrams. In published literature, a wide variety of such diagrams are used, which differ in both normalisation values, number and type of elements and organisation. During this study, the REE contents for granitoids and volcanic rocks are shown normalised to chondrite (normalisation values after McDonough and Sun (1995),

see Table 11-10 Appendix D). Based on the normalised values of REE, the following parameters are calculated:

- Europium anomaly = $Eu/Eu^* = Eu_N / ((Sm_N + Gd_N)/2)$
- fractionation value for REE = $f_{REE} = (La/Yb)_N$
- fractionation value for LREE = $f_{LREE} = (La/Sm)_N$
- fractionation value for HREE = $f_{HREE} = (Gd/Yb)_N$

where $_N$ denotes normalised values, Eu^* denotes the ratio of analysed europium and the standard europium content of chondrite, REE=rare earth elements (La, Ce, Pr, Nd, Sm, Eu, Gd, Tb, Dy, Ho, Er and Yb); LREE=light rare earth elements (La to Eu); HREE=heavy rare earth elements (Eu to Yb).

Europium anomalies smaller than 1 are called “negative” (i.e. actual Eu less than that predicted by a linear relationship between Sm-Eu-Gd), while values greater than 1 denote a “positive” Eu-anomaly (i.e. actual Eu greater than that predicted by a linear relationship between Sm-Eu-Gd). The calculated fractionation values give a first-hand idea of the relative normalised abundances of the two end-members. In REE diagrams, the least mobile REE are placed to the right of the diagram, while towards the left, more mobile elements are shown. Large fractionation values (generally greater than 10) indicate strong depletion (or fractionation) trends, while smaller numbers (less than 10) indicate minor depletion (fractionation) trends.

Multi-element cationic distribution diagrams (SPIDER plots), showing Cs, Rb, Ba, Th, U, Nb, Ta, La, Ce, Pb, Pr, Sr, Nd, Zr, Hf, Sm, Eu, Gd, Tb, Dy, Ho, Er, Yb, Y and Lu for all rocks are normalised to primordial mantle (normalisation values after Sun and McDonough (1989), see Table 11-11 Appendix D). A different multi-element plot is also used for volcanics, showing values normalised to N-type mid-ocean-ridge basalt (normalisation values after Pearce (1996b), see Table 11-12 Appendix D) as well a multi-element plot proposed by Pearce et al. (1984), with normalisation to ocean-ridge granitoid (normalisation values after Pearce et al. (1984), see Table 11-13 Appendix D). Throughout the text,

“negative” or “positive” anomalies are related to relative normalised abundances of the element with respect to the elements on either side in the diagram.

5.2 The Archaean (Group I) Kapiri Mposhi Granite-Gneiss

One sample was collected from what was previously mapped as the Mkushi Gneiss basement complex, but was revealed by SHRIMP geochronology as part of a previously unidentified 2.73 Ga Archaean basement. This sample (KMP1) was collected from an abandoned quarry (Kampoyo quarry on the 1:100000 geological map of the Kapiri Mposhi area (Figure 2-9)) and consists of foliated biotite granite gneiss that is cut by various generations of quartz veins and small pegmatites. The sample was collected from portions of the gneiss away from the veins and pegmatites. Whole-rock major and trace element geochemistry are presented in Table 14-1.

5.2.1 Major element geochemistry

The granite gneiss contains quartz and hypersthene in the norm (Table 5-1) and is thus silica oversaturated. The presence of normative corundum indicates that the granite gneiss is peraluminous. A CIA value of 55 indicates that the gneiss is relatively unaltered, while the low loss on ignition of 0.01% also indicates a low level of alteration.

Table 5-1 Modal composition of sample KMP1 calculated from major element geochemistry.

Normative composition (volume %)	
Quartz	36.07
Orthoclase	11.17
Plagioclase	46.23
Corundum	2.24
Hypersthene	3.36
Magnetite	0.27
Ilmenite	0.4
Apatite	0.26

On a ternary QAP diagram (Le Maître, 1989), the granite gneiss plots in the field of granodiorite and close to the tonalitic field (Figure 5-1 (a)) and would best be referred to as the Kapiri Mposhi Granodiorite Gneiss.

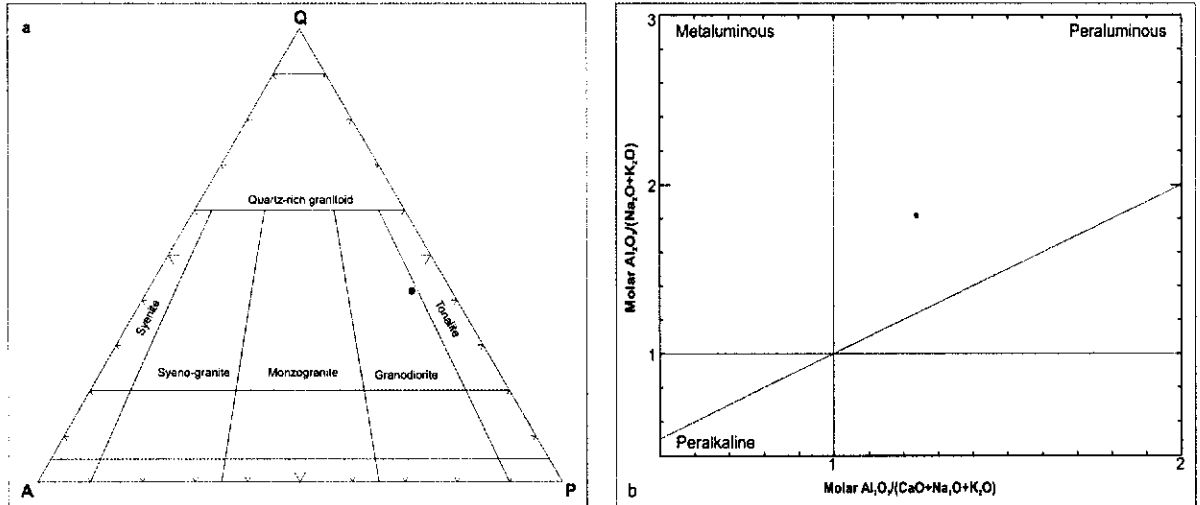


Figure 5-1 (a) QAP diagram indicating a granodioritic composition for the Kapiri Mposhi granite gneiss; (b) Diagram after Maniar and Picolli (1989), characterising the Kapiri Mposhi Granodiorite Gneiss as peraluminous

The Kapiri Mposhi Granodiorite Gneiss has an ASI of 1.23. On a binary diagram proposed by Maniar and Picolli (1989), the strongly peraluminous character of the Kapiri Mposhi Granodiorite Gneiss, which was already indicated by the presence of normative corundum, is apparent (Figure 5-1 (b)). A plot of Na_2O versus K_2O shows the granite gneiss to be sodic in composition (Figure 5-2 (a)).

On the A/CNK versus SiO_2 plot of Clarke (1992) the Kapiri Mposhi Granodiorite Gneiss plots in the S-type field, suggesting derivation from partial melting of metasedimentary source rocks (Figure 5-2 (b)). The diagram also shows the strongly peraluminous character of the gneiss.

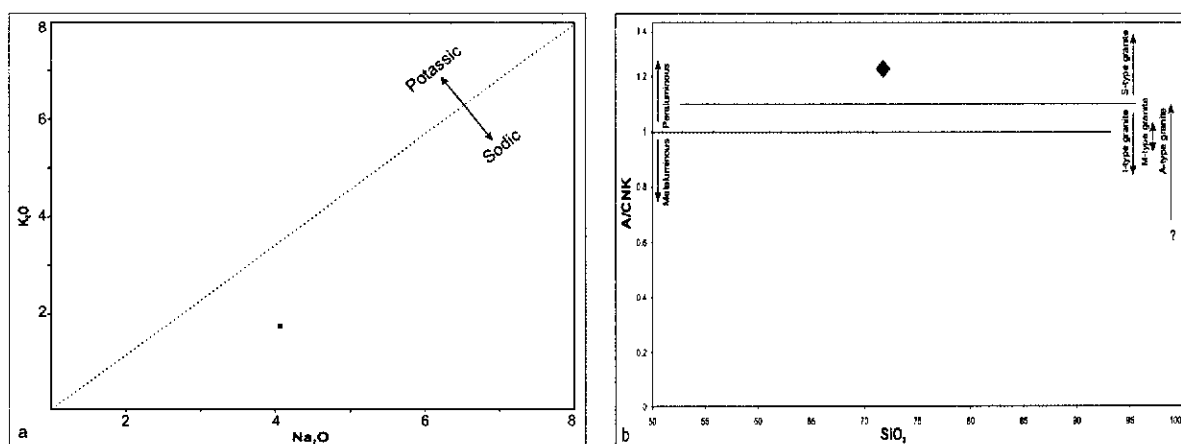


Figure 5-2: (a) binary diagram plotting the K₂O content versus Na₂O content of the Kapiri Mposhi Granodiorite Gneiss showing its sodic character; (b) Plot of SiO₂ vs. ASI after Clarke (1992) suggesting S-type character of the Kapiri Mposhi Granodiorite Gneiss.

5.2.2 Trace elements geochemistry

In a plot proposed by Whalen et al. (1987), showing $(K_2O + Na_2O) / CaO$ versus $(Zr + Nb + Ce + Y)$, the Kapiri Mposhi Granodiorite Gneiss plots in the field of the Orogenic Granite Types (Figure 5-3).

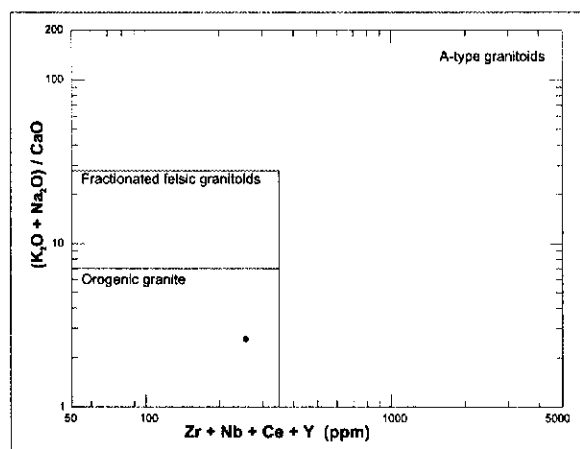


Figure 5-3: Discrimination diagram after Whalen et al. (1987)

The binary diagrams of Y versus Nb and of Rb versus $(Y + Nb)$ by Pearce et al. (1984a) and by Pearce (1996a) (Figure 5-4) suggest the Kapiri Mposhi Granodiorite Gneiss has characteristics consistent with a volcanic arc setting.

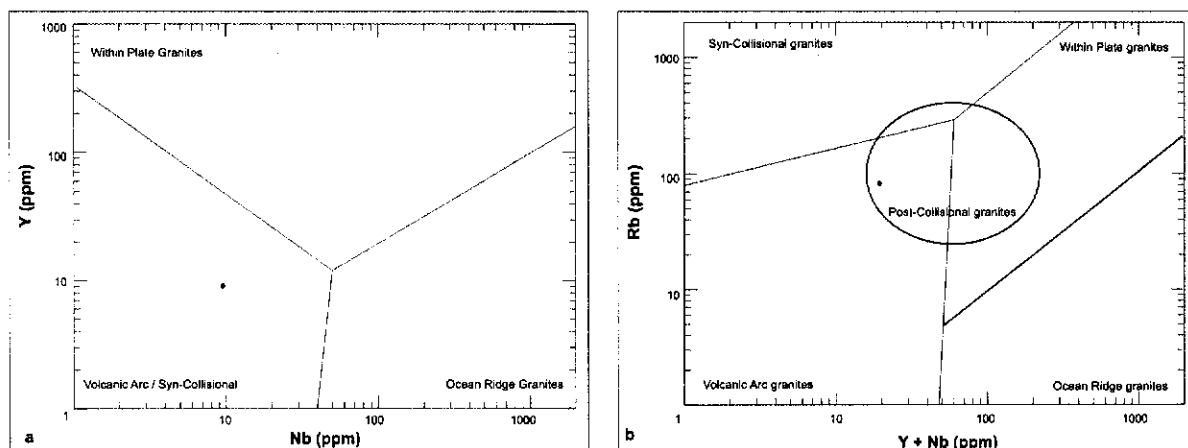


Figure 5-4: Tectonic discrimination diagrams after Pearce (1996a) and Pearce et al. (1984a) suggesting a Volcanic Arc signature for the Kapiri Mposhi granite gneiss.

A chondrite-normalised rare earth element diagram and a primordial mantle normalised multi-element cationic plot for the Kapiri Mposhi Granodiorite Gneiss are shown in Figure 5-5 and Figure 5-6. The granodiorite gneiss shows a strongly fractionated REE pattern ($f_{\text{REE}}=37.84$), with most of the fractionation occurring in the LREE ($f_{\text{LREE}}=5.72$), though minor fractionation in the HREE is still apparent ($f_{\text{HREE}}=3.40$). The granodiorite gneiss also shows a negative Eu anomaly of 0.58, indicating limited plagioclase fractionation.

The SPIDER plot shows strong negative anomalies for Ba, Nb and Eu, and moderately negative Ce, Sr and Yb values. Noticeably, Zr shows a slightly positive anomaly, as does Ta. Strong positive anomalies are recorded for Th and Pb. These features are consistent with granite emplacement in a convergent setting, during which substantial amounts of crust are recycled.

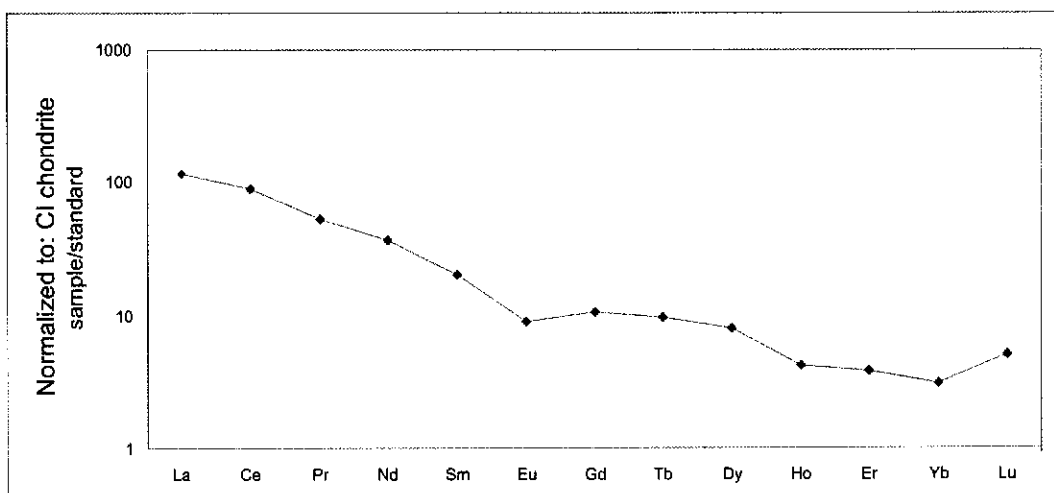


Figure 5-5 Chondrite normalised rare earth element distribution pattern for the Kapiri Mposhi granite gneiss (normalisation values after McDonough and Sun (1995)).

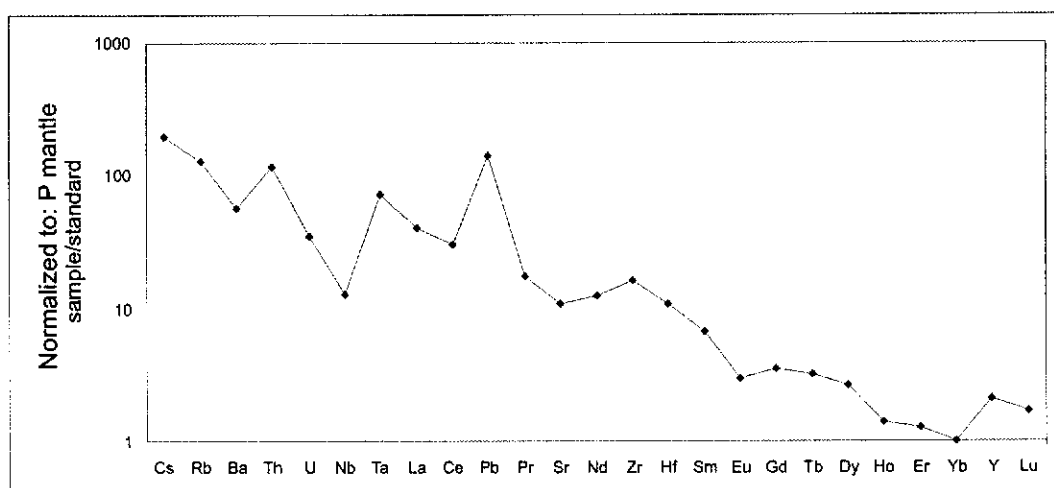


Figure 5-6 Primordial Mantle (P-mantle) normalised multi-element cationic distribution diagram (spidergram) for the Kapiri Mposhi granite gneiss (normalisation values after Sun and McDonough (1989)).

5.2.3 Geotectonic interpretation

Taking into account the obvious limitations of a single sample analysis, the following features characterise the Kapiri Mposhi Granodiorite Gneiss: (a) the gneiss is of peraluminous and sodic character; (b) its overall REE content is relatively high, but not high enough to suggest an intra-plate setting; (c) its Y, Yb and Nb content is relatively high, but not in the range expected for within-plate granites; (d) relative depletion of Ba and Nb and strong enrichment of Pb, Th and Ta, suggest significant amounts of reworked crust in the formation of the granite

precursor; (e) the significant enrichments in Pb and Th may indicate that processes of hydration of subducting oceanic crust played a role in the generation of the magma source. It can be concluded that the geochemical characteristics are in keeping with a volcanic arc setting for the emplacement of the precursor to the Kapiri Mposhi Granodiorite Gneiss.

5.3 Palaeoproterozoic Group II granitoids of the Irumide belt

Eight samples were analysed of the Mkushi Gneiss in the southwestern part of the Irumide belt (Figure 2-9, samples KN1, KN6, MK3, MK4, MK5, MK6, MK12 and CC10) and two samples from the Luwalizi Granite Gneiss in the northeastern part of the Irumide belt (Figure 2-13, samples ISK1 and ISK2). Their whole rock geochemistry is shown in Table 14-2 (major elements) and Table 14-15 (trace elements).

Sample KN1 was collected from strongly foliated biotite granite gneiss in the Kanona map sheet area (Figure 2-10), cut by various small pegmatites. The gneiss shows a strong foliation along a north-northeast direction, dipping steeply southeast, defined by biotite. Stretched K-feldspar defines a shallow to steeply plunging mineral lineation along an east-southeast direction, while the pegmatites are stretched and boudinaged along the same direction. Some secondary epidote was recognised along the pegmatites, and the sample was collected from parts of the outcrop away from the pegmatites. Sample KN6 was collected from deformed and sheared biotite-muscovite granite gneiss in the Kanona map sheet area (Figure 2-10), foliated along a south-southwest direction, dipping shallowly to the west, with a mylonitic lineation defined by stretched K-feldspar along a shallow northeast-plunging direction.

Samples MK3, MK4 and MK5 were collected from Munshiwemba Quarry in the Mkushi map sheet (Figure 2-9). Sample MK3 was collected from strongly sheared biotite granite gneiss in the northern part of the quarry, while MK4 came from an undeformed aplitic dyke in the same location, which appears to cut the gneiss along a shear plane. Sample MK5 was collected from the southern part of

the quarry, and consists of coarse-grained pink granite gneiss, interpreted to be a less-sheared equivalent of sample MK3. Sample MK6 was collected from a flat outcrop of foliated biotite granite gneiss some 20 kilometers east of Munshiwemba Quarry, where the pinkish biotite gneiss is cut by various small pegmatites. All samples were taken well away from the pegmatites.

Sample CC10 was taken from a low-lying flat outcrop of foliated biotite granite gneiss in the Chin'gombe Mission map sheet (Figure 2-9). The gneiss shows a strong biotite foliation along an east-west direction, dipping steeply to the north.

Samples ISK1 and ISK2 were collected from flat outcrops of biotite granite gneiss near Isoka (Isoka map sheet, Figure 2-12). The Luwalizi Granite Gneiss consists of coarse, foliated biotite granite, which contains xenoliths of fine, mafic material. The foliation is defined by K-feldspar phenocrysts, which are aligned along a southwest direction, dipping steeply to the north, but is also expressed in the xenoliths through reoriented biotite.

5.3.1 Major element geochemistry

The Mkushi Gneiss and Luwalizi Granite Gneiss both contain quartz and hypersthene in the norm (Table 5-2) and are silica oversaturated. Normative corundum indicates that the gneisses are peraluminous. The samples have CIA values between 50 and 59, indicating them to represent relatively unaltered rock. The LOI values range from zero to 0.02%, confirming very low levels of alteration.

Table 5-2: Modal composition of Group II granitoids in the Irumide belt calculated from major element chemistry.

	Normative composition									
	Volume %									
	ISK1	ISK2	KN1	KN6	MK3	MK4	MK5	MK6	MK12	CC10
Quartz	36.78	40.99	32.55	35.58	30.14	33.47	43.64	40.51	32.98	37.21
Orthoclase	22.12	30.74	15.86	31.00	30.32	46.55	29.22	24.26	22.38	25.24
Plagioclase	29.23	21.60	44.78	30.15	32.17	18.97	22.67	32.94	37.36	32.96
Corundum	1.95	2.53	0.28	1.73	1.87	0.61	1.80	1.77	3.89	1.32
Hyperssthene	7.63	3.19	5.24	1.14	4.06	0.15	2.08	0.25	2.51	2.55
Magnetite	0.71	0.26	0.43	0.12	0.45	0.02	0.17	0.02	0.21	0.26
Ilmenite	1.41	0.48	0.74	0.16	0.72	0.06	0.30	0.02	0.40	0.35
Apatite	0.16	0.22	0.14	0.12	0.26	0.17	0.12	0.21	0.26	0.10

On the QAP diagram of Le Maître (1989), the Mkushi Gneiss and Luwalizi Granite Gneiss both plot in the monzo-granite field, while the aplite sample (MK4) plots in the syeno-granite field (Figure 5-7 (a)). On a binary diagram after Maniar and Picolli (1989), the Mkushi Gneiss and Luwalizi Granite Gneiss show a distinct peraluminous character (Figure 5-7 (b)).

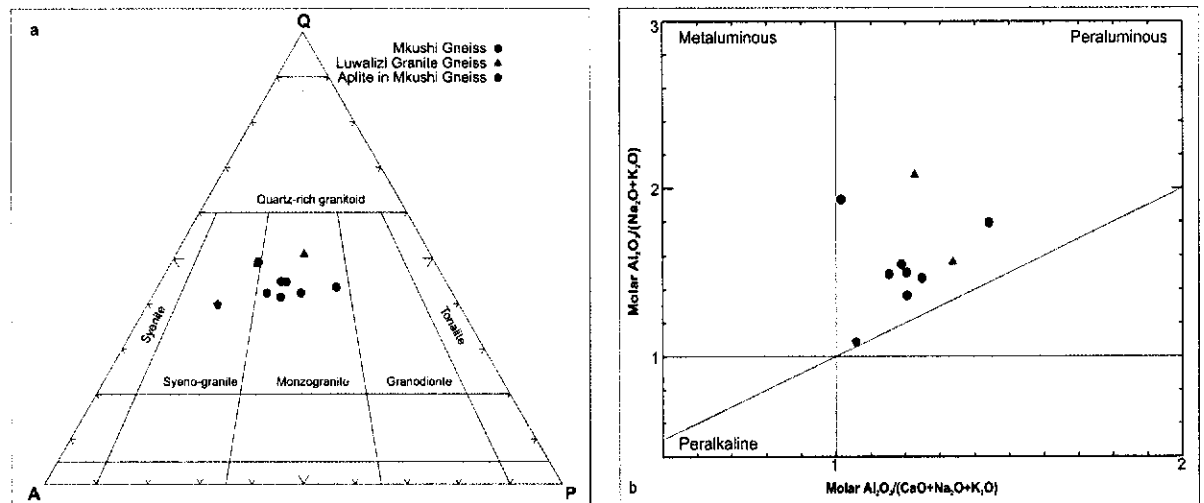


Figure 5-7 (a) QAP diagram indicating monzo-granitic composition of the Mkushi Gneiss and the Luwalizi Granite Gneiss; (b) Diagram after Maniar and Picolli (1989), characterising the Mkushi Gneiss and Luwalizi Granite Gneiss as peraluminous (symbols as in Figure 5-7 (a)).

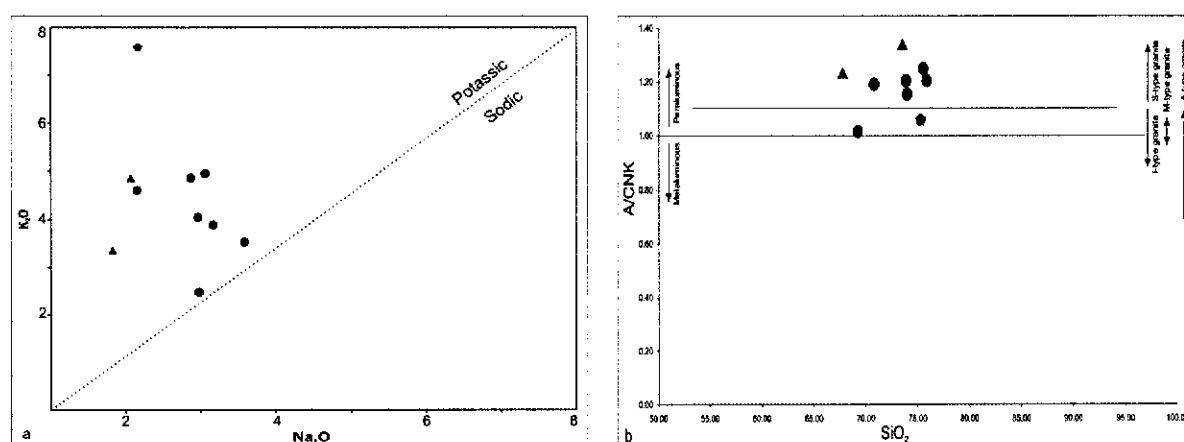


Figure 5-8 (a) Binary diagram plotting the K_2O content versus Na_2O for the Mkushi Gneiss and Luwalizi Granite Gneiss; (b) ASI versus SiO_2 plot for the Mkushi Gneiss and Luwalizi Granite Gneiss. The plot shows that the granite gneisses have predominant S-type characteristics (symbols as in Figure 5-7 (a)).

The binary plot of K_2O versus Na_2O further indicates both granite gneisses to be potassic in nature (Figure 5-8 (a)). The ASI for the Mkushi Gneiss and Luwalizi Granite Gneiss ranges from 1.01 to 1.44, and in the binary plot of ASI versus SiO_2 after Clarke (1992) (Figure 5-8 (b)), the majority of the samples plot with ASI values above 1.10 into the S-type granitoid field. Sample KN1 shows the lowest ASI value of 1.01.

5.3.2 Trace element geochemistry

In a plot after Whalen et al. (1987) (Figure 5-9 (a)), the majority of the samples of the Mkushi Gneiss plot in the orogenic granite type and fractionated granite fields. Luwalizi Granite Gneiss samples ISK1 and ISK2 and Mkushi Gneiss sample CC10 have elevated values (ppm) for Ce, Nb, Y and Zr, and plot into the A-type granite field. It is noteworthy that samples CC10, ISK1 and ISK2 are all about 100 M.y. younger than the typical Mkushi Gneiss (ca. 2050 Ma) and range in age between 1953 ± 6 and 1927 ± 10 Ma.

On a logarithmic plot of Y/Nb versus Yb/Ta after Eby (1992) (Figure 5-9 (b)), sample CC10 plots in the ocean-island basalt field, suggesting a source similar to that of ocean-island basalt. The samples of the Luwalizi Granite Gneiss plot both in and out of the ocean-island field.

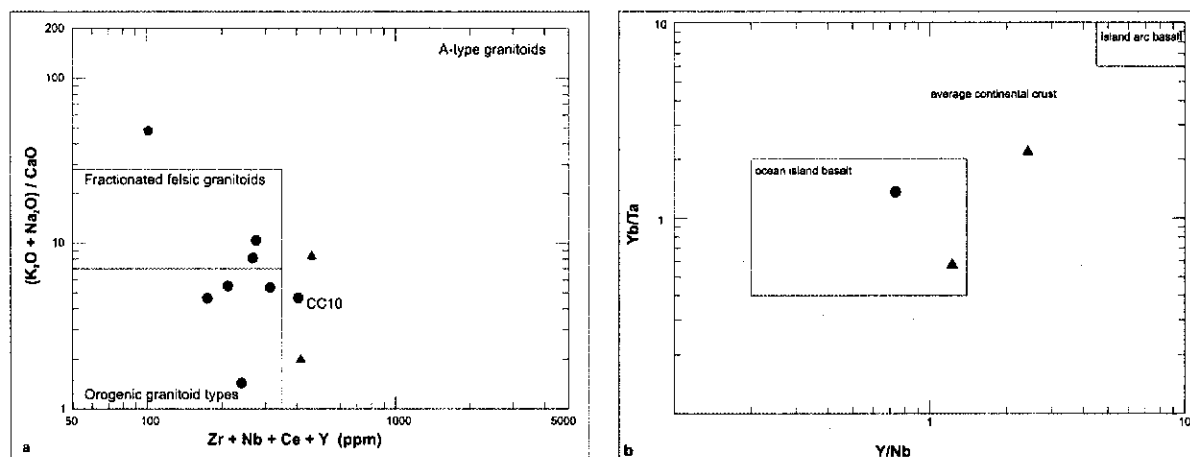


Figure 5-9 (a) Plot after Whalen et al. (1987), showing the Mkushi Gneiss in the Orogenic granite type and fractionated granite fields and the Luwalizi Granite Gneiss in the A-type field. Sample CC10, which is the youngest granite gneiss mapped as part of the Mkushi Gneiss (~1.95 Ga), also plots in the A-type field; (b) Plot of Y/Nb versus Yb/Ta after Eby (1990).

In the diagrams of Pearce et al. (1984) and Pearce (1996) (Figure 5-10), the Mkushi Gneiss has predominant volcanic arc characteristics with samples MK5, KN6 and CC10 showing within-plate characteristics. For the Luwalizi Granite Gneiss, one sample (ISK1) plots within the volcanic arc field, while the other (ISK2) plots in the within-plate field. The younger (1.95 Ga) Mkushi Gneiss (sample CC10) has a significantly higher Y content, and plots in the within-plate field. In the binary diagram showing $(Y + Nb)$ versus Rb , the Mkushi Gneiss and Luwalizi Granite Gneiss both plot within the post-collisional granite field.

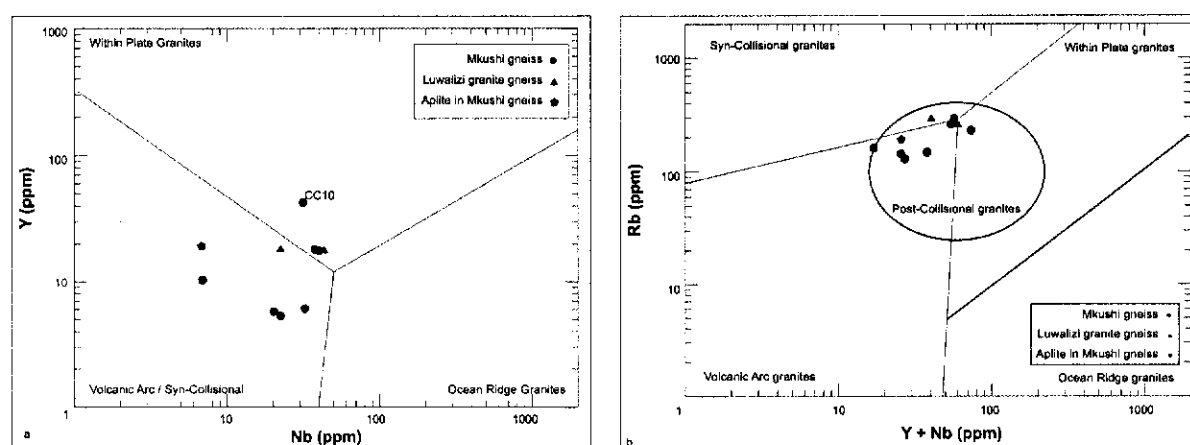


Figure 5-10 (a) Tectonic discrimination diagram after Pearce et al. (1984), depicting the Mkushi Gneiss with predominant volcanic arc / syn-collisional characteristics, and the Luwalizi Granite Gneiss towards the within plate field; (b) tectonic discrimination diagram after Pearce (1996) showing the Mkushi Gneiss and Luwalizi Granite Gneiss straddling syn-collisional, within plate, post-collisional and volcanic arc fields.

Most samples of the Mkushi Gneiss and Luwalizi Granite Gneiss show similar patterns in the chondrite-normalised rare earth element plot (Figure 5-11). The REE patterns are characterised by moderate LREE fractionation and near flat HREE trends. Sample MK12, however, follows an anomalously steep trend, with a fractionation ratio of 50.45, and sample MK6 has an anomalous negative Ce anomaly, indicating a possible sampling or analytical problem, or element mobility and alteration. The aplite (sample MK4) is REE-depleted with respect to the granites and gneisses, and plots well below the rest of the samples along a roughly parallel trend. Fractionation for the samples, excluding MK6, MK 12 and MK4, results in f_{REE} ranging from 6.49 to 35.26. Fractionation is more pronounced in the LREE, with f_{LREE} ranging from 2.83 to 5.91 while f_{HREE} ranges from 1.23 to 4.83. A negative Eu-anomaly is present for most samples ranging from 0.28 to 0.86, but samples MK4 and MK6 record positive Eu-anomalies of 1.23 and 1.46 respectively, possibly indicating that these samples represent plagioclase enriched cumulates.

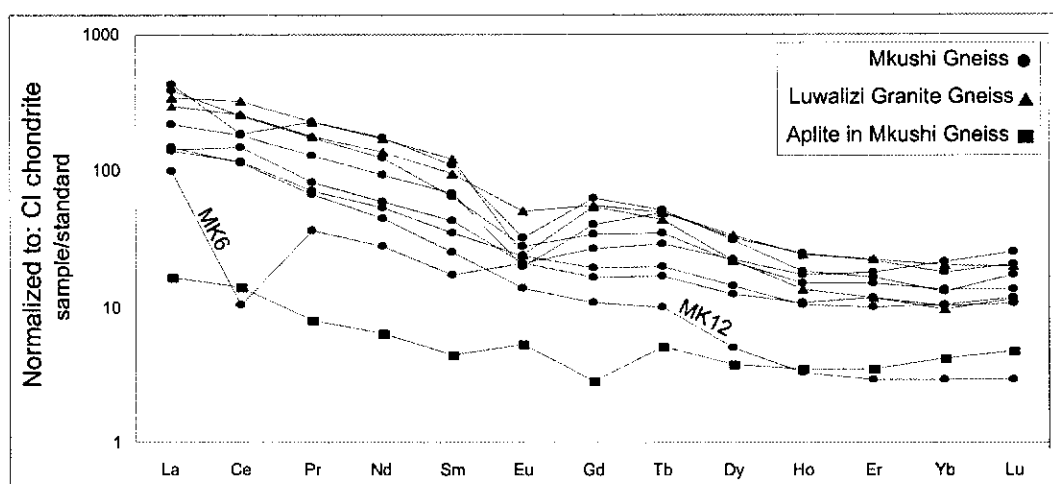


Figure 5-11 Chondrite normalised rare earth element distribution pattern for the Mkushi Gneiss and the Luwalizi Granite Gneiss (normalisation values after McDonough and Sun (1995)).

The SPIDER plots show strong negative anomalies for Nb and Sr, and moderately negative anomalies for Ba, Eu, Zr and Hf, with the exception of samples MK6 and MK12 (Figure 5-12). Strong positive anomalies are recorded for Th and Pb as well as Sm and Nd. Depletion of Nb, Ba, Zr and Hf is commonly associated with granitic rocks that have interacted with a variety of crustal rocks,

including sedimentary rocks (Pearce et al., 1984a). The spider patterns are therefore consistent with the S-type affinity indicated in Figure 5-9.

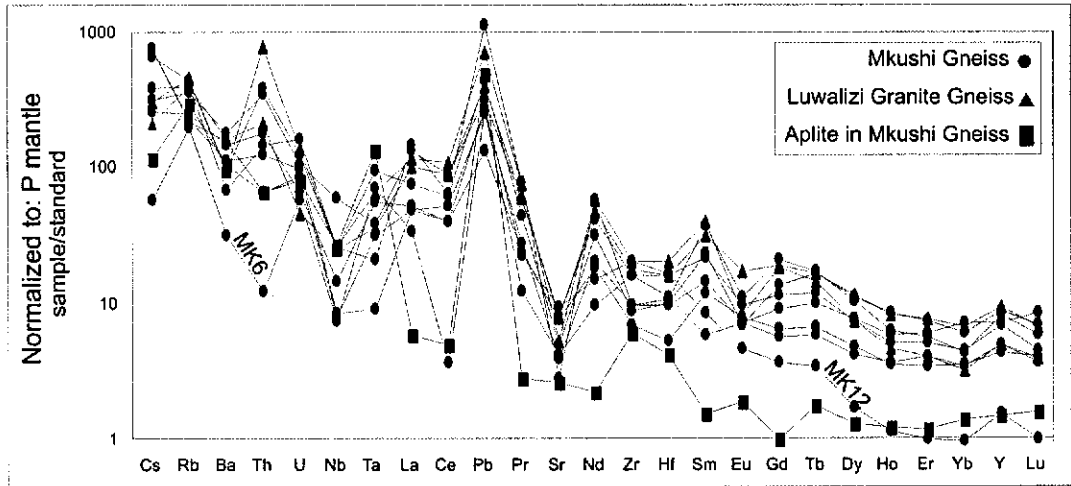


Figure 5-12 P-mantle normalised multi-element cationic plot for the Mkushi Gneiss and Luwalizi Granite Gneiss (normalisation values after Sun and McDonough (1989)).

5.3.3 Geotectonic interpretation

The Mkushi Gneiss and Luwalizi Granite Gneiss show broadly similar characteristics. All Group II granitoids are characterised by peraluminous and potassic compositions. The REE content ranges from moderate to high. Depletion of Nb and Zr-Hf and enrichment in Th and Pb suggest the involvement of continental crust in the formation of Group II granitoids. Negative anomalies for Sr and Eu suggest fractional crystallisation of plagioclase to have been an important factor in the formation of Group II granitoids. Yb, Ta and Nb contents for the younger A-type granitoids suggest a source similar to ocean-island arc to average continental crust, consistent with a subduction setting, perhaps culminating in collision to yield the crust-dominated character.

5.4 *Palaeoproterozoic Mansa plutono-volcanic suite*

Three samples were collected each from the volcanics and granitoids exposed near Mansa (Figure 2-6; samples MA3, 4 and 5 and samples MA1, 2 and 9 respectively). Their whole rock geochemistry is shown in Table 14-3 and Table 14-16.

Sample MA1 was collected from reddish coarse-grained biotite granite, eight kilometers south of Mansa (Figure 2-6). The granite intrudes fine-grained, dark grey volcanic material as evidenced by the occurrence of xenoliths of volcanic material, but the actual intrusive contact was not observed at the outcrop.

Samples MA2 and MA3 were collected from an outcrop where granite and volcanic rock are seen in direct contact. The granite (sample MA2) is reddish brown biotite granite, in which plagioclase and biotite have in part been altered to epidote + calcite (saussurite) and chlorite respectively. The granite intrudes a fine-grained greyish-green volcanic unit (sample MA3), which occurs as elongate rafts in the granite.

Sample MA4 was collected from a large unit of dark grey to greenish layered volcanic, in which cm to dm-thick individual volcanic layers can be identified. The volcanic has an amygdaloidal aspect, with relict amygdales of quartz or greenish epidote.

Sample MA5 was taken from a small outcrop of volcanics along the road to Musonda Falls, comprising dark grey fine-grained rhyolite.

Sample MA9 was collected from a large rounded hill west of Musonda Falls, where reddish coarse biotite granite occurs. The granite is intruded by fine-grained aplites.

5.4.1 Major element geochemistry

Normative calculations on the Mansa Volcanics (samples MA3, 4 and 5) show that these rocks contain highly variable normative quartz ranging from 20.42% in sample MA4 up to 43.63% in sample MA5. All samples also contain hypersthene in the norm indicating their overall silica-saturated character. Sample MA4 contains diopside in the norm indicating its subaluminous character, while samples MA3 and MA5 have normative corundum, showing them to be peraluminous.

Table 5-3: Modal composition of the Mansa Volcanics and Mansa Granitoids of the Bangweulu block calculated from major element chemistry.

	Normative composition					
	Volume %					
	Volcanics			Granitoids		
	MA3	MA4	MA5	MA1	MA2	MA9
Quartz	29.58	20.42	43.63		35.78	43.71
Orthoclase	22.37	20.05	17.73	0.31	25.26	23.79
Plagioclase	40.87	51.75	33.12	2.43	32.14	29.87
Corundum	1.85		1.93		0.88	1.29
Hypersthene	4.00	3.55	1.86	56.81	4.67	1.03
Diopside		2.91		0.80		
Olivine				37.40		
Magnetite	0.34	0.41	0.17	2.09	0.44	0.10
Ilmenite	0.75	0.79	0.41	0.01	0.65	0.18
Apatite	0.24	0.12	0.16	0.15	0.18	0.04

CIA values for the volcanic samples are between 47.5 and 55.6% consistent with relatively unaltered rock. The analysed LOI content for the volcanics is consistently below 0.01% and confirms this.

The Mansa Granitoids similarly show variable silica saturation, with sample MA1 showing no quartz in the norm, and samples MA2 and MA9 containing 35.78 and 43.71% quartz respectively. Based on the anomalous result for sample MA1, which contains abundant quartz in hand specimen yet records low SiO₂ in the geochemical analysis, the major element analysis of this sample is considered flawed and will not be further discussed below. The two silica-oversaturated samples contain normative hypersthene, ranging from 1.03 to 4.67%, and normative corundum, ranging from 0.88 to 1.29%, and represent peraluminous, subalkaline rocks. The CIA index for the granitoids ranges from

52.1 to 54.1%, while LOI values are below 0.01 indicating limited alteration of these rocks.

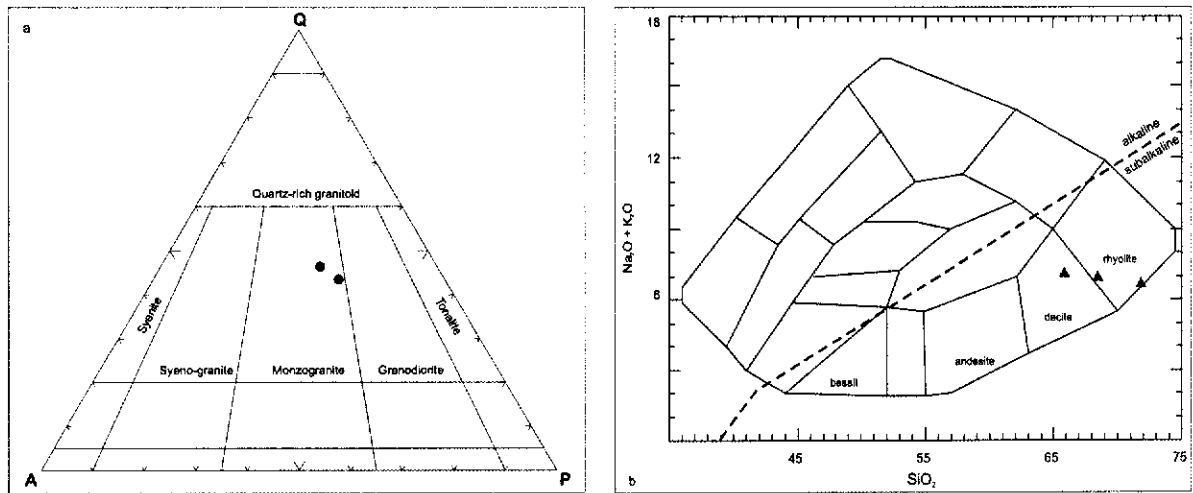


Figure 5-13: (a) QAP diagram indicating monzogranitic composition of the Mansa Granitoids (after Le Maître, (1989)); (b) total alkalis versus silica classification diagram of the Mansa Volcanics after Cox et al. (1979).

The two silica-saturated Mansa Granitoids plot in the monzogranite field of the QAP diagram proposed by Le Maître (1989)(Figure 5-13 (a)).

The three Mansa Volcanics are classified in the diagram proposed by Cox et al. (1979)(Figure 5-13 (b)) as dacite and rhyolite, consistent with their relatively high silica content. The diagram also shows that the volcanics are of subalkaline character.

The Mansa granitoids and volcanics are classified as peraluminous, with the exception of volcanic sample MA4, which plots as metaluminous (Figure 5-14 (a)) on the diagram proposed by Maniar and Picolli (1989). The granites plot as potassic, while the volcanics have broadly subequal K₂O and Na₂O content (Figure 5-14 (b)).

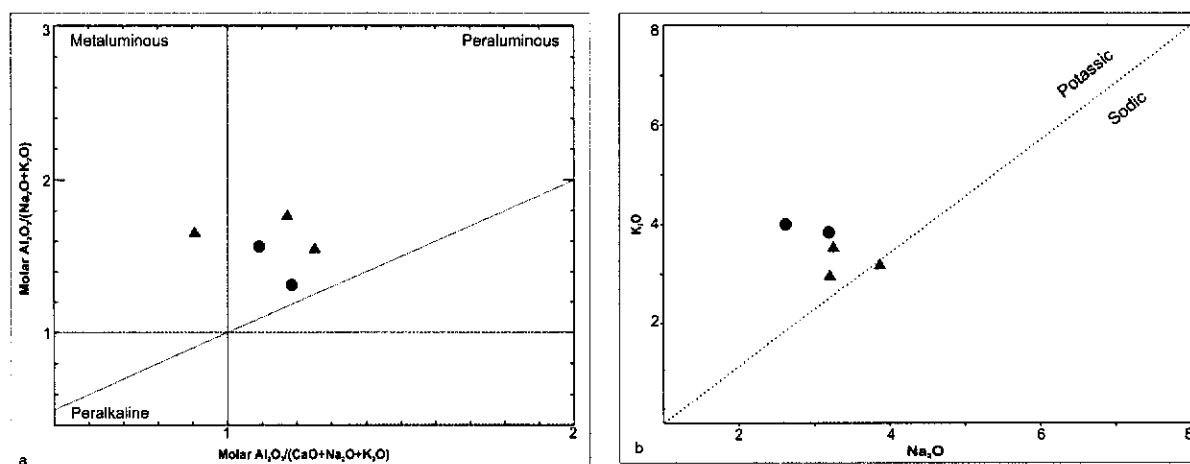


Figure 5-14: (a) Diagram after Maniar and Picolli (1989), characterising the Mansa Granite (circles) and Volcanic (triangles) as peraluminous to metaluminous; (b) binary diagram plotting the K_2O content versus Na_2O for the Mansa Granite (circles) and Volcanic (triangles).

The aluminium saturation index for the granites is slightly over one, and they plot around the boundary of I- and S-type granitoids in the diagram proposed by Clarke (1992)(Figure 5-15 (a)).

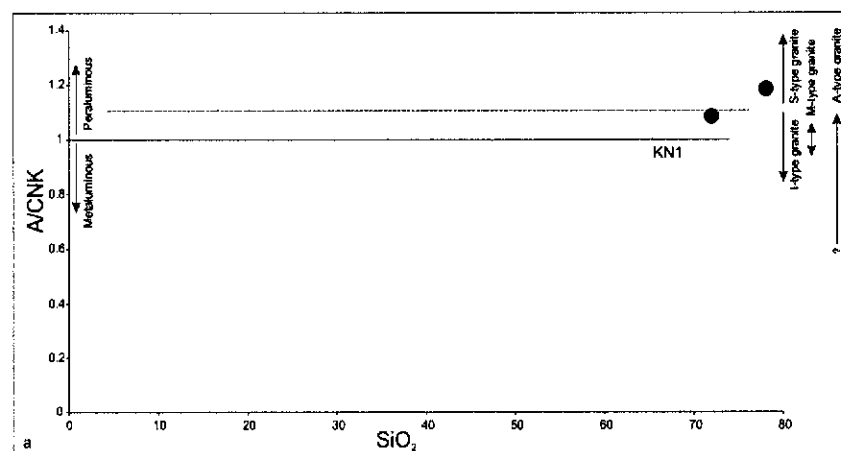


Figure 5-15: ASI versus SiO_2 plot for the Mansa Granites. The granites plot close to the I-type and S-type fields.

5.4.2 Trace element geochemistry

Samples MA9 and MA2 plot in different fields in the tectonic discrimination diagram proposed by Whalen et al. (1987)(Figure 5-16 (a)). Sample MA2 plots in the field of A-type granites, while MA9 plots in the field of fractionated felsic granitoids. The diagram more importantly demonstrates the

relative enrichment in Large Ion Lithophile Elements (LILE) and High Field Strength (HFS)(immobile) elements for both granitoids. The granites plot in the within plate field in the diagram of Pearce et al. (1984) due to relatively high content of Nb and Y (Figure 5-16 (b)).

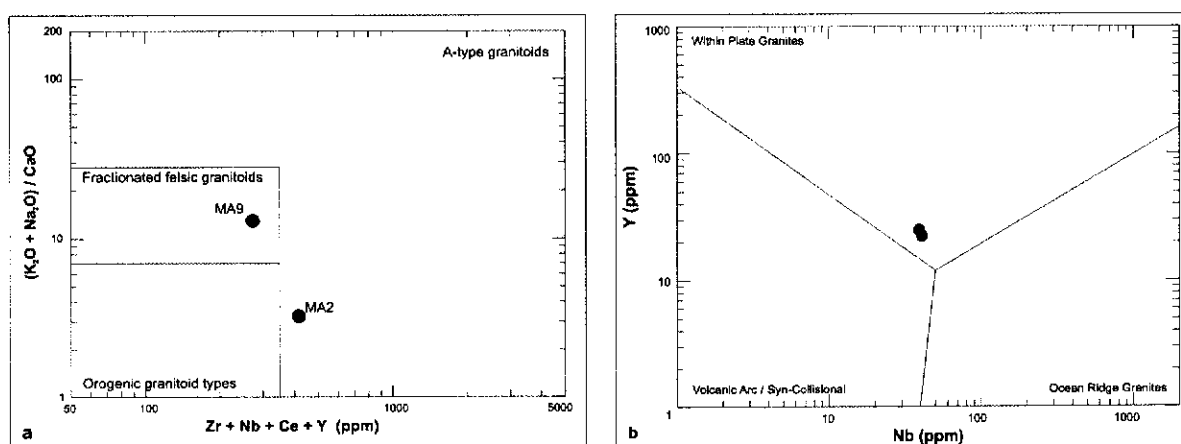


Figure 5-16: (a) Plot after Whalen et al. (1987), showing sample MA9 in the fractionated felsic granite field and sample MA2 in the A-type granite field; (b) Tectonic discrimination diagram after Pearce et al. (1984) depicting the Mansa Granite in the within plate field.

All three Mansa volcanics are silica-oversaturated but have Al_2O_3 wt% values between 13.2 and 16.2%, Ni between 3.9 and 7.4 ppm and Sc between 6.6 and 9.7 ppm, testifying to the fact that they do not comprise cumulates of feldspar, clinopyroxene respectively (Pearce, 1996b). They are classified as subalkaline andesite to basaltic andesite on the Zr/Ti vs. Nb/Y diagram adapted by Pearce (1996b), after Winchester and Floyd (1977), in contrast with their classification as rhyolite and dacite on major element geochemistry and field character (Figure 5-17 (a)). The Zr/Ti vs. Nb/Y diagram does indicate that the samples are suitable for plotting on the ternary diagram $Th-Ta-Hf/3$ proposed by Wood (1980) in an attempt to elucidate their tectonic affinity. The three volcanics plot in the volcanic arc and within plate basalt field proposed by Pearce (1996b)(Figure 5-17 (b)), and thus show a broadly similar geochemical character to the Mansa Granitoids.

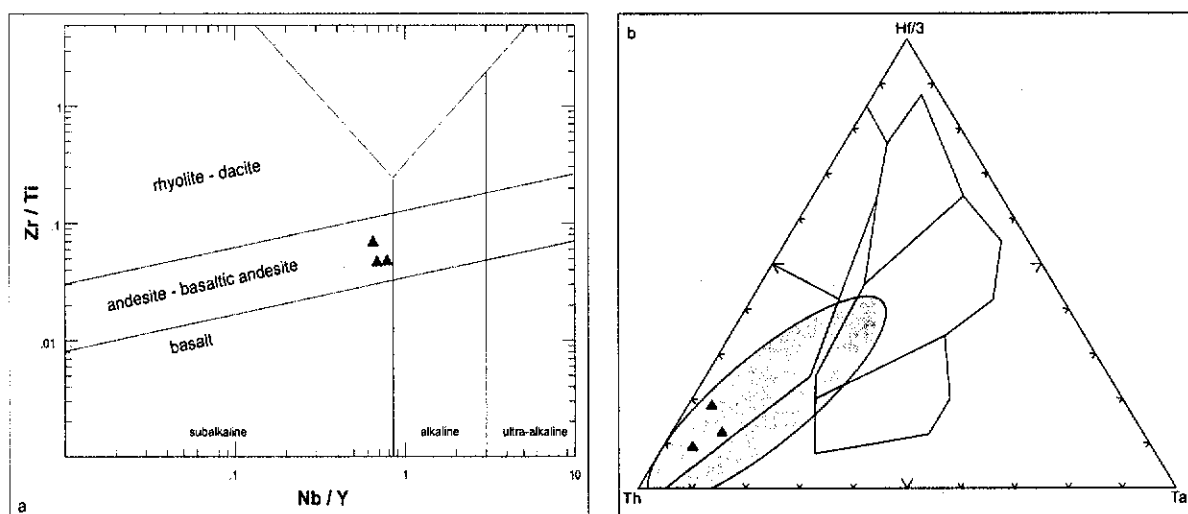


Figure 5-17: (a) Zr/Ti vs. Nb/Y diagram for the Mansa Volcanics (Pearce, 1996b) modified after Winchester and Floyd (1977); (b) Th-Ta-Hf discrimination plot after Wood (1980), showing the volcanics to plot in the field of volcanic arc / within-plate basalt (grey ellipse).

The chondrite-normalised rare earth element plots for the Mansa Granites and Volcanics show remarkably similar characteristics (Figure 5-18). The Mansa Granites have narrowly defined negative Eu-anomalies ranging from 0.56 to 0.59, while two of the Mansa Volcanics (samples MA3 and 4) have no Eu-anomaly, while the other sample (MA5) has a negative Eu-anomaly of 0.67. LREE are relatively fractionated with f LREE ranging from 3.82 to 5.61 for the granites and between 4.05 and 5.50 for the volcanics. HREE show less-fractionated patterns with f HREE ranging from 0.86 to 1.72 for the granites and from 1.74 to 2.25 for the volcanics. The overall fractionation ranges from 8.94 to 20.04 for both suites. The parallelism of the trends supports the interpretation that the volcanics and granites form part of a single co-genetic suite.

Primitive mantle multi-cationic plots for the granitoids show significant negative anomalies for Nb, Sr and Eu (Figure 5-19 and Figure 5-20). The latter two may be indicative of substantial fractionation of plagioclase from the melt through fractional crystallisation, while the Nb anomaly is commonly associated with convergent settings (Pearce et al., 1984a). The observed moderate negative anomalies for Ba, Ta, Ce, Zr-Hf and Ho are also commonly recorded in magma emplaced at convergent margins (Pearce et al., 1984a). Again note the broadly similar pattern for the granites and volcanic rocks, supporting their linked co-genetic origin.

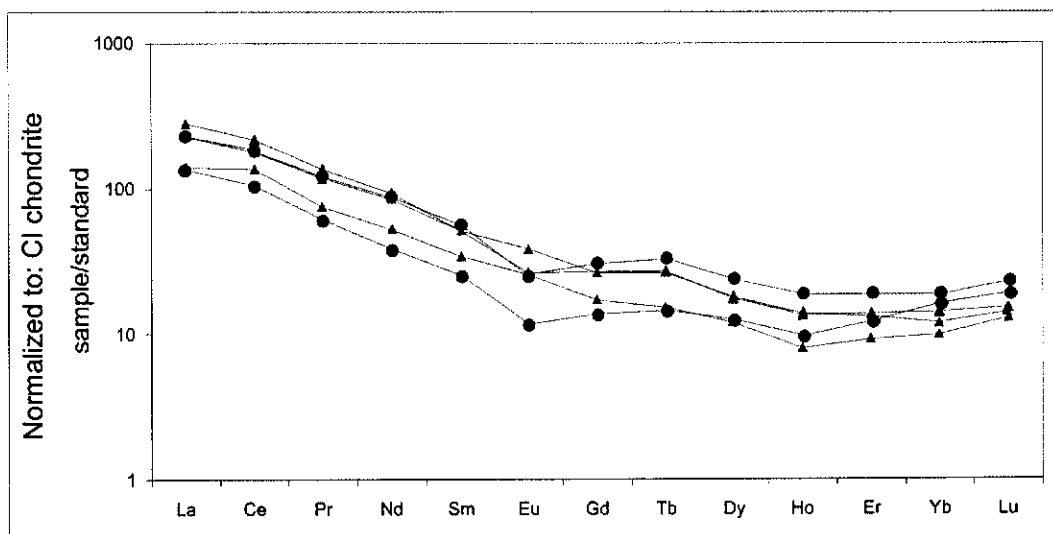


Figure 5-18: CI chondrite normalised rare earth element distribution pattern for the Mansa Granites (normalisation values after McDonough and Sun (1995)).

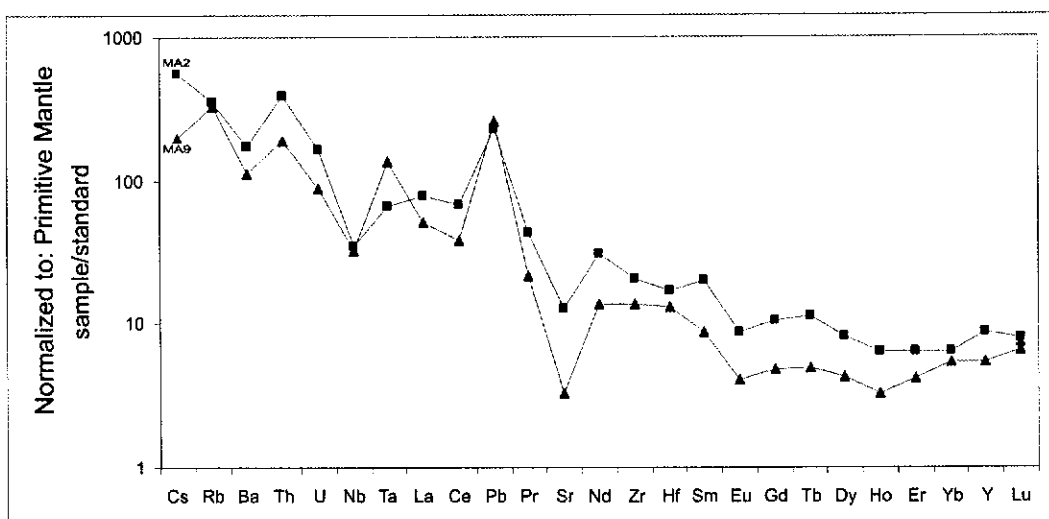


Figure 5-19: Primordial Mantle normalised multi-element cationic distribution diagram (spidergram) for the Mansa Granites (normalisation values after Sun and McDonough (1989)).

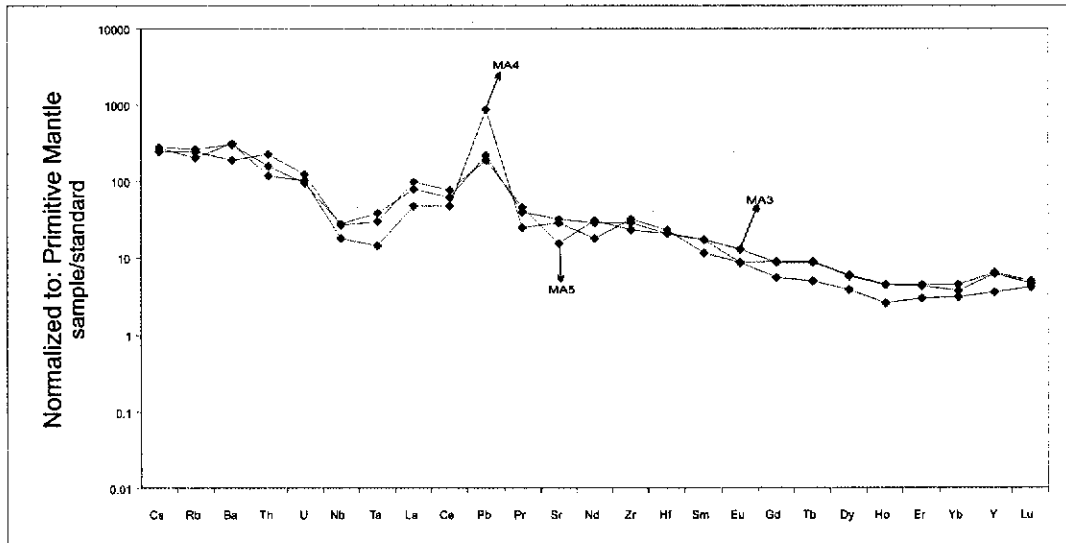


Figure 5-20: Primordial Mantle normalised multi-element cationic distribution diagram (spidergram) for the Mansa Volcanics (normalisation values after Sun and McDonough (1989)).

5.4.3 Geotectonic interpretation

The Mansa Granites and Volcanics show very similar overall geochemical characteristics, supporting the idea that they in fact constitute part of a single plutono-volcanic suite. The Mansa suite displays subalkaline, peraluminous character and is slightly sodic. Its overall REE content is relatively high, giving the granites A-type characteristics, while the elevated Nb and Y content suggests a within-plate character. The volcanics however display high Th content, which coupled with relatively low Ta and Hf gives them a distinct volcanic arc signature. Relative depletions of Ba, Nb, Ta and enrichment in Pb and Th also support a convergent setting. The Mansa plutono-volcanic suite is therefore best interpreted to have been emplaced in a volcanic arc setting.

5.5 *Palaeoproterozoic (Group III) volcanics in the Irumide belt*

This study includes four metavolcanic units which occur within the Manshya River Group sequence, namely the Katibunga Volcanics, the Luswa River Volcanics, the Ilondola Volcanics and the Kachinga Tuff.

The Katibunga Volcanics occur in a fault-bound block, together with metapelite and quartzite of the Manshya River Group. They have been dated at 1871 ± 24 Ma. The volcanics occur predominantly as pillow basalt, and are underlain as well as overlain by clastic deposits dominated by quartzite. Limited schistose sequences within the quartzites are interpreted as possible volcanoclastic deposits, but basic lavas dominate the suite. Thirteen samples of the Katibunga Volcanics were analysed, five collected in 1999 and analysed by Chemex (Canada), and eight more in 2000 and analysed at Curtin University of Technology (see Table 14-4 and Table 14-5 (major elements) and Table 14-17 and Table 14-18 (trace elements)).

Sample KV1 was collected from a location 2 km west of Nakalya Hill (Figure 2-37), and consists of strongly folded and crenulated schist. Based on the abundance of feldspar phenocrysts and alternating layers of quartzite and iron-stained pelite, the rock is interpreted to contain significant volcanoclastic input.

Samples KV4, 5, 7 and 8 were collected from various phases of the basalt and pillow lava occurring at Nakalya Hill (Figure 2-37). Sample KV4 came from aphanitic fresh, dark basalt, with very few amygdales. Sample KV5 was taken from an amygdaloidal dark grey basalt, which contains a few small veinlets of quartz, while sample KV7 was collected from parts of the basalt that showed no veins. Sample KV8 is from a foliated coarse grained gabbro where a younger dolerite intrudes the sequence.

Sample KB2 was collected close to where sample KV1 was taken. The sample came from a metarhyolitic part of the metavolcanic-schist sequence. Sample KB3 was collected from a coarse gabbro to the west of the main basalt outcrop. The gabbro intrudes the metasedimentary / metavolcanic sequence below the main basalts and is interpreted as a feeder dyke to the pillow lavas higher up in the sequence.

Samples KB4, 5, 6, 7, 8 and 9 were collected from various phases of the pillow lavas and basalts on Nakalya Hill. Samples KB4, KB5 and KB6 were sampled from dark grey basalt, with small veinlets of quartz. Samples KB7, KB8

and KB9 were taken from dark grey amygdaloidal basalt in which the pillow lavas occur.

The Luswa River Volcanics occur in a narrow unit, about 50-100 m thick, running parallel to a dominant quartzite ridge of the Manshya River Group (Figure 2-12). The volcanics are very siliceous, greyish-green rocks, in which a primary fabric can be observed as alternating coarse and fine-grained layers. Feldspar phenocrysts can be observed in the coarser layers. Only two samples were analysed (see Table 14-5 and Table 14-18), and were collected from a fine-grained layer (sample LW12) and a coarse grained porphyritic layer (sample LW13) of the rhyolitic tuff.

The Ilondola Volcanics occur a few kilometers west of Ilondola Mission (Figure 2-43), where strongly altered, reddish brown siltstones contain alternating layers of light grey coarse and reddish fine-grained volcanic material. The rock is strongly deformed, and occurs parallel to quartzite ridges ascribed to the Manshya River Group. The thickness of the volcanic unit is estimated at no more than 20 meters. Three samples (IL2, 3 and 4) were collected from the volcanic layer along strike from each other (Figure 2-43 and Table 14-18) from reasonably fresh parts of the rock, but as the entire outcrop is strongly weathered, no major element analysis was conducted.

The Kachinga Tuff is a 300-meter thick unit of light grey rhyolite, which occurs isoclinally folded within the Chimbwe syncline south of Isoka (Figure 2-24). The tuff crops out extensively along a small stream running parallel to the contact with the overlying Kachinga Quartzite, and has been sampled extensively along strike. Nine samples were analysed, taken from all varieties of the Kachinga Tuff (Table 14-6 and Table 14-19). Samples IS3, IS9 and IS10 were collected a few meters above the contact with the underlying Kachinga Pelite, and consist of fine-grained grey metarhyolite. Samples IS19 to IS24 were taken progressively up-sequence from layered units of metavolcanic. Samples IS19 and IS23 consist of a darker grey variety of the Kachinga Tuff, while samples IS20, IS21, IS22 and IS24 were collected from the light grey metarhyolite tuff that dominates the unit.

5.5.1 Major element geochemistry

Normative calculations for the various suites of volcanics in the Irumide belt show a wide variety of compositions, ranging from silica-undersaturated to silica-supersaturated (Table 5-4). The samples from the Katibunga map sheet (samples prefixed KV and KB) are generally silica undersaturated, with the exception of the two samples (KV1 and KB2) collected from rhyolitic schist, which contain over 40% normative quartz. These two samples also show large amounts of normative corundum (10.15 and 12.96%) indicating that they may in part consist of sedimentary material. Their CIA index is very high (77.3 and 80.1%) and equivalent to highly altered granitic samples (Nesbitt and Young, 1982). Samples KV8, KB6, KB7, KB8 and KB9 contain small amounts of normative quartz (up to 10%) and normative hypersthene and can be classified as hypersthene basalts. The remaining samples (KV4, KV5, KV7, KB3 and KB4) generally record no quartz, and variable amounts of normative olivine and hypersthene, and classify as olivine tholeiite. One single sample (sample KB5) contains normative nepheline and olivine placing it in the alkali basalt field. The CIA index for the silica-undersaturated samples ranges from 37.4 to 44.0%, and they represent relatively unaltered samples.

Table 5-4: Modal composition of Group III volcanics in the Irumide belt.

	Normative composition (volume %)								
	KV1	KV4	KV5	KV7	KV8	KB2	KB3	KB4	KB5
Quartz	46.27				0.11	44.64			
Orthoclase	24.66	3.66	3.93	2.82	3.43	29.39	7.34	4.02	3.67
Plagioclase	8.41	51.95	55.73	61.93	56.12	4.22	62.66	62.30	
Nepheline									1.82
Corundum	10.15					12.96			
Hypersthene	8.61	18.30	21.37	15.69	18.67	6.71	4.35	12.19	
Diopside		18.51	14.33	12.56	17.36		17.32	15.81	13.76
Olivine		2.47	1.48	4.73			5.56	3.27	8.84
Magnetite	0.88	2.17	1.59	1.23	1.74	0.74	1.11	0.98	0.87
Ilmenite	0.93	2.56	1.33	0.92	2.15	0.99	1.01	0.80	0.77
Apatite	0.08	0.38	0.24	0.11	0.42	0.36	0.64	0.64	0.86
	KB6	KB7	KB8	KB9	LW12	LW13	IS3	IS9	IS10
Quartz	1.9	10.1	2.57	3.56	46.46	31.57	55.89	51.39	39.28
Orthoclase	0.41	2.29	2.84	6.03	27.21	34.30	15.37	22.17	20.48
Plagioclase	62.05	53.42	65.26	52.33	21.29	27.91	19.86	14.44	29.61
Nepheline									
Corundum					2.09	2.19	3.76	5.08	3.28
Hypersthene	17.26	13.77	18.22	14.99	1.72	2.86	3.42	5.24	5.33
Diopside	14.92	16.26	8.56	17.97					
Olivine									
Magnetite	1.40	1.62	0.91	1.67	0.20	0.32	0.33	0.49	0.50
Ilmenite	1.52	2.04	0.86	3.11	0.46	0.49	0.55	0.68	0.67
Apatite	0.54	0.50	0.78	0.33	0.56	0.37	0.83	0.52	0.84
	IS19	IS20	IS21	IS22	IS23	IS24			
Quartz		45.32	38.62	43.46	36.00	54.43			
Orthoclase	29.44	24.68	16.27	23.61	30.56	13.91			
Plagioclase	55.58	20.06	38.49	28.11	21.08	25.10			
Nepheline									
Corundum	3.79	4.7	2.25	1.56	4.82	2.89			
Hypersthene	7.49	3.73	2.82	1.79	6.02	2.48			
Diopside									
Olivine	1.33								
Magnetite	0.81	0.37	0.32	0.20	0.54	0.26			
Ilmenite	1.15	0.62	0.87	0.38	0.82	0.39			
Anatite	0.41	0.52	0.37	0.89	0.16	0.55			

Samples from the Luswa River Tuff (samples LW12 and LW13) yield modal quartz between 31 and 47% and have normative corundum between 2.1 and 2.2%, making them peraluminous in character. Their CIA index is around 55, comparable to relatively unaltered rocks.

The Kachinga Tuff (samples prefixed IS) is characterised by normative quartz, ranging from 38.6 to 55.9%, and hypersthene ranging from 1.8 to 7.5%. Sample IS19 forms an exception, showing no quartz, but hypersthene and olivine in the norm, and represents the most basic member of the suite. All samples from the Kachinga Tuff have normative corundum (1.6-5.1%) and are peraluminous in character. The CIA index for the Kachinga Tuff samples ranges from 53.9 to 66.0, consistent with relatively low to moderate alteration.

The classification of aphanitic volcanic rocks is achieved based on whole-rock geochemistry, using the diagrams proposed by Cox et al. (1979) and by Streckeisen and Le Maître (1979). The Katibunga Volcanics plot into the basalt field of the TAS diagram (Figure 5-21 (a)), with the exception of KV1 and KB2, which plot into the andesite-dacite fields. These latter samples have high LOI and abnormal Na/K ratios and are therefore suspect. The Luswa River Tuffs plot into the field for rhyolite, because of their high silica content. Sample LW12 plots below and to the right of the proposed volcanic fields, which may indicate limited loss of alkalis during metamorphism. The Kachinga Tuff samples plot in the vicinity of the Luswa River Tuff samples, but also display lower K_2O and Na_2O than expected for typical rhyolites. Sample IS19 has total alkali content greater than 9% and plots into the field of the mugearites. In the $Q' - ANOR$ classification diagram of Streckeisen and Le Maître (1979) (Figure 5-21 (b)), the Katibunga Volcanics dominantly plot as basalt. The two samples of the Luswa River Tuff plot well into the rhyolite field. Samples from the Kachinga Tuff (samples prefixed IS) are predominantly within the rhyolite field, with the exception of IS10 plotting in field of dacites, and IS19 plotting as a trachyte. Note that within each of the suites, the range of normative compositions is relatively restricted, the suite either being dominated by silica oversaturated end members, or by silica-undersaturated end members, with very few intermediate volcanics.

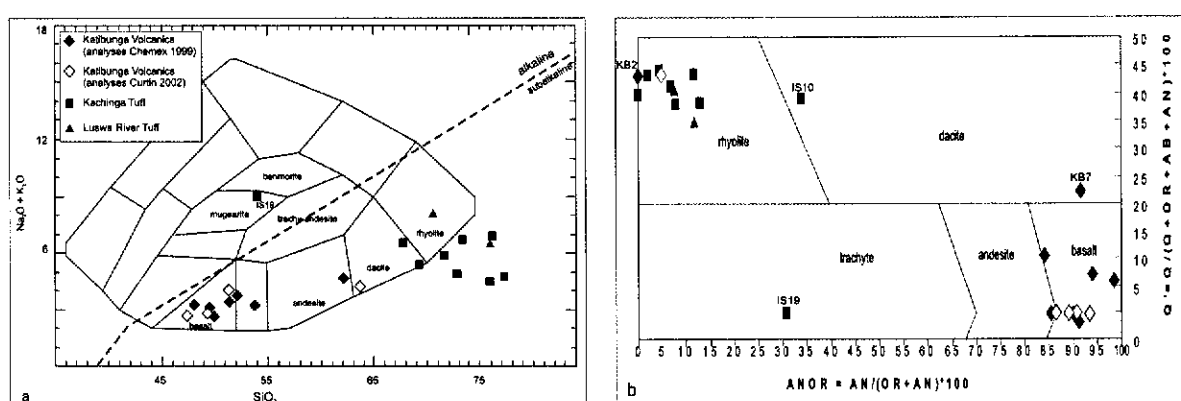


Figure 5-21: (a) Total alkalis versus silica (TAS) diagram of the Irumide volcanics showing the classification fields proposed by Cox et al. (1979); (b) Normative $Q'(F) - ANOR$ diagram after Streckeisen and Le Maître (1979) for the Irumide volcanics.

Using geochemical parameters directly, rather than calculated mesonormative data, a ternary diagram of $Al_2O_3 - FeO_{tot} + TiO_2 - MgO$ was

proposed by Jensen (1976) as a means of classifying basaltic rocks. The diagram is especially well suited to distinguish between calc-alkaline and tholeiitic suites, and works well for high-Mg suites such as komatiites (Figure 5-22 (a)). The Katibunga Volcanics plot in the basaltic fields, and display a wide range of $\text{Al}_2\text{O}_3 / \text{FeO}_{\text{tot}} + \text{TiO}_2$ ratios, spanning the calc-alkaline to tholeiitic basalt fields. This wide range of Al_2O_3 values may indicate varying degrees of alteration within the suite. The silica-saturated members of the Luswa River and Kachinga Tuff plot along the tholeiitic trend line in the field of rhyolites and dacite. The AFM diagram, plotting total alkalis – total iron – MgO, clearly shows the relatively wide scatter of the Katibunga Volcanics, which plot above as well as below the boundary between the tholeiitic and calc-alkaline series. The more evolved acid Luswa and Kachinga Tuffs plot just below the boundary, and are classified as part of the calc-alkaline series of Irvine and Baragar (1971)(Figure 5-22 (b)). Note that there is a distinct lack of intermediate volcanics to allow the determination of a clear trend. The fact that the volcanics are approximately coeval, and have a strongly bimodal character, implies a possible extensional setting.

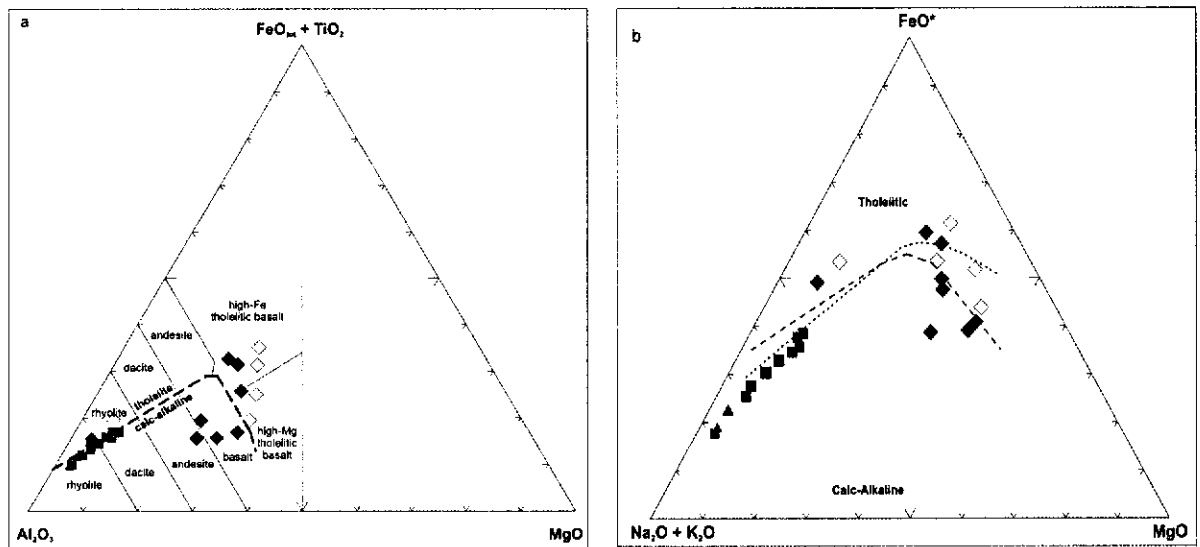


Figure 5-22: (a) Ternary diagram of $\text{Al}_2\text{O}_3 - \text{FeO}_{\text{tot}} + \text{TiO}_2$ and MgO , with classifications fields after Jensen (1976), showing the Irumide volcanics; (b) AFM diagram of the Irumide volcanics showing the boundary between calc-alkaline and tholeiitic series after Kuno (1968)(dotted line) and Irvine and Baragar (1971)(dashed line)(symbols as in Figure 5-21)

In the binary plot proposed by Maniar and Picolli (1989), the Katibunga Volcanics show a high molar proportion of CaO , and plot with metaluminous characteristics (Figure 5-23 (a)). The acid end members of the Irumide volcanics,

the Kachinga and Luswa Tuffs, plot within the peraluminous field. In the binary diagram of K_2O versus Na_2O , the distinction between the Katibunga basalts and the Luswa and Kachinga rhyolitic lavas is pronounced, with the basalts showing low K/Na ratios, and the rhyolitic tuffs predominantly displaying a high K_2O content (Figure 5-23 (b)). The wide scatter of the data points alludes to the possibility of alkali mobility in the volcanics during metamorphism, especially in the isoclinally folded Kachinga Tuff.

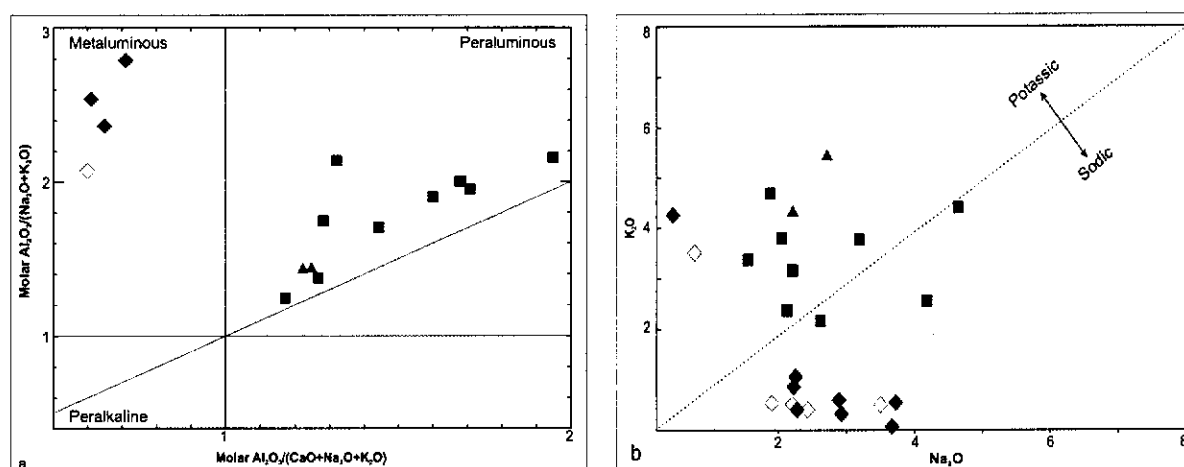


Figure 5-23: (a) Diagram after Maniar and Picolli (1989), characterising the acid end-members of the Irumide volcanics as peraluminous, and the basic members as metaluminous; (b) binary diagram plotting the K_2O content versus Na_2O for the Irumide volcanics, clearly distinguishing the Katibunga basalts as sodic, and the Luswa River and Kachinga Tuff as predominantly potassic (symbols as in Figure 5-21).

5.5.2 Trace elements

The interpretation of volcanic rocks using discrimination diagrams is generally restricted to the least-evolved members of a volcanic suite, i.e. basalts, to avoid the possible geochemical trends imposed by processes of fractionation. Nevertheless, intermediate and acid lavas can be plotted on most diagrams that use only immobile elements, provided they do not include cumulate rocks or sediments. Sedimentary components in metavolcanic rocks can generally be identified from field observations combined with high aluminium and potassium contents. Large CIA values are indicative of high weathering, and, in combination with other factors, may help identify samples of sedimentary character (which are enriched in aluminium). Although none of these criteria constitute proof of the

sedimentary character of a rock, these characteristics are used as indicators, and the samples flagged to be of potential sedimentary character. The three samples of the Ilondola Volcanics (IL2, 3 and 4) are excluded from all but the SPIDER and REE plots, as they represent a mixture of sedimentary and volcanic rock. Samples KV1 and KB2 of the Katibunga Volcanics are characterised by suspiciously high K_2O and CIA values, and are considered unsuitable to be included in the interpretations. Cumulates are readily identified through screening of the geochemical data for abnormally high contents of key immobile elements commonly concentrated in cumulate minerals. The element thresholds used include $Al > 20\text{wt}\%$ (feldspar cumulate), $Sc > 50\text{ ppm}$ (clinopyroxene cumulate), $Ni > 200\text{ ppm}$ (olivine cumulate) (Pearce, 1996b). None of the thresholds are reached, leading to the interpretation that none of the sampled lavas represent cumulates.

In a diagram plotting the ratio Zr/Ti versus Nb/Y , proposed by Winchester and Floyd (1977) and improved by Pearce (1996b), the Katibunga basalts plot in the basalt field, while the more evolved Luswa River and Kachinga Tuff plot towards progressively more alkaline compositions (Figure 5-24 (a)). Although this classification contrasts with the classification of these rocks as rhyolite dacite based on major element geochemistry, this diagram is here used as a filter for selection of permissible evolved rocks to be plotted in the ternary diagrams (Th-Hf-Ta) proposed by Wood (1980) for the discrimination of magma types (cf. Pearce, 1996b). The reason why misclassification can occur is linked to the formation of Zr-Hf bearing phases such as zircon in later stages of the evolution of magma. According to Pearce (1996b), rocks plotting below the basalt – andesite – basaltic andesite line on the Zr/Ti vs. Nb/Y diagram are unlikely to be misclassified on the ternary diagram of Wood (1980). All the Irumide volcanics plot below the threshold line, and are thus interpreted to be suitable for classification on the Th-Hf-Ta ternary diagram.

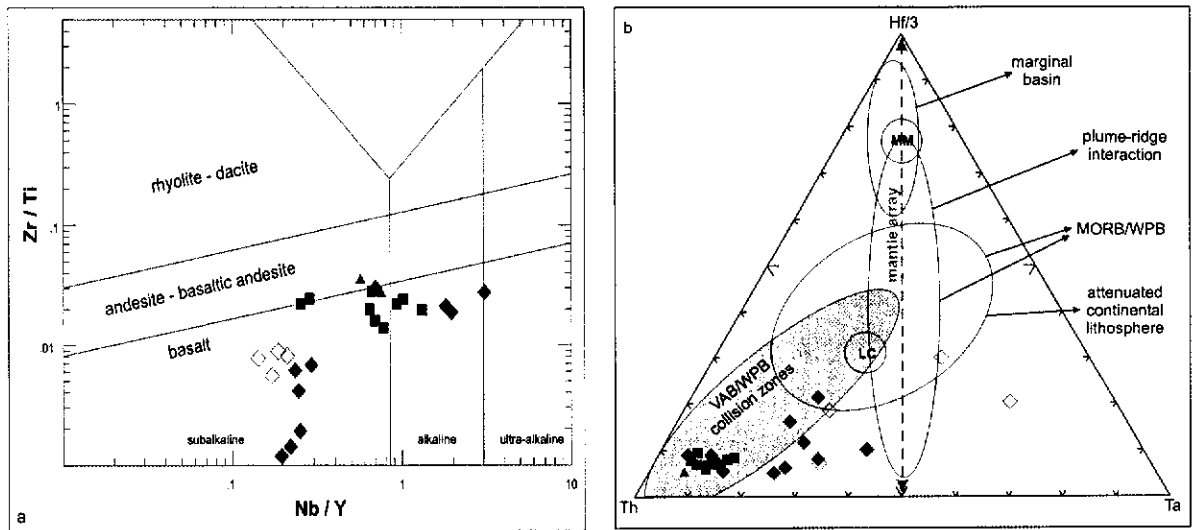


Figure 5-24: (a) Zr/Ti vs. Nb/Y diagram after Winchester and Floyd (1977), with revised fields after Pearce (1996b) showing the Irumide volcanics; (b) Ternary diagram of Th-Hf/3-Ta after Wood (1980) (VAB=Volcanic Arc Basalt; WPB=Within Plate Basalt; MM=MORB Mantle source, LC=Lower Crust; symbols as in Figure 5-21).

The ternary diagram proposed by Wood (1980) involves the three immobile elements Th – Hf – Ta and allows discrimination of volcanic arc magma types from other types, especially MORB. The diagram uses the characteristic that volcanic arc magma types show enrichment in Th, unaccompanied by enrichments in Zr-Hf and Nb-Ta (as in within plate basalts) or enrichment of Nb-Ta (as in alkalic MORB). Increase in Th relative to Hf and Ta pushes the Irumide volcanics towards the Th apex of the diagram, strongly suggesting volcanic arc or within-plate affinities (Figure 5-24 (b)). Many of the Katibunga Volcanics however plot further towards the Ta end of the spectrum, which may suggest either contamination of Ta due to grinding in the tungsten carbide mill, or a genuine, more within plate character.

Another diagram proposed by Pearce (1983) uses the relationship between the immobile elements Th – Ta – Yb to discriminate between active margin, within plate, MORB and ocean island arc magma types (Figure 5-25 (a)). In this diagram, the tantalum enrichment of the Katibunga Volcanics also shifts the data away from the active continental margin into the enriched mantle and intra-plate fields.

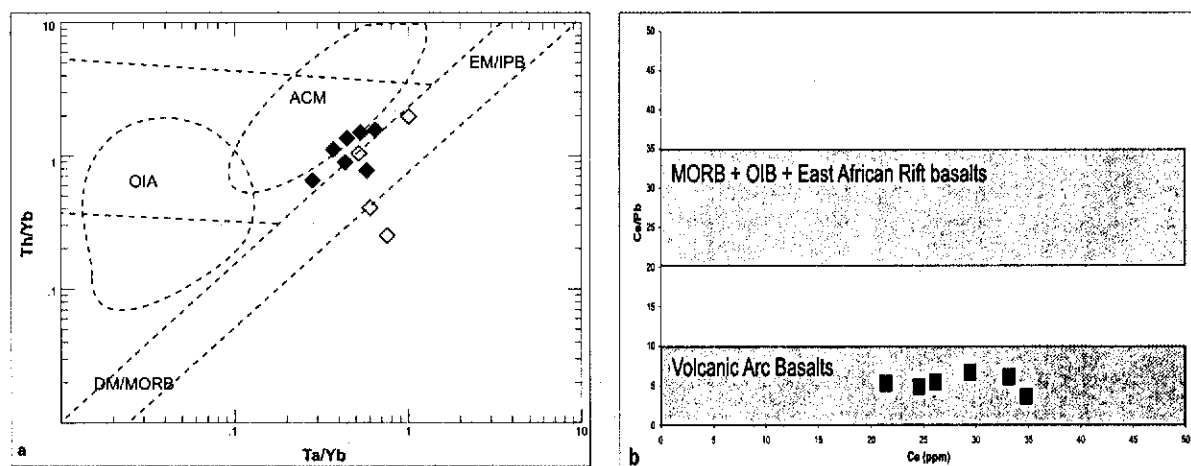


Figure 5-25: (a) Binary plot of Th/Yb vs. Ta/Yb after Pearce (1983), showing proposed fields for ocean island arc (OIA), active continental margin (ACM), enriched mantle (EM), intraplate basalt (IPB), depleted mantle (DM) and mid-ocean ridge basalts (MORB); (b) Binary plot of Ce/Pb vs. Ce showing the fields of volcanic arc basalt and MORB + ocean island basalt + east African rift basalt (fields after Hoffman (1986) and Kampunzu and Mohr (1991)).

In an attempt to further investigate the possible volcanic arc setting for the Katibunga Volcanics, the Ce/Pb ratio is used. It is reported that Ce and Nb are less mobile than Ba and Pb during dehydration processes active in subducting crust, and as such the Ce/Pb ratio can discriminate a subduction setting from a rift setting (Hawkesworth et al., 1997; Sun et al., 2003). Typical Ce/Pb values of ~25 are reported for the East African Rift system, MORB and ocean island basalts (Kampunzu and Mohr, 1991). The Ce/Pb ratios for the Katibunga basalts range from 3.6 to 7.7 and seem to indicate a subduction setting (Figure 5-25 (b)). Again, it must be noted that care must be taken to keep in mind the possible mobility of Ce and Pb during metamorphic or metasomatic processes.

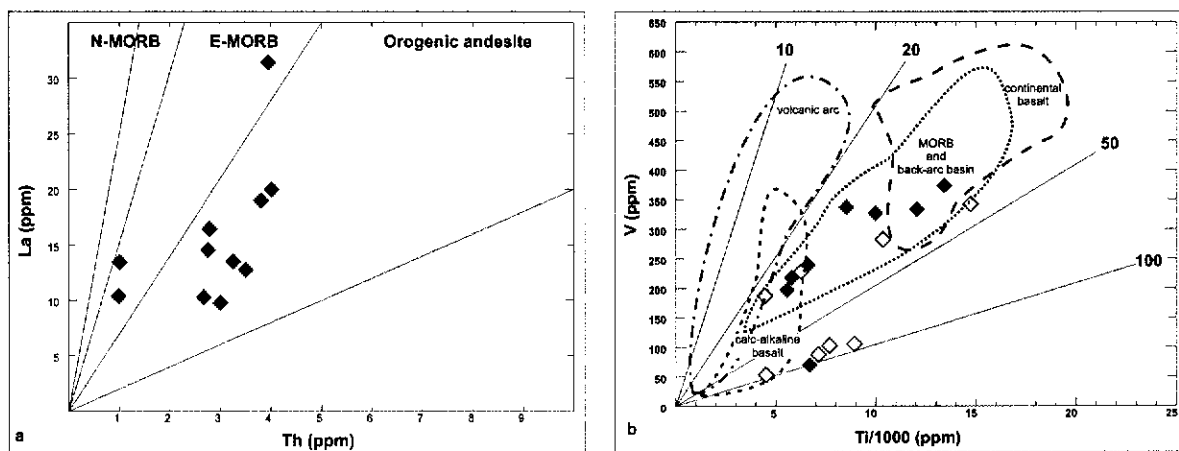


Figure 5-26: (a) Binary diagram of La vs. Th after Gill (1981), classifying the Katibunga Volcanics as predominantly orogenic andesites; (b) Binary diagram of V vs. Ti/1000 after Shervais (1982) demonstrating relatively high Ti/V ratios for the Katibunga Volcanics.

The Katibunga Volcanics display relatively high ratios of Th/La between 0.07 and 0.30, which are commonly associated with arc magmatic rocks. A binary diagram proposed by Gill (1981) indeed plots the Katibunga basalts predominantly in the orogenic andesite field (Figure 5-26 (a)). However, the wide range of Ti/V ratios exhibited by the Katibunga volcanics, with V ranging from 37 to 432 ppm and Ti ranging from 3450 to 20714 ppm, does not allow such clear distinction. In a diagram proposed by Shervais (1982) (Figure 5-26 (b)), the points plot across a wide variety of fields including volcanic arc, calc-alkaline, MORB and back-arc basin.

Chondrite-normalised rare earth element plots for the various volcanics of the Muva Supergroup reveal broadly similar patterns for all silica-saturated volcanics, but are quite distinct for the more mafic Katibunga Volcanics which have overall lower REE content (Figure 5-27, Figure 5-28, Figure 5-29 and Figure 5-30). The rhyolitic tuffs are characterised by relatively steep LREE, and flat HREE trends, with total fractionation values f_{REE} ranging from 5.25 to 29.30. The Ilondola Volcanics show the largest fractionation ranging from 19.1 to 29.30, while the Kachinga Tuffs display the smallest fractionation ranging from 5.24 to 11.75. The Katibunga Volcanics are marked by low overall fractionation values of 2.29 to 4.53. In all samples, fractionation is most extensive in the LREE, ranging from 1.72 to 2.69 for the Katibunga Volcanics, and between 3.22 and 6.25 for the

Ilondola, Luswa River and Kachinga Tuffs. All patterns show very small negative Eu anomalies, ranging from 0.64 to 1.13. Erratic behaviour of Tb in some samples is ascribed to incomplete digestion of refractory phases, especially garnet, in the sample preparation.

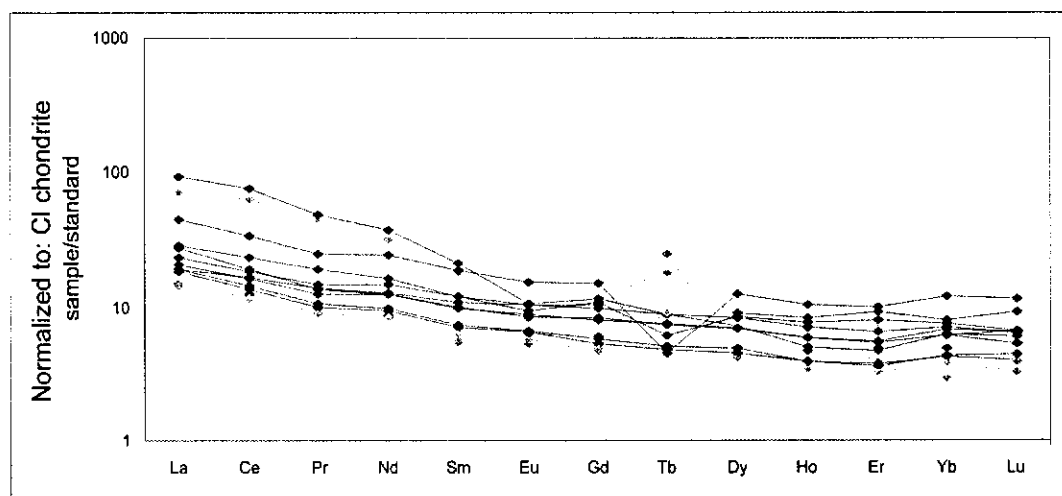


Figure 5-27: Chondrite normalised rare earth element distribution pattern for the Katibunga Volcanics (normalisation values after McDonough and Sun (1995)). Light grey patterns are samples KV1 and KB2, excluded from interpretations.

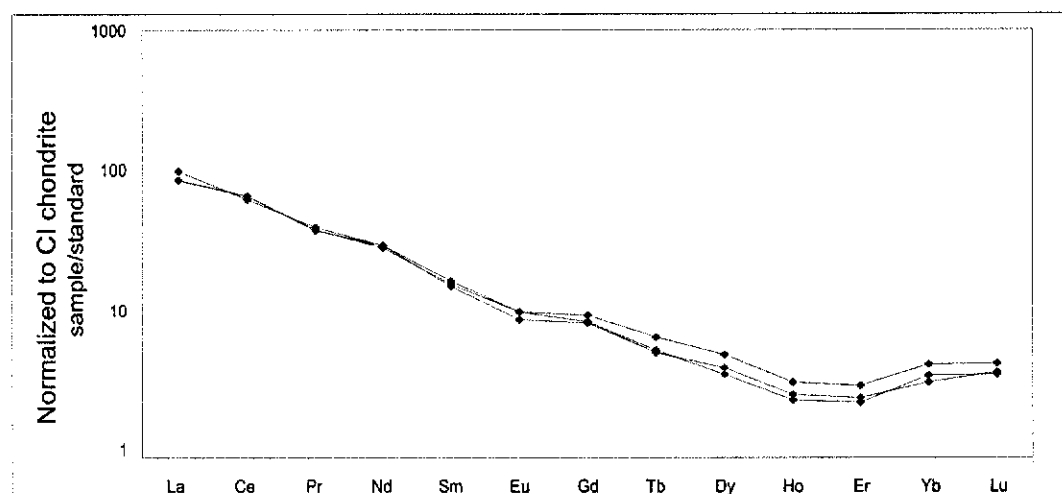


Figure 5-28: Chondrite normalised rare earth element distribution pattern for the Ilondola Volcanics (normalisation values after McDonough and Sun (1995)).

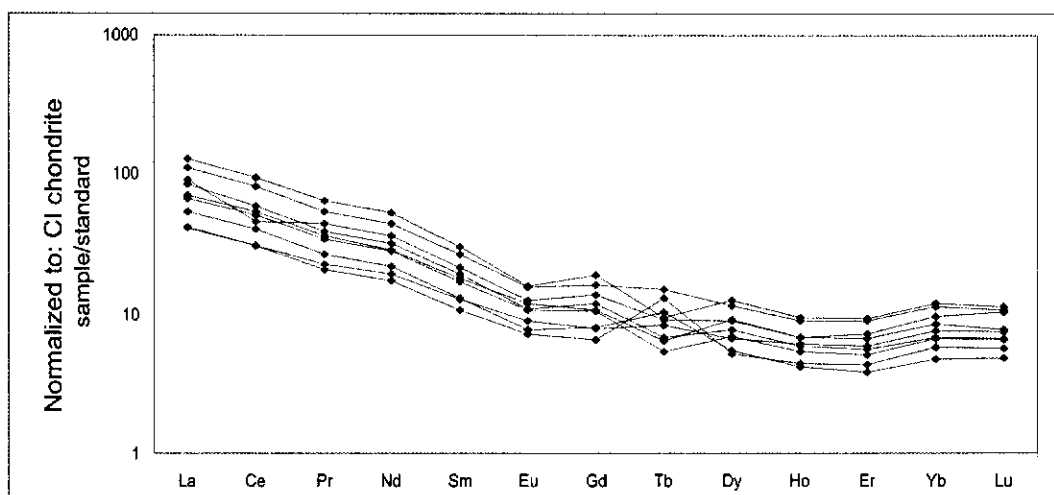


Figure 5-29: Chondrite normalised rare earth element distribution pattern for the Kachinga Tuffs (normalisation values after McDonough and Sun (1995)).

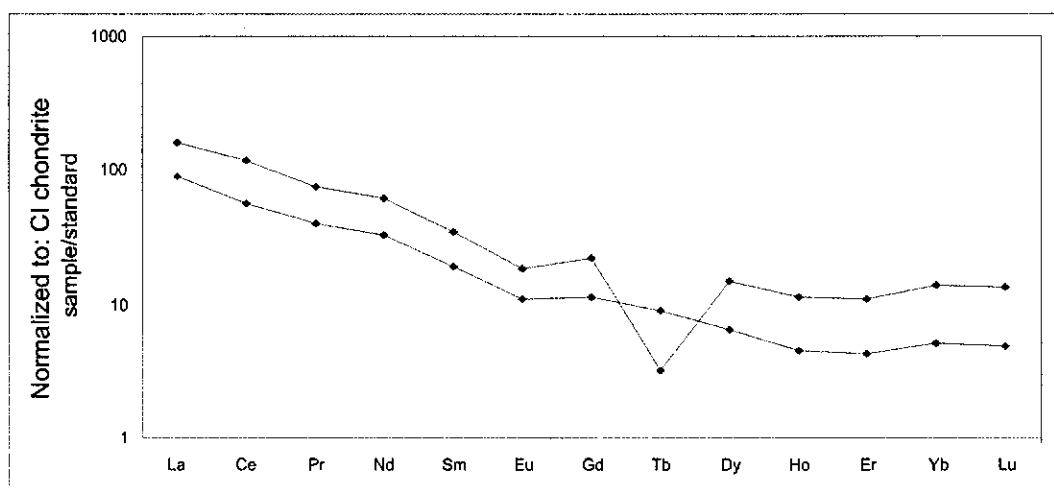


Figure 5-30: Chondrite normalised rare earth element distribution pattern for the Luswa Volcanics (normalisation values after McDonough and Sun (1995)).

An average tholeiitic N-MORB normalised multi-element plot for the Katibunga Volcanics (Figure 5-31), using normalising parameters after Pearce (1996b), shows a pattern consistent with volcanic (continental) arc to within plate basalts, characterised by the negative Nb anomaly (Pearce, 1996b). The low ratio of Ti/Y however is more consistent with a volcanic arc setting than with a within plate setting (Pearce, 1996b). It must be noted, however, that fractional crystallisation can impose negative Ti anomalies (crystallisation of plagioclase, olivine, augite and magnetite), thereby subduing the expected enrichment of Ti over Y typical for within plate basalts (Pearce, 1996b).

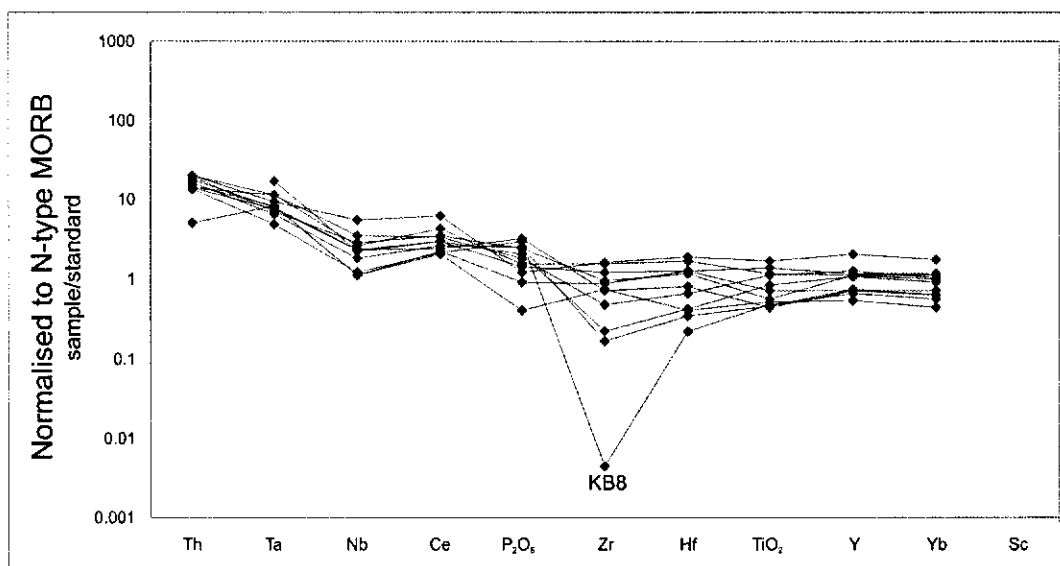


Figure 5-31: MORB normalised rare earth element distribution pattern for the Katibunga Volcanics (normalisation values after Pearce (1996b)).

Primordial mantle normalised multi-element cationic plots for the Irumide volcanics show broadly similar features. All volcanics show pronounced negative Nb and Sr anomalies, moderate negative La and Ce, and pronounced positive Th, Ta and Pb anomalies (Figure 5-32, Figure 5-33, Figure 5-34 and Figure 5-35). The patterns, especially the negative Nb, indicate some crustal involvement in all volcanics (Pearce, 1996b).

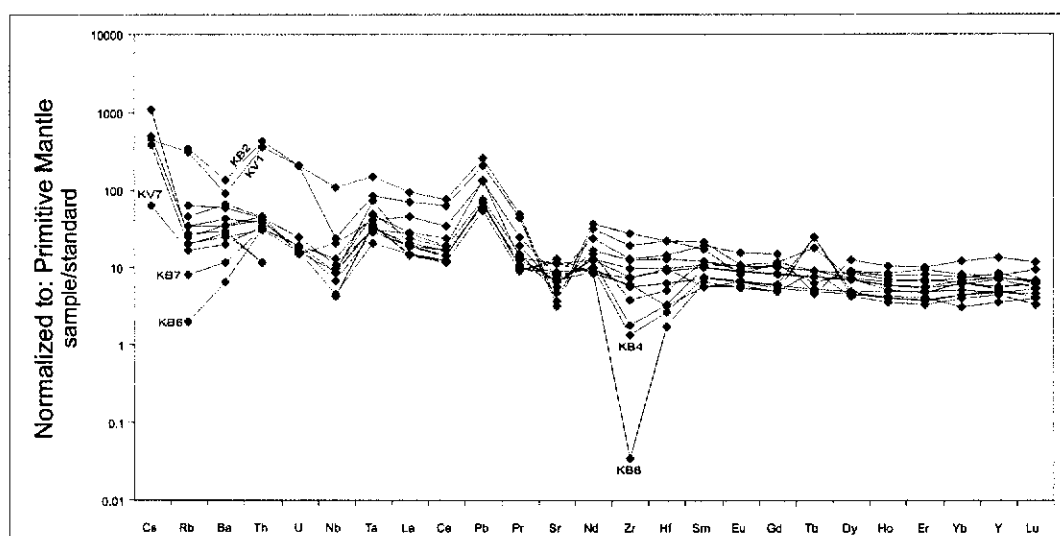


Figure 5-32: Primordial mantle normalised multi-element cationic plot for the Katibunga Volcanics (normalisation values after Sun and McDonough (1989)).

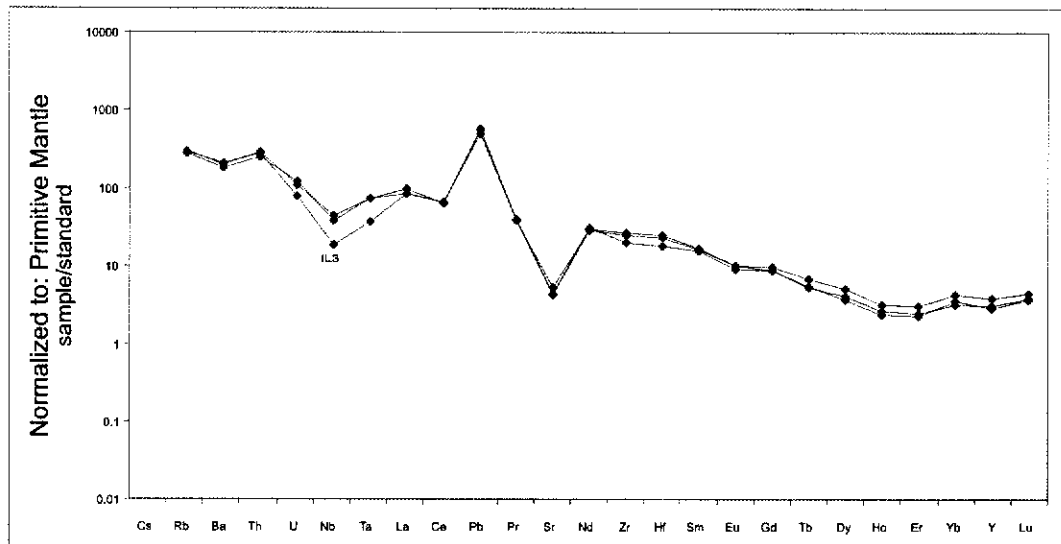


Figure 5-33: Primordial mantle normalised multi-element cationic plot for the Ilondola Volcanics (normalisation values after Sun and McDonough (1989)).

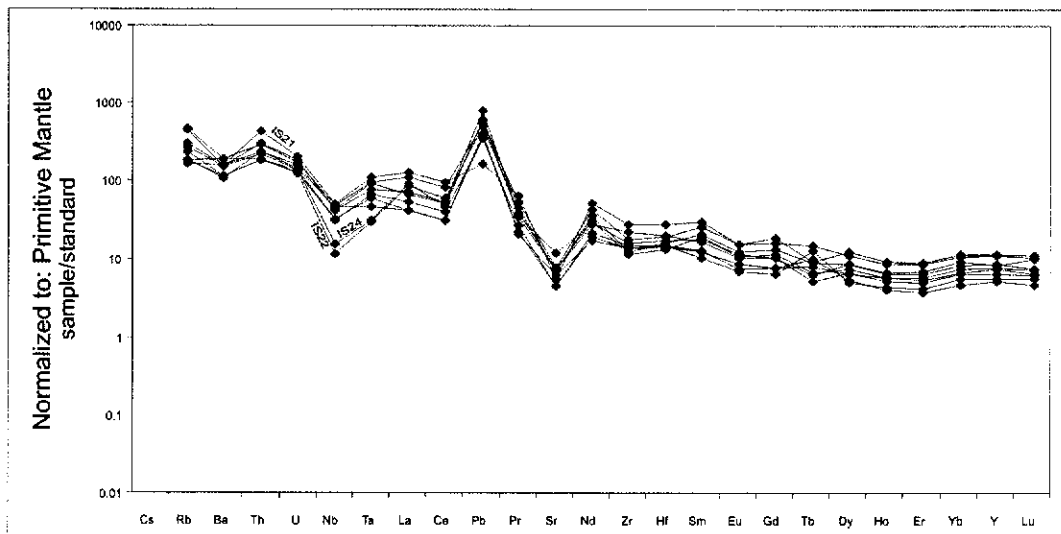


Figure 5-34: Primordial mantle normalised multi-element cationic plot for the Kachinga Tuff (normalisation values after Sun and McDonough (1989)).

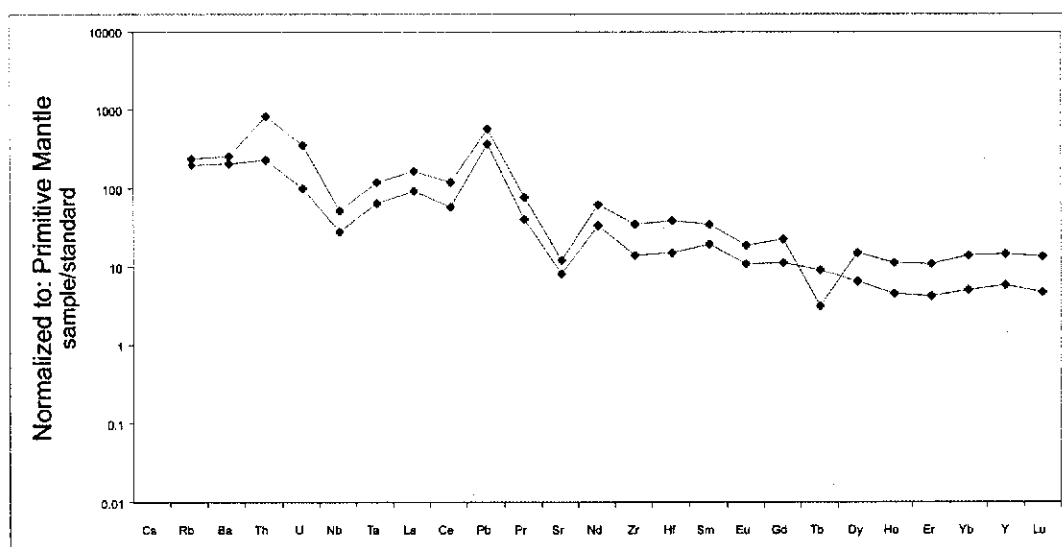


Figure 5-35: Primordial mantle normalised multi-element cationic plot for the Luswa River Volcanics (normalisation values after Sun and McDonough (1989)).

5.5.3 Geotectonic interpretation

Based on the general geochemical characteristics displayed by both acid and basic members of the volcanics in the Irumide belt, and the broadly coeval extrusion ages reported in Chapter 4, the volcanics are interpreted as part of a single volcanic suite. The volcanics are subalkaline in character and show a calc-alkaline trend on the AFM diagram. The Katibunga basalts are metaluminous, while the more evolved acid volcanics have peraluminous compositions. With differentiation, the potassium content rises, and the evolved end member volcanics are potassic in nature, while the more primitive Katibunga basalts are sodic. The absolute trace element abundances are, as one would expect, only ten times that of MORB for the Katibunga Volcanics, but rise up to 100 times that for the acid end members. Relative abundances are, however, strikingly similar between the Katibunga Volcanics and the Ilondola, Luswa and Kachinga suites. REE patterns show moderately fractionated LREE trends, and near-flat HREE trends. Relative enrichment is observed for Y, Ti, Th, Ta and Pb, with depletion for Zr, Nb, Ba and Sr, indicative of crustal involvement. Th-Hf-Ta contents of all volcanics are typical for volcanic arc and within plate settings, with significant enrichment in Th, and low Hf and Ta values. The ratios Th/Yb and Ta/Yb place the Katibunga Volcanics in fields associated with active continental margins or intra-plate settings. Low Ce/Pb ratios for the Katibunga Volcanics allude to processes of Pb enrichment and Ce depletion commonly associated with dehydration processes of subducting crustal slabs at convergent marginal settings, which is one interpretation for the geotectonic setting ascribed to the Irumide volcanics, while an intraplate or continental setting would form an alternative model.

5.6 *Palaeo-Mesoproterozoic (Group IV) granitoids*

Thirteen samples were collected for geochemistry from granitoids and gneisses ascribed to the Group IV suite of intrusions (Table 14-7, Table 14-8 (major elements) and Table 14-20, Table 14-21 (trace elements)). Eleven were collected from the Lukamfwa Hill Granite Gneisses in the southwestern part of the Irumide belt (Figure 2-10), while one sample each was collected from the Musalango Gneiss (sample LW10) and the Lubu Granite Gneiss (sample ML2)(Figure 2-12).

Samples SI/98/2A, SI/98/2B, SI/98/10, SER6-2c, SER6-2 and SR7 were taken from the type locality of the Lukamfwa Hill Granite Gneisses on Lukamfwa Hill, 20 kilometers southeast of Serenje (Figure 2-10). At Lukamfwa Hill, the granite gneiss comprises medium-grained varieties (samples SI/98/2A, SI/98/10 and SER6-2) and coarse-grained porphyritic varieties (samples SI/98/2B, SER6-2c and SR7).

Samples SI/98/3, SER6-3 and SR6 were collected from a low-lying flat outcrop of the Lukamfwa Hill Granite Gneiss, some three kilometers to the east-southeast of Lukamfwa Hill, where it occurs as medium-grained biotite granite gneiss. Sample SR12 was obtained from a small outcrop of biotite granite gneiss thirty-five kilometers west of the Lukamfwa Hill locality.

Sample ND2 was collected from a disused quarry along the Great North Road, where biotite granite gneiss is exposed. The quarry is situated in the Ndabala map sheet, some 50 kilometers west of Lukamfwa Hill. At this location, the strongly foliated biotite granite shows small, discrete shear zones and is intruded by undeformed aplitic dykes and pegmatites.

In the northeastern part of the Irumide belt, sample LW10 was collected from the main outcrop of the Musalango Gneiss in the Luswa River map sheet, where the gneiss occurs in rugged terrain beneath quartzites mapped as part of the Manshya River Group. The rock consists of medium-grained dark grey biotite

gneiss, which is intruded by numerous undeformed amphibolite dykes. Although not studied during the fieldwork, its southern contact consists of a fault zone, along which a thick amphibolite unit occurs. This association of the gneiss with mafic bodies prompted Daly (1986b) to interpret the suite as bimodal, indicative of a rifting event postulated at ca. 1.4 Ga. Dating conducted as part of this study (see Chapter 4) has shown the age of the Musalango Gneiss to be ~1.61 Ga.

The Lubu Granite Gneiss, considered by Daly as part of the Palaeoproterozoic basement to the northeastern Irumide belt (Daly, 1986), was sampled from one locality in the north of the Chinsali map sheet (sample ML2). The gneiss yielded a poorly constrained age of ca. 1.55 Ga (see Chapter 4), and is therefore broadly coeval with the Musalango Gneiss. The Lubu Granite Gneiss is medium-grained pink biotite granite gneiss. At the sampling locality, the granite is intruded by two generations of pegmatite. The older pegmatites are small (cm-scale) and tightly folded, and are cut at a high angle by a younger, undeformed set of pegmatites. Sampling was conducted away from the pegmatites.

5.6.1 Major element geochemistry

Group IV granitoids are silica-oversaturated, with modal quartz ranging from 20.52 to 45.52% (Table 5-5). Most are peraluminous, with modal corundum between 0.04 and 1.95%, but samples SR7 and ND2 have normative diopside and classify as silica-saturated, subaluminous and subalkaline granitoids.

Table 5-5: Modal composition of Group IV granitoids in the Irumide belt.

	Normative composition (Volume %)						
	SI/98/2A	SI/98/2B	SI/98/10	SI/98/3	SR7	SR6	SR12
Quartz	32.07	27.01	32.22	37.71	20.52	38.22	41.89
Orthoclase	30.29	31.89	35.05	34.46	40.04	30.33	32.25
Plagioclase	33.94	37.33	28.23	25.19	31.67	27.59	22.1
Corundum	0.83	0.81	0.15	0.84		1.08	1.35
Diopside					5.67		
Hypersthene	2.23	2.27	3.29	1.41	0.91	20.7	1.73
Magnetite	0.22	0.23	0.36	0.16	0.46	0.3	0.22
Ilmenite	0.29	0.32	0.55	0.22	0.56	0.32	0.34
Apatite	0.14	0.14	0.16		0.16	0.1	0.12

	SER-6-2C	SER 6-2	SER 6-3	ND2	LW10	ML2
Quartz	29.9	30.96	31.24	30.33	31.21	45.72
Orthoclase	37.52	34.41	34.33	29.62	41.47	26.09
Plagioclase	27.39	30.13	30.85	36.44	20.93	25.33
Corundum	1.06	0.06	0.04		1.95	1.12
Diopside				0.39		
Hypersthene	3.13	3.52	2.88	2.42	2.71	1.29
Magnetite	0.46	0.43	0.33	0.31	0.32	0.16
Ilmenite	0.45	0.4	0.31	0.32	0.65	0.28
Apatite	0.1	0.1	0.02	0.7	0.78	

The analysed samples yielded CIA values ranging from 44.5 to 54.1, and low LOI less than 0.72%, and they therefore represent relatively unaltered rocks. On the QAP plot of Le Maître (1989), the granitoids all plot in the field for monzo-granites, with the exception of sample SR7 which classifies as a quartz-syenite. The low normative quartz in this sample is inconsistent with field observations showing abundant quartz. The possibility is therefore raised that this particular sample may have been inadequately dissolved after fusion, making its major element analysis suspect. Rather than deleting it from the database, the sample is plotted along with the others, but identified in the diagrams.

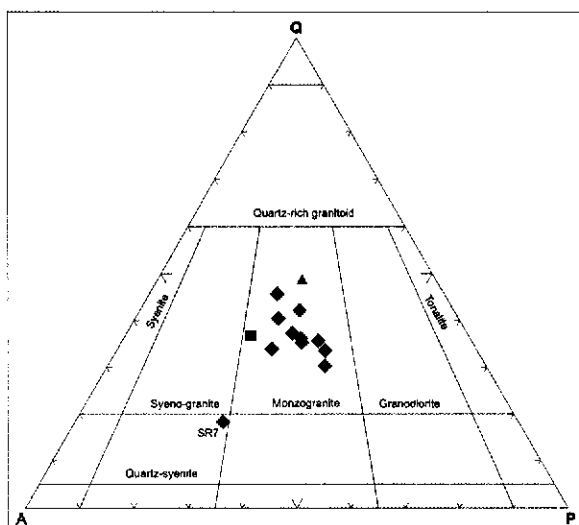


Figure 5-36: QAP diagram indicating a monzo-granitic composition for the Lukamfwa Hill Gneisses (diamond), the Lubu Granite Gneiss (square) and the Musalango Gneiss (triangle).

Group IV granitoids show ASI values ranging from 0.80 to 1.18. The lowest ASI value was recorded in sample SR7, and if this sample is excluded, the ASI ranges from 0.95 to 1.18. The samples are thus peraluminous, with only two samples plotting in the metaluminous field (samples SER6-2c and ND2)(Figure 5-37 (a)). On the binary plot of Na_2O vs. K_2O , the granitoids show a distinctly potassic character, and $\text{K}_2\text{O} / \text{Na}_2\text{O}$ ratios are between 1.33 and 3.00 (Figure 5-37 (b)), although this is not necessarily a primary signature.

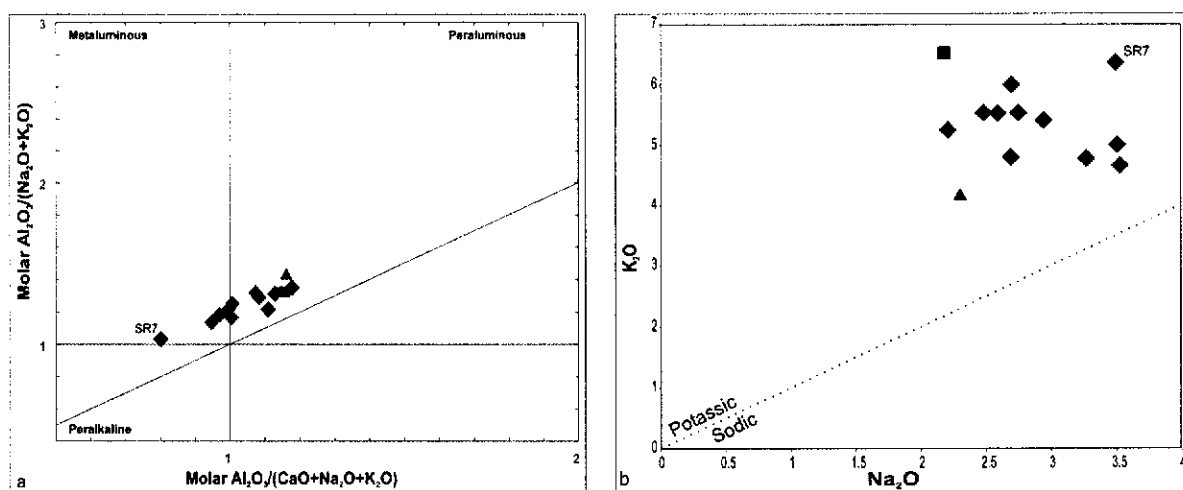


Figure 5-37: (a) Diagram after Maniar and Piccoli (1989), characterising Group IV Granitoids as peraluminous to metaluminous; (b) binary diagram plotting the K_2O content versus Na_2O content for Group IV granite gneisses, showing the potassic character of the suite. Symbols as in Figure 5-36.

On the ASI versus SiO₂ diagram of Clarke (1992), Group IV granitoids plot over a wide range of compositions (Figure 5-38 (a)). Most Lukamfwa Granitoid Gneisses display ASI values below 1.10, suggesting I-type character, but samples SR6, SR12 and SI/98/3 have ASI values greater than 1.10, characteristic for S-type granitoids. Samples of the Lubu Granite Gneiss (ML2) and the Musalango Gneiss also display high ASI values (1.16), and have S-type characteristics.

Based on major element geochemistry, Batchelor and Bowden (1985) proposed a binary multi-cationic plot to discriminate various types of settings (Figure 5-38 (b)). On this diagram, Group IV granitoids plot across the post- and syn-collisional fields, with sample SR12 plotting at the post-collisional extreme, and sample SR7 at the syn-collisional extreme of the spectrum.

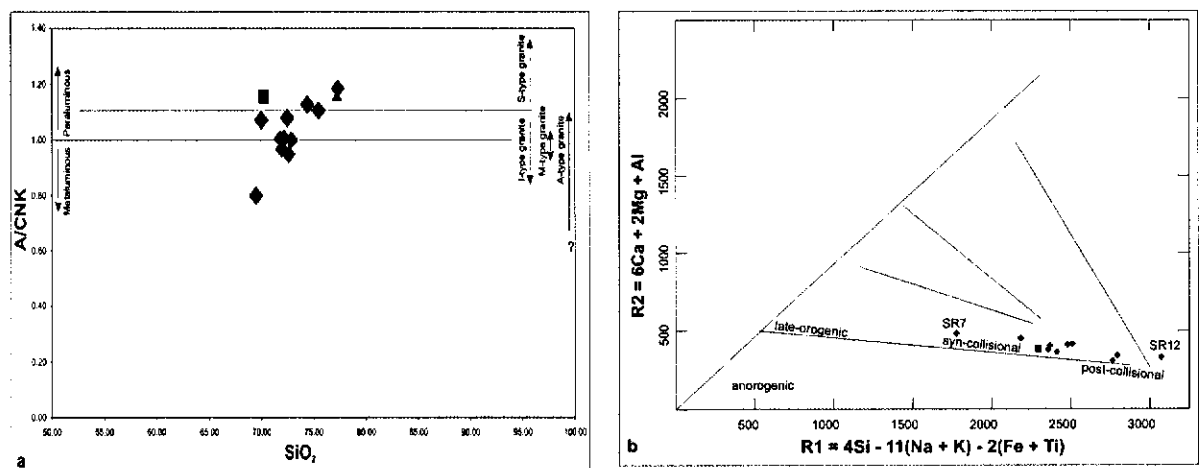


Figure 5-38: (a) Aluminium Saturation Index versus SiO₂ diagram showing Group IV Granite Gneisses to range from A-, I- to S-type granitoids (Clarke, 1992); (b) Plot after Batchelor and Bowden (1985) suggesting syn- to post-collisional setting for Group IV granitoids. Symbols as in Figure 5-36.

5.6.2 Trace element geochemistry

The total REE content of Group IV granitoids is relatively high, ranging between 292 and 1040 ppm. This, coupled with a high ratio of FeO^{*}/MgO (FeO^{*} = total iron as FeO) gives the granitoids a distinct A-type character (Figure 5-39 (a)). Because of the relatively low Nb content of Group IV granitoids relative to true anorogenic granites, the granitoids plot below the line proposed by Eby

(1990), and classify as orogeny-related A-type granitoids (Figure 5-39 (b)). The only exception is the Lubu Granite Gneiss, which plots well into the anorogenic granite field of the plot. A plot of Y/Nb versus Ce/Nb proposed by Eby (1990) also indicates a magma source similar to ocean-island basalt for the Lubu Granite Gneiss, as commonly described for true anorogenic granitoids, and sources similar to average continental crust for the majority of Group IV granitoids, typically reported for I-type granitoids (Figure 5-40).

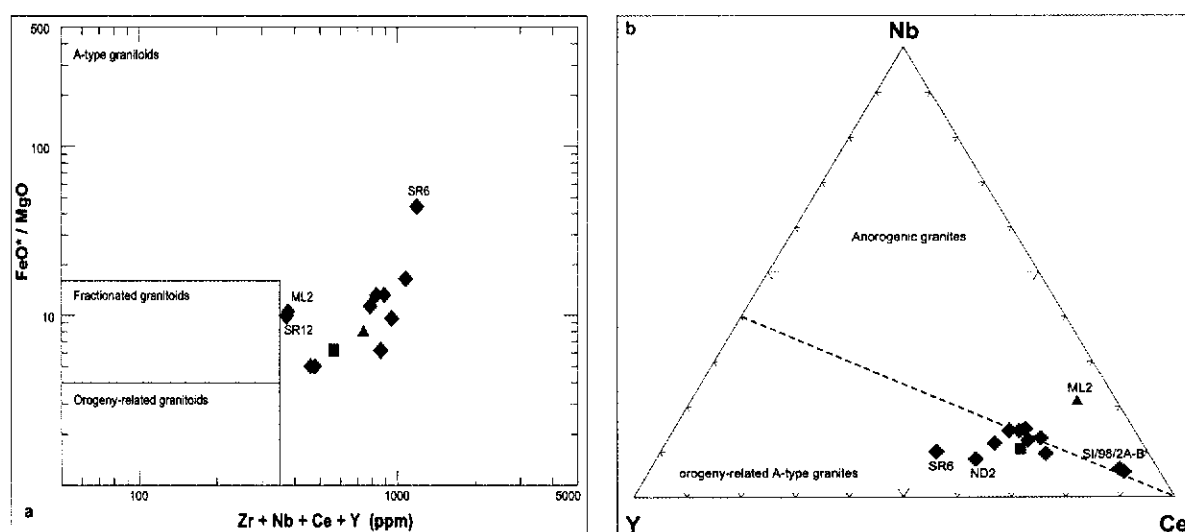


Figure 5-39: (a) binary plot of Zr+Nb+Ce+Y versus FeO*/MgO after Whalen et al. (1987) showing the A-type affinity of Group IV granitoids; (b) Triangular plot of Y-Nb-Ce after Eby (1992), suggesting that the majority of Group IV granite gneisses are orogeny-related A-type granitoids. Sample ML2 (triangle) plots well into the anorogenic granitoid field, having significantly higher Nb content. Symbols as in Figure 5-36.

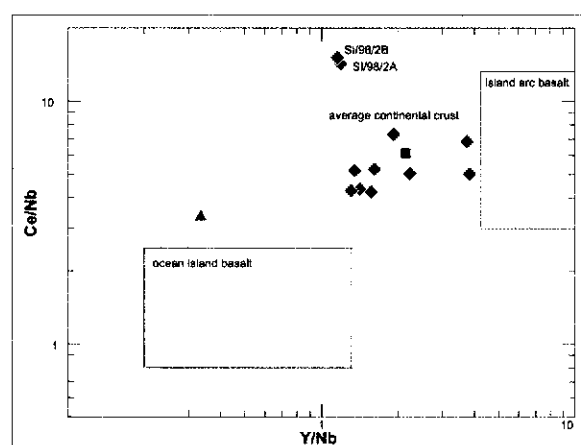


Figure 5-40: Plot of Y/Nb versus Ce/Nb after Eby (1990), suggesting crustal magma sources for Group IV granitoids. Note that the Lubu Granite Gneiss plots closer to an ocean island basalt source commonly associated with anorogenic granitoids. Symbols as in Figure 5-36.

Using the Y-Nb plot of Pearce et al. (1984a), the Lukamfwa Hill Granite Gneiss, Lubu Granite Gneiss and Musalango Gneiss plot in the fields of within-plate granitoids. Samples SI/98/2A-B have low Y and Nb content, and plot in the field for volcanic arc and syn-collisional granite types. On the diagram plotting Y + Nb versus Rb, most granitoids plot in the field of within-plate granitoids, but could also be classified as post-collisional granite types.

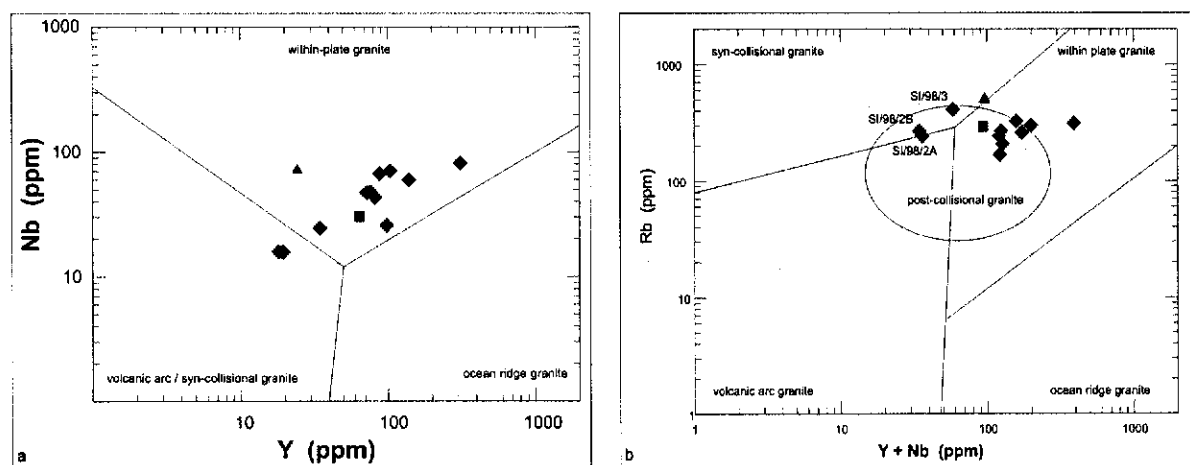


Figure 5-41: Tectonic discrimination diagrams after Pearce (1996a) and Pearce et al. (1984a) suggesting within-plate and post-collisional signatures for Group IV granite gneisses. Symbols as in Figure 5-36.

Chondrite-normalised rare earth element plots for Group IV granitoids show significant enrichment of LREE ($f_{\text{LREE}} = 2.82\text{--}6.98$), a prominent negative Eu anomaly ($0.16\text{--}0.48$) and flat HREE patterns for most samples (Figure 5-42). The Lubu Granite Gneiss (sample ML2) deviates from the pattern of the other Group IV granitoids in that it shows significant HREE depletion. The fractionation ratios f_{LREE} and f_{HREE} for sample ML2 are 4.88 and 7.01 respectively, with a total fractionation ratio f_{REE} of 64.53. Two samples from the earlier analysed batch (samples SI/98/2A and 2B) also show extremely high overall fractionation ratios of 79.82 and 75.29. These samples were taken from the same outcrop and the same rock-type as samples SI/98/10, SER6-2c, SER6-2 and SR7, which show relatively flat HREE trends, and overall fractionation ratios no larger than 18.43. The Lukamfwa Hill, where these samples were taken, locally shows zones of intense shearing, cross-cutting the main fabric of the rock, which may locally have mobilised rare earth elements, resulting in the patterns observed for the samples. It is unclear whether the high fractionation ratios of the two

samples are geologically meaningful or the result of analytical problems, such as incomplete digestion of refractory phases. Samples SI/98/3 and SR6 also stand out from the pattern of the majority of analyses, in that SI/98/3 has an overall lower REE content of 292 ppm, while SR6 displays an overall higher REE content of 1035 ppm. Both samples do show parallel trends with the majority of the other samples and are interpreted to reflect a sampling artefact introduced due to the coarse nature of the Lukamfwa Hill Granite Gneiss.

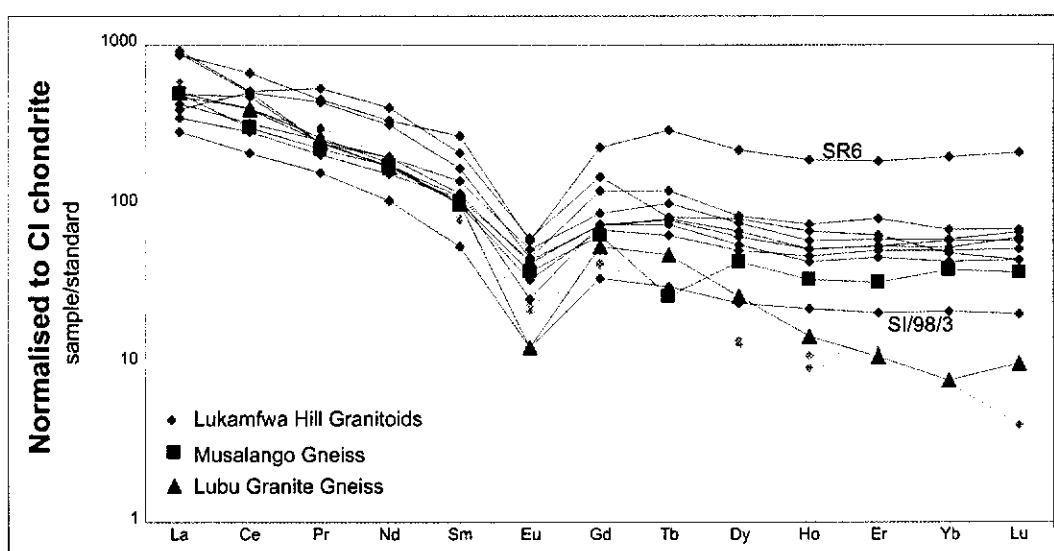


Figure 5-42: Chondrite normalised rare earth element distribution pattern for Group IV granite gneisses (normalisation values after McDonough and Sun (1995)). Light grey samples are samples SI/98/2A and SI/98/2B, which show extremely high fractionation trends.

The multi-cationic plot for Group IV granitoids shows broadly similar patterns for all samples. Negative anomalies are recorded for Ba, Nb, Ce, Sr, Zr, Hf and Eu (Figure 5-43). Samples SI/98/2A, SI/98/2B and ML2 show additional negative anomalies for Yb and Lu. Positive anomalies are observed for Rb, Th, Pb, Nd, Sm and to some extent Gd and Y. All of these features, especially the negative anomalies for Nb-Ta and Zr-Hf, and the positive Pb and Nd, suggest a significant crustal component for the source of these granitoids. This crustal influence is also demonstrated by the A-type character of the granitoids, and the overall high REE content.

A multi-cationic plot, normalised to average ocean ridge granite proposed by Pearce et al. (1984a), shows a fractionation trend and negative anomalies for

Ta-Nb and Zr-Hf commonly associated with volcanic arc, within-plate and syn-collisional settings (Figure 5-44)(Pearce et al., 1984a). According to Pearce et al. (1984a), Zr and Y values, close to the normalising value, and the low normalised Yb values are consistent with a within-plate setting (Pearce et al., 1984a).

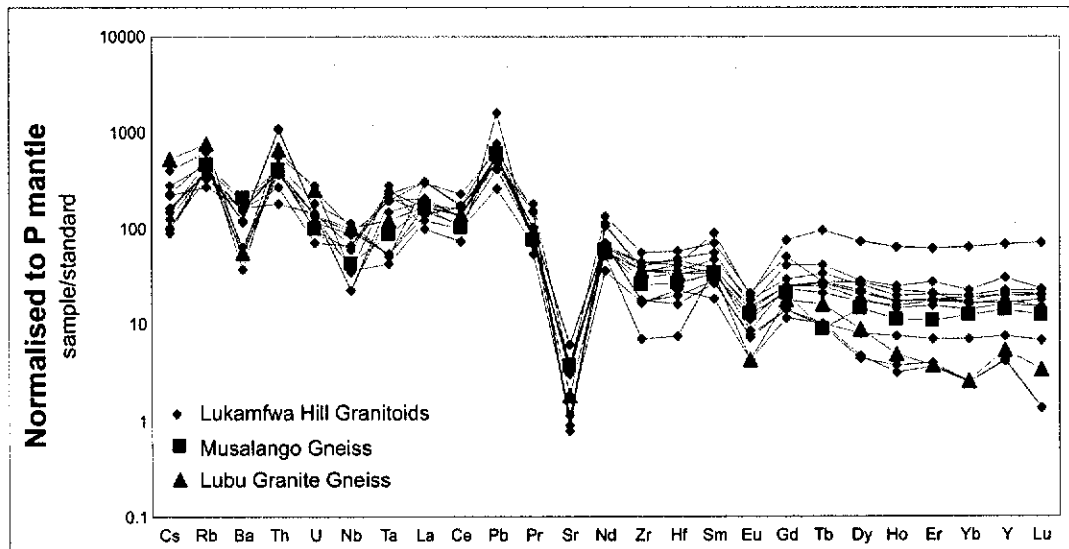


Figure 5-43: Primordial Mantle normalised multi-element cationic distribution diagram (spidergram) for Group IV granite gneisses (normalisation values after Sun and McDonough (1989)).

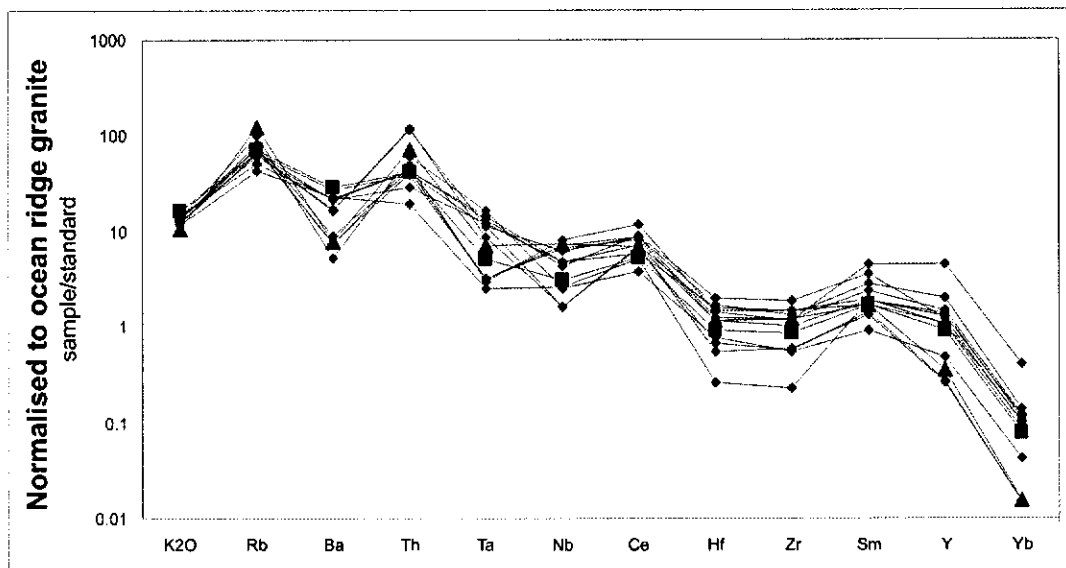


Figure 5-44: Ocean Ridge Granite normalised multi-element plot for Group IV granite gneisses (normalisation values after Pearce et al. (1984)).

5.6.3 Geotectonic interpretation

Group IV granitoids are peraluminous and potassic, and have ASI values ranging from below 0.80 to 1.18 placing them in the S-type to I-type categories. Their major element characteristics classify the granitoids as syn- to post-collisional (Batchelor and Bowden, 1985), while high overall REE contents impart a strong A-type character to the suite (Whalen et al., 1987). The Y-Nb-Ce plot of Eby (1990) characterises the granitoids as orogenic A-type granitoids, with the exception of the Lubu Granite Gneiss, which shows a distinct anorogenic signature. Further discrimination using ratios of Y and Ce over Nb (Eby, 1992) ascribes a magma source similar to average continental crust for the suite, but a source closer to ocean-island basalt for the Lubu Granite Gneiss, a characteristic typical for anorogenic granitoids. The discrimination diagrams of Pearce et al (1984a) and Pearce (1996a) characterise the suite as within-plate to syn-collisional. Moderate enrichment of LREE with respect to chondrite and relatively flat HREE patterns characterise the suite. The Lubu Granite Gneiss, however, shows fractionation of HREE, making it stand apart from the rest of the suite. Relative depletion of Zr-Hf and Nb-Hf, and positive anomalies for Th, Pb, Nd and Y record a strong crustal signature for the suite, which is interpreted to be related to a convergent setting and associated extensive reworking of crustal material.

5.7 *Late-Mesoproterozoic Irumide granitoids*

50 samples were analysed from Group V granitoids, collected from across the entire strike length of the Irumide belt, between Kapiri Mposhi in the southwest and Isoka in the northeast (Table 14-9 to Table 14-14 (major elements) and Table 14-22 to Table 14-27 (trace elements)). Refer to Figure 2-9, Figure 2-10, Figure 2-11, Figure 2-12 and Figure 2-13 for the locations of these samples. The samples are described individually below, from west to east.

Sample KK1 was collected along the road between Kabwe and Kapiri Mposhi from a flat-lying outcrop of coarse porphyritic biotite granite (Figure 2-9).

The granite contains large, angular xenoliths of foliated fine-grained gneiss, but is itself unfoliated. Feldspar phenocrysts are up to several cm in length and define a crude primary magmatic fabric.

Sample MH1 was taken from porphyritic, strongly foliated biotite granite in the south of the Mita Hills map sheet (Figure 2-9). The granite shows a clear steeply-dipping biotite foliation along an east-west direction, which appears to be truncated by late east-northeast trending shear zones, dipping steeply to the south. The granite is intruded by various aplite dykes and pegmatites, which were avoided when taking the sample. Samples MH4 and MH9C were sampled from weakly foliated porphyritic to megacrystic granite in the Mita Hills map sheet (Figure 2-9). These granites are intruded by aplite dykes, and show a prominent primary foliation defined by aligned K-feldspar phenocrysts. Sample MH5 (Figure 2-9) represents a highly sheared porphyritic granite, with a strongly-defined foliation along north-northeasterly trends, dipping steeply to the southeast. The deformation is defined largely by alignment of biotite, but locally the feldspar is stretched into augen.

Samples CC4, CC5 and CC8 were taken from the Chin'gombe Mission map sheet, where foliated, K-feldspar-phyrlic biotite \pm muscovite granites occur (Figure 2-9). These granites are strongly foliated and contain limited amounts of garnet and magnetite. The granitoids are intruded by aplites and contain numerous small pegmatites and late-melt pockets. Locally, strong shearing has transformed the granites into augen gneiss (sample CC8).

Samples MK2 and MK7 were taken from flat outcrops of coarse biotite granite in the Mkushi map sheet (Figure 2-9). In both sampled localities, the granite is coarse-grained, K-feldspar-phyrlic, and contains undeformed pegmatites. A weak foliation along an east-west direction, dipping shallowly to the north, is defined by aligned biotite flakes.

Sample FW1 was collected from unfoliated porphyritic biotite granite in the Fiwila Mission map sheet (Figure 2-9). The granite is intruded by undeformed

aplite dykes, one of which was sampled for geochronological work (sample FW2). The K-feldspar phenocrysts are oriented along a primary magmatic fabric.

Sample ND1 was collected from the Ndabala map sheet, and consists of unfoliated porphyritic biotite granite (Figure 2-9). The granite is associated with coarse monzo-granite (samples ND4 and ND5).

Samples SI/98/11, SI/98/12, SI/98/12b and SR11 were taken from the Sasa Granite in the Serenje map sheet (Figure 2-10). The Sasa Granite is light grey, foliated biotite granite, which crops out in the northwestern part of the Serenje sheet. It forms a dome several tens of kilometers wide, which is surrounded by quartzite hills of the Manshya River Group. Sample SER5-3 was collected to the south of the Sasa Granite, and comprises coarse biotite granite.

Samples SR9 and SQG-2 were collected from an abandoned quarry to the south of Serenje (Figure 2-10) and consist of coarse porphyritic biotite granite. The granite is cut by large, copper-bearing pegmatites and contains dark-grey xenoliths of mafic composition.

Samples SER6-4 and SR5 were taken from a rounded inselberg (Chifuma Hill) in the Serenje sheet, consisting entirely of coarse-grained biotite granite. The granite shows a weak foliation, defined by biotite flakes trending northeast. Samples SI/98/5 and SI/98/6 were taken from a similar hill about 20 kilometers further southeast (Figure 2-10).

KN2A, KN4, KN5, KN7A and KN8 were sampled from various outcrops of porphyritic granitoid in the Kanona map sheet (Figure 2-10). The granitoids are all foliated along northeasterly trends, and contain abundant undeformed K-feldspar phenocrysts defining a crude magmatic foliation. Intrusions of aplite are common, as are small xenoliths of mafic composition, interpreted as partially resorbed mafic dykes. Samples CHT1, CHT2 and CHT6 represent similar granites sampled in the Chitambo Mission sheet (Figure 2-10).

Two samples of the Mununga Granite were taken from a quarry along the main sealed road approximately half-way between Serenje and Mkushi (Figure 2-10) and consist of weakly foliated grey-white biotite-muscovite granite. The granite has a pinkish variety (sample MQG) and a grey-white variety (sample MUN).

Samples CHL2, CHL4 and CHL5 were obtained from coarse biotite granite in the Chilonga Mission map sheet (Figure 2-10 and Figure 2-11). These rocks are biotite \pm muscovite granites, which show a weak to strong northeast-trending biotite foliation. At the location of sample CHL4, discrete shear zones were observed, as were mafic enclaves and small pegmatites. The pegmatites contain quartz and garnet, are unaffected by the foliation, and commonly intrude along the shear zones.

Sample KTB-1 was collected from a flat-lying outcrop consisting of weathered biotite-muscovite granite-gneiss, which contains large rafts of metasedimentary units ascribed to the Manshya River Group (Figure 2-11).

Samples SH8, SH9 and LWC represent parts of the Bemba batholith in the Shiwa N'gandu and Luswa River map sheets (Figure 2-12). The Bemba batholith (Lufila Granite) is unfoliated, reddish, coarse biotite granite, which contains large euhedral K-feldspar phenocrysts that show a clear magmatic foliation. Sample LWC was collected from a dyke-like body of coarse granite intruding the country rock (Manshya River Group), which can be traced back to the main outcrop of the Lufila Granite.

Samples MTG-1, MTG5, LW1 and LW11 were sampled from the Chilubanama Granite in the Luswa River and Chinsali map sheets (Figure 2-12). The Chilubanama Granite, also called the Grey Granite, consists of grey biotite granite, which contains xenoliths of mafic material, and rafts of metasedimentary rock of the Manshya River Group. At the sample locality of MTG1, the granite contains partially resorbed xenoliths with abundant garnet. Zircon analyses of samples of the granite attest to abundant xenocrystic components (samples ZM32 and MTG4), which together with the garnetiferous and metasedimentary xenoliths

are taken to indicate significant crustal assimilation during intrusion. Sample LW2 was obtained from a granodiorite body associated with the Chilubanama Granite in the Luswa River map sheet. The granodiorite is a plagioclase-rich lithology, with minor hornblende.

5.7.1 Major element geochemistry

The majority of Group V granitoids classify as silica-oversaturated, peraluminous, subalkaline rocks, as they contain normative quartz, corundum and hypersthene (Table 5-6). A few granitoids contain normative diopside and hypersthene, and represent subaluminous varieties. The normative quartz content ranges from 14.55% in the most basic member (sample ND5, syeno-granite) to 49.12% in quartz-rich porphyritic granite (sample MH4).

On the QAP diagram of Le Maître (1989), Group V granitoids plot across the fields of monzo-granite and granodiorite (Figure 5-45). Sample LWC plots in the field of tonalite, which is inconsistent with the presence of coarse K-feldspar observed in the field. This may indicate that its geochemical analysis is flawed or that this sample is not representative of the rock as a whole. The most quartz-rich rock (sample MH4) plots in the field of the quartz-rich granitoids, while the most basic members of the suite plot just above the field of the quartz monzonites.

Table 5-6: Modal composition of Group V granitoids in the Irumide belt

	Normative composition (Volume %)									
	SI/98/5	SI/98/6	SI/98/11	SI/98/12	SI/98/12B	MQG1	SQG2	SER5-3	SER6-4	KK1
Quartz	33.28	32.85	31.69	24.54	27.15	29.46	24.10	36.60	26.09	32.00
Orthoclase	34.54	19.52	34.49	14.54	15.47	37.47	25.11	33.69	34.19	31.04
Plagioclase	29.15	37.29	30.64	57.09	53.43	30.84	44.62	25.32	30.08	30.96
Corundum	0.91	1.16	0.04	0.56	0.95			1.96	1.62	1.24
Diopside						0.66	0.23			
Hypersthene	1.71	6.90	2.48	2.72	2.47	1.25	4.59	1.78	5.41	3.48
Magnetite	0.16	0.73	0.31	0.20	0.19	0.18	0.45	0.13	0.60	0.43
Ilmenite	0.23	1.13	0.35	0.28	0.27	0.14	0.66	0.15	1.02	0.57
Apatite	0.02	0.42		0.08	0.08		0.25	0.37	0.99	0.27
	MH1	MH4	MH5	MH8C	CC4	CC5	CC8	MK2	MK7	FW1
Quartz	37.13	49.12	42.74	33.55	41.44	34.70	39.16	42.68	30.60	31.40
Orthoclase	26.58	12.12	24.47	29.07	26.35	22.98	24.15	28.04	32.09	25.08
Plagioclase	32.08	29.96	27.10	31.30	28.33	36.13	32.52	25.76	33.32	35.39
Corundum	1.70	1.73	3.10	2.76	1.47	0.44	1.03	2.06	1.59	1.61
Diopside										
Hypersthene	2.04	5.98	1.98	2.34	1.84	4.23	2.30	1.05	1.79	5.12
Magnetite	0.13	0.42	0.17	0.23	0.19	0.46	0.23	0.08	0.16	0.44
Ilmenite	0.23	0.59	0.29	0.51	0.22	0.77	0.49	0.12	0.29	0.73
Apatite	0.12	0.08	0.16	0.23	0.15	0.29	0.12	0.21	0.15	0.24
	CHT1	CHT2	CHT4	CHT6	ND1	ND4	ND5	KN2A	KN4	KN5
Quartz	34.26	38.38	39.53	38.32	24.34	23.62	14.55	34.12	35.19	32.02
Orthoclase	21.88	22.45	26.25	23.01	46.66	10.45	37.61	30.58	30.66	21.25
Plagioclase	34.19	22.91	31.58	30.54	26.70	46.98	35.86	31.30	29.23	37.87
Corundum		4.95	1.37	1.15	0.37			0.58	2.08	0.52
Diopside	2.43					12.68	3.05			
Hypersthene	4.79	9.58	0.85	5.13	1.40	5.08	7.27	2.38	1.46	6.36
Magnetite	0.68	0.71	0.08	0.60	0.17	0.40	0.56	0.28	0.18	0.61
Ilmenite	1.50	0.76	0.07	0.91	0.23	0.29	0.92	0.52	0.75	1.16
Apatite	0.28	0.27	0.25	0.36	0.13	0.50	0.20	0.23	0.45	0.20
	KN7	KN8	KN8B	SR5	SR9	SR11	MUN	SH8	SH9	LW1
Quartz	41.07	32.15	33.22	38.09	28.04	42.63	38.21	33.04	45.05	35.76
Orthoclase	27.25	32.30	30.45	31.40	26.66	13.70	31.76	33.28	19.97	32.52
Plagioclase	27.40	28.16	30.08	23.22	39.81	40.47	26.21	27.42	29.28	26.58
Corundum	2.18	2.70	1.50	2.37	0.57	0.85	1.37	2.23	1.76	2.44
Diopside										
Hypersthene	1.52	3.54	3.59	3.52	3.65	1.72	1.83	2.04	2.34	1.97
Magnetite	0.15	0.29	0.30	0.40	0.38	0.15	0.24	0.22	0.29	0.21
Ilmenite	0.22	0.56	0.55	0.83	0.70	0.28	0.25	0.30	0.75	0.38
Apatite	0.21	0.29	0.31	0.18	0.20	0.19	0.14	1.46	0.57	0.16
	LW2	LWC	MTG1	MTG5	MGG2	MTGG3	KTB	CHL2	CHL4	CHL5
Quartz	33.22	28.97	29.80	33.10	29.14	30.52	44.71	33.07	39.33	32.23
Orthoclase	24.64	2.64	35.28	29.92	38.52	41.85	27.76	29.67	26.95	21.17
Plagioclase	41.32	64.72	31.98	34.03	29.93	21.45	23.60	32.68	30.43	38.42
Corundum	0.01	2.23	0.40	0.78		1.82	2.60		1.79	0.53
Diopside					0.14			0.68		
Hypersthene	0.33	0.54	1.93	1.66	1.86	3.64	1.00	2.78	1.00	5.24
Magnetite	0.04	0.06	0.19	0.16	0.23	0.25	0.10	0.40	0.09	0.58
Ilmenite	0.02	0.03	0.28	0.17	0.18	0.29	0.13	0.45	0.12	1.44
Apatite	0.42	0.62	0.15	0.17		0.17	0.12	0.27	0.29	0.40

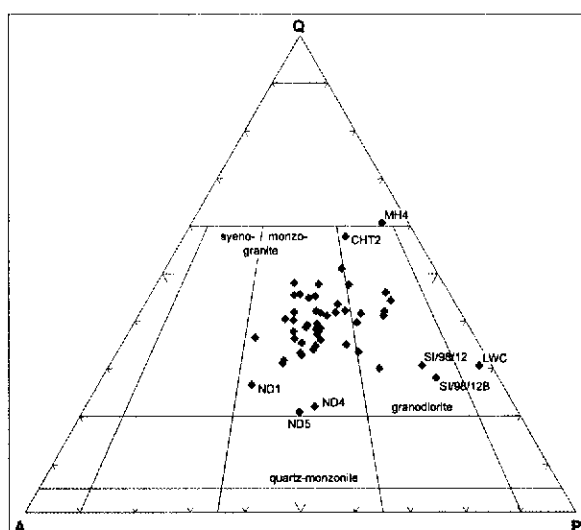


Figure 5-45: QAP diagram for Group V granitoids in the Irumide belt

CIA values range from 38 to 63, with the majority of samples having a CIA index below 50. The LOI values are consistently below 1% confirming that the samples are relatively unaltered. The Aluminium Saturation Index (ASI) for the majority of the samples exceeds 1, and ranges up to 1.73, making Group V suite granitoids predominantly peraluminous in composition. Only six samples have ASI values < 1 , classifying them as metaluminous (Figure 5-46 (a)). Alkali mobility represents a possibility in these rocks.

The granitoids are characterised by potassic compositions, and have K_2O/Na_2O ratios ranging from 0.37 to 2.84. Only six samples display ratios below 1, one of which is sample LWC, which has an anomalously low K_2O/Na_2O ratio of 0.06. Other samples with sodic compositions are the Sasa Granite (samples SI/98/12, SI/98/12B and SR11, $K_2O/Na_2O = 0.45-0.57$), the granodiorite sample of the Luswa River map sheet (sample LW2, $K_2O/Na_2O = 0.83$) and a granodioritic sample from the Ndabala map sheet (sample ND4, $K_2O/Na_2O = 0.37$)(Figure 5-46 (b)).

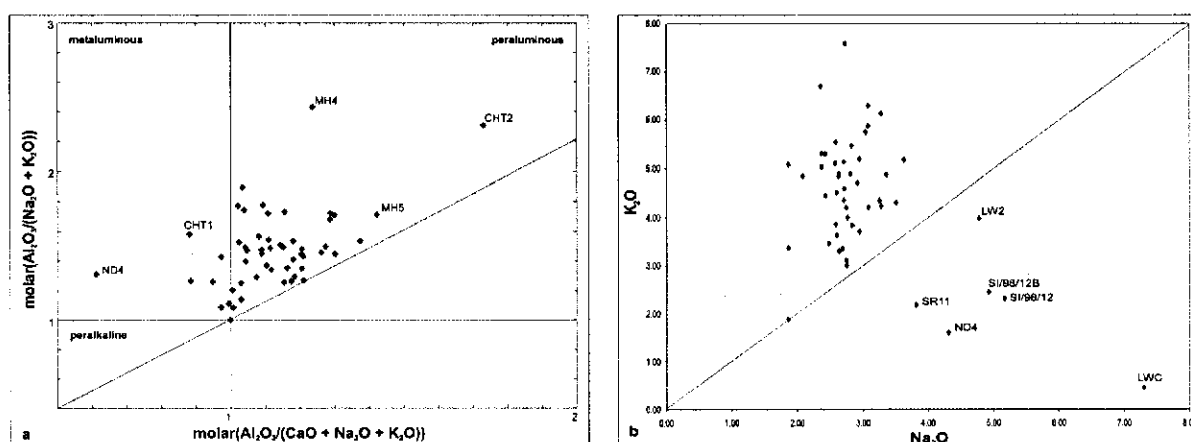


Figure 5-46: (a) Diagram after Maniar and Piccoli (1989), characterising Group V granitoids as peraluminous to metaluminous; (b) binary diagram plotting the K_2O content versus Na_2O content for Group V granitoids, showing the potassic character of the suite.

About half of the samples have ASI values greater than 1.10, classifying them as S-type granitoids on the ASI versus SiO_2 diagram of Clarke (1992) (Figure 5-47 (a)). The remainder of the samples have values below 1.10 and plot in the fields for I-, M- and A-type granitoids. The high ASI for some of the samples may reflect crustal anatexis and partial derivation from deeply buried sedimentary rocks. The tectonic discrimination diagram of Batchelor and Bowden (1985) classifies Group V granitoids across the anatectic syn-collisional and post-orogenic fields, with some samples plotting in the post-orogenic uplift field (Figure 5-47 (b)).

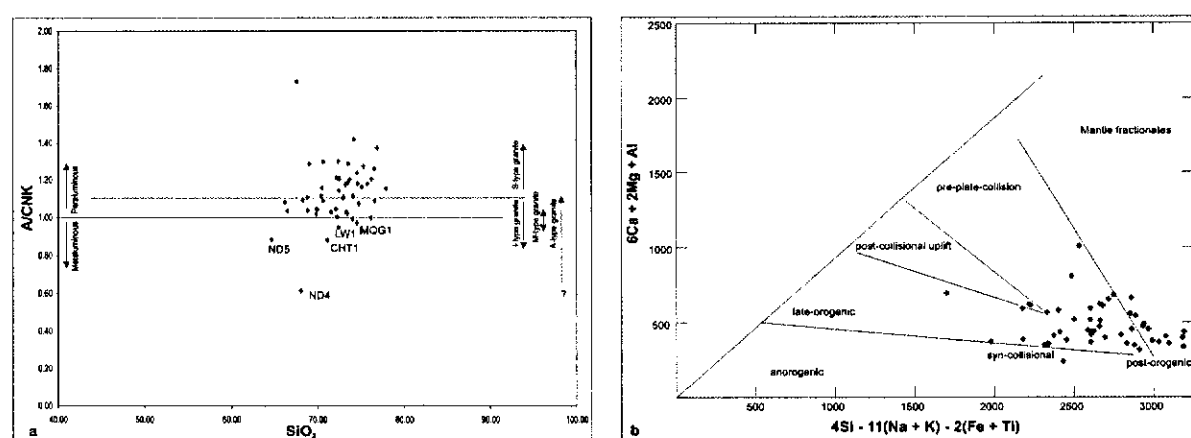


Figure 5-47: (a) Aluminium Saturation Index versus SiO_2 diagram showing Group V granitoids to range from A-, I- to S-type granitoids (Clarke, 1992); (b) Plot after Batchelor and Bowden (1985) suggesting syn- to post-collisional setting for Group V granitoids.

5.7.2 Trace element geochemistry

On a plot proposed by Whalen et al. (1987), using the Ga, Al and Zr content, the granitoids plot across the fields for I-, S- and A-type granitoids (Figure 5-48 (a)). Similar plots are obtained when comparing $Zr + Nb + Ce + Y$ with FeO^*/MgO or with $((K_2O + Na_2O)/CaO)$, as proposed by Whalen et al. (1987).

A triangular plot of Y – Nb – Ce is used to further characterise the granitoids. The granitoids that have distinct A-type characteristics predominantly plot below the line proposed by Eby to distinguish true anorogenic suites from orogeny-related A-type granitoids (Eby, 1990)(Figure 5-48 (b)).

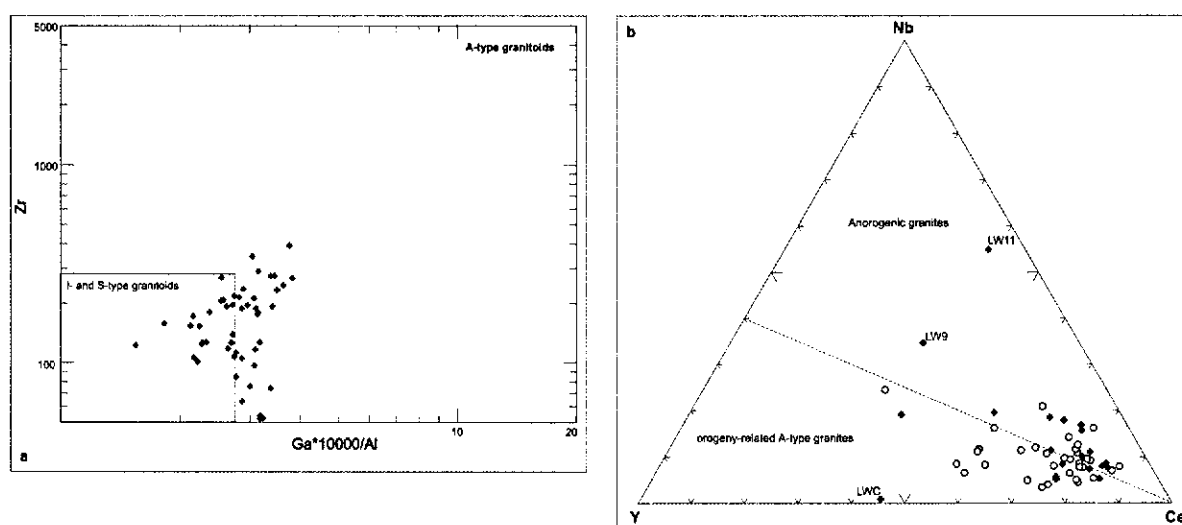


Figure 5-48: (a) binary plot of $Ga \cdot 10000/Al$ versus Zr after Whalen et al. (1987) showing the A-type affinity of a large fraction of Group V granitoids; (b) Triangular plot of Y-Nb-Ce after Eby (1992), suggesting that the majority of Group V Granite Gneisses are orogeny-related A-type granitoids (filled diamonds are data points classified as I- and S-type in the plot of Whalen et al. (1987), open circles are those classified as A-type).

A binary plot of Y/Nb versus Yb/Ta after Eby (1992) further shows that the magma source for Group V granitoids with A-type affinity lies in between that of ocean island basalt and island arc basalt and is similar to compositions typically found in continental crust (Figure 5-49). This confirms that Group V granitoids show closer similarities to syn-tectonic granitoids, emplaced into continental crust, than with those intruded into thinned continental or oceanic crust.

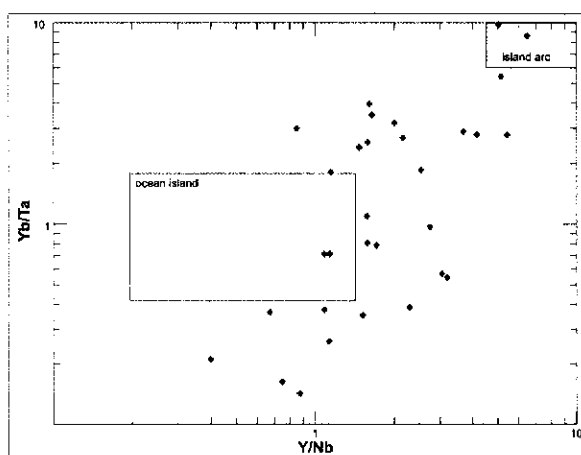


Figure 5-49: Plot of Y/Nb versus Yb/Ta after Eby (1990), suggesting various crustal magma sources for Group V granitoids.

Using the relationships between Y and Nb, Group V granitoids are characterised by within-plate and volcanic-arc / syn-collisional signatures (Figure 5-50 (a))(Pearce et al., 1984b). Relating Y + Nb to Rb, but keeping in mind possible Rb mobility during regional metamorphism, the predominant volcanic-arc and syn-collisional character is confirmed (Figure 5-50 (b)). Using trace element variation diagrams for Rb versus SiO_2 and Ta versus SiO_2 after Pearce et al (1984a)(Figure 5-51), the relatively high Rb content in Group V granitoids suggests a significant crust-dominated geochemistry consistent with a syn-collisional setting rather than a volcanic arc, while relatively elevated Ta contents place the majority of granitoids in the syn-collisional field of the SiO_2 versus Ta diagram.

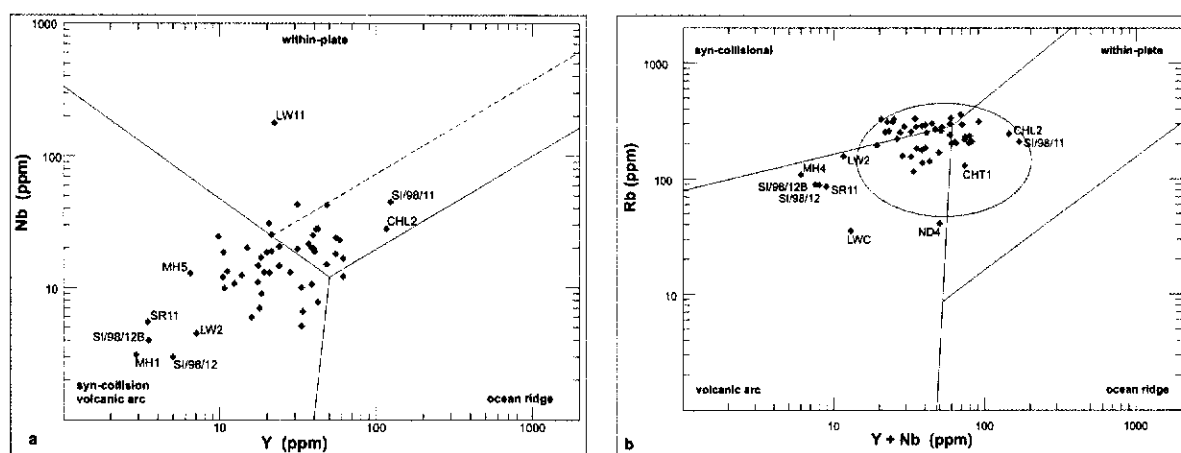


Figure 5-50: Tectonic discrimination diagrams after Pearce (1996a) and Pearce et al. (1984a) suggesting syn- and post-collisional setting for Group V granitoids.

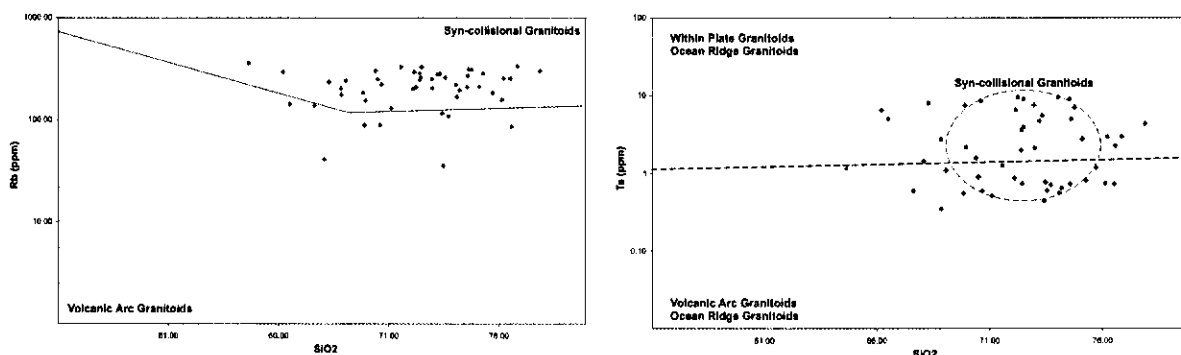


Figure 5-51: Trace element – SiO₂ variation diagram for Group V granitoids

The entire Group V suite shows generally parallel REE patterns, dominated by moderate enrichment in LREE, and flat HREE (Figure 5-52). Anomalous spikes in Tb, Gd and Ce indicate possible analytical problems for that element, but the majority of the suite is characterised by a more or less pronounced negative Eu anomaly (0.14 – 1.01), as could be expected from feldspar-phyric granitoids (Clarke, 1992). Fractionation trends range from 1.8 to 8.1 for HREE, and between 0.8 and 9.7 for LREE, with total fractionation ratios between 2.5 and 118.9. The mean overall fractionation is 29.2, with the majority of samples showing fractionation ratios of 30 or less.

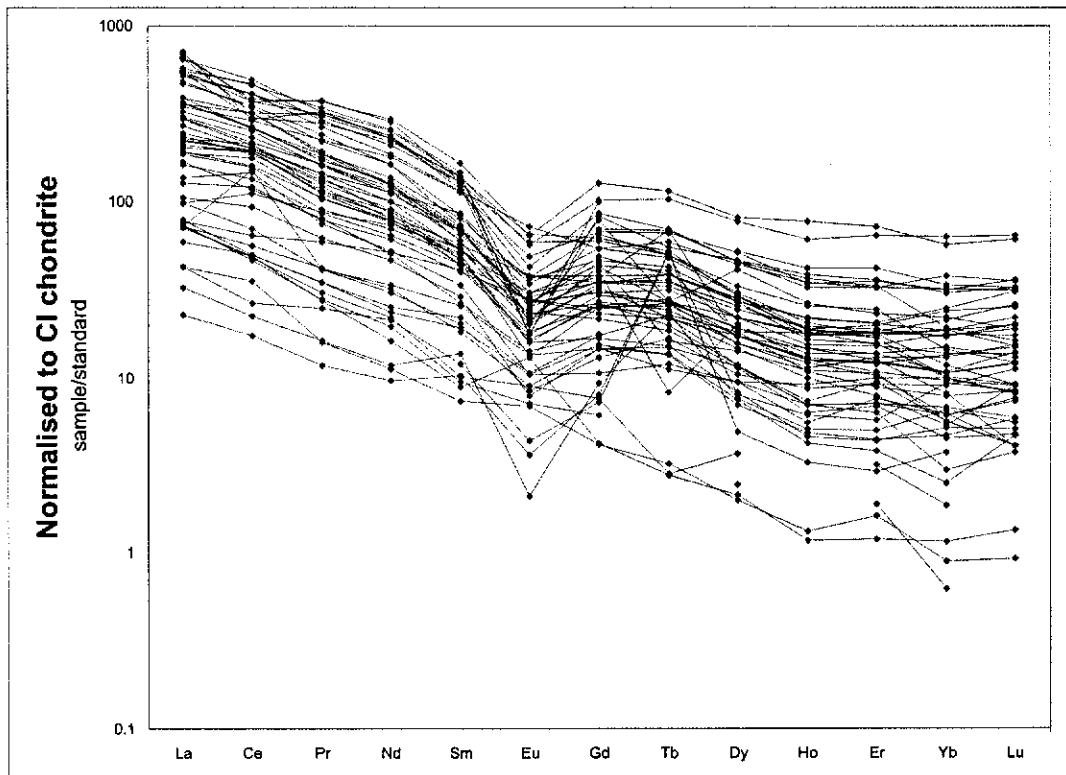


Figure 5-52: REE plot for Group V granitoids (normalisation values after McDonough and Sun (1995)).

The multi-cationic trace element plot for Group V granitoids, normalised to primitive mantle, shows characteristic depletion of Ba, Sr and Eu, and negative Nb, Zr-Hf, Yb and Lu. Strong positive anomalies for Th and Pb, and moderately positive signatures for Nd, Sm, Gd and Y also characterise these plots. Negative anomalies of Ba, Sr and Eu can be ascribed to processes of fractional crystallisation, while the Zr-Hf and Nb-Ta signatures, coupled with the high Pb and Th, suggests significant crustal participation in the generation of Group V granitoids. However, a significant number of samples show subtle differences in trends with slightly positive anomalies for Hf and Ta, and less pronounced positive anomalies for Nd, Th, Sm and Gd, indicating the geochemical complexity of Group V granitoids.

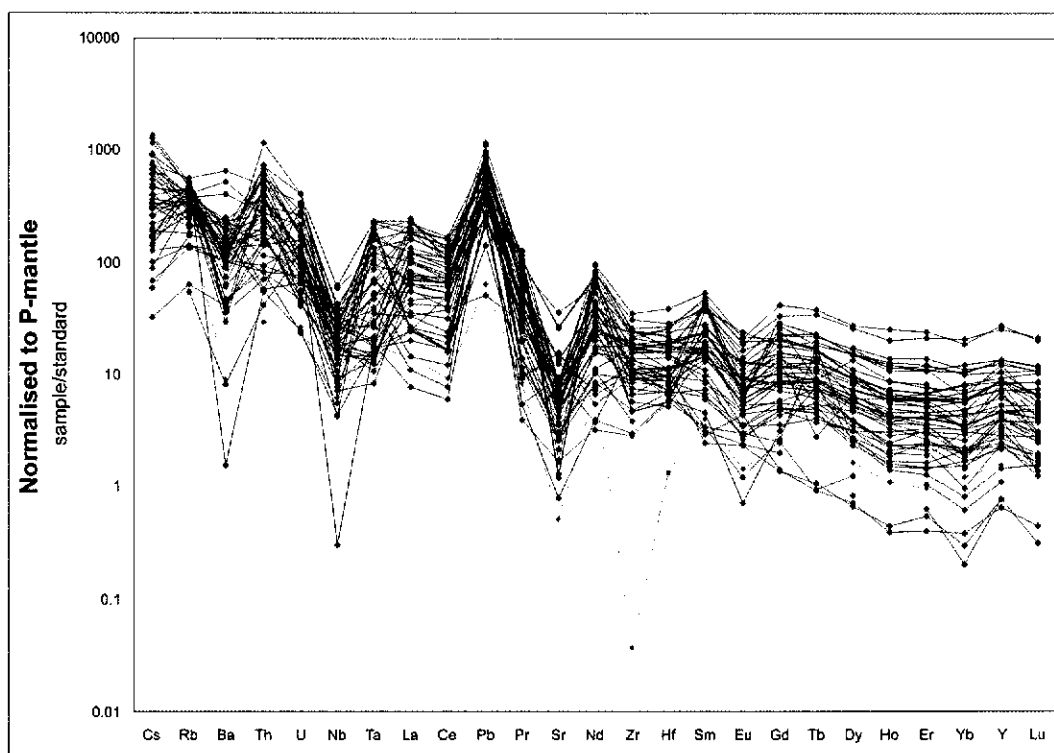


Figure 5-53: Multi-cationic SPIDER plot for Group V granitoids (normalisation values after Sun and McDonough (1989)).

A multi-element plot normalised to ocean-ridge granite after Pearce et al. (1984a) generally shows distinctive negative anomalies for Nb, Zr and Hf, and positive anomalies for Rb, Th, Ce and Sm (Figure 5-54). The relative enrichments of Rb, Ba and Th relative to Ta, and the low normalised values for Y and Yb, are similar to those observed for volcanic arc magmas and crust-dominated within-plate settings (Pearce et al., 1984a).

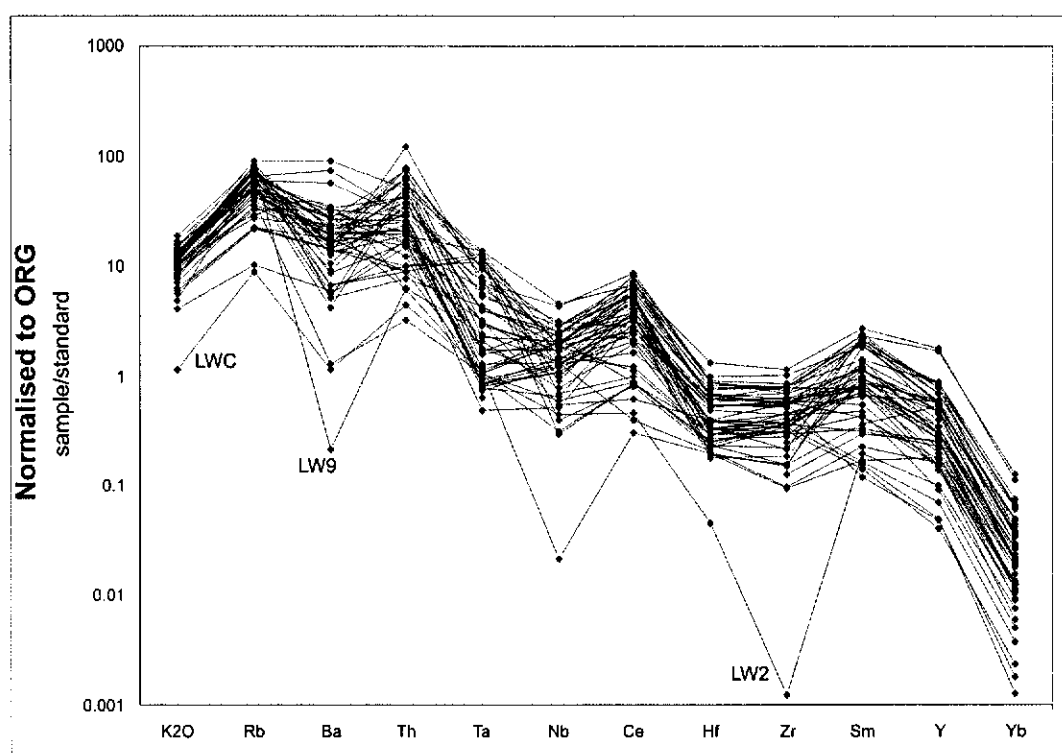


Figure 5-54: Ocean Ridge Granite normalised multi-element plot for Group V granitoids (normalisation values after Pearce et al. (1984)).

5.7.3 Geotectonic interpretation

Group V granitoids are peraluminous and potassic in character. As such they classify as I-, S- and A-type granitoids using the diagram of Clarke (1992). On the diagram of Batchelor and Bowden (1985), the granitoids plot in the syn- and post-collisional fields, consistent with field interpretations and geochronological data confirming their predominant syn-, late- to post-tectonic setting. Because of their varying REE content, some granitoids plot inside the I- and S-type fields of the discrimination diagram of Whalen et al (1987), but about half of the granitoids display a characteristic A-type geochemical signature. Using a ternary diagram after Eby (1990), the granites can be classified predominantly as orogenic A-type granitoids, and their geochemical composition shows similarities with average continental crust. This seems to indicate a significant proportion of crustal reworking, rather than addition of juvenile, ocean island or oceanic-arc magma sources. Using the tectonic discrimination diagrams of Pearce et al. (1984a) and Pearce (1996a), Group V granitoids are indicated as predominantly syn-collisional

and volcanic-arc, and some show within-plate character. Most Group V granitoids also show geochemical similarities with post-collisional granites. REE patterns are characterised by moderately steep LREE, and near-flat HREE trends. A pronounced negative Eu anomaly indicates the significant influence of plagioclase fractionation in the generation of Group V granitoids. Negative anomalies for Ba and Sr in the multi-cationic plots could also indicate fractional crystallisation as an important process. Relative trace element abundances reflect pronounced negative anomalies for Zr-Hf and Nb-Ta, and positive anomalies for Pb and Th, imparting a distinctly crust-dominated pattern, in keeping with the interpretation that the suite was emplaced during the Irumide orogeny, in continental crust, with significant reworking of older LILE-enriched and HFS-depleted crust.

5.8 Differentiation trends

In spite of the fact that the trace and major element fingerprints for all analysed suites appear to be relatively similar, an attempt is made to determine differentiation trends for the various granitoid suites. Given that none of the suites display a wide variation in silica saturation and that samples taken within each suite are widely separated in space, the “trends” only provide a rough indication of magmatic evolution for each suite. Binary variation plots of Na₂O, TiO₂, Zr, MgO, CaO, K₂O, Al₂O₃ and Fe₂O₃ versus SiO₂ are shown in Figure 5-55, Figure 5-56 and Figure 5-57. The first obvious observation for the major element trends is that all granitoid suites plot broadly along similar trends. TiO₂, MgO, CaO and Fe₂O₃ show marked negative correlation trends relative to SiO₂, possibly related to early crystallisation of amphibole, biotite, titanite, rutile, ilmenite/magnetite and plagioclase from the melt, and a possible positive trend for Na₂O that might reflect later crystallisation of albite in the most evolved rocks. Al₂O₃ shows a relatively flat trend as Al₂O₃ is fractionated in various mineral phases both during early and late crystallisation. It is noteworthy that Group II granitoids show a polymodal character, with no points plotting in the SiO₂ range 71-73%. Whether this is an artefact due to the limited number of samples or reflects fractional crystallisation and/or polyphase intrusion is uncertain.

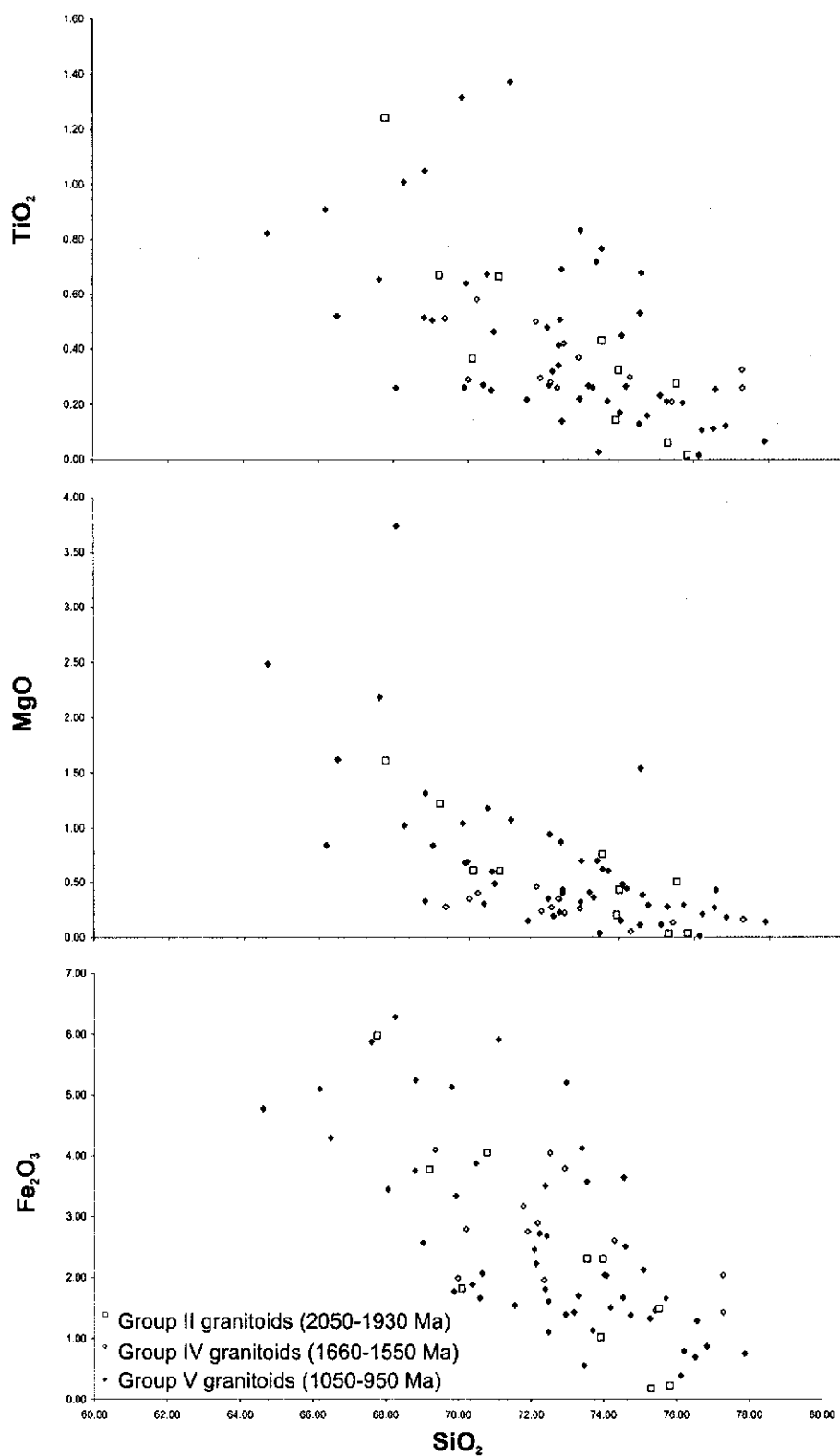


Figure 5-55: Differentiation trends (Harker diagrams) for Group II, Group IV and Group V granitoids in the Irumide belt.

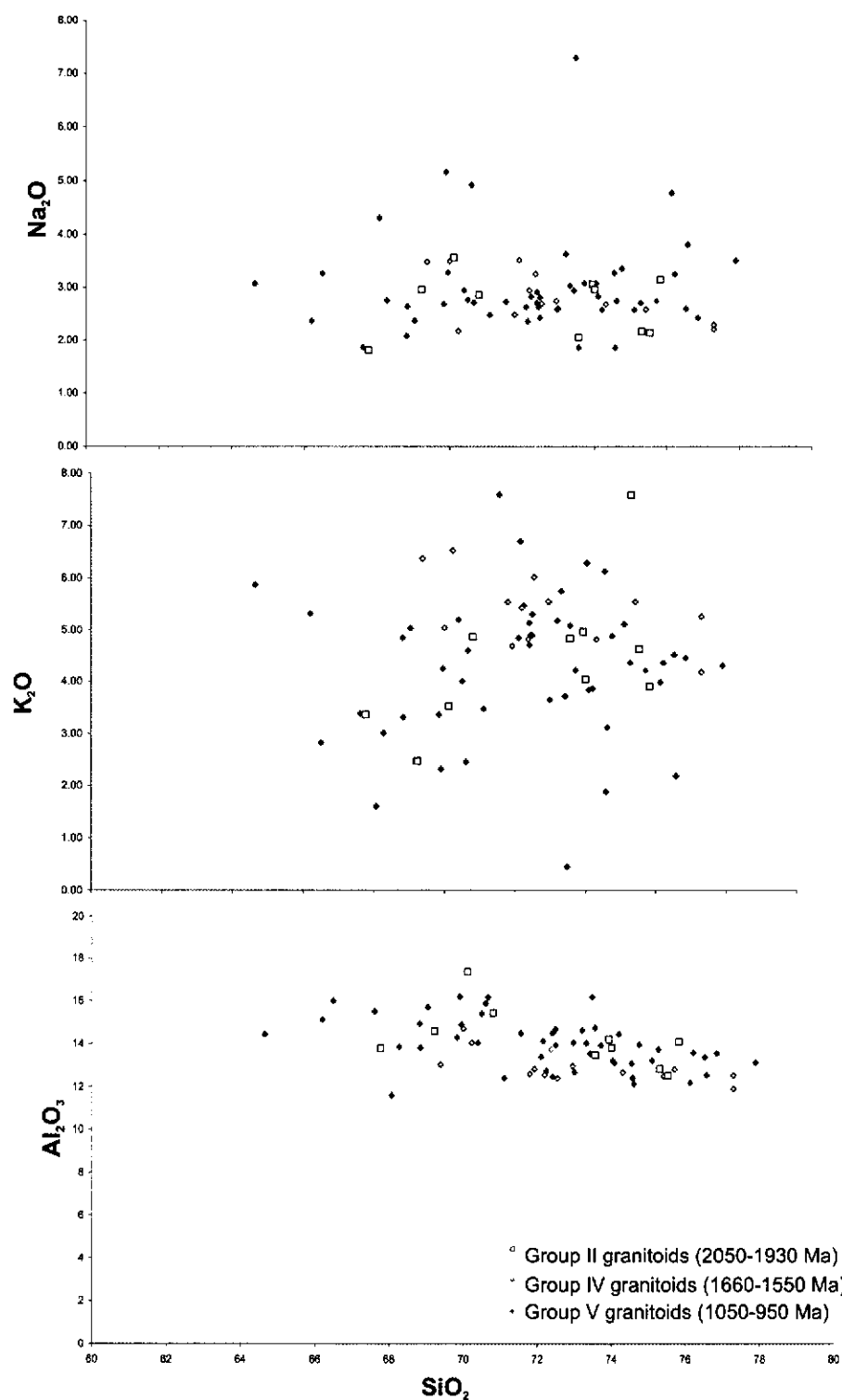


Figure 5-56: Differentiation trends (Harker diagrams) for Group II, Group IV and Group V granitoids in the Irumide belt.

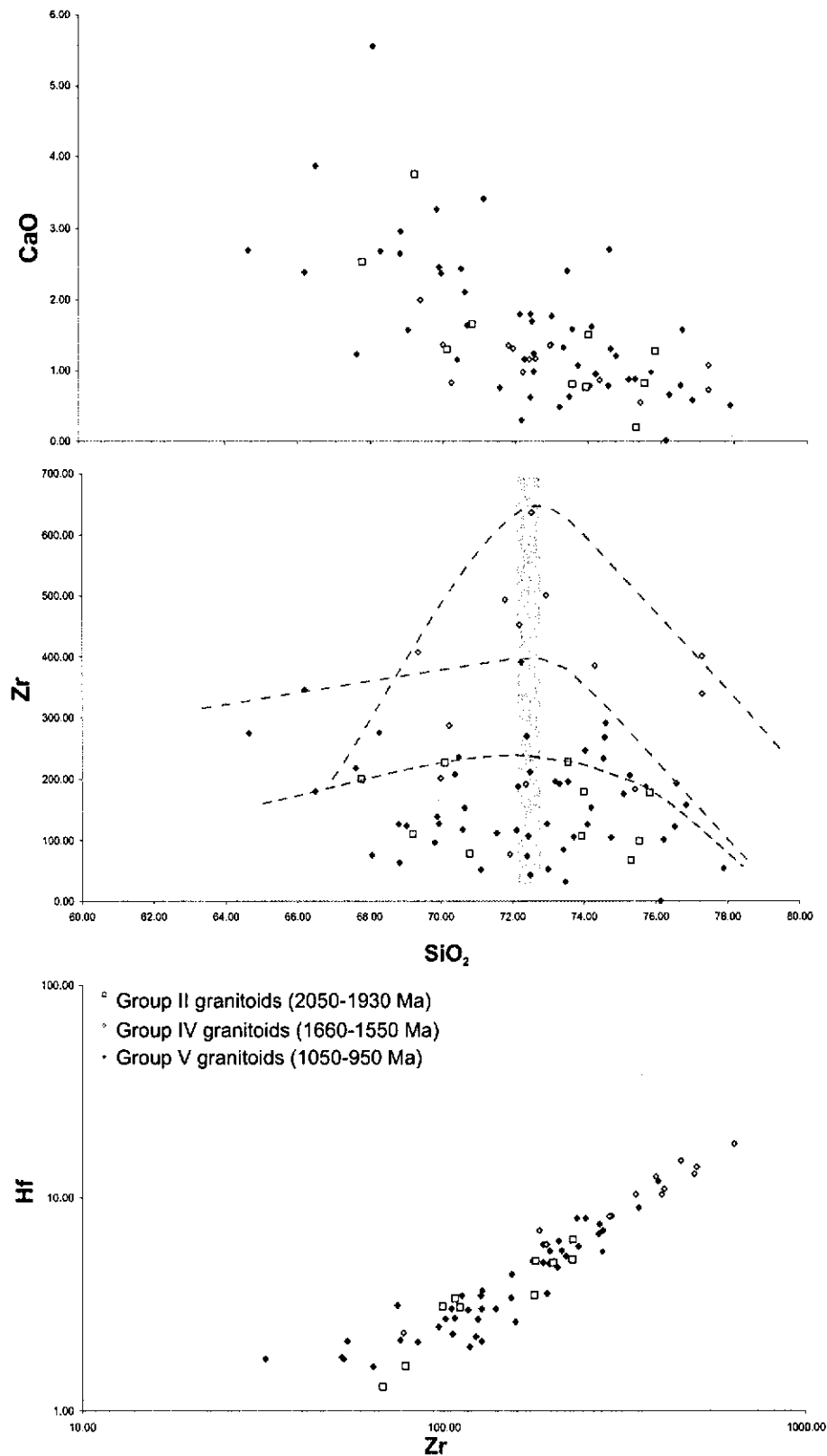


Figure 5-57: Differentiation trends (Harker diagrams) for Group II, Group IV and Group V granitoids in the Irumide belt and log scale diagram showing the relationship between Zr and Hf. The lines on the Zr vs. SiO_2 diagram are trends through the maximum Zr for each suite. The grey zone defines the silica-content range corresponding to the maximum Zr values.

The Zr trends, following the maximum Zr content over the range of SiO₂, indicate saturation for the crystallisation of zircon at around 72 to 73% SiO₂ for Group II, Group IV and Group V granitoids (dashed lines on Figure 5-57 show inferred trends, and grey area defines saturation range), which allows the calculation of a minimum zircon saturation temperature T_{Zr} (see formulae below) of 776°C for Group II, 862°C for Group IV and 773°C for Group V granitoids (Watson and Harrison, 1983; Hanchar and Watson, 2003; Miller et al., 2003).

$$T_{Zr} (^{\circ}\text{C}) = (12900 / (2.95 + M + \ln(476000/Zr_{\text{ppm}}))) - 273$$

where:

$$M = K_{\text{mol}} / (((\text{Al}_2\text{O}_3) / 51 * \text{TOT}_{\text{mol}}) * ((\text{SiO}_2) / 60 * \text{TOT}_{\text{mol}}))$$

where:

$$\text{TOT}_{\text{mol}} = \text{molar } (\text{SiO}_2 + \text{TiO}_2 + \text{Al}_2\text{O}_3 + \text{Fe}_2\text{O}_3 + \text{MnO} + \text{MgO} + \text{CaO} + \text{Na}_2\text{O} + \text{K}_2\text{O} + \text{P}_2\text{O}_5)$$

$$K_{\text{mol}} = \text{molar } (\text{Na}_2\text{O} + \text{K}_2\text{O} + 2\text{CaO}) / \text{TOT}_{\text{mol}}$$

It must be noted that the above formulas assume that all Zr analysed was present in the melt fraction, disregarding possible presence of undissolved Zr in xenocrystic zircon. All calculated T_{Zr} are therefore necessarily maximum temperature estimates.

These relatively high temperature values (>750°C) indicate relatively dry conditions of melting for all three suites, precluding the involvement of subducted oceanic crust, and hydrous melting of the crust. Instead, dehydration melting of hornblende and biotite is the most likely mechanism for the production of the granitoids. These systems require substantial transient heat flux, either in an anorogenic extensional setting, where mantle upwelling can provide the necessary heat, or through processes involving underplating of hot basic magma at the base of the crust or through delamination of the lower crust (Miller et al., 2003).

A strong linear correlation on a log-log plot of Zr versus Hf strongly supports fractional crystallisation of zircon in all granitoids. Contrary to what would be expected if feldspar fractionation had played an important role, such linear trends are very weak in the log-log plots of Eu versus Ba and Eu versus Sr suggesting only limited effects of feldspar fractionation or mobility of Ba and Sr during metamorphism (Figure 5-58).

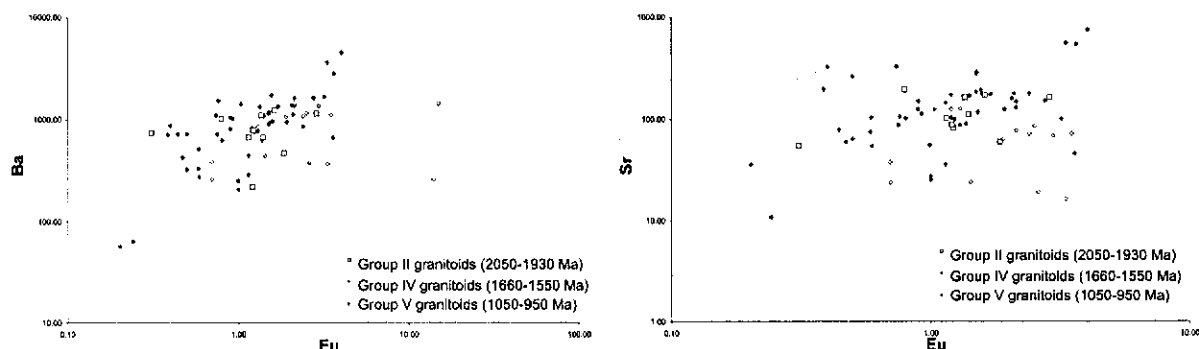


Figure 5-58: Relationships between Ba and Eu and Sr and Eu in Group II, Group IV and Group V granitoids.

5.9 Discussion

The geochemistry of magmatic rocks in northern Zambia, including pre-Irumide lithologies related to the Palaeoproterozoic development of the Bangweulu block and the Ubendian belt, show uniform crust-dominated patterns. All analysed magmatic suites are characterised by relatively high overall REE content and are peraluminous to metaluminous in character, in keeping with significant amounts of crustal melting in their development. High ASI values in granitoids are generally considered to reflect source materials of the magma, rather than the result of fractional crystallisation (Zen, 1986). Peraluminous compositions, such as those that predominate in the granitoids of the Irumide belt and the Bangweulu block, are generally attributed to hydrous melting of mafic rocks (Ellis and Thompson, 1986) or to melting of pelitic or semi-pelitic rocks (Holtz and Johannes, 1991). The former can be readily explained in a convergent setting, where a subducting oceanic plate provides the trigger for melting of mafic mantle material. The latter could occur in convergent settings, where crustal

anatexis would generate crust-derived magmas, or by processes of underplating of mafic hot magma, partially melting the base of the crust.

The Archaean (Group I) Kapiri Mposhi granite gneiss shows a clear volcanic arc signature, with subequal Y and Nb content, low Rb, relatively low total REE, negative anomalies for Zr-Hf, Nb-Ta, and positive anomalies for Th and Pb. Based on the single sample analysed, the granite gneiss is interpreted to record a ~2.7 Ga volcanic arc and forms part of the earlier history of the Bangweulu block.

The Palaeoproterozoic (Group II) Mkushi Gneiss and Luwalizi Granite Gneiss are peraluminous and potassic in composition and show overall REE and Nb, Y and Rb contents consistent with a volcanic-arc setting. Notably, the younger members of the suite show an increase in overall REE content, giving them A-type characteristics possibly indicating an increasing contribution of crustal reworking with time.

The Palaeoproterozoic (Group III) plutono-volcanic suite of the Bangweulu block displays strong volcanic-arc/within-plate signatures characterised by depletions of Ba relative to Rb and Th, and Nb relative to Ce. These plutons and associated volcanics also show enrichment of Pb and Th commonly associated with volcanic arcs. The relatively high REE content of the granitoids and their peraluminous composition is evidence for some crustal reworking in the generation of the suite. It is noteworthy that the geochemical characteristics of the volcanic and granitic samples are similar, in keeping with other evidence that they belong to a single magmatic suite.

The rhyolites and pillow basalts within the Manshya River Group show similar characteristics to the Bangweulu block plutono-volcanic (Group III) suite. The suite displays a calc-alkalic trend, with moderate enrichment of Mg for intermediate members. The volcanics are peraluminous to metaluminous in composition, and their relative abundances of trace elements show consistent depletion of Hf, Ta and Nb, and relative enrichment of Pb and Th, consistent with convergent or within-plate settings. Enrichment of Pb relative to Ce suggests processes of dehydration of subducting oceanic crust, favouring a volcanic arc

setting. The data do not allow distinguishing between within-plate or volcanic arc settings.

The 1.66-1.61 Ga Group IV granitoids are peraluminous to metaluminous and potassic in composition. Their overall REE content is relatively high, with depletions in Zr-Hf and Nb-Ta, which, coupled with enrichments in Th and Pb, indicates a dominant crustal character for the suite. Y, Nb and Ce contents indicate A-type characteristics, while relatively low Nb content suggests an orogeny-related A-type affinity, rather than an anorogenic setting. Only the Lubu Granite Gneiss has a distinct anorogenic signature and may represent anorogenic magmatism at around 1.55 Ga. The Yb, Ta and Th contents of Group IV granitoids suggest a crustal source for the generation of their parent magmas, and the granitoids are interpreted as collision-related granites possibly formed as a response to orogenic collapse and associated delamination of the lithosphere, giving rise to extensive lower crustal melting.

The numerous Group V porphyritic granitoids show uniform major and trace element characteristics. All Group V granitoids are peraluminous to metaluminous and potassic in character. Their overall REE abundances are high, and they are classified as orogeny-related A-type granitoids. Yb, Ta and Hf contents allude to varying source components, while negative anomalies for Zr-Hf and Nb-Ta and positive anomalies for Pb and Th indicate that significant crustal reworking dominated the generation of Group V granitoids. Age data presented in this study indicate that Group V granitoids are syn- to post-kinematic. The strong crustal signature may be the result of processes of underplating of hot magma, crustal delamination or slab break-off to allow significant crustal melting.

An interesting characteristic for all analysed granitoid suites is the relatively similar major element behaviour. The broadly similar trends for all granitoid suites could suggest broadly similar sources, similar melting and mixing mechanisms, similarities in emplacement mechanisms and in the mode of crystallisation. Certain patterns in the binary differentiation diagrams can be ascribed to crystallisation of specific minerals (zircon), while others suggest

possible fractionation of biotite, titanite, rutile, magnetite and/or ilmenite and plagioclase early in the differentiation history.

Saturation of the liquid in zircon occurred at around 72% SiO₂, and allows the calculation of minimum zircon saturation temperatures of 770°C, with Group IV showing the highest temperatures of 862°C. The granitoids of Group II, Group IV and Group V appear to represent relatively hot and dry granitoids, which required substantial heat flux to allow dehydration melting of hornblende and biotite.

6 CHAPTER 6: Sm-Nd Isotope geochemistry

6.1 Introduction

During this study, nineteen samples were analysed for Sm and Nd isotopic composition. The reader is referred to Appendix E for details on the analytical techniques employed. The samples were selected from igneous rocks that had already been dated in this study by the U-Pb SHRIMP zircon technique, and cover the dominant magmatic suites recognised in the Irumide belt. A minimum of two samples were included for each suite, to provide a preliminary idea of the variation in Sm/Nd and isotopic ratios within each suite, and to allow comparison of these ratios in the various generations of magmatism.

In this study both model ages and the difference in isotopic ratio between the rocks and standard reservoirs are reported. The latter is characterised as the calculated difference at the time of extraction of the magma from the chondritic uniform reservoir (CHUR), a widely used model for the isotopic evolution of the mantle during Earth history, using the $\epsilon_{Nd}(T)$ parameter as follows:

$$\epsilon_{Nd}(T) = \frac{\left(\left(\frac{^{143}Nd}{^{144}Nd} \right)_{meas} - \left(\left(\frac{^{147}Sm}{^{144}Nd} \right)_{meas} \times (e^{\lambda T} - 1) \right) \right)}{\left(\left(\frac{^{143}Nd}{^{144}Nd} \right)_{CHUR} - \left(\left(\frac{^{147}Sm}{^{144}Nd} \right)_{CHUR} \times (e^{\lambda T} - 1) \right) \right)}$$

- where: T = emplacement age determined through U-Pb SHRIMP dating on zircon
- meas* = measured isotopic ratio
- CHUR* = chondritic uniform reservoir isotopic ratio. Ratios used during this study after Wasserburg et al. (1981).
- λ = decay constant of ^{147}Sm ($=6.54 \times 10^{-12} \text{ y}^{-1}$)

$\epsilon_{\text{Nd}}(T)$ values provide an estimate of the difference between the initial isotopic ratio of the rock and the corresponding value of the ratio in CHUR at the time of crystallisation of the rock. Positive values of $\epsilon_{\text{Nd}}(T)$ indicate derivation from a source depleted in ^{143}Nd , in other words a source from which magma had already been withdrawn and is as such depleted in LILE elements. A negative $\epsilon_{\text{Nd}}(T)$ indicates derivation from sources with lower Sm/Nd ratios than CHUR. Such rocks were extracted from the CHUR reservoir at earlier times, and have an evolved isotopic composition. Rocks with negative $\epsilon_{\text{Nd}}(T)$ values were therefore derived from, or assimilated, old crustal rocks. An $\epsilon_{\text{Nd}}(T)$ value of zero would indicate derivation from a source of similar composition to CHUR. The $\epsilon_{\text{Nd}}(T)$ parameter therefore provides a powerful means of determining the extent of crustal reworking (negative values), or juvenile addition, in the generation of a rock suite.

Model ages were calculated using two different sets of standard isotopic ratios, one for the chondritic uniform reservoir (CHUR), and one for depleted mantle (DM). The principle followed is to calculate the time needed to evolve from standard ratios of CHUR or depleted mantle, to come to the measured ratios observed in the rock. This “date” is geologically significant only when the Sm/Nd ratios of the rock have not been disturbed since time of separation of Nd from the reservoir through processes other than radioactive decay. If this condition is satisfied, then the calculated “model age” provides an estimate for the total length of time Nd in a rock has resided in the crust. Because of the fact that magmatic processes and magma sources may include both crustal reworking and juvenile addition of magma from standard reservoirs, the “model age” provides only an estimate of the average age of the crust (Arndt and Goldstein, 1987). If the model age is identical or only slightly older than the actual emplacement age of the rock, the rock is termed “juvenile” in character. The ratios used for the calculation of model ages are tabulated in Table 6-1.

Table 6-1: Present day isotopic ratios of a reservoir of chondritic or depleted mantle composition.

	$^{143}\text{Nd}/^{144}\text{Nd}$	$^{147}\text{Sm}/^{144}\text{Nd}$	Reference
Chondritic uniform reservoir	0.512638	0.1966	Wasserburg et al., 1981
Depleted mantle	0.513114	0.222	Michard et al., 1985

The model age calculations were done as follows:

$$T_{CHUR} = \left(\frac{1}{\lambda} \right) \times \ln \left[\frac{\left(\frac{{}^{143}\text{Nd}}{{}^{144}\text{Nd}} \right)_{meas} - 0.512638}{\left(\frac{{}^{147}\text{Sm}}{{}^{144}\text{Nd}} \right)_{meas} - 0.1966} + 1 \right]$$

and

$$T_{DM} = \left(\frac{1}{\lambda} \right) \times \ln \left[\frac{\left(\frac{{}^{143}\text{Nd}}{{}^{144}\text{Nd}} \right)_{meas} - 0.513114}{\left(\frac{{}^{147}\text{Sm}}{{}^{144}\text{Nd}} \right)_{meas} - 0.222} + 1 \right]$$

6.2 Selection of samples

Two samples were selected from the Palaeoproterozoic basement to the Irumide belt (Group II granitoids), including one sample of Mkushi Gneiss (sample MK3) from the type area (Munshiwemba Mine, Figure 2-9), and one sample from the Luwalizi Granite east of Isoka (sample ISK1, Figure 2-13). Both samples have been dated using U-Pb SHRIMP on zircon, and yielded ages of 2042 ± 10 Ma and 1942 ± 6 Ma respectively.

Nine samples were selected from the Irumide volcanics of the Manshya River Group (Group III magmatism), including two samples each from the Kachinga Tuff (samples IS20 and IS23, with sample IS20 dated at 1856 ± 4 Ma, Figure 2-24) and the Luswa River Tuff (samples LW12 and LW13, where sample ZM31 taken from the same outcrop was dated at 1879 ± 13 Ma, Figure 2-12). Five samples were analysed of the Katibunga basalts (samples KB5 – KB9, with sample KB5 dated at 1871 ± 24 Ma, Figure 2-37).

Two samples each were analysed from the Mansa Granitoids and Mansa Volcanics of the Bangweulu block (Group III magmatism). Samples MA1 and MA2 were taken from granitoids, and were dated at 1860 ± 13 and 1862 ± 8 Ma respectively. Samples MA4 and MA5 were collected from volcanics (sample MA5 was dated at 1862 ± 19 Ma, Figure 2-6).

Two samples were analysed of Group IV granitoids. Sample SR7 was collected from the type locality of the Lukamfwa Hill Granitoids in the Serenje map sheet, and dated at 1664 ± 6 Ma (Figure 2-10). Sample SR12 was collected from a biotite granitoid to the west of the Lukamfwa Hill locality (Figure 2-10), and has yielded a U-Pb SHRIMP age of 1639 ± 14 Ma.

Finally, two samples were included from Group V granitoids. Sample SR5 was taken from Chimuma Hill in the Serenje map sheet (Figure 2-10), from the same outcrop as sample SER6-4 which yielded a U-Pb age of 1036 ± 13 Ma. Sample ND4 was taken from a dark grey hornblende-bearing granitoid in the Ndabala map sheet (Figure 2-10), which yielded a date of 1037 ± 16 Ma. The Nd-isotopic results are tabulated in Table 6-2.

Table 6-2: Sm-Nd isotopic data for igneous lithologies in the Irumide belt and the Bangweulu block.

Sample	Nd (ppm)	Sm (ppm)	$^{147}\text{Sm}/^{144}\text{Nd}$ ($\pm 1\sigma$)	$^{143}\text{Nd}/^{144}\text{Nd}$ ($\pm 1\sigma$)	$(^{143}\text{Nd}/^{144}\text{Nd})_{\text{init}}$ ($\pm 1\sigma$)	$\epsilon_{\text{Nd}}(T)$ ($\pm 2\sigma$)	T_{Chur} ($\pm 2\sigma$)	T_{DM} ($\pm 2\sigma$)	SHRIMP age ($\pm 2\sigma$ Ma)
Group II granitoids (Mkushi map sheet and Isoka map sheet)									
MK3	8.2	1.8	0.10465 \pm 0.19853	0.51118 \pm 0.00190	0.50985 \pm 0.00001	-4.2 \pm 0.2	2400 \pm 17	2495 \pm 13	2042 \pm 10
ISK1	16.7	4.1	0.11819 \pm 0.35472	0.51141 \pm 0.00200	0.51141 \pm 0.00001	-4.3 \pm 0.2	2372 \pm 23	2486 \pm 18	1942 \pm 6
Group III Kachinga tuff (Isoka map sheet)									
IS23	13.7	3.4	0.12034 \pm 0.98005	0.51136 \pm 0.01010	0.50990 \pm 0.00005	-6.6 \pm 1.1	2532 \pm 109	2609 \pm 82	1856 \pm 4
IS20	6.7	1.6	0.11797 \pm 0.70341	0.51110 \pm 0.01530	0.51110 \pm 0.00008	-11.3 \pm 1.5	2961 \pm 152	2931 \pm 115	1856 \pm 4
Group III Luswa rhyolite (Luswa River map sheet)									
LW13	2.0	0.5	0.11275 \pm 0.37865	0.51084 \pm 0.00580	0.50937 \pm 0.00003	-14.8 \pm 0.6	3238 \pm 55	3145 \pm 42	1879 \pm 13
LW12	56.5	9.7	0.08312 \pm 0.31347	0.51132 \pm 0.00140	0.51132 \pm 0.00001	1.8 \pm 0.1	1762 \pm 10	1959 \pm 9	1879 \pm 13
Group III Katibunga volcanics (Katibunga map sheet)									
KB9	7.6	2.4	0.15089 \pm 0.19847	0.51176 \pm 0.00150	0.50990 \pm 0.00001	-6.1 \pm 0.2	2909 \pm 31	2884 \pm 20	1871 \pm 24
KB5	1.5	0.4	0.14058 \pm 0.16456	0.51173 \pm 0.00230	0.51000 \pm 0.00001	-4.2 \pm 0.2	2461 \pm 33	2579 \pm 23	1871 \pm 24
KB6	5.7	1.9	0.15877 \pm 0.17863	0.51201 \pm 0.00160	0.51005 \pm 0.00001	-3.1 \pm 0.2	2522 \pm 37	2649 \pm 23	1871 \pm 24
KB7	5.4	1.8	0.16332 \pm 0.47912	0.51213 \pm 0.00410	0.51011 \pm 0.00002	-2.0 \pm 0.5	2338 \pm 109	2555 \pm 63	1871 \pm 24
KB8	2.8	0.9	0.14779 \pm 0.15999	0.51179 \pm 0.00160	0.51179 \pm 0.00001	-4.8 \pm 0.2	2634 \pm 28	2704 \pm 19	1871 \pm 24
Group III Mansa granites (Mansa and Musonda Falls map sheet)									
MA1	15.8	3.4	0.10364 \pm 0.17098	0.51132 \pm 0.00160	0.51005 \pm 0.00001	-2.9 \pm 0.2	2103 \pm 14	2261 \pm 11	1860 \pm 13
MA2	16.4	3.5	0.10324 \pm 0.16883	0.51134 \pm 0.00130	0.51134 \pm 0.00001	-2.3 \pm 0.1	2060 \pm 11	2227 \pm 9	1862 \pm 8
Group III Mansa volcanics (Mansa map sheet)									
MA4	11.0	2.3	0.10085 \pm 0.15118	0.51132 \pm 0.00110	0.51001 \pm 0.00001	-2.1 \pm 0.1	2041 \pm 9	2209 \pm 9	1862 \pm 19
MA5	14.5	2.8	0.09322 \pm 0.20093	0.51118 \pm 0.00180	0.51118 \pm 0.00001	-2.8 \pm 0.2	2084 \pm 14	2234 \pm 11	1862 \pm 19
Group IV granitoids (Serenje map sheet)									
SR7	30.3	8.6	0.13690 \pm 0.09939	0.51138 \pm 0.00380	0.50990 \pm 0.00005	-11.3 \pm 1.0	3113 \pm 229	3031 \pm 156	1664 \pm 6
SR12	81.7	18.8	0.11090 \pm 1.74668	0.51133 \pm 0.00210	0.51133 \pm 0.00001	-7.4 \pm 0.2	2310 \pm 55	2431 \pm 44	1639 \pm 14
Group V granitoids (Serenje and Ndalaba map sheets)									
SR5	12.3	3.0	0.11956 \pm 0.15761	0.51114 \pm 0.00170	0.51032 \pm 0.00001	-18.4 \pm 0.2	2881 \pm 18	2871 \pm 14	1036 \pm 13
ND4	10.4	2.9	0.13289 \pm 0.31091	0.51146 \pm 0.00250	0.51146 \pm 0.00001	-14.6 \pm 0.2	2808 \pm 35	2817 \pm 25	1037 \pm 16
CHUR: $^{143}\text{Nd}/^{144}\text{Nd} = 0.512638$ and $^{147}\text{Sm}/^{144}\text{Nd} = 0.1966$ (Wasserburg et al., 1981)									
DM: $^{143}\text{Nd}/^{144}\text{Nd} = 0.513114$ and $^{147}\text{Sm}/^{144}\text{Nd} = 0.222$ (Michard et al., 1985)									

6.3 Palaeoproterozoic (Group II) granitoids

The Mkushi Gneiss (sample MK3, crystallisation age of 2042 ± 10 Ma) yielded a T_{CHUR} model age of 2400 ± 17 Ma and a T_{DM} model age of 2495 ± 13 Ma indicating that its magma source includes, at least in part, older crustal material with an average crustal residence age of 2.4 Ga (Table 6-2). An initial ϵ_{Nd} value of -4.2 ± 0.2 confirms that the Mkushi Gneiss was not directly derived from a chondritic source, but includes reworked crustal material with higher Sm/Nd ratio than CHUR.

Sample ISK1 (crystallisation age of 1942 ± 6 Ma) yielded a T_{Chur} model age of 2372 ± 23 Ma and a T_{DM} model age of 2486 ± 18 Ma, very similar to those calculated for the Mkushi Gneiss (Table 6-2). The initial ϵ_{Nd} value of -4.2 ± 0.2

also indicates the involvement of older crust in the generation of the Luwalizi Granite Gneiss.

These limited data indicate that the Mkushi Gneiss and the Luwalizi Granite Gneiss were both derived from sources with elevated Sm/Nd ratios and average crustal residence ages from 2.5 to 2.4 Ga, or juvenile magmas that assimilated crust older than 2.4-2.5 Ga.

6.4 Palaeoproterozoic (Group III) Mansa Granitoids and Volcanics

The two volcanics and two granitoids collected from the Mansa area show very similar Nd isotopic data (Table 6-2). A T_{CHUR} model age was obtained of 2103 ± 14 and 2060 ± 11 Ma for samples MA1 and MA2 respectively (crystallisation ages 1860 ± 13 and 1862 ± 8 Ma respectively). The volcanics yielded T_{CHUR} model ages of 2041 ± 9 and 2084 ± 14 Ma for sample MA4 and MA5 respectively (MA4 undated, MA5 has a crystallisation age of 1862 ± 19 Ma). T_{DM} ages are 2261 ± 11 and 2227 ± 9 Ma for the granites and 2209 ± 9 and 2234 ± 11 Ma for the acid volcanics. The granites record initial ϵ_{Nd} values of -2.9 ± 0.2 and -2.3 ± 0.1 , while the volcanics record -2.1 ± 0.1 and -2.8 ± 0.2 . The negative initial ϵ_{Nd} values indicate some involvement of older crustal material in the petrogenesis of the granites and volcanics, while similarities in Nd ratios suggests a similar petrogenesis for both. T_{DM} ages indicate an average crustal residence age of 2.2 Ga. Although the Nd isotopic data do not directly refute the volcanic arc setting envisaged for the suite, the average crustal residence ages calculated for the plutono-volcanic rocks do suggest some participation of pre-existing crust as might occur in an Andean-type setting.

6.5 *Palaeoproterozoic (Group III) Irumide volcanics*

6.5.1 The Luswa River Tuff

Two samples were analysed from the Luswa River rhyolites (crystallisation age of 1879 ± 13). One sample (sample LW12) yielded a slightly positive initial ϵ_{Nd} value of 1.8 ± 0.1 and a T_{chur} model age of 1762 ± 10 Ma. The T_{DM} age for the same sample is 1959 ± 9 Ma (Table 6-2). These features suggest derivation from a depleted mantle source and a juvenile character for the rhyolites. The second sample from the same tuff (sample LW13), however, records an extremely low ϵ_{Nd} value of -14.8 ± 0.6 and extremely old T_{CHUR} model age of 3238 ± 55 Ma. The T_{DM} model age for this sample is 3145 ± 42 Ma, indicating significant participation of older crust in the generation of this magma. At face value, the data would suggest very inhomogeneous conditions in the magma source for the Luswa River Volcanics: on the one hand, part of the magma was sourced directly from depleted mantle with little or no participation of crust, while on the other hand, extensive crustal reworking and mixing occurred to produce ϵ_{Nd} values as low as -14.8 . Because the results for sample LW12 contrast sharply with those for the other volcanic rocks, especially sample LW13, which was collected from the same unit, analysis LW 12 is therefore considered suspect, and not much weight is given to the result.

6.5.2 The Kachinga Tuff

Two samples were analysed from the Kachinga Tuff in the Isoka map sheet (crystallisation age of 1856 ± 4 Ma). The samples yielded ϵ_{Nd} values of -11.3 ± 1.5 and -6.6 ± 1.1 (samples IS20 and IS23 respectively, Table 6-2). Samples IS20 yielded T_{CHUR} and T_{DM} model ages of 2961 ± 152 and 2931 ± 115 Ma, while sample IS23 yielded T_{CHUR} and T_{DM} model ages of 2532 ± 109 and 2609 ± 82 Ma respectively. The data for the Kachinga Tuff samples indicate substantial crustal reworking, with initial ϵ_{Nd} values less than -6.6 ± 1.1 , and T_{DM}

model ages older than 2931 ± 115 Ma. The extremely enriched Nd isotopic signature for the Kachinga Tuff cannot be adequately explained by processes of mixing between subducted oceanic crust and lower crustal melting, but must involve significant amounts of old crustal material. The isotope signature of the rhyolites therefore attests to the existence of crust below the Irumide belt at least 2.9 Ga old.

6.5.3 The Katibunga Volcanics

Five samples were analysed of mafic volcanics near Mpika (crystallisation age of 1871 ± 24 Ma), and are interpreted to belong to one volcanic suite. The samples were collected from an area of several square kilometers and comprise coarse gabbroic and aphanitic basalt lithologies. The volcanics yielded initial ϵ_{Nd} values between -6.1 ± 0.2 and -2.0 ± 0.5 , with T_{CHUR} model ages between 2909 ± 31 and 2338 ± 109 Ma, indicating broadly similar amounts of involvement of older crust in their petrogenesis (Table 6-2). T_{DM} model ages range from 2884 ± 20 to 2555 ± 63 Ma. The negative initial ϵ_{Nd} values indicate participation of older crust in their formation with average crustal residence up to 2884 ± 20 Ma, despite their basaltic composition. Whether this crustal source material represents underlying Sm/Nd-enriched sialic components, or is due to mixing of sediment sources with melt from crustal sources remains unclear.

6.6 Palaeo-Mesoproterozoic (Group IV) granitoids

The two samples analysed from the Lukamfwa Granite Gneisses in the southwest of the Irumide belt yielded initial ϵ_{Nd} values of -11.3 and -7.4 , with T_{CHUR} model ages of 3113 ± 229 and 2310 ± 55 Ma (samples SR7 and SR12, crystallisation ages 1664 ± 6 and 1639 ± 14 Ma respectively, Table 6-2). T_{DM} model ages for the granitoids are 3031 ± 156 and 2431 ± 44 Ma. The negative ϵ_{Nd} values indicate the participation of significant amounts of older crust in their petrogenesis, while the T_{DM} model age of 3031 ± 156 Ma can be considered a minimum age of that crustal component. Either the amount of crustal material

involved in the generation of Group IV granitoids was extensive, or that crust was extremely old. No lithologies of an age exceeding 2.7 Ga have so far been reported from the region.

6.7 *Irumide (Group V) granitoids*

Two syn-Irumide granites were analysed from the southwestern part of the Irumide belt, and yielded emplacement ages of 1037 ± 16 and 1036 ± 13 Ma (samples SR5 and ND4 respectively). Initial ϵ_{Nd} values of -14.6 ± 0.2 and -18.4 ± 0.2 were obtained, indicating that substantial amounts of older crust were involved in the petrogenesis of these granites (Table 6-2). T_{CHUR} model ages are 2881 ± 18 and 2808 ± 35 Ma, and T_{DM} model ages are 2871 ± 14 and 2817 ± 25 Ma. These model ages reflect the participation of underlying crustal material with average crustal residence age of 2.8 Ga. Group V granitoids display the most extensive enrichment in Sm/Nd of all magmatic suites under investigation, attesting to extensive reworking of older crustal sources during Irumide tectonism.

6.8 *Discussion*

Eighteen of the nineteen analysed samples, spanning all magmatic suites identified in the Irumide belt and its foreland (the Bangweulu block), have yielded negative ϵ_{Nd} values, indicative of derivation from Sm/Nd enriched crustal sources with significantly higher $^{143}\text{Nd}/^{144}\text{Nd}$ isotopic composition than the chondritic uniform reservoir. The Nd isotopic data give indirect evidence for the possible existence of underlying older sialic crust. T_{CHUR} crustal residence ages confirm an average crustal residence between 2.05 Ga and 3.24 Ga. Given the possibility of mixing between both juvenile and ancient sources in the generation of the magmas, the oldest T_{CHUR} age of 3.24 Ga may give a minimum age of older sections of crustal material underlying the Irumide belt. A plot of T_{CHUR} model ages versus SHRIMP U-Pb zircon crystallisation ages shows the predominantly reworked nature of the magmatic suites (Figure 6-1).

The Mkushi Gneiss (Group II) has a narrow range of T_{CHUR} model ages between 358 and 430 M.y. older than its emplacement age. The narrow range displayed from the two samples, which were sampled from the far southwestern and northeastern portions of the Irumide belt, suggests the participation of source rocks with similar ages, although variable mixing of source rocks with different ages could fortuitously yield the narrow range observed and cannot be ruled out.

The granites and volcanics of the Bangweulu block near Mansa (Group III) yielded very similar Nd-isotopic ratios. The suite displays T_{CHUR} model ages between 116 and 243 M.y. older than the emplacement. This could indicate that similar source magmas were tapped for the generation of the suite, and that similar amounts of crustal assimilation of an isotopically homogeneous crust occurred.

The Irumide volcanics (Group III) appear to be very variable in terms of Nd-isotopic composition. Two extreme end-members were taken from the Luswa River Tuff, for which one sample yielded a T_{CHUR} age 117 M.y. younger than the emplacement age, and another sample yielded a T_{CHUR} age 1359 M.y. older than the emplacement. These data suggest that parts of the Luswa River Tuffs were generated directly from depleted mantle sources, while other parts were generated through extensive interaction between magma and old crustal sources. As mentioned earlier, because of the highly unusual nature of the single juvenile analysis, not much weight is given to this conclusion. The Kachinga Tuff shows a tighter range with T_{CHUR} ages between 676 and 1105 M.y. older than the emplacement ages. These still suggest highly variable sources collected from a very small area or different degrees of assimilation of older crust, but indicate that in this case participation of older crust was prevalent for all samples. The Katibunga Volcanics define a similar range to the Kachinga Tuff, with T_{CHUR} ages between 467 and 1038 M.y. in excess of the emplacement ages. As is the case with the other volcanic suites, the Katibunga basalts suggest high variability in the source magma, or variable amounts of crustal assimilation.

The Lukamfwa Hill Granite Gneisses (Group IV) define T_{CHUR} model ages 671 and 1461 M.y. older than emplacement. These data attest to the assimilation of older crust in the generation of these granitoids.

Group V granitoids define T_{chur} ages 1771 and 1845 M.y. older than the emplacement ages, suggesting a narrow range of magma sources, which have incorporated significant amounts of older crust.

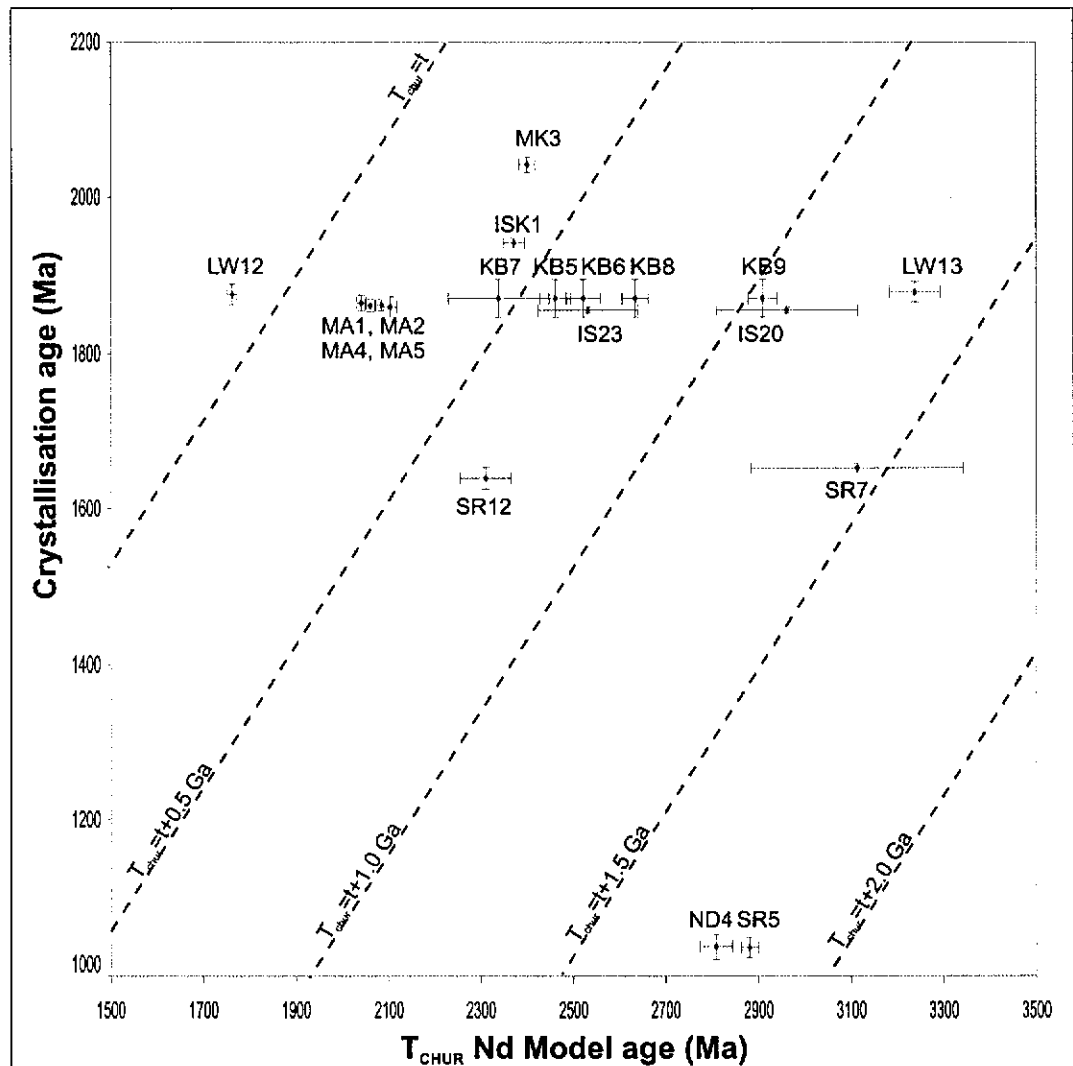


Figure 6-1: T_{chur} model age versus crystallisation age for granitoids and volcanics in the Irumide belt and Bangweulu block, showing the predominantly reworked character of all igneous suites (t =U-Pb SHRIMP emplacement age).

A plot of initial ϵ_{Nd} values versus crystallisation age shows decreasing initial ϵ_{Nd} values with decreasing age (Figure 6-2). The youngest suite has initial ϵ_{Nd} values ranging from -18.4 to -14.6 , while initial ϵ_{Nd} values for the oldest suite

are around -4.3 . The entire range of magmatic suites appears to define a broad growth envelope in which younger suites represent, at least in part, reworked older crust. The Nd-isotopic data therefore suggest that all magmatic suites in the Irumide belt and Bangweulu block were formed through reworking of older crust, with little or no addition of juvenile magma from the depleted mantle. The single sample of the Luswa River Tuff, which has a distinct juvenile signature, provides limited evidence for direct extraction of magma from depleted mantle, but, as this is the only analysis with juvenile character, more work is needed to substantiate this. More work is also needed to investigate why the Katibunga Volcanics have apparently incorporated substantial crustal material, but maintained a basaltic composition.

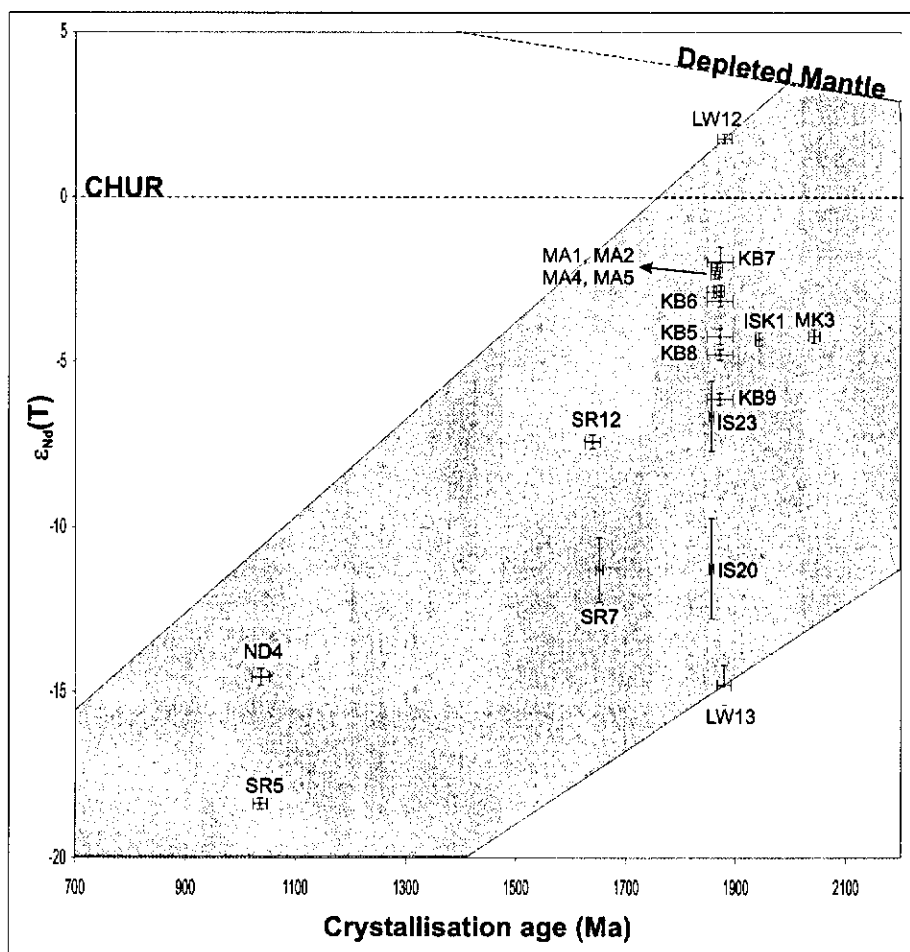


Figure 6-2: Plot of initial ϵ_{Nd} isotopic compositions, relative to that of CHUR (Wasserburg et al., 1981) versus U-Pb SHRIMP zircon crystallisation age. The grey area is the inferred growth envelope modelled on the basis of present day ϵ_{Nd} values for the most juvenile and most ancient end-members.

7 CHAPTER 7: Discussion

7.1 *Regional correlations of the Irumide belt*

7.1.1 Introduction

There are four main regions of Mesoproterozoic tectonism exposed in Zambia and adjacent parts of south-central Africa (Figure 7-1): the Irumide and Kibaran belts on the northwestern and southeastern margins of the Bangweulu block, the Choma-Kalomo block to the west of the Zimbabwe craton, and Mesoproterozoic gneisses in southern Malawi and northwestern Mozambique, adjacent to the eastern and northern margin of the Zimbabwe craton (Cahen et al., 1984; Petters, 1991). Many previous studies have assumed that all these terranes are broadly equivalent and developed during a single orogenic cycle, often termed the “Kibaran cycle”(Kröner, 1977b; Unrug, 1992; Kampunzu, 1997; Kampunzu et al., 2003). In the past, the term “Kibaran” has also been extended to Mesoproterozoic events on the southwestern and southeastern margin of the Kalahari craton in the assumption that the cross-continental Neoproterozoic Damara-Lufilian-Zambezi orogen was the locus of only limited plate motions (Shackleton, 1973; Kröner, 1977b)(Figure 7-1). Most of the proposed correlations were based largely on available geochronological data, which for the Irumide belt were very limited, and which seemed to indicate a continental-scale orogenic event between 1.4 and 1.0 Ga (Burke and Dewey, 1972; Cahen et al., 1984). In view of the new data presented as part of this study, a critical assessment can be made on previously held views and regional correlations in central and southern Africa.

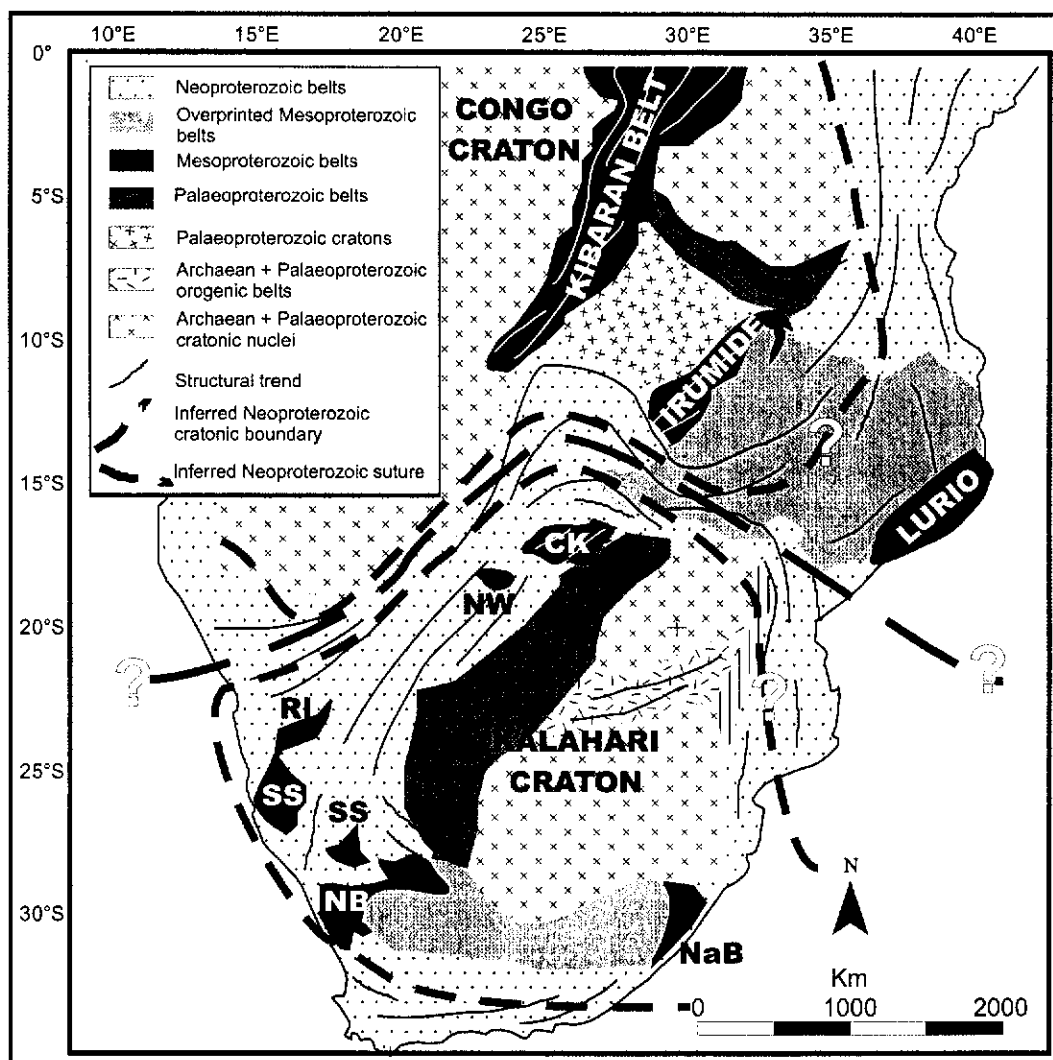


Figure 7-1: Mesoproterozoic tectonic provinces of central and southern Africa. (CK=Choma-Kalomo block; IRUMIDE=Irumide belt; KIBARAN=Kibaran belt; LURIO=foreland to the Lurio belt; NaB=Natal belt; NB=Namaqua belt; NW=northwest Botswana rift; SS=Sinclair sequence; RI=Rehoboth inlier. Question marks indicate uncertain position or continuation of inferred boundaries or suture.

7.1.2 Previous geochronological constraints on Irumide tectonism

There have been two estimates for the timing of Irumide tectonism. Cahen et al. (1984) argued that tectonism occurred at 1355 ± 28 Ma, using a Rb-Sr whole-rock isochron from a phyllonitised granite in northern Malawi, which was interpreted to date resetting of the Rb-Sr clock during the Irumide orogeny (Figure 7-2). Daly (1986b) obtained a broadly similar Rb-Sr whole-rock isochron date of 1407 ± 34 Ma for the Mutangoshi Gneissic Granite near Chinsali (Figure 7-2), but he interpreted this as a pre- to early-tectonic intrusion that preceded the Irumide event. He estimated the age of peak metamorphism and tectonism to be ~ 1100

Ma, based on a whole-rock Rb-Sr date obtained through regression of seven points of the Palaeoproterozoic Mwambwa River Gneiss. More recently, Schenk and Appel (2001) dated metamorphic monazite from a gneiss near Chipata in eastern Zambia (Figure 7-2), placing peak metamorphism in the eastern part of the Irumide belt at 1046 ± 3 Ma. Cox et al. (2002) reported a LA-ICP-MS age of 1043 ± 19 Ma for metamorphic rims on zircon from the Luangwa Gneiss near Luangwa (Figure 7-2), in agreement with the monazite date of Schenk and Appel (2001).

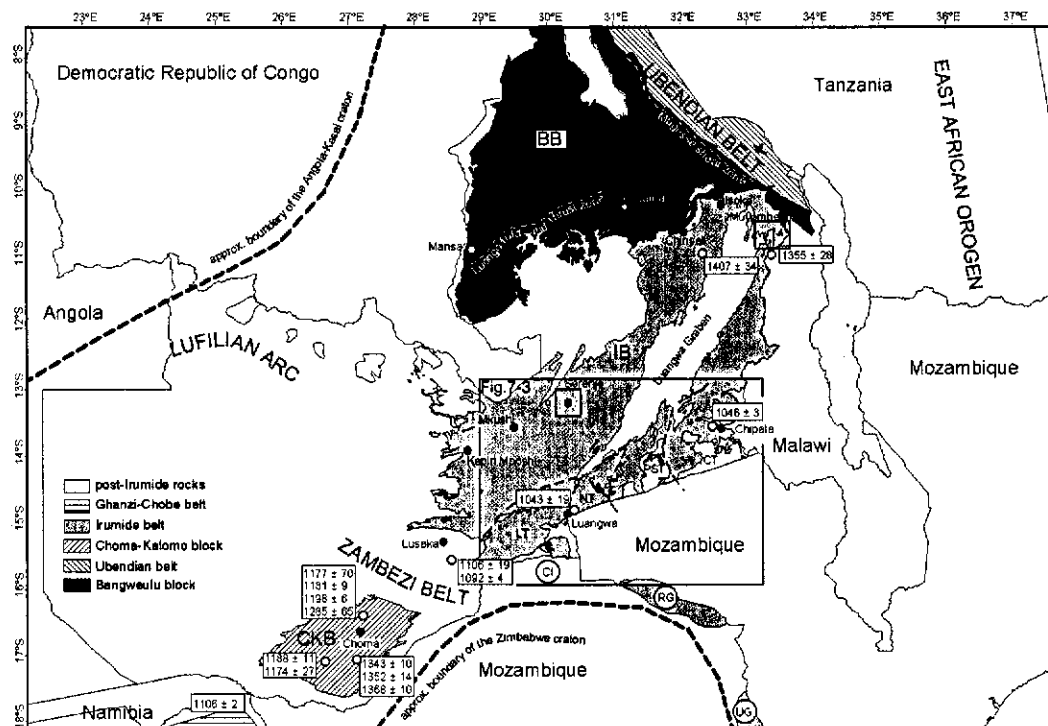


Figure 7-2: Overview of Mesoproterozoic terrains in Zambia. Small squares denote the location of the Serenje map sheet, and the Muyombe map sheet discussed in text. BB=Bangweulu block CI=Chewore Inliers; IB=Irumide belt; LT=Luangwa Terrane; NT=Nyimba Terrane; PST=Petauke-Sinda Terrane; RG=Rushinga Group; UG=Umkondo Group. Box indicates area of Figure 7-3.

7.1.3 Previously proposed correlations

7.1.3.1 *The central African Kibaran belt*

The correlations between the Irumide belt and the Kibaran belt stem from the fact that all available geochronology on both terrains, predominantly consisting of whole-rock Rb-Sr dates, showed a broadly coeval geological

development (Cahen et al., 1967; Cahen, 1970; Cahen et al., 1984; Klerkx, 1987; Tack et al., 1994). Coupled to that, it was observed that the regional trends in both terranes indicated northwest-southeast directed tectonic transport, and that the metasedimentary sequences show comparable continental characteristics (Cahen, 1970; Tembo and Porada, submitted). In the Kibaran belt, extensive granite magmatism has long been considered to have taken place during four magmatic events, spanning between 1350 and 1140 Ma (Klerkx, 1987; Tack et al., 1990; 1994), followed by post-kinematic intrusion of Sn-granites at around 0.97 Ga (Cahen et al., 1984; Caron et al., 1986; Ikingura et al., 1992; Pohl, 1994; Romer and Lehmann, 1995). More recently, this multi-stage evolution, which was predominantly based on whole-rock Rb-Sr dates, has been revised, based on U-Pb dating, into a three-stage model including large volumes of S-type granitoids at ca. 1.38 Ga (Kokonyangi et al., 2001a; 2001b; 2002; Kokonyangi et al., 2004) and, in the eastern part of the Kibaran belt, shear-controlled A-type granitoids emplaced at ca. 1.25 Ga (Tack et al., 1994; Deblond, 1995; Brinckmann et al., 2001), followed by the post-kinematic intrusion of tin-bearing granitoids at ca. 0.97 Ga (Lehmann and Lavreau, 1987; Romer and Lehmann, 1995; Kampunzu et al., 2001). Even with this new well-constrained three-stage evolution for the Kibaran belt, the possibility of a correlation between the Kibaran belt and the Irumide belt remained, largely because age constraints on the Irumide belt have remained equivocal.

Reliable published data, and data presented as part of this study, demonstrate that magmatism in the Irumide belt and its basement is represented at least by five distinct suites: Group I granitoids (2.73 Ga), Group II granitoids (2.05-1.93 Ga); Group III plutono-volcanics (1.88-1.85 Ga); Group IV granitoids (1.65-1.55 Ga) and Group V granitoids (1.05-0.95 Ga). An additional minor ~1.35 Ga magmatic event is recorded in the far northeastern part of the Irumide belt and includes one nepheline-syenite and one biotite granite interpreted as anorogenic plutons (Tembo, 1986; Vrána et al., 2004). With those new robust geochronological constraints, a correlation between the Irumide belt and the Kibaran belt no longer stands up against scrutiny. Neither the 1.38 Ga nor the 1.25 Ga events characterising the Kibaran belt have been identified in the Irumide belt, while none of the magmatic episodes that dominate the history of the Irumide belt

appear to occur in the Kibaran belt. The only magmatic event that broadly coincides for the two regions is the syn-tectonic 1.05 – 0.95 Ga magmatism in the Irumide belt and the post-Kibaran (0.97 Ga) emplacement of tin granitoids in the Kibaran belt. The 0.97 Ga post-Kibaran tin granitoids are commonly interpreted as anorogenic granitoids and could possibly relate to extensional far-field effects of Irumide tectonism. However, according to Pohl (1994) the tin granites were emplaced during a late phase of contraction.

7.1.3.2 Southeastward extension of the Irumide belt

Tectonism in the Irumide belt has previously been linked with Mesoproterozoic events in northern Mozambique and southern Malawi (Andreoli, 1984; Cahen et al., 1984; Sacchi et al., 1984; Daly, 1986b; Pinna et al., 1993). These authors based this correlation on similar northwest-southeast directed tectonic transport and the widespread occurrence of ca. 1100 Ma Rb-Sr dates in northern Mozambique, and suggested that the Irumide belt, Mesoproterozoic lithologies in southern Malawi and northwestern Mozambique and the Lurio belt were part of a linked orogenic system. Recent studies confirm the presence of Mesoproterozoic granitic orthogneisses in the foreland to the Lurio belt, where they were reworked during Neoproterozoic thrusting; similar gneisses occur immediately adjacent to the eastern edge of the Zimbabwe craton. The former yield $^{207}\text{Pb}/^{206}\text{Pb}$ zircon evaporation ages of 1150–929 Ma (Kröner et al., 1997; 2000; 2001), whereas the latter yield U-Pb SHRIMP ages of 1150–1100 Ma (Manhica et al., 2001). In Mozambique, a progressive increase in initial Sr ratio with time was interpreted to document the maturing of an island arc (Pinna et al., 1993). Kröner et al. (1997) reported a zircon xenocryst of 1297 Ma within the Lurio belt, supporting the presence of 1.3 Ga crust in the region. In southern Malawi however, ca. 1.04 – 1.00 Ga magmatism is shown to be entirely juvenile, with initial ϵ_{Nd} values ranging from +2.2 to +3.7 (Kröner et al., 1997). Oliver et al. (1998), Johnson (1999) and Johnson and Oliver (2000; 2004) described allochthonous terranes of accreted oceanic, island-arc and continental-margin lithologies and associated sedimentary assemblages in northeastern Zimbabwe (Chewore Inliers, CI on Figure 7-2). They interpreted an age of 1393 ± 22 Ma for

a plagiogranite to date the age of an ophiolite complex and reported ages ranging between 1.11 and 1.04 Ga for various granitoids in this region. In their interpretation, the occurrence of the ca. 1.4 Ga ophiolite to the southeast of the Irumide belt indicates the existence of an oceanic realm as far back as 1.4 Ga. In their model, the widespread juvenile magmatism between 1.15 and 1.00 Ga recorded in southern Malawi and northwest Mozambique represent continental-margin arc lithologies, later accreted to the southern margin of the Bangweulu block during the Irumide orogeny (Johnson and Rivers, submitted). Whether the Irumide belt reflects an accretionary or a collisional orogen could not be unequivocally stated, but these authors favoured the former. Additional late Mesoproterozoic magmatism in northern Zimbabwe between 1.05 and 1.01 Ga was reported by Hargrove et al. (2003), Dirks et al. (2000) and Müller et al. (2000).

Mapani et al. (2001; submitted) described a series of stacked terranes in eastern Zambia, in what is the southeastward continuation of the Irumide belt to the southeast of the Luangwa Graben (Figure 7-2). They recognised several southeast-dipping, thrust-bound, stacked lithotectonic terranes, which they infer to have been imbricated during Irumide tectonism (Mapani et al., 2001; submitted). Three stacked terranes are dominated by increasingly more distal metasedimentary facies, which they correlate with the Manshya River Group, and which are interpreted as imbricated thrusts of the Irumide belt. Two terranes are considered exotic to the Irumide belt, one of which, the Petauke-Sinda terrane (Figure 7-2), predominantly comprises calc-alkaline intrusives (gabbroic, dioritic, tonalitic and granitic plutons) with supra-subduction zone geochemical signatures (Tembo et al., 2002), together with subordinate supracrustal rocks, and is interpreted as an accreted arc terrane. Preliminary dating of leucocratic biotite granite and foliated biotite gneiss in the Petauke-Sinda terrane yielded zircon LA-ICP-MS ages of 1130-1120 and 938 Ma respectively (Rivers, pers.comm.). The second exotic terrane, termed the Chipata terrane (Figure 7-2), comprises low pressure retrogressed mafic and felsic granulites of supracrustal origin and records a significantly more complex history than the Irumide belt to the northwest. U-Pb SHRIMP dating of parts of the Chipata terrane yielded emplacement ages of 1076 ± 3 Ma, 1050 ± 10 Ma and 1041 ± 9 Ma for various porphyritic biotite granitoids

and an age of 1974 ± 18 Ma for a mafic enclave within the granite (De Waele, unpublished data not reported in this thesis). A U-Pb SHRIMP age on a low Th/U (metamorphic) zircon rim yielded an age of 1047 ± 20 Ma (De Waele, unpublished data not reported in this thesis), confirming the earlier reported U-Pb monazite age of 1046 ± 3 Ma constraining peak metamorphic conditions near Chipata (Schenk and Appel, 2001). In the view of Mapani et al. (2001; submitted), the 1.05 Ga metamorphic ages suggest that the current arrangement of tectonic terranes in eastern Zambia came about during the Irumide orogeny, which they view as having occurred in an Andean or Cordilleran type accretionary orogen.

7.1.3.3 The Choma-Kalomo block of southern Zambia

A critical correlation with respect to regional tectonics is that made across the Neoproterozoic Zambezi belt between the Irumide belt and the Choma-Kalomo block (Figure 7-2). This correlation is based on the apparent alignment of the Irumide belt and Choma-Kalomo block, their similar northeasterly structural trends and their geochronology (Drysdaal et al., 1972; Hanson et al., 1988c). Bulk zircon U-Pb ages of 1352 ± 14 and 1343 ± 6 Ma date the emplacement of two of the main phases of the Choma-Kalomo batholith, whereas a porphyritic granite within the batholith with a U-Pb zircon age of 1198 ± 6 Ma is believed to post-date the main deformation in the Choma-Kalomo block and to provide a lower age limit on the timing of Mesoproterozoic tectonism (Hanson et al., 1988c). To the north of the Choma-Kalomo block near Lusaka, the Mpande Gneiss and Munali Granite yielded U-Pb zircon crystallisation ages of 1106 ± 19 Ma and 1092 ± 4 Ma respectively (Figure 7-2)(Hanson et al., 1988c; Katongo et al., submitted), providing evidence of the existence of late Mesoproterozoic crust below the Zambezi belt.

The older ages reported within the Choma-Kalomo block corresponded closely to the Rb-Sr ages reported by Daly for early to syn-tectonic plutons in the northern Irumide belt (Daly, 1986b), prompting Hanson et al. (1988c) to suggest that the Irumide belt and Choma-Kalomo block represent a single orogen that

occurs on both sides of the Zambezi belt. This correlation was used to suggest limited displacement between the Congo and Kalahari cratons since the late-Mesoproterozoic and found support in the following observations: (i) no Neoproterozoic ophiolites or associated oceanic lithologies had been reported from the Zambezi-Lufilian belt; (ii) age constraints available at the time (predominantly whole-rock Rb-Sr data) suggested the occurrence of a linked Mesoproterozoic orogenic system including the Kibaran belt, Irumide belt, Choma-Kalomo block, Mesoproterozoic lithologies in NW Botswana and central Namibia, Namaqua belt, Natal belt and Lurio belt, and supported the interpretation of the Zambezi belt as an intracratonic feature (Shackleton, 1973; Kröner, 1977b; 1983; Hanson et al., 1988b; Barton et al., 1993; Hanson et al., 1993; Moyes et al., 1993; Wilson et al., 1993; Hanson et al., 1994; Master, 1994; Stern, 1994; Grunow et al., 1996; Kröner et al., 1997; Unrug, 1997; Wilson et al., 1997; Hanson et al., 1998a; Dirks et al., 1999; Dirks and Sithole, 1999; Vinyu et al., 1999; Kampunzu et al., 2000; Hanson, 2003; Kampunzu et al., 2003).

Recent studies and re-interpretation of published work have however identified whiteschist lithologies, ophiolitic complexes and eclogites in northern Zimbabwe and in Zambia (Vrána et al., 1975; Oliver et al., 1998; Johnson and Oliver, 2000; 2002; 2004) and possible relict oceanic crust in the Zambezi belt (John, 2001; John et al., 2003; 2004). The 1.39 Ga Chewore ophiolite provides a minimum age for the existence of an oceanic realm to the southeast of the Bangweulu block. The Chewore inliers also contain a supracrustal sequence dominated by quartzite, which is intruded by a granitoid having a U-Pb SHRIMP zircon age of 1087 ± 9 Ma (Goscombe et al., 2000). Low Th/U rims on this and another granitoid yielded U-Pb ages for peak metamorphism at 1068 ± 21 Ma and 1071 ± 8 Ma, and dated a second metamorphic event at 526 ± 17 Ma (Goscombe et al., 2000). The latter age reflects Pan-African metamorphism, which is interpreted to have extensively reworked the Chewore Inliers. The 1.08-1.06 Ga granitoids and metamorphism are interpreted to record a juvenile addition of crust within the oceanic terrane, similar to the widespread 1.15-0.93 Ga juvenile granitoids reported in northwestern Mozambique, southern Malawi and the Lurio belt (Jourde and Wolff, 1974; Costa et al., 1983; Pinna et al., 1993; Kröner et al., 1997; 2000; 2001; Manhica et al., 2001; Johnson and Oliver, 2004). John (2001)

and John et al. (2001; 2003; 2004) presented P-T estimates and geochemistry on eclogites within the Zambezi belt, which indicate subduction depths up to 90 kilometers, with low geothermal gradients of 8°C / km supporting the subduction of relatively cold crust. The eclogites show similar incompatible element depletion patterns as magmatic rocks formed at recent oceanic spreading centres and are consequently interpreted to be former oceanic crust. Eclogite facies metamorphism was dated using a Sm-Nd garnet-whole-rock isochron age of 595 ± 10 Ma. U/Pb dating on monazites from whiteschist lithologies in both the Copperbelt and Zambezi belt of Zambia indicate that whiteschist formation and subsequent collision between the Congo and Kalahari cratons took place at ca. 530 Ma (John et al., 2004).

The data presented in this study further discredit the proposed link between the Choma-Kalomo block and the Irumide belt by providing the first reliable age constraints on magmatism and peak metamorphism in the Irumide belt. These new data show that the magmatic evolution of the two terranes is markedly different. The two main phases of magmatism recognised in the Choma-Kalomo block, constrained between 1368 ± 10 and 1343 ± 6 Ma, and between 1198 ± 6 Ma and 1174 ± 27 Ma (Hanson et al., 1988a; Bulambo et al., 2004), are not recognised in the Irumide belt, except possibly the Mivula Syenite and Ntendele Metatonalite dated by Vrána et al. (2004). Conversely, the magmatic phases recognised in the Irumide belt, especially the main 1.05 – 0.95 Ga syn- to post-kinematic magmatism, seem to be absent in the Choma-Kalomo block, except perhaps the Phoenix Mine pegmatites. On the basis of these markedly dissimilar geochronological histories, it seems likely that the southern margin of the Bangweulu block was positioned some distance away from the Choma-Kalomo block at around 1350 and 1200 Ma, as it bears no imprint of 1.35 and 1.20 Ga magmatic events, and that the Choma-Kalomo block was similarly some distance from the Irumide belt at around 1000 Ma, as it lacks 1.05-0.95 Ga magmatism. Although profound differences exist between the Choma-Kalomo block and the Irumide belt, striking similarities between the Choma-Kalomo block and the central African Kibaran belt are apparent. Both areas record magmatism at around 1.38-1.35 Ga, and 1.20 Ga. The link between the Kibaran belt and the Choma-Kalomo block had earlier been suggested by Unrug (1992), on the basis of

broad geochronological similarities, similar regional tectonic trends and the occurrence of cassiterite and tin-bearing lithologies in both terranes. The idea that the Choma-Kalomo block may represent a displaced part of the central Kibaran belt certainly merits further investigation.

7.1.3.4 Mesoproterozoic events in the Kalahari craton

The Kalahari craton comprises Archaean and Palaeoproterozoic crust, to which two Mesoproterozoic belts have been added between 1.2 and 1.0 Ga, namely the Namaqua belt of southern Namibia and western South Africa, and the Natal belt of northeastern South Africa (Schultz et al., 1983). The present northwestern margin of the Kalahari craton is the site of the late Mesoproterozoic Kgwebe volcanics in the northwest Botswana rift. These volcanics comprise a bimodal volcanic suite of within-plate tholeiitic basalt and rhyolite (Kampunzu et al., 1998) with zircon U-Pb crystallisation ages of 1106 ± 2 and 1106 ± 4 Ma (Schwartz et al., 1996; Singletary et al., 2003). The northwest Botswana Rift sequences are correlated with the Sinclair sequence of southern Namibia, in which volcanics yielded a zircon U-Pb age of ca. 1.10Ga and granites were emplaced at between 1377 and 1216 Ma (Hoal and Heaman, 1994, 1995). This rifting is interpreted to be the result of extensional stresses related to collision at the southern margin of the Kalahari craton, but is also coeval with the Umkondo mafic igneous province within the Kalahari craton, which is constrained at 1.10 Ga (Hanson et al., 1998b; Wingate, 2001).

The Namaqua and Natal belts have been considered part of a linked orogenic system based on geochronology and aeromagnetic maps (Jacobs et al., 1993; Jacobs and Thomas, 1994). However, the eastern part of the Namaqua belt comprises reworked Archaean and Palaeoproterozoic crust, while the Natal belt consists entirely of juvenile Mesoproterozoic additions to the Kaapvaal craton (Thomas et al., 1993; Jacobs and Thomas, 1994; Clifford et al., 1995; Jacobs et al., 1997; Robb et al., 1999; Grantham et al., 2001; McCourt et al., 2001; Thomas and Jacobs, 2001; Johnston et al., 2002). Both the Natal and Namaqua provinces are characterised by orogenic granitoid intrusion spanning 1.20 – 1.04 Ga. Peak

metamorphic conditions in the Namaqua terrane occurred around 1.15 Ga and 1.02 Ga (Thomas et al., 1994; Robb et al., 1999), while peak conditions in the Natal province are recorded at 1.18 Ga (McCourt et al., 2002) and at 1.06 Ga (Thomas et al., 1996). Fitzsimons (2000) and Jacobs et al. (2003a; 2003b) used similarities in age of plutonism and metamorphism, and the continuation of aeromagnetic anomalies into Dronning Maud Land (Antarctica) to argue that the Namaqua-Natal belt continues into Dronning Maud Land. Jacobs et al. (1993; 2003a; 2003b) considered the Namaqua-Natal-Maud belt the result of indentation tectonics at the southern margin of the Kalahari craton between 1.09 and 1.06 Ga. Dalziel (2000) and Jacobs et al. (2003a; 2003b) suggested that the Llano orogenic belt of Texas could have been the opposing margin to the Namaqua-Natal-Maud belt, and that the Kalahari craton indented into Laurentia at around 1.1 Ga. This model is supported by similarities in age between the Llano and Namaqua-Natal-Maud belts, the compatible kinematic characteristics of both belts, the coeval (1.1 Ga) Keeweenawan and Umkondo magmatic provinces and associated rifts, and the permissible palaeomagnetic position for Laurentia adjacent to Kalahari at 1.10 Ga (Dalziel et al., 2000). In an alternative model, Powell et al. (2001) placed Kalahari away from Laurentia at 1.1 Ga, proposing only a possible convergence with Laurentia at between 1.06 and 1.03 Ga, and a different rotation of the Kalahari craton, placing the Namaqua-Natal province away from the Laurentian margin. A recent paper by Hanson et al. (2004) links coeval intraplate magmatism at ~1.1 Ga in Laurentia and Kalahari to the presence of plume activity beneath the two cratons in the time frame during which Rodinia is assumed to have assembled. Hanson et al. (2004) further suggest that, because palaeomagnetic data show the two cratons cannot be adjacent at 1.1 Ga, this plume activity is very extensive.

7.2 *Regional tectonic interpretation*

7.2.1 Background

Taking into account the new results on the Irumide belt and published data, an attempt will be made to fit the Irumide belt into a tentative tectonic model. In view of the convergent setting of the Irumide belt, three models can reasonably be considered: intracratonic, accretionary or collisional.

An intracratonic setting for the Irumide belt would require the presence of continental crust below the entire orogen, horizontal displacements along basement-cover detachment zones and a dominance of vertical movements and within-plate anorogenic magmatism (Kröner, 1977a, 1977b, 1981, 1983, 1984). This study has demonstrated the presence of 2.05 – 1.93 Ga basement below the Irumide belt, which would argue in favour of an intracratonic setting. Towards the southeast, however, these basement lithologies appear to be missing, as evidenced by the juvenile character of ~1 Ga granitoids in southern Malawi (Kröner et al., 2001) and in northwestern Mozambique (Pinna et al., 1993), possibly indicating that the cratonic margin lies in the poorly documented area to the southeast of the known Irumide belt. Daly (1986b) calculated significant amounts of crustal shortening within the Irumide belt, and ascribed the reported “vertical tectonics” of the Irumide belt (Ackermann and Forster, 1960; Fitches, 1971) to a “pop-up” structure related to overall northwest-verging tectonic transport. Daly (1986b) considered that tectonics in the Irumide belt was related to a continent-continent collision to the present southeast of the Irumide belt, with transmission of stress and displacements over considerable distances within the continental crust. The significant horizontal displacements within the Irumide belt, the apparent presence of basement in the studied area and the apparent lack of basement ages and abundance of more juvenile lithologies to the southeast (northwest Mozambique and southern Malawi) are here taken to indicate that the part of the Irumide belt studied in this thesis lies just inboard of a cratonic margin to the southeast.

Marginal settings (accretionary and collisional) are best seen as end members of a spectrum of orogens, with reported transitions from an accretionary style into a collisional style as reported for the Grenville belt (Rivers and Corrigan, 2000; Gower and Krogh, 2002), the Alpine belt (Stampfli et al., 1998; O'Brien, 2001) and the Himalayan belt (Hodges, 2000; O'Brien, 2001).

Accretionary orogens are formed through subduction of oceanic crust below an older continental block, giving rise to voluminous calc-alkaline magmatism and considerable vertical accretion, coupled with significant lateral accretion due to the addition of oceanic plateaus, microcontinents or oceanic arcs which are riding on the subducting oceanic plate (Windley, 1992). If these juvenile additions are relatively small, subduction may proceed unchanged, or subduction zones may step-back or even flip (Windley, 1992). In other cases terrane accretion may lead to cessation of magmatism and a termination of arc activity altogether (Moores and Twiss, 1995). The main characteristics of accretionary orogens are dominant juvenile calc-alkaline magmatism, longevity of accretionary processes, and extensional and compressive environments (i.e. arc/back arc and accretionary prism), which are overprinted by short regional compressive events (when oceanic arcs or microcontinents accrete)(Murphy and Nance, 1991; Windley, 1992; Sengör and Natal'in, 1996).

Collisional orogens are formed through the introduction of a large buoyant fragment of crust into a consuming margin. Depending on the nature of the fragments of crust involved, collisional orogens can be formed between an arc and a continent or between two continents. The nature of the margins involved, the number of subduction zones, and the direction of subduction all have an impact on the characteristics of the collisional orogen. Generally, collisions will have a significant impact on the geometry of the crust involved and on the kinematics of the plates. In the majority of cases a collision marks the end of subduction processes along a margin (Moores and Twiss, 1995). Collisional processes at one margin often have global repercussions as they offset the budget of subduction. The loss of a consuming margin in a collisional orogen is often balanced by increased rates of subduction elsewhere or the generation of new subduction zones, changing the plate tectonic system worldwide. The numerous available

scenarios that can lead to a collisional orogen mean that no two collisional orogens are alike. The characteristics of a collisional orogeny depend among other things on the shape and physical characteristics of the continents involved and their relative motions. Nevertheless, continental collision is dominantly marked by extensive crustal thickening, bivergent thrust geometry and post-orogenic collapse leading to delamination of the lithosphere, asthenospheric rise and resulting post-orogenic magmatism. An important point to note is that collision is the end phase of convergence, and that accretion of terranes may have preceded collision. It is therefore common to find exotic arcs and/or microcontinents within a collisional belt (e.g. Trans-Hudson Orogen, Hoffman, 1989; e.g. Altaid Orogen, Sengör et al., 1993).

7.2.2 The nature of the foreland and basement to the Irumide belt

Pre-Irumide basement units exposed in the Irumide belt include ~2.05–1.93 Ga igneous rocks, and are related to the Palaeoproterozoic development of the Bangweulu block s.l.. One granitoid within the western Irumide belt was dated at 2.73 Ga, and, together with ~2.7 Ga ages on xenocrystic zircons within granitoids and aplites, indicates a Neoarchaeon component in the Bangweulu block. T_{DM} model ages for granitoids and volcanics within the Irumide belt support the presence of Archaean basement below the Irumide belt, with T_{DM} model ages as old as 3.2 Ga. Direct age constraints on plutono-volcanic rocks of the Bangweulu block s.s. presented in this study refine previously reported ages to 1.87 – 1.86 Ga and record relatively juvenile additions to the Bangweulu block s.l., with some addition of reworked older crust. The presence of Palaeoproterozoic and possibly Archaean basement below the portion of the Irumide belt studied here strongly suggests that the Irumide belt s.s. is entirely underlain by the southeastern continental margin of the Bangweulu block s.l., which in itself appears to comprise three different components (Group I, II and III) which were assembled prior to deposition of the Muva Supergroup at ca. 1.9 Ga.

7.2.3 Supracrustal sequences

The metasedimentary successions exposed in the Irumide belt (Manshya River Group and Kanona Group) appear to be Palaeoproterozoic in age as indicated by: (i) the absence of detrital zircon younger than ~1.85 Ga; (ii) ~1.88-1.85 Ga rhyolites and pillow basalts interstratified within the Muva succession; (iii) occurrence of rafts interpreted to be derived from the Kanona and Manshya River Group in the ~1.65 – 1.60 Ga Lukamfwa Hill Granite Gneiss, Musalongo Gneiss and Lubu Granite Gneiss. Age constraints on a quartzite from the Mporokoso Group on the Bangweulu block support a coeval deposition, indicating that the Manshya River/Kanona Group and Mporokoso Group sedimentary rocks are related to the evolution of the Bangweulu block and the adjacent Palaeoproterozoic Ubendian orogenic system. Detrital provenance data presented for the Kasama Formation on the Bangweulu block, which is interpreted as a fluvial succession derived from the Mporokoso Group succession to the northwest, indicate a maximum age of deposition for these fluvial sediments at 1.43 Ga. No minimum age can be ascribed to this sequence. The Kasama Formation so far represents the only evidence of Mesoproterozoic sedimentation in northern Zambia.

The metasedimentary successions of eastern Zambia and northwestern Mozambique are relatively poorly known. Johns et al. (1989) described three metasedimentary successions in the southeastern Irumide belt. The oldest records two deformation events and consists of granulites and gneisses of presumed sedimentary parentage. These successions were considered to predate deposition of a metasedimentary sequence of quartzite and pelite called the Mchinji Group in Malawi (Thatcher and Wilderspin, 1968). Johns et al. (1989) correlated the Mchinji Group with various sequences in eastern Zambia (Figure 7-3), including parts of the Mwami Formation of Vavrda (1974), the Sasare Group of Phillips (1965) and the Sasare Group plus part of the Fombwe Group of Barr and Drysdall (1972), parts of the Sasare Group of Agar (1983), the Chimpi sequence of Keppie (1995) and the Mpanshya Group of Barr (1974). Agar and Ray (1983) reported that sequences correlated with the Mchinji Group can be laterally traced into the

Manshya River Group. This, together with similar deformation characteristics between the Manshya River Group and the Mchinji Group and its correlatives in eastern Zambia, strongly suggest continuation of the Palaeoproterozoic Muva Supergroup towards the southeast. Vavrda (1974) reported that part of the metasedimentary succession near Chipata is of considerably lower metamorphic grade and appears to post-date Irumide deformation and ascribed these quartzites and pelites to the Mwami Group.

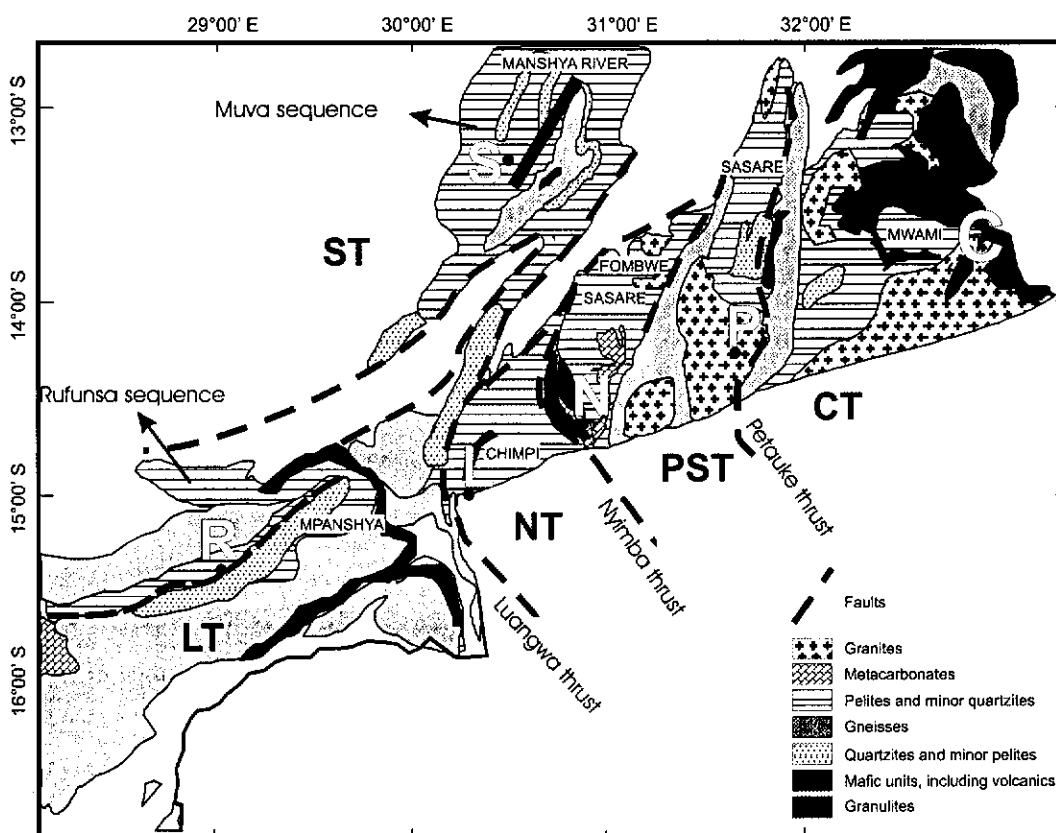


Figure 7-3: Simplified geological map of the southeastern part of the Irumide belt in eastern Zambia, indicating tectonic terranes (black lettering) discussed in the text: ST=Serenje Terrane, LT=Luangwa Terrane, NT=Nyimba Terrane, PST=Petauke-Sinda Terrane, CT=Chipata Terrane. Towns indicated with white lettering: R=Rufunsa, S=Serenje, L=Luangwa, N=Nyimba, P=Petauke and C=Chipata. Possible correlatives of the Muva Supergroup are labelled.

In northwest Mozambique, the Chiure Group was first defined by Jourde and Wolff (1974) to comprise a high- to medium grade supracrustal sequence, structurally overlying high grade migmatites and granulites of the Lurio belt. The group includes mafic rocks at the base, graphitic schist and gneiss with carbonate in the middle, and quartzite, schist and conglomerate at the top but also includes high-pressure mafic rocks, serpentinite and other ultramafic rocks interpreted as

ophiolites (Sacchi et al., 1984). The Chiure Group is intruded by low-K calc-alkalic rocks, gabbro, anorthosite and orogenic granite, and is associated with marine metasedimentary rocks. It was interpreted by Pinna et al. (1993) as a tectonic melange with rocks of various origin including immature island-arc, oceanic sediments, and oceanic crust, and intruded by a wide range of plutons. A better understanding, leading to regional correlations of the supracrustal sequences and a synthesis of events in northern Mozambique, awaits further work and perhaps provides the key to understanding the Irumide belt.

7.2.4 Granitoids within the Irumide belt

During this study, a suite of granitoids was identified within the Irumide belt, which was emplaced at between 1.65 and 1.55 Ga. This is one of the first records of ~1.6 Ga magmatism in southern Africa (cf. Seth et al., 2003). These granitoids contain septae of metasedimentary rocks ascribed to the Manshya River and Kanona Groups, on the basis of preserved ghost stratigraphy not apparent in the older paragneisses of the Mulungwizi Gneiss. This suggests that the 1.65 to 1.55 Ga granitoids were emplaced in situ, within the Bangweulu block and overlying supracrustal sequences. Geochemical data suggest a collisional or within-plate setting for these granitoids, while negative initial ϵ_{Nd} values and T_{DM} model ages between 3.03 and 2.43 Ga suggest significant crustal reworking in their generation. Minimum zircon saturation temperatures of over 860°C suggest relatively dry melting conditions, with significant thermal heat flux in the lower crust. Mechanisms that would provide sufficient heat for dehydration melting include the action of a mantle plume, delamination processes allowing asthenospheric rise during extensional collapse or extensional processes. No ~1.6 Ga metamorphic or structural event has been recognised accompanying this intrusion event within the Irumide belt, leaving the mechanism of emplacement of these granitoids unresolved at present.

Minor late Mesoproterozoic magmatism has been recognised in the far northeastern part of the Irumide belt by Tembo (1986) and Vrána et al. (2004), comprising anorogenic emplacement of the Mivula syenite at 1.36 Ga and the

emplacement of the Ntendele biotite metatonalite at 1.33 Ga. Neither of these intrusions appear to be linked to tectonism at the time, and their significance in the evolution of the Irumide belt is unclear. No additional ~ 1.3 Ga magmatism has been recognised as part of this study, indicating the regionally and volumetrically limited nature of the intrusions. A better understanding of the nature and setting of 1.3 Ga plutonism requires further work.

The main magmatism occurred syn- to late- and post-kinematically and is bracketed between 1.05 and 0.95 Ga, with the majority of intrusions at around 1.03 Ga. These granitoids predominantly show orogenic A-type affinities and are the result of crustal melting of older crust. Their initial ϵ_{Nd} values are strongly negative, and T_{DM} model ages range between 2.87 to 2.81 Ga. Minimum zircon saturation temperatures for the granitoids suggest temperatures in excess of 780°C. The extensive involvement of older crust suggests significant heat influx during their generation. Since the intrusion of the granitoids overlaps with peak metamorphic conditions, this heat flux could be linked to post-orogenic collapse. Other possible processes providing heat flux necessary for extensive reworking of the Bangweulu block basement could involve delamination of the mantle during collisional or accretionary processes to the southeast of the Irumide belt, slab-break off after arrested subduction, impingement of a mantle plume or extensional processes allowing uprise of asthenosphere. Considering the dominance of compressional structures and clear lack of mafic and/or bimodal intrusives in the Irumide belt, the latter is considered the least likely.

7.2.5 Timing of Irumide tectonism

Metamorphic conditions in the Irumide belt have been constrained at 1021 ± 16 and 1018 ± 5 Ma in the southwestern Irumide belt, and at 1004 ± 16 Ma in the northeastern Irumide belt through U-Pb geochronology on low Th/U zircon overgrowths in high-grade granitoids and gneisses. Although these dates are statistically indistinguishable, some minor diachroneity along strike may be present, where peak conditions were reached some 10 M.y earlier in the southwest than in the northeast. This slight diachroneity along strike within the Irumide belt

may be explained through oblique docking of a continental mass with the Bangweulu block (and in extenso the Congo craton) should the Irumide belt be interpreted as collisional, or could indicate the docking of separate smaller crustal fragments at slightly different times should the Irumide belt be accretionary.

Published estimates in the southeastern parts of the Irumide belt place the timing of peak metamorphic conditions at 1046 ± 3 Ma (Chipata granulite, Schenk and Appel, 2001) and 1043 ± 19 Ma (Luangwa Gneiss, Cox et al., 2002). These dates clearly indicate a diachronous metamorphic front across strike, similar to conditions recorded in the Lachlan belt of southeast Australia (Gray and Willman, 1991; Gray, 1997; Foster and Gray, 1999, 2000; Foster et al., 2000) and also recorded in the Appalachians (Keppie, 1989). These older (1.05 Ga) peak metamorphic ages to the southeast (Schenk and Appel, 2001; Cox et al., 2002; Schenk and Appel, 2002), however, document (ultra)high temperature and low-pressure conditions, suggesting that metamorphism is related to intrusion of hot arc magma rather than collision. Goscombe et al. (2000) also dated low-pressure – high-temperature granulite-facies metamorphism in the Chewore inliers at 1.08 Ga, which was related to the voluminous intrusion of hot magma into the arc and metasedimentary rocks. The across-strike variation of peak-metamorphism, as well as the seemingly different metamorphic conditions strongly support an accretionary model for the Irumide belt, culminating in an arc-continent or continent-continent collision at 1.02 Ga.

It is worth noting that a single analysis on a low Th/U rim in the Serenje area yielded a (concordant) date of 554 ± 20 Ma, which is interpreted to document tectonism during the Damara-Lufilian-Zambezi orogeny. Interestingly, K-Ar biotite dates further north in the Serenje map sheet record a thermal overprint between 567 ± 24 Ma and 495 ± 20 Ma, while muscovite does not, having dates between 885 ± 36 and 755 ± 30 Ma (Vail et al., 1968). Although it is unwise to put much weight on these controversial K-Ar constraints, these data do seem to indicate that the thermal front of Neoproterozoic tectonism did not affect lithologies north of Serenje. Vrána et al. (2004) reported $^{40}\text{Ar}/^{39}\text{Ar}$ muscovite ages from the Muyombe sheet in the far northeastern Irumide belt (Figure 7-2) between 888 ± 6 and 852 ± 6 Ma and interpreted younger apparent ages in the first gas

fractions released to indicate limited Neoproterozoic overprints. $^{40}\text{Ar}/^{39}\text{Ar}$ data presented by Daly (1986b) on hornblende from the Chinsali map sheet (Figure 7-2) range between 1017 ± 30 and 907 ± 27 Ma, while K-Ar results on biotite show only a few reset ages of ca. 500 Ma and a predominance of dates around 1.0 Ga. The K-Ar data and $^{40}\text{Ar}/^{39}\text{Ar}$ data for the northeastern Irumide belt thus indicate limited influence of Neoproterozoic tectonism.

7.2.6 Metamorphic grade

The metamorphic grade in the Irumide belt is recorded in metapelites, which show lower greenschist facies assemblages towards the Bangweulu block foreland in the northwest, increasing to upper amphibolite and local granulite facies in the southeast. The abundance of cordierite - andalusite and sillimanite - garnet, and relative paucity of kyanite, indicate medium-pressure (MP) and high-temperature (HT) conditions. In the southeastern extension of the Irumide belt, Mapani et al. (2001) report sillimanite - cordierite and cordierite - garnet assemblages, while near Chipata (Figure 2-5 and Figure 7-3), Schenk and Appel (2001) document ultra high temperature (UHT), low pressure (LP) assemblages of cordierite - hercynite (spinel) - quartz, which formed from garnet and sillimanite. Schenk and Appel (2001) describe a retrograde path with formation of rims of garnet - clinopyroxene - quartz over orthopyroxene in mafic rocks, and neoformation of garnet and sillimanite at the expense of cordierite - spinel - quartz. The formation of kyanite - muscovite \pm chlorite - quartz assemblages indicates that pressures at 550°C, when cordierite broke down, were still quite high. Schenk and Appel (2001) further argued that the UHT conditions in the southeastern Irumide belt are related to massive intrusion of high-temperature granitoids into the metasedimentary pile but point out that ca. 1.05 Ga granitoids were only reported further east in Malawi (Haslam et al., 1986). My own work around Chipata, not included in this study, has yielded zircon U-Pb SHRIMP ages of 1076 ± 3 , 1050 ± 10 and 1041 ± 9 Ma from various granitoids, and low Th/U metamorphic rims have yielded an age of 1047 ± 20 Ma, supporting the presence of syn-kinematic magmatism in the region.

The LP-(U)HT conditions prevalent in the Irumide Orogen do not seem to be in keeping with a collisional setting for the belt, during which extensive crustal thickening, followed by high erosion rates and isostatic rebound, would have led to the exhumation of HP-lithologies within the lower part of the orogen. It must be pointed out, however, that to date no in-depth studies have been conducted on metamorphism in the Irumide belt, leaving any inference based on the available literature speculative.

7.3 *The Rodinia hypothesis*

The possible existence of a late Mesoproterozoic supercontinent, comprising many, if not all, of the Precambrian cratons, has been considered for quite some time (Piper, 1976; Morel and Irving, 1978). More recently, this hypothetical supercontinent, named Rodinia by McMenamin and McMenamin (1990), has been the subject of quite some speculation. Constructions have been proposed and challenged based on geological and palaeomagnetic considerations, none of which can be unequivocally accepted (Piper, 1987; McMenamin and McMenamin, 1990; Dalziel, 1991; Hoffman, 1991; Moores, 1991; Smethurst et al., 1998; Weil et al., 1998; Piper, 2000; Buchan et al., 2001; Powell et al., 2001; Wingate, 2002; Li et al., 2003; Meert and Torsvik, 2003; Pesonen et al., 2003; Pisarevsky et al., 2003; Li et al., 2004). The controversial aspects of any Rodinia construction include the number and nature of participating cratons, their relative position and orientation, and the timing of assembly and break-up.

A very useful tool in testing the workability of a continental configuration is palaeomagnetism. A well-defined palaeopole must satisfy the rigorous criteria proposed by Buchan and Halls (1990), and a grading system has been proposed by Van der Voo (1990) based on seven reliability criteria. This includes a well-defined age of the pole, adequate proof that the magnetic remanence is primary, and adequate structural control over possible post-magnetisation tilting to allow correction. A rigorously defined pole can help disprove a proposed configuration, or can add weight to a proposed model through demonstrating whether a proposed position is allowable or not. Nevertheless, a palaeomagnetically allowable fit

(permissible) can be downgraded to an implausible fit using geological constraints. Geological matching of adjacent continental blocks is mainly based on continuity of tectonic belts and or older lineaments/dyke swarms and on the presence of the expected type of margin (passive or active) for a proposed fit. A plausible fit is characterised by a permissible fit based on reliable paleomagnetic data alone, coupled with a reasonable geological match of adjacent blocks. To date, no consensus has been reached over the exact nature of the Rodinia supercontinent, because the geological, geochronological and palaeomagnetic constraints on Proterozoic palaeogeography are distributed very unevenly in time and space. Palaeomagnetic poles for the period between 1100 and 750 Ma are rare, and those that do exist rarely meet more than three of the reliability criteria of Van der Voo (1990), and must therefore be treated with caution. Figure 7-4 shows one possible model for the Rodinia continent at 1020 Ma after Pisarevski et al. (2003) with a modified position for Siberia after Pisarevski and Natapov (2003). Note that no palaeomagnetic poles are available for the majority of continental masses.

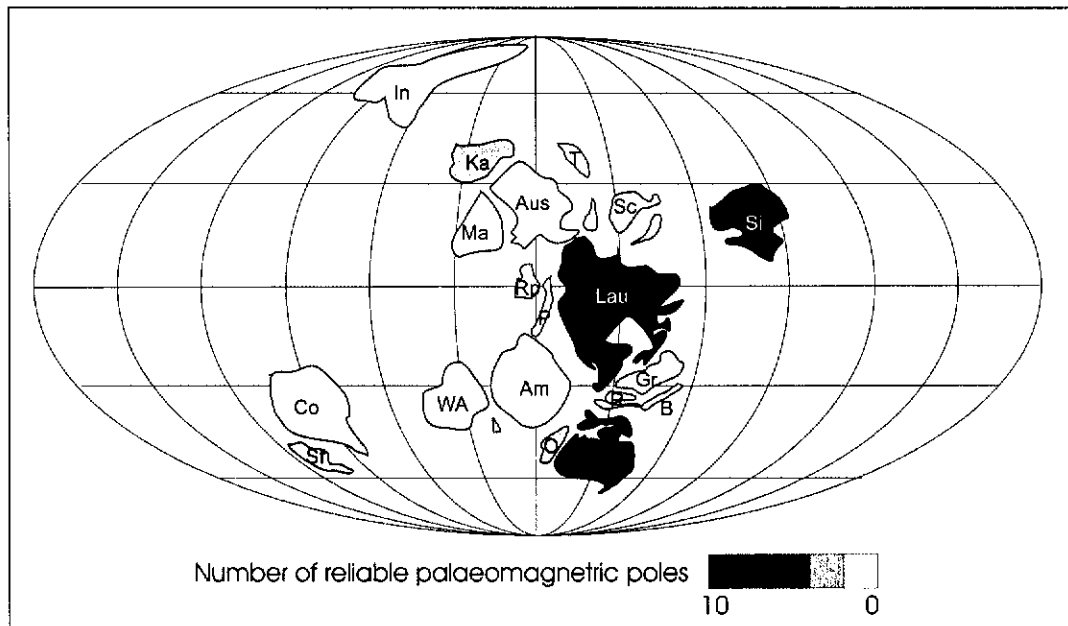


Figure 7-4: One possible configuration of the Rodinia continent at ca. 1.02 Ga, showing the number of palaeomagnetic poles per landmass, which satisfy at least four of the seven criteria of reliability of Van der Voo (1990). The relative position of the continental blocks is taken after Pisarevski et al. (2003) and Pisarevski and Natapov (2003). In=India; Ka=Kalahari; Ma=Mawson; Aus=Australia; T=Tarim; Sc=South China; Si=Siberia; Lau=Laurentia; Rp=Rio de la Plata; P=Pampean terrane; Am=South American cratons; Gr=Greenland; R=Rockall; B=Barentsia; O=Oaxaquia; Ba=Baltica; WA=West Africa; Co=Congo; Sf=Saõ-Francisco.

Over the years, several such configurations have been proposed, which have quite a lot of common characteristics (see examples in Figure 7-5): (i) many reconstructions are centered around Laurentia for which a reasonable number of reliable data are present, and which is flanked by a the Mesoproterozoic Grenville belt and by post-Rodinia passive margins; (ii) east Gondwana (India + Madagascar, (east) Antarctica and Australia), pre-assembled or not, lies to the north of Laurentia; (iii) Baltica generally lies to the south or southeast of Laurentia; (iv) Amazonia, Rio de la Plata and West Africa, for which few reliable palaeomagnetic data are available, are held in fixed relative position to each other, following Trompette (1994).

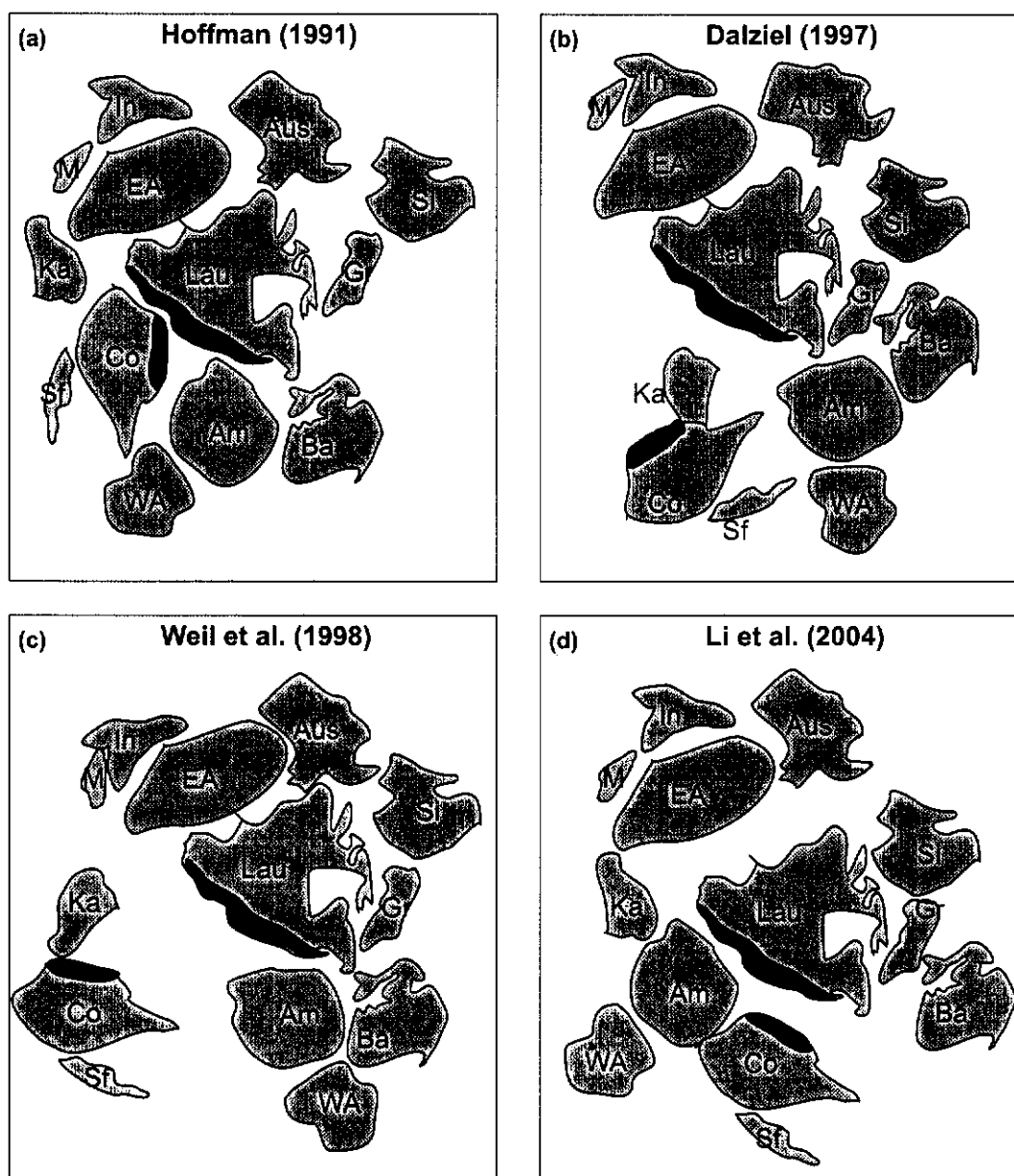


Figure 7-5: Various simplified schematic models for Rodinia, after assembly. The approximate position of the Irumide and Grenville belt are shown in black (M=Madagascar; other abbreviations as in Figure 7-4)(Hoffman, 1991; Dalziel, 1997; Weil et al., 1998; Li et al., 2004).

As can be observed from the models, the Irumide belt can either face another continent (Laurentia in Figure 7-5 (a) and (d)), or is depicted to face an open ocean at ca. 1.0 Ga (Figure 7-5 (b) and (c)). Where the southern margin of the Congo craton (present day coordinates) is juxtaposed to Laurentia (Figure 7-5 (a) and (d)), the Irumide belt would oppose the Grenville belt of northern America. Collisional tectonics in the Grenville is constrained between 1080 and 980 Ma in the north (Gower and Krogh, 2002), which in general terms overlaps with peak conditions in the Irumide belt. In the south, peak conditions on the

Laurentian margin span 1150-1120 Ma (Dalziel et al., 2000), which significantly predates Irumide tectonism. Based on that, a slight modification of the original configuration proposed by Hoffman (1991), rotating the Congo craton so that the Irumide belt faces the Laurentian margin, would be the preferred model. Given the fact that the Irumide belt may represent an accretionary orogen rather than collisional, the options in which the Bangweulu block margin faces an open ocean also need to be considered (Figure 7-5 (b) and (c)).

7.3.1 Conclusions

New and previously published data on the Irumide belt clearly point out that:

- (i) Large parts of the orogen overlie continental crust of the Bangweulu block s.l.
- (ii) The Muva Supergroup supracrustals are the ~1.8 Ga Ubendian molasse deposits. The undeformed portion on the Bangweulu block comprises the Mporokoso Group, while the deformed sequences in the Irumide belt make up the Manshya River and Kanona Groups.
- (iii) No Mesoproterozoic sedimentary basin along the southeastern margin of the Bangweulu block has been identified so far. Either successions deposited along the southeastern margin of the Bangweulu block are yet to be identified, or were eroded during post-orogenic exhumation, or lie further southeast where the geological record is disrupted by Pan-African tectonism.
- (iv) Granitoid magmatism between 1.65 and 1.60 Ga within the Irumide belt, with crust-dominated affinity, documents the first record of a magmatic event at that time along the southeastern margin of the Bangweulu block. T_{DM} crustal residence dates for two granitoids are ~2.4 and ~3.0 Ga, with initial ϵ_{Nd} values of -7.4 to -11.3. No unequivocal structural or metamorphic imprint can be associated with that event, and clarification awaits additional work.
- (v) Regionally defined thrust tectonics show a northwest-vergent geometry with minor southeast-vergent backthrusts.

- (vi) Major syn-, late- and post-kinematic magmatism is characterised by substantial reworking of crust. T_{DM} crustal residence dates for two granitoids are ~2.8 Ga, with initial ϵ_{Nd} values of -14.6 to -18.4.
- (vii) Discrete exotic terranes are present to the southeast of the Irumide belt, including 1.1 Ga juvenile arcs and 1.4 Ga oceanic crust. Extensive Pan-African reworking does, however, obscure their geotectonic setting, and they may have been juxtaposed against the southeastern Irumide belt during Pan-African tectonism.
- (viii) Peak metamorphism is constrained at 1.02 Ga in the Irumide belt s.s., and at 1.05 Ga in the southeast part of the Irumide belt. Metamorphic grade within the Irumide belt s.s. is of MP/HT character, while to the southeast MP/UHT granulite facies prevailed. To date, no detailed work has been conducted on metamorphism in the Irumide belt, and a full understanding of metamorphic conditions awaits future work.

Taken together, the lack of juvenile volcanic arc magmatism along the southeastern margin of the Bangweulu block, voluminous Irumide-age granite magmatism and the apparent termination of orogenic or magmatic activity after 1.02 Ga would argue for a collisional setting for the Irumide belt. The abundance of MP metamorphic assemblages, as opposed to HP assemblages, would be more consistent with an accretionary setting for the belt, although MP assemblages are widely described in collisional orogens as well. The presence of juvenile arcs to the southeast of the Irumide belt can be consistent with both collisional and accretionary settings and, together with the 1.4 Ga Chewore ophiolite documented by Oliver et al. (1998), indicate the presence of an ocean realm to the southeast of the Bangweulu block, within which any number of subduction zones could have been active, forming juvenile ocean island arc complexes. The widespread occurrence of small ultramafic and mafic bodies in NW Mozambique, associated with deep marine sedimentary rocks, and HP assemblages could represent ophiolitic melanges associated with the arc complexes. Nevertheless, extensive Pan-African reworking in the southeastern Irumide belt and further southeast in southern Malawi and northwestern Mozambique, together with the lack of recent studies, hamper a full understanding of the geological history of the region.

The challenge for future research lies in the study of the southeastward extension of the Irumide belt, where lithologies are poorly documented, and where strong overprints by Neoproterozoic events (Zambezi and/or East African orogeny) complicate the understanding of the area. It is quite possible that significant components of the Irumide orogen are located in the area to the southeast of the Luangwa graben, including Mesoproterozoic sediments deposited along the southeastern Bangweulu margin, exotic terranes accreted to that margin during Irumide tectonism (possibly including fragments of an indenting cratonic block), remnant ophiolitic complexes marking the suture between the Bangweulu block and a postulated southern continental block and rift sequences associated with subsequent rifting of the southern craton after collision. Alternatively, such terranes, if ever present, could have been rifted away before Neoproterozoic assembly of the Kalahari and Congo cratons.

8 APPENDIX A: List of samples collected during this study

Table 8-1: Samples collected during this study. ¹thin section made; ²whole-rock major and trace geochemistry conducted; ³zircon U-Pb SHRIMP date obtained; ⁴isotope geochemistry conducted.

ID	UTM coordinates		Geographic coordinates		Map sheet	Description	TS ¹	CH ²	S ³	Nd ⁴	
	Meters		Lat	Long							
	X	Y									
Samples collected in 1998											
SI/98/2A	36L	213117	8520891	-13.3137	30.3684	Serenje	biotite granite (fine grained phase)	N	Y	N	N
SI/98/2B	36L	213117	8520891	-13.3137	30.3684	Serenje	biotite granite (porphyritic phase)	N	Y	N	N
SI/98/3	36L	215717	8518021	-13.3319	30.3920	Serenje	biotite granite	N	Y	N	N
SI/98/5	36L	216935	8511786	-13.3964	30.4018	Serenje	porphyritic granite	N	Y	N	N
SI/98/6	36L	216935	8511786	-13.3964	30.4018	Serenje	porphyritic granite	N	Y	N	N
SI/98/10	36L	211178	8521025	-13.3121	30.3506	Serenje	leucocratic gneiss (Myemba Hills)	N	Y	N	N
SI/98/11	36L	180638	8553354	-13.0152	30.0754	Serenje	foliated biotite granite (Sasa granite)	Y	Y	N	N
SI/98/12	36L	180286	8553398	-13.0147	30.0731	Serenje	foliated biotite granite (Sasa granite)	N	Y	N	N
SI/98/12B	36L	180286	8553398	-13.0147	30.0731	Serenje	foliated biotite granite (Sasa granite)	N	Y	N	N
Collected in 1999 ²											
KV-1	36L	340988	8680938	-11.8911	31.5676	Kalibunga Mission	volcanic	N	Y	N	N
KV-3	36L	340988	8680938	-11.8911	31.5676	Kalibunga Mission	volcanic	Y	N	N	N
KV-4	36L	342628	8680349	-11.8966	31.5826	Kalibunga Mission	volcanic	N	Y	N	N
KV-6	36L	342628	8680349	-11.8966	31.5826	Kalibunga Mission	volcanic	N	Y	N	N
KV-7	36L	342628	8680349	-11.8966	31.5826	Kalibunga Mission	volcanic	N	Y	N	N
KV-8	36L	342628	8680349	-11.8966	31.5826	Kalibunga Mission	volcanic	N	Y	N	N
MTG-1	36L	434521	8617949	-10.8645	32.4381	Chinsali	chibubana granite	N	Y	N	N
MTG-3	36L	434521	8617949	-10.8645	32.4381	Chinsali	chibubana granite	Y	N	N	N
MTG-4	36L	440400	8618110	-10.8636	32.4918	Chinsali	chibubana granite	Y	Y	Y	N
MTG-6	36L	398323	8785898	-10.9522	32.1044	Chinsali	chibubana granite	N	Y	N	N
MTG-8	36L	398323	8785898	-10.9522	32.1044	Chinsali	chibubana granite	Y	N	N	N
MTGG-1	36L	442826	8616360	-10.8796	32.5138	Chinsali	mutangoshi gneissic granite	Y	Y	Y	N
MTGG-2	36L	442826	8616360	-10.8796	32.5138	Chinsali	mutangoshi gneissic granite	N	Y	Y	N
MTGG-3	36L	442826	8616360	-10.8796	32.5138	Chinsali	mutangoshi gneissic granite	N	Y	N	N
MOG-1	36L	285106	8598578	-12.6259	31.0434	Mupamadzi River	grey granite (Mununga Quarry)	N	Y	N	N
SQG-2	36L	199856	8531597	-13.2148	30.2486	Serenje	porphyritic granite (Serenje Quarry)	Y	Y	Y	N
SQX-1	36L	199856	8531597	-13.2148	30.2486	Serenje	pegmatite cutting SQG-2	N	Y	N	N
SASA-2	36L	181355	8554812	-13.0040	30.0832	Serenje	foliated biotite granite (Sasa granite)	Y	N	Y	N
SER-5-3	36L	187279	8541074	-13.1270	30.1349	Serenje	porphyritic granite	N	Y	Y	N
SER-6-2C	36L	211176	8521025	-13.3121	30.3506	Serenje	biotite granite	Y	Y	Y	N
SER-6-2F	36L	211176	8521025	-13.3121	30.3506	Serenje	biotite granite	Y	N	N	N
SER-6-2	36L	211176	8521025	-13.3121	30.3506	Serenje	biotite granite	N	Y	N	N
SER-6-3	36L	215797	8518921	-13.3319	30.3927	Serenje	biotite granite (Lukamwa Hill)	Y	Y	Y	N
SER-6-4	36L	216257	8512779	-13.3873	30.3958	Serenje	porphyritic granite (Chimuma Hill)	Y	Y	Y	N
SER-6-6	36L	220800	8509890	-13.4142	30.4370	Serenje	migmatite (Lukusashi river)	Y	Y	Y	N
SER-6-7	36L	219114	8507940	-13.4314	30.4211	Serenje	migmatite (Fukwe river)	N	Y	Y	N
ZM31	36L	398948	8782043	-10.9851	32.0914	Chinsali	volcanic	Y	N	Y	N
ZM32	36L	399090	8782036	-11.0171	32.0762	Chinsali	granite				
ZM36	36L	285106	8598578	-12.6259	31.0434	Mupamadzi River	grey granite (Mununga Quarry)	N	N	Y	N
Collected in 2000											
IL1	36L	368365	8814255	-10.6911	31.8158	Iiondola Mission	Red Siltstone	Y	N	N	N
IL2	36L	368365	8814255	-10.6911	31.8158	Iiondola Mission	Red Siltstone	Y	N	N	N
IL3	36L	368274	8814018	-10.6932	31.8148	Iiondola Mission	Volcanic	Y	Y	Y	N
IL4	36L	368298	8813769	-10.6955	31.8150	Iiondola Mission	Siltmanite schist	Y	N	N	N
IL5	36L	370473	8820393	-10.6361	31.8538	Iiondola Mission	Sugary Quartzite	N	N	Y	N
IL6	36L	370473	8820393	-10.6361	31.8538	Iiondola Mission	Red Siltstone	N	N	N	N
IL7	36L	370473	8820393	-10.6361	31.8538	Iiondola Mission	Red Siltstone	Y	N	N	N
IL8	36L	360247	8836662	-10.4882	31.7623	Iiondola Mission	Haematite Quartzite	Y	N	Y	N
IL9	36L	369968	8814536	-10.6889	31.8484	Iiondola Mission	Haematite Quartzite	Y	N	Y	N
IL10	36L	377834	8808876	-10.7409	31.9197	Iiondola Mission	Micaceous Quartzite	N	N	Y	N
IL11	36L	382898	8817541	-10.6832	31.9650	Iiondola Mission	Recrystallised Quartz	Y	N	Y	N
IL12	36L	383184	8819412	-10.6463	31.9697	Iiondola Mission	Recrystallised Quartz	Y	N	Y	N
IL13	36L	381572	8787919	-10.9282	31.7689	Iiondola Mission	Recrystallised Quartz	Y	N	Y	N
IL14	36L	383181	8785691	-10.9485	31.7832	Iiondola Mission	Chembwesu Quartzite	N	N	Y	N
IS1	36L	459503	8855920	-10.3237	32.6694	Isoka	Andalusite Schist	Y	N	N	N
IS2	36L	459320	8855283	-10.3294	32.6677	Isoka	Andalusite Schist	Y	N	N	N
IS3	36L	457843	8853618	-10.3443	32.6541	Isoka	Rhyolitic Tuff	Y	Y	Y	N
IS4	36L	458965	8853946	-10.3415	32.6642	Isoka	Andalusite Schist	Y	N	N	N
IS5	36L	458202	8854380	-10.3375	32.6665	Isoka	Andalusite Schist	Y	N	N	N
IS6	36L	457783	8852725	-10.3524	32.6533	Isoka	Biotite Quartzite	Y	N	Y	N
IS7	36L	457631	8852543	-10.3540	32.6520	Isoka	Rhyolitic Tuff	Y	Y	Y	N
IS8	36L	457631	8852543	-10.3540	32.6520	Isoka	Schist	Y	N	N	N
IS9	36L	457631	8852543	-10.3540	32.6520	Isoka	Rhyolitic Tuff	Y	Y	Y	N
IS10	36L	457285	8852201	-10.3571	32.6487	Isoka	Rhyolitic Tuff	Y	Y	Y	N
IS11	36L	457085	8852001	-10.3589	32.6468	Isoka	Rhyolitic Tuff	Y	Y	Y	N
IS12	36L	457016	8852120	-10.3578	32.6464	Isoka	Schist	Y	N	N	N
IS13	36L	458910	8852040	-10.3585	32.6454	Isoka	Schist	Y	N	N	N
IS14	36L	458821	8851843	-10.3603	32.6446	Isoka	Rhyolitic Tuff	Y	Y	Y	N
IS15	36L	457703	8851975	-10.3592	32.6526	Isoka	Andalusite Schist	Y	N	N	N

ID	UTM coordinates		Geographic coordinates		Map sheet	Description	TS ¹	CH ²	S ³	Nd ⁴	
	Meters		Lat	Long							
	X	Y									
Collected in 2000 (continued)											
IS16	36L	457828	8853525	-10.3452	32.6521	Isoka	Sugary Quartzite	Y	N	Y	N
IS17	36L	458200	8852900	-10.3507	32.6390	Isoka	Schist	Y	N	N	N
IS18	36L	457070	8853374	-10.3465	32.6470	Isoka	Schist	Y	N	N	N
IS19	36L	456837	8853282	-10.3473	32.6448	Isoka	Dark Rhyolitic Tuff	Y	Y	Y	N
IS20	36L	456837	8853282	-10.3473	32.6448	Isoka	Rhyolitic Tuff	Y	Y	Y	Y
IS21	36L	456837	8853282	-10.3473	32.6448	Isoka	Rhyolitic Tuff	Y	Y	Y	N
IS22	36L	456837	8853282	-10.3473	32.6448	Isoka	Rhyolitic Tuff	Y	Y	Y	N
IS23	36L	456693	8853338	-10.3468	32.6435	Isoka	Dark Rhyolitic Tuff	Y	Y	Y	Y
IS24	36L	456693	8853338	-10.3468	32.6435	Isoka	Rhyolitic Tuff	Y	Y	Y	N
IS25	36L	462200	8858300	-10.3024	32.6942	Isoka	Quartzite	Y	N	Y	N
KB1	36L	340981	8681210	-11.8886	31.6676	Katibunga Mission	Oriented Rhyolite Sch	Y	N	N	N
KB2	36L	340981	8681210	-11.8886	31.6676	Katibunga Mission	Rhyolite	Y	Y	Y	N
KB3	36L	340851	8681014	-11.8904	31.6664	Katibunga Mission	Gabbro	Y	Y	Y	N
KB4	36L	341707	8679672	-11.9026	31.6741	Katibunga Mission	Basalt	Y	Y	Y	N
KB5	36L	341707	8679672	-11.9026	31.6741	Katibunga Mission	Basalt	Y	Y	Y	Y
KB6	36L	342130	8679928	-11.9003	31.6780	Katibunga Mission	Basalt	Y	Y	Y	Y
KB7	36L	342277	8680082	-11.8990	31.6793	Katibunga Mission	Basalt	Y	Y	Y	Y
KB8	36L	342611	8680909	-11.8915	31.6825	Katibunga Mission	Basalt	Y	Y	Y	Y
KB9	36L	343098	8681226	-11.8887	31.6870	Katibunga Mission	Basalt	Y	Y	Y	Y
LW1	36L	420177	8781538	-10.9920	32.3037	Luswa River	Grey Granite	Y	Y	Y	N
LW2	36L	423119	8774587	-11.0550	32.3299	Luswa River	Luswa Syenite	Y	Y	Y	N
LW3	36L	424090	8772883	-11.0705	32.3386	Luswa River	Recrystallised Quartz	Y	N	Y	N
LW4	36L	424090	8772883	-11.0705	32.3386	Luswa River	Recrystallised Quartz	Y	N	Y	N
LW5	36L	422800	8786000	-11.1325	32.3261	Luswa River	Micaceous Quartzite	Y	N	Y	N
LW6	36L	422818	8783974	-11.1508	32.3261	Luswa River	Micaceous Quartzite	Y	N	Y	N
LW7	36L	425591	8785815	-11.1345	32.3516	Luswa River	Biotite Gneiss	Y	Y	Y	N
LW8	36L	425591	8785815	-11.1345	32.3516	Luswa River	Amphibolite	Y	Y	Y	N
LW9	36L	427977	8785802	-11.1348	32.3734	Luswa River	Pegmaticic Granite	Y	Y	Y	N
LW10	36L	425012	8785724	-11.1352	32.3463	Luswa River	Biotite Gneiss	Y	Y	Y	N
LW11	36L	421575	8774810	-11.0547	32.3157	Luswa River	Biotite Granite	N	Y	Y	N
LW12	36L	398866	8782095	-10.9846	32.0907	Luswa River	Rhyolite	Y	Y	Y	Y
LW13	36L	398866	8782095	-10.9846	32.0907	Luswa River	Rhyolite	N	Y	Y	Y
LW14	36L	398866	8782095	-10.9846	32.0907	Luswa River	Rhyolite	Y	Y	Y	N
LW15	36L	398900	8782100	-10.9846	32.0910	Luswa River	Micaceous Quartzite	Y	N	Y	N
SH1	36L	338955	8780489	-11.1731	31.5591	Shiwa N'Gandu	Micaceous Quartzite	Y	N	Y	N
SH2	36L	338827	8780748	-11.1707	31.5580	Shiwa N'Gandu	Ferruginous Quartzite	Y	N	Y	N
SH3	36L	353210	8781285	-11.1676	31.6895	Shiwa N'Gandu	Recrystallised Quartz	Y	N	Y	N
SH4	36L	354950	8781200	-11.1686	31.7053	Shiwa N'Gandu	Recrystallised Quartz	Y	N	Y	N
SH6	36L	370832	8780660	-11.1753	31.8504	Shiwa N'Gandu	Ferruginous Quartzite	Y	N	Y	N
SH7	36L	380405	8753979	-11.2366	31.9372	Shiwa N'Gandu	Micaceous Quartzite	Y	N	Y	N
SH8	36L	390036	8749282	-11.2801	32.0248	Shiwa N'Gandu	Biotite Granite	Y	Y	Y	N
SH9	36L	394223	8749833	-11.3027	32.0628	Shiwa N'Gandu	Biotite Granite	Y	Y	Y	N
LWC	36L	413835	8754173	-11.2384	32.2429	Luswa River	Granite	N	N	N	N
Collected in 2001											
CC1	36L	771955	8405764	-14.4071	35.5221	Chin'gombe Mission	micaceous quartzite	N	Y	N	N
CC2	36L	772147	8405886	-14.4060	35.5239	Chin'gombe Mission	amphibolite	Y	Y	Y	N
CC3	36L	773017	8406038	-14.4046	35.5320	Chin'gombe Mission	micaceous kyanite quartzite	N	Y	N	N
CC4	36L	778561	8420598	-14.2730	35.5833	Chin'gombe Mission	musc-biot-gneiss	Y	Y	Y	N
CC5	36L	778821	8420240	-14.2762	35.5858	Chin'gombe Mission	porphyritic granite	Y	Y	Y	N
CC6	36L	779737	8407718	-14.3894	35.5943	Chin'gombe Mission	micaceous quartzite	N	Y	N	N
CC7A	36L	778971	8407034	-14.3956	35.5872	Chin'gombe Mission	mixed granite-quartzite	Y	Y	N	N
CC7B	36L	778971	8407034	-14.3956	35.5872	Chin'gombe Mission	mixed granite-quartzite	N	Y	N	N
CC8	36L	778971	8407034	-14.3956	35.5872	Chin'gombe Mission	porphyritic granite	Y	Y	Y	N
CC9	36L	788000	8408522	-14.3821	35.6709	Chin'gombe Mission	garnet amphibolite	N	Y	Y	N
CC10	36L	788820	8407294	-14.3932	35.6785	Chin'gombe Mission	porphyritic granite	Y	Y	N	N
CC11A	36L	807582	8409394	-14.3740	35.8525	Chin'gombe Mission	mylonitic biotite schist	N	Y	N	N
CC11B	36L	807582	8409394	-14.3740	35.8525	Chin'gombe Mission	muscovite-biotite schist	N	Y	N	N
CC12	36L	808403	8409476	-14.3733	35.8602	Chin'gombe Mission	crinulated muscovite schist	N	Y	N	N
CC12B	36L	808403	8409476	-14.3733	35.8602	Chin'gombe Mission	crinulated muscovite schist	N	N	N	N
CC13	36L	810398	8408094	-14.3858	35.8787	Chin'gombe Mission	magnetite bearing quartzite	N	Y	N	N
CHL1	36L	325850	8655106	-12.1221	31.4236	Chilonga Mission	schist	N	Y	N	N
CHL2	36L	334728	8645317	-12.2116	31.5055	Chilonga Mission	biotite gneiss	N	Y	Y	N
CHL3	36L	306508	8655422	-12.1166	31.2482	Chilonga Mission	schist	Y	Y	N	N
CHL4	36L	293978	8641257	-12.2425	31.1313	Chilonga Mission	granite	Y	Y	Y	N
CHL5	36L	285049	8618196	-12.4491	31.0459	Chilonga Mission	granite gneiss	Y	Y	Y	N
CHT1	36L	237826	8581260	-12.7743	30.8046	Chitambo Mission	biotite granite gneiss	Y	Y	Y	N
CHT2	36L	233744	8590210	-12.6930	30.5706	Chitambo Mission	biotite granite gneiss	Y	Y	Y	N
CHT3	36L	241665	8582007	-12.7682	30.6419	Chitambo Mission	muscovite schist	Y	Y	N	N
CHT4	36L	258291	8583960	-12.7534	30.7948	Chitambo Mission	aplite cutting porphyritic granite	N	Y	Y	N

Appendix B: Mineral separation

ID	UTM coordinates		Geographic coordinates		Map sheet	Description	TS ¹	CH ²	S ³	Nd ⁴	
	Meters	Decimal degrees	Lat	Long							
Collected in 2001 (continued)											
CHT5	36L	251502	8590935	-12.6895	30.7337	Chilambo Mission	quartzite	Y	Y	N	N
CHT8	36L	277679	8581736	-12.7766	30.8725	Chilambo Mission	biotite granite gneiss	Y	Y	Y	N
FW1	36L	782982	8487463	-13.6684	35.6242	Fiwila Mission	porphyritic granite	Y	Y	Y	N
FW2	36L	782992	8487463	-13.6684	35.6242	Fiwila Mission	aplite cutting porphyritic granite	Y	Y	Y	N
ISK1	36L	478669	8964875	-10.2443	32.8449	Isoka	porphyritic granite	Y	Y	Y	Y
ISK2	36L	474742	8869408	-10.2030	32.8094	Isoka	porphyritic granite	Y	Y	Y	N
KAS1	36L	308424	8871532	-10.1675	31.2759	Kasama	quartzite	N	Y	N	N
KK1	35L	667006	8419000	-14.2854	34.5491	Kakulu (Mulungushi)	porphyritic granite	N	Y	Y	N
KMP1	35L	680907	8478748	-13.7458	34.6799	Kapiri Mposhi	granite gneiss	Y	Y	Y	N
KN1	36L	240337	8560125	-12.9652	30.6258	Kanona	biotite granite gneiss	N	Y	Y	N
KN2A	36L	261782	8545668	-13.0991	30.8204	Kanona	porphyritic granite	Y	Y	Y	N
KN2B	36L	261782	8545668	-13.0991	30.8204	Kanona	aplite cutting porphyritic granite	Y	Y	Y	N
KN3	36L	261527	8555206	-13.0131	30.8197	Kanona	kyanite quartzite	N	Y	N	N
KN4	36L	268038	8558599	-12.9836	30.8801	Kanona	biotite granite gneiss	Y	Y	Y	N
KN5	36L	268419	8560852	-12.9634	30.8840	Kanona	biotite granite gneiss	Y	Y	Y	N
KN6	36L	272538	8537093	-13.1782	30.9179	Kanona	biotite granite gneiss	Y	Y	Y	N
KN7A	36L	271845	8536077	-13.1872	30.9113	Kanona	biotite granite gneiss	Y	Y	Y	N
KN7B	36L	271845	8536077	-13.1872	30.9113	Kanona	biotite granite gneiss	N	Y	N	N
KN8	36L	270430	8531747	-13.2260	30.8976	Kanona	porphyritic granite	Y	Y	Y	N
KN9A	36L	270430	8531747	-13.2260	30.8976	Kanona	biotite granite gneiss	Y	Y	Y	N
KN9B	36L	270430	8531747	-13.2260	30.8976	Kanona	biotite granite gneiss	Y	Y	N	N
KTB1	36L	373224	8716460	-11.5745	31.8872	Katibunga Mission	biotite muscovite gneiss	N	Y	Y	N
MA1	35L	703280	8752905	-11.2673	34.8928	Mansa	granite	Y	Y	Y	Y
MA2	35L	704363	8753204	-11.2646	34.9028	Mansa	granite	Y	Y	Y	Y
MA3	35L	704363	8753204	-11.2646	34.9028	Mansa	volcanic	Y	Y	Y	N
MA4	35L	705119	8771837	-11.0961	34.9101	Mansa	volcanic	N	N	Y	Y
MA4B	35L	705119	8771837	-11.0961	34.9101	Mansa	volcanic	N	Y	N	N
MA5	35L	700600	8780856	-11.0145	34.8889	Mansa	volcanic	N	Y	Y	Y
MA6	35L	698778	8789360	-10.9375	34.8524	Musonda falls	quartzite	Y	Y	Y	N
MA7	35L	698778	8789360	-10.9375	34.8524	Musonda falls	conglomerate	N	Y	N	N
MA8	35L	698778	8789360	-10.9375	34.8524	Musonda falls	siltstone	N	Y	N	N
MA9	35L	699304	8820014	-10.6601	34.7864	Musonda falls	granite	Y	N	Y	N
MA9B	35L	699304	8820014	-10.6601	34.7864	Musonda falls	aplite cutting granite	N	Y	N	N
MH1	35L	695919	8373506	-14.6977	34.8158	Mita Hills	porphyritic granite	N	Y	Y	N
MH2	35L	700277	8374917	-14.6861	34.8564	Mita Hills	teclonised conglomerate	N	Y	N	N
MH3A	35L	728041	8396022	-14.4948	35.1146	Mita Hills	amphibolite	N	Y	N	N
MH3B	35L	728041	8396022	-14.4948	35.1146	Mita Hills	amphibolite	N	Y	N	N
MH3C	35L	728041	8396022	-14.4948	35.1146	Mita Hills	amphibolite	N	N	Y	N
MH4	35L	735589	8403178	-14.4302	35.1847	Mita Hills	porphyritic granite	N	Y	Y	N
MH5	35L	751887	8414222	-14.3306	35.3360	Mita Hills	musc-biot-garnet-gneiss	Y	Y	Y	N
MH6	35L	755647	8409900	-14.3697	35.3708	Mita Hills	amphibolite	Y	Y	N	N
MH7	35L	756667	8406516	-14.3822	35.3803	Mita Hills	calc-silicate	Y	Y	N	N
MH8A	35L	760151	8394678	-14.5073	35.4125	Mita Hills	metavolcanic	N	Y	N	N
MH8B	35L	760151	8394678	-14.5073	35.4125	Mita Hills	metavolcanic	N	Y	N	N
MH9A	35L	751193	8432140	-14.1685	35.3297	Mita Hills	porphyritic granite+aplite	N	Y	N	N
MH9B	35L	751193	8432140	-14.1685	35.3297	Mita Hills	aplite cutting porphyritic granite	N	Y	Y	N
MH9C	35L	751193	8432140	-14.1685	35.3297	Mita Hills	porphyritic granite	N	N	Y	N
MH10	35L	751041	8436820	-14.1253	35.3283	Mita Hills	porphyritic granite	N	Y	N	N
MK1	35L	765123	8475576	-13.7759	35.4589	Mkushi	micaceous quartzite	Y	Y	Y	N
MK2	35L	763232	8482494	-13.7133	35.4414	Mkushi	biot-musc-granite	Y	Y	Y	N
MK3	35L	731647	8457755	-13.9367	35.1490	Mkushi	granite gneiss	Y	Y	Y	Y
MK4	35L	731647	8457755	-13.9367	35.1490	Mkushi	aplite in granite gneiss	N	Y	Y	N
MK5	35L	731630	8457034	-13.9432	35.1488	Mkushi	pink granite	Y	Y	Y	N
MK6	35L	755048	8457750	-13.9370	35.3856	Mkushi	porphyritic granite	Y	Y	Y	N
MK7	35L	728268	8455259	-13.9592	35.1176	Mkushi	biotite granite gneiss	Y	Y	Y	N
MK8	35L	721965	8501327	-13.5426	35.0601	Mkushi	conglomerate	Y	Y	N	N
MK9	35L	721561	8502349	-13.5333	35.0564	Mkushi	quartzite	N	Y	N	N
MK10	35L	737902	8513128	-13.4361	35.2075	Mkushi	quartzite	Y	Y	N	N
MK11	35L	748850	8505058	-13.5092	35.3086	Mkushi	schist	N	Y	N	N
MK12	35L	748850	8505158	-13.5083	35.3086	Mkushi	biotite granite gneiss	Y	Y	Y	N
MK13A	35L	759668	8492078	-13.6266	35.4076	Mkushi	illimanite schist	Y	N	N	N
MK13B	35L	759668	8492078	-13.6266	35.4076	Mkushi	illimanite schist	N	Y	N	N
ML1	36L	426880	8885937	-10.0498	32.3745	Muliansolo	conglomerate	Y	Y	Y	N
ML2	36L	434165	8838424	-10.4796	32.4367	Shiwa N'Gandu	granite gneiss	Y	Y	Y	N
MUN	36L	285106	8998578	-12.6259	31.0434	Mupamadzi River	mununga granite	Y	Y	Y	N
ND1	35L	811611	8507001	-13.4914	35.8885	Ndabala	porphyritic granite	N	Y	Y	N
ND2	35L	811909	8515465	-13.4149	35.8912	Ndabala	granite gneiss	N	Y	Y	N
ND3	35L	811909	8515465	-13.4149	35.8912	Ndabala	aplite cutting granite gneiss	Y	Y	N	N
ND4	35L	818119	8520019	-13.3736	35.9484	Ndabala	diorite	N	Y	Y	Y
ND6	35L	818015	8539101	-13.2011	35.9472	Ndabala	syenite	N	Y	Y	N

ID	UTM coordinates		Geographic coordinates		Map sheet	Description	TS ¹	CH ²	S ³	Nd ⁴	
	Meters		Decimal degrees								
	X	Y	Lat	Long							
Collected in 2001 (continued)											
ND6	36L	818015	8539101	-13.2011	35.9472	Ndabala	aplite cutting syenite	N	Y	Y	N
SR1	36L	219500	8510422	-13.4091	30.4252	Serenje	musc-sill-garnet schist	N	Y	N	N
SR2	36L	220800	8509890	-13.4142	30.4370	Serenje	migmatite (Lukusashi)	N	Y	N	N
SR3	36L	222708	8503558	-13.4716	30.4534	Serenje	musc-biot-sill-garnet schist	N	Y	N	N
SR4	36L	222910	8503675	-13.4706	30.4553	Serenje	migmatite (Fukwe)	N	Y	N	N
SR5	36L	218257	8512779	-13.3873	30.3958	Serenje	porphyritic granite (Chifuma)	N	Y	Y	Y
SR6	36L	216425	8519406	-13.3277	30.3966	Serenje	biotite granite gneiss	N	Y	Y	N
SR7	36L	215797	8518921	-13.3319	30.3927	Serenje	biotite granite gneiss (Lukamfwa)	N	Y	Y	Y
SR8	36L	217200	8511200	-13.4017	30.4041	Serenje	biot-sill-garnet schist (Kamena)	N	Y	N	N
SR9	36L	199766	8531840	-13.2126	30.2478	Serenje	porphyritic granite	Y	Y	Y	N
SR10	36L	187279	8541074	-13.1270	30.1349	Serenje	porphyritic granite	Y	Y	Y	N
SR11	36L	180278	8553687	-13.0121	30.0731	Serenje	leucocratic granite	N	Y	Y	N
SR12	36L	187170	8524331	-13.2777	30.1306	Serenje	biotite granite gneiss	Y	Y	Y	Y

9 APPENDIX B: Mineral separation

9.1 Crushing

Sample chips were broken into chips of $< 2\text{cm}$ that can fit into a tungsten carbide ring mill used for reduction. The crushing was done either with a jaw crusher (see above) or hydraulic press, and the resulting chips were cleaned on 2mm mesh using tap water. The washing ensured that small grains and surficial dust were removed prior to crushing in the mill. A small amount of dried sample was fed into the ring mill and crushed for several seconds, after which the sample was sieved over 200 to 300 μm disposable mesh. The portion of sample not passing the mesh was put back into the mill, together with the next amount of sample. The procedure was repeated until the entire sample passed through the mesh. In cases where no disposable mesh was available (in Zambia), a 250 μm sieve was used. Prior to each sample, the sieve was meticulously cleaned using water, compressed air, and a steel brush. The sieve was inspected on a light table, and grains that remained lodged in the mesh manually pushed out using a steel pin. The rock powder was thoroughly mixed in a metal bowl, and about 100 grammes was set aside for geochemistry.

9.2 Washing

Prior to heavy liquid separation, it is necessary to wash the sieved sample to remove finer fractions that may pass through filter paper and spoil the liquids during separation. Washing is done in two stages. In the first stage water and decantation is used to remove all suspended particles from the sample. The procedure is repeated until the water on top of the sample appears reasonably clear to the naked eye. The sample can then be rinsed with acetone to remove all excess water, and can then be dried under a heat lamp, or in mildly heated oven (at 60°C).

9.3 Mineral separation

Mineral separation includes three stages, two involving heavy liquid separation and one involving magnetic separation. The heavy liquid separations are based on the use of lithium heteropolytungstate (LST) with density 2.85g/mL, and methylene iodide (MI) with density 3.32g/mL.

9.3.1 LST separation

In the first stage of mineral separation, a liquid called LST (lithium heteropolytungstate) is used, separating a light mineral fraction ($< 2.85 \text{ g/mL}$) from a heavier fraction. LST separation successfully separates quartz and feldspar from accessory phases of interest for geochronologists. A typical LST separation setup (Fig. 9-1) allows separation of ~500 grammes of sample, and consists of a large (1 liter) glass funnel, and assorted glassware (beakers, funnels, stirring rod). Basically 500 grammes of washed sample is mixed with about half a liter of LST liquid, and allowed to settle. The heavy fractions will settle first at the bottom of the flask, while light fractions will float. By repeatedly stirring the mixture, and allowing it to settle (~15 minutes), the heavy grains gradually accumulate from the mixture. LST has a rather large viscosity, making the process rather slow. To achieve a good separation, about two hours must be taken out to allow the sample to settle. The heavy and light fractions can then be collected consecutively from the flask, into marked funnels with filter paper, and the recovered LST can be checked for density and added to the stock bottle for further use. The sample separates are washed with boiling deionised water until all LST has been removed. During the washing stages, sample that remained in the separating flask can be washed into the filter using boiling deionised (DI) water. The recovered LST/water mixture can be evaporated to the correct density, and recovered for reuse. The sample separates on the filter papers are dried under a heat lamp. After drying, the heavy fraction is immediately ready for magnetic separation.

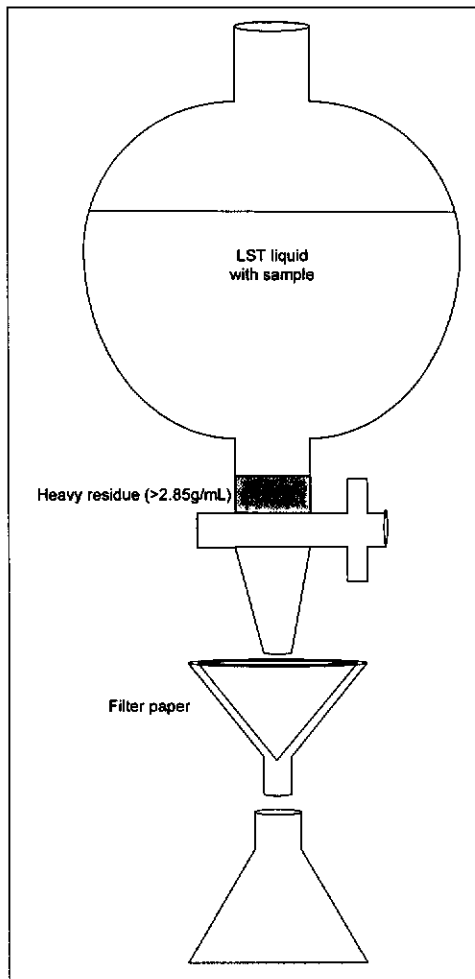


Figure 9-1 Setup for LST heavy liquid separation (a similar setup is used for any heavy liquid separation)

9.3.2 Magnetic separation

A mineral separate from LST separation contains all mineral content with specific density $>2.85 \text{ g/cm}^3$. This excludes quartz and feldspar, but includes more or less magnetic minerals such as magnetite, hematite, garnet, hornblende, pyroxene and biotite, as well as less to non-magnetic minerals such as zircon, rutile, pyrite, kyanite, monazite, apatite and sphene. During magnetic separation, the sample is typically separated into four different fractions, using magnetic properties of the constituent minerals (Table 9-1). Magnetic separation is achieved in a Frantz isodynamic magnetic separator. The magnetic separator consists of a large electromagnet through which mineral mixtures can be passed on a metal trough. The slope of the entire electromagnet and trough assembly can be

modified to control the sample flow. The trough is connected to a vibrator, which can be adjusted to further control the sample-passing rate. The modifiable separation parameters include the tilt of the trough into the magnetic field, and the strength of the electromagnetic field through which the sample flows. The trough splits into a left and right pathway, into which a mineral is either pushed or pulled by the magnetic field depending on its dia- or paramagnetic properties. By varying the strength of the magnetic field and/or tilt of the trough, the minerals can be separated according to their specific magnetic properties. In a first stage, a powerful handmagnet wrapped in a clean piece of paper is used to extract strongly magnetic (ferromagnetic) minerals from the sample. These minerals are attracted to any magnet and can block up the Frantz magnetic separator if not removed. In the following stages, the sample is passed through the Frantz isodynamic separator first using a tilt of 10° and magnet current of 5 Ampères, and then using a tilt of 5° and magnet current of 1.0 Ampères. Each of these separations result in a mineral separate that can be labeled M₀ through M₃ (see Table 9-1). The last fraction includes the minerals of interest for U-Th-Pb geochronology, including zircon and monazite, but also contains more abundant minerals such as apatite and sphene. Inspection under binocular microscope of this M₃ separate at this stage will indicate whether a second heavy liquid separation is required (see below).

Table 9-1 Typical settings for the Frantz Magnetic Separator and resultant mineral separates obtained.

Handmagnet	10° / 0.5 A	5° / 1.0 A	Pass
Fraction M0	Fraction M1	Fraction M2	Fraction M3
Magnetite	Hornblende	Muscovite	Sphene
Pyrrhotite	Garnet	Diopside	Apatite
	Olivine	Tremolite	Andalusite
	Chloritoid	Enstatite	Monazite
	Biotite	Spinel	Xenotime
	Chlorite	Staurolite (light)	Leucoxene
	Staurolite (dark)	(Clino)Zoisite	Rutile
	Hypersthene	Tourmaline (light)	Zircon
	Augite		Pyrite
	Epidote		Kyanite
	Tourmaline (dark)		Sillimanite

9.3.3 MI Heavy Liquid Separation

An M3 heavy mineral separate that has passed the magnetic separation, and therefore only consists of non- or very low magnetic minerals, is often unsuitable for direct picking of zircon. Zircon can in fact be largely undetectable because of the often copious amounts of more abundant phases such as kyanite, sillimanite, rutile, apatite and sphene. A further separate is therefore commonly obtained using a dense liquid called Methylene Iodide (MI). MI is a liquid with specific density of 3.32 g/cm^3 , and therefore ideal to separate apatite (s.d.= 3.10-3.35) and sillimanite (s.d.= 3.23-3.27) from the heavier sphene, zircon and monazite. A similar setup as that used for LST separation is adopted, albeit smaller to fit the smaller size of the non-magnetic heavy mineral sample. A small amount of MI liquid is placed in the separating funnel, and the heavy mineral separate added. Because of the lower viscosity of MI liquid compared to LST liquid, separation of the floating from sinking fraction is achieved just minutes after stirring. The fractions are collected on marked filter papers and washed using acetone (not DI water). The MI can be recovered from the acetone/MI mixture and reused. The samples are dried and placed in marked sample bottles (separates M4 (s.g. between 2.85 and 3.32) and MI (s.g. > 3.32)). The heavy separate (MI) can be immediately inspected under binocular microscope for presence of zircon, monazite and rutile.

10 APPENDIX C: SHRIMP Analytical procedure

10.1 SHRIMP II

A Secondary Ion Mass Spectrometer (SIMS) combines the sampling precision of an ion gun with the analytical capabilities of a mass spectrometer. Essentially, ions are generated in an ion-source, accelerated and directed towards a target, where the ion-beam (primary beam) sputters material from the sample. This target material is ionised, accelerated and focused into a secondary beam, and directed towards a source slit and into the mass-spectrometer component of the SIMS, where its make-up can be analysed.

The SHRIMP II is essentially a large ion microprobe coupled to a double focusing mass analyser. The machine has been modelled to a turning radius of 1 meter for a homogeneous field magnetic analyser (magnet), which required a 1.27 meter electrostatic analyser, resulting in a total run-length from source slit to collector slit of 7 meters. Because of the large path of the secondary beam, a double focusing arrangement, including an electrostatic analyser to allow energy focusing, and a homogeneous field magnetic analyser, separated by an electrostatic quadrupole lens, was selected to maximise signal at the collector slit. The SHRIMP II comprises three main component groups, namely the source, the mass analysers (energy and directional focusing) and the collector (Figure 10-1).

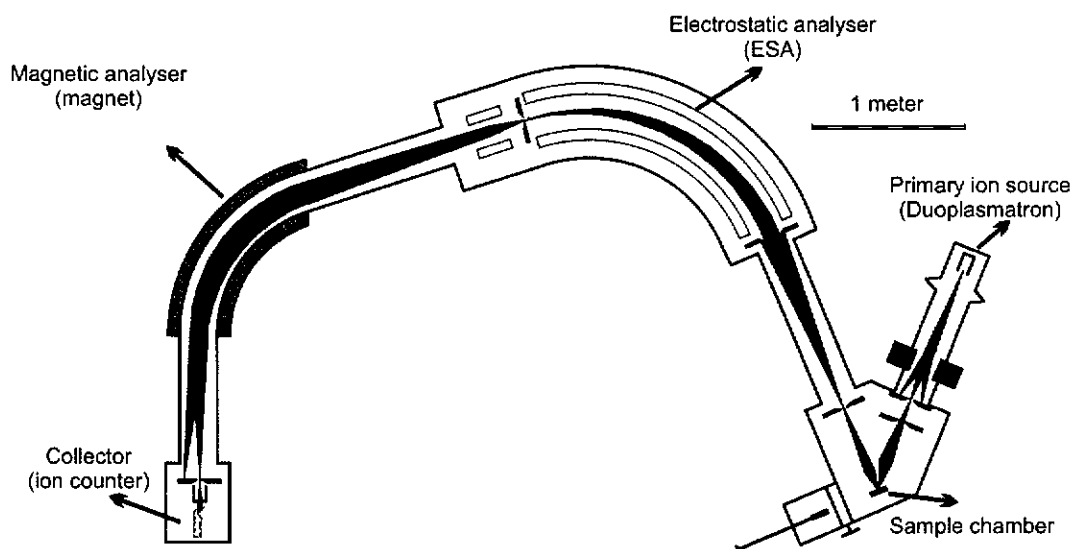


Figure 10-1 Simplified diagram of the SHRIMP II (adapted from Australian Scientific Instruments documentation)

10.1.1 The Source

The source refers to the component where primary (oxygen) ions are produced in a cold-hollow-cathode duoplasmatron. The ions are accelerated and focused to strike the target at 45 degrees in the horizontal plane. As the duoplasmatron produces O_2^+ , O^+ and, because of impurities in the oxygen supply, NO^+ , OH^+ and other minor species, a velocity filter (the Wien filter) is applied to remove unwanted species so that the primary beam consists of a single ion species (O_2^+). The primary beam passes through an aperture called the Köhler aperture, which ensures a uniform ion density and sharply defined diameter of the beam. The use of Köhler illumination leads to the sputtering of a sharply defined, flat-bottomed slightly elliptical crater, from which the secondary ion emission is constant, reproducible and readily calibrated (Williams, 1998)(Figure 10-2).

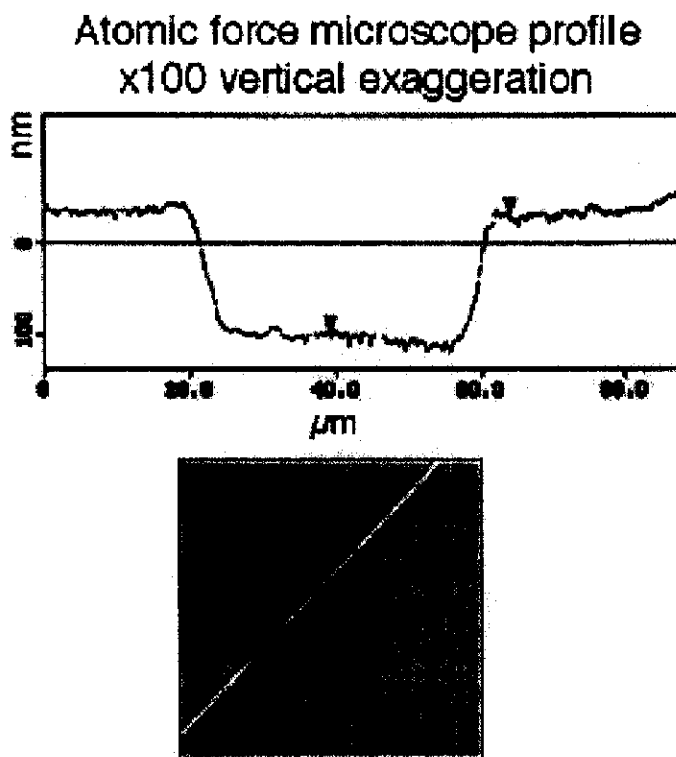


Figure 10-2 Geometry of a typical SHRIMP spot. Note the sharply defined crater edge and the flat bottom of the pit (picture taken from Australian Scientific Instruments documentation).

10.1.2 The Mass Analysers

The material sputtered from a sample area consists of a complex mixture of atomic and molecular combinations of all elements in the primary beam and target. Some of this extracted material is ionised and accelerated at right angles to the sample surface along a secondary ion beam. This secondary beam passes through a set of electrostatic lenses and steering plates, which match the phase-space characteristics of the beam to the tolerances of the electrostatic and mass analysers. The beam then enters the electrostatic analyser (ESA), which provides an energy-dependent offset to the secondary beam, to compensate for the energy dispersion of the magnet. This energy dependent focusing arrangement maximises the transmission of the beam towards the source slit of the magnet. The source slit of the magnet is rather wide (80 μm), again to maximise signal, and the large turning radius of the magnetic analyser (1 meter) compensates for the resultant loss in sensitivity. The magnetic field in the (electro)magnet can be adjusted to direct specific mass species towards a single detector slit.

10.1.3 The Detector

Ion counting employs a single electron multiplier with an effective dead time of 20 ns. Each mass species is directed into the detector slit by cyclic stepping of the magnetic field. As each species has a different focal point, the collector stage is moved to the optimal focal length for each mass. The exact setting of both collector position and magnetic field are stored in a “run-table”, which is calibrated to a standard prior to an analysis session. The run-table also stores the count and dead times for each species. Short-term beam instability is monitored by dividing the set count time for each mass in ten time segments. The dispersion of observed counts is compared with that expected from Poisson counting statistics, and significant outliers rejected. Each set of scans is repeated several times (between 5 and 7 times in this study) and shows a linear increase or decrease with time as analysis proceeds. The linear variation is a direct result of sputtering characteristics and matrix effects at the target site, and the progressive deepening of the analysis spot. Deviation from linearity reflects either target heterogeneity on a sub-micron scale, or could signify primary or secondary beam instability during the course of an analysis. Although theoretically such aberrations can be manually removed to “improve” an analysis, in this study, significantly erratic analyses were discarded entirely prior to data reduction.

10.2 Zircon selection and mounting

Zircons were handpicked under a binocular microscope from the non-magnetic heavy mineral fraction. The crystals were picked dry using a needle, and stuck to double-sided adhesive tape on a glass slide. In case of granitoids, gneisses or volcanics, for which an emplacement age was anticipated, only relatively clear, uncracked, eu- to subhedral crystals were selected. For high-grade gneisses, large zircons were selected, which showed internal zoning and possible core-rim associations, as well as euhedral single growth crystals and rounded zircons presumed to be metamorphic in character. Between 50 and 150 grains were mounted for each sample, depending on availability and quality of the zircons. For

the quartzites, which form part of this study, a minimum of 100 zircons were mounted covering the entire range of morphologies, colour, and size.

Perth Consortium internal zircon standard CZ3, chips from a gem sized Sri Lankan zircon, were mounted together with the unknowns. The CZ3 standard has no detectable variation of isotopic composition, parent/daughter ratios and elemental concentrations at the resolution of the SHRIMP II. The adopted age of CZ3 is 564 Ma, and isotopic ratios are known to be concordant. The CZ3 standard has a Uranium content of 550 ppm, and is characterised by a non metamict crystal structure, no inclusions or defects and no common Pb making it an ideal standard for zircon dating.

A phenolic ring was placed on the glass slide, centred over the mounted grains, and a 5:1 mixture of Buehler Epoxide Resin and Hardener carefully poured inside. To minimise potential bubbles in the resin, the mixture was placed in an ultrasonic bath for a couple of minutes prior to casting. The cast was allowed to set for 24 hours, after which the phenolic ring was removed. The glass slide and epoxy mount were placed on a grinding machine, and the top surface grinded parallel to the glass slide to obtain a final thickness of about 4 mm. After grinding, the mount was wrenched off the tape and should have two opposing parallel faces. The zircons are at this stage secured just below the surface of the mount, and needed to be exposed and polished for analysis. Using a succession of waterproof abrasive papers, both sides of the mount were polished. On the side with the zircons, extreme care was taken to gently polish using coarse paper until most grains were exposed roughly mid-section. The level of exposure was monitored by visual inspection under binocular microscope with both transmitted and reflected light. Once a sufficient exposure had been achieved, the mount was cleaned and progressively finer abrasive papers used to refine the polish, continuously taking care to check the polished surface under the microscope. After the finest abrasive paper, the mount was thoroughly cleaned in an ultrasonic bath using ethanol, and then further polished on 3 μm and 1 μm polishing pads. Care was taken to thoroughly clean the mount in between each polishing pad to avoid contamination. After polishing, the mount was labelled at the back, and

went through a rigorous cleaning procedure to minimise surficial contamination. The cleaning includes successive rinses, and wiping of the mount surface using organic and inorganic solvents (propan-2-OL and petroleum spirit (ether)), followed by wiping and rinsing with soap solution and deionised water. The cleaned mount was then coated with a thin ultra-pure gold coat, which makes the surface conductive. During the course of this study, a gold coating was only applied once prior to imaging on the electron microscope (see below). The coating retained sufficient conductivity after SEM work so that no new coating was required prior to SHRIMP analysis.

10.3 Imaging

Optical imaging was conducted on a binocular petrographic microscope, with fitted digital camera system. CL imaging was carried out on a Phillips XL 30 Scanning Electron Microscope fitted with CL detector. The Electron Microscope was operated with an accelerating voltage of 15 keV, and the working distance was ~18 mm. Obtained images were directly saved as digital files and were printed out on a laserprinter. All images were used during analysis to allow careful selection of analysis spots. The sites were marked and labelled during the SHRIMP session.

10.4 Analytical technique (SHRIMP)

U, Th and Pb isotopic data were collected on the Sensitive High Mass Resolution Ion Microprobe (SHRIMP II) at Curtin University following procedures similar to those described by Nelson (1997). A detailed account of the operation of the SHRIMP ion microprobe is given in Williams (1998), and only the salient points are discussed below. During the analyses presented in this thesis, the current of the O₂⁻ beam during an analytical session was between 2.2 and 4.1 nA on CZ3 zircon, resulting in a sensitivity of 15-30 cps / nA / ppm Pb. A köhler aperture of 70 µm was selected, resulting in an incident primary beam diameter of around 25 µm. Analyses on unknowns were interspersed with analyses of in-

house CZ3 standard, for which an age of 564 Ma, U content of 550 ppm and $^{206}\text{Pb}/^{238}\text{U}$ of 0.09143 was adopted (Pidgeon et al., 1994). Measured compositions were corrected for common lead using non-radiogenic ^{204}Pb (see details below). Analyses that displayed high counts on ^{204}Pb , were abandoned, so that applied corrections are minimal and insensitive to the chosen isotopic composition of common Pb. In all analyses, the component of common Pb related to surface contamination was minimised through the meticulous cleaning procedure prior to loading and rastering the primary beam over the analysed area for up to 2 minutes prior to analysis. Common Pb counts were therefore observed to be constant and low. An average crustal Pb isotopic composition following the model of Stacey and Kramers (1975) was used in the common Pb correction, appropriate to the age of the zircon. Data processing was done using the excel add-ins Squid and Isoplot (Ludwig, 2001b, 2001a). All decay constants are those recommended by Steiger and Jäger (1977), but for calculation of the ages, the errors on these constants are not applied. The 2σ error on the weighted mean calibration ratio ($\alpha = (^{206}\text{Pb}^+ / ^{238}\text{U}^+) / (^{238}\text{UO}^+ / ^{238}\text{U}^+)^2$); (Claoué-Long et al., 1995)) are reported in the data tables. All ages are reported at 95% confidence level, while Mean Square of Weighted Deviates (MSWD) values are reported to give an estimate of the goodness of fit of the population for a calculated age. The obtained age populations for detrital analyses were further evaluated using an excel-based utility called “AgeDisplay”, based on methodologies described by Sircombe (2000; 2004). For the visual communication of data, the diagrams proposed by Tera and Wasserburg (1974) and Wetherill (1956) are used. In the few cases that common Pb correction proved to be inadequate, uncorrected values are plotted on a Tera-Wasserburg plot, and a regression line forced through the data points and the common Pb composition calculated for the age of the sample (Stacey and Kramers, 1975). The intercept of this regression line was interpreted as the best date estimate for the zircon population.

10.5 Standardisation and calibration of SHRIMP II

In the process of sputtering material from the sample surface, signals collected for the various masses over the various scans are observed to rise or fall.

This linear change is a direct result of the different extraction behaviour of each species and is also dependent on crater depth and surface charging effects as analysis proceeds. This characteristic of the sputtering process, aggravated by the fact that SHRIMP II uses sequential counting on a single collector rather than simultaneous counting in a multi collector setup, means that calculated isotopic ratios do not reflect the true isotopic make up of the target. The differences are relatively minor for the various species of a single element (the various isotopes of Pb), but become significant for inter-element ratios (such as ratios of $^{238}\text{U}/^{206}\text{Pb}$). Furthermore, the inter-element discrimination is not fixed, but can vary both within each analytical session, as from day to day, so that internal calibration is necessary for each session. As the inter-element discrimination can vary within a session, calibration involves repeated, interspersed analysis of a standard. Claué-Long et al. (1995) reported that during measurement of a reference zircon standard and unknown zircons, small variations in $^{206}\text{Pb}^+/^{238}\text{U}^+$ correlated well with variations in UO^+/U^+ . The relationship between the two ratios is best described through a power law:

$$^{206}\text{Pb}^+/^{238}\text{U}^+ = A (\text{UO}^+/\text{U}^+)^2$$

or

$$\ln(^{206}\text{Pb}^+/^{238}\text{U}^+) = \ln(A) + 2.\ln(\text{UO}^+/\text{U}^+)$$

This second equation describes a straight line with slope 2 and Y-intercept $\ln(A)$. Experimental work has indeed shown that for zircon, the average value for the slope is 2.0 (Claoué-Long et al., 1995). A sufficient number of analyses on standard zircon during a single session, allows the definition of a “calibration line”, which is used to calculate values of $(^{206}\text{Pb}^+/^{238}\text{U}^+)_{\text{standard}}$ at the value for $(\text{UO}^+/\text{U}^+)_{\text{unknown}}$. Through this, it is assumed that the ionic ratios are identical to the atomic ratios. The Uranium concentration is likewise calculated through calibration of $(\text{Zr}_2\text{O}^+/\text{U}^+)$ against (UO^+/U^+) , following a power law with an exponent value of 0.66 (Claoué-Long et al., 1995).

$$\text{Zr}_2\text{O}^+/\text{U}^+ = A (\text{UO}^+/\text{U}^+)^{0.66}$$

and

$$U_{\text{unknown}} = U_{\text{standard}} \left(\frac{Zr_2O^-/U_{\text{standard}}^+}{Zr_2O^+/U_{\text{unknown}}^+} \right)$$

$^{232}\text{Th}/^{238}\text{U}$ ratios are calculated through:

$$(^{232}\text{Th}/^{238}\text{U}) = [0.03446 (UO^+/U^+) + 0.868] \cdot (^{232}\text{ThO}^+/^{238}\text{UO}^+) \text{ (Williams, 1998)}$$

Pb and Th concentrations are calculated from $^{206}\text{Pb}/^{238}\text{U}$, $^{232}\text{Th}/^{238}\text{U}$ and the Pb isotopic composition.

10.6 Data quality and processing

A typical data file from SHRIMP II consists of a text file with a range of data including sample (spot) number, time and date of the start of analysis, actual detector counts for each scan and mass species and associated standard deviations. Standard deviations reported in the text file include errors from ion counting, background correction, and are multiplied by the parameter \sqrt{F} . F is a measure of the goodness of fit of a regression line across the scans and is given by:

$$F = \text{variance}(\text{observed})/\text{variance}(\text{expected})$$

where variance(expected) is the variance expected from Poisson counting statistics alone.

Along with the text file, the control software of the SHRIMP II (Labview) also produces a printed sheet after each analysis, recording slightly more data including the sample (spot) number, time and date of the analysis, the run-table employed, and tabulated detector counts per mass peak and per scan. The software also calculates various statistical parameters for linear regression across the

various scans per mass, and calculates uncorrected as well as common Pb corrected isotopic ratios and corresponding ages. Values of $\ln(^{206}\text{Pb}/^{238}\text{U})$ and $\ln(^{238}\text{UO}/^{238}\text{U})$, which are important for the calibration diagrams, are also reported on the printout.

Data reduction was carried out using a software plug-in for excel called “Squid” (Ludwig, 2001b), while another plug-in called Isoplot was used for further calculation and evolution diagrams. The plug-in allows direct import of the text file, and automatically processes the raw data, propagating analytical errors introduced by the correction of measured compositions for common Pb, and by the calibration of $^{206}\text{Pb}^*/^{238}\text{U}$ ratios. Errors are propagated at each step of the data reduction in terms of the variance, σ^2 , of each quantity, using the general principle of error propagation (Geyh and Schleicher, 1990):

$$\sigma_x^2 = \sigma_u^2 \left(\frac{\partial x}{\partial u} \right)^2 + \sigma_v^2 \left(\frac{\partial x}{\partial v} \right)^2 + \dots + 2\sigma_{uv} \left(\frac{\partial x}{\partial u} \right) \left(\frac{\partial x}{\partial v} \right) + \dots$$

in which the third term can be ignored if the variables are independent.

10.7 Correction for common Pb

Ordinary (common) Pb, incorporated during crystallisation or later geochemical processes, as well as Pb contamination of the sample complicates the determination of the lead produced by radioactive decay. Even though the amount of common Pb is minor for a mineral like zircon, corrections need to be made to come to an accurate age estimate.

Common Pb content is best defined as:

$$f = ^{206}\text{Pb}_c / (^{206}\text{Pb}_c + ^{206}\text{Pb}^*)$$

where f =proportion of common Pb in total Pb; Pb_c denotes common Pb and Pb^* denotes radiogenic Pb.

There are three methods currently applied to calculate f , based on measured ^{204}Pb (204 method), ^{207}Pb (207 method) and ^{208}Pb (208 method).

The ^{204}Pb isotope presents the most direct estimate of the amount of ordinary lead, since this isotope is not produced by the radioactive decay of uranium or thorium. For this reason, as well as the fact that the measurement of ^{204}Pb is (just) within the capabilities of SHRIMP II, this correction method has been applied for the majority of samples. The proportion $^{204}\text{Pb}_{\text{common}}$ in total ^{204}Pb is given by:

$$f_{204} = \frac{\left(\frac{^{204}\text{Pb}}{^{206}\text{Pb}} \right)_{\text{total}}}{\left(\frac{^{204}\text{Pb}}{^{206}\text{Pb}} \right)_c}$$

The 204 method suffers from low precision, predominantly because ^{204}Pb is the least abundant Pb isotope, but also because its measurement in the ion microprobe can be susceptible to isobaric interferences with Rare Earth Elements. Where, due to incorrect centering on ^{204}Pb , common Pb correction yielded unsatisfactory results, a modified “semi-total-Pb/U isochron” approach was applied (Tera and Wasserburg, 1972). In this approach, the $^{207}\text{Pb}/^{206}\text{Pb}$ and $^{238}\text{U}/^{206}\text{Pb}$ ratios are plotted, uncorrected for common Pb, on a Tera-Wasserburg diagram, together with the calculated $^{207}\text{Pb}/^{206}\text{Pb}$ ratio of Pb at the time of formation of the zircon on the $^{207}\text{Pb}/^{206}\text{Pb}$ axis. A regression of the uncorrected data to common Pb yields an intercept on the concordia, which is interpreted as the best estimate of the age of the population.

10.8 Composition of common Pb

Common lead contains the isotopes ^{204}Pb , ^{206}Pb , ^{207}Pb and ^{208}Pb and the ratios are both regionally and temporally variable. Stacey and Kramers (1975) proposed a two-stage model of Pb evolution through geological time, which can be applied to calculate the ratios $^{206}\text{Pb}/^{204}\text{Pb}$, $^{207}\text{Pb}/^{204}\text{Pb}$ and $^{208}\text{Pb}/^{204}\text{Pb}$. During this study, the proportions of common Pb were very low, and corrections insensitive to the choice of common Pb composition. Because surface contamination was limited through both rigorous cleaning procedures of the mount surface, and rastering of the primary beam prior to each analysis, common Pb was assumed to be contributed by the mineral alone. A calculated composition for the age of the mineral was thus considered the most suitable approach.

11 APPENDIX D: Geochemical procedures

During this study, 111 samples were analysed for both major and trace elements using ICP-MS, ICP-OES and AAS techniques. The results are reported separately for major elements and trace elements (see Appendix G).

11.1 Determining water content

Porcelain crucibles were cleaned with water and dried in an oven at $\sim 105^{\circ}\text{C}$ for at least one hour. When dry they were removed from the oven and allowed to cool down. The empty crucible was then put on a Sartorius balance and ~ 5 grammes of sample powder accurately weighed. The crucible was then transferred to a pre-heated oven at $\sim 105^{\circ}\text{C}$, and left overnight (minimum 8 hours). The crucibles were then taken from the oven, and allowed to cool in a desiccator. The weight was then determined on the balance, and the difference attributed to loss of H_2O .

11.2 Determining Carbonate and Organic content (LOI)

After having determined the content of H_2O in a sample, the crucible was directly transferred into a pre-heated muffle furnace at $\sim 1050^{\circ}\text{C}$. It was allowed to stay at $\sim 1050^{\circ}\text{C}$ for a minimum of 8 hours. It was then moved into a desiccator to cool down. The weight was then obtained, and the difference in weight related to the total LOI in the sample.

11.3 Hydrofluoric acid digestion (ICP-MS)

The digestion technique used is different for analysis of trace elements and analysis of major elements in rock samples. The aim for traces (ICP-MS) is to dissolve all phases (including refractory minerals such as zircon and garnet),

while simultaneously volatilising silica as a gaseous fluoride. The technique used during this work was adapted from Crock and Lichte (1982). Approximately 50 mg of rock powder was transferred into cleaned and dried Teflon canisters, and carefully weighed on a sensitive balance. 30 ml of a 4:1 mixture of purified $\text{HNO}_3/\text{HClO}_4$ was then added, together with 20 ml HF (50% solution). The Teflon sample holder was then put on a hot plate at $\sim 140^\circ\text{C}$ overnight, to allow full digestion of the sample. When the sample was dry and cooled down, 1 ml HNO_3 , 0.5 ml HCl and 5 ml MilliQ H_2O was added to redissolve the sample. Then the sample was transferred into plastic sample holders and topped up to a total weight of $\sim 50\text{g}$. The exact weight of the actual sample powder, and the exact weight of the final digestion was carefully recorded. Prior to ICP-MS analysis, 1 ml of sample was mixed with 9 ml of MilliQ and an internal Rh-Ir standard for drift calibration.

11.4 Sample fusion (ICP-OES)

To analyse major elements, the mineral matrix was prepared for digestion through a fusion process. The melting temperature for the mineral matrix is lowered through adding lithium tetraborate ($\text{Li}_2\text{B}_4\text{O}_7$) flux (neither Li, nor B will interfere with the analysis of the majors). A mixture of rock powder and flux was placed into a platinum crucible and fused at $\sim 970^\circ\text{C}$ in a furnace for 60 minutes. The resulting fusion beads were redissolved on a hotplate at $\sim 40\text{-}50^\circ\text{C}$ in a 3% HCl solution, which was then volumetrically diluted in 250 ml flasks, and ready for analysis. Standardisation and data quality were achieved by running standard and blank solutions at regular intervals.

11.5 Analysis of trace and rare earth elements through ICP-MS

Trace elements were analysed in ALS Chemex (Canada) and in the department of Applied Chemistry of Curtin University of Technology. At Curtin University of Technology, a VG PQ3 ICP-MS instrument was used, fitted with a Scott double pass – constant temperature (10°C) spray chamber and Meinhardt

Nebuliser. Each analysis consisted of a 60 second uptake, 90 second analysis, and 60 second washout sequence, with two scans per second over the range of elements. Registration was done using 19 channels per atomic mass unit (amu), using a 320 ms dwell time. Standards were introduced with concentration of 1, 2, 5, 10 and 20 ppb, while internal Rh and Ir standards were applied for internal drift correction.

For the analysis of trace elements through ICP-MS, a digested rock sample is introduced into hot plasma, using a stream of Ar carrier gas, which in itself forms and maintains the plasma. Temperatures inside the plasma reach ~6000°K, with pressures up to ~760 Torr, rapidly stripping the atoms of their valence electrons. The positively charged ions are accelerated to a set of apertures into an interface region, which enables extraction of the ions without compromising the high vacuum (10^{-4} Torr) in the mass spectrometer. The interface chamber itself is pumped to 10^{-3} Torr with a large capacity rotary vacuum pump, which removes the majority of the Ar atoms. Once the ions are in the mass spectrometer chamber, they are focused by an electromagnetic lens system and directed down the mass analyser. Ions with specific m/z ratios are transmitted sequentially to the ion detection system, while ions with lower or higher mass/charge ratios have different trajectories and are lost. The detector consists of combined electron multiplier and low gain analog detector, one of which is selected depending on the ion-beam intensity. A schematic representation of a Quadrupole ICP system is displayed in Figure 11-1.

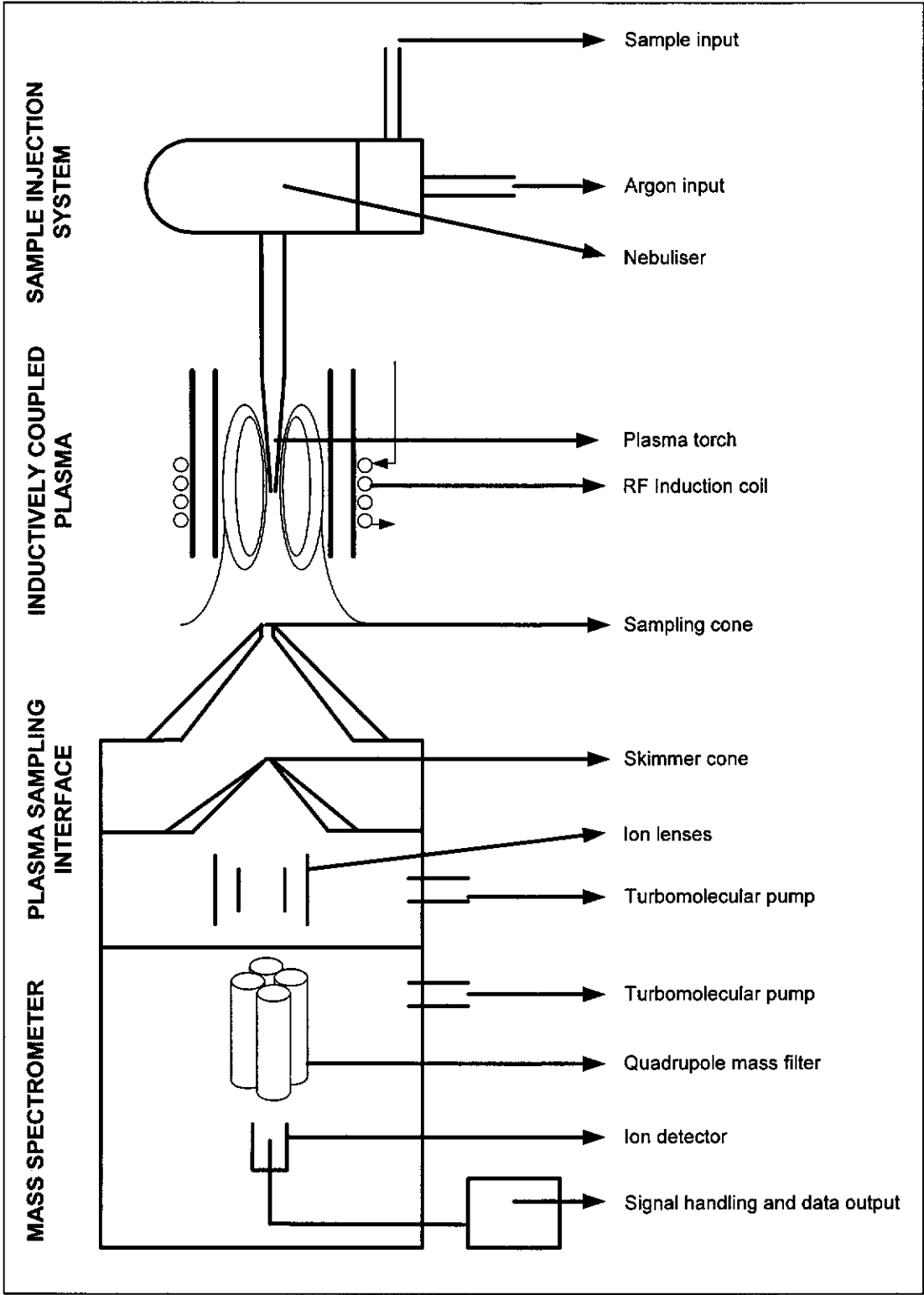


Figure 11-1 Diagram of a Quadrupole Induced Coupled Plasma Mass Spectrometer (ICP-MS) system.

11.6 External standards

Multi-elemental laboratory standards and commercially produced Standard Reference Materials (SRM) were selected and the SRM prepared in the same way as the unknowns. Six standards were selected to cover the expected range in the unknowns (see Tables 11-1, 11-2, 11-3 and 11-4). The standards were used to generate calibration curves from which the composition of unknown samples could be inferred as an external check.

Table 11-1 Measured values for standards (weight %, major elements)

	SRM1	SRM 2	SRM 4	SRM 6	SRM50	SRM50	SRM50	SRM50
SiO ₂	76.73	64.45	52.74	40.12	51.18	51.50	50.83	51.77
Al ₂ O ₃	12.63	16.97	17.83	0.23	15.01	15.66	15.11	15.05
Fe ₂ O ₃	2.13	1.57	7.96	16.39	8.62	8.14	8.97	8.00
MnO					0.17	0.17	0.18	0.17
MgO	0.04	0.45	6.92	41.93	7.47	7.50	7.53	7.64
CaO	0.75	0.71	10.58	0.33	10.75	10.82	10.39	11.05
Na ₂ O	3.19	0.62	2.46	0.16	1.79	2.29	2.41	2.69
K ₂ O	4.99	15.08	0.29	0.03	0.59	0.69	0.60	0.54
TiO ₂	0.11	0.04	0.22	0.02	0.84	0.85	0.84	0.90
P ₂ O ₅	0.01	0.13	0.19	0.09	0.14	0.16	0.15	0.15

Table 11-2 Quoted values for standards (weight %, major elements)

	SRM1	SRM2	SRM4	SRM6	SRM50	SY2
SiO ₂	75.70	63.63	52.64	39.02	48.20	56.20
Al ₂ O ₃	12.08	17.33	16.49		12.13	9.56
Fe ₂ O ₃	2.04	1.44	9.00	16.96		2.55
MnO					0.13	0.25
MgO		0.46	7.50	43.51	4.56	1.62
CaO	0.78	0.68	11.51	0.28	7.72	5.69
Na ₂ O	3.36	0.43	2.46		0.85	1.60
K ₂ O	4.99	15.36	0.25		0.25	1.85
TiO ₂			0.20	0.02	1.03	0.18
P ₂ O ₅	0.01	0.12			0.16	0.47

Table 11-3 Measured values for standard (ppm, trace elements)

	SY2	SY2	SY2	SRM1	SRM1	SRM1	SRM6	SRM6	SRM6	SRM50	SRM50	SRM50
As	17.78	17.09	17.30	19.40	19.30	20.79	0.66	0.62	0.57	1.09	1.27	1.11
Ba	468	468	460	120.9	120.0	121.1	10.00	9.18	9.33	220	224	226
Be	22.84	21.86	22.00	8.10	7.75	8.17	0.01	0.01	0.01	0.53	0.50	0.54
Bi	0.10			0.26	0.28	0.30	0.011			0.01		
Cd	0.22	0.20	0.21	0.12	0.11	0.12	0.02	0.02	0.02	0.12	0.10	0.09
Ce	178.0	173.9	175.0	201	195	201		0.17	0.19	32.9	32.9	32.4
Co	8.63	8.85	8.60	0.40	0.36	0.38	208	207	207	40.0	40.7	40.1
Cr	9.87	9.85	9.50	11.54	12.00	12.04	2870	2986	2834	357	354	354
Cu	5.35	5.22	5.20	12.41	12.00	12.63	10.00	9.43	9.94	84.0	85.6	82.1
Dy	18.62	18.39	18.00	17.33	17.00	17.52		0.03	0.03	4.60	4.22	4.27
Er	12.45	12.92	12.40	10.58	10.50	10.44		0.02	0.03		2.08	2.11
Eu	2.37	2.27	2.42	0.38	0.35	0.39				1.18	1.10	1.10
Ga	27.89	28.97	29.00	28.04	27.00	28.32	0.40	0.45	0.44	16.30	15.53	16.35
Gd	16.54	16.88	17.00	13.69	14.00	13.72		0.02	0.02	4.30	4.25	4.27
Ge	1.37	1.26	1.30	0.81		0.77		2.48	2.35		1.74	1.43
Hf	7.47	7.44	7.70	12.98	12.40	12.23			0.08		2.80	2.67
Ho	3.72	3.68	3.80	3.52	3.60	3.61		0.01	0.01		0.76	0.67
La	78.3	77.3	75.0	109.3	109.0	110.2	0.20	0.19	0.17	16.20	16.35	16.50
Li	96.2	95.7	95.0	11.98	12.00	11.72		3.88	4.01		6.87	6.13
Lu	2.72	2.72	2.70	2.09	2.00	2.16		0.01	0.01	0.43	0.37	0.43
Mn	2449	2476	2478	155.9	154.9	154.0	1704	1716	1715	1317	1328	1312
Mo	1.57	1.45	1.80	2.72	2.84	2.69	0.77	0.73	0.84		0.59	0.59
Nb	29.02	28.83	29.00	53.7	53.0	52.4		0.96	0.96	10.00	10.49	10.45
Nd	74.6	73.8	73.0	72.1	72.0	72.4		0.06	0.05	17.80	17.25	17.42
Ni	9.81	9.81	9.90	6.83	8.00	6.94	2040	2089	2099	85.0	83.3	87.6
Pb	86.5	88.4	85.0	40.9	40.0	40.7	1.32	1.31	1.24	25.00	25.9	25.4
Pr	18.83	18.09	18.80	20.00	19.50	20.08		0.02	0.02		3.83	3.47
Rb	222	216	217	330	325	324		0.79	0.88	14.00	14.11	13.83
Sb	0.22	0.25	0.25	1.16	1.19	1.13		0.28	0.28	0.34	0.33	0.34
Sm	16.31	16.58	16.10	15.81	15.80	16.06		0.02	0.01	3.80	3.92	3.89
Sn	5.32	5.33	5.70	3.27	3.30	3.26	0.15	0.16	0.15	0.80	0.79	0.75
Sr	273	269	271	9.76	10.00	9.93	3.00	3.29	3.19	195	197	199
Ta	2.14	2.15	2.01	5.02	4.90	5.03					0.85	0.78
Tb	2.49	2.53	2.50	2.75	3.00	2.71					0.68	0.59
Th	385	383	379	51.9	51.0	51.4	0.15	0.12	0.17	6.00	6.05	6.04
Ti	896	884	899	695		677	120	121	121.5	5155	5111	5187
Tl	1.36	1.30	1.50	0.93	0.93	0.96	0.016			0.10		
Tm	2.14	2.03	2.10	1.86	2.00	1.95		0.01			0.34	0.31
U	287	284	284	15.44	15.00	15.61	0.14	0.15	0.16		0.41	0.37
V	50.5	49.2	50.0	2.13	2.00	2.32	40.0	37.4	38.7	216	213	215
W	0.72	0.71	0.76	1.48	1.45	1.48	0.19	0.18	0.16		0.48	0.47
Y	123.0	129.6	128.0	142.9	143.0	144.1		0.17	0.17	23.00	23.2	22.8
Yb	16.76	16.95	17.00	14.17	14.20	14.14		0.05	0.05	2.73	2.51	2.52
Zn	250	252	248	51.8	50.0	51.1	90.0	88.8	89.3	81.0	80.6	80.4
Zr	274	278	280	303	300	303	8.00	7.96	7.95	86.0	85.2	85.5

Table 11-4 Quoted values for standards (ppm, trace elements)

	SRM1	SRM2	SRM4	SRM6	SRM50	SY2
Ag		0.03	0.03			0.029
As	19.30	0.25	0.40	0.66	1.09	17.30
Ba	120.0	2420	102.0	10.0	220	460
Be	7.75	1.61	0.35		0.53	22.00
Bi	0.28	0.02	0.01	0.011	0.01	0.111
Cd	0.11	0.01	0.07	0.019	0.12	0.21
Ce	195	12.00	6.00		32.9	175
Co	0.36	3.00	58.0	208	40	8.60
Cr	12.00	12.00		2870	357	9.50
Cs	1.06	6.68	0.22	0.05		2.40
Cu	12.00	19.00	14.00	10.0	84	5.20
Dy	17.00	0.40	1.00		4.60	18.00
Er	10.50	0.12	0.67			12.40
Eu	0.35	0.30	0.63		1.18	2.42
Ga	27.00	11.00	16.00	0.4	16.3	29.0
Gd	14.00	0.83	0.91		4.30	17.00
Ge			1.54			1.30
Hf	12.40	0.46	0.38			7.70
Ho	3.60	0.05	0.22			3.80
La	109.0	5.00	3.00	0.2	16.2	75
Li	12.00					95
Lu	2.00	0.01	0.20		0.43	2.70
Mn	154.9	77.5	1394	1703.81		
Mo	2.84	0.76	0.89	0.77		0.53
Nb	53.0				10.00	29.0
Nd	72.0	6.00	3.00		17.8	73
Ni			120.0	2040	85	10.00
Pb	40.0	2.39	2.48	1.32	25.0	85
Pd	0.01	0.01	0.01			0.015
Pr	19.50	1.39	0.77			18.80
Rb	325	530	5.00		14.00	217
Sb	1.19	0.05	0.05		0.34	0.25
Sc	0.90	3.60	37.4			7.00
Se	0.01					20.00
Sm	15.80		0.80		3.80	16.10
Sn	3.30	0.48	0.27	0.15	0.80	5.70
Sr	10.00	62.0	260		195	271
Ta	4.90	0.03	0.07			2.01
Tb	3.00	0.10	0.17			2.50
Te	0.01					0.002
Th	51.0	1.00	0.42	0.15	6.00	379
Tl	0.93	1.12	0.02	0.016	0.10	1.50
Tm	2.00		0.10			2.10
U		0.37	0.28	0.14		284
V		10.00	220	40.0	216	50.0
W	1.45		0.19	0.19		0.76
Y	143.0	1.14	7.00		23.0	128
Yb	14.20		0.70		2.73	17.00
Zn	50.0	10.00	68.0	90.0	81	248
Zr	300	20.0	14.00		86	280

11.7 Blanks

Blanks were prepared using the same procedure as the unknowns, and contain impurities and background of the various consumables applied in sample digestion. The blanks were used as control of the quality of the sample preparation procedure. During our study the values for blanks were below detection limits, and no correction was necessary.

11.8 Calibration

Signal intensities were measured for all analysed isotopes in a blank as well as in standards, and plotted in calibration curves, which were then used to infer the unknowns. Instrument drift (temporal variation of signal intensity with time) was corrected for by interspersing standard analyses with unknowns. Ideally, standards should be species with masses without interferences in the matrix and for this study ^{103}Rh and ^{192}Ir were used.

11.9 Data quality and processing

To assess the precision and accuracy of the ICP-MS analyses, several duplicates were analysed. Duplicates were taken from one and the same sample vial (rock powder), and processed separately. Moderate variations were detected, and are interpreted to relate mainly to sampling effects on the rock powder, rather than the analyses itself. Duplicate analyses for major and trace elements are shown in Table 11-5 and Table 11-6 respectively, while minimum detection limits for major and trace elements are shown in Table 11-7 and Table 11-8.

Table 11-5 Duplicate analyses (major elements)

SAMPLE	LW8		IS21		KB3		LW2		LW9		SH8		CC8		KN2B		MK5		MH5		KN8	
	(1)	(2)	(1)	(2)	(1)	(2)	(1)	(2)	(1)	(2)	(1)	(2)	(1)	(2)	(1)	(2)	(1)	(2)	(1)	(2)	(1)	(2)
SiO ₂	44.17	45.70	75.21	73.40	50.04	48.01	78.08	78.13	75.21		73.59	70.40	71.32	74.10	75.40	77.12	72.91	75.53	72.97	74.20	69.04	72.45
Al ₂ O ₃	13.62	16.16	12.11	13.25	17.10	18.25	12.41	12.19	14.55		13.94	14.05	13.91	13.12	12.93	12.26	12.65	12.53	13.99	14.46	15.72	14.55
Fe ₂ O ₃	14.06	11.18	3.28	2.74	10.64	8.66	0.51	0.39	0.68		2.34	1.88	2.82	2.04	0.49	0.37	1.92	1.49	1.88	1.51	2.67	2.68
MnO	0.19	0.19	0.04	0.03	0.18	0.13		0.00			0.01	0.01	0.04				0.04		0.03			
MgO	11.12	11.38	0.77	0.57	5.92	5.36	0.02	0.01	0.06		0.47	0.30	0.55	0.48	0.03	0.04	0.61	0.50	0.48	0.44	0.84	0.87
CaO	8.88	8.74	0.65	0.45	10.90	12.44	0.02	0.01	0.73		1.33	1.15	1.95	1.82	1.05	0.92	1.05	0.82	1.11	0.95	1.57	1.70
Na ₂ O	2.16	2.34	4.32	4.19	2.49	2.25	5.24	4.78	5.14		3.02	2.95	3.47	2.84	3.08	2.61	2.84	2.15	3.16	2.59	2.37	2.63
K ₂ O	0.77	0.87	2.40	2.54	0.95	1.04	3.67	3.98	3.29		5.12	5.19	4.79	3.84	5.81	5.24	5.82	4.83	4.80	3.86	5.03	4.90
TiO ₂	1.47	1.81	0.78	0.78	0.85	0.83	0.02	0.02	0.02		0.29	0.27	0.46	0.45	0.02	0.02	0.29	0.28	0.25	0.27	0.50	0.51
P ₂ O ₅	0.20	0.01	0.10	0.16		0.29		0.22				0.73	0.10	0.06		0.09		0.06		0.08	0.14	0.16
H ₂ O		0.10		0.20		0.11		0.10		0.14		0.17										
LOI		0.42	0.00	0.79		1.92		0.27		0.57		0.63		0.01		0.00		0.01		0.01	0.01	0.01
TOTAL	96.64	98.50	99.64	99.13	99.05	99.30	99.97	98.10	99.68	0.70	100.11	97.74	99.42	98.54	98.81	96.68	97.93	97.99	98.58	98.36	97.79	100.45

Table 11-6 Duplicate analyses (trace elements)

SAMPLE	LW8		IS21		KB3		LW2		LW9		SH8	
	(1)	(2)	(1)	(2)	(1)	(2)	(1)	(2)	(1)	(2)	(1)	(2)
B	-	-	-	-	-	-	-	-	-	-	-	-
Ba	134	181	817	1089	279	409	52.9	63.5	22.0	10.9	673	756
Be	-	-	-	-	-	-	-	-	-	-	-	-
Bi	-	-	-	-	-	-	-	-	-	-	-	-
Cd	-	-	-	-	-	-	-	-	-	-	-	-
Ce	12.40	18.12	140	168	24.10	34.80	11.40	16.31	13.30	13.84	158	161
Co	76.9	94.9	47.8	52.3	63.2	75.4	43.8	51.5	57.1	61.7	40.9	37.5
Cr	929	2040	18.00	39.75	76.00	145	-	-	-	-	-	-
Cs	-	-	-	-	-	-	-	-	-	-	-	-
Cu	107.0	168.9	12.00	10.76	78.0	117.9	5.00	1.09	5.00	1.27	11.00	2.58
Dy	5.00	5.92	9.00	9.26	4.30	5.20	0.90	1.19	2.80	1.87	5.20	4.98
Er	2.40	2.51	5.10	4.44	2.60	2.74	0.40	0.46	1.30	0.79	2.50	1.73
Eu	1.50	1.95	2.20	2.63	1.00	1.51	0.20	0.24	0.10	0.12	1.00	1.24
Ga	18.00	18.68	17.00	14.73	22.00	21.94	32.00	30.70	20.00	18.18	24.00	18.09
Gd	5.00	5.92	11.30	11.19	3.80	4.84	1.30	1.43	2.40	1.85	8.50	8.11
Ge	-	-	-	-	-	-	-	-	-	-	-	-
Hf	3.00	2.31	18.00	8.65	2.00	2.86	-	-	2.00	1.89	6.00	6.24
Ho	0.90	0.99	1.80	1.54	0.90	0.98	0.20	0.18	0.50	0.27	1.00	0.69
In	-	-	-	-	-	-	-	-	-	-	-	-
La	4.90	7.85	66.7	87.9	12.20	19.12	6.70	10.06	6.60	7.64	79.1	86.0
Li	-	-	-	-	-	-	-	-	-	-	-	-
Lu	0.30	0.35	0.80	0.82	0.40	0.49	-	-	0.20	0.13	0.30	0.22
Mn	-	-	-	-	-	-	-	-	-	-	-	-
Mo	-	-	-	-	-	-	-	-	-	-	-	-
Nb	7.00	2.27	24.00	35.49	9.00	7.82	12.00	4.49	20.00	13.29	30.00	20.53
Nd	11.90	16.00	63.7	71.1	12.20	17.26	7.10	9.68	5.70	5.35	60.9	58.9
Ni	345	496	16.00	11.89	70.0	86.8	-	-	-	-	9.00	8.05
Pb	-	-	9.00	11.74	6.00	9.69	-	-	53.0	82.5	42.0	54.8
Pd	-	-	-	-	-	-	-	-	-	-	-	-
Pr	2.10	2.67	17.00	17.72	2.90	3.80	1.80	2.29	1.70	1.49	17.60	15.60
Rb	51.8	61.55	95.80	103.6	31.90	41.29	136.0	157.4	286	314	309	303
Sb	-	-	-	-	-	-	-	-	-	-	-	-
Sc	-	-	-	-	-	-	-	-	-	-	-	-
Se	-	-	-	-	-	-	-	-	-	-	-	-
Sm	4.20	5.45	11.70	13.37	3.30	4.44	1.40	1.78	2.30	2.03	10.70	10.67
Sn	3.00	0.87	3.00	3.06	2.00	1.14	-	0.63	10.00	12.41	8.00	6.22
Sr	200	245	115.0	121.1	192	241	16.10	10.87	15.00	16.33	110.0	100
Ta	-	0.29	2.20	4.55	0.60	1.27	2.00	0.74	3.50	1.64	2.40	1.57
Tb	0.90	0.87	1.60	1.02	0.70	0.83	0.20	1.85	0.50	0.86	1.10	0.30
Th	-	-	34.00	37.30	3.00	3.81	-	-	5.00	4.90	54.0	50.9
Ti	-	-	-	-	-	-	-	-	-	-	-	-
Tl	-	-	-	-	-	-	-	-	1.10	0.32	0.80	0.17
Tm	0.30	0.43	0.80	1.38	0.40	0.18	-	-	0.20	0.52	0.30	0.21
U	-	-	4.90	4.31	-	-	-	-	6.50	6.68	7.00	5.98
V	229	271	51.0	60.6	260	336	-	-	-	-	19.00	17.99
W	29.00	4.30	388	41.15	110.0	13.05	435.0	33.05	525	44.4	365	27.27
Y	24.10	34.65	46.8	54.4	23.90	33.98	5.20	7.09	15.00	11.19	29.00	24.10
Yb	2.10	2.82	5.40	5.86	2.30	3.40	0.40	0.60	1.40	1.04	2.10	1.55
Zn	94.00	118.9	27.00	37.24	77.0	100.5	5.00	8.65	17.00	24.26	45.0	47.8
Zr	129.0	76.59	682	309	88.0	86.6	15.90	0.41	33.60	33.5	230	208

SAMPLE	CC8		KN2B		MK5		MH5		KN8		KB7	
(1)	(2)	(1)	(2)	(1)	(2)	(1)	(2)	(1)	(2)	(1)	(2)	(1)
B	-	-	-	-	-	-	-	-	3.37	5.78	-	-
Ba	1070	1099	440	438	554	676	707	725	2854	3685	82.3	84.06
Be	-	-	-	-	-	-	-	-	5.20	5.97	1.16	1.15
Bi	-	-	-	-	-	-	-	-	0.08	0.08	-	-
Cd	-	-	-	-	-	-	-	-	0.03	0.02	0.11	0.11
Ce	180	154	22.30	11.23	105	112	81.2	56.8	178	193	33.17	36.29
Co	14.00	13.47	14.70	12.37	88.8	82.1	11.40	10.44	18.17	18.96	80.7	80.9
Cr	-	-	-	-	-	-	11.00	16.76	22.11	24.15	36.07	37.36
Cs	1.90	1.35	1.30	0.89	5.20	5.29	7.60	6.22	4.77	5.92	-	-
Cu	11.00	6.54	7.00	3.57	10.00	5.75	10.00	5.95	7.45	8.58	113.3	118.5
Dy	7.10	6.28	3.90	1.92	8.70	8.10	2.90	1.83	7.25	7.43	6.25	6.52
Er	4.10	3.17	2.30	1.22	4.80	3.59	1.40	0.60	2.70	2.81	3.21	3.24
Eu	1.60	1.41	0.30	0.18	1.20	1.15	0.80	0.44	3.64	3.33	1.77	1.81
Ga	23.00	17.66	24.00	18.67	17.00	14.06	21.00	15.36	17.83	19.91	18.05	18.55
Gd	9.50	7.06	3.50	1.56	8.90	8.13	5.10	2.91	12.36	11.96	5.96	6.21
Ge	-	-	-	-	-	-	-	-	2.20	19.91	2.11	2.22
Hf	10.00	3.45	5.00	3.57	5.00	3.08	4.00	4.35	2.69	2.71	1.61	1.19
Ho	1.40	1.04	0.70	0.37	1.70	1.39	0.50	0.23	1.02	1.13	1.18	1.21
In	-	-	-	-	-	-	-	0.01	0.02	0.02	-	-
La	93.80	75.6	10.50	4.09	52.9	51.7	40.1	25.00	169.5	154.7	16.51	18.33
Li	-	-	-	-	-	-	-	-	59.54	61.32	11.01	10.90
Lu	0.60	0.62	0.50	0.34	0.60	0.52	0.20	0.11	0.22	0.22	0.49	0.47
Mn	-	-	-	-	-	-	-	-	487	515	2134	2206
Mo	-	-	-	-	-	-	-	-	0.08	0.19	0.21	0.18
Nb	22.00	10.62	18.00	20.20	17.00	17.72	12.00	12.83	19.97	19.70	9.38	8.44
Nd	67.10	50.6	10.70	4.40	44.0	43.4	35.10	21.29	102.1	105.8	20.19	21.3
Ni	-	-	-	-	-	-	5.00	6.63	10.79	11.04	36.21	37.1
Pb	20.00	17.69	34.00	27.32	33.00	31.92	41.0	34.85	62.93	78.5	5.46	5.53
Pd	-	-	-	-	-	-	-	-	0.02	0.02	-	-
Pr	19.80	14.62	2.80	1.12	12.00	12.08	9.60	5.73	29.85	28.67	4.13	4.37
Rb	174.0	168.4	176.0	171.2	274	291	215.0	194.7	241	261	5.28	5.33
Sb	-	-	-	-	-	-	-	-	0.04	0.03	0.13	0.19
Sc	-	-	-	-	-	-	-	-	8.46	7.42	-	-
Se	-	-	-	-	-	-	-	-	-	-	-	-
Sm	10.90	10.08	3.30	1.61	9.20	10.27	6.30	4.31	19.87	18.68	5.40	5.49
Sn	3.00	1.37	2.00	0.98	5.00	1.96	2.00	1.26	1.94	2.32	2.46	2.45
Sr	192.0	171.2	107.0	72.2	106.0	103.4	136.0	79.0	550	567	102	106.7
Ta	2.70	0.56	5.60	2.26	9.80	3.93	2.00	0.65	1.09	0.74	2.06	1.88
Tb	1.30	1.26	0.70	0.37	1.50	1.83	0.60	0.49	1.89	1.80	0.98	1.00
Th	30.00	20.07	17.00	7.18	37.00	33.19	25.00	18.93	22.85	23.19	2.79	2.62
Ti	-	-	-	-	-	-	-	-	-	-	13424	13270
Tl	0.60	0.68	0.60	0.66	1.00	1.27	0.90	1.13	1.26	1.66	-	-
Tm	0.60	0.60	0.40	0.24	0.70	0.54	0.20	0.08	0.34	0.37	-	-
U	4.40	2.68	7.50	3.40	3.90	2.64	4.80	2.23	1.20	2.01	0.42	0.43
V	29.00	38.35	-	-	21.00	30.31	16.00	21.68	56.6	55.1	374	373
W	91.00	4.54	165.0	13.29	672	51.0	83.0	6.54	9.73	11.71	23.54	23.22
Y	40.6	38.64	17.20	10.49	48.90	39.87	14.30	6.49	38.45	31.25	38.64	40.2
Yb	3.90	3.88	2.90	1.77	4.30	2.97	1.30	0.40	1.63	1.88	3.59	3.68
Zn	44.00	50.31	5.00	7.97	28.00	35.50	38.00	42.70	55.3	59.5	119.1	118.2
Zr	376	126.4	107.0	101.4	172	99.1	147.0	154.1	124.0	107.2	42.78	29.83

Table 11-7 Minimum Detection Limits for major elements analyses by ICP-OES method.

	MDL (%)
SiO ₂	0.01
Al ₂ O ₃	0.01
Fe ₂ O ₃	0.01
MnO	0.01
MgO	0.01
CaO	0.01
Na ₂ O	0.05
K ₂ O	0.05
TiO ₂	0.01
P ₂ O ₅	0.1
H ₂ O	0.1
LOI	0.01

Table 11-8 Minimum Detection Limits for trace analyses by ICP-MS method

MDL (ppm)		MDL (ppm)		MDL (ppm)	
Ba	2	Hf	0.1	Sn	0.5
Be	0.1	Ho	0.1	Sr	0.1
Bi	0.1	La	0.5	Ta	0.1
Cd	0.1	Li	0.1	Tb	0.1
Ce	0.5	Lu	0.1	Th	0.05
Co	0.2	Mn	0.5	Ti	10
Cr	10	Mo	0.1	Tl	0.5
Cs	0.05	Nb	0.2	Tm	0.1
Cu	2	Nd	0.5	U	0.05
Dy	0.1	Ni	2	V	2
Er	0.1	Pb	1	W	0.1
Eu	0.1	Pr	0.1	Y	0.05
Ga	0.5	Rb	0.05	Yb	0.1
Gd	0.1	Sb	0.1	Zn	5
Ge	1	Sc	2	Zr	0.5
		Sm	0.1		

11.10 Analysis of major elements through ICP-OES.

During this study, a JY38 Sequential ICP-OES was used to analyse major elements (Si, Al, Fe, Mn, Mg, Ca, K, Na, Ti and P). The instrument is fitted with a Scott double pass spray chamber (not temperature controlled), and Meinhardt Nebuliser. Emission peaks were defined using between 9 and 15 points, measuring 0.5 seconds per point. A reference wavelength of 193.0310 nm (Carbon) was used. Sample uptake was set at 50 seconds, followed by a washout of 20 seconds. The spectrometer was calibrated using standard solutions with concentration ranges 0-100 ppm for each of the elements. The built-in software integrated counts below the Gaussian approximation of each peak. Background subtraction was based on manual input of one point on each side of calibration peaks. Multi-element standards, with concentration ranges 0-100 ppm were analysed every ten unknowns to allow quality control. Emission spectra for Na and K are known not to be optimal at the operating temperatures of the plasma (8000°C). Their emission was optimised by lowering the plasma temperature for those peaks through an increase of Ar to the plasma. For the samples analysed in 2001, a malfunction of the solenoid responsible for the increase of Ar in the plasma, seriously affected precision. For those analyses, K and Na were determined separately using conventional Atomic Absorption Spectrometry (AAS).

The ICP-OES (Inductively Coupled Plasma – Atomic Emission Spectrometer) technique uses plasma at 8000°C to energise ions to emit light. A high-resolution diffraction grating based optical system separates the emitted light according to wavelength, and a photomultiplier detector measures the light. Comparison of atomic emission with standards provides a means for quantitative analysis. Compared to the ICP-MS technique, ICP-OES lacks the ability to measure isotopic concentrations and isotope ratios or ion concentrations at very low levels. On the other hand, spectral analysis is not hampered by the same interferences as Mass Spectrometry, making it an ideal complementary tool for geochemical analysis. The spectral lines used for ICP-OES analysis are given in Table 11-9.

Table 11-9 Wavelengths used on ICP-OES

Element	Wavelength (Nanometer)
P	213.618
Si	251.611
Mn	257.61
Fe	259.94
Mg	279.553
Ti	336.121
Ca	393.367
Al	396.152
Na	589.592
K	766.49

11.11 Analysis of K and Na using Atomic Absorption Spectrometry

Due to technical problems encountered with the ICP-OES system, Atomic Absorption Spectrometry (AAS) was used in some cases to determine K and Na content. The analyses were conducted on a Varian SpectrAA10, using an oxidising air-acetylene flame. Counts were integrated over 5 seconds. The samples were diluted 10 times to fall within the analytical range and a standard set of 0-2 and 0-5 ppm Na (589.6 nm); 0-2 ppm K (766.5 nm) and 0-8 ppm K (769.9 nm).

11.12 Calculation and plotting tools

For the calculation of the normative compositions of the rocks (CIPW norm), an Excel[®] program was used developed by Kurt Hollocher (Geology Department, Union College, Schenectady, NY, 12308, hollochk@union.edu).

The treatment of whole rock geochemical data, involves a substantial amount of plotting of data in diagrams. A range of standard diagrams is used in this thesis to depict certain trends or affinities of the lithologies. These diagrams often include various fields and or lines after published work, showing the relation between the Irumide rocks and various well-studied or reference rock suites. For

the treatment of the data presented in this thesis, a range of plotting tools have been used which include:

- Newpet[®] for DOS (by Daryl Clarke, Memorial University of Newfoundland, Canada)
- Petroplot[®] (Su et al., 2003)
- Microsoft Excel[®]

Diagrams were in most cases finalised in CorelDraw[®] 10.

11.13 Normalisation values

Table 11-10: Normalisation values for CI-chondrite after McDonough and Sun (1995).

Element	Normalisation value CI-Chondrite
La	0.237
Ce	0.613
Pr	0.0928
Nd	0.457
Sm	0.148
Eu	0.0563
Gd	0.199
Tb	0.0361
Dy	0.246
Ho	0.0546
Er	0.16
Yb	0.161
Lu	0.0246

Table 11-11: Normalisation values for Primordial Mantle after Sun and McDonough (1989).

Element	Normalisation value Primordial Mantle
Cs	0.0079
Rb	0.635
Ba	6.989
Th	0.085
U	0.021
Nb	0.713
Ta	0.041
La	0.687
Ce	1.775
Pb	0.071
Pr	0.276
Sr	21.1
Nd	1.354
Zr	11.2
Hf	0.309
Sm	0.444
Eu	0.168
Gd	0.596
Tb	0.108
Dy	0.737
Ho	0.164
Er	0.48
Yb	0.493
Y	4.55
Lu	0.074

Table 11-12: Normalisation values for N-MORB after Pearce (1996b)

Element	Normalisation value N-MORB
Th	0.2
Ta	0.18
Nb	2.7
Ce	10
P2O5	0.12
Zr	90
Hf	2.4
TiO2	1.45
Y	30
Yb	3.4
Sc	40

Table 11-13: Normalisation values for Ocean-Ridge Granitoid after Pearce et al. (1984a).

Element	Normalisation value Ocean-Ridge Granitoid
K ₂ O	0.4
Rb	4
Ba	50
Th	0.8
Ta	0.7
Nb	10
Ce	35
Hf	9
Zr	340
Sm	9
Y	70
Yb	80

12 APPENDIX E: Isotope geochemistry

12.1 Mass Spectrometry

All isotopic measurements were made on a VG-354 multicollector mass spectrometer with software interface. The multicollector system consists of nine Faraday collectors: one axial collector (Ax), four higher mass collectors (H1-H4), and four lower mass collectors (L1-L4). The axial collector can be changed to the Daly photomultiplier for measurement of small ion beams, using a simple selection in the software.

In Thermal Ionisation Mass Spectrometry (TIMS), a small amount of acid dissolved sample is ionised through heating of the Rhenium or Tantalum filament to temperatures in excess of 900°C. The ions are accelerated in an electric field ($eV = \frac{1}{2}mv^2$ (where e =charge; V =accelerating voltage; m =mass of the ion; v =velocity of the ion)). The ions are subsequently focused through an electrical lens system, and channelled through a magnetic field where they are diverted into an orbit with radius dependent on ionic mass. The radius can be calculated through the following equation:

$$r_m = \frac{m.v}{e.B}$$

where r_m = radius (cm); m = ionic mass (amu); v = velocity (m/s); e = charge; B = magnetic field (gauss).

This equation indicates that, with constant magnetic field and accelerating voltage, the radius of the ion is only dependent on the charge and the ionic mass.

The precision obtained through the ID-TIMS method is a direct result of the fact that ionisation yields from the filaments are high, that the method avoids mass interferences by using single atomic samples, and that a known amount of

material with known (and often unusual) isotopic composition is added to the unknown sample. This material is referred to as the “spike”, and allows very accurate determination of isotopic composition of the unknown. The sample digestion and chemical separation that precedes an ID-TIMS analysis is described in the following sections.

12.2 Sample digestion and spiking

The sample holder and digestion setup consists for each sample of a bomb consisting of a conical end Teflon canister to hold the sample, and a fitting cap, which when fitted together form a flat ended cylinder. The conical fitting and external shape is meant to ensure tight fit in the metal holders, and ensures that the canister can stand high pressures and does not deform under high temperature. Some protecting Teflon pads and a mantle ensures that the Teflon canister does not come in direct contact with the metal holder (Fig. 12-1). The metal holder consists of a screw cap and holder, which puts the Teflon sample canister under slight pressure allowing better digestion and avoiding leakage.

The canisters, Teflon pads and mantles are thoroughly cleaned prior to sample digestion to avoid contamination, first in deionised water with lint free cloth, and then in a 70% HNO_3 bath at 80°C on a hot plate for 24 hours. The HNO_3 is washed out with a hot bath of deionised water on a hot plate for another 24 hours. The metal sample holders are cleaned with deionised water and lint free cloth, followed by an ultrasonic bath for five minutes, to remove loose particles and possible dust coating. The holders are dried and cleaned with PROPAN-2-OL to remove water, and stored in a dust free environment.

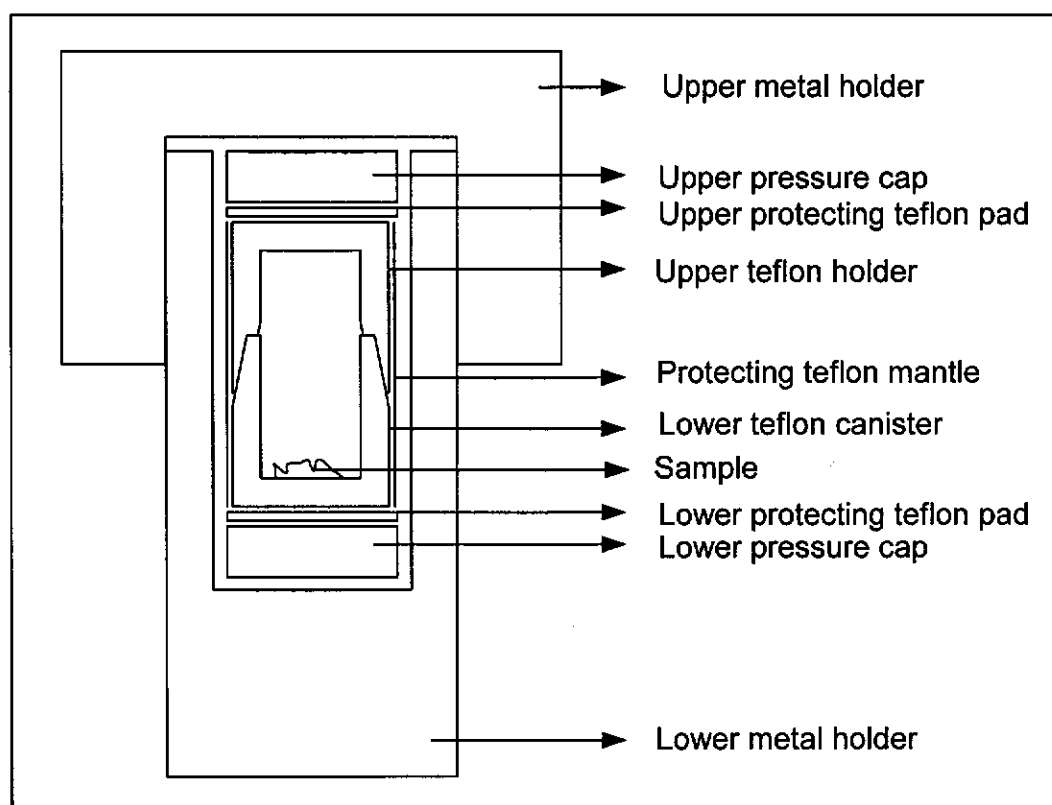


Figure 12-1 Schematic representation of the sample holder and casing for digestion of the sample in hydrofluoric acid (HF).

Samples are crushed and powdered in a tungsten ring mill, taking care to crush a representative part for the sample. In fine-grained rocks this involves crushing of ~200 grammes (g) of sample, and quartering off to ~1 g. For medium to coarse grained samples up to 1 kilogram (kg) of sample may be crushed and quartered down to obtain a representative sample of ~1 g. About 100 milligram (mg) of sample powder is transferred to a Teflon bomb and weighed on a Sartorius Ultra Micro balance. The sample is spiked with ~25-50 mg of ^{147}Sm / ^{150}Nd spike of known isotopic composition (depending on expected concentrations in the sample). ~1 ml HF acid is added to submerge the sample, and the Teflon bombs are placed into the metal screw-cap holders (see Fig. 12-1). The sample is then transferred into an oven at ~180°C for 12 hours, to allow time for complete digestion. When taking the sample from the oven, about one hour is allowed for cooling, after which visual inspection reveals whether the entire sample has been successfully digested. If full digestion has not been achieved, some HNO_3 can be added to the bomb, and the sample allowed to digest further in

the oven for another 12 hours. When the sample has been fully digested, the Teflon bombs are taken from the metal holders, opened, and allowed to evaporate on a hot plate at no more than 60°C. Care is taken not to overheat the sample at this stage, as that would cause insoluble fluorides to be formed. When the samples are completely dry, the residue is redissolved in 6M HCl, and allowed to evaporate on a hot plate at 60°C. This step ensures that all HF is removed from the sample. When the sample is completely dry again, the residue is dissolved in a minimal amount of 2M HCl. The redissolved sample is first placed in a centrifuge, to separate colloidal and undissolved impurities. The liquid phases can then be passed through the column separation (see below). After first separation of REE, the collected REE fraction is evaporated down to dryness on a hot plate at 60°C. The fraction is then redissolved in 0.2M HCl for treatment on the second separation (see below). The redissolved REE fraction is passed onto the Sm-Nd column, and Sm and Nd fractions collected. These are finally evaporated to dryness and ready for loading on filaments.

12.3 Chemical separation

The separation of atomic species prior to loading on filaments is an important step in the preparation for ID-TIMS analysis. Chemical separation is achieved in an “ultra-clean” laboratory, using highly purified chemicals and Teflon/glassware. Each sample digestion and separation is accompanied by a blank, to monitor background levels. The specific methodologies applied for separation of Rb and Sr from Rare Earth Elements, and for separating Sm from Nd are outlined below.

12.3.1 Separation of REE from lighter elements

Cation Exchange resin AG 50W × 8 200-400 mesh hydrogen form is used for the separation of REE from lighter elements. The resin is placed on top of a tungsten wool filter in a small glass column, through gravity (sedimentation) and calibrated using standard single cation solutions and Chlorophosphonazo III

metallochromic indicator. During this study, calibration was done to extract Rb, Sr and REE, but for reasons of time, only the REE fraction was collected for further separation and analysis. Once the volumes and molarities of HCl are defined for each column to separate the elements, the procedure can be repeated to allow separation of Rb, Sr and REE from an unknown. The calibration results are schematically shown in Figure 12-2.

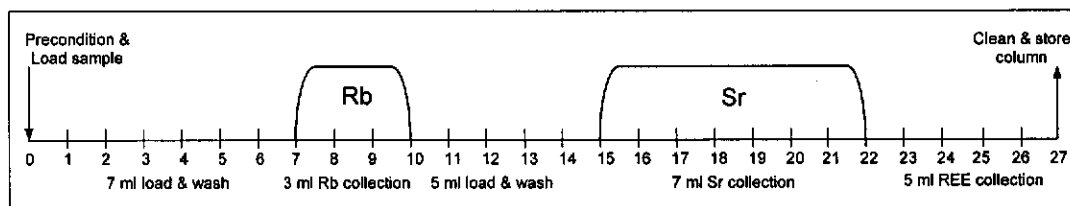


Figure 12-2: Schematic representation of the calibration of cation exchange columns used to separate Rb, Sr and REE in this study. Rb is collected in 2ml after 7ml wash in 2M HCl. Sr is collected in 7ml after 5ml wash in 4M HCl. REE are collected in 5ml of 6M HCl straight after the Sr peak.

12.3.2 Separation of Sm and Nd

The separation of REE is based on Reverse-Phase Partition Chromatography, using a column of polytrifluorochloroethylene (Kel-F) impregnated with di(2-ethylhexyl)-orthophosphoric acid (HDEHP)(Sochacka and Siekierski, 1964; Kiss, 1992). The HDEHP is packed in dilute HCl solution, and the packing protected with a tungsten wool filter on top, to avoid disturbing the filter when loading solutions. Calibration proceeds similarly to that for the cation-exchange columns, again in sequential order with first Nd and then Sm passing through the column. The solution used to separate Nd from Sm is 0.2M and 0.4M HCl respectively. Collection windows for both Nd and Sm are defined for each individual column, and a separation of minimum 2ml must be achieved between peaks to acquire satisfactory separation (Figure 12-3 and Figure 12-4). If Nd passes through too fast, inadequate separation of Ba from Nd may result in complications with the separates. Normally about 10ml of 0.2M HCl must precede extraction of Nd for it to be reasonably free of Ba.

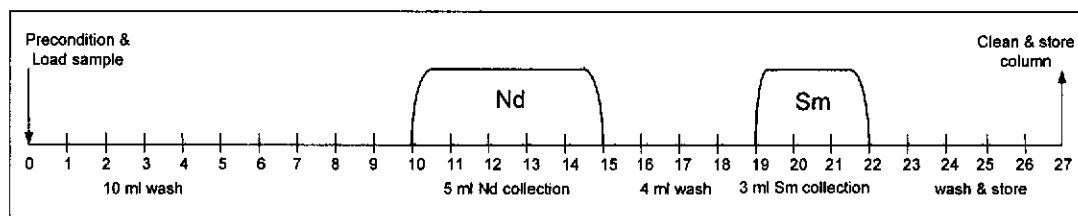


Figure 12-3: Schematic representation of the calibration of Kel-F / HDPEP column # 1 used in the study to separate Nd from Sm.

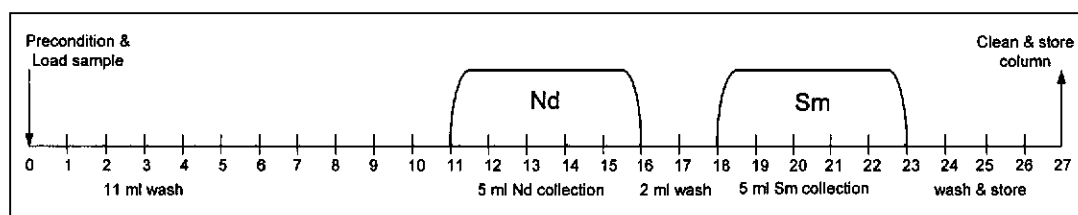


Figure 12-4: Schematic representation of the calibration of Kel-F / HDPEP columns # 2, #3 and #4 used in the study to separate Nd from Sm.

12.4 Sample loading

To concentrate the sample residues of each isotopic separation, it is necessary to redissolve each separate into one drop of HNO_3 followed by one drop of H_3PO_4 . Further slight evaporation on the hot plate produces a gel-like droplet in which all residue is dissolved. Just prior to loading the material on a filament, one drop of HNO_3 is added to make about 100 μl of total solution. The Sm, Nd and Rb fractions of sample, blank and standard (for Sm and Rb no standard is necessary) are loaded onto a triple Remium (3RE) filament configuration (Fig. 12-5).

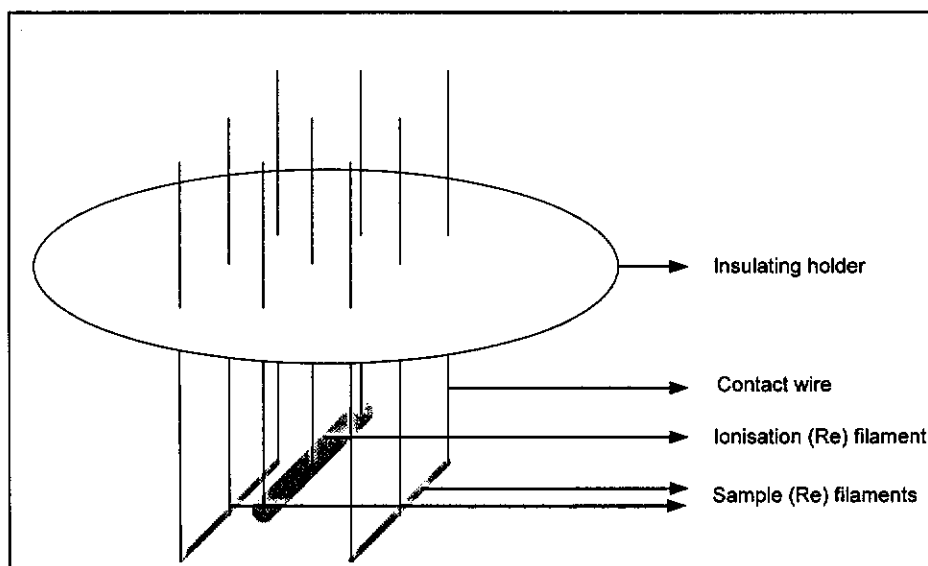


Figure 12-5 Triple Rhenium filament configuration used for Sm, Nd and Rb Thermal Ionisation mass Spectrometry (TIMS)

About 50 μl of redissolved sample solution is loaded onto the external two Re filaments by putting a droplet onto the slightly heated filament. The droplet is slowly evaporated, and finally “burnt” onto the filament by gradually increasing the current through the wire. The same system of loading is applied for the Sr extracts, which are loaded onto a single Tantalum (1Ta) filament configuration (Fig. 12-6).

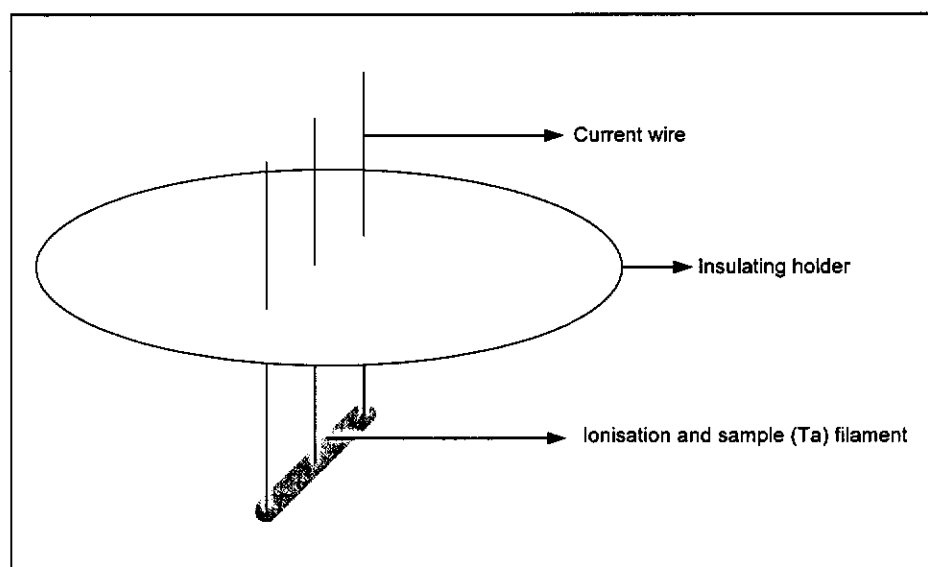


Figure 12-6 Single Tantalum (1Ta) filament configuration used for TIMS analysis of Sr.

The typical filament configuration for a mass spectrometer run of one unknown, one standard and one blank looks as follows (Table 12-1). The filaments are loaded in the TIMS sample tray and placed into the sample lock in the evening and are pumped down to vacuum overnight.

Table 12-1 Typical filament configuration for a mass spectrometer run of Sm, Nd, Rb and Sr

Filament nr	Filament type	Sample designation	Element
1	3Re	Unknown	Nd
2	3Re	Blank	Nd
3	3Re	Unknown	Sm
4	3Re	Blank	Sm
5	3Re	Standard	Nd
6	3Re	Unknown	Rb
7	3Re	Blank	Rb
8	1Ta	Unknown	Sr
9	1Ta	Blank	Sr
10	1Ta	Standard	Sr

12.5 Operating procedures

The VG-354 mass spectrometer is software controlled through a menu driven program. This program controls the detector setting, readings, voltmeters and sequencing of analyses. The software allows manual control to change and save detector settings. A series of hardware control panels allow the manual control of beam deflectors, filament temperatures and manual magnet control for beam deflection. The filaments are loaded in a carousel that can hold up to 24 samples. Each sample can be manually rotated into place for analysis.

12.6 Internal instrument corrections

The instrumental factors affecting precision of mass spectrometry analysis include beam stability, gain and cup-efficiency. If ionic charges for a given set of

isotopes are identical, detector spacing can be set such that different isotopes are measured simultaneously. By progressively shifting the detector array one unit towards lower mass (multicollector jumping mode), it is possible to overcome cup efficiency problems. Since all ratios are calculated from measurements acquired during one jump, the results are independent of the beam stability and are gain free. Isotopic ratios are calculated and corrected for mass fractionation through an internal programme following Turner (1982). A typical analysis is set up to run in ten blocks of ten measurements, for which each geometric mean is calculated. A data printout is generated during analysis, which includes raw background counts and raw detector counts, as well as corrected isotopic ratios and analytical errors (2σ level) per block of ten measurements, and for the total number of measurements.

13 APPENDIX F: SHRIMP analytical data

In the following tables, analyses are reported in the order they were analysed during the session. Details on each analytical session are provided at the bottom of each table, including the date, and the number and error on standard analyses.

Table 13-1 SHRIMP analytical data for sample KMP-1 (biotite granite gneiss, Kapiri Mposhi map sheet). Spot name ending with r denotes an analysis on a rim.

Spot Name	f^{206} (%)	U (ppm)	Th (ppm)	Th/U	$^{207}\text{Pb}/^{206}\text{Pb}$ ($\pm 1\sigma$)	$^{206}\text{Pb}/^{238}\text{U}$ ($\pm 1\sigma$)	$^{207}\text{Pb}/^{206}\text{Pb}$ Age ($\pm 1\sigma$ Ma)	C(%)
KMP1-1	0.160	361	109	0.31	0.18520 \pm 0.00058	0.49807 \pm 0.00196	2700.0 \pm 5.1	96.5
KMP1-2	5.328	300	192	0.66	0.23768 \pm 0.02128	0.60223 \pm 0.06121	3104.5 \pm 142.7	97.9
KMP1-1r	1.134	559	358	0.66	0.18360 \pm 0.00145	0.45528 \pm 0.00159	2685.7 \pm 13.0	90.1
KMP1-3	1.946	714	440	0.64	0.18677 \pm 0.00507	0.44983 \pm 0.00260	2713.9 \pm 44.7	88.2
KMP1-4	0.087	597	416	0.72	0.18951 \pm 0.00043	0.53337 \pm 0.00163	2737.9 \pm 3.7	100.6
KMP1-5	0.421	665	226	0.35	0.18727 \pm 0.00067	0.40214 \pm 0.00154	2718.3 \pm 5.9	80.2
f^{206} = the proportion of common ^{206}Pb in the total ^{206}Pb ; Th/U = $^{232}\text{Th}/^{238}\text{U}$; %C = % concordance								
All ratios and ages corrected for common Pb using measured ^{204}Pb and composition appropriate to the age of the zircon (Stacey and Kramers, 1975)								
Analyses conducted during a single session (31/03/2003). 10 CZ3 standard analyses yielded a 2σ error of the mean of 0.36%								

Table 13-2 SHRIMP analytical data for sample MK-3 (biotite granite gneiss, Mkushi map sheet). Spot names ending with r denote analyses on a rim, spot names ending with c denote analyses on core.

Spot Name	f^{206} (%)	U (ppm)	Th (ppm)	Th/U	$^{207}\text{Pb}/^{206}\text{Pb}$ ($\pm 1\sigma$)	$^{206}\text{Pb}/^{238}\text{U}$ ($\pm 1\sigma$)	$^{207}\text{Pb}/^{206}\text{Pb}$ Age ($\pm 1\sigma$ Ma)	C(%)
MK3-1	0.038	228	194	0.88	0.12646 \pm 0.00066	0.36575 \pm 0.00188	2049.3 \pm 9.2	98.1
MK3-2r	0.024	770	56	0.08	0.12404 \pm 0.00047	0.35671 \pm 0.00101	2015.1 \pm 6.7	97.6
MK3-3r	0.002	891	88	0.10	0.12515 \pm 0.00034	0.36597 \pm 0.00100	2031.0 \pm 4.8	99.0
MK3-4r	0.000	137	122	0.91	0.12605 \pm 0.00082	0.36105 \pm 0.00244	2043.6 \pm 11.6	97.2
MK3-4c	0.089	466	411	0.91	0.12560 \pm 0.00054	0.32834 \pm 0.00133	2037.3 \pm 7.7	89.8
f^{206} = the proportion of common ^{206}Pb in the total ^{206}Pb ; Th/U = $^{232}\text{Th}/^{238}\text{U}$; %C = % concordance								
All ratios and ages corrected for common Pb using measured ^{204}Pb and composition appropriate to the age of the zircon (Stacey and Kramers, 1975)								
Analyses conducted during a single session (31/03/2003). 10 CZ3 standard analyses yielded a 2σ error of the mean of 0.36%								

Table 13-3 SHRIMP analytical data for sample MK-5 (pink granite gneiss, Mkushi map sheet). Spot names ending with r denote analyses on a rim, spot names ending with c denote analyses on core.

Spot Name	f^{206} (%)	U (ppm)	Th (ppm)	Th/U	$^{207}\text{Pb}/^{206}\text{Pb}$ ($\pm 1\sigma$)	$^{206}\text{Pb}/^{238}\text{U}$ ($\pm 1\sigma$)	$^{207}\text{Pb}/^{206}\text{Pb}$ Age ($\pm 1\sigma$ Ma)	C(%)
¹ MK5-1	0.167	569	351	0.64	0.12591 \pm 0.00064	0.35801 \pm 0.00496	2041.6 \pm 9.0	96.6
¹ MK5-2	0.013	681	369	0.56	0.12508 \pm 0.00027	0.36034 \pm 0.00460	2029.9 \pm 3.9	97.7
¹ MK5-3	0.712	687	408	0.61	0.12480 \pm 0.00065	0.31352 \pm 0.00400	2026.0 \pm 9.2	86.8
² MK5-4	0.090	804	367	0.47	0.12116 \pm 0.00048	0.32508 \pm 0.00095	1973.4 \pm 7.1	91.9
² MK5-5r	0.034	587	329	0.58	0.12669 \pm 0.00044	0.36302 \pm 0.00221	2052.5 \pm 6.2	97.3
² MK5-6	0.050	505	409	0.84	0.12639 \pm 0.00129	0.37341 \pm 0.00170	2048.3 \pm 18.0	99.9
² MK5-7	0.280	224	139	0.64	0.12665 \pm 0.00079	0.35236 \pm 0.00197	2051.9 \pm 11.0	94.8
f^{206} = the proportion of common ^{206}Pb in the total ^{206}Pb ; Th/U = $^{232}\text{Th}/^{238}\text{U}$; %C = % concordance All ratios and ages corrected for common Pb using measured ^{204}Pb and composition appropriate to the age of the zircon (Stacey and Kramers, 1975) Analyses conducted during two sessions (¹ 28/02/2003 and ² 31/03/2003). Session ¹ : 10 CZ3 standard analyses yielded a 2 σ error of the mean of 0.98% Session ² : 10 CZ3 standard analyses yielded a 2s error of the mean of 0.36%								

Table 13-4 SHRIMP analytical data for sample CC-10 (porphyritic granite, Chin'gombe Mission map sheet).

Spot Name	f^{206} (%)	U (ppm)	Th (ppm)	Th/U	$^{207}\text{Pb}/^{206}\text{Pb}$ ($\pm 1\sigma$)	$^{206}\text{Pb}/^{238}\text{U}$ ($\pm 1\sigma$)	$^{207}\text{Pb}/^{206}\text{Pb}$ Age ($\pm 1\sigma$ Ma)	C(%)
CC10-1.1	0.000	693	612	0.91	0.12058 \pm 0.00034	0.37259 \pm 0.01464	1964.9 \pm 5.1	103.9
CC10-2.1	0.851	460	343	0.77	0.11507 \pm 0.00428	0.30681 \pm 0.01212	1881.0 \pm 67.0	91.7
CC10-3.1	0.163	514	296	0.60	0.11950 \pm 0.00046	0.35108 \pm 0.01380	1948.7 \pm 6.9	99.5
CC10-4.1	0.426	167	121	0.75	0.11864 \pm 0.00203	0.34657 \pm 0.01371	1935.9 \pm 30.6	99.1
CC10-5.1	0.051	403	283	0.72	0.11942 \pm 0.00050	0.33052 \pm 0.01300	1947.6 \pm 7.5	94.5
CC10-6.1	0.005	390	273	0.72	0.11898 \pm 0.00046	0.33719 \pm 0.01326	1940.9 \pm 6.9	96.5
f^{206} = the proportion of common ^{206}Pb in the total ^{206}Pb ; Th/U = $^{232}\text{Th}/^{238}\text{U}$; %C = % concordance All ratios and ages corrected for common Pb using measured ^{204}Pb and composition appropriate to the age of the zircon (Stacey and Kramers, 1975) Analyses conducted during a single session (06/07/2003). 16 CZ3 standard analyses yielded a 2 σ error of the mean of 2.10%								

Table 13-5 SHRIMP analytical data for sample KN-1 (biotite granite gneiss, Kanona map sheet).

Spot Name	f^{206} (%)	U (ppm)	Th (ppm)	Th/U	$^{207}\text{Pb}/^{206}\text{Pb}$ ($\pm 1\sigma$)	$^{206}\text{Pb}/^{238}\text{U}$ ($\pm 1\sigma$)	$^{207}\text{Pb}/^{206}\text{Pb}$ Age ($\pm 1\sigma$ Ma)	C(%)
KN1-1	0.002	335	198	0.61	0.12935 \pm 0.00067	0.30750 \pm 0.00816	2089.1 \pm 9.1	82.7
KN1-2	0.005	268	68	0.26	0.12518 \pm 0.00068	0.33974 \pm 0.00833	2031.3 \pm 9.6	92.8
KN1-3	0.041	307	112	0.38	0.12539 \pm 0.00056	0.36288 \pm 0.00896	2034.3 \pm 7.9	98.1
KN1-4	0.000	440	215	0.51	0.12547 \pm 0.00045	0.35235 \pm 0.00855	2035.5 \pm 6.4	95.6
KN1-5	0.000	414	200	0.50	0.12570 \pm 0.00044	0.37025 \pm 0.00899	2038.7 \pm 6.1	99.6
KN1-6	0.007	386	223	0.60	0.12647 \pm 0.00046	0.37061 \pm 0.00901	2049.4 \pm 6.4	99.2
f^{206} = the proportion of common ^{206}Pb in the total ^{206}Pb ; Th/U = $^{232}\text{Th}/^{238}\text{U}$; %C = % concordance All ratios and ages corrected for common Pb using measured ^{204}Pb and composition appropriate to the age of the zircon (Stacey and Kramers, 1975) Analyses conducted during a single session (08/06/2003). 12 CZ3 standard analyses yielded a 2 σ error of the mean of 1.56%								

Appendix F: zircon U-Pb SHRIMP analytical data

Table 13-6 SHRIMP analytical data for sample ISK-1 (Luwalizi Granite Gneiss, Isoka map sheet).

Spot Name	f ₂₀₆ (%)	U (ppm)	Th (ppm)	Th/U	²⁰⁷ Pb/ ²⁰⁶ Pb (±1σ)	²⁰⁶ Pb/ ²³⁸ U (±1σ)	²⁰⁷ Pb/ ²⁰⁶ Pb Age (±1σ Ma)	C(%)
ISK1-1	0.029	253	179	0.73	0.11875 ±0.00068	0.33595 ±0.00342	1937.5 ±10.2	96.4
ISK1-2	0.028	2669	110	0.04	0.11800 ±0.00055	0.36163 ±0.00369	1926.1 ±8.3	103.3
ISK1-3	0.855	93	175	1.93	0.11577 ±0.00191	0.34508 ±0.00413	1892.0 ±29.8	101.0
ISK1-4	0.077	565	110	0.20	0.11893 ±0.00050	0.34189 ±0.00322	1940.1 ±7.6	97.7
ISK1-5	0.061	521	109	0.22	0.11895 ±0.00042	0.34748 ±0.00325	1940.6 ±6.4	99.1
ISK1-6	0.212	945	169	0.19	0.11838 ±0.00110	0.32209 ±0.00634	1931.9 ±16.7	93.2
ISK1-7	0.000	504	204	0.42	0.11916 ±0.00038	0.34803 ±0.00340	1943.6 ±5.7	99.1
ISK1-8	0.060	396	156	0.41	0.11917 ±0.00050	0.33942 ±0.00345	1943.8 ±7.5	96.9
ISK1-9	0.194	785	595	0.78	0.12008 ±0.00122	0.34865 ±0.00318	1957.4 ±18.2	98.5
f ₂₀₆ = the proportion of common ²⁰⁶ Pb in the total ²⁰⁶ Pb; Th/U = ²³² Th/ ²³⁸ U; %C = % concordance								
All ratios and ages corrected for common Pb using measured ²⁰⁴ Pb and composition appropriate to the age of the zircon (Stacey and Kramers, 1975)								
Analyses conducted during a single session (29/09/2002). 15 CZ3 standard analyses yielded a 2σ error of the mean of 0.51%								

Table 13-7 SHRIMP analytical data for sample ISK-2 (Luwalizi Granite Gneiss, Isoka map sheet).

Spot Name	f ₂₀₆ (%)	U (ppm)	Th (ppm)	Th/U	²⁰⁷ Pb/ ²⁰⁶ Pb (±1σ)	²⁰⁶ Pb/ ²³⁸ U (±1σ)	²⁰⁷ Pb/ ²⁰⁶ Pb Age (±1σ Ma)	C(%)
ISK2-1	0.688	103	29	0.29	0.11666 ±0.00146	0.35250 ±0.00409	1905.7 ±22.5	102.1
ISK2-2	0.181	300	391	1.34	0.11926 ±0.00065	0.30654 ±0.00299	1945.2 ±9.8	88.6
ISK2-3	0.071	502	308	0.63	0.11781 ±0.00041	0.33415 ±0.00310	1923.3 ±6.2	96.6
ISK2-4	0.000	949	29	0.03	0.11919 ±0.00135	0.35460 ±0.01018	1944.2 ±20.2	100.6
ISK2-5	0.059	277	26	0.10	0.11879 ±0.00081	0.34057 ±0.00336	1938.1 ±12.2	97.5
f ₂₀₆ = the proportion of common ²⁰⁶ Pb in the total ²⁰⁶ Pb; Th/U = ²³² Th/ ²³⁸ U; %C = % concordance								
All ratios and ages corrected for common Pb using measured ²⁰⁴ Pb and composition appropriate to the age of the zircon (Stacey and Kramers, 1975)								
Analyses conducted during a single session (29/09/2002). 15 CZ3 standard analyses yielded a 2σ error of the mean of 0.51%								

Table 13-8 SHRIMP analytical data for sample MA1 (Mansa Granite, Mansa map sheet).

Spot Name	f ₂₀₆ (%)	U (ppm)	Th (ppm)	Th/U	²⁰⁷ Pb/ ²⁰⁶ Pb (±1σ)	²⁰⁶ Pb/ ²³⁸ U (±1σ)	²⁰⁷ Pb/ ²⁰⁶ Pb Age (±1σ Ma)	C(%)
MA1-1	0.033	481	447	0.96	0.11382 ±0.00039	0.32521 ±0.00302	1861.3 ±6.3	97.5
MA1-2	0.010	310	336	1.12	0.11375 ±0.00047	0.33116 ±0.00318	1860.2 ±7.4	99.1
MA1-3	0.315	196	270	1.42	0.11245 ±0.00086	0.32055 ±0.00334	1839.4 ±13.8	97.4
MA1-4	0.446	161	219	1.41	0.11366 ±0.00116	0.29450 ±0.00323	1858.7 ±18.4	89.5
f ₂₀₆ = the proportion of common ²⁰⁶ Pb in the total ²⁰⁶ Pb; Th/U = ²³² Th/ ²³⁸ U; %C = % concordance								
All ratios and ages corrected for common Pb using measured ²⁰⁴ Pb and composition appropriate to the age of the zircon (Stacey and Kramers, 1975)								
Analyses conducted during a single session (30/09/2002). 17 CZ3 standard analyses yielded a 2σ error of the mean of 0.51%								

Table 13-9 SHRIMP analytical data for sample MA2 (Mansa Granite, Mansa map sheet).

Spot Name	f^{206} (%)	U (ppm)	Th (ppm)	Th/U	$^{207}\text{Pb}/^{206}\text{Pb}$ ($\pm 1\sigma$)	$^{206}\text{Pb}/^{238}\text{U}$ ($\pm 1\sigma$)	$^{207}\text{Pb}/^{206}\text{Pb}$ Age ($\pm 1\sigma$ Ma)	C(%)
MA2-1	0.054	249	176	0.73	0.11405 \pm 0.00063	0.33122 \pm 0.00330	1865.0 \pm 9.9	98.9
MA2-2	0.104	166	177	1.10	0.11254 \pm 0.00088	0.34415 \pm 0.00480	1840.9 \pm 14.1	103.6
MA2-3	0.070	195	198	1.05	0.11409 \pm 0.00073	0.33393 \pm 0.00340	1865.5 \pm 11.6	99.6
MA2-4	0.000	209	226	1.12	0.11432 \pm 0.00058	0.33588 \pm 0.00351	1869.2 \pm 9.2	99.9
MA2-5	0.338	290	212	0.75	0.11379 \pm 0.00074	0.32660 \pm 0.00319	1860.9 \pm 11.7	97.9
MA2-6	0.037	312	278	0.92	0.11387 \pm 0.00066	0.33103 \pm 0.00320	1862.0 \pm 10.4	99.0
MA2-7	0.100	151	133	0.91	0.11383 \pm 0.00090	0.34458 \pm 0.00366	1861.4 \pm 14.3	102.5
MA2-8	0.083	168	189	1.16	0.11402 \pm 0.00079	0.33662 \pm 0.00353	1864.5 \pm 12.6	100.3
MA2-9	0.064	365	257	0.73	0.11381 \pm 0.00049	0.33550 \pm 0.00320	1861.2 \pm 7.8	100.2
f^{206} = the proportion of common ^{206}Pb in the total ^{206}Pb ; Th/U = $^{232}\text{Th}/^{238}\text{U}$; %C = % concordance All ratios and ages corrected for common Pb using measured ^{204}Pb and composition appropriate to the age of the zircon (Stacey and Kramers, 1975) Analyses conducted during a single session (30/09/2002). 17 CZ3 standard analyses yielded a 2σ error of the mean of 0.51%								

Table 13-10 SHRIMP analytical data for sample MA3 (Mansa Volcanic, Mansa map sheet).

Spot Name	f^{206} (%)	U (ppm)	Th (ppm)	Th/U	$^{207}\text{Pb}/^{206}\text{Pb}$ ($\pm 1\sigma$)	$^{206}\text{Pb}/^{238}\text{U}$ ($\pm 1\sigma$)	$^{207}\text{Pb}/^{206}\text{Pb}$ Age ($\pm 1\sigma$ Ma)	C(%)
MA3-1	0.177	453	398	0.91	0.11101 \pm 0.00051	0.31363 \pm 0.00295	1816.1 \pm 8.3	96.8
MA3-2	0.057	143	134	0.97	0.11498 \pm 0.00082	0.33843 \pm 0.00514	1879.5 \pm 12.8	100.0
MA3-3	0.104	195	296	1.57	0.11344 \pm 0.00068	0.33107 \pm 0.00350	1855.3 \pm 10.8	99.4
MA3-4	0.258	71	68	0.99	0.11287 \pm 0.00134	0.34240 \pm 0.00425	1846.1 \pm 21.5	102.8
MA3-5	0.040	222	264	1.23	0.11389 \pm 0.00061	0.33492 \pm 0.00345	1862.4 \pm 9.6	100.0
MA3-6	0.073	299	247	0.85	0.11392 \pm 0.00051	0.34081 \pm 0.00329	1862.9 \pm 8.1	101.5
MA3-7	0.043	165	229	1.43	0.11527 \pm 0.00070	0.33163 \pm 0.00359	1884.1 \pm 10.9	98.0
MA3-8	0.089	159	151	0.98	0.11338 \pm 0.00082	0.33783 \pm 0.00358	1854.3 \pm 13.0	101.2
MA3-9	0.060	326	427	1.35	0.11480 \pm 0.00051	0.33399 \pm 0.00382	1876.7 \pm 8.0	99.0
f^{206} = the proportion of common ^{206}Pb in the total ^{206}Pb ; Th/U = $^{232}\text{Th}/^{238}\text{U}$; %C = % concordance All ratios and ages corrected for common Pb using measured ^{204}Pb and composition appropriate to the age of the zircon (Stacey and Kramers, 1975) Analyses conducted during a single session (30/09/2002). 17 CZ3 standard analyses yielded a 2σ error of the mean of 0.51%								

Table 13-11 SHRIMP analytical data for sample MA5 (Mansa Volcanic, Mansa map sheet).

Spot Name	f^{206} (%)	U (ppm)	Th (ppm)	Th/U	$^{207}\text{Pb}/^{206}\text{Pb}$ ($\pm 1\sigma$)	$^{206}\text{Pb}/^{238}\text{U}$ ($\pm 1\sigma$)	$^{207}\text{Pb}/^{206}\text{Pb}$ Age ($\pm 1\sigma$ Ma)	C(%)
MA5-1	0.020	620	679	1.13	0.11484 \pm 0.00032	0.34711 \pm 0.00323	1877.3 \pm 5.1	102.3
MA5-2	0.298	72	63	0.91	0.11368 \pm 0.00137	0.33917 \pm 0.00412	1859.0 \pm 21.8	101.3
MA5-3	0.446	667	739	1.14	0.10816 \pm 0.00247	0.27965 \pm 0.00299	1768.6 \pm 41.7	89.9
MA5-4	0.260	57	77	1.39	0.11392 \pm 0.00143	0.32764 \pm 0.00418	1862.8 \pm 22.7	98.1
f^{206} = the proportion of common ^{206}Pb in the total ^{206}Pb ; Th/U = $^{232}\text{Th}/^{238}\text{U}$; %C = % concordance All ratios and ages corrected for common Pb using measured ^{204}Pb and composition appropriate to the age of the zircon (Stacey and Kramers, 1975) Analyses conducted during a single session (30/09/2002). 17 CZ3 standard analyses yielded a 2σ error of the mean of 0.51%								

Appendix F: zircon U-Pb SHRIMP analytical data

Table 13-12 SHRIMP analytical data for sample MA9 (Musonda Falls Granite, Musonda Falls map sheet).

Spot Name	f^{206} (%)	U (ppm)	Th (ppm)	Th/U	$^{207}\text{Pb}/^{206}\text{Pb}$ ($\pm 1\sigma$)	$^{206}\text{Pb}/^{238}\text{U}$ ($\pm 1\sigma$)	$^{207}\text{Pb}/^{206}\text{Pb}$ Age ($\pm 1\sigma$ Ma)	C(%)
MA9-1	0.037	134	127	0.98	0.11373 ± 0.00079	0.34248 ± 0.00374	1859.8 ± 12.6	102.1
MA9-2	0.000	208	261	1.29	0.11398 ± 0.00058	0.33645 ± 0.00386	1863.9 ± 9.2	100.3
MA9-3	0.221	138	94	0.71	0.11254 ± 0.00094	0.33072 ± 0.00358	1840.9 ± 15.1	100.1
MA9-4	0.218	298	311	1.08	0.11408 ± 0.00064	0.31857 ± 0.00310	1865.4 ± 10.1	95.6
MA9-5	0.024	148	175	1.22	0.11529 ± 0.00072	0.33386 ± 0.00355	1884.4 ± 11.2	98.6
MA9-6	0.096	93	125	1.40	0.11373 ± 0.00098	0.33623 ± 0.00415	1859.8 ± 15.6	100.5
MA9-7	0.990	115	123	1.11	0.11368 ± 0.00160	0.29036 ± 0.00341	1859.1 ± 25.3	88.4
MA9-8	0.029	187	162	0.89	0.11459 ± 0.00064	0.33443 ± 0.00354	1873.5 ± 10.0	99.3
MA9-9	0.550	182	133	0.75	0.11331 ± 0.00138	0.28272 ± 0.00306	1853.1 ± 22.0	86.6

f^{206} = the proportion of common ^{206}Pb in the total ^{206}Pb ; Th/U = $^{232}\text{Th}/^{238}\text{U}$; %C = % concordance
All ratios and ages corrected for common Pb using measured ^{204}Pb and composition appropriate to the age of the zircon (Stacey and Kramers, 1975)
Analyses conducted during a single session (30/09/2002). 17 CZ3 standard analyses yielded a 2σ error of the mean of 0.51%

Table 13-13 SHRIMP analytical data for sample MA6 (Quartzite, Kabweluma Formation, Mporokoso Group, Mansa map sheet).

Spot Name	f^{206} (%)	U (ppm)	Th (ppm)	Th/U	$^{207}\text{Pb}/^{206}\text{Pb}$ ($\pm 1\sigma$)	$^{206}\text{Pb}/^{238}\text{U}$ ($\pm 1\sigma$)	$^{207}\text{Pb}/^{206}\text{Pb}$ Age ($\pm 1\sigma$ Ma)	C(%)
MA6-1*	0.131	87	93	1.10	0.11161 ± 0.00119	0.33476 ± 0.00586	1825.8 ± 19.3	102.0
MA6-2*	0.061	391	235	0.62	0.12176 ± 0.00044	0.36177 ± 0.00578	1982.2 ± 6.5	100.4
MA6-3*	0.100	31	58	1.89	0.11264 ± 0.00205	0.33377 ± 0.00695	1842.5 ± 33.0	100.8
MA6-4*	0.033	133	88	0.69	0.12175 ± 0.00111	0.36544 ± 0.00613	1982.0 ± 16.2	101.3
MA6-5*	0.213	99	34	0.35	0.13468 ± 0.00129	0.42679 ± 0.00755	2159.9 ± 16.7	106.1
MA6-6*	0.400	27	31	1.19	0.11106 ± 0.00180	0.34475 ± 0.00723	1816.8 ± 29.4	105.1
MA6-7*	0.054	441	568	1.33	0.12248 ± 0.00043	0.36000 ± 0.00574	1992.6 ± 6.2	99.5
MA6-8*	0.195	158	95	0.62	0.12026 ± 0.00082	0.35695 ± 0.00605	1960.1 ± 12.2	100.4
MA6-9*	0.093	278	187	0.69	0.12056 ± 0.00058	0.36523 ± 0.00598	1964.5 ± 8.6	102.2
MA6-10*	0.066	28	22	0.79	0.13576 ± 0.00170	0.38511 ± 0.00787	2173.8 ± 21.9	96.6
MA6-11*	0.042	194	180	0.96	0.11447 ± 0.00066	0.34301 ± 0.00564	1871.5 ± 10.4	101.6
MA6-12*	0.170	70	85	1.25	0.11031 ± 0.00146	0.34077 ± 0.00612	1804.5 ± 24.1	104.8
MA6-13*	0.058	313	365	1.21	0.12053 ± 0.00051	0.36007 ± 0.00580	1964.0 ± 7.6	100.9
MA6-14*	0.432	194	217	1.16	0.11171 ± 0.00094	0.30593 ± 0.00503	1827.3 ± 15.3	94.2
MA6-15*	0.056	225	126	0.58	0.11956 ± 0.00060	0.35208 ± 0.00573	1949.6 ± 8.9	99.7
MA6-16*	0.062	204	86	0.43	0.12236 ± 0.00066	0.36986 ± 0.00606	1991.0 ± 9.5	101.9
MA6-17*	0.116	141	115	0.84	0.11306 ± 0.00080	0.34384 ± 0.00574	1849.2 ± 12.8	103.0
MA6-18*	0.157	138	126	0.94	0.11545 ± 0.00077	0.34714 ± 0.00580	1886.9 ± 12.0	101.8
MA6-2.1#	0.131	87	93	1.10	0.12114 ± 0.00091	0.36462 ± 0.00655	1973.1 ± 13.3	101.6
MA6-2.2#	0.061	391	235	0.62	0.11221 ± 0.00092	0.32673 ± 0.00598	1835.5 ± 14.8	99.3
MA6-2.3#	0.100	31	58	1.89	0.12645 ± 0.00095	0.36261 ± 0.00694	2049.2 ± 13.3	97.3
MA6-2.4#	0.033	133	88	0.69	0.13897 ± 0.00128	0.40703 ± 0.00803	2214.4 ± 16.0	99.4
MA6-2.5#	0.213	99	34	0.35	0.11402 ± 0.00148	0.34277 ± 0.00652	1864.5 ± 23.5	101.9
MA6-2.6#	0.400	27	31	1.19	0.11172 ± 0.00165	0.33885 ± 0.00665	1827.6 ± 26.7	102.9
MA6-2.7#	0.054	441	568	1.33	0.18630 ± 0.00147	0.51587 ± 0.01027	2709.7 ± 13.0	99.0
MA6-2.8#	0.195	158	95	0.62	0.11151 ± 0.00117	0.32774 ± 0.00583	1824.2 ± 19.0	100.2
MA6-2.9#	0.093	278	187	0.69	0.11347 ± 0.00061	0.31661 ± 0.00531	1855.7 ± 9.8	95.6
MA6-2.10#	0.066	28	22	0.79	0.12358 ± 0.00043	0.36232 ± 0.00605	2008.6 ± 6.2	99.2
MA6-2.11#	0.042	194	180	0.96	0.12126 ± 0.00059	0.35021 ± 0.00604	1974.9 ± 8.7	98.0

f^{206} = the proportion of common ^{206}Pb in the total ^{206}Pb ; Th/U = $^{232}\text{Th}/^{238}\text{U}$; %C = % concordance
All ratios and ages corrected for common Pb using measured ^{204}Pb and composition appropriate to the age of the zircon (Stacey and Kramers, 1975)
Analyses conducted on the same mount, during two separate sessions
Session 1 (07/10/2002): 2σ error in standard calibration for 19 CZ3 standards was 0.78% (analyses denoted with *)
Session 2 (01/03/2003): 2σ error in standard calibration for 8 CZ3 standards was 1.38% (analyses denoted with #)

Table 13-14 SHRIMP analytical data for sample KAS (Mwela Quartzite, Kasama Formation, Kasama map sheet).

Spot Name	f^{206} (%)	U (ppm)	Th (ppm)	Th/U	$^{207}\text{Pb}/^{206}\text{Pb}$ ($\pm 1\sigma$)	$^{206}\text{Pb}/^{238}\text{U}$ ($\pm 1\sigma$)	$^{207}\text{Pb}/^{206}\text{Pb}$ Age ($\pm 1\sigma$ Ma)	C(%)
KAS-1*	0.079	319	147	0.48	0.17358 ± 0.00055	0.48384 ± 0.00783	2592.5 ± 5.3	98.1
KAS-2*	0.086	110	46	0.43	0.12310 ± 0.00092	0.35927 ± 0.00610	2001.7 ± 13.3	98.9
KAS-3*	0.071	127	124	1.01	0.12121 ± 0.00087	0.36376 ± 0.00610	1974.1 ± 12.8	101.3
KAS-4*	0.235	354	232	0.68	0.11471 ± 0.00072	0.30468 ± 0.00488	1875.3 ± 11.3	91.4
KAS-5*	0.086	249	163	0.68	0.09039 ± 0.00064	0.23813 ± 0.00387	1433.7 ± 13.5	96.0
KAS-6*	0.000	157	252	1.65	0.12163 ± 0.00071	0.36095 ± 0.00597	1980.3 ± 10.4	100.3
KAS-7*	0.078	166	57	0.35	0.12717 ± 0.00073	0.37953 ± 0.00637	2059.2 ± 10.2	100.7
KAS-8*	0.505	483	474	1.01	0.10776 ± 0.00251	0.24683 ± 0.00408	1761.8 ± 42.6	80.7
KAS-9*	0.133	190	104	0.56	0.12689 ± 0.00076	0.33364 ± 0.00557	2055.3 ± 10.5	90.3
KAS-10*	0.220	83	82	1.02	0.11004 ± 0.00107	0.32852 ± 0.00572	1800.1 ± 17.8	101.7
KAS-11*	0.022	202	156	0.80	0.12556 ± 0.00074	0.37436 ± 0.00610	2036.8 ± 10.4	100.6
KAS-12*	0.000	127	130	1.06	0.11538 ± 0.00124	0.32068 ± 0.00576	1885.8 ± 19.3	95.1
KAS-13*	0.000	130	80	0.64	0.12186 ± 0.00068	0.36238 ± 0.00605	1983.6 ± 9.9	100.5
KAS-14*	0.078	111	84	0.78	0.11600 ± 0.00099	0.30067 ± 0.00509	1895.4 ± 15.4	89.4
KAS-15*	0.007	156	90	0.60	0.11743 ± 0.00065	0.35136 ± 0.00580	1917.4 ± 10.0	101.2
KAS-16*	0.230	78	58	0.77	0.12047 ± 0.00120	0.34901 ± 0.00610	1963.2 ± 17.8	98.3
KAS-17*	0.098	136	137	1.04	0.11400 ± 0.00075	0.33860 ± 0.00566	1864.2 ± 11.8	100.8
KAS-18*	0.045	281	173	0.64	0.11869 ± 0.00050	0.35515 ± 0.00573	1936.6 ± 7.6	101.2
KAS-2.1#	0.507	70	75	1.10	0.11234 ± 0.00159	0.32701 ± 0.00606	1837.5 ± 25.6	99.3
KAS-2.2#	0.474	442	354	0.83	0.11574 ± 0.00067	0.20346 ± 0.00340	1891.4 ± 10.4	63.1
KAS-2.3#	0.000	245	195	0.82	0.11519 ± 0.00067	0.32496 ± 0.00559	1882.9 ± 10.5	96.3
KAS-2.4#	0.000	81	64	0.82	0.11613 ± 0.00102	0.33714 ± 0.00618	1897.5 ± 15.7	98.7
KAS-2.5#	0.154	80	188	2.42	0.11504 ± 0.00119	0.32755 ± 0.00605	1880.5 ± 18.7	97.1
KAS-2.6#	0.017	49	16	0.35	0.13533 ± 0.00129	0.39786 ± 0.00837	2168.2 ± 16.6	99.6
KAS-2.7#	0.012	169	106	0.65	0.11543 ± 0.00106	0.32372 ± 0.00556	1886.7 ± 16.6	95.8
KAS-2.8#	0.113	198	287	1.50	0.11386 ± 0.00076	0.31911 ± 0.00544	1861.9 ± 12.0	95.9
KAS-2.9#	0.070	170	146	0.89	0.11317 ± 0.00077	0.33494 ± 0.00575	1850.9 ± 12.2	100.6
KAS-2.10#	0.258	81	49	0.62	0.12203 ± 0.00139	0.35313 ± 0.00648	1986.1 ± 20.2	98.2
KAS-2.11#	0.060	280	231	0.85	0.11436 ± 0.00057	0.32863 ± 0.00551	1869.8 ± 9.0	98.0
KAS-2.12#	0.023	240	186	0.80	0.11043 ± 0.00058	0.32360 ± 0.00557	1806.5 ± 9.5	100.0
KAS-2.13#	0.248	66	41	0.64	0.10880 ± 0.00126	0.33609 ± 0.00635	1779.4 ± 21.1	105.0
KAS-2.14#	0.032	303	202	0.69	0.11418 ± 0.00051	0.33295 ± 0.00567	1867.0 ± 8.1	99.2
KAS-2.15#	0.063	139	104	0.77	0.11318 ± 0.00083	0.33962 ± 0.00593	1851.0 ± 13.2	101.8
f^{206} = the proportion of common ^{206}Pb in the total ^{206}Pb ; Th/U = $^{232}\text{Th}/^{238}\text{U}$; %C = % concordance								
All ratios and ages corrected for common Pb using measured ^{204}Pb and composition appropriate to the age of the zircon (Stacey and Kramers, 1975)								
Analyses conducted on the same mount, during two separate sessions								
Session 1 (07/10/2002): 2σ error in standard calibration for 19 CZ3 standards was 0.78% (analyses denoted with *)								
Session 2 (01/03/2003): 2σ error in standard calibration for 8 CZ3 standards was 1.38% (analyses denoted with #)								

Appendix F: zircon U-Pb SHRIMP analytical data

Table 13-15 SHRIMP analytical data for sample IL14 (Chembewesu Quartzite, Manshya River Group, Ilondola Mission map sheet).

Spot Name	f^{206} (%)	U (ppm)	Th (ppm)	Th/U	$^{207}\text{Pb}/^{206}\text{Pb}$ ($\pm 1\sigma$)	$^{206}\text{Pb}/^{238}\text{U}$ ($\pm 1\sigma$)	$^{207}\text{Pb}/^{206}\text{Pb}$ Age ($\pm 1\sigma$ Ma)	C(%)
IL14.1	0.000	116	109	0.98	0.13059 \pm 0.00163	0.32856 \pm 0.00730	2105.9 \pm 21.9	89.5
IL14.2	0.120	154	142	0.95	0.12692 \pm 0.00106	0.32248 \pm 0.00703	2055.8 \pm 14.8	90.2
IL14.3	0.080	218	78	0.37	0.12617 \pm 0.00168	0.31923 \pm 0.00683	2045.3 \pm 23.6	89.8
IL14.4	0.000	275	309	1.16	0.11489 \pm 0.00070	0.28674 \pm 0.00609	1878.2 \pm 11.0	89.1
IL14.5	0.175	197	163	0.85	0.11556 \pm 0.00105	0.28699 \pm 0.00629	1888.6 \pm 16.4	88.6
IL14.6	0.482	94	61	0.67	0.11373 \pm 0.00208	0.28326 \pm 0.00644	1859.8 \pm 33.1	89.0
IL14.7	0.126	134	167	1.29	0.12702 \pm 0.00121	0.31596 \pm 0.00696	2057.2 \pm 16.8	88.5
IL14.8	0.080	365	202	0.57	0.12576 \pm 0.00067	0.32226 \pm 0.00678	2039.6 \pm 9.4	90.8
IL14.9	0.284	282	185	0.68	0.12570 \pm 0.00085	0.32027 \pm 0.00680	2038.6 \pm 12.0	90.4
IL14.10	0.077	397	236	0.61	0.13250 \pm 0.00063	0.33689 \pm 0.00705	2131.4 \pm 8.3	90.3
IL14.11	0.458	92	114	1.29	0.15722 \pm 0.00166	0.41726 \pm 0.00937	2426.0 \pm 17.9	95.2
IL14.12	0.250	182	117	0.66	0.12486 \pm 0.00103	0.34817 \pm 0.00748	2026.9 \pm 14.5	97.7
IL14.13	0.239	176	167	0.98	0.12728 \pm 0.00096	0.35552 \pm 0.00766	2060.7 \pm 13.3	97.9
IL14.14	0.380	127	51	0.42	0.18127 \pm 0.00148	0.47939 \pm 0.01045	2664.5 \pm 13.5	97.3
IL14.15	0.476	127	136	1.11	0.12541 \pm 0.00158	0.35878 \pm 0.00786	2034.6 \pm 22.3	99.9
IL14.16	0.301	220	92	0.43	0.12227 \pm 0.00092	0.35321 \pm 0.00752	1989.6 \pm 13.4	100.8
IL14.17	0.243	215	138	0.66	0.19696 \pm 0.00126	0.46935 \pm 0.00998	2801.2 \pm 10.5	91.0
IL14.18	0.338	195	55	0.29	0.12446 \pm 0.00145	0.36398 \pm 0.00780	2021.1 \pm 20.6	101.8
IL14.19	0.165	291	71	0.25	0.12497 \pm 0.00077	0.35649 \pm 0.00750	2028.4 \pm 11.0	99.7
IL14.20	0.595	85	42	0.51	0.12357 \pm 0.00215	0.35999 \pm 0.00815	2008.4 \pm 30.8	101.5
IL14.21	0.228	425	117	0.29	0.12415 \pm 0.00097	0.32514 \pm 0.00679	2016.7 \pm 13.8	92.6
IL14.22	0.211	194	81	0.43	0.12687 \pm 0.00095	0.35843 \pm 0.00767	2055.0 \pm 13.2	98.8
IL14.23	0.200	169	66	0.40	0.12433 \pm 0.00099	0.36246 \pm 0.00781	2019.2 \pm 14.1	101.5
IL14.24	0.159	292	187	0.66	0.12565 \pm 0.00090	0.37240 \pm 0.00785	2038.0 \pm 12.6	103.0
IL14.25	0.622	94	189	2.09	0.12322 \pm 0.00167	0.35176 \pm 0.00783	2003.4 \pm 24.0	99.7
IL14.26	0.063	268	137	0.53	0.13794 \pm 0.00072	0.39795 \pm 0.00841	2201.5 \pm 9.1	100.8
IL14.27	0.385	162	57	0.36	0.12503 \pm 0.00112	0.36429 \pm 0.00788	2029.3 \pm 15.9	101.5
IL14.28	0.444	296	207	0.72	0.12429 \pm 0.00088	0.31440 \pm 0.00664	2018.7 \pm 12.5	89.8
IL14.29	0.211	212	66	0.32	0.12516 \pm 0.00099	0.37105 \pm 0.00791	2031.0 \pm 14.0	103.0
IL14.30	0.123	130	92	0.73	0.12595 \pm 0.00113	0.36992 \pm 0.00807	2042.2 \pm 15.9	102.2
IL14.31	0.398	126	173	1.42	0.11745 \pm 0.00126	0.34770 \pm 0.00763	1917.8 \pm 19.2	103.2
IL14.32	0.196	132	89	0.70	0.12705 \pm 0.00117	0.36786 \pm 0.00802	2057.5 \pm 16.3	100.9
IL14.33	0.461	54	73	1.40	0.12452 \pm 0.00195	0.36980 \pm 0.00885	2022.0 \pm 27.8	103.2
IL14.34	0.082	224	36	0.17	0.12658 \pm 0.00084	0.36980 \pm 0.00786	2051.1 \pm 11.7	101.7
IL14.35	0.206	230	125	0.56	0.12623 \pm 0.00084	0.36748 \pm 0.00782	2046.1 \pm 11.8	101.4
IL14.36	0.262	214	122	0.59	0.12645 \pm 0.00090	0.36214 \pm 0.00771	2049.2 \pm 12.6	100.0
IL14.37	0.274	110	98	0.92	0.12749 \pm 0.00136	0.36037 \pm 0.00797	2063.6 \pm 18.9	98.9
IL14.38	0.173	38	80	2.19	0.22420 \pm 0.00220	0.59940 \pm 0.01478	3011.1 \pm 15.8	103.2
IL14.39	0.148	195	42	0.22	0.12547 \pm 0.00087	0.37394 \pm 0.00801	2035.5 \pm 12.3	103.5
IL14.40	0.148	249	55	0.23	0.12481 \pm 0.00094	0.37077 \pm 0.00785	2026.1 \pm 13.3	103.2
IL14.41	0.265	280	130	0.48	0.13635 \pm 0.00082	0.34304 \pm 0.00731	2181.3 \pm 10.5	89.6
IL14.42	0.122	232	189	0.84	0.12694 \pm 0.00081	0.36525 \pm 0.00776	2056.0 \pm 11.3	100.4
IL14.43	0.350	87	69	0.81	0.11516 \pm 0.00190	0.33712 \pm 0.00765	1882.4 \pm 29.7	102.3
IL14.44	0.074	184	105	0.59	0.12359 \pm 0.00088	0.35860 \pm 0.00770	2008.7 \pm 12.7	101.1
IL14.45	0.122	261	250	0.99	0.20305 \pm 0.00086	0.51948 \pm 0.01098	2850.9 \pm 6.9	97.1
IL14.46	0.146	271	103	0.39	0.12446 \pm 0.00080	0.33288 \pm 0.00703	2021.1 \pm 11.3	94.3
IL14.47	0.174	125	79	0.66	0.12529 \pm 0.00120	0.36810 \pm 0.00806	2032.9 \pm 17.0	102.2
f^{206} = the proportion of common ^{206}Pb in the total ^{206}Pb ; Th/U = $^{232}\text{Th}/^{238}\text{U}$; %C = % concordance								
All ratios and ages corrected for common Pb using measured ^{204}Pb and composition appropriate to the age of the zircon (Stacey and Kramers, 1975)								
Analyses conducted during a single session (21/06/2002); 2σ error in standard calibration for 9 CZ3 standards was 1.61%								

Table 13-16 SHRIMP analytical data for sample MK8 (Basal Conglomerate, Kanona Group Group, Mkushi map sheet).

Spot Name	f^{206} (%)	U (ppm)	Th (ppm)	Th/U	$^{207}\text{Pb}/^{206}\text{Pb}$ ($\pm 1\sigma$)	$^{206}\text{Pb}/^{238}\text{U}$ ($\pm 1\sigma$)	$^{207}\text{Pb}/^{206}\text{Pb}$ Age ($\pm 1\sigma$ Ma)	C(%)
MK8-1	0.335	108	22	0.21	0.12478 ± 0.00144	0.37353 ± 0.01409	2025.6 ± 20.5	101.0
MK8-2	0.081	80	35	0.45	0.12699 ± 0.00114	0.36965 ± 0.01339	2056.8 ± 15.9	98.6
MK8-3	0.269	126	78	0.64	0.11977 ± 0.00099	0.36701 ± 0.01381	1952.8 ± 14.7	103.1
MK8-4	0.299	116	45	0.40	0.12637 ± 0.00137	0.37165 ± 0.01401	2048.0 ± 19.2	99.5
MK8-5	0.361	103	86	0.86	0.12420 ± 0.00100	0.39504 ± 0.01490	2017.4 ± 14.3	106.0
MK8-6	0.456	127	100	0.81	0.12662 ± 0.00304	0.36286 ± 0.01366	2051.6 ± 42.4	97.2
MK8-7	0.438	250	180	0.74	0.12340 ± 0.00192	0.30782 ± 0.01172	2006.0 ± 27.6	84.0
f^{206} = the proportion of common ^{206}Pb in the total ^{206}Pb ; Th/U = $^{232}\text{Th}/^{238}\text{U}$; %C = % concordance								
All ratios and ages corrected for common Pb using measured ^{204}Pb and composition appropriate to the age of the zircon (Stacey and Kramers, 1975)								
Analyses conducted during a single session (07/04/2003); 2σ error in standard calibration for 19 CZ3 standards was 1.77%								

Table 13-17 SHRIMP analytical data for sample ZM 31 (Luswa rhyolite, Luswa River map sheet)

Spot Name	f^{206} (%)	U (ppm)	Th (ppm)	Th/U	$^{207}\text{Pb}/^{206}\text{Pb}$ ($\pm 1\sigma$)	$^{206}\text{Pb}/^{238}\text{U}$ ($\pm 1\sigma$)	$^{207}\text{Pb}/^{206}\text{Pb}$ Age ($\pm 1\sigma$ Ma)	C(%)
ZM31-1.1	0.000	77	80	1.08	0.11503 ± 0.00115	0.34953 ± 0.00778	1880.4 ± 18.0	102.8
ZM31-2.1	0.012	113	120	1.10	0.11584 ± 0.00105	0.31998 ± 0.00640	1892.9 ± 16.4	94.5
ZM31-3.1	0.000	116	77	0.69	0.11588 ± 0.00096	0.33379 ± 0.00679	1893.5 ± 14.8	98.1
ZM31-4.1	0.000	70	76	1.11	0.11597 ± 0.00134	0.33851 ± 0.00784	1894.9 ± 20.7	99.2
ZM31-5.1	0.112	272	361	1.37	0.11450 ± 0.00079	0.33027 ± 0.00624	1872.1 ± 12.4	98.3
ZM31-6.1	0.327	236	332	1.45	0.11467 ± 0.00106	0.33938 ± 0.00646	1874.7 ± 16.7	100.5
ZM31-7.1	0.013	131	81	0.64	0.11498 ± 0.00103	0.35138 ± 0.00716	1879.6 ± 16.2	103.3
ZM31-8.1	0.000	88	59	0.69	0.11356 ± 0.00125	0.32159 ± 0.00687	1857.1 ± 19.8	96.8
ZM31-9.1	0.025	96	121	1.29	0.11532 ± 0.00141	0.33691 ± 0.00717	1884.8 ± 22.0	99.3
ZM31-10.1	0.062	460	492	1.11	0.11543 ± 0.00063	0.35144 ± 0.00669	1886.7 ± 9.8	102.9
f^{206} = the proportion of common ^{206}Pb in the total ^{206}Pb ; Th/U = $^{232}\text{Th}/^{238}\text{U}$; %C = % concordance								
All ratios and ages corrected for common Pb using measured ^{204}Pb and composition appropriate to the age of the zircon (Stacey and Kramers, 1975)								
Analyses conducted during a single session (14/11/1999). 14 CZ3 standard analyses yielded a 2σ error of the mean of 1.11%								

Table 13-18 SHRIMP analytical data for sample IS20 (Kachinga rhyolitic tuff, Isoka map sheet).

Spot Name	f^{206} (%)	U (ppm)	Th (ppm)	Th/U	$^{207}\text{Pb}/^{206}\text{Pb}$ ($\pm 1\sigma$)	$^{206}\text{Pb}/^{238}\text{U}$ ($\pm 1\sigma$)	$^{207}\text{Pb}/^{206}\text{Pb}$ Age ($\pm 1\sigma$ Ma)	C(%)
IS20-20	0.137	118	85	0.75	0.11278 ± 0.00083	0.33165 ± 0.00378	1844.8 ± 13.2	100.1
IS20-21	0.002	83	70	0.88	0.11525 ± 0.00114	0.33104 ± 0.00412	1883.8 ± 17.8	97.9
IS20-22	0.037	122	146	1.23	0.11373 ± 0.00096	0.33884 ± 0.00389	1859.9 ± 15.2	101.1
IS20-18	0.000	137	183	1.38	0.11380 ± 0.00073	0.33698 ± 0.00378	1860.9 ± 11.6	100.6
IS20-17	0.334	112	100	0.92	0.11158 ± 0.00115	0.32882 ± 0.00389	1825.3 ± 18.7	100.4
IS20-16	0.085	199	215	1.11	0.11505 ± 0.00070	0.32931 ± 0.00346	1880.6 ± 10.9	97.6
IS20-15	0.197	99	92	0.96	0.11220 ± 0.00103	0.33116 ± 0.00417	1835.4 ± 16.7	100.5
f^{206} = the proportion of common ^{206}Pb in the total ^{206}Pb ; Th/U = $^{232}\text{Th}/^{238}\text{U}$; %C = % concordance								
All ratios and ages corrected for common Pb using measured ^{204}Pb and composition appropriate to the age of the zircon (Stacey and Kramers, 1975)								
Analyses conducted during a single session (07/09/2002). 12 CZ3 standard analyses yielded a 2σ error of the mean of 0.65%								

Appendix F: zircon U-Pb SHRIMP analytical data

Table 13-19 SHRIMP analytical data for sample KB-5 (Basalt, Katibunga Mission map sheet).

Spot Name	f^{206} (%)	U (ppm)	Th (ppm)	Th/U	$^{207}\text{Pb}/^{206}\text{Pb}$ ($\pm 1\sigma$)	$^{206}\text{Pb}/^{238}\text{U}$ ($\pm 1\sigma$)	$^{207}\text{Pb}/^{206}\text{Pb}$ Age ($\pm 1\sigma$ Ma)	C(%)
¹ KB5-1.1	0.348	59	69	1.21	0.11211 \pm 0.00252	0.30327 \pm 0.00411	1833.9 \pm 40.7	93.1
² KB5-1	0.714	128	169	1.36	0.11329 \pm 0.00363	0.31196 \pm 0.00755	1852.9 \pm 57.9	94.5
² KB5-2	1.205	135	65	0.50	0.16934 \pm 0.00362	0.43508 \pm 0.00978	2551.1 \pm 35.8	91.3
² KB5-3	0.641	132	304	2.37	0.11552 \pm 0.00211	0.33711 \pm 0.00768	1888.1 \pm 32.8	99.2
² KB5-4	0.110	142	183	1.34	0.11483 \pm 0.00114	0.32910 \pm 0.00742	1877.1 \pm 17.8	97.7
² KB5-5	0.524	165	87	0.55	0.11547 \pm 0.00161	0.32795 \pm 0.00723	1887.2 \pm 25.1	96.9
² KB5-6	1.719	112	195	1.80	0.11051 \pm 0.00210	0.30587 \pm 0.00681	1807.9 \pm 34.6	95.2
f^{206} = the proportion of common ^{206}Pb in the total ^{206}Pb ; Th/U = $^{232}\text{Th}/^{238}\text{U}$; %C = % concordance All ratios and ages corrected for common Pb using measured ^{204}Pb and composition appropriate to the age of the zircon (Stacey and Kramers, 1975) Analyses conducted during two sessions (¹ 07/09/2002 and ² 04/12/2003). Session ¹ : 12 CZ3 standard analyses yielded a 2 σ error of the mean of 0.65% Session ² : 16 CZ3 standard analyses yielded a 2 σ error of the mean of 1.15%								

Table 13-20 SHRIMP analytical data for sample MTGG-1 (Mutangoshi Gneissic Granite, Chinsali map sheet). Spot names ending with r denote analyses on a rim, spot names ending with c denote analyses on core.

Spot Name	f^{206} (%)	U (ppm)	Th (ppm)	Th/U	$^{207}\text{Pb}/^{206}\text{Pb}$ ($\pm 1\sigma$)	$^{206}\text{Pb}/^{238}\text{U}$ ($\pm 1\sigma$)	$^{207}\text{Pb}/^{206}\text{Pb}$ Age ($\pm 1\sigma$ Ma)	C(%)
MTGG1-1	0.025	1519	364	0.25	0.07177 \pm 0.00021	0.15839 \pm 0.00260	979.4 \pm 6.1	96.8
MTGG1-2	0.068	540	197	0.38	0.07304 \pm 0.00042	0.16698 \pm 0.00277	1015.1 \pm 11.6	98.1
MTGG1-3r	0.063	1265	217	0.18	0.07279 \pm 0.00027	0.16835 \pm 0.00276	1008.0 \pm 7.5	99.5
MTGG1-3c	0.643	264	112	0.44	0.12030 \pm 0.00099	0.34978 \pm 0.00586	1960.7 \pm 14.7	98.6
MTGG1-4c	0.000	227	107	0.49	0.07443 \pm 0.00059	0.16034 \pm 0.00274	1053.1 \pm 16.0	91.0
MTGG1-5	0.445	673	248	0.38	0.07256 \pm 0.00053	0.15909 \pm 0.00270	1001.7 \pm 14.8	95.0
MTGG1-6c	1.178	109	78	0.74	0.07366 \pm 0.00206	0.16557 \pm 0.00294	1032.1 \pm 56.7	95.7
MTGG1-6r	0.000	636	246	0.40	0.07369 \pm 0.00030	0.17452 \pm 0.00289	1033.0 \pm 8.2	100.4
MTGG1-7c	0.034	860	336	0.40	0.07352 \pm 0.00029	0.17377 \pm 0.00286	1028.3 \pm 8.0	100.4
MTGG1-7r	0.042	670	245	0.38	0.07349 \pm 0.00035	0.17052 \pm 0.00282	1027.5 \pm 9.7	98.8
MTGG1-8	0.000	291	160	0.57	0.07318 \pm 0.00053	0.17448 \pm 0.00294	1019.0 \pm 14.7	101.7
MTGG1-9	0.000	221	123	0.57	0.07380 \pm 0.00054	0.17427 \pm 0.00296	1036.1 \pm 14.7	100.0
MTGG1-10	0.000	221	123	0.57	0.07380 \pm 0.00054	0.17427 \pm 0.00296	1036.1 \pm 14.7	100.0
MTGG1-12	0.041	401	755	1.95	0.11992 \pm 0.00042	0.34792 \pm 0.00578	1955.1 \pm 6.2	98.4
f^{206} = the proportion of common ^{206}Pb in the total ^{206}Pb ; Th/U = $^{232}\text{Th}/^{238}\text{U}$; %C = % concordance All ratios and ages corrected for common Pb using measured ^{204}Pb and composition appropriate to the age of the zircon (Stacey and Kramers, 1975) Analyses conducted during a single session (26/03/2002). 16 CZ3 standard analyses yielded a 2 σ error of the mean of 0.81%								

Table 13-21 SHRIMP analytical data for sample MTGG-2 (Mutangoshi Gneissic Granite, Chinsali map sheet). Spot names ending with c denote analyses on core.

Spot Name	f_{206} (%)	U (ppm)	Th (ppm)	Th/U	$^{207}\text{Pb}/^{206}\text{Pb}$ ($\pm 1\sigma$)	$^{206}\text{Pb}/^{238}\text{U}$ ($\pm 1\sigma$)	$^{207}\text{Pb}/^{206}\text{Pb}$ Age ($\pm 1\sigma$ Ma)	C(%)
MTGG2-5	0.030	179	36	0.21	0.07279 \pm 0.00073	0.18023 \pm 0.00282	1008.0 \pm 20.5	106.0
MTGG2-13	2.944	2758	15	0.01	0.07241 \pm 0.00204	0.17611 \pm 0.00261	997.5 \pm 57.3	104.8
MTGG2-4	0.000	301	159	0.55	0.07477 \pm 0.00044	0.18089 \pm 0.00273	1062.4 \pm 11.8	100.9
MTGG2-16c	3.492	124	111	0.93	0.12224 \pm 0.00271	0.35845 \pm 0.00568	1989.2 \pm 39.4	99.3
MTGG2-10c	0.396	87	117	1.38	0.12150 \pm 0.00122	0.36072 \pm 0.00587	1978.3 \pm 17.9	100.4
MTGG2-19	8.241	1879	43	0.02	0.07312 \pm 0.01154	0.15088 \pm 0.00267	1017.4 \pm 319.7	89.0
f_{206} = the proportion of common ^{206}Pb in the total ^{206}Pb ; Th/U = $^{232}\text{Th}/^{238}\text{U}$; %C = % concordance All ratios and ages corrected for common Pb using measured ^{204}Pb and composition appropriate to the age of the zircon (Stacey and Kramers, 1975) Analyses conducted during a single session (26/03/2002). 16 CZ3 standard analyses yielded a 2σ error of the mean of 0.81%								

Table 13-22 SHRIMP analytical data for sample LW-10 (Musalango Gneiss, Luswa River map sheet).

Spot Name	f_{206} (%)	U (ppm)	Th (ppm)	Th/U	$^{207}\text{Pb}/^{206}\text{Pb}$ ($\pm 1\sigma$)	$^{206}\text{Pb}/^{238}\text{U}$ ($\pm 1\sigma$)	$^{207}\text{Pb}/^{206}\text{Pb}$ Age ($\pm 1\sigma$ Ma)	C(%)
¹ LW10-1	0.000	55	47	0.88	0.10202 \pm 0.00121	0.27148 \pm 0.00388	1661.2 \pm 22.0	93.2
¹ LW10-2	0.090	69	57	0.85	0.09954 \pm 0.00117	0.27964 \pm 0.00374	1615.4 \pm 22.0	98.4
¹ LW10-3	0.150	75	63	0.87	0.09906 \pm 0.00134	0.27641 \pm 0.00360	1606.4 \pm 25.2	97.9
¹ LW10-4	0.426	50	36	0.75	0.09350 \pm 0.00189	0.27859 \pm 0.00412	1498.0 \pm 38.3	105.8
¹ LW10-5	0.280	64	42	0.67	0.09479 \pm 0.00177	0.25952 \pm 0.00354	1523.9 \pm 35.1	97.6
¹ LW10-6	0.212	115	85	0.76	0.09707 \pm 0.00115	0.27708 \pm 0.00327	1568.6 \pm 22.2	100.5
¹ LW10-7	1.840	84	55	0.67	0.08926 \pm 0.00295	0.23250 \pm 0.00303	1409.8 \pm 63.3	95.6
¹ LW10-9	0.034	64	55	0.89	0.09879 \pm 0.00115	0.27653 \pm 0.00465	1601.4 \pm 21.7	98.3
¹ LW10-10	1.601	59	45	0.79	0.09288 \pm 0.00312	0.27515 \pm 0.00397	1485.4 \pm 63.6	105.5
² LW10-11	0.132	164	96	0.60	0.09807 \pm 0.00129	0.27897 \pm 0.00670	1587.7 \pm 24.5	99.9
² LW10-12	0.205	48	35	0.76	0.10017 \pm 0.00194	0.27610 \pm 0.00719	1627.3 \pm 36.0	96.6
² LW10-13	0.335	82	83	1.05	0.09742 \pm 0.00192	0.26469 \pm 0.00658	1575.3 \pm 36.9	96.1
² LW10-14	0.176	93	83	0.93	0.10079 \pm 0.00283	0.27730 \pm 0.00687	1638.7 \pm 52.0	96.3
f_{206} = the proportion of common ^{206}Pb in the total ^{206}Pb ; Th/U = $^{232}\text{Th}/^{238}\text{U}$; %C = % concordance All ratios and ages corrected for common Pb using measured ^{204}Pb and composition appropriate to the age of the zircon (Stacey and Kramers, 1975) Analyses conducted during two sessions (¹ 07/09/2002 and ² 01/04/2003). Session ¹ : 12 CZ3 standard analyses yielded a 2σ error of the mean of 0.65% Session ² : 9 CZ3 standard analyses yielded a 2σ error of the mean of 1.93%								

Appendix F: zircon U-Pb SHRIMP analytical data

Table 13-23 SHRIMP analytical data for sample ML-2 (Lubu Granite Gneiss, Chinsali map sheet).

Spot Name	f^{206} (%)	U (ppm)	Th (ppm)	Th/U	$^{207}\text{Pb}/^{206}\text{Pb}$ ($\pm 1\sigma$)	$^{206}\text{Pb}/^{238}\text{U}$ ($\pm 1\sigma$)	$^{207}\text{Pb}/^{206}\text{Pb}$ Age ($\pm 1\sigma$ Ma)	C(%)
¹ ML2-1	0.070	171	279	1.69	0.09497 \pm 0.00075	0.25688 \pm 0.00261	1527.5 \pm 14.9	96.5
¹ ML2-8	0.232	262	517	2.04	0.09504 \pm 0.00078	0.25790 \pm 0.00252	1528.9 \pm 15.5	96.7
¹ ML2-5	3.913	326	572	1.81	0.09224 \pm 0.00632	0.25073 \pm 0.00259	1473.5 \pm 129.9	97.9
¹ ML2-10	4.250	256	445	1.80	0.09288 \pm 0.00432	0.23290 \pm 0.00240	1486.6 \pm 88.0	90.8
¹ ML2-11	3.107	284	472	1.72	0.09402 \pm 0.00362	0.21551 \pm 0.00211	1509.3 \pm 72.7	83.4
¹ ML2-12	0.777	415	687	1.71	0.09322 \pm 0.00157	0.24262 \pm 0.00223	1492.5 \pm 31.8	93.8
¹ ML2-13	1.260	195	322	1.70	0.09205 \pm 0.00175	0.23712 \pm 0.00240	1468.9 \pm 36.0	93.4
² ML2-21	0.037	265	498	1.94	0.09616 \pm 0.00069	0.26961 \pm 0.00638	1550.8 \pm 13.4	99.2
² ML2-22	4.673	283	461	1.68	0.10711 \pm 0.00822	0.21757 \pm 0.00524	1749.9 \pm 140.6	72.5
² ML2-23	0.725	319	407	1.32	0.09641 \pm 0.00160	0.24507 \pm 0.00579	1555.9 \pm 31.2	90.8
² ML2-24	0.392	348	568	1.69	0.09517 \pm 0.00095	0.25925 \pm 0.00610	1531.5 \pm 18.8	97.0
f^{206} = the proportion of common ^{206}Pb in the total ^{206}Pb ; Th/U = $^{232}\text{Th}/^{238}\text{U}$; %C = % concordance All ratios and ages corrected for common Pb using measured ^{204}Pb and composition appropriate to the age of the zircon (Stacey and Kramers, 1975) Analyses conducted during two sessions (¹ 08/09/2002 and ² 01/04/2003). Session ¹ : 5 CZ3 standard analyses yielded a 2 σ error of the mean of 1.07% Session ² : 9 CZ3 standard analyses yielded a 2 σ error of the mean of 1.93%								

Table 13-24 SHRIMP analytical data for sample SER 6-2c (Lukamfwa Hill Granite Gneiss, Serenje map sheet). Spot names ending with r denote analyses on a rim, spot names ending with c denote analyses on core.

Spot Name	f^{206} (%)	U (ppm)	Th (ppm)	Th/U	$^{207}\text{Pb}/^{206}\text{Pb}$ ($\pm 1\sigma$)	$^{206}\text{Pb}/^{238}\text{U}$ ($\pm 1\sigma$)	$^{207}\text{Pb}/^{206}\text{Pb}$ Age ($\pm 1\sigma$ Ma)	C(%)
SER62-26c	0.989	65	53	0.84	0.10376 \pm 0.00389	0.30047 \pm 0.00779	1692.5 \pm 69.2	100.1
SER62-26r	0.047	770	452	0.61	0.10228 \pm 0.00028	0.28729 \pm 0.00622	1665.8 \pm 5.0	97.7
SER62-27	0.146	316	326	1.07	0.10317 \pm 0.00056	0.29634 \pm 0.00664	1681.8 \pm 10.0	99.5
SER62-28	0.615	82	76	0.96	0.09960 \pm 0.00194	0.30221 \pm 0.00755	1616.7 \pm 36.2	105.3
SER62-29	0.246	100	81	0.84	0.10405 \pm 0.00191	0.26150 \pm 0.00583	1697.6 \pm 33.8	88.2
SER62-32	0.040	2804	2342	0.86	0.10179 \pm 0.00027	0.28702 \pm 0.00617	1657.1 \pm 4.9	98.2
SER62-36	0.368	588	214	0.38	0.10021 \pm 0.00041	0.26012 \pm 0.00586	1627.9 \pm 7.6	91.6
SER62-37	0.108	489	390	0.82	0.10257 \pm 0.00070	0.30040 \pm 0.00676	1671.1 \pm 12.6	101.3
SER62-40	0.433	112	125	1.16	0.10214 \pm 0.00179	0.29847 \pm 0.00660	1663.4 \pm 32.4	101.2
SER62-41c	14.976	3965	2136	0.56	0.10197 \pm 0.00801	0.10059 \pm 0.00293	1660.2 \pm 145.4	37.2
SER62-41r	0.542	148	98	0.69	0.10007 \pm 0.00198	0.29888 \pm 0.00661	1625.3 \pm 36.9	103.7
f^{206} = the proportion of common ^{206}Pb in the total ^{206}Pb ; Th/U = $^{232}\text{Th}/^{238}\text{U}$; %C = % concordance All ratios and ages corrected for common Pb using measured ^{204}Pb and composition appropriate to the age of the zircon (Stacey and Kramers, 1975) Analyses conducted during a single session (01/03/2002). 16 CZ3 standard analyses yielded a 2 σ error of the mean of 1.18%								

Table 13-25 SHRIMP analytical data for sample SER 6-3 (Lukamfwa Hill Granite Gneiss, Serenje map sheet).

Spot Name	f^{206} (%)	U (ppm)	Th (ppm)	Th/U	$^{207}\text{Pb}/^{206}\text{Pb}$ ($\pm 1\sigma$)	$^{206}\text{Pb}/^{238}\text{U}$ ($\pm 1\sigma$)	$^{207}\text{Pb}/^{206}\text{Pb}$ Age ($\pm 1\sigma$ Ma)	C(%)
SER63-1	0.056	470	339	0.74	0.10201 \pm 0.00043	0.29684 \pm 0.00644	1861.0 \pm 7.8	100.9
SER63-2	0.183	320	259	0.84	0.10158 \pm 0.00092	0.29511 \pm 0.00721	1853.1 \pm 16.7	100.8
SER63-5	0.187	467	361	0.80	0.10014 \pm 0.00104	0.29069 \pm 0.00628	1826.6 \pm 19.3	101.1
SER63-7	0.102	403	303	0.78	0.10176 \pm 0.00033	0.29662 \pm 0.00642	1856.6 \pm 6.0	101.1
SER63-6	0.062	378	309	0.84	0.10205 \pm 0.00074	0.29462 \pm 0.00654	1861.7 \pm 13.4	100.2
SER63-8	0.359	331	356	1.11	0.10071 \pm 0.00214	0.28016 \pm 0.00610	1837.2 \pm 39.4	97.2
SER63-22	0.195	420	331	0.81	0.10099 \pm 0.00107	0.29160 \pm 0.00644	1842.3 \pm 19.7	100.4
SER63-29	0.057	501	288	0.59	0.10042 \pm 0.00070	0.27852 \pm 0.00635	1831.8 \pm 13.0	97.1
SER63-15	0.082	339	255	0.78	0.10193 \pm 0.00051	0.30028 \pm 0.00666	1859.6 \pm 9.2	102.0
SER63-19	0.178	308	233	0.78	0.09915 \pm 0.00124	0.27707 \pm 0.00600	1808.1 \pm 23.2	98.0
f^{206} = the proportion of common ^{206}Pb in the total ^{206}Pb ; Th/U = $^{232}\text{Th}/^{238}\text{U}$; %C = % concordance All ratios and ages corrected for common Pb using measured ^{204}Pb and composition appropriate to the age of the zircon (Stacey and Kramers, 1975) Analyses conducted during a single session (01/03/2002). 16 CZ3 standard analyses yielded a 2σ error of the mean of 1.18%								

Table 13-26 SHRIMP analytical data for sample SR12 (Lukamfwa Hill Granite Gneiss, Serenje map sheet).

Spot Name	f^{206} (%)	U (ppm)	Th (ppm)	Th/U	$^{207}\text{Pb}/^{206}\text{Pb}$ ($\pm 1\sigma$)	$^{206}\text{Pb}/^{238}\text{U}$ ($\pm 1\sigma$)	$^{207}\text{Pb}/^{206}\text{Pb}$ Age ($\pm 1\sigma$ Ma)	C(%)
SR12-1	0.215	141	110	0.81	0.10132 \pm 0.00092	0.29495 \pm 0.00309	1848.4 \pm 16.8	101.1
SR12-2	0.000	198	204	1.07	0.10007 \pm 0.00155	0.28166 \pm 0.00288	1825.3 \pm 28.8	98.4
SR12-3	0.136	139	84	0.63	0.09898 \pm 0.00095	0.27508 \pm 0.00369	1804.9 \pm 17.9	97.6
SR12-4	0.067	179	138	0.79	0.10155 \pm 0.00076	0.29499 \pm 0.00294	1852.7 \pm 13.8	100.8
SR12-8	0.823	138	142	1.06	0.10024 \pm 0.00376	0.28273 \pm 0.00313	1828.6 \pm 69.7	98.6
SR12-9	0.093	103	117	1.17	0.10149 \pm 0.00121	0.29459 \pm 0.00361	1851.5 \pm 22.2	100.8
SR12-10	0.088	222	256	1.19	0.10082 \pm 0.00066	0.29085 \pm 0.00335	1839.3 \pm 12.2	100.4
f^{206} = the proportion of common ^{206}Pb in the total ^{206}Pb ; Th/U = $^{232}\text{Th}/^{238}\text{U}$; %C = % concordance All ratios and ages corrected for common Pb using measured ^{204}Pb and composition appropriate to the age of the zircon (Stacey and Kramers, 1975) Analyses conducted during a single session (08/09/2002). 5 CZ3 standard analyses yielded a 2σ error of the mean of 1.07%								

Table 13-27 SHRIMP analytical data for sample ND-2 (biotite granite gneiss, Ndabala map sheet).

Spot Name	f^{206} (%)	U (ppm)	Th (ppm)	Th/U	$^{207}\text{Pb}/^{206}\text{Pb}$ ($\pm 1\sigma$)	$^{206}\text{Pb}/^{238}\text{U}$ ($\pm 1\sigma$)	$^{207}\text{Pb}/^{206}\text{Pb}$ Age ($\pm 1\sigma$ Ma)	C(%)
ND2-1	0.070	103	82	0.83	0.09989 \pm 0.00142	0.28323 \pm 0.00373	1822.0 \pm 26.5	99.1
ND2-2	0.000	185	144	0.80	0.10018 \pm 0.00061	0.29307 \pm 0.00349	1827.4 \pm 11.3	101.8
ND2-3	0.091	229	196	0.88	0.10031 \pm 0.00067	0.28161 \pm 0.00337	1829.7 \pm 12.5	98.1
ND2-4	0.025	181	154	0.88	0.10110 \pm 0.00097	0.28361 \pm 0.00661	1844.5 \pm 17.8	97.9
f^{206} = the proportion of common ^{206}Pb in the total ^{206}Pb ; Th/U = $^{232}\text{Th}/^{238}\text{U}$; %C = % concordance All ratios and ages corrected for common Pb using measured ^{204}Pb and composition appropriate to the age of the zircon (Stacey and Kramers, 1975) Analyses conducted during a single session (08/03/2003). 14 CZ3 standard analyses yielded a 2σ error of the mean of 0.66%								

Appendix F: zircon U-Pb SHRIMP analytical data

Table 13-28 SHRIMP analytical data for sample SH8 (Bemba batholith, Chinsali map sheet).

Spot Name	f^{206} (%)	U (ppm)	Th (ppm)	Th/U	$^{207}\text{Pb}/^{206}\text{Pb}$ ($\pm 1\sigma$)	$^{206}\text{Pb}/^{238}\text{U}$ ($\pm 1\sigma$)	$^{207}\text{Pb}/^{206}\text{Pb}$ Age ($\pm 1\sigma$ Ma)	C(%)
SH8-1	0.952	689	235	0.35	0.07306 \pm 0.00099	0.15975 \pm 0.00205	1015.8 \pm 27.3	94.1
SH8-2	1.247	269	219	0.84	0.07143 \pm 0.00142	0.12831 \pm 0.00175	969.9 \pm 40.6	80.2
f^{206} = the proportion of common ^{206}Pb in the total ^{206}Pb ; Th/U = $^{232}\text{Th}/^{238}\text{U}$; %C = % concordance								
All ratios and ages corrected for common Pb using measured ^{204}Pb and composition appropriate to the age of the zircon (Stacey and Kramers, 1975)								
Analyses conducted during a single session (28/02/2003). 10 CZ3 standard analyses yielded a 2σ error of the mean of 0.98%								

Table 13-29 SHRIMP analytical data for sample LW-2 (Luswa River Syenite, Luswa River map sheet).

Spot Name	f^{206} (%)	U (ppm)	Th (ppm)	Th/U	$^{207}\text{Pb}/^{206}\text{Pb}$ ($\pm 1\sigma$)	$^{206}\text{Pb}/^{238}\text{U}$ ($\pm 1\sigma$)	$^{207}\text{Pb}/^{206}\text{Pb}$ Age ($\pm 1\sigma$ Ma)	C(%)
LW2-1	0.334	163	87	0.55	0.07036 \pm 0.00135	0.16688 \pm 0.00192	939.0 \pm 39.3	105.9
LW2-2	0.844	68	221	3.36	0.06581 \pm 0.00287	0.16812 \pm 0.00244	800.5 \pm 91.4	125.1
LW2-9	0.307	196	34	0.18	0.06984 \pm 0.00124	0.16932 \pm 0.00188	923.6 \pm 36.4	109.2
LW2-3	0.036	196	63	0.33	0.07220 \pm 0.00090	0.16983 \pm 0.00187	991.7 \pm 25.4	102.0
LW2-4	0.120	261	255	1.01	0.07078 \pm 0.00077	0.15796 \pm 0.00168	951.2 \pm 22.2	99.4
LW2-10	1.293	559	695	1.28	0.07170 \pm 0.00202	0.16308 \pm 0.00161	977.5 \pm 57.5	99.6
LW2-5	0.138	354	239	0.70	0.07042 \pm 0.00065	0.15807 \pm 0.00161	940.7 \pm 18.9	100.6
LW2-6	0.099	255	216	0.88	0.07085 \pm 0.00063	0.15605 \pm 0.00166	953.1 \pm 18.2	98.1
f^{206} = the proportion of common ^{206}Pb in the total ^{206}Pb ; Th/U = $^{232}\text{Th}/^{238}\text{U}$; %C = % concordance								
All ratios and ages corrected for common Pb using measured ^{204}Pb and composition appropriate to the age of the zircon (Stacey and Kramers, 1975)								
Analyses conducted during a single session (07/09/2002). 12 CZ3 standard analyses yielded a 2σ error of the mean of 0.65%								

Table 13-30 SHRIMP analytical data for sample ZM32 (Chilubanama Granite, Luswa River map sheet)

Spot Name	f^{206} (%)	U (ppm)	Th (ppm)	Th/U	$^{207}\text{Pb}/^{206}\text{Pb}$ ($\pm 1\sigma$)	$^{206}\text{Pb}/^{238}\text{U}$ ($\pm 1\sigma$)	$^{207}\text{Pb}/^{206}\text{Pb}$ Age ($\pm 1\sigma$ Ma)	C(%)
ZM32-1.1	0.315	268	286	1.10	0.11369 \pm 0.00123	0.31815 \pm 0.00871	1859.3 \pm 19.5	95.8
ZM32-2.1	0.119	464	404	0.90	0.10135 \pm 0.00123	0.29651 \pm 0.00809	1649.0 \pm 22.6	101.5
ZM32-3.1	1.024	414	434	1.08	0.07062 \pm 0.00173	0.16744 \pm 0.00478	946.4 \pm 50.1	105.5
ZM32-4.1	23.894	471	393	0.86	0.08282 \pm 0.00822	0.14496 \pm 0.00408	1265.0 \pm 193.8	69.0
ZM32-5.1	0.042	78	63	0.84	0.12553 \pm 0.00216	0.35921 \pm 0.01072	2036.3 \pm 30.5	97.2
ZM32-6.1	0.750	90	45	0.52	0.06751 \pm 0.00277	0.16150 \pm 0.00488	853.4 \pm 85.4	113.1
f^{206} = the proportion of common ^{206}Pb in the total ^{206}Pb ; Th/U = $^{232}\text{Th}/^{238}\text{U}$; %C = % concordance								
All ratios and ages corrected for common Pb using measured ^{204}Pb and composition appropriate to the age of the zircon (Stacey and Kramers, 1975)								
Analyses conducted during a single session (14/11/1999). 14 CZ3 standard analyses yielded a 2σ error of the mean of 1.11%								

Table 13-31 SHRIMP analytical data for sample MTG-4 (Chilubanama Granite, Chinsali map sheet). Spot names ending with r denote analyses on a rim, spot names ending with c denote analyses on core.

Spot Name	f^{206} (%)	U (ppm)	Th (ppm)	Th/U	$^{207}\text{Pb}/^{206}\text{Pb}$ ($\pm 1\sigma$)	$^{206}\text{Pb}/^{238}\text{U}$ ($\pm 1\sigma$)	$^{207}\text{Pb}/^{206}\text{Pb}$ Age ($\pm 1\sigma$ Ma)	C(%)
MTG4-9r	0.000	435	9	0.02	0.07315 \pm 0.00038	0.17075 \pm 0.00255	1018.1 \pm 10.4	99.8
MTG4-10r	0.000	587	10	0.02	0.07289 \pm 0.00042	0.16688 \pm 0.00247	1010.8 \pm 11.7	98.4
MTG4-8r	0.000	577	9	0.02	0.07296 \pm 0.00032	0.17056 \pm 0.00259	1012.9 \pm 9.0	100.2
MTG4-7r	0.033	216	131	0.63	0.12369 \pm 0.00053	0.35853 \pm 0.00550	2010.1 \pm 7.6	98.3
MTG4-10c	0.082	1201	26	0.02	0.07368 \pm 0.00029	0.17054 \pm 0.00250	1032.9 \pm 7.8	98.3
MTG4-9c	0.235	124	146	1.22	0.07099 \pm 0.00103	0.17281 \pm 0.00275	957.1 \pm 29.6	107.4
MTG4-6c	0.253	521	63	0.12	0.07348 \pm 0.00053	0.16841 \pm 0.00250	1027.1 \pm 14.6	97.7
MTG4-4r	0.265	564	39	0.07	0.07130 \pm 0.00053	0.16329 \pm 0.00242	966.0 \pm 15.1	100.9
MTG4-1c	0.236	268	29	0.11	0.12620 \pm 0.00076	0.40044 \pm 0.00685	2045.7 \pm 10.7	106.1
MTG4-4c	0.656	132	81	0.63	0.12419 \pm 0.00118	0.35275 \pm 0.00549	2017.2 \pm 16.8	96.6
MTG4-1r	1.041	522	139	0.27	0.07170 \pm 0.00091	0.16941 \pm 0.00252	977.3 \pm 25.9	103.2
MTG4-8c	2.478	218	282	1.34	0.08996 \pm 0.00222	0.24300 \pm 0.00374	1424.8 \pm 47.0	98.4
MTG4-5c	4.327	624	820	1.36	0.07249 \pm 0.00260	0.14984 \pm 0.00225	999.7 \pm 72.9	90.0
f^{206} = the proportion of common ^{206}Pb in the total ^{206}Pb ; Th/U = $^{232}\text{Th}/^{238}\text{U}$; %C = % concordance								
All ratios and ages corrected for common Pb using measured ^{204}Pb and composition appropriate to the age of the zircon (Stacey and Kramers, 1975)								
Analyses conducted during a single session (26/03/2002). 16 CZ3 standard analyses yielded a 2σ error of the mean of 0.81%								

Table 13-32 SHRIMP analytical data for sample LW-1 (Chilubanama Granite, Luswa River map sheet).

Spot Name	f^{206} (%)	U (ppm)	Th (ppm)	Th/U	$^{207}\text{Pb}/^{206}\text{Pb}$ ($\pm 1\sigma$)	$^{206}\text{Pb}/^{238}\text{U}$ ($\pm 1\sigma$)	$^{207}\text{Pb}/^{206}\text{Pb}$ Age ($\pm 1\sigma$ Ma)	C(%)
LW1-7	0.617	44	54	1.27	0.09440 \pm 0.00279	0.26390 \pm 0.00411	1516.2 \pm 55.8	99.6
LW1-4	0.970	57	83	1.50	0.08642 \pm 0.00296	0.25221 \pm 0.00372	1347.5 \pm 66.2	107.6
LW1-2	0.392	498	1001	2.08	0.09277 \pm 0.00059	0.23907 \pm 0.00232	1483.2 \pm 12.1	93.2
LW1-1	0.762	87	82	0.97	0.09554 \pm 0.00242	0.27213 \pm 0.00503	1538.8 \pm 47.7	100.8
LW1-5	0.282	402	670	1.72	0.07268 \pm 0.00077	0.16794 \pm 0.00169	1005.0 \pm 21.4	99.6
LW1-6	0.697	34	51	1.56	0.09377 \pm 0.00229	0.26772 \pm 0.00450	1503.4 \pm 46.2	101.7
f^{206} = the proportion of common ^{206}Pb in the total ^{206}Pb ; Th/U = $^{232}\text{Th}/^{238}\text{U}$; %C = % concordance								
All ratios and ages corrected for common Pb using measured ^{204}Pb and composition appropriate to the age of the zircon (Stacey and Kramers, 1975)								
Analyses conducted during a single session (07/09/2002). 12 CZ3 standard analyses yielded a 2σ error of the mean of 0.65%								

Table 13-33 SHRIMP analytical data for sample KK-1 (porphyritic granite, Kakulu (Mulungushi) map sheet).

Spot Name	f^{206} (%)	U (ppm)	Th (ppm)	Th/U	$^{207}\text{Pb}/^{206}\text{Pb}$ ($\pm 1\sigma$)	$^{206}\text{Pb}/^{238}\text{U}$ ($\pm 1\sigma$)	$^{207}\text{Pb}/^{206}\text{Pb}$ Age ($\pm 1\sigma$ Ma)	C(%)
KK1-1	0.271	182	208	1.18	0.07202 \pm 0.00125	0.16528 \pm 0.00111	986.5 \pm 35.3	99.9
KK1-2	0.268	117	130	1.15	0.07107 \pm 0.00163	0.16747 \pm 0.00138	959.3 \pm 46.9	104.0
KK1-3	0.426	262	126	0.50	0.07244 \pm 0.00233	0.16346 \pm 0.00098	998.3 \pm 65.3	97.8
KK1-4	0.920	56	74	1.35	0.07090 \pm 0.00391	0.16310 \pm 0.00207	954.6 \pm 112.6	102.0
KK1-5	0.000	183	166	0.94	0.07316 \pm 0.00073	0.17005 \pm 0.00112	1018.3 \pm 20.3	99.4
KK1-6	0.000	171	189	1.15	0.07442 \pm 0.00076	0.16554 \pm 0.00112	1052.8 \pm 20.7	93.8
f^{206} = the proportion of common ^{206}Pb in the total ^{206}Pb ; Th/U = $^{232}\text{Th}/^{238}\text{U}$; %C = % concordance								
All ratios and ages corrected for common Pb using measured ^{204}Pb and composition appropriate to the age of the zircon (Stacey and Kramers, 1975)								
Analyses conducted during a single session (31/03/2003). 10 CZ3 standard analyses yielded a 2σ error of the mean of 0.36%								

Appendix F: zircon U-Pb SHRIMP analytical data

Table 13-34 SHRIMP analytical data for sample MH-4 (porphyritic granite, Mita hills map sheet).

Spot Name	f^{206} (%)	U (ppm)	Th (ppm)	Th/U	$^{207}\text{Pb}/^{206}\text{Pb}$ ($\pm 1\sigma$)	$^{206}\text{Pb}/^{238}\text{U}$ ($\pm 1\sigma$)	$^{207}\text{Pb}/^{206}\text{Pb}$ Age ($\pm 1\sigma$ Ma)	C(%)
¹ MH4-1	0.089	88	77	0.90	0.07264 \pm 0.00091	1.71845 \pm 0.03341	1003.9 \pm 25.4	101.7
¹ MH4-2	2.762	167	124	0.76	0.07159 \pm 0.00290	1.00004 \pm 0.04290	974.4 \pm 82.5	63.8
¹ MH4-3	0.142	394	636	1.67	0.07331 \pm 0.00091	1.72059 \pm 0.04192	1022.6 \pm 25.1	99.1
² MH4-4	0.743	1418	444	0.32	0.07233 \pm 0.00160	1.42415 \pm 0.03171	995.4 \pm 44.9	86.4
² MH4-5	1.938	425	206	0.50	0.07493 \pm 0.00734	1.54638 \pm 0.15199	1066.7 \pm 197.0	84.3
² MH4-6	0.127	301	168	0.58	0.07465 \pm 0.00073	1.61686 \pm 0.01781	1059.0 \pm 19.7	88.8
f^{206} = the proportion of common ^{206}Pb in the total ^{206}Pb ; Th/U = $^{232}\text{Th}/^{238}\text{U}$; %C = % concordance All ratios and ages corrected for common Pb using measured ^{204}Pb and composition appropriate to the age of the zircon (Stacey and Kramers, 1975) Analyses conducted during two sessions (¹ 28/02/2003 and ² 31/03/2003). Session ¹ : 10 CZ3 standard analyses yielded a 2 σ error of the mean of 0.98% Session ² : 10 CZ3 standard analyses yielded a 2 σ error of the mean of 0.36%								

Table 13-35 SHRIMP analytical data for sample MH-9c (porphyritic granite, Mita hills map sheet).

Spot Name	f^{206} (%)	U (ppm)	Th (ppm)	Th/U	$^{207}\text{Pb}/^{206}\text{Pb}$ ($\pm 1\sigma$)	$^{206}\text{Pb}/^{238}\text{U}$ ($\pm 1\sigma$)	$^{207}\text{Pb}/^{206}\text{Pb}$ Age ($\pm 1\sigma$ Ma)	C(%)
¹ MH9-1	0.133	363	294	0.84	0.07346 \pm 0.00065	1.67234 \pm 0.02688	986.2 \pm 31.0	99.9
¹ MH9-2	0.253	120	79	0.68	0.07302 \pm 0.00183	1.69526 \pm 0.04895	1050.4 \pm 30.6	95.5
¹ MH9-3	0.019	615	452	0.76	0.07418 \pm 0.00032	1.79513 \pm 0.02427	1077.0 \pm 14.6	96.8
² MH9-4	1.354	696	504	0.75	0.07486 \pm 0.00656	1.75921 \pm 0.15444	1064.7 \pm 176.1	95.3
² MH9-5	0.041	491	343	0.72	0.07386 \pm 0.00048	1.71359 \pm 0.01305	1037.8 \pm 13.1	96.6
² MH9-6	0.037	808	632	0.81	0.07342 \pm 0.00037	1.76861 \pm 0.01042	1025.6 \pm 10.1	101.2
² MH9-7	0.125	628	442	0.73	0.07333 \pm 0.00059	1.77452 \pm 0.01590	1023.1 \pm 16.2	101.9
² MH9-1	0.133	363	294	0.84	0.07346 \pm 0.00065	1.67234 \pm 0.02688	986.2 \pm 31.0	99.9
f^{206} = the proportion of common ^{206}Pb in the total ^{206}Pb ; Th/U = $^{232}\text{Th}/^{238}\text{U}$; %C = % concordance All ratios and ages corrected for common Pb using measured ^{204}Pb and composition appropriate to the age of the zircon (Stacey and Kramers, 1975) Analyses conducted during two sessions (¹ 28/02/2003 and ² 31/03/2003). Session ¹ : 10 CZ3 standard analyses yielded a 2 σ error of the mean of 0.98% Session ² : 10 CZ3 standard analyses yielded a 2 σ error of the mean of 0.36%								

Table 13-36 SHRIMP analytical data for sample CC-5 (porphyritic granite, Chin'gombe Mission map sheet).

Spot Name	f^{206} (%)	U (ppm)	Th (ppm)	Th/U	$^{207}\text{Pb}/^{206}\text{Pb}$ ($\pm 1\sigma$)	$^{206}\text{Pb}/^{238}\text{U}$ ($\pm 1\sigma$)	$^{207}\text{Pb}/^{206}\text{Pb}$ Age ($\pm 1\sigma$ Ma)	C(%)
CC5-1.1	0.098	327	151	0.48	0.07301 \pm 0.00078	0.17914 \pm 0.00706	1014.2 \pm 21.7	104.7
CC5-2.1	0.000	145	57	0.40	0.07454 \pm 0.00109	0.17549 \pm 0.00697	1056.0 \pm 29.4	98.7
CC5-3.1	0.000	195	102	0.54	0.07671 \pm 0.00110	0.17598 \pm 0.00699	1113.6 \pm 28.5	93.8
CC5-3.2	0.684	338	204	0.62	0.07234 \pm 0.00186	0.16622 \pm 0.00660	995.5 \pm 52.3	99.6
CC5-4.1	0.000	311	133	0.44	0.07398 \pm 0.00071	0.17326 \pm 0.00685	1040.9 \pm 19.3	99.0
CC5-5.1	0.000	198	110	0.57	0.07375 \pm 0.00071	0.17047 \pm 0.00674	1034.7 \pm 19.5	98.1
f^{206} = the proportion of common ^{206}Pb in the total ^{206}Pb ; Th/U = $^{232}\text{Th}/^{238}\text{U}$; %C = % concordance All ratios and ages corrected for common Pb using measured ^{204}Pb and composition appropriate to the age of the zircon (Stacey and Kramers, 1975) Analyses conducted during a single session (06/07/2003). 16 CZ3 standard analyses yielded a 2 σ error of the mean of 2.10%								

Table 13-37 SHRIMP analytical data for sample CC-8 (porphyritic granite, Chin'gombe Mission map sheet).

Spot Name	f^{206} (%)	U (ppm)	Th (ppm)	Th/U	$^{207}\text{Pb}/^{206}\text{Pb}$ ($\pm 1\sigma$)	$^{206}\text{Pb}/^{238}\text{U}$ ($\pm 1\sigma$)	$^{207}\text{Pb}/^{206}\text{Pb}$ Age ($\pm 1\sigma$ Ma)	C(%)
CC8-1.1	0.000	476	214	0.46	0.07414 ± 0.00053	0.17374 ± 0.00683	1045.3 ± 14.4	98.8
CC8-2.1	0.000	257	139	0.56	0.07360 ± 0.00062	0.16806 ± 0.00664	1030.4 ± 17.0	97.2
CC8-3.1	0.000	393	178	0.47	0.07376 ± 0.00050	0.17462 ± 0.00687	1034.8 ± 13.8	100.3
CC8-4.1	0.000	406	260	0.66	0.07421 ± 0.00049	0.17340 ± 0.00682	1047.2 ± 13.2	98.4
CC8-5.1	0.652	361	164	0.47	0.07191 ± 0.00146	0.15855 ± 0.00625	983.3 ± 41.3	96.5
CC8-6.1	0.063	570	230	0.42	0.07341 ± 0.00048	0.17011 ± 0.00668	1025.4 ± 13.3	98.8
f^{206} = the proportion of common ^{206}Pb in the total ^{206}Pb ; Th/U = $^{232}\text{Th}/^{238}\text{U}$; %C = % concordance								
All ratios and ages corrected for common Pb using measured ^{204}Pb and composition appropriate to the age of the zircon (Stacey and Kramers, 1975)								
Analyses conducted during a single session (06/07/2003). 16 CZ3 standard analyses yielded a 2σ error of the mean of 2.10%								

Table 13-38 SHRIMP analytical data for sample MK-7 (biotite granite gneiss, Mkushi map sheet). Spot name ending with r denotes analysis on a rim.

Spot Name	f^{206} (%)	U (ppm)	Th (ppm)	Th/U	$^{207}\text{Pb}/^{206}\text{Pb}$ ($\pm 1\sigma$)	$^{206}\text{Pb}/^{238}\text{U}$ ($\pm 1\sigma$)	$^{207}\text{Pb}/^{206}\text{Pb}$ Age ($\pm 1\sigma$ Ma)	C(%)
¹ MK7-1	0.660	199	415	2.16	0.07376 ± 0.00118	1.65756 ± 0.03473	1034.9 ± 32.2	94.1
¹ MK7-2	1.670	333	284	0.88	0.12323 ± 0.00248	4.45448 ± 0.10767	2003.4 ± 35.8	74.9
¹ MK7-2r	0.530	1815	64	0.04	0.06881 ± 0.00056	1.39160 ± 0.02089	892.9 ± 16.7	98.8
² MK7-3	1.569	261	422	1.67	0.07879 ± 0.00201	1.59315 ± 0.04186	1166.9 ± 50.6	75.6
² MK7-4	1.296	192	228	1.23	0.07985 ± 0.00253	1.28480 ± 0.04190	1193.2 ± 62.6	59.6
² MK7-5	2.088	1199	175	0.15	0.06873 ± 0.00366	1.13515 ± 0.06128	890.7 ± 110.0	81.9
f^{206} = the proportion of common ^{206}Pb in the total ^{206}Pb ; Th/U = $^{232}\text{Th}/^{238}\text{U}$; %C = % concordance								
All ratios and ages corrected for common Pb using measured ^{204}Pb and composition appropriate to the age of the zircon (Stacey and Kramers, 1975)								
Analyses conducted during two sessions (¹ 28/02/2003 and ² 31/03/2003).								
Session ¹ : 10 CZ3 standard analyses yielded a 2σ error of the mean of 0.98%								
Session ² : 10 CZ3 standard analyses yielded a 2σ error of the mean of 0.36%								

Table 13-39 SHRIMP analytical data for sample FW-1 (porphyritic granite, Fiwila Mission map sheet).

Spot Name	f^{206} (%)	U (ppm)	Th (ppm)	Th/U	$^{207}\text{Pb}/^{206}\text{Pb}$ ($\pm 1\sigma$)	$^{206}\text{Pb}/^{238}\text{U}$ ($\pm 1\sigma$)	$^{207}\text{Pb}/^{206}\text{Pb}$ Age ($\pm 1\sigma$ Ma)	C(%)
FW1-1	0.452	2020	422	0.22	0.07069 ± 0.00064	1.69632 ± 0.03287	948.5 ± 18.5	109.1
FW1-2	0.108	1069	382	0.37	0.07417 ± 0.00057	1.78742 ± 0.03402	1046.0 ± 15.6	99.3
FW1-3	0.484	203	359	1.82	0.07207 ± 0.00183	1.77925 ± 0.05690	988.0 ± 51.6	107.5
FW1-4	1.112	389	499	1.32	0.07156 ± 0.00266	1.64344 ± 0.06824	973.4 ± 75.9	102.0
FW1-5	0.000	1327	148	0.12	0.07464 ± 0.00043	1.88767 ± 0.03439	1058.9 ± 11.6	102.5
FW1-6	1.112	712	776	1.13	0.07299 ± 0.00166	1.70267 ± 0.04924	1013.7 ± 46.2	99.4
FW1-7	0.517	982	617	0.65	0.07217 ± 0.00097	1.79415 ± 0.03954	990.7 ± 27.3	107.9
f^{206} = the proportion of common ^{206}Pb in the total ^{206}Pb ; Th/U = $^{232}\text{Th}/^{238}\text{U}$; %C = % concordance								
All ratios and ages corrected for common Pb using measured ^{204}Pb and composition appropriate to the age of the zircon (Stacey and Kramers, 1975)								
Analyses conducted during a single session (07/04/2003). 7 CZ3 standard analyses yielded a 2σ error of the mean of 1.65%								

Appendix F: zircon U-Pb SHRIMP analytical data

Table 13-40 SHRIMP analytical data for sample FW-2 (aplite cutting porphyritic granite, Fiwila Mission map sheet).

Spot Name	f^{206} (%)	U (ppm)	Th (ppm)	Th/U	$^{207}\text{Pb}/^{206}\text{Pb}$ ($\pm 1\sigma$)	$^{206}\text{Pb}/^{238}\text{U}$ ($\pm 1\sigma$)	$^{207}\text{Pb}/^{206}\text{Pb}$ Age ($\pm 1\sigma$ Ma)	C(%)
FW2-1	0.391	120	70	0.60	0.12523 \pm 0.00195	6.35520 \pm 0.16284	2032.1 \pm 27.5	99.4
FW2-2	1.017	345	94	0.28	0.08254 \pm 0.00436	1.99952 \pm 0.11282	1258.3 \pm 103.2	82.9
FW2-3	0.089	968	96	0.10	0.12607 \pm 0.00055	6.44670 \pm 0.11521	2043.9 \pm 7.8	99.5
FW2-4	0.210	191	87	0.47	0.19366 \pm 0.00273	14.32643 \pm 0.33874	2773.5 \pm 23.2	99.8
FW2-5	0.325	209	72	0.36	0.11233 \pm 0.00173	4.56871 \pm 0.11198	1837.4 \pm 27.9	90.7
FW2-6	0.056	1375	122	0.09	0.12414 \pm 0.00067	6.47916 \pm 0.11706	2016.5 \pm 9.5	102.6
FW2-7	0.134	307	22	0.07	0.12370 \pm 0.00145	6.33304 \pm 0.13892	2010.3 \pm 20.8	101.3
FW2-8	0.597	77	40	0.54	0.12984 \pm 0.00281	7.04491 \pm 0.22442	2095.8 \pm 38.1	102.1
FW2-9	0.465	114	237	2.16	0.13000 \pm 0.00483	6.53413 \pm 0.31931	2097.9 \pm 65.2	95.5
FW2-10	0.884	185	87	0.49	0.12534 \pm 0.00216	6.23497 \pm 0.16391	2033.6 \pm 30.5	97.7
FW2-11	0.086	343	221	0.67	0.11927 \pm 0.00262	6.15944 \pm 0.17685	1945.3 \pm 39.3	105.4
FW2-12	0.549	157	115	0.76	0.10069 \pm 0.00251	4.11285 \pm 0.13133	1636.9 \pm 46.4	102.2
FW2-13	0.066	648	83	0.13	0.16268 \pm 0.00073	8.84789 \pm 0.16048	2483.7 \pm 7.6	86.3
f^{206} = the proportion of common ^{206}Pb in the total ^{206}Pb ; Th/U = $^{232}\text{Th}/^{238}\text{U}$; %C = % concordance All ratios and ages corrected for common Pb using measured ^{204}Pb and composition appropriate to the age of the zircon (Stacey and Kramers, 1975) Analyses conducted during a single session (07/04/2003). 7 CZ3 standard analyses yielded a 2σ error of the mean of 1.65%								

Table 13-41 SHRIMP analytical data for sample CHT-6 (porphyritic granite, Chitambo Mission map sheet).

Spot Name	f^{206} (%)	U (ppm)	Th (ppm)	Th/U	$^{207}\text{Pb}/^{206}\text{Pb}$ ($\pm 1\sigma$)	$^{206}\text{Pb}/^{238}\text{U}$ ($\pm 1\sigma$)	$^{207}\text{Pb}/^{206}\text{Pb}$ Age ($\pm 1\sigma$ Ma)	C(%)
CHT6-1	0.869	144	117	0.84	0.07304 \pm 0.00306	1.74172 \pm 0.08690	1015.1 \pm 84.8	101.3
CHT6-2	1.150	147	178	1.25	0.06558 \pm 0.00336	1.53049 \pm 0.08469	792.9 \pm 107.5	127.1
CHT6-3	0.460	415	282	0.70	0.07373 \pm 0.00161	1.71450 \pm 0.04876	1034.2 \pm 44.1	97.1
CHT6-4	0.225	300	214	0.74	0.07371 \pm 0.00113	1.74871 \pm 0.04221	1033.5 \pm 30.9	99.0
CHT6-5	2.414	148	111	0.77	0.06606 \pm 0.00561	1.43724 \pm 0.12602	808.3 \pm 177.7	116.9
CHT6-6	0.680	164	175	1.11	0.07541 \pm 0.00311	1.73153 \pm 0.07990	1079.3 \pm 82.9	92.0
CHT6-7	0.778	113	99	0.91	0.07232 \pm 0.00356	1.66512 \pm 0.09000	994.9 \pm 100.2	100.1
CHT6-8	1.591	93	124	1.38	0.06590 \pm 0.00529	1.50833 \pm 0.12608	803.3 \pm 168.0	123.2
CHT6-9	1.253	140	143	1.06	0.07048 \pm 0.00587	1.62685 \pm 0.13995	942.3 \pm 170.7	105.9
f^{206} = the proportion of common ^{206}Pb in the total ^{206}Pb ; Th/U = $^{232}\text{Th}/^{238}\text{U}$; %C = % concordance All ratios and ages corrected for common Pb using measured ^{204}Pb and composition appropriate to the age of the zircon (Stacey and Kramers, 1975) Analyses conducted during a single session (07/04/2003). 7 CZ3 standard analyses yielded a 2σ error of the mean of 1.65%								

Table 13-42 SHRIMP analytical data for sample KN-2a (porphyritic granite, Kanona map sheet).

Spot Name	f^{206} (%)	U (ppm)	Th (ppm)	Th/U	$^{207}\text{Pb}/^{206}\text{Pb}$ ($\pm 1\sigma$)	$^{206}\text{Pb}/^{238}\text{U}$ ($\pm 1\sigma$)	$^{207}\text{Pb}/^{206}\text{Pb}$ Age ($\pm 1\sigma$ Ma)	C(%)
KN2a-1	0.000	204	282	1.43	0.07378 ± 0.00071	0.17375 ± 0.00411	1035.6 ± 19.4	99.7
KN2a-2	0.018	225	117	0.54	0.08606 ± 0.00084	0.16993 ± 0.00347	1339.6 ± 18.8	75.5
KN2a-3	0.000	116	177	1.58	0.07873 ± 0.00095	0.17796 ± 0.00374	1165.3 ± 24.0	90.6
KN2a-4	0.000	165	146	0.91	0.08220 ± 0.00130	0.17712 ± 0.00365	1250.3 ± 30.8	84.1
KN2a-5	0.000	1421	882	0.64	0.07915 ± 0.00119	0.17420 ± 0.00352	1176.0 ± 29.7	88.0
KN2a-6	0.056	131	147	1.16	0.07527 ± 0.00096	0.17795 ± 0.00370	1075.7 ± 25.7	98.1
KN2a-7	0.000	236	176	0.77	0.07668 ± 0.00075	0.17284 ± 0.00352	1113.0 ± 19.6	92.3
KN2a-8	0.066	247	144	0.60	0.07634 ± 0.00082	0.17257 ± 0.00351	1103.9 ± 21.4	93.0
f^{206} = the proportion of common ^{206}Pb in the total ^{206}Pb ; Th/U = $^{232}\text{Th}/^{238}\text{U}$; %C = % concordance								
All ratios and ages corrected for common Pb using measured ^{204}Pb and composition appropriate to the age of the zircon (Stacey and Kramers, 1975)								
Analyses conducted during a single session (08/06/2003). 12 CZ3 standard analyses yielded a 2σ error of the mean of 1.56%								

Table 13-43 SHRIMP analytical data for sample KN-5 (porphyritic granite, Kanona map sheet). Spot name ending with r denotes analysis on a rim, spot name ending with c denotes analysis on a core.

Spot Name	f^{206} (%)	U (ppm)	Th (ppm)	Th/U	$^{207}\text{Pb}/^{206}\text{Pb}$ ($\pm 1\sigma$)	$^{206}\text{Pb}/^{238}\text{U}$ ($\pm 1\sigma$)	$^{207}\text{Pb}/^{206}\text{Pb}$ Age ($\pm 1\sigma$ Ma)	C(%)
KN5-1	0.000	456	212	0.48	0.07463 ± 0.00046	0.17865 ± 0.00358	1058.6 ± 12.5	100.1
KN5-2	0.098	181	356	2.03	0.08078 ± 0.00128	0.17909 ± 0.00369	1216.0 ± 31.1	87.3
KN5-3r	0.050	2299	231	0.10	0.07580 ± 0.00109	0.13595 ± 0.00294	1089.8 ± 28.9	75.4
KN5-3c	0.025	332	177	0.55	0.07797 ± 0.00081	0.17663 ± 0.00356	1146.1 ± 20.7	91.5
KN5-4	0.000	273	138	0.52	0.07652 ± 0.00075	0.17761 ± 0.00360	1108.6 ± 19.6	95.1
KN5-5	0.021	247	120	0.50	0.07979 ± 0.00066	0.17543 ± 0.00356	1191.8 ± 16.3	87.4
KN5-6	0.000	338	180	0.55	0.07487 ± 0.00054	0.17867 ± 0.00360	1065.1 ± 14.4	99.5
KN5-7	0.000	281	132	0.49	0.07650 ± 0.00060	0.17752 ± 0.00359	1108.1 ± 15.6	95.1
KN5-8	0.000	298	153	0.53	0.07624 ± 0.00059	0.18036 ± 0.00365	1101.3 ± 15.4	97.1
f^{206} = the proportion of common ^{206}Pb in the total ^{206}Pb ; Th/U = $^{232}\text{Th}/^{238}\text{U}$; %C = % concordance								
All ratios and ages corrected for common Pb using measured ^{204}Pb and composition appropriate to the age of the zircon (Stacey and Kramers, 1975)								
Analyses conducted during a single session (08/06/2003). 12 CZ3 standard analyses yielded a 2σ error of the mean of 1.56%								

Table 13-44 SHRIMP analytical data for sample KN-7 (biotite granite gneiss, Kanona map sheet). Spot name ending with r denotes analysis on a rim, spot name ending with c denotes analysis on a core.

Spot Name	f^{206} (%)	U (ppm)	Th (ppm)	Th/U	$^{207}\text{Pb}/^{206}\text{Pb}$ ($\pm 1\sigma$)	$^{206}\text{Pb}/^{238}\text{U}$ ($\pm 1\sigma$)	$^{207}\text{Pb}/^{206}\text{Pb}$ Age ($\pm 1\sigma$ Ma)	C(%)
KN7-2	0.000	506	155	0.32	0.12212 ± 0.00108	0.33971 ± 0.00680	1987.4 ± 15.8	94.9
KN7-3r	0.399	2878	39994	14.36	0.19049 ± 0.01292	0.07975 ± 0.00159	2746.4 ± 111.5	18.0
KN7-3c	0.000	184	258	1.45	0.19596 ± 0.00156	0.41147 ± 0.00899	2792.8 ± 13.1	79.5
KN7-4	0.000	209	30	0.15	0.12215 ± 0.00064	0.37122 ± 0.00753	1987.8 ± 9.3	102.4
KN7-5	0.049	230	87	0.39	0.11920 ± 0.00307	0.34343 ± 0.00939	1944.3 ± 46.0	97.9
KN7-6	0.010	259	818	3.26	0.08331 ± 0.00069	0.15308 ± 0.00310	1276.5 ± 16.2	71.9
KN7-7	0.032	740	235	0.33	0.07422 ± 0.00038	0.17678 ± 0.00352	1047.6 ± 10.2	100.2
KN7-8	0.003	973	825	0.88	0.12417 ± 0.00028	0.36971 ± 0.00738	2017.0 ± 4.1	100.5
f^{206} = the proportion of common ^{206}Pb in the total ^{206}Pb ; Th/U = $^{232}\text{Th}/^{238}\text{U}$; %C = % concordance								
All ratios and ages corrected for common Pb using measured ^{204}Pb and composition appropriate to the age of the zircon (Stacey and Kramers, 1975)								
Analyses conducted during a single session (08/06/2003). 12 CZ3 standard analyses yielded a 2σ error of the mean of 1.56%								

Appendix F: zircon U-Pb SHRIMP analytical data

Table 13-45 SHRIMP analytical data for sample KN-8 (porphyritic granite, Kanona map sheet). Spot name ending with r denotes analysis on a rim, spot name ending with c denotes analysis on a core.

Spot Name	f^{206} (%)	U (ppm)	Th (ppm)	Th/U	$^{207}\text{Pb}/^{206}\text{Pb}$ ($\pm 1\sigma$)	$^{206}\text{Pb}/^{238}\text{U}$ ($\pm 1\sigma$)	$^{207}\text{Pb}/^{206}\text{Pb}$ Age ($\pm 1\sigma$ Ma)	C(%)
KN8-1	0.018	245	191	0.81	0.08522 \pm 0.00068	0.19321 \pm 0.00399	1320.4 \pm 15.6	86.2
KN8-1c	0.007	117	58	0.51	0.12664 \pm 0.00092	0.37348 \pm 0.00773	2051.8 \pm 12.8	99.7
KN8-2	0.000	496	1171	2.44	0.08071 \pm 0.00091	0.16912 \pm 0.00338	1214.4 \pm 22.2	82.9
KN8-3	0.000	107	124	1.19	0.08184 \pm 0.00128	0.17658 \pm 0.00371	1241.6 \pm 30.7	84.4
KN8-4	0.031	406	88	0.23	0.12828 \pm 0.00255	0.32698 \pm 0.00657	2074.5 \pm 35.0	87.9
KN8-4r	0.000	315	176	0.58	0.07506 \pm 0.00059	0.16945 \pm 0.00343	1070.0 \pm 15.8	94.3
KN8-5	0.000	382	256	0.69	0.07682 \pm 0.00057	0.16490 \pm 0.00331	1116.4 \pm 14.9	88.1
KN8-6	0.033	310	228	0.76	0.07609 \pm 0.00140	0.17208 \pm 0.00356	1097.4 \pm 36.7	93.3
KN8-7	0.000	321	134	0.43	0.10008 \pm 0.00164	0.24025 \pm 0.00483	1625.6 \pm 30.4	85.4
KN8-8	0.002	378	348	0.95	0.07472 \pm 0.00063	0.17771 \pm 0.00357	1060.9 \pm 17.0	99.4
KN8-9	0.000	113	164	1.50	0.08671 \pm 0.00137	0.17318 \pm 0.00364	1354.1 \pm 30.4	76.0
KN8-10	0.002	725	586	0.83	0.07918 \pm 0.00047	0.17180 \pm 0.00342	1176.7 \pm 11.9	86.9
KN8-11	0.091	215	267	1.29	0.07687 \pm 0.00091	0.17315 \pm 0.00353	1117.9 \pm 23.6	92.1
f^{206} = the proportion of common ^{206}Pb in the total ^{206}Pb ; Th/U = $^{232}\text{Th}/^{238}\text{U}$; %C = % concordance								
All ratios and ages corrected for common Pb using measured ^{204}Pb and composition appropriate to the age of the zircon (Stacey and Kramers, 1975)								
Analyses conducted during a single session (08/06/2003). 12 CZ3 standard analyses yielded a 2σ error of the mean of 1.56%								

Table 13-46 SHRIMP analytical data for sample ND-1 (porphyritic granite, Ndabala map sheet). Spot names ending with r denote analyses on a rim, spot names ending with c denote analyses on core.

Spot Name	f^{206} (%)	U (ppm)	Th (ppm)	Th/U	$^{207}\text{Pb}/^{206}\text{Pb}$ ($\pm 1\sigma$)	$^{206}\text{Pb}/^{238}\text{U}$ ($\pm 1\sigma$)	$^{207}\text{Pb}/^{206}\text{Pb}$ Age ($\pm 1\sigma$ Ma)	C(%)
ND1-1	1.348	1300	486	0.39	0.07944 \pm 0.00934	0.16120 \pm 0.00216	1183.1 \pm 232.3	81.4
ND1-2	0.000	288	419	1.50	0.07371 \pm 0.00052	0.17831 \pm 0.00219	1033.5 \pm 14.3	102.3
ND1-3	0.777	238	266	1.16	0.08212 \pm 0.00285	0.16971 \pm 0.00211	1248.3 \pm 67.9	81.0
ND1-4	0.291	1057	481	0.47	0.07402 \pm 0.00165	0.17261 \pm 0.00190	1042.0 \pm 44.9	98.5
ND1-5r	0.512	999	532	0.55	0.07818 \pm 0.00160	0.16041 \pm 0.00176	1151.5 \pm 40.6	83.3
ND1-5c	0.003	1864	493	0.27	0.07314 \pm 0.00025	0.17789 \pm 0.00201	1017.7 \pm 6.9	103.7
ND1-7	4.316	1926	917	0.49	0.10095 \pm 0.02577	0.15316 \pm 0.00437	1641.7 \pm 473.8	56.0
ND1-8	6.367	1718	490	0.29	0.12801 \pm 0.08145	0.14736 \pm 0.00752	2070.8 \pm 1121.2	42.8
ND1-9	0.000	1977	55	0.03	0.07348 \pm 0.00021	0.17610 \pm 0.00203	1027.2 \pm 5.8	101.8
ND1-10	0.014	2459	1017	0.43	0.07322 \pm 0.00024	0.17671 \pm 0.00191	1020.2 \pm 6.6	102.8
f^{206} = the proportion of common ^{206}Pb in the total ^{206}Pb ; Th/U = $^{232}\text{Th}/^{238}\text{U}$; %C = % concordance								
All ratios and ages corrected for common Pb using measured ^{204}Pb and composition appropriate to the age of the zircon (Stacey and Kramers, 1975)								
Analyses conducted during a single session (08/03/2003). 14 CZ3 standard analyses yielded a 2σ error of the mean of 0.66%								

Table 13-47 SHRIMP analytical data for sample ND-4 (diorite, Ndabala map sheet).

Spot Name	f^{206} (%)	U (ppm)	Th (ppm)	Th/U	$^{207}\text{Pb}/^{206}\text{Pb}$ ($\pm 1\sigma$)	$^{206}\text{Pb}/^{238}\text{U}$ ($\pm 1\sigma$)	$^{207}\text{Pb}/^{206}\text{Pb}$ Age ($\pm 1\sigma$ Ma)	C(%)
ND4-1	0.000	324	370	1.18	0.07357 \pm 0.00053	0.17253 \pm 0.00205	1029.7 \pm 14.7	99.6
ND4-2	0.071	271	288	1.10	0.07353 \pm 0.00078	0.17504 \pm 0.00206	1028.7 \pm 21.6	101.1
ND4-3	0.071	398	650	1.69	0.07364 \pm 0.00053	0.17264 \pm 0.00200	1031.7 \pm 14.5	99.5
ND4-4	0.011	306	328	1.11	0.07444 \pm 0.00054	0.17156 \pm 0.00210	1053.5 \pm 14.5	96.9
f^{206} = the proportion of common ^{206}Pb in the total ^{206}Pb ; Th/U = $^{232}\text{Th}/^{238}\text{U}$; %C = % concordance								
All ratios and ages corrected for common Pb using measured ^{204}Pb and composition appropriate to the age of the zircon (Stacey and Kramers, 1975)								
Analyses conducted during a single session (08/03/2003). 14 CZ3 standard analyses yielded a 2σ error of the mean of 0.66%								

Table 13-48 SHRIMP analytical data for sample ND-5 (syenite, Ndabala map sheet).

Spot Name	f_{206} (%)	U (ppm)	Th (ppm)	Th/U	$^{207}\text{Pb}/^{206}\text{Pb}$ ($\pm 1\sigma$)	$^{206}\text{Pb}/^{238}\text{U}$ ($\pm 1\sigma$)	$^{207}\text{Pb}/^{206}\text{Pb}$ Age ($\pm 1\sigma$ Ma)	C(%)
ND5-1	0.721	263	332	1.31	0.07687 ± 0.00134	0.16182 ± 0.00190	1117.9 ± 34.8	86.5
ND5-2	0.097	230	311	1.39	0.07293 ± 0.00090	0.17429 ± 0.00208	1012.1 ± 24.9	102.3
ND5-3	0.036	241	253	1.09	0.07347 ± 0.00083	0.17202 ± 0.00204	1027.0 ± 23.0	99.6
ND5-4	0.623	242	401	1.72	0.07501 ± 0.00128	0.16700 ± 0.00204	1068.7 ± 34.4	93.2
f_{206} = the proportion of common ^{206}Pb in the total ^{206}Pb ; Th/U = $^{232}\text{Th}/^{238}\text{U}$; %C = % concordance								
All ratios and ages corrected for common Pb using measured ^{204}Pb and composition appropriate to the age of the zircon (Stacey and Kramers, 1975)								
Analyses conducted during a single session (08/03/2003). 14 CZ3 standard analyses yielded a 2σ error of the mean of 0.66%								

Table 13-49 SHRIMP analytical data for sample SASA 2 (Sasa Granite, Serenje map sheet)

Spot Name	f_{206} (%)	U (ppm)	Th (ppm)	Th/U	$^{207}\text{Pb}/^{206}\text{Pb}$ ($\pm 1\sigma$)	$^{206}\text{Pb}/^{238}\text{U}$ ($\pm 1\sigma$)	$^{207}\text{Pb}/^{206}\text{Pb}$ Age ($\pm 1\sigma$ Ma)	C(%)
SASA2-1	2.481	48	110	2.38	0.06921 ± 0.01622	0.17652 ± 0.00516	905.1 ± 482.9	115.8
SASA2-2	0.707	912	780	0.88	0.07271 ± 0.00054	0.17402 ± 0.00413	1005.8 ± 15.1	102.8
SASA2-3c	0.268	465	281	0.62	0.07472 ± 0.00128	0.16978 ± 0.00398	1060.9 ± 34.5	95.3
SASA2-3r	0.823	1932	467	0.25	0.07254 ± 0.00113	0.15492 ± 0.00333	1001.0 ± 31.6	92.8
SASA2-5	0.301	417	404	1.00	0.07653 ± 0.00149	0.14188 ± 0.00340	1109.0 ± 39.0	77.1
SASA2-10	1.723	228	279	1.26	0.07278 ± 0.00333	0.16983 ± 0.00427	1008.0 ± 92.7	100.3
SASA2-11	0.294	1974	66	0.03	0.07403 ± 0.00064	0.16416 ± 0.00387	1042.3 ± 17.3	94.0
SASA2-12c	0.858	1059	371	0.36	0.07295 ± 0.00087	0.17077 ± 0.00367	1012.7 ± 24.1	100.4
SASA2-12r	0.311	1133	326	0.30	0.07414 ± 0.00265	0.17338 ± 0.00375	1045.3 ± 72.1	98.6
SASA2-15	0.890	186	266	1.48	0.07038 ± 0.00357	0.17803 ± 0.00399	939.5 ± 104.0	112.4
SASA2-17	0.945	252	329	1.35	0.07226 ± 0.00112	0.16976 ± 0.00407	993.3 ± 31.5	101.8
SASA2-18	1.335	193	279	1.49	0.07682 ± 0.00499	0.14176 ± 0.00329	1116.6 ± 129.6	76.5
f_{206} = the proportion of common ^{206}Pb in the total ^{206}Pb ; Th/U = $^{232}\text{Th}/^{238}\text{U}$; %C = % concordance								
All ratios and ages corrected for common Pb using measured ^{204}Pb and composition appropriate to the age of the zircon (Stacey and Kramers, 1975)								
Analyses conducted during a single session (01/03/2002). 16 CZ3 standard analyses yielded a 2σ error of the mean of 1.18%								

Table 13-50 SHRIMP analytical data for sample SER 5-3 (porphyritic granite, Serenje map sheet)

Spot Name	f_{206} (%)	U (ppm)	Th (ppm)	Th/U	$^{207}\text{Pb}/^{206}\text{Pb}$ ($\pm 1\sigma$)	$^{206}\text{Pb}/^{238}\text{U}$ ($\pm 1\sigma$)	$^{207}\text{Pb}/^{206}\text{Pb}$ Age ($\pm 1\sigma$ Ma)	C(%)
SER53-1.1	0.041	257	248	1.00	0.07388 ± 0.00076	0.17373 ± 0.00329	1038.2 ± 20.8	99.5
SER53-2.1	0.001	252	123	0.50	0.07371 ± 0.00075	0.17480 ± 0.00336	1033.7 ± 20.4	100.5
SER53-3.1	0.416	117	198	1.74	0.07069 ± 0.00229	0.16569 ± 0.00341	948.5 ± 66.4	104.2
SER53-4.1	0.000	813	761	0.97	0.07387 ± 0.00042	0.17557 ± 0.00321	1037.9 ± 11.5	100.5
SER53-5.1	0.000	317	292	0.95	0.07488 ± 0.00069	0.17544 ± 0.00332	1065.4 ± 18.5	97.8
SER53-6.1	0.054	244	261	1.10	0.07259 ± 0.00080	0.17680 ± 0.00341	1002.5 ± 22.5	104.7
SER53-7.1	0.101	513	455	0.92	0.07327 ± 0.00073	0.16920 ± 0.00344	1021.4 ± 20.1	98.7
SER53-8.1	0.170	457	409	0.92	0.07259 ± 0.00068	0.17488 ± 0.00331	1002.6 ± 19.0	103.6
SER53-9.1	0.420	189	197	1.08	0.07034 ± 0.00173	0.16331 ± 0.00334	938.2 ± 50.6	103.9
SER53-10.1	4.930	346	392	1.17	0.07239 ± 0.00472	0.16601 ± 0.00330	997.1 ± 132.5	99.3
f_{206} = the proportion of common ^{206}Pb in the total ^{206}Pb ; Th/U = $^{232}\text{Th}/^{238}\text{U}$; %C = % concordance								
All ratios and ages corrected for common Pb using measured ^{204}Pb and composition appropriate to the age of the zircon (Stacey and Kramers, 1975)								
Analyses conducted during a single session (14/11/1999). 14 CZ3 standard analyses yielded a 2σ error of the mean of 1.11%								

Appendix F: zircon U-Pb SHRIMP analytical data

Table 13-51 SHRIMP analytical data for sample SER 6-4 (porphyritic granite, Serenje map sheet).

Spot Name	f^{206} (%)	U (ppm)	Th (ppm)	Th/U	$^{207}\text{Pb}/^{206}\text{Pb}$ ($\pm 1\sigma$)	$^{206}\text{Pb}/^{238}\text{U}$ ($\pm 1\sigma$)	$^{207}\text{Pb}/^{206}\text{Pb}$ Age ($\pm 1\sigma$ Ma)	C(%)
SER64-1.1	0.632	171	382	2.31	0.07237 \pm 0.00174	0.14368 \pm 0.00283	996.3 \pm 48.8	86.9
SER64-2.1	0.000	260	71	0.28	0.07517 \pm 0.00078	0.17481 \pm 0.00332	1073.1 \pm 20.9	96.8
SER64-3.1	0.000	1252	248	0.20	0.07398 \pm 0.00036	0.18155 \pm 0.00328	1040.8 \pm 9.9	103.3
SER64-4.1	0.000	237	712	3.11	0.07339 \pm 0.00078	0.17228 \pm 0.00333	1024.7 \pm 21.6	100.0
SER64-5.1	0.000	449	670	1.54	0.07283 \pm 0.00066	0.17375 \pm 0.00328	1009.1 \pm 18.3	102.3
SER64-6.1	0.701	50	99	2.04	0.06717 \pm 0.00406	0.16809 \pm 0.00428	842.9 \pm 125.7	118.8
SER64-7.1	0.000	1038	140	0.14	0.07344 \pm 0.00042	0.17694 \pm 0.00349	1026.0 \pm 11.6	102.4
SER64-8.1	0.603	898	292	0.34	0.07516 \pm 0.00099	0.15197 \pm 0.00281	1072.8 \pm 26.5	85.0
SER64-9.1	0.000	889	979	1.14	0.12301 \pm 0.00044	0.37536 \pm 0.00694	2000.4 \pm 6.4	102.7
SER64-10.1	0.292	213	562	2.73	0.07507 \pm 0.00403	0.17522 \pm 0.00373	1070.4 \pm 107.8	97.2
f^{206} = the proportion of common ^{206}Pb in the total ^{206}Pb ; Th/U = $^{232}\text{Th}/^{238}\text{U}$; %C = % concordance								
All ratios and ages corrected for common Pb using measured ^{204}Pb and composition appropriate to the age of the zircon (Stacey and Kramers, 1975)								
Analyses conducted during a single session (14/11/1999). 14 CZ3 standard analyses yielded a 2σ error of the mean of 1.11%								

Table 13-52 SHRIMP analytical data for sample SQG (porphyritic granite, Serenje map sheet).

Spot Name	f^{206} (%)	U (ppm)	Th (ppm)	Th/U	$^{207}\text{Pb}/^{206}\text{Pb}$ ($\pm 1\sigma$)	$^{206}\text{Pb}/^{238}\text{U}$ ($\pm 1\sigma$)	$^{207}\text{Pb}/^{206}\text{Pb}$ Age ($\pm 1\sigma$ Ma)	C(%)
SQG-72	0.000	460	463	1.04	0.07474 \pm 0.00051	0.17773 \pm 0.00270	1061.6 \pm 13.7	99.3
SQG-70	0.000	187	88	0.49	0.07616 \pm 0.00114	0.18443 \pm 0.00825	1099.4 \pm 29.9	99.3
SQG-26	0.004	402	187	0.48	0.07480 \pm 0.00040	0.16799 \pm 0.00253	1063.0 \pm 10.8	94.2
SQG-60	0.012	689	348	0.52	0.07370 \pm 0.00031	0.16831 \pm 0.00249	1033.3 \pm 8.5	97.1
SQG-7	0.027	699	259	0.38	0.07329 \pm 0.00034	0.17155 \pm 0.00253	1021.9 \pm 9.5	99.9
SQG-17	0.040	136	90	0.68	0.07244 \pm 0.00083	0.17304 \pm 0.00273	998.4 \pm 23.3	103.0
SQG-77	0.042	133	97	0.76	0.07241 \pm 0.00069	0.18131 \pm 0.00288	997.6 \pm 19.3	107.7
SQG-48	0.043	702	346	0.51	0.07362 \pm 0.00034	0.16623 \pm 0.00245	1031.2 \pm 9.4	96.1
SQG-20	0.074	411	249	0.62	0.07357 \pm 0.00061	0.17071 \pm 0.00257	1029.8 \pm 16.9	98.7
SQG-1	0.088	233	144	0.64	0.07264 \pm 0.00060	0.17245 \pm 0.00263	1003.8 \pm 16.8	102.2
SQG-14	1.201	575	284	0.51	0.07218 \pm 0.00129	0.16418 \pm 0.00251	990.9 \pm 36.3	98.9
f^{206} = the proportion of common ^{206}Pb in the total ^{206}Pb ; Th/U = $^{232}\text{Th}/^{238}\text{U}$; %C = % concordance								
All ratios and ages corrected for common Pb using measured ^{204}Pb and composition appropriate to the age of the zircon (Stacey and Kramers, 1975)								
Analyses conducted during a single session (26/03/2002). 16 CZ3 standard analyses yielded a 2σ error of the mean of 0.81%								

Table 13-53 SHRIMP analytical data for sample ZM 36 (Mununga Granite, Mupamadzi River map sheet).

Spot Name	f^{206} (%)	U (ppm)	Th (ppm)	Th/U	$^{207}\text{Pb}/^{206}\text{Pb}$ ($\pm 1\sigma$)	$^{206}\text{Pb}/^{238}\text{U}$ ($\pm 1\sigma$)	$^{207}\text{Pb}/^{206}\text{Pb}$ Age ($\pm 1\sigma$ Ma)	C(%)
ZM36-1.1	0.000	91	94	1.07	0.07842 ± 0.00227	0.17709 ± 0.00381	1157.5 ± 57.4	90.8
ZM36-2.1	0.193	145	138	0.98	0.07180 ± 0.00144	0.17875 ± 0.00354	980.3 ± 40.7	108.1
ZM36-3.1	0.000	32	30	0.95	0.08094 ± 0.00861	0.17282 ± 0.00519	1220.0 ± 209.1	84.2
ZM36-4.1	0.026	491	269	0.57	0.07344 ± 0.00055	0.17008 ± 0.00315	1026.2 ± 15.1	98.7
ZM36-5.1	0.014	487	298	0.63	0.07348 ± 0.00063	0.17624 ± 0.00326	1027.3 ± 17.5	101.9
ZM36-6.1	0.358	64	65	1.05	0.06967 ± 0.00246	0.16523 ± 0.00395	918.6 ± 72.8	107.3
ZM36-7.1	0.015	568	340	0.62	0.07328 ± 0.00067	0.16720 ± 0.00314	1021.7 ± 18.5	97.6
ZM36-8.1	0.174	206	164	0.82	0.07253 ± 0.00189	0.16960 ± 0.00379	1000.9 ± 52.9	100.9
ZM36-9.1	0.081	567	359	0.65	0.07358 ± 0.00069	0.17231 ± 0.00322	1030.0 ± 19.0	99.5
ZM36-10.1	0.054	615	292	0.49	0.07418 ± 0.00060	0.17079 ± 0.00318	1046.4 ± 16.3	97.1

f^{206} = the proportion of common ^{206}Pb in the total ^{206}Pb ; Th/U = $^{232}\text{Th}/^{238}\text{U}$; %C = % concordance
 All ratios and ages corrected for common Pb using measured ^{204}Pb and composition appropriate to the age of the zircon (Stacey and Kramers, 1975)
 Analyses conducted during a single session (14/11/1999). 14 CZ3 standard analyses yielded a 2σ error of the mean of 1.11%

Table 13-54 SHRIMP analytical data for sample CHL-5 (porphyritic granite, Chilonga Mission map sheet).

Spot Name	f^{206} (%)	U (ppm)	Th (ppm)	Th/U	$^{207}\text{Pb}/^{206}\text{Pb}$ ($\pm 1\sigma$)	$^{206}\text{Pb}/^{238}\text{U}$ ($\pm 1\sigma$)	$^{207}\text{Pb}/^{206}\text{Pb}$ Age ($\pm 1\sigma$ Ma)	C(%)
CHL5-1	0.506	227	368	1.68	0.07432 ± 0.00129	1.79657 ± 0.05688	1050.3 ± 34.9	99.1
CHL5-2	0.723	269	488	1.87	0.07373 ± 0.00221	1.69087 ± 0.07479	1034.0 ± 60.6	95.9
CHL5-3	0.610	244	44	0.18	0.07236 ± 0.00213	1.71635 ± 0.06805	996.1 ± 59.9	102.7
CHL5-4	0.069	130	351	2.78	0.07794 ± 0.00232	1.94345 ± 0.07815	1145.3 ± 59.1	93.6
CHL5-5	0.066	328	586	1.85	0.07694 ± 0.00086	1.91776 ± 0.05474	1119.6 ± 22.4	95.7
CHL5-6	0.547	268	185	0.71	0.07340 ± 0.00218	1.74131 ± 0.06934	1024.9 ± 60.2	99.9
CHL5-7	0.635	421	418	1.03	0.07197 ± 0.00121	1.65353 ± 0.05147	985.1 ± 34.3	100.9
CHL5-8	0.582	332	454	1.41	0.07228 ± 0.00165	1.70937 ± 0.05026	993.7 ± 46.4	102.7

f^{206} = the proportion of common ^{206}Pb in the total ^{206}Pb ; Th/U = $^{232}\text{Th}/^{238}\text{U}$; %C = % concordance
 All ratios and ages corrected for common Pb using measured ^{204}Pb and composition appropriate to the age of the zircon (Stacey and Kramers, 1975)
 Analyses conducted during a single session (07/04/2003). 7 CZ3 standard analyses yielded a 2σ error of the mean of 1.65%

Appendix F: zircon U-Pb SHRIMP analytical data

Table 13-55 SHRIMP analytical data for sample SER 6-6 (migmatite, Serenje map sheet). Spot names ending with r denote analyses on a rim, spot names ending with c denote analyses on core.

Spot Name	f^{206} (%)	U (ppm)	Th (ppm)	Th/U	$^{207}\text{Pb}/^{206}\text{Pb}$ ($\pm 1\sigma$)	$^{206}\text{Pb}/^{238}\text{U}$ ($\pm 1\sigma$)	$^{207}\text{Pb}/^{206}\text{Pb}$ Age ($\pm 1\sigma$ Ma)	C(%)
¹ SER66-5r	0.037	1878	14	0.01	0.07337 \pm 0.00025	0.16909 \pm 0.00364	1024.2 \pm 6.9	98.3
¹ SER66-19r	0.063	2356	23	0.01	0.07293 \pm 0.00028	0.16645 \pm 0.00357	1011.9 \pm 7.8	98.1
¹ SER66-17r	0.497	2859	33	0.01	0.07307 \pm 0.00066	0.16175 \pm 0.00353	1016.0 \pm 18.4	95.1
¹ SER66-16r	0.063	2322	23	0.01	0.07165 \pm 0.00099	0.16537 \pm 0.00355	976.1 \pm 28.1	101.1
¹ SER66-15r	0.046	1784	16	0.01	0.07334 \pm 0.00017	0.16696 \pm 0.00359	1023.4 \pm 4.8	97.3
¹ SER66-9r	0.123	1855	15	0.01	0.07296 \pm 0.00043	0.16697 \pm 0.00359	1012.7 \pm 11.8	98.3
¹ SER66-5c	0.843	208	66	0.33	0.12615 \pm 0.00139	0.35630 \pm 0.00778	2045.0 \pm 19.4	96.1
¹ SER66-19c	0.068	354	88	0.26	0.12714 \pm 0.00054	0.34267 \pm 0.00837	2058.8 \pm 7.5	92.3
¹ SER66-17c	0.238	218	42	0.20	0.12523 \pm 0.00130	0.35197 \pm 0.00796	2032.1 \pm 18.4	95.7
¹ SER66-16c	0.077	298	126	0.44	0.12645 \pm 0.00046	0.36676 \pm 0.00834	2049.2 \pm 6.4	98.3
¹ SER66-15c	0.063	932	60	0.07	0.12456 \pm 0.00143	0.35838 \pm 0.00959	2022.6 \pm 20.3	97.6
¹ SER66-9c	0.078	534	78	0.15	0.12650 \pm 0.00091	0.36595 \pm 0.00884	2049.9 \pm 12.7	98.1
² SER66-1r	0.227	3138	37	0.01	0.07282 \pm 0.00031	0.17188 \pm 0.00205	1009.0 \pm 8.7	101.3
² SER66-2r	0.000	1486	12	0.01	0.07318 \pm 0.00021	0.16505 \pm 0.00198	1019.0 \pm 5.9	96.6
² SER66-3r	0.026	1758	14	0.01	0.07299 \pm 0.00019	0.16973 \pm 0.00203	1013.6 \pm 5.3	99.7
² SER66-4r	0.305	1843	18	0.01	0.07297 \pm 0.00030	0.16042 \pm 0.00195	1013.0 \pm 8.3	94.7
f^{206} = the proportion of common ^{206}Pb in the total ^{206}Pb ; Th/U = $^{232}\text{Th}/^{238}\text{U}$; %C = % concordance								
All ratios and ages corrected for common Pb using measured ^{204}Pb and composition appropriate to the age of the zircon (Stacey and Kramers, 1975)								
Analyses conducted during two sessions (¹ 01/03/2002 and ² 28/02/2003).								
Session ¹ : 16 CZ3 standard analyses yielded a 2 σ error of the mean of 1.18%								
Session ² : 10 CZ3 standard analyses yielded a 2 σ error of the mean of 0.98%								

Table 13-56 SHRIMP analytical data for sample SER 6-7 (migmatite, Serenje map sheet). Spot names ending with r denote analyses on a rim, spot names ending with c denote analyses on core.

Spot Name	f^{206} (%)	U (ppm)	Th (ppm)	Th/U	$^{207}\text{Pb}/^{206}\text{Pb}$ ($\pm 1\sigma$)	$^{206}\text{Pb}/^{238}\text{U}$ ($\pm 1\sigma$)	$^{207}\text{Pb}/^{206}\text{Pb}$ Age ($\pm 1\sigma$ Ma)	C(%)
¹ SER67-1r	0.319	1169	9	0.01	0.07311 \pm 0.00092	0.16775 \pm 0.00387	1017.0 \pm 25.5	98.3
¹ SER67-10r	0.105	1395	8	0.01	0.07226 \pm 0.00078	0.15396 \pm 0.00332	993.3 \pm 21.8	92.9
¹ SER67-11r	0.181	1389	9	0.01	0.07222 \pm 0.00071	0.16282 \pm 0.00357	992.1 \pm 19.9	98.0
¹ SER67-15r	0.103	1434	38	0.03	0.07820 \pm 0.00057	0.15819 \pm 0.00340	1151.9 \pm 14.4	82.2
¹ SER67-24r	0.112	913	15	0.02	0.07939 \pm 0.00042	0.17463 \pm 0.00376	1181.8 \pm 10.4	87.8
¹ SER67-19	0.047	1629	9	0.01	0.07371 \pm 0.00097	0.16451 \pm 0.00356	1033.5 \pm 26.5	95.0
¹ SER67-4	0.129	1224	7	0.01	0.07240 \pm 0.00085	0.16246 \pm 0.00350	997.2 \pm 23.8	97.3
¹ SER67-13	0.057	1632	48	0.03	0.07927 \pm 0.00047	0.17485 \pm 0.00378	1178.9 \pm 11.7	88.1
¹ SER67c-1	0.383	187	86	0.47	0.14189 \pm 0.00106	0.38480 \pm 0.00839	2250.4 \pm 12.9	93.3
¹ SER67-10c	0.257	526	180	0.35	0.12437 \pm 0.00084	0.26813 \pm 0.00588	2019.8 \pm 11.9	75.8
¹ SER67-11c	0.211	261	49	0.19	0.12507 \pm 0.00100	0.32424 \pm 0.00866	2029.8 \pm 14.2	89.2
¹ SER67-15c	0.062	1859	234	0.13	0.11677 \pm 0.00254	0.28833 \pm 0.00728	1907.4 \pm 39.1	85.6
¹ SER67-24c	0.221	247	91	0.38	0.12570 \pm 0.00137	0.35995 \pm 0.01156	2038.6 \pm 19.3	97.2
¹ SER67-19c	0.074	361	163	0.47	0.12441 \pm 0.00093	0.34859 \pm 0.00770	2020.4 \pm 13.3	95.4
¹ SER67-4c	0.048	505	35	0.07	0.12401 \pm 0.00054	0.37734 \pm 0.00814	2014.8 \pm 7.8	102.4
¹ SER67-13c	0.179	351	286	0.84	0.12542 \pm 0.00082	0.36404 \pm 0.00808	2034.7 \pm 11.5	98.4
² SER67-1r	0.000	1137	7	0.01	0.07378 \pm 0.00072	0.16117 \pm 0.00320	1035.6 \pm 19.6	93.0
² SER67-2r	0.017	1342	7	0.01	0.07452 \pm 0.00073	0.16849 \pm 0.00382	1055.5 \pm 19.7	95.1
² SER67-3r	0.017	1610	7	0.00	0.05865 \pm 0.00055	0.08056 \pm 0.00160	554.2 \pm 20.4	90.1
² SER67-4r	0.005	1356	9	0.01	0.07335 \pm 0.00031	0.16479 \pm 0.00328	1023.7 \pm 8.6	96.1
f^{206} = the proportion of common ^{206}Pb in the total ^{206}Pb ; Th/U = $^{232}\text{Th}/^{238}\text{U}$; %C = % concordance								
All ratios and ages corrected for common Pb using measured ^{204}Pb and composition appropriate to the age of the zircon (Stacey and Kramers, 1975)								
Analyses conducted during two sessions (¹ 01/03/2002 and ² 28/02/2003).								
Session ¹ : 16 CZ3 standard analyses yielded a 2 σ error of the mean of 1.18%								
Session ² : 12 CZ3 standard analyses yielded a 2 σ error of the mean of 1.56%								

14 APPENDIX G Whole Rock geochemistry analytical data

Table 14-1: Major and trace element geochemistry of sample KMP 1 (sample batch #4 collected in 2001 and analysed at Curtin University of Technology; n.a.=not analysed).

Major elements weight%		Trace elements ppm							
SiO ₂	71.77	Ba	398	Ga	19.28	Ni	5.17	Ti	n.a.
Al ₂ O ₃	15.54	Be	1.23	Gd	2.10	Pb	10.09	Tl	0.47
Fe ₂ O ₃	2.40	Bi	0.02	Ge	0.97	Pr	4.86	Tm	0.10
MnO	n.a.	Cd	0.03	Hf	3.36	Rb	81.1	U	0.74
MgO	0.76	Ce	54.6	Ho	0.23	Sb	0.04	V	40.5
CaO	2.20	Co	84.4	La	27.8	Sc	4.91	W	53.5
Na ₂ O	4.07	Cr	13.10	Li	40.8	Sm	3.03	Y	9.65
K ₂ O	1.76	Cs	1.57	Lu	0.12	Sn	0.85	Yb	0.50
TiO ₂	0.37	Cu	3.49	Mn	292	Sr	233	Zn	45.5
P ₂ O ₅	0.13	Dy	1.95	Mo	0.21	Ta	2.93	Zr	182
H ₂ O	n.a.	Er	0.61	Nb	9.10	Tb	0.35		
LOI	0.01	Eu	0.50	Nd	16.92	Th	9.93		
TOTAL	99.00								

Table 14-2: Major element geochemistry (weight %) of the Mkushi Gneiss and the Luwalizi Granite Gneiss (sample batch #4 collected in 2001 and analysed at Curtin University of Technology; n.a.=not analysed).

	KN1	KN6	MK3	MK4	MK5	MK6	MK12	CC10	ISK1	ISK2
SiO ₂	69.22	73.94	70.81	75.31	75.53	75.83	70.12	74.00	67.78	73.56
Al ₂ O ₃	14.60	14.22	15.45	12.84	12.53	14.11	17.37	13.82	13.79	13.49
Fe ₂ O ₃	3.76	1.02	4.05	0.17	1.49	0.23	1.82	2.31	5.97	2.31
MnO	n.a.	n.a.	n.a.	n.a.	n.a.	n.a.	n.a.	n.a.	n.a.	n.a.
MgO	1.22	0.20	0.61	0.03	0.50	0.04	0.61	0.43	1.61	0.76
CaO	3.76	0.77	1.66	0.20	0.82	1.28	1.31	1.51	2.54	0.81
Na ₂ O	2.96	3.06	2.86	2.17	2.15	3.15	3.57	2.97	1.81	2.06
K ₂ O	2.48	4.96	4.87	7.59	4.63	3.90	3.52	4.04	3.36	4.84
TiO ₂	0.67	0.14	0.66	0.06	0.28	0.02	0.37	0.33	1.24	0.43
P ₂ O ₅	0.07	0.06	0.13	0.09	0.06	0.11	0.13	0.05	0.08	0.11
H ₂ O	n.a.	n.a.	n.a.	n.a.	n.a.	n.a.	n.a.	n.a.	n.a.	n.a.
LOI	0.01	0.01	0.01	0.02	0.01	0.00	0.01	0.01	0.01	0.01
TOTAL	98.74	98.38	101.10	98.45	97.99	98.66	98.80	99.46	98.18	98.37

Table 14-3: Major element geochemistry (weight %) of the Mansa Granitoids and Volcanics (sample batch #4 collected in 2001 and analysed at Curtin University of Technology; n.a.=not analysed; # denotes suspect analysis (see text for details)).

	MA1#	MA2	MA9	MA3	MA4	MA5
SiO ₂	46.77	72.03	77.98	68.59	66.05	75.83
Al ₂ O ₃	0.43	13.30	12.19	16.21	16.23	13.17
Fe ₂ O ₃	14.16	3.84	0.85	2.98	3.57	1.49
MnO	n.a.	n.a.	n.a.	n.a.	n.a.	n.a.
MgO	34.47	0.92	0.23	0.99	1.20	0.46
CaO	0.30	2.04	0.55	2.58	4.52	1.14
Na ₂ O	0.20	2.57	3.15	3.23	3.84	3.18
K ₂ O	0.04	3.99	3.84	3.52	3.16	2.97
TiO ₂	0.01	0.60	0.17	0.68	0.73	0.37
P ₂ O ₅	0.06	0.09	0.02	0.12	0.06	0.08
H ₂ O	n.a.	n.a.	n.a.	n.a.	n.a.	n.a.
LOI	0.05	0.02	0.01	0.01	0.02	0.01
TOTAL	96.43	99.37	98.97	98.90	99.36	98.69

Table 14-4: Major element geochemistry (weight %) of the Katibunga Volcanics (samples KV-2, KV4, KV-5, KV-7 and KV-8 of sample batch #2, collected in 1999 and analysed by Chemex Canada; samples KB2, KB3, KB4, KB5 and KB6 of sample batch #3, collected in 2000 and analysed at Curtin University of Technology; n.a.=not analysed).

	KV-1	KV-4	KV-5	KV-7	KV-8	KB2	KB3	KB4	KB5	KB6
SiO ₂	63.75	47.42	48.12	49.23	51.32	62.13	48.01	51.39	48.54	52.17
Al ₂ O ₃	18.66	13.40	15.38	16.91	13.06	22.44	18.25	17.10	18.75	14.50
Fe ₂ O ₃	6.93	16.24	12.10	9.57	13.31	5.89	8.68	7.83	6.84	10.87
MnO	0.03	0.23	0.17	0.16	0.20	0.02	0.13	0.11	0.09	0.19
MgO	1.14	6.45	7.72	8.19	6.34	0.84	5.36	7.50	5.53	6.17
CaO	0.24	10.05	10.30	10.31	8.55	0.15	12.44	11.21	10.86	8.92
Na ₂ O	0.75	2.20	1.89	2.42	3.51	0.44	2.25	2.89	3.74	3.68
K ₂ O	3.51	0.50	0.54	0.40	0.48	4.24	1.04	0.59	0.53	0.06
TiO ₂	0.76	2.00	1.05	0.75	1.73	0.82	0.83	0.67	0.64	1.23
P ₂ O ₅	0.04	0.17	0.11	0.05	0.19	0.16	0.29	0.30	0.39	0.25
H ₂ O	n.a.	n.a.	n.a.	n.a.	n.a.	0.08	0.11	0.11	0.07	0.06
LOI	n.a.	n.a.	n.a.	n.a.	n.a.	4.12	1.92	1.44	1.76	1.12
TOTAL	95.81	98.66	97.38	97.99	98.69	101.32	99.30	101.12	97.75	99.20

Table 14-5: Major element geochemistry (weight %) of the Katibunga and Luswa River Volcanics (sample batch #3 collected in 2000 and analysed at Curtin University of Technology).

	KB7	KB8	KB9	LW12	LW13
SiO ₂	53.78	49.86	49.56	76.11	70.65
Al ₂ O ₃	13.10	18.37	14.22	11.97	14.94
Fe ₂ O ₃	12.59	7.13	12.72	1.78	2.78
MnO	0.20	0.12	0.27	0.03	0.03
MgO	4.44	6.68	5.51	0.28	0.40
CaO	8.97	10.59	10.22	0.73	1.03
Na ₂ O	2.92	2.27	2.22	2.20	2.72
K ₂ O	0.32	0.40	0.84	4.30	5.42
TiO ₂	1.65	0.70	2.48	0.42	0.44
P ₂ O ₅	0.22	0.36	0.15	0.29	0.19
H ₂ O	0.10	0.14	0.11	0.14	0.18
LOI	0.73	2.09	0.98	0.46	0.54
TOTAL	99.02	98.71	99.27	98.70	99.32

Table 14-6: Major element geochemistry (weight %) of the Isoka Volcanics (sample batch #3 collected in 2000 and analysed at Curtin University of Technology).

	IS3	IS9	IS10	IS19	IS20	IS21	IS22	IS23	IS24
SiO ₂	76.11	72.93	69.34	54.07	71.75	73.40	76.20	67.93	77.45
Al ₂ O ₃	11.50	13.32	15.08	21.71	14.56	13.25	11.55	16.27	11.31
Fe ₂ O ₃	2.78	4.07	4.23	6.69	3.13	2.74	1.73	4.53	2.18
MnO	0.02	0.03	0.03	0.08	0.03	0.03	0.02	0.05	0.02
MgO	0.64	0.96	0.97	1.84	0.66	0.57	0.30	1.20	0.40
CaO	0.63	0.37	2.42	2.52	0.61	0.45	0.31	0.86	0.66
Na ₂ O	2.12	1.54	2.20	4.65	2.04	4.19	3.19	1.88	2.62
K ₂ O	2.36	3.35	3.15	4.39	3.77	2.54	3.74	4.67	2.16
TiO ₂	0.49	0.59	0.60	0.99	0.54	0.78	0.35	0.72	0.35
P ₂ O ₅	0.41	0.25	0.41	0.19	0.25	0.18	0.45	0.08	0.27
H ₂ O	0.21	0.31	0.23	0.19	0.19	0.20	0.11	0.25	0.18
LOI	1.14	2.21	1.73	1.32	1.36	0.79	0.70	1.84	0.88
TOTAL	98.42	99.94	100.40	98.65	98.89	99.13	98.66	100.28	98.49

Table 14-7: Major element geochemistry (weight %) of the Lukamfwa Hill Granitoids (samples SI/98/2A, SI/98/2B, SI/98/3 and SI/98/10 of sample batch #1 collected in 1998 and analysed at Chemex Canada; samples SER6-2C, SER6-2 and SER6-3 of sample batch #2, collected in 1999 and analysed by Chemex Canada; n.a.=not analysed).

	SI/98/2A	SI/98/2B	SI/98/3	SI/98/10	SER-6-2C	SER 6-2	SER 6-3
SiO ₂	72.38	70.00	75.42	71.80	72.55	72.95	72.20
Al ₂ O ₃	13.74	14.72	12.49	12.60	12.39	12.97	12.55
Fe ₂ O ₃	1.96	1.99	1.46	3.16	4.04	3.78	2.89
MnO	0.04	0.07	0.07	0.06	0.09	0.08	0.05
MgO	0.35	0.35	0.13	0.46	0.22	0.26	0.27
CaO	1.16	1.37	0.55	1.36	1.17	1.36	0.98
Na ₂ O	3.26	3.50	2.59	2.49	2.70	2.75	2.95
K ₂ O	4.82	5.04	5.54	5.54	6.02	5.55	5.43
TiO ₂	0.26	0.29	0.21	0.50	0.42	0.37	0.28
P ₂ O ₅	0.07	0.07	0.00	0.08	0.05	0.05	0.01
H ₂ O	n.a.	n.a.	n.a.	n.a.	n.a.	n.a.	n.a.
LOI	n.a.	n.a.	n.a.	n.a.	n.a.	n.a.	n.a.
TOTAL	98.04	97.40	98.46	98.05	99.65	100.12	97.61

Table 14-8: Major element geochemistry (weight %) of the Lukamfwa Hill Granite Gneiss, the Lubu Granite Gneiss (sample ML2) and the Musalango Gneiss (sample LW10)(samples ND2, SR5, SR7 and SR12 of sample batch #4 collected in 2001 and analysed at Curtin University of Technology; samples ML2 and LW10 of sample batch #3 collected in 2000 and analysed at Curtin University of Technology; n.a.=not analysed).

	ND2	SR6	SR7	SR12	ML2	LW10
SiO ₂	71.92	74.31	69.38	77.30	77.30	70.24
Al ₂ O ₃	12.83	12.67	13.03	12.54	11.91	14.05
Fe ₂ O ₃	2.76	2.61	4.10	2.04	1.43	2.79
MnO	n.a.	n.a.	n.a.	n.a.	n.a.	0.03
MgO	0.24	0.05	0.28	0.16	0.16	0.40
CaO	1.31	0.87	2.00	0.73	1.08	0.83
Na ₂ O	3.52	2.69	3.49	2.21	2.30	2.18
K ₂ O	4.69	4.82	6.38	5.26	4.18	6.53
TiO ₂	0.30	0.30	0.51	0.33	0.26	0.58
P ₂ O ₅	0.09	0.05	0.08	0.06	0.00	0.39
H ₂ O	n.a.	n.a.	n.a.	n.a.	n.a.	0.17
LOI	0.00	0.00	0.01	0.01	0.01	0.56
TOTAL	97.66	98.37	99.23	100.62	98.62	98.75

Table 14-9: Major element geochemistry (weight %) of Porphyritic Granitoids (samples SI/98/5, SI/98/6, SI/98/11, SI/98/12 and SI/98/12B of sample batch #1 collected in 1998 and analysed by Chemex Canada; samples MQG-1, SQG-2, SER5-3, SER6-4 and SER6-6 of sample batch #2 collected in 1999 and analysed by Chemex Canada; n.a.=not analysed).

	SI/98/5	SI/98/6	SI/98/11	SI/98/12	SI/98/12B	MQG-1	SQG-2	SER 5-3	SER 6-4
SiO ₂	72.97	68.28	72.25	69.90	70.61	74.55	68.76	72.50	66.20
Al ₂ O ₃	14.06	13.86	12.74	16.20	15.90	13.09	14.88	13.94	15.12
Fe ₂ O ₃	1.39	6.28	2.72	1.77	1.66	1.67	4.00	1.10	5.10
MnO	0.04	0.10	0.04	0.01	0.01	0.04	0.06	0.03	0.04
MgO	0.32	1.02	0.19	0.68	0.60	0.11	0.83	0.43	0.84
CaO	1.37	2.69	1.16	2.46	2.11	0.79	2.69	0.99	2.39
Na ₂ O	2.59	2.76	2.83	5.17	4.93	3.28	3.70	2.43	2.37
K ₂ O	5.54	3.01	5.47	2.32	2.46	6.13	3.99	5.30	5.31
TiO ₂	0.22	1.01	0.32	0.26	0.25	0.13	0.61	0.14	0.91
P ₂ O ₅	0.01	0.21	0.00	0.04	0.04	<0.01	0.13	0.18	0.49
H ₂ O	n.a.	n.a.	n.a.	n.a.	n.a.	n.a.	n.a.	n.a.	n.a.
LOI	n.a.	n.a.	n.a.	n.a.	n.a.	n.a.	n.a.	n.a.	n.a.
TOTAL	98.51	99.22	97.72	98.81	98.57	99.79	99.65	97.04	98.77

Table 14-10: Major element geochemistry (weight %) of Porphyritic Granitoids (sample batch #4 collected in 2001 and analysed at Curtin University of Technology; n.a.=not analysed)

	KK1	MH1	MH4	MH5	MH9C	CC4	CC5	CC8
SiO ₂	68.82	73.72	74.58	74.20	70.67	75.72	73.43	74.10
Al ₂ O ₃	14.94	13.94	12.41	14.46	16.17	12.82	13.56	13.12
Fe ₂ O ₃	3.74	1.13	3.63	1.51	2.07	1.66	4.12	2.04
MnO	n.a.	n.a.	n.a.	n.a.	n.a.	n.a.	n.a.	n.a.
MgO	0.33	0.61	1.54	0.44	0.49	0.29	0.70	0.48
CaO	2.65	1.07	2.71	0.95	1.64	0.98	2.41	1.62
Na ₂ O	2.08	3.08	1.86	2.59	2.72	2.75	2.95	2.84
K ₂ O	4.85	4.22	1.89	3.86	4.60	4.21	3.72	3.84
TiO ₂	0.51	0.21	0.53	0.27	0.46	0.21	0.72	0.45
P ₂ O ₅	0.14	0.06	0.04	0.08	0.12	0.08	0.15	0.06
H ₂ O	n.a.	n.a.	n.a.	n.a.	n.a.	n.a.	n.a.	n.a.
LOI	0.01	0.01	0.00	0.01	0.01	0.01	0.00	0.01
TOTAL	98.07	98.03	99.19	98.36	98.94	98.71	101.74	98.54

Table 14-11: Major element geochemistry (weight %) of Porphyritic Granitoids (sample batch #4 collected in 2001 and analysed at Curtin University of Technology; n.a.=not analysed).

	MK2	MK7	FW1	CHT1	CHT2	CHT4	CHT6	ND1	ND4	ND5
SiO ₂	76.53	73.21	70.50	71.11	67.62	77.89	73.00	71.56	68.07	64.65
Al ₂ O ₃	13.39	14.64	15.41	12.40	15.52	13.12	12.69	14.49	11.60	14.44
Fe ₂ O ₃	0.69	1.43	3.87	5.91	5.87	0.75	5.20	1.54	3.43	4.77
MnO	n.a.	n.a.	n.a.	n.a.	n.a.	n.a.	n.a.	n.a.	n.a.	n.a.
MgO	0.27	0.41	1.18	1.07	2.18	0.14	0.69	0.15	3.74	2.48
CaO	0.79	0.49	2.44	3.42	1.23	0.51	1.77	0.76	5.56	2.70
Na ₂ O	2.60	3.63	2.77	2.48	1.87	3.51	2.61	2.73	4.31	3.08
K ₂ O	4.52	5.18	4.00	3.47	3.38	4.31	3.64	7.59	1.61	5.87
TiO ₂	0.11	0.27	0.67	1.37	0.65	0.07	0.84	0.22	0.26	0.82
P ₂ O ₅	0.11	0.08	0.12	0.14	0.13	0.13	0.18	0.07	0.24	0.10
H ₂ O	n.a.	n.a.	n.a.	n.a.	n.a.	n.a.	n.a.	n.a.	n.a.	n.a.
LOI	0.02	0.01	0.01	0.01	0.02	0.01	0.02	0.01	0.01	0.10
TOTAL	99.01	99.33	100.97	101.38	98.46	100.43	100.63	99.12	98.83	98.92

Table 14-12: Major element geochemistry (weight %) of Porphyritic Granitoids (sample batch #4 collected in 2001 and analysed at Curtin University of Technology); sample KN2A was collected from an aplite associated with the porphyritic granite (n.a.=not analysed).

	KN2A	KN2B	KN4	KN5	KN7	KN8	SR5	SR9	SR11	MUN
SiO ₂	72.11	77.12	72.50	68.84	75.28	69.04	73.56	69.95	76.58	75.11
Al ₂ O ₃	13.40	12.26	14.69	13.82	13.74	15.72	14.75	14.90	12.54	13.22
Fe ₂ O ₃	2.46	0.37	1.61	5.24	1.33	2.57	3.56	3.33	1.28	2.13
MnO	n.a.	n.a.	n.a.	n.a.	n.a.	n.a.	n.a.	n.a.	n.a.	n.a.
MgO	0.35	0.04	0.40	1.31	0.28	0.84	0.62	0.69	0.43	0.11
CaO	1.80	0.92	1.24	2.96	0.89	1.57	1.59	2.37	1.58	0.88
Na ₂ O	2.63	2.61	2.81	2.64	2.71	2.37	1.86	3.28	3.82	2.58
K ₂ O	4.85	5.24	4.90	3.31	4.36	5.03	5.08	4.25	2.19	5.11
TiO ₂	0.48	0.02	0.69	1.05	0.21	0.50	0.77	0.64	0.26	0.23
P ₂ O ₅	0.11	0.09	0.23	0.10	0.11	0.14	0.09	0.10	0.10	0.07
H ₂ O	n.a.	n.a.	n.a.	n.a.	n.a.	n.a.	n.a.	n.a.	n.a.	n.a.
LOI	0.00	0.00	0.01	0.00	0.01	0.01	0.01	0.01	0.01	0.00
TOTAL	98.19	98.68	99.07	99.28	98.91	97.79	101.89	99.51	98.78	99.44

Table 14-13: Major element geochemistry (weight %) of Porphyritic Granitoids (samples SH8, SH9, LW1, LW2, LWC and LW11 of sample batch #3 collected in 2000 and analysed at Curtin University of Technology; samples MTG-4, MTG-5, MGG-2 and MTGG-3 of sample batch #3 collected in 1999 and analysed by Chemex Canada; n.a.=not analysed).

	SH8	SH9	LW1	LW2	LWC	LW11	MTG-1	MTG-5	MGG-2
SiO ₂	70.40	74.62	72.41	76.13	73.48	51.51	73.32	74.76	74.04
Al ₂ O ₃	14.05	12.14	14.51	12.19	16.19	24.52	14.04	13.97	13.22
Fe ₂ O ₃	1.88	2.51	1.80	0.39	0.56	3.13	1.70	1.38	2.04
MnO	0.01	0.04	0.02	0.00	0.00	0.09	0.01	0.04	0.04
MgO	0.30	0.38	0.34	0.01	0.04	0.15	0.36	0.29	0.15
CaO	1.15	1.31	0.62	0.01	0.63	0.97	1.33	1.21	0.79
Na ₂ O	2.95	2.75	2.71	4.78	7.30	8.18	3.04	3.36	3.08
K ₂ O	5.19	3.12	5.13	3.98	0.45	8.44	5.75	4.88	6.29
TiO ₂	0.27	0.68	0.34	0.02	0.03	0.64	0.26	0.16	0.17
P ₂ O ₅	0.73	0.28	0.08	0.22	0.32	0.40	0.08	0.09	0.00
H ₂ O	0.17	0.18	0.10	0.10	0.14	0.13	n.a.	n.a.	n.a.
LOI	0.63	0.54	0.53	0.27	0.46	0.95	n.a.	n.a.	n.a.
TOTAL	97.74	98.54	98.61	98.10	99.60	99.13	99.89	100.14	99.82

Table 14-14: Major element geochemistry (weight %) of Porphyritic Granitoids (sample batch #4 collected in 2001 and analysed at Curtin University of Technology; n.a.=not analysed).

	KTB1	CHL2	CHL4	CHL5
SiO ₂	76.85	72.41	76.22	69.83
Al ₂ O ₃	13.56	12.47	13.59	14.30
Fe ₂ O ₃	0.87	3.49	0.79	5.13
MnO	n.a.	n.a.	n.a.	n.a.
MgO	0.18	0.22	0.21	1.04
CaO	0.58	1.80	0.66	3.27
Na ₂ O	2.43	2.92	3.26	2.89
K ₂ O	4.46	4.71	4.36	3.36
TiO ₂	0.12	0.41	0.11	1.32
P ₂ O ₅	0.06	0.13	0.15	0.21
H ₂ O	n.a.	n.a.	n.a.	n.a.
LOI	0.01	0.01	0.01	0.01
TOTAL	99.11	98.58	99.35	101.15

Table 14-15: Trace element geochemistry (ppm) of the Mkushi Gneiss and the Luwalizi Granite Gneiss (sample batch #4 collected in 2001 and analysed at Curtin University of Technology; n.a.=not analysed).

	KN1	KN6	MK3	MK4	MK5	MK6	MK12	CC10	ISK1	ISK2
Ba	789	473	1112	741	676	221	1024	0.02	1163	675
Be	2.46	4.47	2.77	2.15	1.84	2.19	1.90	0.06	2.79	2.99
Bi	0.22	0.16	0.07	0.21	0.08	0.01	0.10	0.07	0.06	0.06
Cd	0.05	0.02	0.03	0.04	0.02	0.02	0.02	0.15	0.05	0.07
Ce	92	114	72.0	8.75	112	6.46	71.0	0.35	158	197
Co	21.87	9.30	63.3	94	82.1	60.2	46.5	0.34	60.4	52.6
Cr	29.80	7.22	31.11	6.76	13.29	2.65	12.00	1.90	49.0	23.09
Cs	6.06	3.09	6.02	0.92	5.29	0.45	2.08	1.61	1.69	2.48
Cu	4.74	3.88	5.29	357	5.75	1.76	6.99	0.84	26.53	13.50
Dy	5.60	7.76	3.59	0.95	8.10	3.13	1.27	1.30	8.49	5.51
Er	2.93	2.72	1.63	0.57	3.59	1.92	0.47	1.62	3.64	1.92
Eu	1.22	1.85	1.36	0.31	1.15	1.21	0.79	0.93	2.88	1.40
Ga	18.33	16.36	17.60	11.11	14.06	15.96	20.19	4.05	28.2	19.31
Gd	5.41	12.78	3.92	0.59	8.13	3.39	2.21	2.20	11.40	11.08
Ge	18.33	16.36	1.02	2.16	14.06	0.45	0.71	2.44	3.60	19.31
Hf	3.06	3.36	1.62	1.30	3.08	3.48	5.10	2.21	4.93	6.34
Ho	0.97	1.03	0.59	0.20	1.39	0.61	0.18	2.54	1.36	0.76
La	34.0	101	33.7	4.02	51.7	23.5	35.5	5.39	71.1	81.3
Li	41.4	47.2	70.0	3.47	33.8	16.64	21.8	5.02	36.8	39.4
Lu	0.63	0.44	0.30	0.12	0.52	0.27	0.07	6.92	0.50	0.29
Mn	1223	172	972	29.8	462	45.9	354	7.98	1402	430
Mo	0.26	0.40	0.49	0.38	0.41	0.16	0.12	9.66	0.73	0.14
Nb	6.09	18.12	5.74	19.19	17.72	5.27	10.32	16.21	17.74	18.44
Nd	27.37	79.7	24.99	3.02	43.4	13.13	20.7	5.34	63.5	78.5
Ni	13.21	3.76	12.77	1.96	5.20	1.12	4.14	42.8	22.14	12.19
Pb	18.19	81.2	9.71	34.9	31.9	19.04	19.76	2.87	29.4	51.9
Pr	7.72	21.37	6.66	0.76	12.08	3.45	6.27	30.07	16.59	21.05
Rb	147	262	143	192	291	128	159	21.75	261	293
Sb	0.04	0.06	0.07	0.11	0.09	0.08	0.06	21.75	0.10	1.18
Sc	11.30	2.68	14.67	1.28	5.70	0.50	2.98	22.65	25.74	8.27
Sm	6.45	16.40	5.30	0.68	10.27	2.63	3.81	31.28	14.22	17.93
Sn	1.24	3.26	1.89	0.78	1.96	0.28	1.09	12.28	0.91	1.09
Sr	82.4	59.8	165	55.0	103	88.9	196	39.9	165	112
Ta	0.37	0.86	1.28	5.43	3.93	2.88	2.28	56.7	1.50	2.72
Tb	1.07	1.89	0.74	0.19	1.83	0.62	0.37	91.5	1.80	1.59
Th	10.56	12.75	5.61	5.66	33.2	1.06	15.55	6.17	18.55	68.8
Ti	n.a.	n.a.	n.a.	n.a.	n.a.	n.a.	n.a.	157	n.a.	n.a.
Tl	0.91	1.25	0.72	0.65	1.27	0.42	0.88	32.6	1.15	1.26
Tm	0.61	0.37	0.26	0.07	0.54	0.25	0.08	46.7	0.52	0.30
U	2.11	3.47	1.81	1.70	2.64	1.22	1.40	174	0.95	2.97
V	83.8	11.75	108	9.79	30.3	11.64	31.4	15.09	192	43.0
W	5.23	7.20	27.07	61.7	51.0	45.0	30.2	231	22.87	35.6
Y	32.2	37.1	20.05	6.79	39.9	22.2	6.84	180	43.0	22.39
Yb	3.56	2.14	1.73	0.69	2.97	1.68	0.48	1256	3.35	1.57
Zn	80.7	24.99	76.5	23.9	35.5	7.35	70.0	352	164	69.1
Zr	111	107	78.2	67.6	99	178	227	n.a.	201	228

Table 14-16: Trace element geochemistry (ppm) of the Mansa Granitoids and Volcanics (sample batch #4 collected in 2001 and analysed at Curtin University of Technology; n.a.=not analysed).

	MA1	MA2	MA9	MA3	MA4	MA5
Ba	991	1218	788	2095	2145	1286
Be	2.32	2.47	4.13	2.37	2.74	3.44
Bi	0.08	0.27	0.07	0.10	0.18	0.09
Cd	0.02	0.02	0.05	0.02	0.07	0.03
Ce	122	120	68.66	109	83.9	133
Co	51.0	63.5	130	31.4	32.1	42.4
Cr	19.18	15.31	8.07	11.73	11.22	7.90
Cs	3.74	4.49	1.58	2.22	2.09	1.93
Cu	28.6	23.44	2.93	25.24	64.0	9.61
Dy	5.63	5.92	3.11	4.40	2.90	4.24
Er	2.99	3.03	1.98	2.07	1.46	2.19
Eu	1.50	1.44	0.67	2.17	1.45	1.46
Ga	17.37	16.94	17.55	20.77	20.70	18.78
Gd	6.35	6.31	2.81	5.23	3.39	5.27
Ge	1.61	1.49	1.41	2.10	1.32	1.54
Hf	4.68	5.24	4.07	6.35	7.17	6.39
Ho	1.06	1.05	0.54	0.75	0.43	0.73
La	58.4	54.0	34.94	53.1	32.8	66.1
Li	44.7	41.7	10.48	53.9	33.4	25.61
Lu	0.52	0.59	0.48	0.34	0.31	0.37
Mn	744	785	292	885	885	1065
Mo	1.57	1.04	1.56	1.08	0.52	0.55
Nb	22.30	24.81	23.26	19.39	12.73	18.90
Nd	40.9	42.2	18.55	39.0	24.04	42.0
Ni	12.89	10.25	2.67	7.37	6.49	3.94
Pb	18.34	16.62	18.75	15.60	61.6	13.36
Pr	11.61	12.00	6.00	11.01	6.92	12.60
Rb	225	225	208	165	128	155
Sb	0.17	0.18	0.11	0.18	0.27	0.25
Sc	10.73	9.56	5.02	8.65	6.59	9.67
Sm	8.52	8.82	3.89	7.64	5.06	7.50
Sn	1.72	1.68	1.32	1.36	1.15	1.37
Sr	251	270	69	660	593	322
Ta	1.97	2.76	5.55	1.59	0.59	1.21
Tb	1.23	1.23	0.52	0.94	0.54	0.96
Th	30.1	33.0	16.14	13.21	9.89	19.40
Ti	n.a.	n.a.	n.a.	n.a.	n.a.	n.a.
Tl	0.74	0.92	0.78	0.51	0.81	0.51
Tm	0.48	0.49	0.38	0.37	0.26	0.41
U	3.93	3.49	1.84	1.98	2.12	2.56
V	84	69.7	19.93	73.1	76.3	34.5
W	26.58	35.0	80	17.73	11.44	22.14
Y	40.9	39.3	24.16	28.4	16.30	29.4
Yb	2.99	3.09	2.65	1.88	1.58	2.24
Zn	60.5	50.7	35.02	51.5	112	55.1
Zr	200	232	154	321	355	257

Table 14-17: Trace element geochemistry (ppm) of the Katibunga Volcanics (KV samples of sample batch #2, collected in 1999 and analysed by Chemex Canada; samples KB of sample batch #3, collected in 2000 and analysed at Curtin University of Technology; n.a.=not analysed).

	KV-1	KV-4	KV-5	KV-7	KV-8	KB2	KB3	KB4	KB5	KB6
Ba	640	199	212	141	251	947	409	299	240	46.4
Be	n.a.	n.a.	n.a.	n.a.	n.a.	4.29	1.00	0.75	0.71	0.90
Bi	n.a.	n.a.	n.a.	n.a.	n.a.	n.a.	n.a.	n.a.	n.a.	n.a.
Cd	n.a.	n.a.	n.a.	n.a.	n.a.	0.13	0.10	0.07	0.08	n.a.
Ce	114	30.0	22.5	21.0	42.5	136	34.8	26.2	24.60	29.45
Co	20.5	62.5	61	46	51	25.75	75.4	73.0	65.1	68.7
Cr	n.a.	n.a.	n.a.	n.a.	n.a.	152	145	666	594	105
Cs	3.6	3.10	4.00	0.50	8.80	n.a.	n.a.	n.a.	n.a.	n.a.
Cu	20	50	60	65	95	9.03	118	155	86.6	133
Dy	5.4	6.80	3.70	3.30	6.40	5.41	5.20	3.71	3.42	5.28
Er	3.4	4.50	2.40	2.00	3.90	2.33	2.74	1.86	1.80	2.69
Eu	1.4	1.80	1.10	1.00	1.60	1.82	1.51	1.14	1.12	1.47
Ga	27	22	18.00	18.00	16.00	26.3	21.94	16.35	17.04	15.99
Gd	7.1	6.30	3.70	2.90	6.60	7.02	4.84	3.51	3.26	5.07
Ge	n.a.	n.a.	n.a.	n.a.	n.a.	n.a.	n.a.	n.a.	n.a.	n.a.
Hf	7	3.00	3.00	1.00	4.00	7.02	2.86	0.83	1.94	1.03
Ho	1.1	1.40	0.80	0.70	1.30	0.83	0.98	0.66	0.67	0.98
La	49.5	13.50	10.50	10.00	20.00	65.1	19.12	13.38	12.78	14.53
Li	n.a.	n.a.	n.a.	n.a.	n.a.	57.9	16.97	17.92	22.29	13.04
Lu	0.5	0.70	0.40	0.30	0.50	0.46	0.49	0.30	0.34	0.40
Mn	n.a.	n.a.	n.a.	n.a.	n.a.	n.a.	n.a.	n.a.	n.a.	n.a.
Mo	n.a.	n.a.	n.a.	n.a.	n.a.	n.a.	n.a.	n.a.	n.a.	n.a.
Nb	17	6.00	3.00	3.00	7.00	79.8	7.82	4.90	6.26	6.28
Nd	44	17.5	12.00	11.50	22.5	51.4	17.26	13.58	13.13	17.42
Ni	25	65	130	80	40	36.8	86.8	118	120	53.6
Pb	15.00	n.a.	n.a.	n.a.	n.a.	18.85	9.69	4.81	5.06	4.39
Pr	12.50	3.90	2.80	2.60	5.40	13.66	3.80	2.99	2.80	3.54
Rb	197.5	12.80	18	10.80	16.0	225	41.3	21.65	22.37	1.27
Sb	n.a.	n.a.	n.a.	n.a.	n.a.	n.a.	n.a.	0.23	0.39	n.a.
Sc	n.a.	n.a.	n.a.	n.a.	n.a.	n.a.	n.a.	n.a.	n.a.	n.a.
Sm	7.90	4.90	2.50	2.50	5.40	9.50	4.44	3.37	3.23	4.49
Sn	4.00	n.a.	1.00	n.a.	1.00	4.86	1.14	0.85	0.82	1.08
Sr	68.6	139	149	251	120	78.4	241	183	173	149
Ta	3.5	3.00	1.50	1.50	2.00	6.35	1.27	1.18	1.43	1.34
Tb	1.97	n.a.	2.75	2.71	0.68	0.97	0.83	0.57	0.54	0.81
Th	31	1.00	1.00	3.00	4.00	37.3	3.81	3.24	3.49	2.74
Ti	n.a.	n.a.	n.a.	n.a.	n.a.	6702	8533	6538	5786	9978
Tl	0.50	n.a.	1.86	1.95	0.34	0.39	0.44	0.30	0.31	0.45
Tm	1.64	n.a.	0.93	0.96	n.a.	1.05	0.18	0.11	n.a.	n.a.
U	4.5	n.a.	n.a.	n.a.	n.a.	4.42	0.53	0.40	0.35	0.41
V	55	335	230	190	285	73.3	336	240	221	328
W	37	46	31	21.0	33	12.66	13.05	17.54	18.30	15.65
Y	24.5	35.5	21.5	16.5	34	26.2	34.0	22.9	21.92	32.5
Yb	3.1	4.00	2.50	1.50	3.80	3.19	3.40	2.17	2.21	3.08
Zn	60	115	75	60	95	71.2	100	81.7	72.2	103
Zr	220	112	81	68	142	311	86.6	15.30	64.5	19.89

Table 14-18: Trace element geochemistry (ppm) of the Katibunga, Luswa River and Ilondola Volcanics (sample batch #3 collected in 2000 and analysed at Curtin University of Technology; n.a.=not analysed).

	KB7	KB8	KB9	LW12	LW13	IL2	IL3	IL4
Ba	82.3	175	459	1418	1749	1448	1504	1322
Be	1.16	0.62	1.33	1.63	2.60	2.05	2.04	3.09
Bi	n.a.	n.a.	n.a.	n.a.	0.27	0.36	0.30	0.28
Cd	0.11	0.00	0.17	0.09	0.23	0.10	0.09	0.09
Ce	33.2	21.46	60.6	101	210	121.6	122.2	115.3
Co	80.7	59.6	80.6	52.2	63.3	7.79	7.19	6.38
Cr	36.1	558	206	18.18	36.60	262	286	287
Cs	n.a.	n.a.	n.a.	n.a.	n.a.	n.a.	n.a.	n.a.
Cu	113	83.8	124	10.19	28.95	13.00	20.25	20.96
Dy	6.25	3.16	9.31	4.79	11.12	3.85	2.77	3.10
Er	3.21	1.62	4.89	2.07	5.30	1.49	1.14	1.23
Eu	1.77	0.92	2.61	1.85	3.11	1.75	1.76	1.55
Ga	18.05	15.46	21.94	12.62	18.61	26.86	26.38	25.32
Gd	5.96	2.98	9.04	6.77	13.30	5.87	5.30	5.26
Ge	n.a.	n.a.	n.a.	n.a.	n.a.	n.a.	n.a.	n.a.
Hf	1.61	0.54	4.51	4.69	11.75	7.97	7.26	5.77
Ho	1.18	0.58	1.75	0.75	1.88	0.54	0.41	0.44
La	16.51	10.43	31.4	62.1	111	61.1	60.4	70.4
Li	11.01	23.0	21.87	19.93	31.18	45.30	27.36	26.23
Lu	0.49	0.25	0.87	0.36	1.00	0.33	0.28	0.29
Mn	n.a.	n.a.	n.a.	n.a.	n.a.	n.a.	n.a.	n.a.
Mo	0.21	n.a.	0.50	n.a.	n.a.	n.a.	n.a.	n.a.
Nb	9.38	3.32	14.68	20.01	36.8	32.08	13.59	27.99
Nd	20.19	11.79	33.3	44.7	83.5	41.8	40.4	42.4
Ni	36.2	105	93.2	6.95	12.66	19.28	23.59	39.07
Pb	5.46	4.01	9.32	26.02	39.8	40.08	36.98	42.37
Pr	4.13	2.52	7.01	11.10	20.89	10.90	11.05	11.44
Rb	5.28	13.07	29.65	125	147	199	193	184
Sb	0.13	n.a.	n.a.	n.a.	0.35	0.16	n.a.	0.78
Sc	n.a.	n.a.	n.a.	n.a.	n.a.	n.a.	n.a.	n.a.
Sm	5.40	2.93	8.54	8.54	15.60	7.76	7.34	7.04
Sn	2.46	0.59	0.92	1.93	3.83	4.16	3.65	3.81
Sr	102	275	167	172	256	112.6	92.0	96.5
Ta	2.06	0.87	1.68	2.67	4.89	3.10	1.57	3.09
Tb	0.98	1.00	0.50	0.98	0.35	0.75	0.61	0.58
Th	2.79	2.66	3.94	19.44	66.9	25.62	24.47	21.74
Ti	13424	5550	20714	3450	6603	8956	7695	7149
Tl	0.50	0.51	0.27	0.40	0.12	0.25	0.21	0.19
Tm	n.a.	n.a.	n.a.	0.52	1.57	0.92	0.89	0.95
U	0.42	0.34	0.32	2.09	7.27	2.33	1.73	2.68
V	374	198	432	37.3	60.6	106.7	102.7	89.7
W	23.54	13.19	12.95	37.1	54.0	5.05	5.20	4.49
Y	38.6	20.00	61.2	26.96	65.9	18.07	13.44	14.49
Yb	3.59	1.95	6.06	2.54	6.91	2.17	1.80	1.63
Zn	119	73.5	186	31.63	55.0	25.53	16.63	13.47
Zr	42.8	0.40	147	155	393	311	285	229

Table 14-19: Trace element geochemistry (ppm) of the Isoka Volcanics (sample batch #3 collected in 2000 and analysed at Curtin University of Technology; n.a.=not analysed).

	IS3	IS9	IS10	IS19	IS20	IS21	IS22	IS23	IS24
Ba	751	796	1088	1074	1077	1089	1321	1301	807
Be	2.05	2.14	2.85	6.58	2.93	1.80	1.99	3.94	3.30
Bi	0.27	0.28	0.20	0.72	0.19	n.a.	0.22	0.34	0.36
Cd	0.07	0.09	0.13	0.07	0.07	0.15	0.06	0.10	n.a.
Ce	54.4	72.2	91.3	95.3	54.6	168	104	144	81.6
Co	43.1	28.71	31.9	28.4	29.7	52.3	35.6	50.8	49.8
Cr	87.4	89.5	124	111.3	41.4	39.7	27.17	138	31.4
Cs	n.a.	n.a.	n.a.	n.a.	n.a.	n.a.	n.a.	n.a.	n.a.
Cu	18.91	32.77	21.55	14.22	34.7	10.76	15.14	69.3	25.73
Dy	3.78	4.04	5.07	6.61	4.92	9.26	5.69	8.41	6.59
Er	2.06	1.84	2.42	3.43	2.81	4.44	2.65	4.22	3.17
Eu	1.19	1.29	1.77	1.98	1.49	2.63	1.82	2.61	2.11
Ga	13.97	15.32	20.05	27.6	16.48	14.73	13.44	24.5	14.22
Gd	3.87	4.72	6.25	6.37	4.63	11.19	7.04	9.58	8.08
Ge	n.a.	n.a.	n.a.	n.a.	n.a.	n.a.	n.a.	n.a.	n.a.
Hf	4.61	4.60	6.25	5.39	4.49	8.65	4.18	5.93	5.04
Ho	0.72	0.68	0.87	1.12	0.99	1.54	0.96	1.47	1.10
La	28.38	37.0	45.6	48.4	28.85	88	57.8	76.1	62.3
Li	33.16	27.06	43.2	41.9	22.15	9.76	15.82	41.3	18.16
Lu	0.42	0.35	0.48	0.76	0.55	0.82	0.49	0.79	0.57
Mn	n.a.	n.a.	n.a.	n.a.	n.a.	n.a.	n.a.	n.a.	n.a.
Mo	n.a.	0.23	0.26	n.a.	n.a.	n.a.	n.a.	n.a.	n.a.
Nb	33.3	22.45	30.2	30.0	22.78	35.49	8.44	34.2	11.23
Nd	23.51	29.80	38.2	39.1	26.12	71	42.9	59.3	49.0
Ni	19.87	16.80	12.45	37.5	10.86	11.89	10.40	43.2	11.43
Pb	28.42	24.76	42.5	55.9	25.27	11.74	35.0	37.7	43.7
Pr	5.73	7.42	9.55	10.07	6.31	17.72	10.71	14.76	12.16
Rb	118	151	192	289	171	104	114	299	115
Sb	0.42	n.a.	n.a.	n.a.	n.a.	0.16	n.a.	0.16	0.26
Sc	n.a.	n.a.	n.a.	n.a.	n.a.	n.a.	n.a.	n.a.	n.a.
Sm	4.68	5.74	7.52	7.94	5.60	13.37	8.58	11.73	9.45
Sn	1.76	1.97	2.59	2.70	2.42	3.06	1.84	3.37	2.04
Sr	136	98.0	155	258	98	121	163	165	149
Ta	1.91	2.69	3.73	3.15	2.47	4.55	1.22	3.88	1.29
Tb	1.40	1.10	0.58	0.69	0.89	1.02	0.73	1.61	0.97
Th	20.01	15.78	20.00	25.9	18.24	37.3	16.02	24.4	15.44
Ti	4737	4636	6375	7760	4704	6598	3580	7710	3567
Tl	0.70	0.53	0.34	0.32	0.43	0.57	0.49	0.72	0.43
Tm	1.26	0.53	0.51	0.61	0.81	1.38	0.67	0.54	0.51
U	2.93	2.66	3.34	3.86	2.90	4.31	2.56	3.52	2.84
V	78.5	78.9	105	131.8	60.3	60.6	42.9	99	50.2
W	25.17	19.94	25.43	6.72	21.11	41.1	23.59	22.42	33.6
Y	25.71	24.14	30.19	39.0	35.6	54.4	34.4	50.8	40.4
Yb	2.86	2.33	3.28	4.68	3.74	5.86	3.34	5.48	4.14
Zn	61.4	70.7	75.5	178	59.0	37.24	47.2	164	67.7
Zr	155	170	255	180	156	309	131	204	144

Table 14-20: Trace element geochemistry (ppm) of the Lukamfwa Hill Granitoids (samples SI of sample batch #1 collected in 1998 and analysed at Chemex Canada; samples SER of sample batch #2, collected in 1999 and analysed by Chemex Canada; n.a.=not analysed).

	SI/98/2A	SI/98/2B	SI/98/3	SI/98/10	SER-6-2C	SER 6-2	SER 6-3
Ba	835	857	263	1075	1125	1095	379
Be	n.a.	n.a.	n.a.	n.a.	n.a.	n.a.	n.a.
Bi	n.a.	n.a.	n.a.	n.a.	n.a.	n.a.	n.a.
Cd	n.a.	n.a.	n.a.	n.a.	n.a.	n.a.	n.a.
Ce	231	241	130	247	314	199.5	306
Co	32.5	29.0	47.5	28.0	19.0	20.0	14.0
Cr	n.a.	n.a.	n.a.	n.a.	n.a.	n.a.	n.a.
Cs	1.20	1.00	3.20	0.70	0.80	1.30	2.20
Cu	15.00	10.00	15.00	35	n.a.	25	5.00
Dy	3.40	3.20	5.90	12.70	20.30	13.60	20.9
Er	1.70	1.90	3.30	8.20	10.20	7.50	13.20
Eu	1.20	1.30	0.70	1.90	3.50	2.40	2.60
Ga	22	22	17.00	18.00	23	24	24
Gd	8.40	8.50	6.80	13.90	29.7	15.00	24.4
Ge	n.a.	n.a.	n.a.	n.a.	n.a.	n.a.	n.a.
Hf	6.00	5.00	7.00	13.00	18.00	14.00	15.00
Ho	0.50	0.60	1.20	2.60	3.70	2.40	4.10
La	141	133	67.5	113	217	102	212
Li	n.a.	n.a.	n.a.	n.a.	n.a.	n.a.	n.a.
Lu	0.10	0.10	0.50	1.30	1.10	1.10	1.70
Mn	n.a.	n.a.	n.a.	n.a.	n.a.	n.a.	n.a.
Mo	n.a.	n.a.	n.a.	n.a.	n.a.	n.a.	n.a.
Nb	16.00	16.00	25	47	43	47	61
Nd	94.5	93	49	83	183	91	144.5
Ni	0.00	0.00	0.00	0.00	5.00	5.00	5.00
Pb	40	40	115	35	30	30	35
Pr	28.3	27	14.9	24.4	50	23.4	40.7
Rb	258	265	406	269	209	241	300
Sb	n.a.	n.a.	n.a.	n.a.	n.a.	n.a.	n.a.
Sc	n.a.	n.a.	n.a.	n.a.	n.a.	n.a.	n.a.
Sm	12.70	11.90	8.10	14.80	31.0	17.30	25.1
Sn	2.00	2.00	12.00	9.00	4.00	5.00	6.00
Sr	126.5	128	24	63.3	72	72.7	19.10
Ta	8.00	6.00	11.50	10.00	9.50	8.50	8.00
Tb	1.10	1.00	1.10	2.30	3.00	2.70	4.40
Th	93	96	49	35	35	23	33
Ti	n.a.	n.a.	n.a.	n.a.	n.a.	n.a.	n.a.
Tl	0.50	0.50	1.00	0.50	2.00	0.50	0.50
Tm	0.10	0.10	0.40	1.30	0.93	1.10	1.90
U	3.00	3.00	6.00	3.00	2.00	1.50	2.50
V	20	20	10.00	20	5.00	5.00	0.00
W	198	143	261	183	176	175	147
Y	19	18.5	34	76	82.5	74	137
Yb	1.20	1.20	3.40	8.20	8.00	7.00	11.10
Zn	55	55	70	40	100	90	90
Zr	192	202	184	494	637	501	453

Table 14-21: Trace element geochemistry (ppm) of the Lukamfwa Hill Granitoids (samples ND2, SR5, SR7 and SR12 of sample batch #4 collected in 2001 and analysed at Curtin University of Technology; samples ML2 and LW10 of sample batch #3 collected in 2000 and analysed at Curtin University of Technology; n.a.=not analysed).

	ND2	SR6	SR7	SR12	ML2	LW10
Ba	1169	370	1375	448	387	1456
Be	3.69	6.20	6.96	3.98	6.67	2.37
Bi	0.03	0.15	0.09	0.03	0.07	n.a.
Cd	0.02	0.08	0.57	0.03	0.04	0.11
Ce	175	409	306	288	244	185
Co	40.9	6.78	15.93	10.35	101	45.3
Cr	6.92	6.37	7.83	7.08	9.78	11.53
Cs	1.78	1.19	0.77	1.82	4.27	n.a.
Cu	3.23	13.85	12.82	2.60	6.09	12.81
Dy	16.87	54.0	19.00	15.61	6.42	10.67
Er	8.67	29.65	9.73	8.69	1.74	5.14
Eu	2.52	3.33	2.97	1.43	0.70	2.14
Ga	24.75	21.23	28.93	19.52	26.69	16.70
Gd	14.77	45.1	17.68	15.07	10.78	12.80
Ge	24.75	21.23	28.93	19.52	1.95	n.a.
Hf	2.32	12.61	10.99	10.40	10.36	8.16
Ho	2.86	10.47	3.21	2.87	0.80	1.82
La	83.2	207	94.1	118	118	116
Li	18.54	6.46	9.46	16.49	119	87.5
Lu	1.51	5.24	1.65	1.46	0.24	0.91
Mn	535	563	1234	455	515	n.a.
Mo	1.92	0.80	0.64	0.96	2.64	n.a.
Nb	25.69	81.3	70.7	66.8	73.3	30.2
Nd	71.4	152	90.0	80.3	78.9	80.6
Ni	2.13	3.22	2.78	2.58	4.53	5.49
Pb	18.76	45.7	55.5	40.0	42.93	44.1
Pr	19.21	41.8	22.63	22.47	23.21	20.71
Rb	172	310	267	329	494	292
Sb	0.11	0.04	0.05	0.03	0.10	n.a.
Sc	10.20	2.11	8.30	2.60	6.06	n.a.
Sm	16.38	39.8	20.87	16.79	15.14	15.26
Sn	2.81	7.56	9.60	6.26	6.16	5.78
Sr	86.4	16.32	69.0	24.11	37.79	77.6
Ta	1.73	2.06	2.21	2.24	5.02	3.59
Tb	2.98	10.50	3.66	2.90	1.75	0.95
Th	15.63	39.4	31.8	34.95	58.2	34.3
Ti	n.a.	n.a.	n.a.	n.a.	n.a.	4587
Tl	0.64	1.40	1.25	1.47	1.79	0.18
Tm	1.43	4.90	1.70	1.59	0.24	1.46
U	3.05	3.87	2.90	2.83	5.40	2.06
V	15.05	6.83	17.09	13.17	21.04	33.4
W	25.43	7.20	14.41	11.44	59.6	38.8
Y	96.0	311	101	88.6	24.42	64.2
Yb	8.63	32.12	9.70	9.49	1.24	6.17
Zn	97.6	219	617	84.4	77.2	55.1
Zr	77.3	386	408	339	401	288

Table 14-22: Trace element geochemistry (ppm) of Porphyritic Granitoids (samples SI of sample batch #1 collected in 1998 and analysed by Chemex Canada; samples MQG-1, SQG-2, SER5-3, SER6-4 and SER6-6 of sample batch #2 collected in 1999 and analysed by Chemex Canada; n.a.=not analysed).

	SI/98/5	SI/98/6	SI/98/11	SI/98/12	SI/98/12B	MQG-1	SQG-2	SER 5-3	SER 6-4
Ba	822	866	669	725	878	207	1015	327	1130
Be	n.a.	n.a.	n.a.	n.a.	n.a.	n.a.	n.a.	n.a.	n.a.
Bi	n.a.	n.a.	n.a.	n.a.	n.a.	n.a.	n.a.	n.a.	n.a.
Cd	n.a.	n.a.	n.a.	n.a.	n.a.	n.a.	n.a.	n.a.	n.a.
Ce	141	224	232	29.5	28.5	248	121	34.5	225
Co	26.5	30	19.00	24	24.5	19.00	20.00	25	22.5
Cr	n.a.	n.a.	n.a.	n.a.	n.a.	n.a.	n.a.	n.a.	n.a.
Cs	1.60	4.30	0.70	1.00	0.80	2.40	3.60	7.20	3.10
Cu	10.00	25	5.00	20.00	10.00	5.00	10.00	5.00	25
Dy	2.90	11.20	20.00	0.90	0.60	11.40	4.20	2.30	8.20
Er	1.50	5.30	11.50	0.50	0.30	5.80	2.00	1.60	3.90
Eu	1.20	2.40	3.60	0.50	0.40	1.00	1.70	0.50	2.10
Ga	16.00	24.00	24.00	22.00	21.00	23.0	21.0	12.00	23.00
Gd	6.50	17.00	25.1	1.50	1.20	16.50	7.40	2.90	13.00
Ge	n.a.	n.a.	n.a.	n.a.	n.a.	n.a.	n.a.	n.a.	n.a.
Hf	3.00	7.00	12.00	3.00	2.00	8.00	6.00	n.a.	9.00
Ho	0.40	2.00	4.20	n.a.	n.a.	2.10	0.80	0.50	1.40
La	71	162.5	159	17.00	17.50	122	63.0	17.00	130.5
Li	n.a.	n.a.	n.a.	n.a.	n.a.	n.a.	n.a.	n.a.	n.a.
Lu	0.10	0.40	1.50	n.a.	n.a.	0.80	0.10	0.20	0.30
Mn	n.a.	n.a.	n.a.	n.a.	n.a.	n.a.	n.a.	n.a.	n.a.
Mo	n.a.	n.a.	n.a.	n.a.	n.a.	n.a.	n.a.	n.a.	n.a.
Nb	9.00	24	45.00	3.00	4.00	15.00	11.00	7.00	28
Nd	52.5	127.5	131.5	10.00	9.00	104	45.5	14.50	106.5
Ni	n.a.	n.a.	n.a.	n.a.	n.a.	10.00	n.a.	n.a.	n.a.
Pb	70	30	20.00	10.00	15.00	45.0	25.00	35	40
Pr	14.90	34.8	34.40	2.80	2.60	28.0	13.10	3.90	28.9
Rb	252	235	211	88.8	89.6	210	159	329	295
Sb	n.a.	n.a.	n.a.	n.a.	n.a.	n.a.	n.a.	n.a.	n.a.
Sc	n.a.	n.a.	n.a.	n.a.	n.a.	n.a.	n.a.	n.a.	n.a.
Sm	8.80	18.90	23.90	1.50	1.40	18.00	7.80	2.70	17.10
Sn	3.00	9.00	4.00	2.00	1.00	3.00	2.00	5.00	3.00
Sr	173.5	180	45.9	265	329	25.6	202	64.2	179.5
Ta	7.50	8.00	9.50	7.50	8.50	9.00	6.00	9.00	6.50
Tb	0.80	2.50	4.10	0.10	0.00	1.97	2.49	0.40	1.80
Th	37	53	15.00	8.00	7.00	41.0	28.0	8.00	48
Ti	n.a.	n.a.	n.a.	n.a.	n.a.	n.a.	n.a.	n.a.	n.a.
Tl	1	0.5	n.a.	n.a.	n.a.	0.50	2.14	0.50	0.50
Tm	0.10	0.60	1.60	n.a.	n.a.	1.64	1.36	0.30	0.40
U	2.50	3.50	1.00	1.50	0.50	4.00	2.50	3.00	2.00
V	15.00	85	10.00	20.00	15.00	n.a.	40.0	10.00	40
W	190	151	187	200	211	184	123	235	144
Y	18.50	55	123.5	5.00	3.50	48.0	17.50	18.00	42.5
Yb	0.90	3.10	9.20	0.30	0.10	4.90	1.30	1.60	2.30
Zn	20.00	85	75	25	20	55.0	55.0	10.00	75
Zr	127	276	392	139	118	234	215	43	346

Table 14-23: Trace element geochemistry (ppm) of Porphyritic Granitoids (sample batch #4 collected in 2001 and analysed at Curtin University of Technology; n.a.=not analysed).

	KK1	MH1	MH4	MH5	MH9C	CC4	CC5	CC8
Ba	1401	1110	1432	725	1347	0.01	n.a.	0.02
Be	3.37	1.54	5.57	1.26	2.82	0.04	0.05	0.05
Bi	0.12	0.03	0.06	0.08	0.02	0.05	0.04	0.05
Cd	0.05	n.a.	0.02	0.01	0.02	0.09	0.70	0.36
Ce	192	30.1	129	56.8	127	0.17	0.27	0.60
Co	75.1	15.76	16.14	10.44	12.96	0.22	0.34	0.62
Cr	6.97	10.10	11.58	16.76	9.09	1.60	0.97	1.37
Cs	1.17	0.47	3.65	6.22	2.05	1.18	0.44	0.56
Cu	13.99	2.90	14.19	5.95	5.80	0.54	0.69	1.04
Dy	6.66	0.52	4.26	1.83	2.81	0.81	0.78	1.26
Er	3.22	0.19	1.90	0.60	1.10	0.92	1.56	1.41
Eu	2.06	0.74	1.03	0.44	1.33	0.72	0.54	0.68
Ga	23.72	15.09	23.78	15.36	18.06	3.65	2.76	3.54
Gd	9.27	0.84	5.09	2.91	4.32	2.64	1.39	2.68
Ge	2.25	0.25	23.78	15.36	1.54	1.26	1.99	3.17
Hf	2.12	2.29	6.76	4.35	3.38	0.85	1.75	3.88
Ho	1.21	0.06	0.71	0.23	0.34	1.76	1.51	1.35
La	83.6	16.91	53.1	25.00	68.3	3.63	4.24	6.28
Li	24.66	15.99	66.6	94.1	24.11	4.93	2.11	3.45
Lu	0.37	0.03	0.37	0.11	0.11	5.11	4.61	7.06
Mn	593	158	640	288	388	7.12	7.04	4.54
Mo	0.44	0.05	0.54	0.14	0.16	7.01	5.89	10.08
Nb	25.06	3.12	25.31	12.83	12.40	11.10	7.27	14.62
Nd	62.1	7.39	40.2	21.29	39.3	3.82	9.53	5.69
Ni	3.86	7.27	4.30	6.63	3.85	16.95	12.95	10.62
Pb	47.2	16.04	36.4	34.8	32.6	3.21	12.86	6.54
Pr	17.14	2.55	10.61	5.73	12.51	15.41	5.02	20.07
Rb	204	109	270	195	223	18.33	18.75	17.66
Sb	0.08	0.08	0.08	0.04	0.04	18.33	18.75	17.66
Sc	6.74	1.73	3.51	1.93	5.31	25.7	26.31	17.69
Sm	11.84	1.31	6.88	4.31	6.42	18.37	20.78	38.6
Sn	0.95	0.37	2.33	1.26	0.70	11.24	17.63	13.47
Sr	161	333	126	79.0	168	34.7	29.3	19.75
Ta	2.74	0.71	0.72	0.65	0.59	36.5	27.62	50.6
Tb	1.55	0.10	1.00	0.49	0.67	55.1	29.8	75.6
Th	34.62	4.77	12.51	18.93	21.03	2.96	4.40	3.53
Ti	n.a.	n.a.	n.a.	n.a.	n.a.	112	73.2	154
Tl	1.12	0.38	1.55	1.13	0.93	n.a.	n.a.	n.a.
Tm	0.49	0.03	0.37	0.08	0.16	22.92	62.8	38.3
U	0.95	0.53	1.44	2.23	1.62	42.3	95.5	50.3
V	29.17	32.1	36.11	21.68	36.9	115	194	171
W	45.5	11.10	8.51	6.54	5.20	9.89	12.02	12.01
Y	39.4	2.90	21.48	6.49	13.82	184	116	168
Yb	3.01	0.18	2.17	0.40	0.71	189	84.7	126
Zn	79.5	30.3	93.0	42.7	46.2	1032	1762	1099
Zr	127	106	269	154	153	351	608	427

Table 14-24: Trace element geochemistry (ppm) of Porphyritic Granitoids (sample batch #4 collected in 2001 and analysed at Curtin University of Technology; n.a.=not analysed).

	MK2	MK7	FW1	CHT1	CHT2	CHT4	CHT6	ND1	ND4	ND5
Ba	331	721	1195	0.03	0.02	277	960	776	290	4595
Be	3.89	4.18	4.06	0.09	0.04	8.22	3.54	2.03	3.47	8.48
Bi	0.03	0.01	0.04	0.04	0.12	0.16	0.11	0.01	0.05	0.15
Cd	0.01	0.03	n.a.	0.82	0.25	0.05	0.05	n.a.	n.a.	0.03
Ce	30.3	96.7	193	0.92	0.34	30.36	121	119	67.9	248
Co	12.75	73.5	36.3	0.89	0.38	56.2	55.7	22.87	49.5	38.96
Cr	8.60	7.86	27.23	0.96	0.52	8.46	16.01	7.10	9.00	56.2
Cs	3.74	1.13	5.47	0.51	0.60	10.34	3.95	1.31	0.26	5.94
Cu	12.82	7.40	18.11	1.85	0.62	3.10	22.98	3.05	2.30	69.8
Dy	2.32	4.29	4.75	2.37	0.88	4.47	10.93	2.89	7.00	7.28
Er	1.13	1.96	2.20	2.77	0.89	2.93	5.24	1.00	3.27	2.86
Eu	0.58	0.75	1.51	0.60	0.97	0.59	1.93	1.30	1.14	4.04
Ga	10.34	19.89	22.22	3.61	1.31	20.90	20.54	20.02	17.42	24.46
Gd	2.12	5.05	6.12	2.01	1.88	3.46	10.71	5.25	6.86	10.85
Ge	0.53	19.89	22.22	5.66	2.07	20.90	20.54	20.02	1.25	3.62
Hf	2.23	5.58	5.87	5.02	2.08	2.13	1.75	3.45	2.15	5.55
Ho	0.38	0.69	0.75	2.51	3.25	0.98	1.89	0.38	1.17	0.95
La	13.95	45.2	91	12.57	3.83	18.52	57.0	51.3	23.19	126
Li	30.7	29.64	77.4	1.79	5.29	24.35	40.6	26.30	21.97	61.2
Lu	0.19	0.30	0.32	13.46	5.34	0.64	0.86	0.09	0.76	0.47
Mn	384	189	507	6.00	7.24	563	794	127	975	1259
Mo	0.17	0.27	0.18	16.52	7.33	0.36	0.44	0.45	0.14	1.71
Nb	5.97	30.82	13.03	20.42	8.42	21.61	16.66	9.89	7.77	27.81
Nd	10.76	34.7	56.6	13.09	13.04	11.60	51.3	41.3	33.6	84.2
Ni	1.80	3.27	11.62	12.18	14.60	2.95	6.38	2.64	6.73	30.74
Pb	30.9	17.02	48.1	7.51	15.22	42.1	33.38	42.9	3.62	25.06
Pr	3.25	9.67	17.70	22.80	17.88	3.21	13.28	11.69	8.09	24.20
Rb	254	280	252	19.73	21.25	301	205	329	41.1	361
Sb	0.06	0.05	0.04	19.73	21.25	0.10	0.03	0.13	0.10	0.19
Sc	2.06	4.09	8.75	31.69	23.74	4.99	11.09	3.79	5.78	16.53
Sm	2.84	7.49	10.36	61.3	23.99	3.28	12.57	8.05	7.95	16.99
Sn	1.88	2.11	4.65	18.09	29.37	1.31	2.65	0.79	0.86	1.82
Sr	74.9	87.9	291	43.9	31.2	54.7	126	88.2	146	761
Ta	0.72	4.69	0.89	81.6	31.8	4.32	2.10	1.25	1.44	1.15
Tb	0.43	0.93	0.95	81.6	43.5	0.82	2.11	0.72	1.39	1.74
Th	7.06	27.12	50.2	3.78	56.8	11.86	16.95	38.9	13.89	40.99
Ti	n.a.	n.a.	n.a.	176	95.2	n.a.	n.a.	n.a.	n.a.	n.a.
Tl	1.05	0.86	1.13	n.a.	n.a.	1.37	0.93	1.20	0.23	0.94
Tm	0.17	0.31	0.38	44.2	96.0	0.55	0.89	0.11	0.63	0.53
U	1.63	5.59	3.50	118	107	7.08	1.66	2.02	1.15	7.20
V	14.98	18.59	67.5	153	126	12.69	46.5	11.71	88.8	185
W	10.06	56.1	11.76	8.50	138	39.81	34.59	16.89	17.52	12.44
Y	15.90	20.65	28.13	131	139	36.90	61.4	10.71	42.2	41.00
Yb	0.98	1.72	2.40	52.0	218	3.40	6.06	0.47	4.01	2.78
Zn	19.02	21.67	70.1	1650	819	24.54	85.3	25.82	109	126
Zr	122	197	236	996	1606	53.9	52.7	112	75.7	275

Table 14-25: Trace element geochemistry (ppm) of Porphyritic Granitoids (sample batch #4 collected in 2001 and analysed at Curtin University of Technology; n.a.=not analysed).

	KN2A	KN2B	KN4	KN5	KN7	KN8	SR5	SR9	SR11	MUN
Ba	1643	438	1056	944	520	2854	1551	967	712	448
Be	3.11	6.98	7.39	3.20	2.62	5.20	3.01	2.86	1.22	2.70
Bi	0.05	0.02	0.05	0.12	0.04	0.08	0.07	0.02	n.a.	0.08
Cd	0.02	0.02	0.02	0.03	0.01	0.03	n.a.	0.02	0.03	0.03
Ce	117	11.23	117	108	88.6	178	91.7	81.7	21.74	285
Co	16.65	12.37	63.8	24.69	6.57	18.17	27.52	31.50	28.89	49.7
Cr	8.77	2.86	9.09	24.88	7.70	22.11	12.86	12.21	7.22	8.73
Cs	2.71	0.89	7.19	5.45	2.45	4.77	2.08	2.68	0.55	2.89
Cu	5.54	3.57	3.72	14.78	2.56	7.45	12.32	9.14	3.07	2.29
Dy	6.04	1.92	2.01	5.37	1.70	7.25	2.83	3.88	0.48	11.23
Er	3.00	1.22	0.69	2.80	0.70	2.70	1.13	1.65	0.26	5.16
Eu	2.14	0.18	0.90	1.52	0.59	3.64	0.76	1.58	0.39	1.14
Ga	20.73	18.67	22.60	19.84	17.46	17.83	21.82	17.36	16.46	20.74
Gd	6.96	1.56	3.36	6.06	3.07	12.36	2.94	4.91	0.81	13.80
Ge	1.50	0.23	22.60	19.84	1.18	2.20	21.82	17.36	0.49	20.74
Hf	2.96	3.57	5.61	1.61	4.68	2.69	4.87	3.64	3.54	5.01
Ho	1.06	0.37	0.25	0.97	0.26	1.02	0.38	0.66	0.07	1.78
La	47.6	4.09	48.5	44.0	32.11	169	17.00	38.22	10.06	132
Li	32.35	3.22	89.6	41.9	56.3	59.5	30.77	30.91	18.33	31.32
Lu	0.49	0.34	0.12	0.55	0.14	0.22	0.14	0.18	0.02	0.78
Mn	451	148	351	859	322	487	508	425	166	400
Mo	0.81	0.41	0.26	0.57	0.04	0.08	0.38	0.23	0.11	1.14
Nb	19.87	20.20	24.59	5.12	18.55	19.97	10.78	13.10	5.48	23.04
Nd	37.6	4.40	35.46	35.59	23.99	102	15.43	29.39	5.08	93.6
Ni	2.78	1.62	4.19	10.71	3.66	10.79	5.84	4.98	3.10	2.80
Pb	27.35	27.32	62.9	19.05	46.3	62.9	44.7	19.53	16.87	35.03
Pr	10.33	1.12	10.28	9.58	6.88	29.85	3.84	7.98	1.49	26.61
Rb	203	171	332	177	285	241	259	156	86.2	212
Sb	0.07	0.03	0.04	0.09	0.06	0.04	0.05	0.04	0.07	0.06
Sc	8.29	2.13	3.33	10.99	3.03	8.46	3.27	6.27	2.41	7.34
Sm	8.42	1.61	6.55	7.94	4.94	19.87	3.76	6.50	1.08	19.08
Sn	1.29	0.98	2.70	1.09	2.31	1.94	1.05	1.28	1.02	2.12
Sr	131	72.2	151	118	105	550	106	178	199	36.03
Ta	0.86	2.26	3.92	0.35	0.81	1.09	0.60	2.15	2.24	2.76
Tb	1.20	0.37	0.55	1.14	0.49	1.89	0.54	0.96	0.12	2.46
Th	12.84	7.18	30.14	12.41	32.85	22.85	15.76	15.35	7.11	29.75
Ti	n.a.	n.a.	n.a.	n.a.	n.a.	n.a.	n.a.	n.a.	n.a.	n.a.
Tl	0.97	0.66	1.80	0.75	1.18	1.26	1.44	0.76	0.51	1.08
Tm	0.45	0.24	0.11	0.50	0.10	0.34	0.19	0.22	0.05	0.78
U	1.50	3.40	2.73	3.26	2.55	1.20	0.90	0.86	0.98	2.23
V	23.22	7.03	31.59	92.9	18.58	56.6	46.1	42.1	22.33	12.02
W	12.18	13.29	55.9	3.88	5.18	9.73	13.76	30.66	32.5	39.2
Y	39.8	10.49	9.80	33.14	10.60	38.4	12.38	19.28	3.44	58.4
Yb	2.75	1.77	0.83	2.99	0.74	1.63	1.09	0.98	0.14	5.15
Zn	59.0	7.97	56.9	79.1	46.9	55.3	85.2	53.3	45.7	79.7
Zr	117	101	212	63.6	207	124	196	127	193	176

Table 14-26: Trace element geochemistry (ppm) of Porphyritic Granitoids (samples SH8, SH9, LW1, LW2, LWC and LW11 of sample batch #3 collected in 2000 and analysed at Curtin University of Technology; samples MTG-4, MTG-5, MGG-2 and MTGG-3 of sample batch #3 collected in 1999 and analysed by Chemex Canada; n.a.=not analysed).

	SH8	SH9	LW1	LW2	LW11	LWC	MTG-1	MTG-5	MGG-2
Ba	756	638	1360	63.5	242	56.6	910	630	253
Be	2.40	2.44	3.46	5.76	2.93	13.15	n.a.	n.a.	n.a.
Bi	n.a.	n.a.	0.16	0.16	n.a.	n.a.	n.a.	n.a.	n.a.
Cd	0.07	0.11	0.12	n.a.	0.13	n.a.	n.a.	n.a.	n.a.
Ce	161	301	207	16.31	124	10.66	213	72	281
Co	37.5	27.07	29.9	51.5	27.3	30.4	13.00	12.50	19.00
Cr	12.95	9.15	13.84	1.92	2.34	0.14	n.a.	n.a.	n.a.
Cs	n.a.	n.a.	n.a.	n.a.	n.a.	n.a.	2.40	9.20	2.60
Cu	2.58	9.31	11.42	1.09	6.14	17.36	n.a.	n.a.	n.a.
Dy	4.98	10.09	4.52	1.19	4.53	1.97	3.50	2.30	12.90
Er	1.73	3.68	1.41	0.46	1.57	0.91	1.70	1.20	6.70
Eu	1.24	1.37	1.71	0.24	1.86	0.20	1.50	0.80	1.00
Ga	18.09	19.12	18.47	30.70	26.4	12.10	24.0	20.0	24.0
Gd	8.11	15.59	8.67	1.43	6.42	1.57	9.00	3.50	19.90
Ge	n.a.	n.a.	n.a.	n.a.	n.a.	n.a.	n.a.	n.a.	n.a.
Hf	6.24	8.21	7.49	0.41	4.24	1.76	6.00	3.00	8.00
Ho	0.69	1.44	0.59	0.18	0.65	0.33	0.60	0.30	2.30
La	86	153	113	10.06	46.3	5.38	111	39.5	137
Li	50.6	52.8	36.7	1.15	18.42	35.1	n.a.	n.a.	n.a.
Lu	0.22	0.47	0.21	n.a.	0.18	0.21	0.10	0.10	0.80
Mn	n.a.	n.a.	n.a.	n.a.	n.a.	n.a.	n.a.	n.a.	n.a.
Mo	0.29	n.a.	n.a.	n.a.	n.a.	n.a.	n.a.	n.a.	n.a.
Nb	20.53	42.6	18.52	4.49	178	0.22	20.00	12.00	18.00
Nd	58.9	114	73.8	9.68	47.9	4.38	73	23.00	116
Ni	8.05	3.93	4.26	0.87	1.11	1.27	n.a.	n.a.	n.a.
Pb	54.8	61.8	52.8	4.60	4.59	23.70	55.0	40.0	45.0
Pr	15.60	29.88	20.05	2.29	12.64	1.09	22.0	7.40	31.6
Rb	303	314	288	157	339	35.5	283	311	221
Sb	n.a.	n.a.	n.a.	n.a.	n.a.	n.a.	n.a.	n.a.	n.a.
Sc	n.a.	n.a.	n.a.	n.a.	n.a.	n.a.	n.a.	n.a.	n.a.
Sm	10.67	20.41	12.44	1.78	8.17	1.52	10.80	3.90	21.50
Sn	6.22	3.39	2.49	0.63	3.49	3.08	1.00	6.00	4.00
Sr	100	90.5	177	10.87	335	35.7	186	103	27.6
Ta	1.57	4.94	1.97	0.74	16.67	0.76	5.50	7.00	9.50
Tb	0.30	0.98	1.45	1.85	0.20	1.87	0.59	n.a.	n.a.
Th	50.9	99.1	58.6	2.54	3.44	3.54	63.0	25.0	45.0
Ti	1972	2925	2647	103	4863	140	n.a.	n.a.	n.a.
Tl	0.17	0.23	0.78	0.82	n.a.	0.88	0.31	0.01	n.a.
Tm	0.21	1.48	0.14	1.53	0.32	0.67	n.a.	n.a.	n.a.
U	5.98	8.46	3.62	0.56	0.66	2.64	4.50	3.00	4.00
V	17.99	22.68	27.8	13.14	14.21	16.05	15.00	10.00	n.a.
W	27.3	20.76	22.93	33.0	22.7	15.99	106	113	186
Y	24.1	48.4	19.94	7.09	22.30	12.77	15.00	10.50	55.0
Yb	1.55	3.53	1.26	0.60	1.32	1.49	0.90	1.00	5.40
Zn	47.8	58.3	62.0	8.65	101	10.15	50.0	50.0	75
Zr	208	291	270	0.41	173	32.0	193	105	247

Table 14-27: Trace element geochemistry (ppm) of Porphyritic Granitoids (sample batch #4 collected in 2001 and analysed at Curtin University of Technology; n.a.=not analysed).

	KTB1	CHL2	CHL4	CHL5
Ba	253	0.05	0.01	0.02
Be	2.55	0.06	0.06	0.13
Bi	0.08	0.04	0.03	0.05
Cd	0.01	0.29	1.39	0.70
Ce	39.11	1.62	0.22	0.46
Co	67.2	1.57	0.27	0.49
Cr	9.05	5.37	1.40	1.32
Cs	10.89	3.62	2.95	0.55
Cu	15.51	3.33	0.47	1.01
Dy	5.41	3.72	0.61	1.38
Er	2.46	3.19	0.47	2.14
Eu	0.99	1.17	1.02	1.01
Ga	12.38	4.19	6.09	5.33
Gd	5.82	1.71	5.49	2.06
Ge	0.65	10.30	1.47	2.88
Hf	2.61	10.12	1.45	2.99
Ho	1.00	1.36	5.32	7.31
La	18.18	19.03	2.58	6.88
Li	49.9	3.11	2.70	2.48
Lu	0.43	20.16	2.59	7.56
Mn	348	50.8	44.9	18.66
Mo	0.38	20.51	3.00	10.13
Nb	18.80	25.68	3.83	12.04
Nd	23.38	8.16	1.98	10.11
Ni	3.13	28.00	14.70	6.58
Pb	31.50	5.55	2.70	15.19
Pr	5.48	33.8	13.07	9.83
Rb	336	21.10	15.04	22.02
Sb	0.09	21.10	15.04	22.02
Sc	3.44	48.4	40.7	27.59
Sm	6.14	116	17.67	33.8
Sn	2.98	71.8	59.2	53.8
Sr	55.8	10.35	77.7	120
Ta	2.96	98.5	13.80	45.9
Tb	0.98	129	23.18	52.1
Th	6.09	4.14	2.95	6.70
Ti	n.a.	180	42.9	118
Tl	1.42	n.a.	n.a.	n.a.
Tm	0.43	16.87	12.61	82.6
U	2.40	96.9	24.72	116
V	16.14	101	59.5	150
W	40.6	9.00	9.41	14.41
Y	40.3	246	255	186
Yb	2.86	74.3	101	96.7
Zn	24.84	1695	427	1392
Zr	158	597	241	982

15 REFERENCES

- Ackermann, E.H., 1936. Das problem der Mkushi-Gneise am NW-rand der Rhodesischen masse. *Geologische Rundschau*, 27: 81-87.
- Ackermann, E.H., 1950. Ein neuer faltengurtel in Nordrhodesien und seine tectonische stellung im Afrikanischen grundgebirge. *Geologische Rundschau*, 38: 24-39.
- Ackermann, E.H., 1960. Strukturen im untergrund eines intrakratonischen doppelorogens (Irumiden Nordrhodesien). *Geologische Rundschau*, 50: 538-553.
- Ackermann, E.H. and Forster, A., 1960. Grundzüge der stratigraphie und struktur des Irumide Orogen, 21st International Geological Congress, pp. 182-192.
- Agar, R.A. and Ray, A.K., 1983. The geological map of the Petauke area. Geological Survey of Zambia, Lusaka.
- Andersen, L.S. and Unrug, R., 1984. Geodynamic evolution of the Bangweulu block, northern Zambia. *Precambrian Research*, 25: 187-212.
- Andreoli, M.A.G., 1984. Petrochemistry, tectonic evolution and metasomatic mineralisations of Mozambique Belt granulites from southern Malawi and Tete (Mozambique). In: S.N. Punukollu and S.C.P. Andrews (Editors), *Proterozoic; evolution, mineralization, and orogenesis*. Precambrian Research. Elsevier, Amsterdam, International, pp. 161-186.
- Andrews-Speed, C.P., 1986. Gold-bearing fluvial and associated tidal marine sediments of Proterozoic age in the Mporokoso basin, northern Zambia. *Sedimentary Geology*, 48: 193-222.
- Andrews-Speed, C.P., 1989. The Mid-Proterozoic Mporokoso basin, northern Zambia: sequence stratigraphy, tectonic setting and potential for gold and uranium mineralisation. *Precambrian Research*, 44: 1-17.
- Armstrong, R.A., Robb, L.J., Master, S., Kruger, F.J. and Mumba, P.A.C.C., 1999. New U-Pb age constraints on the Katangan Sequence, Central African Copperbelt. In: F. Tembo, B. De Waele and S. Nkamba (Editors), *IGCP 418 2nd fieldmeeting*. Geological Society of Zambia, Kitwe, Zambia, pp. 48-49.
- Arndt, N.T. and Goldstein, S.L., 1987. Use and abuse of crust-formation ages. *Geology (Boulder)*, 15(10): 893-895.
- Ayres, H.R., 1974. The geology of the Shiwa N'Gandu area; explanation of degree sheet 1131, NE quarter. 64, Geological Survey of Zambia, Lusaka.
- Ayres, H.R., 1998. The geological map of the Shiwa Ng'andu area. Geological Survey Department of Zambia, Lusaka.
- Barr, M.W.C., 1974. The pre-Karoo geology of the Rufunsa area, Zambia, with special reference to structure and metamorphism. PhD Thesis, University of Leeds.
- Barr, M.W.C. and Drysdall, A.R., 1972. The geology of the Sasare area; explanation of degree sheet 1131, SW quarter. 30, Geological Survey of Zambia, Lusaka.
- Barton, C.M., Carney, J.N., Crow, M.J., Dunkley, P.N. and Simango, S., 1993. Geological and structural framework of the Zambezi belt, northeastern Zimbabwe. In: R.H. Findlay, R. Unrug, M.R. Banks and J.J. Veevers (Editors), *Gondwana eight: assembly, evolution and dispersal*. Balkema, Rotterdam, pp. 55-68.
- Batchelor, R.A. and Bowden, P., 1985. Petrogenetic interpretation of granitoid rocks series using multicationic parameters. *Chemical Geology*, 48: 43-55.
- Bauer, W. and Jacobs, J., 2001. The neoproterozoic suture between east and west Gondwana - New results from central Dronning Maud Land, Antarctica. *Gondwana Research*, 4(2): 147-149.
- Best, M.G. and Christiansen, E.H., 2000. *Igneous Petrology*. Blackwell Science Inc., 455 pp.
- Bevington, P.R. and Robinson, D.K., 1992. *Data reduction and error analysis for the physical sciences*. McGraw-Hill, New York.
- Boven, A., Theunissen, K., Sklyarov, E., Klerkx, J., Melnikov, A., Mruma, A. and Punzalan, L., 1999. Timing of exhumation of a high-pressure granulite terrane of the Palaeoproterozoic Ubende belt (west Tanzania). *Precambrian Research*, 93: 119-137.
- Brewer, M.S., Haslam, H.W., Darbyshire, P.F.P. and Davis, A.E., 1979. Rb-Sr age determinations in the Bangweulu block, Luapula Province, Zambia. 79/5, Institute of Geological Sciences, London.

- Brinckmann, J., Lehmann, B., Hein, U., Höhndorf, A., Mussallam, K., Weiser, T. and Timm, F., 2001. La géologie et la minéralisation primaire de l'or de la chaîne Kibarienne, nord-ouest du Burundi, Afrique orientale. *Geologische Jahrbuch Reihe, D 101*: 3-195.
- Buchan, K., Ernst, R., Hamilton, M., Mertanen, S., Pesonen, L.J. and Elmin, S.-A., 2001. Rodinia: the evidence from integrated paleomagnetism and U-Pb geochronology. *Precambrian Research*, 110: 9-32.
- Buchan, K.L. and Halls, H.C., 1990. Palaeomagnetism of Proterozoic dyke swarms of the Canadian Shield. In: A.J. Parker, P.C. Rickwood and D.H. Tucker (Editors), *Mafic dykes and emplacement mechanisms*. Balkema, Rotterdam, pp. 209-230.
- Bulanbo, M., De Waele, B., Kampunzu, A.B. and Tembo, F., 2004. SHRIMP U-Pb geochronology of the Choma-Kalomo block (Zambia) and geological implications, 20th Colloquium of African Geology, Orléans, France, pp. 96.
- Burke, K.C. and Dewey, J.F., 1972. Orogeny in Africa, *African Geology; Structural Geology*. Univ. Ibadan, Dep. Geol., Ibadan, Nigeria, pp. 583-608.
- Cahen, L., 1970. Igneous activity and mineralisation episodes in the evolution of the Kibariide and Katangide orogenic belts of central Africa. In: T.N. Clifford and I.G. Gass (Editors), *African Magmatism and tectonics*, pp. 97-117.
- Cahen, L., Delhal, J. and Deutsch, S., 1967. Rb-Sr Geochronology of some granitic rocks from the Kibaran belt (central Katanga, republic of Congo). *Annales of the Museum for Central Africa*, 8(59).
- Cahen, L., Snelling, N.J., Delhal, J., Vail, J.R., Bonhomme, M. and Ledent, D., 1984. The geochronology and evolution of Africa. Oxford University Press, Oxford, 512 pp.
- Caron, J.-P.H., Kampunzu, A.B., Lwango, B.L., Manteka, B. and Nkanika, R.W., 1986. Les Ressources minérales d'âge proterozoïque moyen en Afrique équatoriale et l'évolution géodynamique de la chaîne Kibarienne. *UNESCO Geology for Economic Development Newsletter*, 5: 139-152.
- Carruthers, H., 2000. The geological map of the Chin'gombe area. Geological Survey Department of Zambia, Lusaka.
- Cawood, P.A., Nemchin, A., Freeman, M. and Sircombe, K., 2003. Linking source and sedimentary basin: detrital zircon record of sediment flux along a modern river system and implications for provenance studies. *Earth and Planetary Science Letters*, 210: 259-268.
- Chappell, B.W., 1999. Aluminium saturation in I- and S-type granites and the characterisation of fractionated haplogranites. *Lithos*, 46: 535-551.
- Chappell, B.W. and White, A.J.R., 1974. Two contrasting granite types. *Pacific Geology*, 8: 173-174.
- Chappell, B.W. and White, A.J.R., 1992. I-type and S-type granites in the Lachlan Fold Belt. *Transactions of the Royal Society of Edinburgh-Earth Sciences*, 83: 1-26.
- Cherniak, D.J. and Watson, E.B., 2000. Pb diffusion in zircon. *Chemical Geology*, 172: 5-24.
- Chisela, S., in press. The Geological map of the Kakulu area. Geological Survey Department of Zambia, Lusaka.
- Claoué-Long, J., Compston, W., Roberts, J. and Fanning, C.M., 1995. Two Carboniferous ages: a comparison of SHRIMP zircon dating with conventional zircon ages and ⁴⁰Ar/³⁹Ar analysis. In: W.A. Berggren, D.V. Kent, M.-P. Aubry and J. Hardenbol (Editors), *Geochronology, time scales and global stratigraphic correlation*. SEPM (Society of Sedimentary Petrology) Special Publication, pp. 3-21.
- Clarke, D.B., 1992. *Granitoid rocks*. Chapman & Hall, London, 283 pp.
- Clifford, T.N., Barton, E.S., Retief, E.A., Rex, D.C. and Fanning, C.M., 1995. A crustal progenitor for the intrusive anorthosite-charnockite kindred of the cupriferous Koperberg suite, O'Kiep District, Namaqualand, South Africa: new isotope data for the country rocks and intrusives. *Journal of Petrology*, 36: 231-258.
- Clifford, T.N., Gass, I.G. and Kennedy, W.Q., 1970. *African magmatism and tectonics*. Hafner Pub. Co., Darien, Connecticut, USA, 461 pp.
- Collins, A.S., Kröner, A., Fitzsimons, I.C.W. and Razakamanana, T., 2003. Detrital footprint of the Mozambique Ocean: U/Pb SHRIMP and Pb evaporation zircon geochronology of metasediments in Eastern Madagascar. *Tectonophysics*, 375: 77-99.
- Compston, W., Williams, I.S. and Meyer, C., 1984. U-Pb geochronology of zircons from lunar breccia 73217 using a sensitive high mass-resolution ion microprobe. *Journal of Geophysical Research*, 89: 525-534.
- Cordiner, R.J., 1994. The geological map of the Chitambo Mission area. Geological Survey Department of Zambia, Lusaka.

- Cordiner, R.J., 2000. The geological map of the Kanona area. Geological Survey Department of Zambia, Lusaka.
- Costa, M., Casati, C. and Di Bartolomeo, G., 1983. Cartografia geológica e prospecção Mineira e geoquímica das províncias de Nampula e da Zâmbia, área de Alto Ligonha. AQUATER SpA, Instituto Nacional de Geologia, Maputo.
- Cox, K.G., Bell, J.D. and Pankhurst, R.J., 1979. The interpretation of igneous rocks. George Allen & Unwin, London, 445 pp.
- Cox, R., Coleman, D.S., Chokel, C.B., DeOreo, S.B., Wooden, J.L., Collins, A.S., De Waele, B., Kröner A., submitted. Proterozoic tectonostratigraphy and paleogeography of central Madagascar derived from detrital zircon U-Pb age populations. *Journal of Geology*, 114(4).
- Cox, R.A., Rivers, T., Mapani, B., Tembo, D. and De Waele, B., 2002. New U-Pb data for the Irumide belt: LAM-ICP-MS results for Luangwa Terrane. In: G.S.o. Namibia (Editor), 11th IAGOD Quadrennial Symposium and Geocongress, technical meeting IGCP 440: Assembly and Breakup of Rodinia, Windhoek, Namibia, pp. 10.
- Crock, J.G. and Lichte, F.E., 1982. Determination of rare earth elements in geologic materials by inductively couple argon plasma/atomic emission spectrometry. *Analytical Chemistry*, 54: 1329-1332.
- Cvetkovic, D., 1973. The geology of the Mita hills area; explanation of degree sheet 1429, NW quarter. 34, Geological Survey Department of Zambia, Lusaka.
- Cvetkovic, D., 1992. The geological map of the Mita Hills area. Geological Survey Department of Zambia, Lusaka.
- Daly, M.C., 1986a. The intracratonic Irumide belt of Zambia and its bearing on collision orogeny during the Proterozoic of Africa. In: M.P. Coward and A. Ries (Editors), *Collisional Tectonics*. Geological Society of London, London, pp. 321-328.
- Daly, M.C., 1986b. The tectonic and thermal evolution of the Irumide belt, Zambia. PhD Thesis, University of Leeds, Leeds, 326 pp.
- Daly, M.C., 1994a. The geological map of the Chinsali area. Geological Survey Department of Zambia, Lusaka.
- Daly, M.C., 1994b. The geological map of the Isoka area. Geological Survey Department of Zambia, Lusaka.
- Daly, M.C., 1994c. The geological map of the Mulilansolo Mission area. Geological Survey Department of Zambia, Lusaka.
- Daly, M.C., 1995a. The geology of Chinsali and Mutangoshi Hills area; explanation of degree sheet 1032, SE and SW quarter. 79, Geological Survey Department of Zambia, Lusaka.
- Daly, M.C., 1995b. The geology of Mulilansolo Mission and Isoka areas; explanation of degree sheet 1032, NE and NW quarter. 84, Geological Survey Department of Zambia, Lusaka.
- Daly, M.C., Chakraborty, S.K., Kasolo, P., Musiwa, M., Mumba, P., Naidu, B., Namateba, C., Ngambi, O. and Coward, M.P., 1984. The Lufilian arc and Irumide belt of Zambia: results of a geotraverse across their intersection. *Journal of African Earth Sciences*, 2(4): 311-318.
- Daly, M.C. and Unrug, R., 1982. The Muva Supergroup, northern Zambia. *Transactions of the Geological Society of South Africa*, 85: 155-165.
- Dalziel, I.W.D., 1991. Pacific margins of Laurentia and East Antarctica as a conjugate rift pair: evidence and implications for an Eocambrian supercontinent. *Geology*, 19: 598-601.
- Dalziel, I.W.D., 1997. Neoproterozoic-Paleozoic geography and tectonics; review, hypothesis. *Geological Society of America Bulletin*, 109(1): 16-42.
- Dalziel, I.W.D., Mosher, S. and Gahagan, L.M., 2000. Laurentia-Kalahari collision and the assembly of Rodinia. *Journal of Geology*, 108: 499-513.
- De Waele, B., 1997. Geology and stratigraphy of the Mupamadzi river area and correlation with the adjoining areas within the Irumide belt. *Zambian Journal of Applied Earth Sciences*, 11(1): 34-48.
- De Waele, B. and Mapani, B., 1998. Geology, stratigraphy and correlation of the Irumide belt, Mkushi-Mpika Block, Conference on the Role of a National Geological Survey in Sustainable Development. Geological Survey Department of Botswana, Gaborone, Botswana, pp. 132-133.
- De Waele, B. and Mapani, B., 2002. Geology and correlation of the central Irumide belt. *Journal of African Earth Sciences*, 35(3): 385-397.
- De Waele, B., Wingate, M.T.D., Fitzsimons, I.C.W. and Mapani, B.S.E., 2003. Untying the Kibaran knot: A reassessment of Mesoproterozoic correlations in southern Africa based on SHRIMP U-Pb data from the Irumide belt. *Geology*, 31(6): 509-512.

- Deblond, A., 1995. Lamprophyres of Burundi: a review, Royal Museum of Central Africa, Tervueren.
- Dickin, A.P., 1995. Radiogenic Isotope Geology. Cambridge University Press, Cambridge, 490 pp.
- Dirks, P.H.G.M., Kröner, A., Jelsma, H.A., Maneya, C. and Jamal, D.L., 2000. Pb-Pb zircon ages and a tectonic framework for the Zambezi belt. *Journal of African Earth Sciences*, 30(18th Colloquium of African Geology): 23-24.
- Dirks, P.H.G.M., Kröner, A., Jelsma, H.A., Sithole, T.A. and Vinyu, M.L., 1999. Structural relations and Pb-Pb zircon ages for a crustal-scale Pan African shear zone in the Zambezi Belt, northwest Zimbabwe. *Journal of African Earth Sciences*, 28: 427-442.
- Dirks, P.H.G.M. and Sithole, T.A., 1999. Eclogites in the Makuti gneisses of Zimbabwe: implications for the tectonic evolution of the Zambezi Belt in southern Africa. *Journal of Metamorphic Geology*, 17(6): 593-612.
- Dodson, M.H., Cavanagh, B.J., Thatcher, E.C. and Aftalion, M., 1975. Age limits for the Ubendian metamorphic episode in northern Malawi. *Geological Magazine*, 112: 403-410.
- Drysdall, A.R., Johnson, R.L., Moore, T.A. and Thieme, J.G., 1972. Outline of the geology of Zambia. *Geologie en Mijnbouw*, 51: 265-276.
- Eby, G.N., 1990. The A-type granitoids: A review of their occurrence and chemical characteristics and speculations on their petrogenesis. *Lithos*, 26: 115-134.
- Eby, G.N., 1992. Chemical subdivision of the A-type granitoids: Petrogenetic and tectonic implications. *Geology*, 20: 641-644.
- Ellis, D.J. and Thompson, A.B., 1986. Subsolvus and partial melting reactions in the quartz-excess $\text{CaO}+\text{MgO}+\text{Al}_2\text{O}_3+\text{SiO}_2+\text{H}_2\text{O}$ system under water-excess and water-deficient conditions to 10 kb; some implications for the origin of peraluminous melts from mafic rocks. *Journal of Petrology*, 27(1): 91-121.
- Faure, G., 1997. Principles of isotope geology. Cambridge University Press, Cambridge, 506 pp.
- Fitches, W.R., 1966. Preliminary report on the geology of the Mafingi Hills area of N. Malawi and Zambia. 10, Research Institute for African Geology, Leeds.
- Fitches, W.R., 1967. Progress report on the Mafingi Hills area of N. Malawi and Zambia. 11, Research Institute for African Geology, Leeds.
- Fitches, W.R., 1968a. New K-Ar age determinations from the Pre-Cambrian Mafingi Hills area of Zambia and Malawi. 12, Research Institute for African Geology, Leeds.
- Fitches, W.R., 1968b. Structural and stratigraphic relations in the Precambrian rocks of the Mafingi Hills area of northern Malawi and Zambia. PhD Thesis, University of Leeds, Leeds.
- Fitches, W.R., 1970. A part of the Ubendian orogenic belt in N. Malawi and Zambia. *Geologische Rundschau*, 59: 444-458.
- Fitches, W.R., 1971. Sedimentation and tectonics at the northern end of the Irumide orogenic belt, N. Malawi and Zambia. *Geologische Rundschau*, 59: 444-458.
- Fitzsimons, I.C.W., 2000. Grenville-age basement provinces in East Antarctica: Evidence for three separate collisional orogens. *Geology*, 28(10): 879-882.
- Forster, A., 1965. Der kristallin sockel im östlichen Nordrhodesien und sein verband mit anderen baueinheiten Zentral- und Ostafrikas. *Geotektonische Forschungen*, 20(I-II): 115.
- Foster, D.A. and Gray, D.R., 1999. Deformation rates and timing of deformation in the western Lachlan Orogen, eastern Australia. In: Anonymous (Editor), Geological Society of America, 1999 annual meeting. Abstracts with Programs - Geological Society of America, pp. 301.
- Foster, D.A. and Gray, D.R., 2000. Evolution and structure of the Lachlan fold belt (orogen) of eastern Australia. *Annual Reviews of Earth and Planetary Sciences*, 28: 47-80.
- Foster, D.A., Gray, D.R. and VandenBerg, A.H.M., 2000. Timing of orogenic events in the Lachlan Orogen; discussion and reply. *Australian Journal of Earth Sciences*, 47(4): 813-822.
- Geyh, M.A. and Schleicher, H., 1990. Absolute age determination. Springer-Verlag, Berlin, 503 pp.
- Gill, J.B., 1981. Orogenic andesites and plate tectonics. Springer Verlag, Berlin, Germany, 401 pp.
- Goscombe, B., Armstrong, R.A. and Barton, J.M., 2000. Geology of the Chewore Inliers, Zimbabwe: Constraining the Mesoproterozoic to Palaeozoic evolution of the Zambezi belt. *Journal of African Earth Sciences*, 30(3): 589-627.
- Gower, C.F. and Krogh, T.E., 2002. A U-Pb geochronological review of the Proterozoic history of the eastern Grenville Province. *Canadian Journal of Earth Sciences*, 39: 795-829.

- Grantham, G.H., Eglinton, B.M. and Armstrong, R.A., 2001. The Geochronology of some lithologies from sheet 3018A, Leliefontein, Namaqua metamorphic province. In: S. McCourt (Editor), IGCP 418 4th Fieldmeeting. University of Durban-Westville, Durban, South Africa.
- Gray, A., 1930. The Correlation of the ore-bearing sediments of the Katanga and the Rhodesian Copperbelt. *Economic Geology*, 25: 783-804.
- Gray, D.R., 1997. Tectonics of the southeastern Australian Lachlan fold belt; structural and thermal aspects. In: P. Burg Jean and M. Ford (Editors), *Orogeny through time*. Geological Society of London Special Publication, London, pp. 149-177.
- Gray, D.R. and Willman, C.E., 1991. Deformation in the Ballarat slate belt, central Victoria, and implications for the crustal structure across Southeast Australia. *Australian Journal of Earth Sciences*, 38(2): 171-201.
- Grunow, A.M., Hanson, R. and Wilson, T.J., 1996. Were aspects of Pan-African deformation linked to Iapetus opening? *Geology (Boulder)*, 24(12): 1063-1066.
- Guernsey, T.D., 1951. A Summary of the provisional geological features of northern Rhodesia. *Colonial Geological Mineral Resources*, 1: 121-151.
- Halligan, R., 1963. The Proterozoic rocks of Tanganyika. 34, Geological Survey of Tanganyika, Dar Es Salaam.
- Hanchar, J.M. and Miller, C.F., 1993. Zircon zonation patterns as revealed by cathodoluminescence and backscattered electron images: implications for interpretation of complex crustal histories. *Chemical Geology*, 110: 1-13.
- Hanchar, J.M. and Watson, B.E., 2003. Zircon saturation thermometry. In: J.M. Hanchar and P.W.O. Hoskin (Editors), *Zircon. Reviews in Mineralogy and Geochemistry*. The Mineralogical Society of America, Washington, USA, pp. 89-112.
- Hanson, R.E., 2003. Proterozoic geochronology and tectonic evolution of southern Africa. In: M. Yoshida, B.F. Windley and S. Dasgupta (Editors), *Proterozoic East Gondwana: Supercontinent Assembly and Breakup*. Geological Society of London Special Publication, London, pp. 427-463.
- Hanson, R.E., Crowley, J.L., Bowring, S.A., Ramezani, J., Cose, W.A., Dalziel, I.W.D., Pancake, J.A., Seidel, E.K., Blenkinsop, T.G. and Mukwakwami, J., 2004. Coeval large-scale magmatism in the Kalahari and Laurentian cratons during Rodinia assembly. *Science*, 304(5674): 1126.
- Hanson, R.E., Hargrove, U.S., Martin, M.A., Bowring, S.A., Krol, M.A., Hodges, K.V., Munyanyiwa, H. and Blenkinsop, T.G., 1998a. New Geochronological constraints on the tectonic evolution of the Pan-African Zambezi belt, south-central Africa., *Gondwana 10: Event stratigraphy of Gondwana. Journal of African Earth Sciences*, pp. 104-105.
- Hanson, R.E., Martin, M.W., Bowring, S.A. and Munyanyiwa, H., 1998b. U-Pb zircon age for the Umkondo dolerites, eastern Zimbabwe: 1.1 Ga large igneous province in southern Africa/East Antarctica and possible Rodinia correlations. *Geology*, 26: 1143-1146.
- Hanson, R.E., Wardlaw, M.S., Wilson, T.J. and Mwale, G., 1993. U-Pb zircon ages from the Hook Granite massif and Mwembeshi Dislocation: Constraints on Pan-African deformation, plutonism, and transcurrent shearing in central Zambia. *Precambrian Research*, 63: 189-209.
- Hanson, R.E., Wilson, T.J., Brueckner, H.K., Onstott, T.C., Wardlaw, M.S., Johns, C.C. and Hardcastle, K.C., 1988a. Reconnaissance geochronology, tectonothermal evolution, and regional significance of the Middle Proterozoic Choma-Kalomo block, southern Zambia. *Precambrian Research*, 42: 39-61.
- Hanson, R.E., Wilson, T.J. and Munyanyiwa, H., 1994. Geologic evolution of the Neoproterozoic Zambezi orogenic belt in Zambia. *Journal of African Earth Sciences*, 18(2): 135-150.
- Hanson, R.E., Wilson, T.J. and Wardlaw, M.S., 1988b. Deformed batholiths in the Pan African Zambezi belt, Zambia: Age and implications for regional Proterozoic tectonics. *Geology*, 16: 1134-1137.
- Hanson, R.E., Wilson, T.J., Wardlaw, M.S., Brueckner, H.K. and Onstott, T.C., 1988c. Geochronology of the middle Proterozoic Choma-Kalomo Block, southern. In: Anonymous (Editor), *Geological Society of America, 1988 centennial celebration*. Geological Society of America (GSA), Boulder, CO, United States.
- Hargrove, U.S., Hanson, R.E., Martin, W.M., Blenkinsop, T.G., Bowring, S.A., Walker, N. and Munyanyiwa, H., 2003. Tectonic evolution of the Zambezi orogenic belt: geochronological, structural and petrological constraints from northern Zimbabwe. *Precambrian Research*, 123: 159-186.

- Haslam, H.W., Rundle, C.C. and Brewer, M.S., 1986. Rb-Sr studies of metamorphic and igneous events in eastern Zambia. *Journal of African Earth Sciences*, 5(5): 447-453.
- Hawkesworth, C., Turner, S., Peate, D., McDermott, F. and van Calsteren, P., 1997. Elemental U and Th variations in island arc rocks: implications for U-series isotopes. *Chemical Geology*, 139(1-4): 207-221.
- Hoal, B.G. and Heaman, L.M., 1994. The Sinclair Sequence: U-Pb age constraints., Proterozoic Crustal and Metallogenic Evolution. Geological Society of Namibia and Geological Survey of Namibia, Windhoek, Namibia, pp. 29.
- Hoal, B.G. and Heaman, L.M., 1995. The Sinclair Sequence: U-Pb age constraints from the Awasib Mountain area. *Namibian Geological Survey Communications*, 10: 83-91.
- Hodges, K.V., 2000. Tectonics of the Himalaya and southern Tibet from two perspectives. In: W. Geissman John and F. Glazner Allen (Editors), Special focus on the Himalaya. Geological Society of America, Bulletin, pp. 324-350.
- Hoffman, P.F., 1989. Precambrian geology and tectonic history of North America. In: A.W. Bally and A.R. Palmer (Editors), The geology of North America; an overview. Geol. Soc. Am., Boulder, CO, United States, pp. 447-512.
- Hoffman, P.F., 1991. Did the breakout of Laurentia turn Gondwanaland inside-out? *Science*, 252(5011): 1409-1412.
- Hofmann, A.W., Jochum, K.P., Seufert, M. and White, W.M., 1986. Nb and Pb in oceanic basalts: new constraints on mantle evolution. *Earth and Planetary Science Letters*, 79: 33-54.
- Holmes, A., 1951. The sequence of Precambrian orogenic belts in south and central Africa., 18th International Geological Congress, London, pp. 254-269.
- Holtz, F. and Johannes, W., 1991. Genesis of peraluminous granites; I, Experimental investigation of melt compositions at 3 and 5 Kb and various H₂O activities. *Journal of Petrology*, 32(5): 935-958.
- Hoskin, P.W.O. and Black, L.P., 2000. Metamorphic zircon formation by solid-state recrystallization of protolith igneous zircon. *Journal of Metamorphic Geology*, 18(4): 423-439.
- Ikingura, J.R., Reynolds, P.H., Watkinson, D.H. and Bell, K., 1992. ⁴⁰Ar-³⁹Ar Dating of micas from granites of NE Kibaran belt (Karagwe-Ankolean), NW Tanzania. *Journal of African Earth Sciences*, 15(3-4): 501-511.
- Irvine, T.N. and Baragar, W.R.A., 1971. A guide to the chemical classification of the common volcanic rocks. *Canadian Journal of Earth Sciences*, 8: 523-548.
- Jackson, G.C.A., 1932. The geology of the N'Changa District, northern Rhodesia. *Quarterly Journal of the Geological Society of London*, 88: 443-515.
- Jacobs, J., Bauer, W. and Fanning, C.M., 2003a. New age constraints for Grenville-age metamorphism in western central Dronning Maud Land (East Antarctica), and implications for the palaeogeography of Kalahari in Rodinia. *International Journal of Earth Sciences*, 92(3): 301-315.
- Jacobs, J., Falter, M., Thomas, R.J., Kunz, J. and Jebberger, E.K., 1997. Ar-Ar thermochronological constraints on the structural evolution of the Mesoproterozoic Natal Metamorphic Province, SE Africa. *Precambrian Research*, 86: 71-92.
- Jacobs, J., Fanning, C.M. and Bauer, W., 2003b. Timing of Grenville-age vs. Pan-African medium- to high grade metamorphism in western Dronning Maud Land (East Antarctica) and significance for correlations in Rodinia and Gondwana. *Precambrian Research*, 125(1-2): 1-20.
- Jacobs, J., Fanning, C.M., Henjes-Kunst, F., Olesch, M. and Paech, H.-J., 1998. Continuation of the Mozambique belt into East Antarctica: Grenville-age metamorphism and polyphase Pan-African high-grade events in central Dronning-Maud Land. *Journal of Geology*, 106: 385-406.
- Jacobs, J. and Thomas, R.J., 1994. Oblique collision at about 1.1 Ga along the southern margin of the Kaapvaal craton, south-east Africa. *Geologische Rundschau*, 83: 322-333.
- Jacobs, J., Thomas, R.J. and Weber, K., 1993. Accretion and indentation tectonics at the southern margin of the Kaapvaal craton during the Kibaran (Grenville) orogeny. *Geology*, 21: 203-206.
- Jensen, L.S., 1976. A new cation plot for classifying subalkalic volcanic rocks, Miscellaneous Paper 66. Ontario Geological Survey, Ontario, Canada.
- Johannsen, A., 1931. A descriptive petrography of the igneous rocks, 1. University of Chicago Press, Chicago, 267 pp.

- John, T., 2001. Subduction and continental collision in the Lufilian Arc - Zambezi belt orogen: A petrological, geochemical, and geochronological study of eclogites and whiteschists (Zambia). PhD Thesis, University of Kiel, Kiel, 78 pp.
- John, T., Schenk, V., Haase, K., Scherer, E. and Tembo, F., 2003. Evidence for a Neoproterozoic ocean in south-central Africa from mid-oceanic-ridge-type geochemical signatures and pressure-temperature estimates of Zambian eclogites. *Geology*, 31(3): 243-246.
- John, T., Schenk, V., Mezger, K. and Tembo, F., 2004. Timing and PT evolution of whiteschist metamorphism in the Lufilian Arc-Zambezi belt Orogen (Zambia): Implications for the assembly of Gondwana. *Journal of Geology*, 112: 71-90.
- Johns, C.C., Liyungu, K., Mabuku, S., Mwale, G., Sakungo, F., Tembo, D., Vallance, G. and Barr, M.W.C., 1989. The stratigraphic and structural framework of eastern Zambia: Results of a geotraverse. *Journal of African Earth Sciences*, 9: 123-136.
- Johnson, S., 1999. A Kibaran aged marginal basin and island-arc complex in northern Zimbabwe. In: B. De Waele, F. Tembo and R.M. Key (Editors), Abstracts Volume IGCP 418/419. Geological Society of Zambia, Lusaka, pp. 6.
- Johnson, S. and Rivers, T., submitted. Mesoproterozoic to Early Palaeozoic magmatic and tectonothermal history of central, southern Africa: a review. *Journal of the Geological Society of London*.
- Johnson, S., Rivers, T. and De Waele, B., in press. A Review of the Mesoproterozoic to early Palaeozoic magmatic and tectonothermal history of south-central Africa: implications for Rodinia and Gondwana. *Journal of the Geological Society of London*.
- Johnson, S.P. and Oliver, G.J.H., 2000. Mesoproterozoic oceanic subduction, island-arc formation and the initiation of back-arc spreading in the Kibaran belt of central, southern Africa: evidence from the ophiolite terrane, Chewore inliers, northern Zimbabwe. *Precambrian Research*, 103: 125-146.
- Johnson, S.P. and Oliver, G.J.H., 2002. High fO_2 metasomatism during whiteschist metamorphism. *Journal of Petrology*, 43: 271-290.
- Johnson, S.P. and Oliver, G.J.H., 2004. Tectonothermal history of the Karouera Arc, northern Zimbabwe. *Precambrian Research*, 130: 71-97.
- Johnsson, M.J., 1993. The system controlling the composition of clastic sediments. In: M.J. Johnsson and A. Basu (Editors), Processes controlling the composition of clastic sediments. Special Paper. Geological Society of America, Boulder, Colorado, pp. 1-19.
- Johnston, S.T., McCourt, S., Bisnath, A. and Mitchell, A.A., 2002. The Tugela terrane, Natal belt: Kibaran magmatism and tectonism along the south-east margin of the Kaapvaal Craton. *South African Journal of Geology*, 105(1): 1-14.
- Jourde, G. and Wolff, J.P., 1974. Open File Report - Géologie et minéralisation des degrés carrés, BRGM, Instituto Nacional de Geologica, Maputo.
- Kampunzu, A.B., 1997. The Kibaran orogenic cycle (Ca. 1400-1000 Ma); review and new perspectives in the framework of Rodinia reconstruction. In: R. Cox and D. Ashwal Lewis (Editors), Proceedings of the UNESCO-IUGS-IGCP-348/ 368 international symposium and field workshop on Proterozoic geology of Madagascar; abstract volume. Gondwana Research Group Miscellaneous Publication. Osaka City University, Department of Geosciences, Faculty of Science, Gondwana Research Group, Osaka, Japan, pp. 34.
- Kampunzu, A.B., Akanayang, P., Mapeo, R.B.M., Modie, B.N. and Wendorff, M., 1998. Geochemistry and tectonic significance of Mesoproterozoic Kgwebe metavolcanic rocks in northwest Botswana: implications for the evolution of the Kibaran Namaqua-Natal Belt. *Geological Magazine*, 135: 669-683.
- Kampunzu, A.B., Armstrong, R.A., Kokonyangi, J. and Ngulube, D.A., 2001. Kibaran geochronology, timing of orogenic events and petrogenetic implications for the source of the Kibaran tin granites. In: S. McCourt (Editor), IGCP 418 4th fieldmeeting. University of Durban-Westville, Durban, South Africa.
- Kampunzu, A.B., Armstrong, R.A., Modisi, M.P. and Mapeo, R.B.M., 2000. Ion microprobe ages on detrital zircon grains from the Ghanzi Group: Implications for the identification of a Kibaran-age crust in northwest Botswana. *Journal of African Earth Sciences*, 30(3): 579-587.
- Kampunzu, A.B., Milesi, J.P. and Deschamps, Y., 2003. Africa within Rodinia supercontinent: evidence from the Kibaran orogenic system, Geological Society of America. Geological Society of America, Seattle, USA, pp. paper number 124-3.
- Kampunzu, A.B. and Mohr, P., 1991. Magmatic evolution and petrogenesis in the East African Rift system. In: A.B. Kampunzu and R.T. Lubala (Editors), Magmatism in extensional

- structural settings; the Phanerozoic African Plate. Springer-Verlag, Berlin, Federal Republic of Germany, pp. 85-136.
- Katongo, C., Köller, F., Klötzli, U., Koeberl, C., Tembo, F. and De Waele, B., submitted. Petrography, geochemistry and geochronology of key granitoid rocks in the Neoproterozoic-Paleozoic Lufilian - Zambezi belt, Zambia: implications for the tectonic setting and regional correlation. *Journal of African Earth Sciences*.
- Kempe, U., Gruner, T., Nasdala, L. and Wolf, D., 2000. Relevance of cathodoluminescence for the interpretation of U-Pb zircon ages, with an example of an application to a study of zircons from the Saxonian granulite complex, Germany. In: M. Pagel, V. Barbin, P. Blanc and D. Ohnenstetter (Editors), *Cathodoluminescence in Geology*. Springer-Verlag, Berlin, pp. 415-455.
- Kennedy, W.Q., 1964. The differentiation of Africa during the Pan African thermo-tectonic episode. *Annual Report Institute of African Geology and Department of Earth Sciences*, 8.
- Keppie, J.D., 1989. Northern Appalachian Terranes and their accretionary history. *Geological Society of America Special Paper*, 230: 159-192.
- Keppie, S.D., 1995. The geology of the Nyimba area; explanation of degree sheet 1430, SE quarter. 38, Geological Survey of Zambia, Lusaka.
- Kerr, C.D., 1975. The geology of the Fiwila mission area, explanation of degree sheet 1329, SE quarter. 68, Geological Survey Department of Zambia, Lusaka.
- Kerr, C.D., 1994. The Geological map of the Fiwila Mission area. Geological Survey Department of Zambia, Lusaka.
- Key, R.M., Liyungu, A.K., Njamu, F.M., Banda, J., Mosley, P.N., Somwe, V. and Armstrong, R.A., 2001a. The geology and stream sediment geochemistry of the Mwinilunga sheet; explanation of that part of 1:250 000 Sheet SC-35-13 that lies in Zambia. 5, Geological Survey Department of Zambia, Lusaka.
- Key, R.M., Liyungu, A.K., Njamu, F.M., Somwe, V., Banda, J., Mosley, P.N. and Armstrong, R.A., 2001b. The western arm of the Lufilian Arc in NW Zambia and its potential for copper mineralisation. *Journal of African Earth Sciences*, 33(3-4): 503-528.
- Kiss, E., 1992. Separation of rare earth elements by reverse-phase partition chromatography. Preparation of KEL-F column supporting DI(2-ethylexyl)-orthophosphoric acid., Research School of Earth Sciences. Australian National University, Canberra.
- Klerkx, J., 1987. Crustal evolution of the northern Kibaran Belt, eastern and central Africa. In: A. Kröner (Editor), *Proterozoic Lithospheric Evolution*. American Geophysical Union and the Geological Society of America, pp. 217-233.
- Klerkx, J., Theunissen, K. and Delvaux, D., 1998. Persistent fault controlled basin formation since the Proterozoic along the Western Branch of the East African Rift. *Journal of African Earth Sciences*, 26(3 SU -): 347-361.
- Kokonyangi, J., Armstrong, R.A., Kampunzu, A.B. and Yoshida, M., 2001a. SHRIMP U-Pb zircon geochronology of granitoids in the Kibaran type area, Mitwabe-Central Katanga (Congo). *Gondwana Research*, 4: 661-663.
- Kokonyangi, J., Armstrong, R.A., Kampunzu, A.B., Yoshida, M. and Okudaira, T., 2002. Magmatic evolution of the Kibarides belt (Katanga, Congo) and implications for Rodinia reconstruction: Field observations, U-Pb SHRIMP geochronology and geochemistry of granites. In: G.S.o. Namibia (Editor), 11th IAGOD Quadrennial Symposium and Geocongress. Geological Survey of Namibia, Windhoek, Namibia, pp. 5.
- Kokonyangi, J., Armstrong, R.A., Kampunzu, A.B., Yoshida, M. and Okudaira, T., 2004. U-Pb zircon geochronology and petrology of granitoids from Mitwaba (Katanga, Congo): implications for the evolution of the Mesoproterozoic Kibaran belt. *Precambrian Research*, 132: 79-106.
- Kokonyangi, J., Okudaira, T., Kampunzu, A.B. and Yoshida, M., 2001b. Geological evolution of the Kibarides belt, Mitwaba, Democratic Republic of Congo, central Africa. *Gondwana Research*, 4: 663-664.
- Kröner, A., 1977a. Precambrian mobile belts of southern and eastern Africa: Ancient sutures or sites of ensialic mobility? A case for crustal evolution towards plate tectonics. *Tectonophysics*, 40: 101-135.
- Kröner, A., 1977b. *Precambrian Plate Tectonics*. Elsevier, Amsterdam, 801 pp.
- Kröner, A., 1981. Precambrian crustal evolution and continental drift. *Geologische Rundschau*, 70: 412-428.
- Kröner, A., 1983. Proterozoic mobile belts compatible with the plate tectonic concept. In: G.M. Medaris, C.W. Byers, D.M. Mikelson and W.G. Shanks (Editors), *Proterozoic Geology*:

- Selected Papers from an International Proterozoic Symposium. Geological Society of America Memoir. Geological Society of America, pp. 59-74.
- Kröner, A., 1984. Fold belts and plate tectonics in the Precambrian. In: N.A. Bogdanov (Editor), Abstracts; 27th international geological congress. International Geological Congress, pp. 334-335.
- Kröner, A., Dirks, P.H.G.M. and Jamal, D.L., 2000. Archaean, Kibaran and Pan-African zircon ages for granitoid rocks in northwestern Mozambique, GeoLuanda, Luanda, Angola.
- Kröner, A., Sacchi, R., Jaeckel, P. and Costa, M., 1997. Kibaran magmatism and Pan-African granulite metamorphism in northern Mozambique: Single zircon ages and regional implications. *Journal of African Earth Sciences*, 25(3): 467-484.
- Kröner, A., Willner, A.P., Hegner, E., Jaeckel, P. and Nemchin, A., 2001. Single zircon ages, PT evolution and Nd isotopic systematics of high-grade gneisses in southern Malawi and their bearing on the evolution of the Mozambique belt in south eastern Africa. *Precambrian Research*, 109: 257-291.
- Kuno, H., 1968. Differentiation of basalt magmas, Basalts; the Poldervaart treatise on rocks of basaltic composition, Vol. 2. Interscience Publications, New York-London, pp. 623-688.
- Le Maitre, R.W., 1989. A classification of igneous rocks and glossary of terms: recommendations of the International Union of Geological Sciences subcommission on the systematics of igneous rocks. Blackwell, Oxford, 193 pp.
- Legg, C., 1976. The geology and mineralisation of the Mkushi copper deposits. 38, Geological Survey Department of Zambia, Lusaka.
- Lehmann, B. and Lavreau, J., 1987. Tin granites of the northern Kibaran belt, central Africa (Kivu/Zaire, Rwanda, Burundi). In: G. Matheis and H. Schandelmeier (Editors), 14th Colloquium of African Earth Sciences. Balkema, Berlin, pp. 33-36.
- Lenoir, J.L., Liégeois, J.-P., Theunissen, K. and Klerkx, J., 1994. The Palaeoproterozoic Ubendian shear belt in Tanzania: Geochronology and structure. *Journal of African Earth Sciences*, 19(3): 169-184.
- Li, Z.X., Evans, D.A.D. and Zhang, S., 2004. A 90° spin on Rodinia: possible causal links between the Neoproterozoic supercontinent, superplume, true polar wander and low-latitude glaciation. *Earth and Planetary Science Letters*, 220(3-4): 409-421.
- Li, Z.X., Li, X.H., Kinny, P.D., Wang, J., Zhang, S. and Zhou, H., 2003. Geochronology of Neoproterozoic syn-rift magmatism in the Yangtze Craton, South China and correlations with other continent: evidence for a mantle superplume that broke up Rodinia. *Precambrian Research*, 122: 85-109.
- Lucacik, E., 1998a. The Geological map of the Ilondola Mission area. Geological Survey Department of Zambia, Lusaka.
- Lucacik, E., 1998b. The geology of the Ilondola Mission area; explanation of quarter degree sheet 1031, SE quarter. 95, Geological Survey Department of Zambia, Lusaka.
- Ludwig, K.R., 1998. On the treatment of concordant uranium-lead ages. *Geochimica et Cosmochimica Acta*, 62: 665-676.
- Ludwig, K.R., 2001a. Isoplot/Ex rev. 2.49, Berkely Geochronology Centre, Berkely, California.
- Ludwig, K.R., 2001b. Squid 1.02: A User's Manual. 2, Berkeley Geochronology Center, Berkeley.
- Manhica, A.D.S.T., Grantham, G.H., Armstrong, R.A., Guise, P.G. and Kruger, F.J., 2001. Polyphase deformation and metamorphism at the Kalahari craton-Mozambique belt boundary. In: J.A. Miller, R.A. Holdsworth, I.S. Buick and M. Hand (Editors), *Continental Reactivation and Reworking*. Geological Society of London Special Publication, London, pp. 303-322.
- Maniar, P.D. and Piccoli, P.M., 1989. Tectonic discrimination of granitoids. *Geological Society of America Bulletin*, 101: 635-643.
- Mapani, B., 1999. Tectonic and metamorphic evolution of the Serenje and adjoining areas. In: B. De Waele, F. Tembo and R.M. Key (Editors), Abstracts Volume IGCP 418/419. Geological Society of Zambia, Lusaka, pp. 16.
- Mapani, B. and Moore, T.A., 1995a. The Geological map of the Serenje area. Geological Survey Department of Zambia, Lusaka.
- Mapani, B.S.E., 1992. Stratigraphy and correlation of the Serenje and adjoining areas. *Zambian Journal of Applied Earth Sciences*, 6(1): 1-8.
- Mapani, B.S.E. and Moore, T.A., 1995b. The geology of the Serenje area, explanation of degree sheet 1330, NW quarter. 51, Geological Survey Department of Zambia, Lusaka.

- Mapani, B.S.E., Rivers, T., De Waele, B., Tembo, F. and Katongo, C., submitted. Terrane subdivision of the Irumide Orogen in Zambia: A testable tectonic hypothesis. *Tectonophysics*.
- Mapani, B.S.E., Rivers, T., Tembo, F. and Katongo, C., 2001. Terrane Mapping in the eastern Irumide and Mozambique belts: Implications for the assembly and dispersal of Rodinia. In: S. McCourt (Editor), IGCP 418 4th fieldmeeting. University of Durban-Westville, Durban, South Africa.
- Marten, B.E., 1968. The geology of the Chalabesa Mission area; explanation of degree sheet 1131, NW quarter. 23, Geological Survey Department of Zambia, Lusaka.
- Master, S., 1994. Geodynamic evolution and correlation of the Magondi belt (Zimbabwe): implications for the Palaeoproterozoic history of Botswana. *The Botswana Journal of Earth Sciences*, 2: 25-32.
- McConnell, R.B., 1950. Outline of the geology of Ufipa and Ubende, Geological Survey of Tanganyika, Dar Es Salaam.
- McCourt, S., Armstrong, R.A. and Bisnath, A., 2002. U-Pb zircon ages from the Tugela terrane, Natal belt, South Africa: constraints on accretion tectonic associated with the assembly of Rodinia. In: G.S.o. Namibia (Editor), Technical meeting IGCP 418. Geological Survey of Namibia, Windhoek, Namibia, pp. 6.
- McCourt, S., Armstrong, R.A. and S.T., J., 2001. New U-Pb SHRIMP ages from the Tugela Terrane, Natal belt, South Africa: Insights into the Assembly of Rodinia., Geological Society of Australia, Rodinia symposium. From basins to mountains: Rodinia at the turn of the Century. Tectonic Special Research Center, Perth, Australia, pp. 80.
- McDonough, W.F. and Sun, S.-S., 1995. The composition of the Earth. *Chemical Geology*, 120: 228.
- McDougall, I. and Harrison, T.M., 1999. Geochronology and thermochronology by the ⁴⁰Ar/³⁹Ar method. Oxford University Press, Oxford, 269 pp.
- McMenamin, M.A.S. and McMenamin, D.L.S., 1990. The emergence of animals: the Cambrian breakthrough. University Press, New York.
- Meert, J., Torsvik, T.H., Eide, E.A. and Nedelec, A., 1997. A paleomagnetic review of Gondwana assembly including preliminary paleomagnetic results from Madagascar. In: R. Cox and D. Ashwal Lewis (Editors), Proceedings of the UNESCO-IUGS-IGCP-348/ 368 international symposium and field workshop on Proterozoic geology of Madagascar; abstract volume. Gondwana Research Group Miscellaneous Publication. Osaka City University, Department of Geosciences, Faculty of Science, Gondwana Research Group, Osaka, Japan, pp. 52.
- Meert, J.G., 2002. Paleomagnetic evidence for a Paleo-Mesoproterozoic supercontinent Columbia. *Gondwana Research*, 5: 207-216.
- Meert, J.G., 2003. A synopsis of events related to the assembly of eastern Gondwana. *Tectonophysics*, 362(1-4): 1-40.
- Meert, J.G. and Torsvik, T.H., 2003. The making and unmaking of a supercontinent: Rodinia revisited. *Tectonophysics*, 375: 261-288.
- Meert, J.G. and Van der Voo, R., 1995. The making of Gondwana 800-550 Ma. In: Anonymous (Editor), Geological Society of America, 1995 annual meeting. Geological Society of America (GSA), Boulder, CO, United States.
- Meert, J.G. and Van der Voo, R., 1997. The assembly of Gondwana 800-550 Ma. *Journal of Geodynamics*, 23: 223-235.
- Mendelsohn, F., 1961. The geology of the northern Rhodesian Copperbelt. Macdonald, London, 523 pp.
- Miller, C.F., Meschter, M.S. and Mapes, R.W., 2003. Hot and cold granites? Implications of zircon saturation temperatures and preservation of inheritance. *Geology (Boulder)*, 31(6): 529-532.
- Möller, A., O'Brien, P.J., Kennedy, A. and Kröner, A., 2002. Polyphase zircon in ultrahigh-temperature granulites (Rogaland, SW Norway): constraints for Pb diffusion in zircon. *Journal of Metamorphic Geology*, 20(8): 727-740.
- Möller, A., O'Brien, P.J., Kennedy, A. and Kröner, A., 2003. Linking growth episodes of zircon and metamorphic textures to zircon chemistry: an example from the ultrahigh-temperature granulites of Rogaland (SW Norway). In: D. Vance, I. Villa and W. Müller (Editors), Geochronology: linking the isotopic record with petrology and textures. Geological Society of London Special Publications, pp. 65-81.
- Moore, T.A., 1967a. The Geological map of the Bwana Mkubwa area. Geological Survey Department of Zambia, Lusaka.

- Moore, T.A., 1967b. The geology of the Ndola and Bwana Mkubwa areas, explanation of degree sheets 1228, part of SE quarter, and 1328, part of NE quarter. 20, Geological Survey Department of Zambia, Lusaka.
- Moore, E.M., 1991. Southwest US - East Antarctic (SWEAT) connection: a hypothesis. *Geology*, 19: 425-428.
- Moore, E.M. and Twiss, R.J., 1995. *Tectonics*. W.H. Freeman and Company, New York, 415 pp.
- Morel, P. and Irving, E., 1978. Tentative Paleoacontinental maps for the early Proterozoic. *Journal of Geology*, 86: 535-561.
- Morton, A.C., 1985. Heavy minerals in provenance studies. In: G.G. Zuffa (Editor), *Provenance of arenites*. D. Reidel, Dordrecht, pp. 249-277.
- Mosley, P.N., 1994. The Geological map of the Mtofwe area. Geological Survey Department of Zambia, Lusaka.
- Mosley, P.N. and Marten, B.E., 1994. The Geological map of the Katibunga Mission area. Geological Survey Department of Zambia, Lusaka.
- Mosley, P.N. and Marten, B.S., 1979. The Geology of the Katibunga mission area, explanation of degree sheet 1131, SE quarter. 81, Geological Survey Department of Zambia, Lusaka.
- Moyes, A.B., Barton, J.M.J. and Groenewald, P.B., 1993. Late Proterozoic to early Palaeozoic tectonism in Dronning Maud Land, Antarctica: supercontinental fragmentation and amalgamation. *Journal of the Geological Society of London*, 150: 833-842.
- Müller, M.A., Kröner, A., Baumgartner, L.P., Dirks, P.H.G.M. and Jelsma, H.A., 2000. Evolution of Neoproterozoic high-grade rocks in the Mavuradonha Mountains, Zambezi belt, northeast Zimbabwe. *Journal of African Earth Sciences*, 30(18th Colloquium of African Geology): 64-65.
- Murphy, J.B. and Nance, R.D., 1991. Supercontinent model for the contrasting character of Late Proterozoic orogenic belts. *Geology*, 19: 469-472.
- Namateba, C., 1994. The geology of the Mafinga Hills area; explanation of degree sheet 0933, SW quarter. 93, Geological Survey Department of Zambia, Lusaka.
- Nemchin, A.A., Giannini, L.M., Bodorkos, S. and Oliver, N.H.S., 2001. Ostwald ripening as a mechanism for zircon overgrowth formation during high-grade metamorphism: theoretical constraints, a numerical model and its application to pelitic migmatites of the Tickalara Metamorphics, northwestern Australia. *Geochimica et Cosmochimica Acta*, 65(16): 2771-2787.
- Nesbitt, H.W. and Young, G.M., 1982. Early Proterozoic climates and plate motions inferred from major element chemistry of lutites. *Nature*, 299: 715-717.
- Newton, A.R., 1959. On the syenite of Mivula Hill, Eastern province. *Records of the Geological Survey of Zambia*: 14-17.
- Ng'ambi, O., Boelrijk, N.A.I.M., Priem, H.N.A. and Daly, M.C., 1986. Geochronology of the Mkushi Gneiss complex, central Zambia. *Precambrian Research*, 32: 279-295.
- Ngoyi, K., Liégeois, J.-P., Demaiffe, D. and Dumont, P., 1991. Age tardi-ubendien (Protérozoïque inférieur) des dômes granitiques de l'arc cuprifère zaïro-zambien. *Comptes Rendu de l'Académie de Sciences*, 313(II): 83-89.
- O'Brien, P.J., 2001. Subduction followed by collision; Alpine and Himalayan examples. In: C. Rubie David and D. van der Hilst Rob (Editors), *Processes and consequences of deep subduction*. *Physics of the Earth and Planetary Interiors*, pp. 277-291.
- Oliver, G.J.H., Johnson, S.P., Williams, I.S. and Herd, D.A., 1998. Relict 1.4 Ga oceanic crust in the Zambezi Valley, northern Zimbabwe: Evidence for Mesoproterozoic supercontinental fragmentation. *Geology*, 26: 571-573.
- Padget, P., 1959. The Geology of the Mafingi Mountains area of northern Rhodesia and Nyasaland. *Transactions of the Geological Society of South Africa*, 62: 139-145.
- Page, B.G.N., 1962. The stratigraphical and structural relationships of the Abercorn sandstones, the Plateau Series and Basement rocks of the Kawimbe area, Abercorn district, northern Rhodesia. *Annual Report Institute of African Geology and Department of Earth Sciences*, 6: 29.
- Page, T.C., 1973. The Geology of the Chilonga Mission area; explanation of degree sheet 1231, NW quarter. 56, Geological Survey Department of Zambia, Lusaka.
- Paquette, J.-L. and Nédélec, A., 1998. A new insight into Pan-African tectonics in the East-West Gondwana collision zone by U-Pb zircon dating of granites from central Madagascar. *Earth and Planetary Science Letters*, 155: 45-56.
- Pearce, J.A., 1983. Role of the sub-continental lithosphere in magma genesis at active continental margins. In: C.J. Hawkesworth and M.J. Norry (Editors), *Continental basalts and mantle*

- xenoliths; papers prepared for a UK Volcanic Studies Group meeting at the University of Leicester. Shiva Publ., Nantwich, United Kingdom, pp. 230-249.
- Pearce, J.A., 1996a. Sources and settings of granitic rocks. *Episodes*, 19: 120-125.
- Pearce, J.A., 1996b. A user's guide to basalt discrimination diagrams. In: H. Bailes Alan et al. (Editors), *Trace element geochemistry of volcanic rocks; applications for massive sulphide exploration*. Geological Association of Canada, Short Course Notes, John's, NF, Canada, pp. 79-113.
- Pearce, J.A., Harris, N.B.W. and Tindle, A.G., 1984a. Trace element discrimination diagrams for the tectonic interpretation of granitic rocks. *Journal of Petrology*, 25: 956-983.
- Pearce, J.A., Lippard, S.J. and Roberts, S., 1984b. Characteristics and tectonic significance of supra-subduction zone ophiolites. In: B.P. Kokelaar and M.F. Howells (Editors), *Marginal basin geology; volcanic and associated sedimentary and tectonic processes in modern and ancient marginal basins*. Geological Society Special Publication, London, pp. 74-94.
- Pesonen, L.J., Elming, S.-A., Mertanen, S., Pisarevsky, S., D'Agrella-Filho, M.S., Meert, J.G., Schmidt, P.W., Abrahamsen, N. and Bylund, G., 2003. Palaeomagnetic configuration of continents during the Proterozoic. *Tectonophysics*, 375(1-4): 289-324.
- Petters, S.W., 1991. *Regional Geology of Africa*. Lecture Notes in Earth Sciences, 40. Springer-Verlag, 722 pp.
- Phillips, K.A., 1955. Relationship between the Muva system and the Plateau series in northern Rhodesia. spec., Association de Services Geologiques Africaines, Nairobi.
- Phillips, K.A., 1965. The Geology of the Petauke - Mwanjawantu area; Explanation of Degree Sheet 1431, NW and part of SW quarters. 15, Geological Survey of Zambia, Lusaka.
- Pidgeon, R.T., Furfaro, D., Kennedy, A.K., Nemchin, A.A. and Van Bronswijk, W., 1994. Calibration of zircon standards for the Curtin SHRIMP II. *United States Geological Survey circular*, 1107: 251.
- Pinna, P., Jourde, G., Calvez, J.Y., Mroz, J.P. and Marques, J.M., 1993. The Mozambique belt in northern Mozambique; Neoproterozoic (1100-850 Ma) crustal growth and tectogenesis, and superimposed Pan-African (800-550 Ma) tectonism. *Precambrian Research*, 62(1-2): 1-59.
- Piper, J.D.A., 1976. Palaeomagnetic Evidence for a Proterozoic super-continent. *Philosophical Transactions of the Royal Society of London, A*. 280: 469-490.
- Piper, J.D.A., 1987. *Palaeomagnetism and the continental crust*. Open University Press, Milton Keynes, 434 pp.
- Piper, J.D.A., 2000. The Neoproterozoic supercontinent: Rodinia or Palaeopangaea? *Earth and Planetary Science Letters*, 176: 131-146.
- Pisarevsky, S.A. and Natapov, L.M., 2003. Siberia and Rodinia. *Tectonophysics*, 375: 221-245.
- Pisarevsky, S.A., Wingate, M.T.D., Powell, C.M., Johnson, S. and Evans, D.A.D., 2003. Models of Rodinia assembly and fragmentation. In: M. Yoshida, B. Windley and S. Dasgupta (Editors), *Proterozoic East Gondwana: Supercontinent Assembly and Breakup*. Geological Society of London Special Publication, pp. 35- 55.
- Pitcher, W.S., 1997. *The Nature and origin of Granite*. Chapman & Hall, London, 408 pp.
- Pohl, W., 1994. Metallogeny of the northeastern Kibaran belt, central Africa - recent perspectives. *Ore Geology Reviews*, 9: 105-130.
- Porada, H. and Berhorst, V., 2000. Towards a new understanding of the Neoproterozoic-Early Palaeozoic Lufilian and Zambezi Belts in Zambia and the Democratic Republic of Congo. *Journal of African Earth Sciences*, 30: 717-771.
- Powell, C.M., Jones, D.L., Pisarevsky, S.A. and Wingate, M.T.D., 2001. Palaeomagnetic constraints on the position of the Kalahari Craton in Rodinia. In: C.M. Powell and J.G. Meert (Editors), *Assembly and breakup of Rodinia*. Elsevier. Amsterdam, International. 2001.
- Priem, H.N.A., Boelrijk, N.A.I.M., Hebeda, E.H., Verdurmen, A.E.A.T. and Verschure, R.H., 1979. Isotopic age determinations on granitic and gneissic rocks from the Ubendian-Usagaran system in southern Tanzania. *Precambrian Research*, 9(3-4): 227-239.
- Rainaud, C., Armstrong, R.A., Master, S. and Robb, L.J., 1999. A fertile Palaeoproterozoic magmatic arc beneath the Central African Copperbelt. In: C.J.e.a. Stanley (Editor), *Mineral Deposits: Processes to Processing*. Balkema, London, pp. 1427-1430.
- Rainaud, C., Master, S., Armstrong, R.A. and Robb, L.J., 2003. A cryptic Mesoarchean terrane in the basement to the central African Copperbelt. *Journal of the Geological Society of London*, 160: 11-14.
- Rainaud, C.L., Armstrong, R.A., Master, S., Robb, L.J. and Mumba, P.A.C.C., 2002. Contributions to the geology and mineralisation of the central African Copperbelt: I. Nature

- and geochronology of the pre-Katangan basement. In: G.S.o. Namibia (Editor), 11th IAGOD Quadrennial Symposium and Gecongress. Geological Survey of Namibia, Windhoek, Namibia, pp. 5.
- Rainbird, R.H., Heaman, L.M. and Young, G., 1992. Sampling Laurentia: Detrital zircon geochronology offers evidence for an extensive Neoproterozoic river system originating from the Grenville Orogen. *Geology*, 20: 351-354.
- Ramsay, C.R. and Ridgway, J., 1977. Metamorphic patterns in Zambia and their bearing on problems of Zambian tectonic history. *Precambrian Research*, 4: 321-337.
- Ray, G.E., 1974. The structural and metamorphic geology of northern Malawi. *Journal of the Geological Society of London*, 140: 427-440.
- Ray, G.E. and Crow, M.J., 1975. A review of some age determinations from the Misuku belt of northern Malawi. *Records of the Geological Survey of Malawi*, 8: 49-66.
- Reichwalder, P. and Brandon, A., 1992. The Geological map of the Luano Valley area. Geological Survey Department of Zambia, Lusaka.
- Ridgway, J. and Ramsay, C.R., 1986. A provisional metamorphic map of Zambia - explanatory notes. *Journal of African Earth Sciences*, 5(5): 441-446.
- Ring, U., 1993. Aspects of the kinematic history and mechanisms of superposition of the Proterozoic mobile belts of eastern Central Africa (northern Malawi and southern Tanzania). *Precambrian Research*, 62: 207-226.
- Ring, U., 1999. Volume loss, fluid flow, and coaxial versus noncoaxial deformation in retrograde, amphibolite facies shear zones, northern Malawi, east-central Africa. *Geological Society of America Bulletin*, 111(1): 123-142.
- Ring, U., Kröner, A., Layer, P., Buchwaldt, R. and Toulkeredis, T., 1999. Deformed A-type granites in northern Malawi, east-central Africa: pre- or syntectonic. *Journal of the Geological Society of London*, 156: 695-714.
- Ring, U., Kröner, A. and Toulkeredis, T., 1997. Palaeoproterozoic granulite-facies metamorphism and granitoid intrusions in the Ubendian-Usagaran Orogen of northern Malawi, east-central Africa. *Precambrian Research*, 85: 27-51.
- Rivers, T. and Corrigan, D., 2000. Convergent margin on southeastern Laurentia during the Mesoproterozoic: tectonic implications. *Canadian Journal of Earth Sciences*, 37: 359-383.
- Robb, L.J., Armstrong, R.A. and Waters, D.J., 1999. The history of granulite-facies metamorphism and crustal growth from single zircon U-Pb geochronology: Namaqualand, South Africa. *Journal of Petrology*, 40: 1747-1770.
- Roberts, M.P. and Finger, F., 1997. Do U-Pb zircon ages from granulites reflect peak metamorphic conditions? *Geology*, 25: 319-322.
- Rogers, J.J.W., Unrug, R. and Sultan, M., 1995. Tectonic assembly of Gondwana. *Journal of Geodynamics*, 19(1): 1-34.
- Romer, R.L. and Lehmann, B., 1995. U-Pb columbite age of Neoproterozoic Ta-Nb mineralization in Burundi. *Economic Geology and the Bulletin of the Society of Economic Geologists*, 90(8): 2303-2309.
- Ross, G.M., Parrish, R.R. and Winston, D., 1992. Provenance and U-Pb geochronology of the Mesoproterozoic Belt Superior group (northern United States): Implications for age of deposition and pre-Panthalassa plate reconstructions. *Earth & Planetary Science Letters*, 113: 57-76.
- Rubatto, D. and Gebauer, D., 2000. Use of Cathodoluminescence for U-Pb Zircon dating by Ion Microprobe: Some examples from the Western Alps. In: M. Pagel, V. Barbin, P. Blanc and D. Ohnenstetter (Editors), *Cathodoluminescence in Geosciences*. Springer-Verlag, Berlin, pp. 373-400.
- Sacchi, R., Cadoppi, P. and Costa, M., 2000. Pan-African reactivation of the Lurio segment of the Kibaran belt system: A reappraisal from recent age determinations in northern Mozambique. *Journal of African Earth Sciences*, 30(3): 629-639.
- Sacchi, R., Merques, J., Costa, M. and Casati, C., 1984. Kibaran events in the southernmost Mozambique belt. *Precambrian Research*, 25: 141-159.
- Schandelmeier, H., 1980. Regionale gliederung des Prakambriums und aspekte der krustentwicklung um Mambwe/nordost-Zambia. PhD Thesis, Technical University of Berlin, Berlin, 134 pp.
- Schandelmeier, H., 1981. The Precambrian of NE Zambia in relation to the dated Kate, Mambwe and Luchewe intrusives. *Geologische Rundschau*, 70(2): 956-971.

- Schandelmeier, H., 1983. The geochronology of post-Ubendian granitoids and dolerites from the Mambwe area, northern province, Zambia. Report Institute of Geological Sciences, 83(1): 40-46.
- Schenk, V. and Appel, P., 2001. Anti-clockwise P-T path during ultrahigh-temperature (UHT) metamorphism at ca. 1050 Ma in the Irumide Belt of Eastern Zambia. *Berichte der Deutschen Mineralogischen Gesellschaft, Beihefte zum European Journal of Mineralogy*, 13: 161.
- Schenk, V. and Appel, P., 2002. UHT-metamorphism in the Irumide belt of Zambia: an anti-clockwise P-T path and concordant monazite age at 1.05 Ga. In: N. Ennih and G. Abdelsalam Mohamed (Editors), 19th Colloquium of African Geology, El Jadida, Morocco, pp. 165.
- Schultz, K.J., Tankard, A.J., Jackson, M.P.A., Eriksson, K.A., Hobday, D.K., Hunter, D.R. and Minter, W.E.L., 1983. Crustal evolution of South Africa; 3.8 billion years of Earth history; book review. *American Journal of Science*, 283(9): 987-988.
- Schwartz, M.O., Kwok, Y.Y., Davis, D.W. and Akanyang, P., 1996. Geology, geochronology and regional correlation of the Ghanzi Ridge, Botswana. *South African Journal of Geology*, 99: 245-250.
- Searle, D.L., 1972. The Stratigraphy of the Plateau Series of Senga Hill area. *Records of the Geological Survey of Zambia*, 12: 55-62.
- Sengör, A.M.C. and Natal'in, B.A., 1996. Turcic-type orogeny and its role in the making of the continental crust. *Annual Reviews of Earth and Planetary Sciences*, 24: 263-337.
- Sengör, A.M.C., Natal'in, B.A. and Burtman, V.S., 1993. Evolution of the Altaid tectonic collage and Paleozoic crustal growth in Eurasia. *Nature*, 364: 299-307.
- Seth, B., Armstrong, R.A., Brandt, S., Villa, I.M. and Kramers, J.D., 2003. Mesoproterozoic U-Pb and Pb-Pb ages of granulites in NW Namibia: reconstructing a complete orogenic cycle. *Precambrian Research*, 126: 147-168.
- Shackleton, R.M., 1973. Correlation of structures across Precambrian orogenic belts in Africa. In: D.H. Tarling and S.K. Runcorn (Editors), *Implications of Continental Drift to the Earth Sciences*. Academic press, London, pp. 1091-1095.
- Shackleton, R.M., 1996. The final collision between East and West Gondwana: where is it? *Journal of African Earth Sciences*, 23: 271-287.
- Shervais, J.W., 1982. Ti-V plots and the petrogenesis of modern and ophiolitic lavas. *Earth and Planetary Science Letters*, 59(1): 101-118.
- Singletary, S., Hanson, R.E., Martin, M.W., Crowley, J.L., Bowring, S.A., Key, R.M., Ramokate, L.V., Direng, B.B. and Krol, M.A., 2003. Geochronology of basement rocks in the Kalahari Desert, Botswana, and implications for regional Proterozoic tectonics. *Precambrian Research*, 121: 47-71.
- Sircombe, K., 2002. Reconnaissance detrital zircon geochronology provenance of the Palaeoproterozoic Ashburton Formation; implications for Pilbara and Yilgarn amalgamation. In: V.P. Preiss (Editor), *Geoscience 2002; expanding horizons; abstracts of the 16th Australian geological convention*. Geological Society of Australia. Sydney, N.S.W., Australia. 2002.
- Sircombe, K.N., 2000. The usefulness and limitations of binned frequency histograms and probability density distributions for displaying absolute age data. 13, Geological Survey of Canada, Ottawa, Canada.
- Sircombe, K.N., 2004. Age Display: an EXCEL workbook to evaluate and display univariate geochronological data using binned frequency histograms and probability density distributions. *Computers and Geoscience*, 30: 21-31.
- Sircombe, K.N., Bleeker, W. and Stern, R.A., 2001. Archean provenance; a systematic detrital zircon investigation of supracrustals in the Slave Craton, Canada. In: K.F. Cassidy, J.M. Dunphy and M.J. van Kranendonk (Editors), *Fourth international Archean symposium; extended abstracts*. AGSO - Australian Geological Survey Organisation. Canberra, Australia. 2001.
- Smethurst, M.A., Khrumov, A. and Torsvik, T.H., 1998. Palaeomagnetic constraints on the Neoproterozoic - Paleozoic drift history of the Siberian platform: Rodinia to Pangea. *Earth Science Reviews*, 43: 1-24.
- Smith, A.G., 1965. The Geological map of the Kapiri Mposhi area. Geological Survey Department of Zambia, Lusaka.
- Smith, A.G., 1966. The geology of the Kapiri Mposhi area; explanation of degree sheet 1328, SE quarter. 18, Geological Survey Department of Zambia, Lusaka.

- Smith, A.G., 2000. The Geological map of the Ndabala area. Geological Survey Department of Zambia, Lusaka.
- Smith, A.G. and Kerr, C.D., 1975. The geology of the Ndabala area, explanation of degree sheet 1329, NE quarter. 67, Geological Survey Department of Zambia, Lusaka.
- Sochacka, R.J. and Siekierski, S., 1964. Reverse-phase partition chromatography with di-(2-ethylhexyl) orthophosphoric acid as the stationary phase. Part 1: separation of rare earths. *Journal of Chromatography*, 16: 376-384.
- Stacey, J.S. and Kramers, J.D., 1975. Approximation of terrestrial lead isotopic evolution by a two-stage model. *Earth and Planetary Science Letters*, 26: 207-221.
- Stampfli, G.M., Mosar, J., Marquer, D., Marchant, R., Baudin, T. and Borel, G., 1998. Subduction and obduction processes in the Swiss Alps. In: A. Vauchez and O. Meissner Rolf (Editors), *Continents and their mantle roots. Tectonophysics*, pp. 159-204.
- Steiger, R.H. and Jäger, E., 1977. Subcommission on geochronology: convention on the use of decay constants in geo- and cosmochemistry. *Earth and Planetary Science Letters*, 36: 359-362.
- Stern, R.J., 1994. Arc assembly and continental collision in the Neoproterozoic East African Orogen: implications for the consolidation of Gondwanaland. *Reviews of Earth and Planetary Sciences*, 22: 319-351.
- Stillman, C.J., 1965a. The Geological map of the Mkushi area. Geological Survey Department of Zambia, Lusaka.
- Stillman, C.J., 1965b. The Geological map of the Musofu River area. Geological Survey Department of Zambia, Lusaka.
- Stillman, C.J., 1965c. The geology of the Musofu river and Mkushi areas; explanation of degree sheet 1329, part of NW quarter and SW quarter. 12, Geological Survey Department of Zambia, Lusaka.
- Streckeisen, A. and Le Maître, R.W., 1979. A chemical approximation to the modal QAPF classification of the igneous rocks. *Neues Jahrbuch fuer Mineralogie. Abhandlungen*, 136(2): 169-206.
- Su, Y., Langmuir, C.H. and Asimow, P.D., 2003. PetroPlot: A plotting and data management tool set for Microsoft Excel. *Geochemistry, Geophysics, Geosystems (G-cubed)*, 4(3): 1-14.
- Sun, S. and McDonough, W.F., 1989. Chemical and isotopic systematics of ocean basalts: implications for mantle composition and processes. In: A.D.N. Saunders, M.J. (Editor), *Magmatism in the Ocean Basins. Geological Society of London Special Publication*, pp. 313-345.
- Sun, W., Kamenetsky, V.S. and Bennet, V.C., 2003. Mechanisms of Re enrichment in subduction related magmas, 13th V.M. Goldschmidt conference. Cambridge Publications, Kurashiki, Japan, pp. 456.
- Sykes, J.M.D., 1994. The geological map of the Luswa River area. Geological Survey Department of Zambia, Lusaka.
- Sykes, J.M.D., 1995. The geology of the Luswa River area, degree sheet 1132, NW quarter. 76, Geological Survey Department, Lusaka.
- Tack, L., De, P.P., Liégeois, J.P., Nimpagaritse, G., Ntungicimpaye, A. and Midende, G., 1990. Late Kibaran magmatism in Burundi. *Journal of African Earth Sciences*, 10(4): 733-738.
- Tack, L., Liégeois, J.P., Deblond, A. and Duchesne, J.C., 1994. Kibaran A-type granitoids and mafic rocks generated by two mantle sources in a late orogenic setting (Burundi). *Precambrian Research*, 68(3-4): 323-356.
- Tembo, F., 1986. Petrology and Geochemistry of Syenite Intrusions in the Eastern Province of Zambia. Msc. Thesis, University of Zambia, Lusaka.
- Tembo, F. and Porada, H., submitted. Recognition and correlation of Mesoproterozoic Muva Supergroup rocks in the Neoproterozoic Lufilian and Zambezi belts of Zambia. Gondwana Research.
- Tembo, F., Rivers, T., Mapani, B., De Waele, B. and Katongo, C., 2002. Terrane mapping of the Irumide Orogen in eastern Zambia: Reconnaissance geochemistry of the meta-igneous rocks. In: G.S.o. Namibia (Editor), 11th IAGOD Quadrennial Symposium and Geocongress. Geological Survey of Namibia, Windhoek, Namibia, pp. 9.
- Tera, F. and Wasserburg, G.J., 1972. U-Th-Pb systematics in three Apollo 14 basalts and the problem of initial Pb in lunar rocks. *Earth and Planetary Science Letters*, 14(3): 281-304.
- Tera, F. and Wasserburg, G.J., 1974. U-Th-Pb systematics on lunar rocks and inferences about lunar evolution and the age of the Moon, 5th Lunar Science conference. *Geochimica Cosmochimica Acta*, pp. 1571-1599.

- Thatcher, E.C., 1974. The geology of the Nyika area. 40, Geological Survey of Malawi, Zomba, Malawi.
- Thatcher, E.C. and Wilderspin, K.E., 1968. The geology of the Mchinji-Upper-Bua area. 24, Geological Survey Department of Malawi, Zomba, Malawi.
- Thieme, J.G., 1970. The geology of the Mansa area; explanation of degree sheet 1128 parts of NW Quarter and NE Quarter. 26, Geological Survey Department of Zambia, Lusaka.
- Thieme, J.G., 1971. The geology of the Musonda Falls area: explanation of degree sheet 1028, SE quarter. 32, Geological Survey Department of Zambia, Lusaka.
- Thieme, J.G. and Johnson, R.L., 1981. The Geological map of Zambia. Geological Survey Department of Zambia, Lusaka.
- Thomas, R.J., Agenbacht, A.L.D., Cornell, D.H. and Moore, J.M., 1994. The Kibaran of southern Africa: Tectonic evolution and metallogeny. *Ore Geology Reviews*, 9: 131-160.
- Thomas, R.J., Eglinton, B.M. and Bowring, S.A., 1993. Dating of cessation of Kibaran magmatism in Natal, South Africa. *Journal of African Earth Sciences*, 16(3): 247-252.
- Thomas, R.J., H, D.B.C. and Bowring, S.A., 1996. A comparative study of the Mesoproterozoic late orogenic porphyritic granitoids of Southwest Namaqualand and Natal, South Africa. In: R.J. Thomas, R.M. Shackleton and S. Muhongo (Editors), IGCP 348 (Mozambique and related belts). *Journal of African Earth Sciences*. Pergamon, London-New York, International, pp. 485-508.
- Thomas, R.J. and Jacobs, J., 2001. Polyphase tectonic events revealed by titanite fission dating in SE Africa and positioning the western front of the East Antarctic Orogen. *Gondwana Research*, 4(2): 195-198.
- Trompette, R., 1994. Geology of western Gondwana (2000-500 Ma). Pan-African-Brasiliano aggregation of South America and Africa. Balkema, Rotterdam, 350 pp.
- Turner, P.J., 1982. Multicollection in thermal ionisation mass spectrometry. 02.485, VG Isotopes Ltd., Cheshire.
- Unrug, R., 1982. The Kasama Formation: lithostratigraphy, palaeogeography and regional position, Palaeogeography of Zambia. Geological Society of Zambia, Lusaka, pp. 2-8.
- Unrug, R., 1984. The Mid-Proterozoic Mporokoso Group of northern Zambia: stratigraphy, sedimentation and regional position. *Precambrian Research*, 24: 99-121.
- Unrug, R., 1992. Kibaran terranes with cassiterite mineralisation in the Zambezi belt, Zambia and Zimbabwe. *IGCP Bulletin*, 4: 121-124.
- Unrug, R., 1997. Rodinia to Gondwana; the geodynamic map of Gondwana supercontinent assembly. *GSA Today*, 7(1): 1-6.
- Vail, J.R., Snelling, N.J. and Rex, D.C., 1968. Pre-Katangan geochronology of Zambia and adjacent parts of central Africa. *Canadian Journal of Earth Sciences*, 5: 621-628.
- Van de Velde, P. and De Waele, B., 1997. The geological map of the Mupamadzi River area. The Geological Survey Department of Zambia, Lusaka.
- Van de Velde, P. and De Waele, B., 1998. The geology of the Mupamadzi river area, explanation of degree sheet 1231, SW quarter. 105, Geological Survey Department of Zambia, Lusaka.
- Van der Voo, R., 1990. The reliability of paleomagnetic data. *Tectonophysics*, 184(1): 1-9.
- Van Tuijl, M.M. and Verhoog, B.J., 1995a. The geological map of the Kalungu area. Geological Survey Department of Zambia, Lusaka.
- Van Tuijl, M.M. and Verhoog, B.J., 1995b. The geological map of the Mututa Hills area. Geological Survey Department of Zambia, Lusaka.
- Van Tuijl, M.M. and Verhoog, B.J., 1995c. The geology of the Kalungu and Mututa Hills area; explanation of degree sheet 0932, SE and SW quarter. 85, Geological Survey Department of Zambia, Lusaka.
- Vavra, G., 1990. On the kinematics of zircon growth and its petrogenetic significance: a cathodoluminescence study. *Contributions to Mineralogy and Petrology*, 106: 90-99.
- Vavra, G., 1993. A guide to quantitative morphology of accessory zircon. *Chemical Geology*, 110: 15-28.
- Vavra, G., 1994. Systematics of internal zircon morphology in major Variscan granitoid types. *Contributions to Mineralogy and Petrology*, 117: 331-344.
- Vavra, G., Gebauer, D., Schmid, R. and Compston, W., 1996. Multiple zircon growth and recrystallization during polyphase Late Carboniferous to Triassic metamorphism in granulites of the Ivrea Zone (Southern Alps): An ion microprobe (SHRIMP) study. *Contributions to Mineralogy and Petrology*, 122(4): 337-358.

- Vavra, G., Schmid, R. and Gebauer, D., 1999. Internal morphology, habit and U-Th-Pb microanalysis of amphibolite-to-granulite facies zircons: geochronology of the Ivrea Zone (Southern Alps). *Contributions to Mineralogy and Petrology*, 134: 380-404.
- Vavrdá, I., 1974. The geology of the Chipata area: explanation of degree sheet 1332, SE quarter, 41. Geological Survey Department of Zambia, Lusaka, 22 pp.
- Verhoog, B.J. and Van Tuijl, M.M., 1995a. The geology of the Chozi area; explanation of degree sheet 0932, NW quarter. 84, Geological Survey Department of Zambia, Lusaka.
- Verhoog, B.J. and Van Tuijl, M.M., 1995b. The geology of the Makasa area; explanation of degree sheet 931, SE quarter. 86, Geological Survey Department of Zambia, Lusaka.
- Verhoog, B.J. and Van Tuijl, M.M., 1995c. The geology of the Nakonde area; explanation of degree sheet 0932 NE quarter. 84, Geological Survey Department of Zambia, Lusaka.
- Vinyu, M.L., Hanson, R.E., Martin, M.W., Bowring, S.A., Jelsma, H.A., Krol, M.A. and Dirks, P.H.G.M., 1999. U/Pb and $^{40}\text{Ar}/^{39}\text{Ar}$ geochronological constraints on the tectonic evolution of the easternmost part of the Zambezi orogenic belt, northeast Zimbabwe. *Precambrian Research*, 98: 67-82.
- Vrána, S., Kachlík, V., Kröner, A., Marheine, D., Seifert, A.V., Íááek, V. and Babûrek, J., 2004. Ubendian basement and its late Mesoproterozoic and early Neoproterozoic structural and metamorphic overprint in northeastern Zambia. *Journal of African Earth Sciences*, 38: 1-21.
- Vrána, S., Prasad, G. and Fediukova, E., 1975. Metamorphic kyanite eclogites in the Lufilian Arc of Zambia. *Contributions to Mineralogy and Petrology*, 51: 139-160.
- Wasserburg, G.J., Jacobsen, S.B., DePaolo, D.J., McCulloch, M.T. and Wen, T., 1981. Precise determination of Sm/Nd ratios, Sm and Nd isotopic abundances in standard solutions. *Geochimica et Cosmochimica Acta*, 45: 2311-2323.
- Watson, E.B. and Harrison, T.M., 1983. Zircon saturation revisited: temperature and composition effects in a variety of crustal magma types. *Earth and Planetary Science Letters*, 64: 295-304.
- Weil, A.B., Van der Voo, R., Mac Niocaill, C. and Meert, J.G., 1998. The Proterozoic supercontinent Rodinia: Palaeomagnetically derived reconstruction for 1100 to 800 Ma. *Earth and Planetary Science Letters*, 154: 13-24.
- Wetherill, G.W., 1956. Discordant uranium-lead ages. *Transactions American Geophysical Union*, 37: 320-326.
- Whalen, J.B., Currie, K.L. and Chappell, B.W., 1987. A-type granites - geochemical characteristics, discrimination and petrogenesis. *Contributions to Mineralogy and Petrology*, 95(4): 407-419.
- Williams, I.S., 1998. U-Th-Pb geochronology by ion microprobe. In: M.A. McKibben, W.C. Shanks III and W.I. Ridley (Editors), *Applications of microanalytical techniques to understanding mineralizing processes. Reviews in Economic Geology*, pp. 1-35.
- Wilson, T.J., Grunow, A.M. and Hanson, R.E., 1997. Gondwana Assembly: the view from southern Africa and East Gondwana. *Journal of Geodynamics*, 23: 263-286.
- Wilson, T.J., Hanson, R.E. and Wardlaw, M.S., 1993. Late Proterozoic evolution of the Zambezi belt: implications for regional Pan-African tectonics and shear displacements in Gondwana. In: R.H. Findlay, R. Unrug, M.R. Banks and J.J. Veevers (Editors), *Gondwana Eight: Assembly, Evolution and Dispersal*. Balkema, Rotterdam, pp. 69-82.
- Winchester, J.A. and Floyd, P.A., 1977. Geochemical discrimination of different magma series and their differentiation products using immobile elements. *Chemical Geology*, 20: 325-343.
- Windley, B., 1992. Proterozoic collisional and accretionary orogens. In: K.C. Condie (Editor), *Proterozoic crustal evolution. Developments in Precambrian Geology*. Elsevier, Amsterdam, Netherlands, pp. 419-446.
- Wingate, M.T.D., 2001. SHRIMP baddeleyite age for an Umkondo dolerite sill, Nyanga Mountains, eastern Zimbabwe. *South African Journal of Geology*, 104: 13-22.
- Wingate, M.T.D., Pisarevski, S.A., Evans, D.A.D., 2002. Rodinia connections between Australia and Laurentia: no SWEAT, or AUSWUS. *Terra Nova*, 14: 121-128.
- Wood, D.A., 1980. The application of a Th-Hf-Ta diagram to problems of tectonomagmatic classification and to establishing the nature of crustal contamination of basaltic lavas of the British Tertiary volcanic province. *Earth and Planetary Science Letters*, 50(1): 11-30.
- Zen, E., 1986. Aluminium enrichment in silicate melts by fractional crystallization: some mineralogic and petrographic constraints. *Journal of Petrology*, 27: 1095-1117.
- Zhao, G., Cawood, P.A., Wilde, S.A. and Sun, M., 2002. Review of global 2.1-1.8 Ga orogens: implications for a pre-Rodinia supercontinent. *Earth-Science Reviews*, 59(1-4): 125-162.

